SEISMIC HAZARD AND SEISMIC SLOPE STABILITY ASSESSMENT OF DARJEELING SIKKIM HIMALAYAS, INDIA

Thesis submitted in partial fulfillment
of the requirements for the degree of

Doctor of Philosophy in **Civil Engineering**

by

G. N. SHINY NEHARIKA
20162314
neharika.s@research.iiit.ac.in

International Institute of Information Technology, Hyderabad
(Deemed to be University)
Hyderabad - 500 032, INDIA
MAY 2023

CERTIFICATE

It is certified that the work contained in this thesis, **“**Seismic hazard and seismic slope stability assessment of Darjeeling Sikkim Himalayas, INDIA**,”** by Mrs. G. N. SHINY NEHARIKA**,** has been carried out under my supervision and is not submitted elsewhere for a degree.

Date: 22-06-2023

Advisor:
Dr. K.S.Rajan
Professor
Lab of Spatial Informatics,
International Institute of Information Technology,
Hyderabad – 500 032,
Telangana– (INDIA),
Email: rajan@iiit.ac.in

Advisor:
Dr. D. Neelima Satyam
Professor
Department of Civil Engineering,
Indian Institute of Technology Indore,
Khandwa Road, Simrol-453552,
Madhya Pradesh– (INDIA)
Email: neelima.satyam@iiti.ac.in

Dedicated to everlasting father, my master, and saviour

Jesus Christ

And

My beloved mother and brother, ***Kunta Varalaxmi & Sunny Nehar***

ACKNOWLEDGEMENT

To accomplish my thesis, many unsung individuals provided me with assistance, guidance, encouragement, time, love, and energy. I am grateful to all those people who are in my piece of research challenge to gain a Ph.D.

After Jesus Christ, first and foremost, I would like to express my sincere gratitude to my supervisor Dr. D. Neelima Satyam, for the guidance, patience, and motivation at every stage of the thesis work. More than that u always says, “I share a very special bond with her she is the one who spent more time with me like for 10 years and more than a student she is a part of my family” What can I achieve more than this in my life. Next, I would specially thank Dr. K. S. Rajan for providing all the support, thoughts, and time given to me throughout my research. After my completion of my final defence exam u said “Congratulations Dr. Neharika, All the Best and take care” your words mean lot to me sir. I profusely thank both of my guides for all they did toward completing my work, and I am privileged to have had the opportunity to work under them.

I want to thank my committee members for providing a comfortable environment during my defense and for the intense comments, ideas, and suggestions you shared.

Besides my advisors, I thank all the academic office staff of IIIT-H. I want to express special thanks to Y. V. S. K. Kishore, from the Academic office, for all the help and cooperation throughout my study period with so much of patience and kindness.

Thanks to my lab mates in IIIT-H, Swathi, Ambica, and Nitin (IIT Indore), for all discussions and assistance in preparing my thesis. Special thanks to Nitin Tiwari for his heartful support and encouragement during my work.

I owe my gratitude to my friends who solace me in the best and most challenging times during my education. Your support and encouragement have lifted me up countless times. My heartfelt thanks to my friend Ishwarya Asala for standing by me during the best and worst with moral certainty and constant encouragement in the entire journey of fulfilment of my PhD study. I would also thank my friend Manideep kanagala for his encouragement and advice when I am confused during my wretched days; your words given me much needed clarity in life. I would also thank my friend Ramakanth Bollempally for the time you spent to strengthen me with patience and care. I would like to thank my friend SRK (Siva Rama

Krishna) for your heartful words and encouragement during few depressed days. I am truly grateful for all your unwavering presence in my life especially in my toughest moments.

Special thanks to my friend and husband, Gollapudi Tejesh, for making me strong and made me believe I could do it. I sincerely thank him for making me independent in life.

Deeply from my heart, with love and faith, I owe a debt of gratitude to thank my beloved mother and brother for believing that I could do it and highly appreciated patience. Amma, no words to express the love, care, help, support, and encouragement you showered on me. Your prayer for me sustained me this far. Thanks for sticking around in my worst to hold and help me pricelessly. And I sincerely thank my brother Nehar for continuously believing, trusting, and given a shoulder to lean on. Annya thanks for boundless love and caring you have shown on me, I confidently say that no one can replace your caring on me. You both have immense hope on me, but I feel I have achieved very little in life, I promise you I will make you proud with many achievements in coming days. Your unwavering love, care and support means the world.

I sincerely thank all my Kunta family members for understanding me (Special thanks to April, Sahana, and Samyana for Joy, you provided me), my many unnamed friends and all my well-wishers.

I thank myself for making myself strong in numerous instances when no one else was present in countless struggles, fluctuations, health issues, heartbreaks with the unwavering faith in God. I have achieved something truly special in life but truly overjoyed to have earned my PhD degree in so many struggles. I owe all my life and success to my best friend, my love, my advisor, my everything to my best friend Son of Christ. I thank you Christ for holding me through all difficulties. I proudly say that you are the one who let me supported to finish my degree. I have experienced your support and love every single minute. I will keep on trusting you for my future.

My heartfelt thanks to all.

Neharika

ABSTRACT

The Himalayan region, spanning 2,500 kilometers in northern India, is highly prone to seismic activity. Situated in seismic zones IV and V, this region experiences frequent and devastating earthquakes, responsible for 70% of the world's fatal landslides. Factors such as steep slopes, heavy rainfall, uneven topography, geological conditions, climate, and unplanned urbanization exacerbate the susceptibility of the Himalayan landscape to landslides during earthquakes. The ongoing collision between the Indian and Eurasian plates generates faults and stress, making the region a high-risk area for future earthquakes. Khattri's 1999 research suggests a 56% probability of a magnitude 8.5 or greater earthquake occurring in the Himalayan seismic gap within the next century. Therefore, earthquake-induced landslides are a significant concern, necessitating enhanced preparedness to mitigate social and economic setbacks.

To assess slope stability under seismic conditions, researchers employ deterministic, probabilistic, and statistical techniques. While predicting earthquakes with absolute certainty is impossible, seismic hazard studies estimate expected ground motion levels. These studies play a vital role in identifying ground shaking intensities that can trigger slope failures, quantifying hazards associated with specific locations. Integrated seismic hazard assessments, considering slope properties, enable the evaluation of likely ground motion scenarios. Therefore, conducting comprehensive and up-to-date seismic hazard studies is crucial to assess future landslide hazards in the earthquake-prone Himalayan region.

Several seismic hazard analyses have been conducted in the Himalayan region, resulting in the development of peak ground acceleration for specific locations. However, challenges exist in using these ground intensities to accurately predict seismic vulnerability. Outdated or macro-level hazard maps, infrequent updates to earthquake databases, lack of expanded prediction equations, generalized GIS databases, data uncertainties, and stochastic-based earthquake catalogs contribute to these challenges. Depth ranges and maximum magnitude evaluations are crucial in seismic hazard assessments. Previous studies used standard or average depth ranges, but this study incorporated appropriate focal depths for point and linear sources. It also utilized a probabilistic approach called Regional Rupture Character (RRC) to estimate maximum magnitudes, setting it apart from studies using different ground motion

prediction equations (GMPEs). Furthermore, the study introduced a fully probabilistic technique, called fully probabilistic seismic hazard assessment (FPSHA), to assess ground motion triggering landslides, a novel approach for the region.

This study conducted seismic hazard analyses for the Darjeeling Sikkim Himalayan region using three frameworks: deterministic seismic hazard analysis (DSHA), probabilistic seismic hazard analysis (PSHA), and fully probabilistic seismic hazard analysis (FPSHA). DSHA emphasized seismic sources as the primary threat but did not consider uncertainties in the earthquake database and GMPE, potentially impacting results. While deterministic hazard maps evaluate intolerable failure consequences, they lack probabilistic information. PSHA, considering uncertainties in the earthquake database, provides estimates of ground motion exceedance over a specific time period. PSHA ground motions were significantly lower than those from DSHA, possibly due to inclusion of uncertainties. However, PSHA ground motions varied compared to FPSHA, which integrated PSHA with a dynamic slope stability model considering slope properties. FPSHA assessed the most probable ground motion scenarios for landslide triggering over the next 50 years for all slope models. Significant differences in ground motion levels were observed between FPSHA and both DSHA and PSHA, attributed to uncertainties in slope models, GMPE, and seismic source models.

It is apparent from this research that seismic landslide hazards can be overestimated or underestimated when relying solely on DSHA and PSHA approaches. While PSHA provides probabilistic ground motions based on historical earthquakes, it is recommended for general seismic infrastructure design. FPSHA, on the other hand, estimates ground motions based on earthquake statistics and soil properties, offering suitable design ground motions for landslide triggering conditions. By considering all possible earthquake scenarios leading to slope instability, FPSHA accounts for specific conditions that can trigger landslides.

The updated hazard maps and design charts developed in this study have various applications. They can be utilized in seismic infrastructure design, hazard zoning mapping, landslide monitoring, seismic slope stability analysis, land use planning, code requirements, and implementation of mitigation measures. These outcomes play a crucial role in pre-disaster prevention by facilitating earthquake-resistant design and enhancing post-disaster rescue preparedness. Furthermore, the findings can be employed to develop region-specific ground motion attenuation relationships, synthesize ground motions, and inform various engineering applications.

CONTENTS

Chapter **Page**

List of Figures

List of Tables

LIST OF ABBREVIATIONS

SSA	- Slope Stability Analysis
SHA	- Seismic Hazard Analysis
DSH	- Darjeeling Sikkim Himalayas
DSHA	- Deterministic Seismic Hazard Analysis
PSHA	- Probabilistic Seismic Hazard Analysis
NDM	- Newmark's Displacement Model
EC	- Earthquake Catalogue
GMPE	- Ground Motion Prediction Equation
PGA/pga	- Peak Ground Acceleration
PSA	- Peak Spectral Acceleration
FPSHA	- Fully Probabilistic Seismic Hazard Analysis
MCS	- Monte Carlo Simulation
SA	- Spectral Acceleration
UHRS	- Uniform Hazard Response Spectra
USGS	- United States Geological Survey
IAEG	- International Association of Engineering Geology
EPOCH	- European Programme On Climate and Natural Hazards
AGS	- Australian Geomechanics Society
FOS/FS	- Factor of Safety
MCE	- Maximum Credible Earthquake
LEM	- Limit Equilibrium Method
FDM	- Finite Difference Method
FEM	- Finite Element Method
SSR	- Shear Strength Reduction
BEM	- Boundary Element Method
PEM	- Point Estimation Method

FTB	- Fold Thrust Belt
MCT	- Main Central Thrust
MBT	- Main Boundary Thrust
HER	- Eastern Himalayan Region
UNESCO	- United Nations Educational, Scientific and Cultural Organization
DHR	- Darjeeling Himalayan Railway
NH	- National Highway
SOI	- Survey of India
IS	- Indian Standard
PDF	- Probability Density Function
CDF	- Cumulative Density Function
MFT	- Main Frontal thrust
DH	- Darjeeling Himalayas
STD	- South Tibetan Detachment
IMD	- Indian Metrological Department
SEISAT	- Seimotectonic Atlas
GSI	- Geological Survey of India
TFL	- Total Fault Length
ISC	- International Seismological Center
ISS	- International Seismological Summary
ISR	- Institute of seismological Research
ISC-GEM	- International Seismological Center and Global Earthquake Model
GCMT	- Global Centroid Moment Tensor database
IRIS	- Incorporated Research Institutions for Seismology
NGAR	- Next Generation Attenuation Relations
SPT	- Standard Penetration Test
MASW	- Multichannel Analysis of Surface Wave
ASCE	- American Society of Civil engineers
NEHRP	- The National earthquake hazard reduction program
EPRI	- Electrical Power Research Institute

RLD	- Rupture Length Distance
GR	- Gutenberg-Ritcher

Chapter 1

Introduction

1.1 Overview

An earthquake is a natural phenomenon that leads to significant geomorphological transformations, such as ground surface displacement, elevation changes, and rotational movements. It also induces various geological hazards, including liquefaction, landslides, structural damage, mudflows, alterations in the water table, and tsunamis, by vigorously shaking the Earth's surface in both vertical and horizontal directions. The Indian Himalayan region, characterized by the ongoing collision between the Eurasian and Indian tectonic plates, is particularly susceptible to substantial earthquakes [1]. Consequently, there has been a notable increase in landslides throughout the Himalayas in the past five decades [2].

Notably, the Himalayan region frequently experiences slope failures triggered by significant earthquakes with a magnitude equal to or greater than 7.0. Figure 1.1 illustrates some of the landslides triggered by the M_w 6.9 Sikkim Nepal earthquake on September 18, 2011. These landslides inflicted severe damage to the hills of Sikkim, followed by areas in Darjeeling, West Bengal, and Bihar. Tragically, they resulted in loss of life, destruction of temples and structures, and prolonged isolation of towns and villages for over three weeks. Subsequent heavy rainfall in the affected regions exacerbated the situation, leading to extensive slope erosion and instability, and triggering additional landslides. This cyclical process persisted, intensifying the overall impact.


gettyimages
DIPTENDU DUTTA
127501116

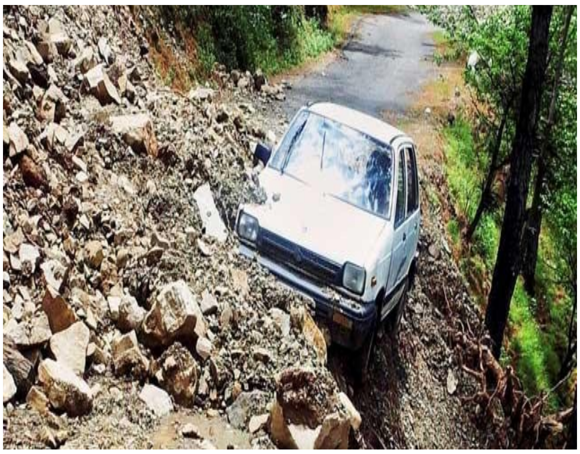

Figure 1.1 Damages on roads and buildings at DSH during the 2011 Sikkim earthquake

(https://savethehills.blogspot.com/2011/)

Following the earthquake, during the rainy season, approximately 354 new landslides and 48 reactivated landslides were recorded, causing substantial damage to roads and bridges [3]. Khattri [4] indicates a 56% probability of an earthquake with a magnitude (M_w) greater than 8.5 occurring in the Himalayan seismic gap within the next 100 years. Consequently, the region's current situation raises concerns about mitigating social and economic setbacks. However, estimating recurrence intervals between significant earthquakes remains challenging in many studies on Himalayan landslides. Therefore, conducting seismic hazard studies is considered a crucial initial step in the region to provide preliminary insights into future hazards.

In this research, a seismic hazard analysis (SHA) study has been conducted for a 300 km study area, employing three methodologies: deterministic SHA (DSHA), probabilistic SHA (PSHA), and finite-fault PSHA (FPSHA). This study utilizes an updated site-specific database, established procedures, and seismotectonic data to assess the seismic hazard distribution in terms of peak ground acceleration (PGA) and peak spectral acceleration (PSA) at various periods. The results obtained from the SHA are valuable for seismic slope stability analysis of landslides and landslide hazard assessment in the study region. Moreover, this subset of SHA and site-specific analysis aids in refining the hazard estimation process for the region. The PGA hazard maps generated through this research will significantly contribute to seismic design considerations for various civil engineering structures within the 300 km study area.

1.2 Scope and objective of the thesis

The thesis aims to provide site-specific peak ground accelerations (PGA) using three distinct methodologies for 300 km of the study area, with the primary objective of identifying the best suitable method for selecting scenario-triggering conditions for landslides.

Objectives of the study area

The study encompasses the following specific objectives:

- Identification of Seismic Sources: Conduct an extensive review of available literature and historical data to identify relevant seismic sources within the study area. This information will be utilized to compile an improved earthquake catalogue, estimate earthquake recurrence characteristics, and develop a comprehensive seismo-tectonic map.

- Deterministic Seismic Hazard Analysis: Utilize a deterministic seismic hazard framework to estimate maximum considered ground motions in the 300km study area, considering active tectonic faults, and generate PGA hazard maps as the main outcome of this analysis.
- Probabilistic Seismic Hazard Analysis: Employ a probabilistic seismic hazard framework to quantify design ground motions associated with the 300km study area incorporating seismo-tectonics, and produce PGA hazard maps, hazard curves, Uniform Hazard Response Spectrum (UHRS), and de-aggregation charts specific to the study area over the next 50 years.
- Fully Probabilistic Seismic Hazard Analysis: the objective is to evaluate the potential ground motions capable of triggering landslides within the 300km study area over a 50-year period, incorporating active tectonic faults and soil parameters through a fully probabilistic seismic hazard technique, resulting in the creation of design charts tailored to 3160 slope models.
- Case study: Select the Tindharia landslide site to assess the variations in site-specific design ground motions resulting from the three different approaches.

By accomplishing these objectives, the thesis aims to contribute to a comprehensive understanding of PGA hazard assessment methodologies and their implications for landslide susceptibility in the study area.

1.3 Organization of thesis

The thesis is structured into nine chapters, each addressing specific aspects of the research.

Chapter one provides an overview of past earthquake-induced landslide failures and highlights the importance of site-specific hazard studies in the study region. It presents the problem statement, research scope, objectives, and the organization of the thesis.

Chapter two offers a concise review of landslide hazard assessment studies and emphasizes the significance of seismic hazard studies within them. It examines previous studies, identifies gaps in the existing literature, and discusses advanced methods in seismic hazard analysis.

Chapter three focuses on providing detailed information about the study area, including its location, seismicity, geology, topography, and climatic conditions, gathered from various sources.

Chapter four presents a comprehensive seismic hazard framework, methodology, and methods employed in the Seismic Hazard Analysis (SHA). It covers the preparation of the earthquake catalogue, including event de-clustering, homogenization, and completeness check. Additionally, it discusses the selection of region-specific ground motion prediction equations (GMPE) used to estimate Peak Ground Acceleration (PGA) for the study area, along with factors influencing GMPE such as local site effects, focal depths, and distance to the site.

Chapter five focuses on the methodology and application of deterministic SHA in the study area. It describes the implementation of Deterministic SHA (DSHA) using QGIS and Microsoft Excel, utilizing the earthquake catalogue and considering active tectonics. This chapter presents the development of PGA hazard and spectral acceleration maps at different time periods for the study area using QGIS software.

Chapter six delves into the methodology and application of Probabilistic SHA (PSHA), accounting for uncertainties in seismic sources and GMPE. It covers seismicity parameters, hazard maps, curves, Uniform Hazard Response Spectrum (UHRS), and de-aggregation analysis for the overall study area and various site locations using R-CRISIS software. The site-specific 475-year hazard map derived from this study serves as input for seismic design purposes.

Chapter seven introduces an improved Fully Probabilistic SHA (FPSHA) framework, encompassing data selection, PSHA, geological investigations, landslide probability assessment, and calibration model. This chapter adopts a multi-stage hazard approach considering uncertainties in seismic sources, GMPE, and slope models. It involves the preparation of 3160 slope models based on geomechanical characteristics gathered from relevant research publications. The design charts developed in this chapter provide insight into the most probable ground motion triggering landslides over the next 50 years for all slope models.

Chapter eight presents a case study of the Tindharia landslide, where DSHA, PSHA, and FPSHA analyses were conducted to examine the variation in site-specific design ground motions from each approach. It discusses the identification of the best-fit ground motion for landslide events.

Chapter nine concludes the thesis by summarizing the main research findings and offering recommendations for future studies. The references and annexure sections follow.

Chapter 2

Literature Review

2.1 Introduction

Details of various landslide hazard assessment studies and highlights the significance of seismic hazard studies within these assessments are discussed in this chapter. It emphasizes the presence of uncertainty in ground motion analysis, which is crucial in landslide studies. Seismic Hazard Analysis (SHA) serves as an initial step in determining site-specific ground motion for selected locations. Hence, the chapter presents a detailed review of the existing literature on seismic hazard studies, along with newly improvised techniques employed in SHA. The literature review demonstrates that while numerous site-specific seismic hazard studies have been conducted worldwide, their importance remains paramount in the seismic design of specific areas. Moreover, it acknowledges the prevalent uncertainties surrounding earthquake scenarios. To address these challenges, this study adopts three different approaches to estimate site-specific design ground motion, and the uncertainties associated with these methodologies are thoroughly discussed. By summarizing extensive publications, this chapter aims to provide an up-to-date understanding of the research area's current state of the art while identifying research gaps that require further exploration.

2.2 Landslide triggered due to earthquake.

Landslides and earthquakes are interrelated natural hazards that have historically caused significant damage and severe landslides. Earthquake-induced landslides have wide-ranging impacts on people, socio-economic conditions, the environment, and infrastructure [5]. While multiple factors can contribute to landslide occurrence, seismic activity plays a prominent role [6]. The Himalayan region, known for its active seismicity, experiences frequent landslides as a direct consequence. The interaction between earthquakes and landslides creates a chain effect [7], wherein each event can occur independently or conditionally, resulting in an amplified hazard potential, even with a relatively low probability of occurrence [8].

The triggering factors of earthquakes on landslides encompass various aspects, such as earthquake magnitude, strong ground motion and its characteristics, epicentral distance, and duration. Each earthquake event has unique characteristics, influenced by factors like faults, epicenter location, magnitude, seismic waves, and aftershocks. When the Earth's crust is subjected to stress, it releases stored strain energy abruptly, leading to rupture and failure. Earthquake-induced landslides predominantly occur near faults, providing pathways for energy release, which affects weathered soil and rock, resulting in landslides. Strong ground motion is the primary agent triggering landslides, influencing the intensity of movement in the form of soil strength reduction or shear stress increase. Various types of landslides, including slides, falls, spreads, and slumps, have been observed during earthquake-induced events [9]. Two types of landslide failures can occur during earthquakes: newly triggered landslides and reactivation of pre-existing landslides. The persistence of landslides over the long term is particularly hazardous in the Himalayan region due to factors such as heavy rainfall, unfavorable geological conditions, steep slopes, and ongoing human activities like population growth and economic development.

2.2.1 Seismic landslide hazard assessment

Keefer [6] conducted the first comprehensive investigation on earthquake-induced landslides spanning from 1811 to 1980. Subsequently, numerous studies have been carried out and updated since then. However, uncertainties persist regarding earthquakes and landslides, necessitating the exploration of linkages between different models and studies to enhance our understanding of this complex system. Researchers have examined the relationship between an earthquake's ground motion and slope displacements [10] [11]. Despite the development of various studies and models, earthquake triggering mechanisms remain poorly understood. It has been found that a minimum magnitude of 4.0 or higher is required to trigger a landslide[12]. Keefer's study from 1984 to 2002 indicated an increase in the number of landslides with larger magnitudes. However, subsequent research from 1998 to 2009 demonstrated that moderate earthquakes can also induce numerous landslides. Additionally, landslides have been observed to occur not necessarily concurrently with the earthquake but a few days before or after the main shock. In some cases, the main shock's intensity may not be sufficient to trigger slope failure, but subsequent aftershocks can initiate landslides [13]. Employing countermeasures and scenario formulation can be effective in mitigating the associated hazards.

Various approaches, including deterministic, statistical, and probabilistic methods, have been utilized since the early 20th century to assess the seismic stability of slopes. Deterministic approaches used for slope stability evaluation under dynamic loading conditions include pseudo-static analysis [14], Newmark's sliding block model (Newmark, 1965), numerical analysis methods [15][16][17], and testing methods. The pseudo-static approach, commonly employed in standard seismic slope stability analysis, simplifies the earthquake effects by representing them with an equivalent static force [11]. However, this method has its limitations and is considered conservative. Subsequently, researchers have employed finite element methods, a type of stress-deformation analysis, for complex slopes, external loadings, and heterogeneous soils [18][19]. Newmark's method, which considers sliding blocks, is used to evaluate permanent displacements. Testing methods, such as shake table tests, are used on simple surfaces and small scales, typically limited to a single input ground motion. Each of these methods is applied in different situations to assess landslide hazards and conduct susceptibility assessments [20]. However, accurate soil properties and knowledge of the ground motion remain crucial for the application of these methods.

Many researchers have developed landslide susceptibility maps using statistical or probabilistic approaches on regional or global scales. Due to the difficulty of identifying material parameters on a large scale, most hazard maps estimate slope parameters through Geographic Information System (GIS) analysis tools [21]. These maps provide a general evaluation of hazard levels at various sites. Susceptibility maps focus on areas prone to landsliding based on physical parameters, regardless of triggering conditions [22]. Probability hazard maps, expressed in terms of a 475-year design ground intensity, consider triggering conditions [23], although earthquake scenarios are often not site-specific. In many cases, the peak ground acceleration (PGA) required to initiate slope failure is obtained from 475-year, 10% probability seismic hazard maps [24].

2.3 Literature review

This chapter addresses the challenge of mitigating earthquake-induced landslide hazards by providing site-specific design peak ground accelerations (PGA’s) for specific locations or sites. The objective is to generate individual PGAs that consider different landslide mechanisms separately. The chapter focuses on an in-depth examination of seismic hazard studies and their methodologies, which offer design-oriented ground motion assessments.

2.3.1 Seismic hazard analysis

Seismic hazard studies play a crucial role in assessing various natural phenomena associated with earthquakes, including landslides, liquefaction, and tsunamis. These studies aim to evaluate the design of peak ground acceleration (PGA) hazard maps for specific regions within a defined timeframe. Accurate seismic hazard assessments and appropriate ground motion estimations are instrumental in ensuring the safety of constructions, informing land-use planning decisions, conducting dynamic slope stability analyses, and facilitating disaster mitigation and management efforts. Previous seismic hazard studies provide valuable insights into ground acceleration in seismic design, thereby addressing critical concerns. Consequently, this chapter focuses on reviewing existing seismic study publications, employing different approaches, both in the present study area and worldwide, to assess the research landscape and identify knowledge gaps.

Numerous researchers have conducted seismic hazard studies across various regions in India due to its active tectonic settings. These studies aim to generate seismic hazard maps and estimate strong ground motions. Assessing earthquake hazards is crucial for determining the severity of ground motion at specific sites within developing countries like India, as it informs earthquake-resistant stability analyses for new buildings, power plants, dams, slopes, land use planning, and the assessment of remedial measures. The seismic zonation map provided by the Indian standard design code BIS [25] is widely used in the country, classifying regions into four subclasses (II, III, IV, and V) based on different zone factors. However, this map offers only a general understanding of earthquake hazard and risk due to the inherent uncertainties involved. Several seismic studies in India have indicated the need for revisions to the hazard values provided by BIS-1893 (2002), necessitating region-specific seismic hazard studies conducted through different criteria and approaches to develop PGA-related hazard maps.

Each seismic hazard study makes specific assumptions and employs distinct data collection methods for earthquake events, tectonics, geology, attenuation relationships, seismic sources, and ground motion prediction equations (GMPE’s) to generate hazard zonation maps. While each approach has its merits, the hazard values derived from previous research can result in either underestimation or overestimation. Underestimation poses safety risks, while overestimation incurs unnecessary costs. With rapid urbanization, accurate seismic hazard studies for specific sites have become imperative to safeguard infrastructure from earthquake damage. To develop site-specific design ground motions and hazard maps, seismic hazard studies have traditionally employed two globally accepted techniques: deterministic and probabilistic approaches. Moreover, advancements in scientific knowledge and technologies have led to the development of modern approaches, such as scenario-based neo-deterministic seismic hazard assessment (NDSHA) and improvised full probabilistic approaches. The forthcoming sections provide detailed information on these methods and related publications.

2.3.1.1 Commonly used methods

Both the deterministic and probabilistic approaches in seismic hazard assessment follow a similar set of fundamental steps, with the initial stages being identical [26]. The deterministic approach aims to estimate the most severe ground motion scenario by considering the maximum possible magnitude (M_{max}) and the closest potential source distance (R_{min}) to the site [27]. On the other hand, probabilistic studies have been conducted since 1984, focusing on quantifying seismic hazard by considering uncertainties associated with earthquake location, timing, and magnitude [27].

2.3.1.1.1 Deterministic Seismic Hazard Analysis (DSHA)

The Deterministic Seismic Hazard Analysis (DSHA) is a simplified approach used to assess seismic hazards for specific sites or regions by assuming a particular earthquake scenario. This method is typically employed prior to conducting probabilistic hazard assessments and is particularly useful for worst-case scenarios. In DSHA, the maximum controlling earthquake is determined, which represents the maximum magnitude within the source zone at a finite distance from the site.

While DSHA provides a reliable estimate of seismic hazard due to its time-invariant nature, it lacks consideration for all potential earthquake sources in terms of their size, location, and recurrence rate. As a result, the approach has fewer published works compared to Probabilistic Seismic Hazard Analysis (PSHA). However, many researchers support DSHA over PSHA due to its lower uncertainty regarding earthquake occurrences.

DSHA is considered beneficial for emergency planning and critical facility assessments [28][29][30][31]. Some criticisms of PSHA include the inability to properly model dependencies between uncertain parameters, uncertainties in the mathematical formulation of ground motion, and limitations in representing frequency of ground motion [32]. DSHA, despite not addressing the frequency of ground motion, remains a valuable approach for decision-making and seismic hazard assessment [33].

Several studies have conducted deterministic seismic hazard mapping for different regions in India using the DSHA approach. Parvez et al. [34] performed the initial attempt to develop a deterministic seismic hazard map for the entire Indian subcontinent, reporting a maximum design ground acceleration of 1.3g. Kolathayar et al. [35] updated this work, preparing deterministic seismic hazard maps for India with observed PGA values ranging from 0.35 to 0.05g at the bedrock level. Other studies employed DSHA for specific cities or regions in India, such as Bangalore [36], northeast India [37], Chennai City [38], Kolkata [39], Lucknow region [1], and Mumbai [40]. Shukla and Choudhury [41] evaluated seismic ground motion using DSHA for major cities in Gujarat. Ramakrishnan et al. [42] conducted DSHA for the north and central Himalayas, with observed PGA values ranging from 0.7 to 0.1g.

The most recent version of the India seismic zonation map, based on the Indian standard design code BIS [43], assigns zonal factors considering previous earthquake activities rather than SHA. However, some researchers have found that the design values recommended by the Indian standards (1893:2016) were not conservative [35][40]. The deterministic seismic hazard map and relative PGAs for the present study area have not been fully reported or updated. Therefore, this study aims to conduct a DSHA analysis specifically for the study area, as detailed in Chapter 5.

2.3.1.1.2 Probabilistic Seismic Hazard Analysis (PSHA)

Probabilistic Seismic Hazard Assessment (PSHA) is regarded as a more cost-effective and intelligent approach that incorporates infinite deterministic hazards. It involves analyzing all potential earthquakes and uncertainties to determine the probability of exceeding a specific peak ground acceleration (PGA) or intensity within a given period. By considering uncertainties, this method adds complexity but enables engineers to reduce risks and address safety concerns effectively [44]. PGA and PSA hazard maps are utilized to evaluate specific risk levels.

The concept of PSHA was initially developed by Cornell in 1968 [45], introducing associated uncertainties. Since 1984, numerous studies have been conducted worldwide to quantify seismic hazards resulting from earthquakes in specific cities or regions, including several publications adopting the PSHA methodology. Various authors have employed different approaches and models to generate hazard zonation maps for cities, states, and regions, resulting in a diverse range of recommendations.

Historically, seismic hazard studies in India began with the development of a national seismic hazard map in 1935 by the Geological Survey of India (GSI), which identified seven seismic zones ranging from 0 to VI [46]. These early regionalization studies and seismic maps assigned seismic hazards to zones based on deterministic assessments without considering probabilities of peak ground motion parameters [46-56]. However, these maps lacked a comprehensive understanding of geodynamics processes and were based solely on geotectonic concepts and earthquake distributions.

To develop seismic areas with suitable design ground motion parameters that will not be exceeded within a given time, probabilistic seismic hazard maps were generated by incorporating statistical models, seismic source zones, historical data, frequency-magnitude relations, source-to-site distance, and acceleration-attenuation functions [45] [57]. Quantitative methods, such as the Modified Mercalli Intensity (MMI) scale, were utilized to create hazard maps. Researchers have adopted probabilistic seismic studies to evaluate expected ground motion resulting from future earthquakes, employing various attenuation relations and developing PGA hazard maps. Multiple attenuation models using a weighting scheme have also been employed, leading to significant improvements in seismic hazard studies over time.

The Bureau of Indian Standards (BIS) has revised the seismic zonation map of India several times, with the most recent revisions occurring in 1996, 1970, 1984, 2002, and 2016. Previous studies on seismic hazard assessments in India have employed various methodologies and models, including [58-64]. These studies utilized a single ground motion prediction equation (GMPE) for the entire country and generally underestimated the hazard levels [65] due to limited identified areal source zones and attenuation relationships. Researchers subsequently shifted their focus from regional hazard maps to city-specific assessments, resulting in studies for various cities and regions throughout India.

For slope stability analysis, probabilistic seismic hazard maps (with a return period of 475 years) are commonly used to determine the appropriate design ground motion. Numerous studies have developed hazard maps using different methodologies, resulting in varying 475-year PGA hazard values for the present study area (as summarized in Table 2.1). However, earlier seismic studies were conducted on a larger scale, such as for the entire country, states, or regions. PGA hazard maps prepared by different researchers differ significantly due to variations in the selection of prediction equations and site classes. Therefore, this study aims to conduct a small-scale PSHA using appropriate site classes and recently developed prediction equations to derive the suitable design ground acceleration.

In summary, PSHA has proven to be a valuable and evolving methodology for seismic hazard assessment in India and worldwide. By considering uncertainties and employing probabilistic approaches, engineers can better understand and mitigate risks associated with earthquakes, leading to improved safety in infrastructure development.

Table 2.1 Report on prior studies for the Darjeeling Sikkim Himalayan region.

S. no	**Researcher**	**Area**	**Remarks** (10% probability of exceedance in 50 years–475 years return period)	**Attenuation model**	**PGA**
1	Bhatia et al. [63]	Entire India	Based on 86 areal seismic source zones under the Global Seismic Hazard Assessment Program (rock site condition)	Joyner and Boore [66]	0.35
2	NDMA [67]	India	The contours showing the distribution of PGA presented for bedrock and different soil classes	Developed regional attenuation relations using simulated ground motion data	0.16
3	Nath and Thingbaijam [68]	India	India Aerial sources have been considered in the analysis Studied at Rock site condition	GMPEs based on the different seismotectonic settings for various	0.36

				regions have been used.	
4	Manik and Nath [69]	Darjeeling–Sikkim Himalaya	Spatial distribution of PGA at the surface level	NGP models have been developed based on the empirical formulation of Boore and Atkinson [70] and Campbell and Bozorgnia [71] Ground motion prediction models for three tectonic types	0.579
5	Giardini et al.[72]	Asia.	Site classification rock Global seismic hazard assessment program.	Huo and Hu [73]	0.32
6	Nath et al. [74]	Entire West Bengal	Rock level	14 GMPAs for three seismotectonic provinces were selected through suitability testing; and appropriate weighting in	0.42

				a logic tree framework	
7.	Maiti et al. [75]	Entire West Bengal	Rock level	14 regional and global prediction relations are incorporated and integrated with appropriate ranks and weights in a logic tree framework.	0.42
			Tectonic seismogenic source (hypocentral depth: 0–25km)		0.325
			Tectonic seismogenic source (hypocentral depth: 25–70km)		0.175
			Layered polygonal seismogenic source (hypocentral depth: 0–25km)		0.250
			Layered polygonal seismogenic source (hypocentral depth: 25–70km)		0.110
			At the firm rock site condition conforming to B/C site class (Vs: 620–760 m/s)		0.445
			Surface consistent		0.714

2.3.1.2 Advanced approaches

Many of the advanced seismic hazard assessment methods involve combining deterministic and probabilistic approaches or incorporating additional mathematical relations. By combining different techniques, researchers aim to enhance the reliability and precision of hazard assessments, ultimately leading to more robust and informed decision-making in the field of seismic risk management.

2.3.1.2.1 Neo-Deterministic Seismic Hazard Analysis

The multi-scenario-based neo-deterministic methodology has been developed for seismic hazard assessment [32] [76] with the aim of evaluating seismic risks at specific sites using a large set of modeled earthquake scenarios. One key difference between this approach and the deterministic seismic hazard analysis (DSHA) lies in the utilization of synthetic seismograms in the neo-deterministic approach and ground motion prediction equations (GMPE) in the DSHA. The neo-deterministic seismic hazard analysis (NDSHA) relies on physically simulating wave propagation in seismically active regions [77]. This scenario-based approach to seismic hazard analysis is developed to address the limited availability of seismological, geophysical, and geological data for the study area.

It employs generated or scenario-based earthquake events and a stochastic earthquake catalogue generated from seismic source models for assessing earthquake-induced landslide hazards. Realistic synthetic time series are used to develop scenario-based earthquake ground motions that are particularly useful for earthquake engineering purposes [32]. The NDSHA maps provide conservative estimates of seismic hazards and find application in assessing strategic buildings, heritage sites, and conducting seismic microzoning in urban areas worldwide. However, it is important to acknowledge that this methodology introduces uncertainties regarding ground scenarios and earthquake events.

2.3.1.2.2 Improvised fully probabilistic approach.

In the aforementioned studies, the consideration of uncertainties in selecting expected ground motion levels has been largely overlooked. However, there has been a growing focus among researchers on establishing mathematical relationships between seismic hazard assessment and landslide-causing factors, such as topography and geology, to aid in mitigating earthquake-induced landslides [78][79]. Although various methods are widely employed for landslide assessment, most of these studies acknowledge the uncertainty surrounding earthquake scenarios and tend to provide conservative estimations of seismic landslide hazards. Nonetheless, the concept of rational risk management that effectively addresses data uncertainties has emerged with the advent of fully probabilistic approaches in the late 20th century.

The framework of the fully probabilistic approach involves estimating slope failure under seismic loading by considering all possible ground shaking levels, typically inferred from Newmark's model [80][81] or a consistent earthquake scenario for seismic slope stability [82]. Based on empirical relations derived from Newmark's method, the critical acceleration of the slope (a_c) is calculated and combined with probabilistic seismic hazard assessment to determine the probability of slope failure under seismic action in the future [80]. This approach effectively handles uncertainties in the data and provides a rational framework for hazard management. Some researchers have utilized this approach to establish the annual exceedance frequency for specific sliding displacements [83][84] [80]. However, no previous research has applied this method to the present study area. Consequently, in this study, a fully probabilistic seismic hazard analysis is conducted for the study area in Chapter 7.

2.4 Understanding the Research gaps and motivation.

The literature review aimed to identify the causes and impacts of landslides and identify research gaps that warrant further investigation. The review revealed several areas within the field of landslides that require additional research.

Firstly, while numerical simulations of slopes during earthquakes require well-defined soil properties, the selection of appropriate design ground motion remains subjective and is often overlooked in most landslide hazard assessments.

Secondly, the regional-specific hazard maps developed for the study area are general in nature, covering relatively large areas. This can result in either underestimation or overestimation of hazard levels, as identified by [75] and [74].

Thirdly, probabilistic hazard maps based on the Probabilistic Seismic Hazard Assessment (PSHA) methodology are commonly used in the study area. However, these hazard maps have not been updated with the latest earthquake catalogues (EC), nor have they incorporated new methodologies and ground motion prediction equations specific to the study area.

Fourthly, previous seismic hazard analyses have predominantly focused on tectonic and seismo-tectonic factors, neglecting the combined influence of soil characteristics and seismic activity in the study area.

Lastly, although a few studies have explored the use of Fully Probabilistic Seismic Hazard Assessment (FPSHA) in evaluating site-specific ground motion for seismic hazard assessment in landslides, there is a lack of comprehensive investigation and understanding of these three methods for the purpose of seismic slope design.

These identified research gaps underscore the need for further exploration and investigation in the field of landslides. By addressing these gaps, we can enhance our understanding of landslides and improve our ability to prevent and mitigate their detrimental effects.

2.5 Conclusion

The comprehensive review of past earthquake-induced landslides in the Darjeeling Sikkim Himalayas, along with the associated seismic hazards, highlights the importance of considering both well-measured material properties and subjective ground-motion selection. Seismic hazard analysis methods play a crucial role in assessing site-specific design ground motion. Therefore, this chapter provides a detailed review of seismic hazard analysis within the study area, as well as relevant publications from both the study region and the wider country. Additionally, various approaches for determining site-specific design ground intensity are discussed.

The literature review reveals that many researchers have developed PGA hazard maps at regional or global scales, employing either deterministic or probabilistic methodologies. However, these hazard maps are often based on outdated earthquake catalogues, employ outdated ground motion prediction equations (GMPE's), or estimate slope parameters using generalized global information system (GIS) tools. Furthermore, the hazard values derived by previous researchers for the study region lack site-specificity, and there is considerable uncertainty regarding the appropriate site-specific earthquake scenario. To address these limitations, this study develops updated, site-specific deterministic, probabilistic hazard maps, and design charts for the present study area, employing the Dynamic Seismic Hazard Analysis (DSHA), Probabilistic Seismic Hazard Analysis (PSHA), and Fully Probabilistic Seismic Hazard Analysis (FPSHA) methodologies.

The next chapter focuses on the input parameters required for seismic hazard analysis, including the earthquake catalogue, past earthquake data, seismo-tectonics, local site effects, GMPE's, and soil parameters. A detailed explanation of the three selected methodologies and the most suitable seismic hazard approach for assessing seismic slope stability is presented in subsequent chapters.

Site Characteristics of the study area

3.1 Location of the study area

The present study encompasses a 300 km radial distance, covering the entirety of the Darjeeling Sikkim Himalayas (DSH) region, as illustrated in Figure 3.1. This region is situated in the foothills of the eastern Himalayas and is characterized by significant folded thrust faults, as documented by Medlicott [85]. It is positioned to the west of the Nepal Himalayas and to the east of the Bhutan Himalayas. The study area comprises mountain peaks, deep valleys, and ecologically sensitive areas, which are susceptible to slight to moderate earthquakes and landslides. These geological phenomena are influenced by the region's active and complex tectonic features, young geology, and diverse climatic conditions.

The Tindharia landslide, located in the Darjeeling district of West Bengal, India, is center of 300 km radial seismic hazard analysis (SHA) conducted in this study. It serves as a prominent case study in Chapter 7. This historic landslide occurred during the 2011 Sikkim Nepal earthquake and led to the devastating destruction of the Darjeeling toy train track, a renowned world heritage site and a major tourist attraction.

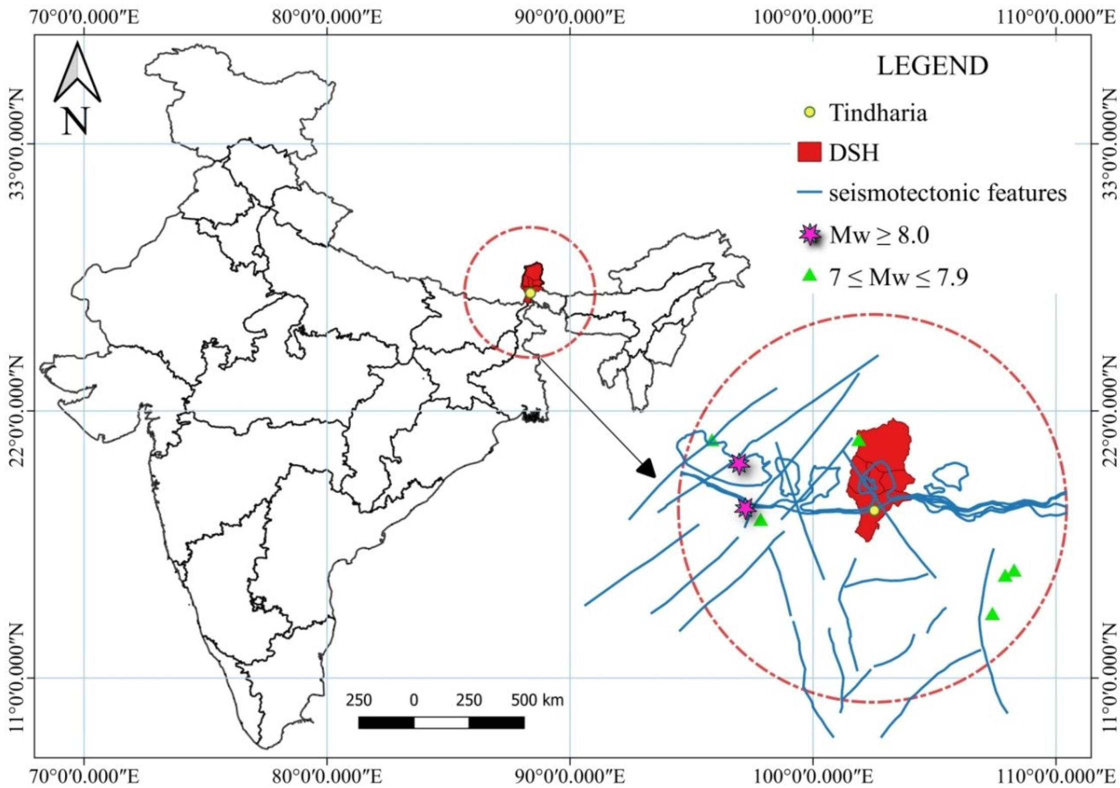

Figure 3.1 Geographic location of DSH and Tindharia landslide (India) with major earthquake events and seismotectonic features within a 300 km radius.

The study area, encompassing a 300 km radius, is surrounded by significant seismic events, including the 1833 earthquake with a magnitude of M_w 8.1 and the 1934 Bihar-Nepal earthquake with a magnitude of Mw 8.4, along with several earthquakes above magnitude 6.5. The region exhibits complex tectonic characteristics, characterized by slight to moderate seismic activity. Considering the earthquake occurrences and prominent tectonic features such as the main central thrust (MCT) and main boundary thrust (MBT), the selection of a 300 km radius in this study is based on the practice of incorporating all active sources within the zone of influence from the study area's center.

3.2 Details of topography

The study area is located within the DSH (Darjeeling-Sikkim Himalayas) region of the Eastern Himalayas. It exhibits a diverse topography, with elevations ranging from 15 to 3602 meters and slopes ranging from 0° to 79.23°. The area is characterized by towering mountain ranges such as Kanchenjunga and deep valleys intersected by rivers and streams, particularly in the Darjeeling Himalayas.

The Darjeeling district can be divided into two distinct sections: the southern plain terrain, known as Terai, and the northern hilly topography. Figure 3.2(a) illustrates this division. The elevations in the plain land and hilly terrain range from 15 to 422 meters and 422 to 3602 meters, respectively. Similarly, the slopes in the plain land vary from 0° to 18.64°, while in the hilly terrain, they range from 18.64° to 79.23°, as depicted in Figures 3.2 (a and b) [86].

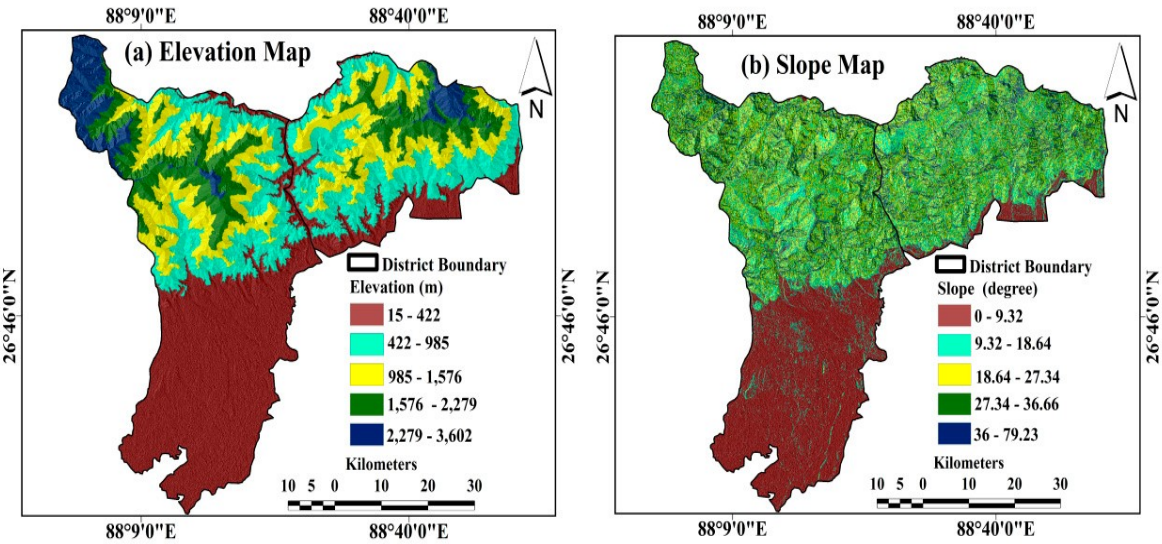

Figure 3.2 (a) Elevation and **(b)** slope map of Darjeeling [86].

The drainage system within the study area is strongly influenced by the topography, as a multitude of streams flow from the hilly terrain towards the plain terrain. The district is traversed by several significant rivers, including Teesta, Mahananda, Rangeet, Mechi, Balason, and Murti.

In addition to its complex landforms, the region is characterized by weak geology, high seismic activity, substantial rainfall, slope instability, and the presence of narrow and deep valleys prone to gully erosion. Consequently, the study area is subject to the combined effects of earthquakes, rainfall, and human activities, which have resulted in the occurrence of numerous critical landslides.

3.3 Geological details

The DSH region is situated in an area where the Eurasian and Indian plates converge, forming an almost perpendicular alignment with the Himalayan deformation front. The geological composition of the region is characterized by the presence of metamorphic rocks, specifically within the active Himalayan fold thrust belt (FTB), as well as High-grade gneiss rocks, which form a half window within the DSH.

For a more comprehensive understanding of the geological formations in the region, please refer to Figure 3.3 (a) for Sikkim and Figure 3.3 (b) for Darjeeling.

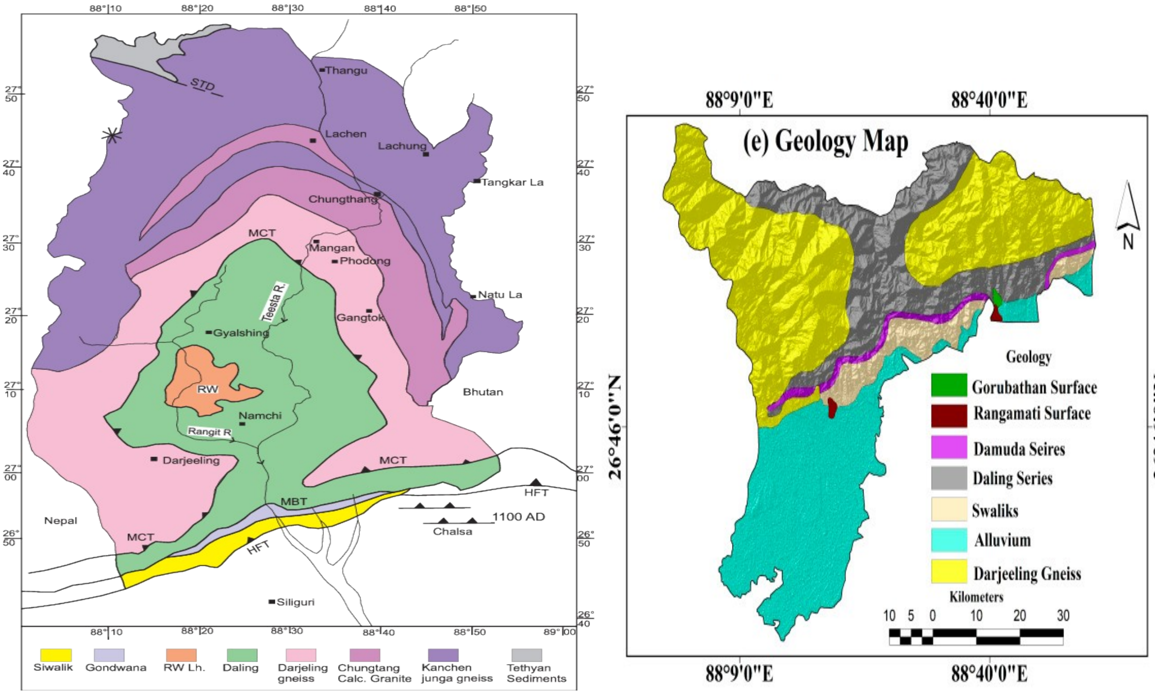

(a) (b)

Figure 3.3 Geological map of **(a)** Sikkim Himalayas [87] and **(b)** Darjeeling [86].

The DSH region encompasses the Main Central Thrust (MCT), Main Boundary Thrust (MBT), and Main Frontal Thrust (MFT) faults within the fold thrust belt (FTB). These faults delineate the rock units present in the region [88]. Early geological investigations and classifications were conducted by Mallet [89] in the Darjeeling, Sikkim, and Nepal regions, followed by subsequent studies and observations in the mid-19th century [90] [91].

The geological composition of the Darjeeling hills comprises three distinct belts: the Siwalik frontal range as the outer belt, the Damuda range as a narrow middle belt, and the metamorphic rocks belonging to the Darjeeling and Daling groups as the inner belt [92]. The Darjeeling plain in the Terai landscape exhibits alluvium and raised terraces due to the presence of a transverse drainage system [93], as depicted in Figure 3.3b. The inner range of the Daling and Darjeeling Gneiss groups consists of high-grade metamorphosed rocks. The young, folded range in the DH is characterized by sedimentary rocks undergoing active erosion, contributing to high susceptibility to landslides in the region [94].

The geological formations in the DH exhibit variations in soil and rock types based on elevation and slope. The predominant rock types include high-grade gneiss, quartzite, schist, phyllite, shales, and sandstone [91][95][96]. Soil classifications encompass mountain and glacial soil, brown hill soil, forest soil, brown forest soil, terai soil, and tea soil [92]. The soils range from red and gritty in the uphill areas to dark and fertile in the plains, with silty or silty loam textures predominating along riverbanks. The geological formations of the Darjeeling Himalayas also contain various minerals such as copper, coal, iron ore, mica, lead, graphite, zinc, nickel, and silica sand [97]. The geological sequence in the entire DH, from the lowland plain to the higher regions, consists of six formations, with detailed characteristics provided in Table 3.1.

Table 3.1 Geological formation of DH [89][91][98]

Series	**Age** [99]	**Lithological characteristics**
Alluvium (Pleistocene)	1.8 million years to 10,000 years (recent to sub recent formation)	Composed of sand, silt, clay, and some bands of gravel
Raised Terrace (Pleistocene)	1.8 million years (recent to sub recent formation)	Deposit at confluences of rivers composed of gravels, pebbles, and boulders mixed with clay and sand
Siwalik (Miocene)	26 million years	Mudstone, sandstone with bands of siltstone, shale, clay, and lignite
Damuda series (Premian (equivalent to Gondwanas)	280 million years	Coarse-grained hard sandstone, quartzites, seams of graphitic coal, carbonaceous shale, and slates belong to the Damuda series and minor bands of limestone
Daling series (Precambrian)	3787 million years	Greenish slates comprised of chlorite–sericite schist, chlorite shales, phyllites and schist associated with quartzite, chlorite–quartz schist, and slate
Darjeeling Gneiss (Precambrian)	3787 million years	Highly foliated due to metamorphism, golden silvery mica-schist, carboniferous mica-schist, and coarse-grained gneiss It contains minerals of garnet,

		sillimanite, kainite, and staurolite and carries subordinate bands of quartzite

3.4 Seismo-tectonic details

Based on geographical statistics, approximately 54% of India's land is considered vulnerable to earthquakes due to its complex and diverse tectonic framework. The seismic activity in the country is classified into three major zones based on the tectonic settings: subduction zones (such as Hindukush-Pamir, Indo-Myanmar Arc, and Andaman-Sumatra belt), tectonically active shallow crust regions (including the Himalayas, South Tibetan plateau, and northwest frontier provinces), and stable continental regions (such as Peninsular India).

The study area under consideration falls within the tectonically active eastern Himalayas in India. The increased seismicity in the Himalayan region is attributed to the northward movement of the Indian plate at a rate of approximately 5 cm per year, colliding with the Eurasian plate [100]. This collision has resulted in the formation of the massive Himalayan Mountain range and is considered one of the fastest-moving plates globally. The Himalayan orogenic belt, located north of India, stretches for about 2500 km from north to south [100]. This region is characterized by high seismic activity and is prone to major earthquakes with a magnitude (M) of ≥ 8.

The Himalayas can be divided into five tectonostratigraphic zones based on distinct rock domains: the higher Himalaya (3500-8880m), Sub Himalaya (Siwaliks) (1000-4000/4800m), lesser Himalaya (400-2400m), Tethys Himalayas (Tibetan Himalayan zone) (4000-6000m) [91], and Gangetic plain (Terai), as illustrated in Figure 3.4. The Himalayas are further divided into three regions: western, eastern, and central Himalayas. The eastern Himalayan region, characterized by high seismic activity, falls under zone V according to IS: 1893 (2002) [25] classification. The entire area exhibits numerous geological structures resulting from multiple phases of the deformational process [101]. Specifically, the Eastern Himalayas are further subdivided into three geographic regions: Assam Himalayas, Darjeeling-Sikkim Himalayas (DSH), and Bhutan Himalayas.

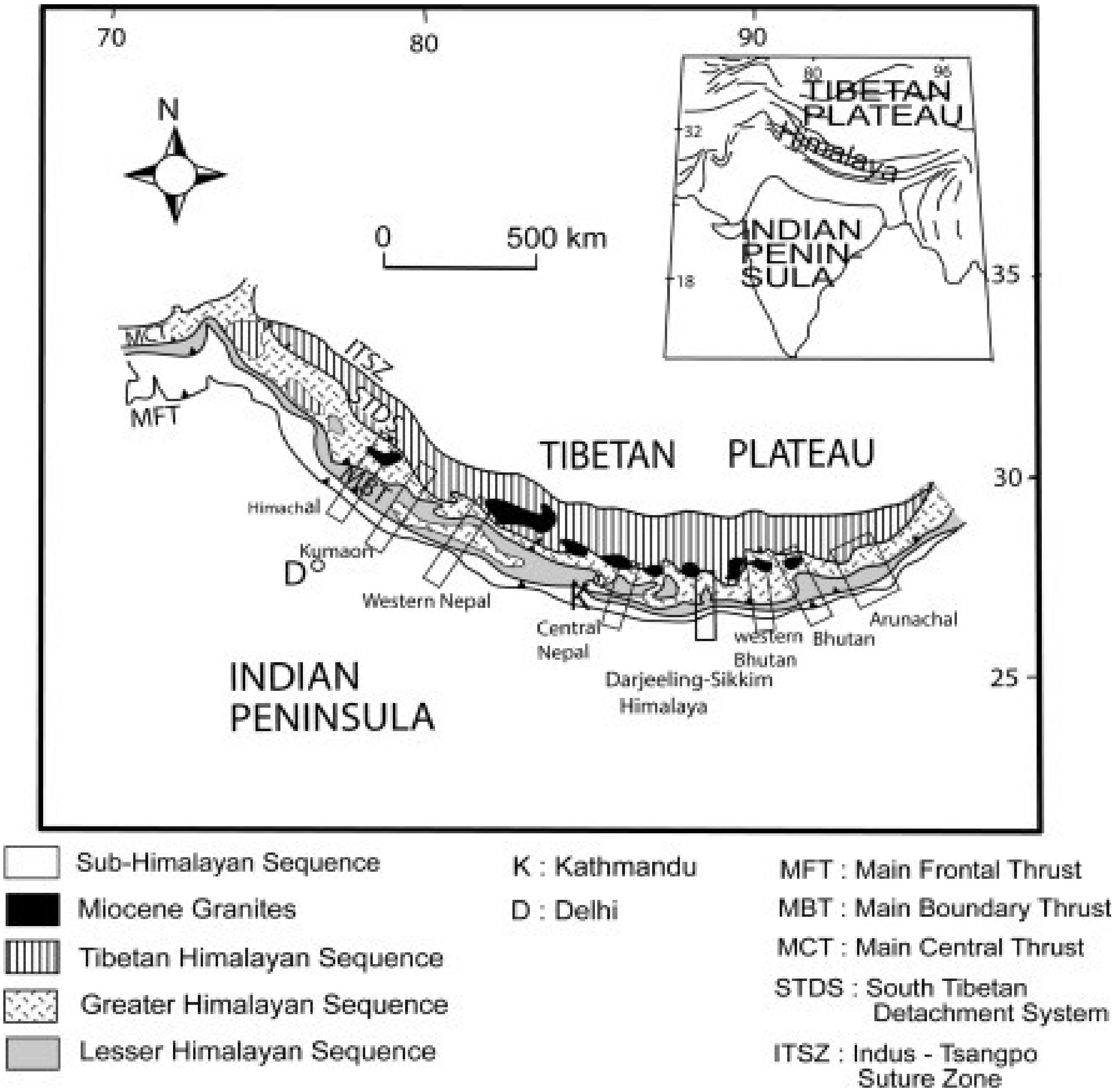

Figure 3.4 Lithotectonic map of the Himalayas [102].

The central part of the study region, specifically Darjeeling, is situated in the lesser and Siwalik Himalayas, which are separated by two significant faults known as the Main Central Thrust (MCT) and Main Boundary Thrust (MBT). The Darjeeling-Sikkim Himalayas (DSH) region is part of the Himalayan fold thrust belt (FTB), characterized by major folded thrust faults [85]. The area is surrounded by prominent active tectonic features, including faults, lineaments, and thrusts, as depicted in Figure 3.5. The region is susceptible to earthquakes, as evidenced by numerous earthquake shocks, although seismic epicenters are not observed. The presence of the Tista lineament in the Darjeeling Himalayan region has been associated with high-magnitude earthquakes [103]. Detailed information about the major earthquakes occurring within a 300 km radius of the study area can be found in Chapter 4.

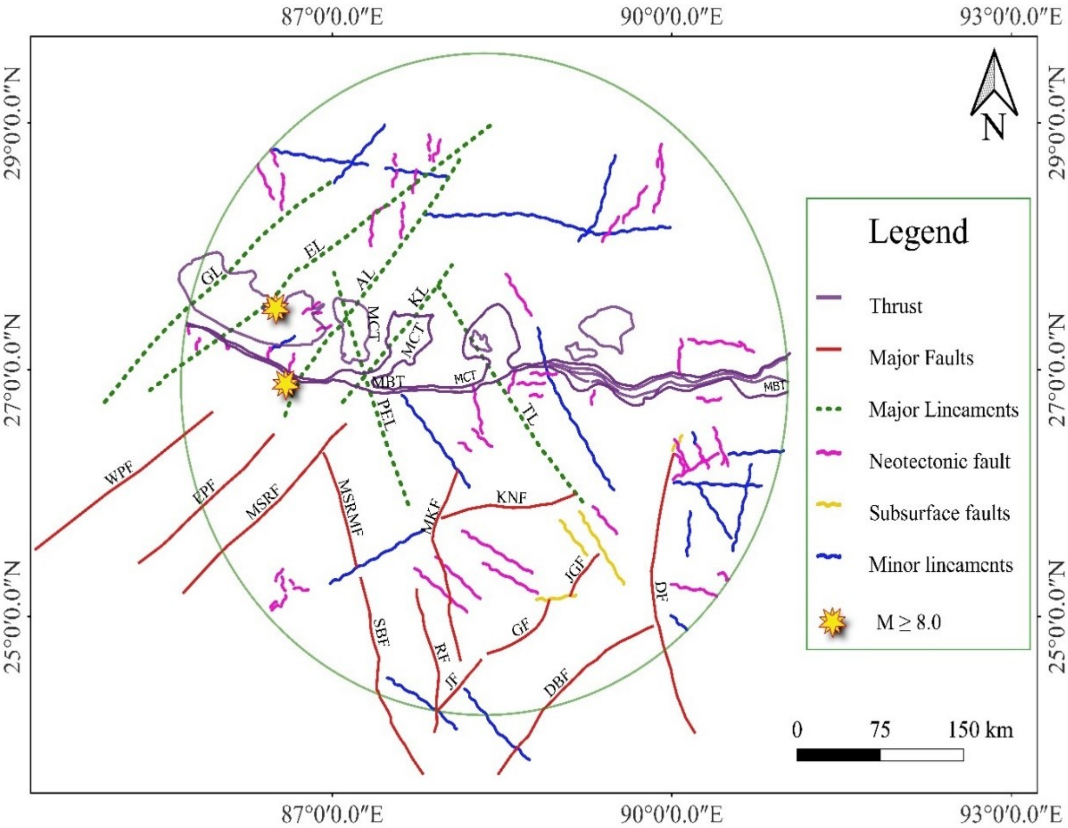

Figure 3.5 Seismo-tectonic details within the study area.

Considering the seismic strain gaps observed in the subduction zone of the Himalayas, it is anticipated that India may experience significant earthquakes in the future [104]. These earthquakes have the potential to cause secondary damage, including landslides, liquefaction, and rockfalls, which pose substantial risks to human safety and infrastructure. The occurrence of such events can have wide-ranging impacts on various aspects of human life.

3.5 Climatic conditions

The climate encompasses meteorological parameters such as precipitation, temperature, humidity, sunshine, and cloudiness, which are primarily influenced by wind patterns. The study region and its surroundings exhibit distinctive climatic conditions due to factors such as topography, ridges and valleys, geographical location, and neighboring mountain ranges. The area exhibits three climatic zones based on elevation: tropical, sub-alpine, and temperate. These zones are characterized by four distinct seasons: pre-monsoon (summer), monsoon, post-monsoon, and winter [105].

Situated in a humid tropical belt, the climate in the southeastern plains of the study area is warm and humid, with variations depending on elevation, reflecting typical tropical and sub-tropical conditions. Conversely, the northern hills experience cold winters, pleasant summers, and occasional snowfall [105].

Rainfall patterns vary with altitude, with the northern hills receiving less rainfall compared to the plains. The rainy season typically starts in May and lasts until October, with the highest rainfall occurring in June and July. The annual rainfall in the study area exceeds 3200 mm, with daily rainfall often exceeding 600 mm. Rainfall is a critical trigger for slope instability as the penetration of rainwater reduces shear strength, leading to devastating landslides [106][107]. Rainfall also contributes to surface runoff and erosion, further exacerbating slope instability. Therefore, accurate rainfall data is essential for analyzing rainfall-induced slope stability.

Temperature ranges from 4 °C to 42 °C in the plains and -5 °C to 27 °C in the hills, depending on elevation. Temperatures decrease with increasing altitude and can reach freezing point during the monsoon season. The lowest temperatures are observed in the winter months from December to March, with January being the coldest month when temperatures often drop below 0°. The northern hills experience high humidity throughout the year, while the plains have lower humidity levels during drier months such as March to April. The district maintains high humidity year-round, with levels not dropping below 60% even during the summer months from March to April [108]. Relative humidity during the monsoon season in higher altitudes ranges from 85% to 99% and gradually decreases with decreasing altitude. In comparison, relative humidity during dry months (March to April) ranges from 45% to 60% [97].

3.6 Conclusion

This chapter focuses on the selection and location of the study area. The chosen area is situated within the lesser Himalayan terrain, characterized by prominent mountain peaks such as Kanchenjunga. A comprehensive 300km radius map of the study area has been developed, highlighting key tectonic features. Data pertaining to seismo-tectonic aspects, geological composition, geotechnical properties, topography, and climatic conditions have been gathered to facilitate the seismic hazard analysis (SHA) process.

The study area is encompassed by a range of active tectonic faults, lineaments, and thrust zones, varying in scale from major to minor. Notably, the presence of the Tista lineament, along with the MCT and MBT thrusts, has been associated with significant earthquakes of magnitude greater than 7.5 M_w. Past seismic activity records and geotechnical assessments indicate that the study area is highly susceptible to earthquakes and landslides.

Furthermore, the study area is characterized by hilly terrain, with elevations ranging from 15 to 3602 meters and slope angles varying from 0 to 79.23°. It forms part of the tectonic-stratigraphic sequence of metamorphic rocks within the fold thrust belt of the Himalayas. The unique combination of complex landforms, weak geological formations, high rainfall, slope instability, and the presence of narrow and deep valleys with gully erosion render the study region highly vulnerable to critical earthquakes and landslides.

Chapter 4

Seismic hazard analysis framework

4.1. Introduction

Seismic hazard studies play a crucial role in accurately assessing the potential impact of future seismic events at specific locations. These studies involve the integration of various mathematical models to address uncertainties and challenges associated with earthquake prediction. A key parameter in designing earthquake-resistant structures, mitigating existing ones, and enforcing code provisions is the prediction of site-specific ground motion.

Relying solely on ground-shaking intensity data from nearby stations and previous regional studies is unreliable due to uncertainties related to location, magnitude, and seismic source characteristics. Moreover, ground motion is influenced by regional tectonics, geological features, seismotectonic depth ranges, as well as the use of appropriate Ground Motion Prediction Equations (GMPE's). Consequently, site-specific micro-level studies, incorporating updated data, are indispensable for accurately assessing the specific risks associated with particular areas.

Thus, the present study emphasizes the importance of conducting Seismic Hazard Analysis (SHA) that takes into account local site conditions and utilizes region-specific GMPE's. This chapter provides a comprehensive overview of the steps involved in conducting SHA, including the identification of seismic sources, collection of earthquake data, preparation of Earthquake Catalogs (ECs), calculation of distances from the site to the seismic sources, and selection of appropriate GMPEs. The chapter concludes by summarizing the key concepts discussed throughout.

4.2 Evaluation of SHA

4.2.1 SHA Methodology

Earthquakes, as natural phenomena, result from the sudden movement or rupture of faults, leading to ground shaking. Seismic Hazard Analysis (SHA) aims to assess the varying levels of earthquake effects. This study serves as a key tool for understanding future seismic events by drawing evidence from past events and historical periods. Several parameters are utilized to classify seismic hazards, including strong motion duration [109], peak ground acceleration [45], soil liquefaction [111], landslides [112], response spectral amplitudes [113][114][115][116], and surface faulting [117][118].

Of these parameters, earthquake ground acceleration has been extensively studied and received significant attention, primarily due to its potential for causing extensive economic losses in most earthquakes. Ground-shaking intensity is typically characterized by ground motion acceleration or spectral acceleration (SA) within a probabilistic or deterministic framework [119]. Ground motion is an integral component considered in provisional seismic codes and design standards in modern countries for several decades. Additionally, it plays a crucial role in assessing the potential for landslides and liquefaction at specific sites or areas.

The primary objective of any seismic hazard study is to ensure that structures can withstand a certain level of ground shaking without experiencing significant damage. By comprehensively analyzing seismic parameters and accurately characterizing ground motion, such studies contribute to the development of robust structural designs and the establishment of appropriate safety standards. These efforts aim to safeguard human lives and minimize the economic consequences associated with earthquakes.

4.2.2 SHA approaches

The theoretical formulation of seismic hazard analysis was initially conducted by Cornell in 1968. This analysis refers to the quantitative estimation of earthquake-induced ground motion within a specified time period for a particular area or site [120]. In the present study, three distinct approaches are employed: deterministic, probabilistic, and an improvised fully probabilistic method.

The deterministic approach involves calculating the hazard parameter for a specific earthquake scenario, assuming it occurs at a fixed distance from the seismic source to the site [122][123][124]. On the other hand, Probabilistic Seismic Hazard Analysis (PSHA) incorporates all potential earthquakes while considering uncertainties related to earthquake location, timing, magnitude, and ground motion models [45][113][115][27].

The improvised fully probabilistic approach has been utilized to assess the total probability of slope failure under all possible ground motions. It combines uncertainties associated with slope models, Ground Motion Prediction Equations (GMPE’s), and seismic source models. This approach provides a comprehensive assessment of sustainability by selecting earthquake scenarios that yield consistent seismic slope failure probabilities [82].

All these methods require input data to initiate the seismic hazard analysis. The input data encompasses an earthquake catalogue, GMPE selection, active tectonics characterization, local site effects assessment, focal depth determination, and distance calculation between the site and seismic sources. This chapter focuses on preparing the necessary input data for hazard assessment.

4.2.3 Framework of SHA

The initial phase involves the selection of the study area and defining its boundary radius. This step aims to establish the specific region under investigation. Subsequently, the preparation of a refined earthquake catalogue (EC) becomes essential for evaluating seismic hazards accurately. The EC is constructed based on a compilation of historical earthquake data, including information on magnitude, time, date, location, and depth. To ensure the reliability of the catalogue, each stage undergoes thorough verification to address potential uncertainties, such as homogenization, de-clustering, and completeness checks.

In addition, an appropriate attenuation model is selected to estimate the final hazard for the chosen study site or area. This attenuation relation takes into account various factors, including the distance between the seismic source and the site, the soil conditions at the site (such as shear wave velocity), and the focal mechanism of the earthquakes. Each of these components is extensively examined and assessed to determine the most suitable function for hazard estimation.

All the aforementioned input data play a vital role in conducting Deterministic Seismic Hazard Analysis (DSHA), Probabilistic Seismic Hazard Analysis (PSHA), and the improvised Fully Probabilistic Seismic Hazard Analysis (FPSHA). Detailed analyses of these methodologies are expounded upon in Chapters 5, 6, and 7 of the study.

The initial step in identifying seismic sources entails selecting the site of interest and determining the radius of the influencing zone. The study area selection, comprehensive site description, and rationale behind choosing a radius of 300 km are elaborated upon in Chapter 3, Section 3.1. Following this, the earthquake catalogue preparation process is described in subsequent sections.

This study aims to comprehensively understand seismic hazards and enhance the resilience of the studied region. By employing meticulous procedures and utilizing gathered input data, it enables informed decision-making, improves structural design practices, and fosters better preparedness for seismic events.

4.3 Preparation of Earthquake Catalogue (EC)

The collection of earthquake databases in the form of a catalogue is a fundamental step in seismotectonic and seismic studies. This crucial process involves data collection, homogenization, de-clustering, and completeness checks. These steps ensure the reliability and quality of the collected data, providing a solid foundation for further analysis and assessment in the field of seismology.

4.3.1 Data collection

Within the defined 300km radius, a comprehensive collection of seismic sources has been accomplished. These seismic sources can be categorized into seismic source zones or linear seismic sources, with the latter representing tectonic features such as faults and lineaments. Descriptions of the seismic sources may take the form of lines, points, or areas in proximity to the site, and their delineation is based on seismo-tectonic information [122].

The identification of geographical seismic sources begins with the acquisition of geological and seismological evidence. The distribution of epicenters across a wide region is indicative of an area source zone, while seismicity clustering around an active fault is indicative of a line source. In cases where the associated fault is not readily identifiable, the geometric center of the area is assumed to be the epicenter, represented as a point source. Within this study, two seismic source modes are considered: point sources and linear sources.

By incorporating these various seismic source modes, this study ensures a comprehensive assessment of potential seismic hazards. The consideration of both points and linear sources provides a robust foundation for evaluating the seismic activity within the designated area and contributes to a more accurate understanding of the associated risks.

4.3.1.1 Linear seismic sources

In Chapter 3, it was established that the study area is characterized by numerous active tectonic features that contribute to seismic hazards in the region. This study focuses on these active tectonic features, including faults, lineaments, thrust zones, and shear zones.

To compile the linear seismic sources, the study relies on India's Seismo-tectonic Atlas (SEISAT) published by the Geological Survey of India (GSI) [125]. SEISAT is a highly regarded reference manual widely utilized by researchers in the field. The study specifically refers to SEISAT for identifying linear sources, such as faults, lineaments, and shear zones. Five sheets (12, 13, 14, 23, and 24) of SEISAT maps covering a 30x40 area with a scale of 1:1,000,000 were collected. These sheets were then scanned and georeferenced in the QGIS software.

Through careful processing, the maps were combined to create a comprehensive digitized map, from which the linear sources were extracted using QGIS software. Approximately 30 tectonic features encompassing thrusts, major and minor faults, subsurface faults, and major and minor lineaments were identified, as illustrated in Figure 3.5. However, for the purpose of this study, only 20 major active tectonic features were selected and utilized. Detailed information on these major tectonic features, including fault types, total fault lengths (TFL), and the observed maximum earthquake, is summarized in Table 4.1.

Table 4.1 Details of the major tectonic features in the site area.

S.No	Fault name	Fault code	Fault Type	Observed M_w
1	Jangipur Gaibandha Fault	JGF	Strike slip	6.0
2	Gaibandha Fault	GF	Strike-slip	5.5
3	Dhubri Fault	DF	Reverse	7.6
4	Katihar Nailphamuri Fault	KNF	Normal fault	5.5
5	West Patna Fault	WPF	Normal fault	5.2
6	Sainthia Bahmani Fault	SBF	Normal fault	5.7
7	Gouri Shankar Lineament	GSL	Strike slip	6.1
8	Everest Lineament	EL	Strike slip	6.1
9	Arun Lineament	AL	Oblique Reverse	5.6
10	Kanchenjunga Lineament	KL	Normal fault	7.0
11	Purnea Everest Lineament	PEL	Normal fault	6.1

12	Tista Lineament	TL	Strike slip	5.7
13	Main Boundary Thrust	MBT	Reverse	8.3
14	Main Central Thrust	MCT	Reverse	8.0
15	Debagram Bongra Fault	DBF	Normal fault	5.4
16	East Patna Fault	EPF	Normal fault	4.2
17	Munger sahastra Ridge Fault	MSRF	Normal fault	4.3
18	Rajmahal Fault	RF	Normal fault	4.9
19	Jangipur Fault	JF	Normal fault	4.8
20	Malda kishanganj Fault	MKF	Normal fault	4.5

Three types of faults have been identified. Namely, strike-slip faulting, reverse faulting, and normal faulting. The ground amplitudes change depending on the style of faulting.

4.3.1.2 Point sources

In addition to the linear seismic sources, it is important to consider earthquake events that are not directly associated with these sources. While most earthquakes occur along the boundaries of tectonic plates, some events also occur in regions far from these boundaries. To ensure a comprehensive interpretation in seismic hazard analysis (SHA), point sources are also taken into account.

For the study analysis, earthquake data spanning from 1934 to 2021 with magnitudes ranging from 4.0 to 8.5 were collected. This dataset includes additional information such as focal depth, distance from the site, year of occurrence, and event time. The instrumental seismic data were obtained from various reputable sources, including the United States Geological Survey (USGS), International Seismological Centre (ISC), International Seismological Summary, Institute of Seismological Research (ISR), Global Earthquake Model, Global Centroid Moment Tensor database (GCMT), and Incorporated Research Institutions for Seismology (IRIS).

As instrumental data before 1900 is not available, information from this period is referred to as pre-instrumental or historical data. Such data was gathered from well-published literature, including journal articles, books, reports, historical records, newspaper articles, Indian office records, and British libraries. Various sources were consulted, including publications by [127-137] compiled a comprehensive earthquake catalogue covering the period from 810 BC to 2012 by extensively researching a variety of sources.

In total, approximately 2,344 raw earthquakes were collected from instrumental and literature sources. Among these, 2,195 earthquakes were obtained from instrumental data sources within a 300 km radius of the study site, spanning the period from 1930 to 2021. The remaining 149 earthquakes were gathered from literature sources covering the period from 1800 to 2021, as summarized in Table 4.2.

To ensure data quality, the raw dataset was carefully processed to address duplicate events, dependent events, and non-homogenization of magnitudes. Duplicate events were removed using Microsoft Excel, while dependent events were eliminated using the time-distance window method in ZMAP software. A detailed procedure for de-clustering is explained in Section 4.3.3. The homogenization of magnitudes is evaluated in the subsequent section, ensuring the reliability and consistency of the dataset used for further analysis.

Table 4.2 Summary of the raw EC from 1800 to 2021.

SI no.	Magnitude	Instrumental data sources					Literature
		USGS	ISC-Bulletin	ISC	GCMT	IRIS	
1.	$4 \le M \le 4.9$	228	274	830		212	92
2.	$5 \le M \le 5.9$	257	84	237	1	28	39
3.	$6 \le M \le 6.9$	10	6	17	1	2	5
4.	$7 \le M \le 7.9$	2	2	1		1	8
5.	$M \ge 8.0$	1	0	1			5
Total		498	366	1086	2	243	149

4.3.2 Homogenization of magnitudes

The raw earthquake catalog exhibits heterogeneity in terms of magnitude scales, including local magnitude (M_L), surface-wave magnitude (M_S), duration magnitude (M_D), body wave magnitude (M_b), moment magnitude (M_w), moment magnitude from inversion of the W-phase (M_{ww}), and centroid moment magnitude from the inversion of long-period surface waves (M_{wc}). To ensure consistency and comparability, the standardized magnitudes are categorized as reported magnitudes (M_{rep}) which include M_L, M_S, M_D, M_b, and M_m, and proxy values for moment magnitude (M_{wp}) which encompass M_{wL}, M_{ws}, M_{wd}, M_{wb}, and M_{wm}. A detailed breakdown of the dataset containing different magnitude types is presented in Table 4.3. Through this approach, the study achieves a harmonized representation of earthquake magnitudes for further analysis and interpretation.

Table 4.3 Different magnitude types in the raw EC.

Magnitude types	M_S	M_b	M_w	M_{wb}	M_{wc}	M_{ww}
No. of earthquakes	105	1814	408	2	7	8

In order to ensure meaningful analysis and capture the seismicity patterns of a region accurately, it is essential to apply a uniform magnitude scaling [138]. However, the limitations inherent in different magnitude scales, as reported by Das and Wason [139], can compromise the accuracy of converted magnitudes and lead to saturation effects in the case of large earthquakes. As a result, moment magnitude (M_w) is considered in this study due to its distinct advantages.

Moment magnitude directly derives from the seismic moment, which is a measure of the true size of an earthquake [140][141]. It is calculated based on the product of fault and rupture area, and unlike other magnitude types, it does not saturate at higher magnitude levels. Therefore, different scales of magnitudes utilized in this study are converted into a common scale, namely moment magnitude.

To establish the conversion equations for various magnitude types, regression analysis has been conducted at regional and global scales. Several studies, including [141-151], have developed these conversion relations. It should be noted that these equations may vary depending on source characteristics and stress drop [144], making regional conversion equations more preferable [152].

In this study, surface wave magnitude (Ms) and body wave magnitude (Mb) are converted to moment magnitude (Mw) using Equations 4.1, 4.2, and 4.3 from Scordilis [141]. By employing these conversion equations, the seismic magnitudes across different scales are standardized to moment magnitude, facilitating consistent and reliable analysis of seismic events.

$$M_W = 0.675 M_S + 2.10 \; For \; 3 \leq M_W \leq 6.1 \quad (4.1)$$

$$M_W = 1.01 M_S + 0.21 \; For \; 6.2 \leq M_W \leq 8.2 \quad (4.2)$$

$$M_W = 0.854 M_b + 1.26 \qquad \text{For } 3.5 \leq M_b \leq 6.2 \quad (4.3)$$

Meanwhile, local magnitudes (M_l) are changed to moment magnitudes (M_w) using Equation 4.4 from Deniz and Yucemen [153].

$$M_W = 1.57 M_l - 2.66 \quad (4.4)$$

Once the earthquake catalog is homogenized, the next step is to decluster the data by removing repeated and dependent events, ensuring a reliable and unbiased dataset for seismic hazard analysis.

4.3.3. De-clustering of catalogue

De-clustering is a crucial process that aims to separate dependent earthquakes, such as aftershocks and foreshocks, from independent earthquakes in the seismicity catalog [154]. These dependent events are influenced by previous earthquakes and are caused by factors like after slip, stress changes, and seismic swarms. On the other hand, independent events, such as the main shocks, are not triggered by preceding earthquakes but occur due to tectonic loading and seismic activity.

In this study, earthquake events were collected from various sources, which may contain dependent events like foreshocks and aftershocks. To ensure reliable results, the dataset was carefully examined to identify and remove duplicate events with similar or slightly different magnitudes. Specifically, 36 duplicate events were identified and eliminated using Microsoft Excel. After this step, the earthquake catalog consisted of 2,308 events.To further refine the dataset and eliminate dependent events, a de-clustering process was performed using the time–distance window method implemented in ZMAP software. Figure 4.1 provides a visual representation of the earthquake catalog before de-clustering, encompassing both dependent and independent events within a 300 km radius.

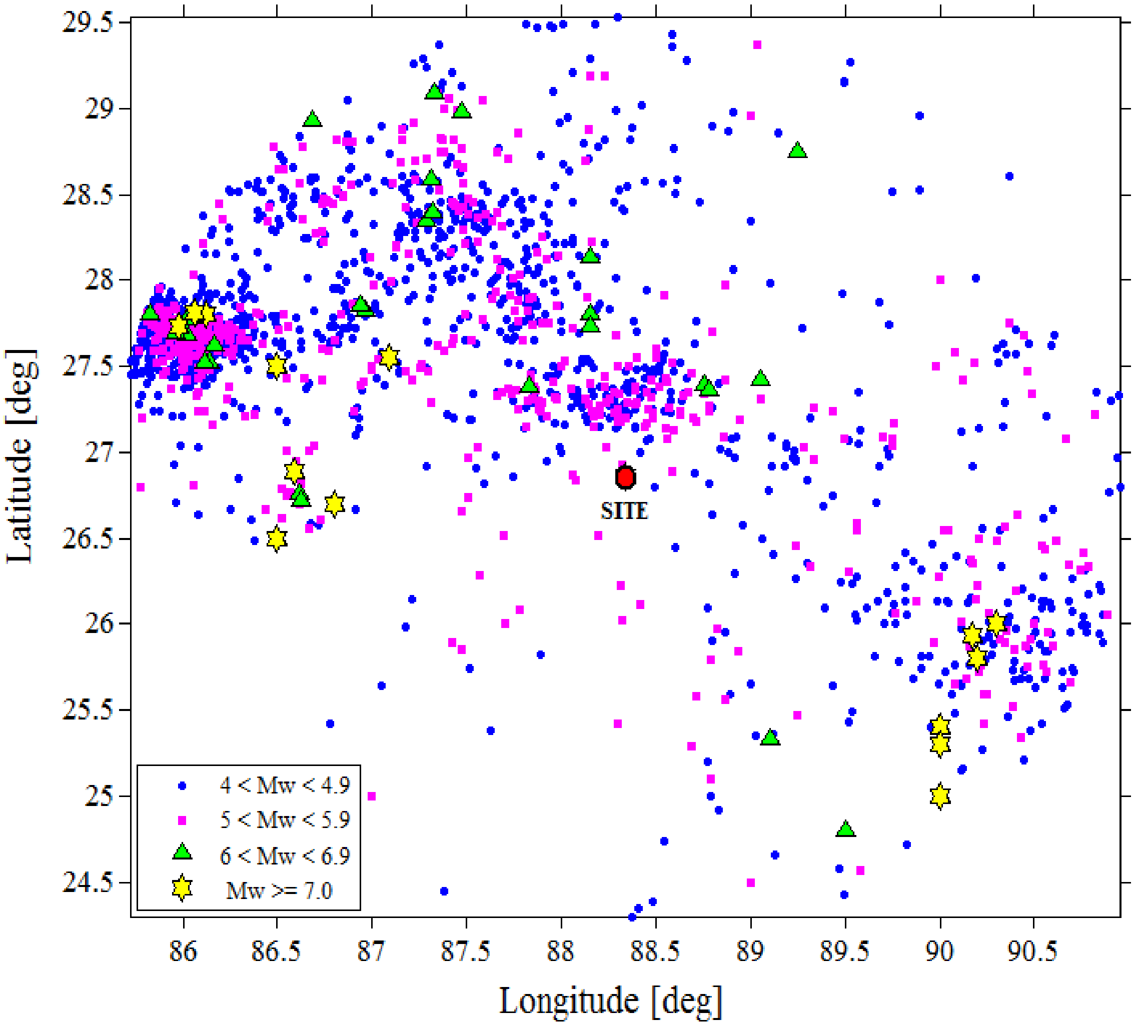

Figure 4.1 EC before de-clustering.

Various algorithms have been developed to separate dependent events from the raw seismicity catalog based on temporal and spatial variabilities. Knopoff [155] introduced an algorithm that removes aftershocks exhibiting a Poisson distribution. Gardner and Knopoff [156] proposed the window method, which utilizes time and distance as functions of the main event magnitude. Events falling within specific time and distance windows are considered main shocks, while the remaining events are categorized as dependent events. Over the years, researchers have proposed different de-clustering algorithms, ranging from deterministic to stochastic approaches [154] [157-160]. These algorithms vary in their spatio-temporal window parameters, leading to differences in result interpretation. Among the available methods, the window method by Gardner and Knopoff [156] and the cluster method suggested by Reasenberg [154] are commonly used due to their simplicity and availability of source codes. The Gardner and Knopoff [156] method focus on the main shock while disregarding secondary and high-order aftershocks. On the other hand, the Reasenberg algorithm employs a linked window method that connects aftershocks within an earthquake cluster, considering the highest magnitude as the main event.

In this study, the Gardner and Knopoff [156] window method is implemented to de-cluster the dependent events using ZMAP software [161]. Specific window sizes, as depicted in Equations 4.5 and 4.6, are employed by the algorithm. Table 4.4 presents the length and time window durations according to Gardner and Knopoff [156].

$$d = 10^{0.1238 * M_w + 0.983}, \tag{4.5}$$

$$t = 10^{0.032 * M_w + 2.7389} \left(if\ M_w \geq 6.5 \right), else\ t = 10^{0.5409 * M_w - 0.547}, \tag{4.6}$$

Where t is time in days, d is the distance in km, and M_w is the earthquake magnitude.

Table 4.4 Aftershock identification window [156].

Magnitude (M_w)	2.5	3	3.5	4	4.5	5	5.5	6	6.5	7	7.5	8
Length (km)	20	22.5	26	30	35	40	47	54	61	70	81	94
Time (days)	6	11.5	22	42	83	155	290	510	790	915	960	985

The raw earthquake catalog (EC), consisting of 2308 events, was processed using the Gardner and Knopff [156] window method within the ZMAP software. This de-clustering approach successfully identified approximately 1986 events (86.048%) as dependent events. The de-clustered catalog, depicted in Figure 4.2, shows 322 events represented by blue dots. Further analysis revealed the presence of more than six earthquake clusters, comprising a total of six events (1.8634%) as shown in Figure 4.3.

Following the de-clustering process, it was determined that 87.9119% of the events within the raw database, totaling 2308 events, were categorized as dependent events. The remaining 316 events were identified as main shock events, as illustrated in Figure 4.4. The magnitudes of the events before and after de-clustering are presented in Table 4.5. Additionally, Figure 4.5 provides a visual representation of the primary events within the study area.

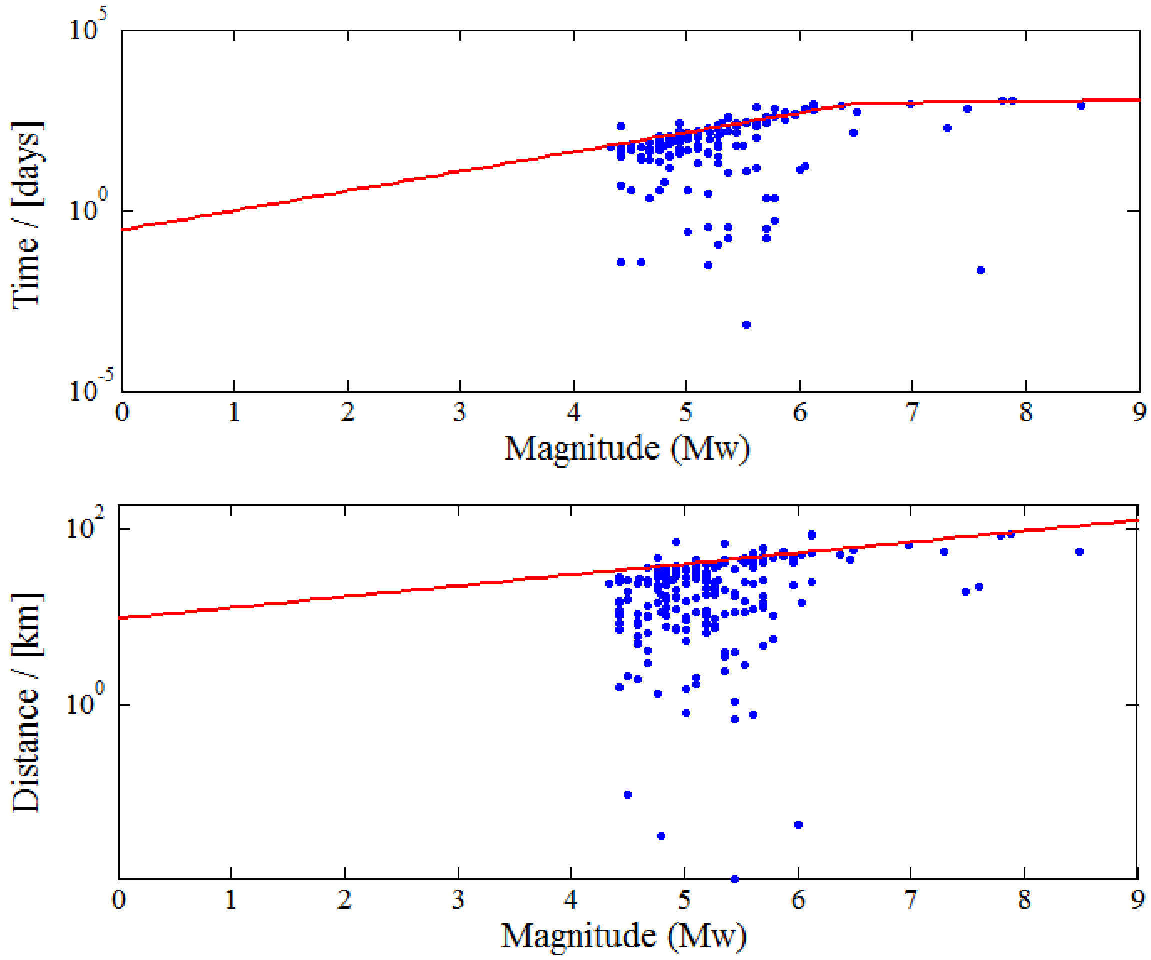

Figure 4.2 Time and distance window map displaying a de-clustered catalogue that contains 322 events.

Table 4.5 Before and after de-clustering earthquake events in the EC.

Magnitude (M_w)		4–4.9	5–5.9	6–6.9	7–7.9	>8.0
No. of events	Before de-clustering	1620	629	40	12	7
	After de-clustering	166	127	14	6	2

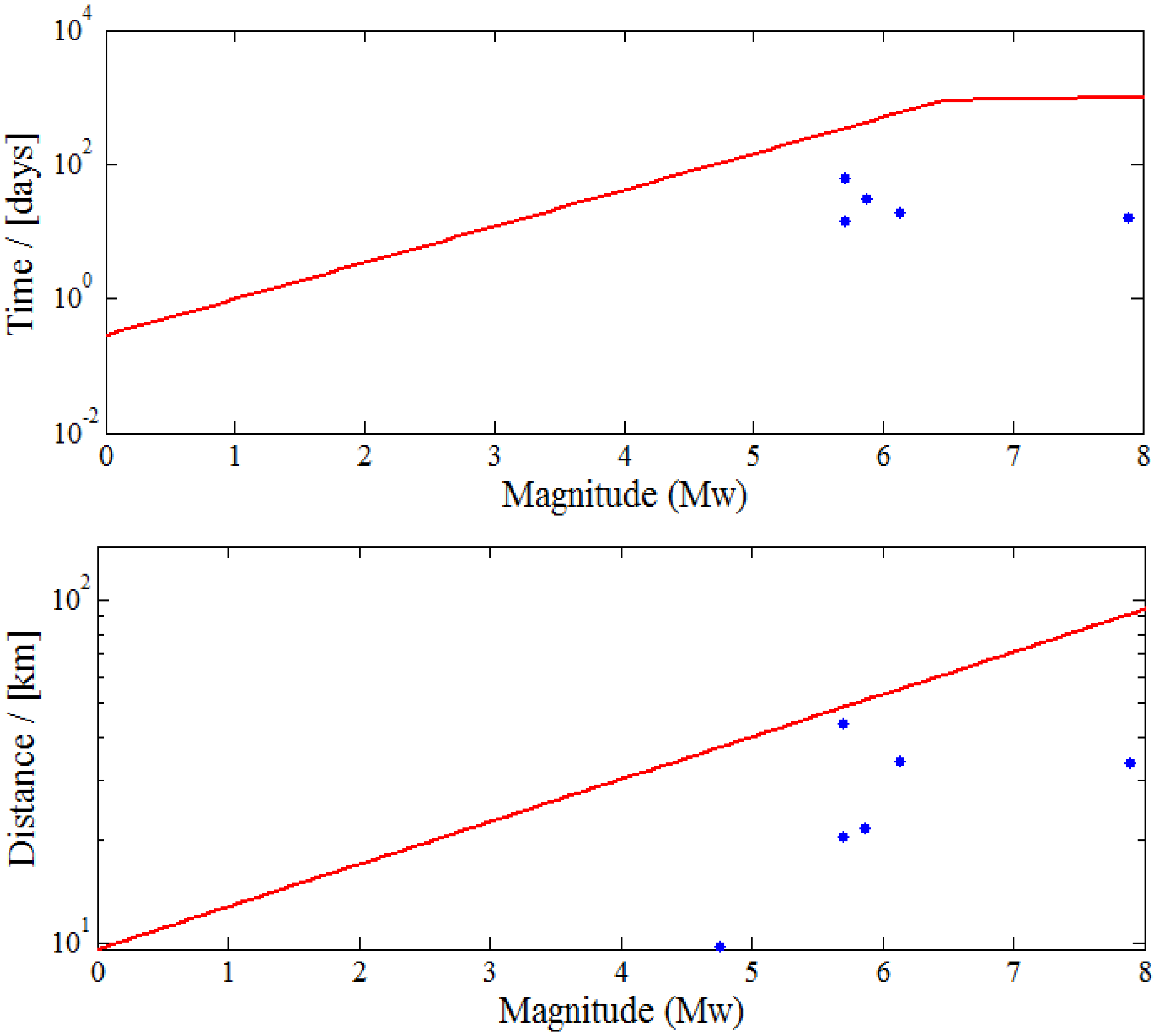

Figure 4.3 Time and distance window map displaying a de-clustered catalogue that contains six events.

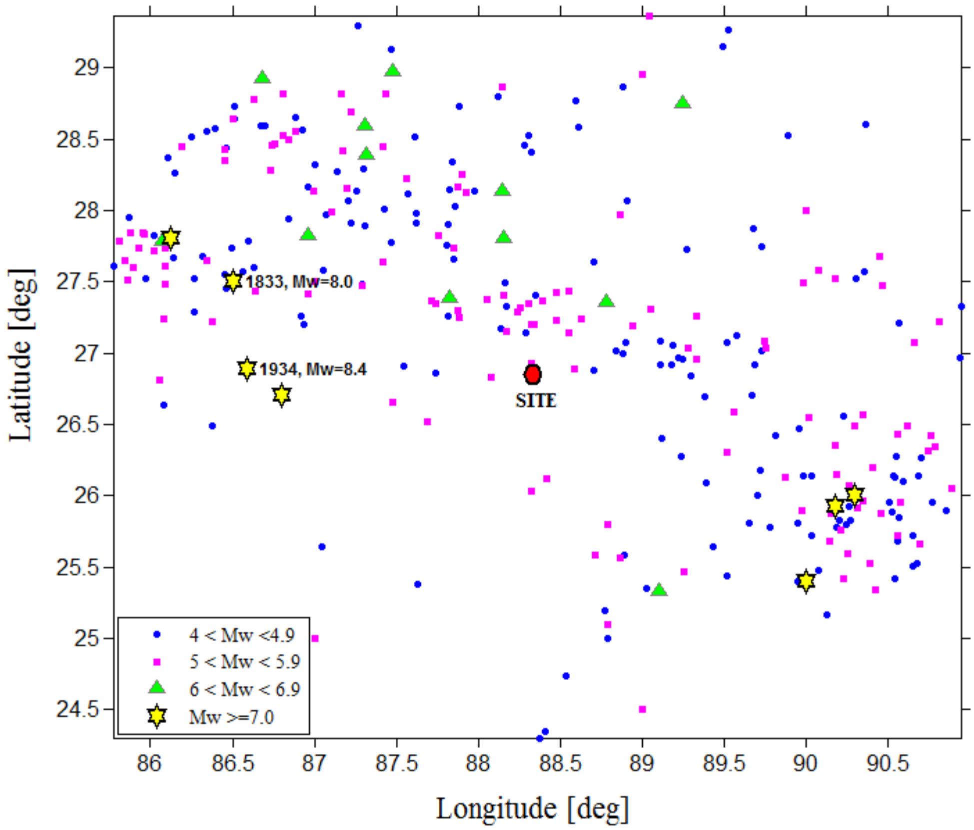

Figure 4.4 Distribution of 316 de-clustered main earthquake events within 300km of the site area.

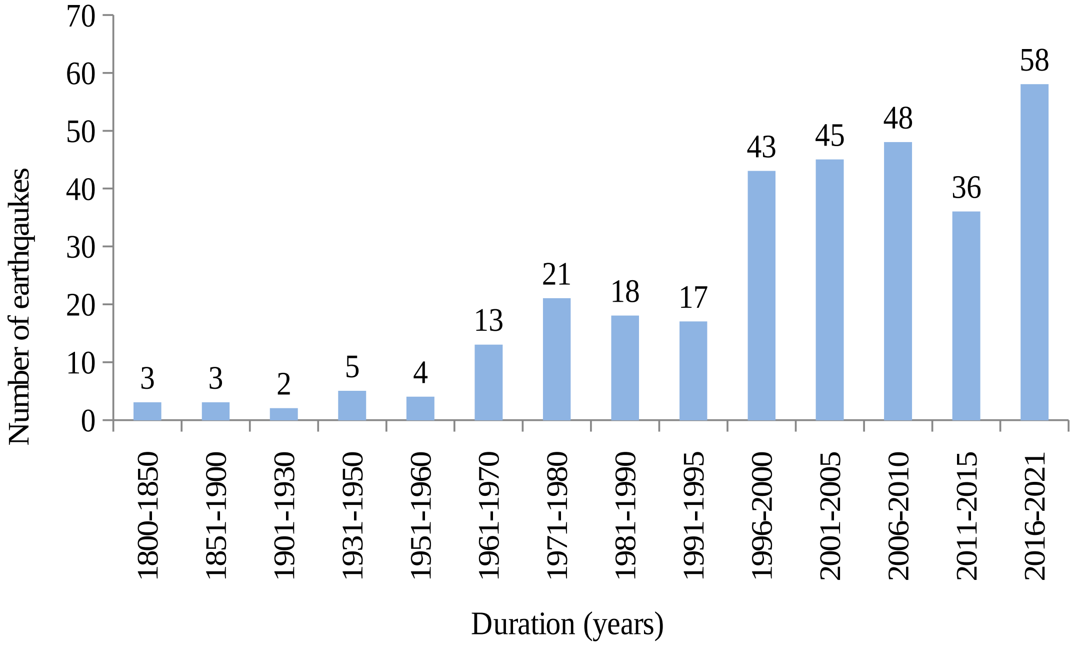

Figure 4.5 Bar chart of earthquake magnitude distribution with duration and frequency of occurrence.

4.3.4 Completeness check

The final earthquake catalog, obtained after de-clustering, is recommended for a quantitative assessment of completeness to ensure more accurate results, which are crucial for further hazard analysis. Utilizing the catalog directly may lead to underestimated outcomes due to potential gaps in event coverage or incomplete data for certain years. The irregularities in temporal and spatial monitoring network data coverage can result in missed events, particularly those of smaller magnitudes or those occurring concurrently with significant events.

To assess the completeness of earthquake data in terms of both quantity and quality across different magnitude ranges and time periods, statistical methods are employed. Two commonly used approaches for completeness assessment are based on magnitude and time. Regarding magnitude, the minimum magnitude in the catalog at which 100% of events are detected within a given space-time volume is determined, representing the magnitude of completeness (M_c). Events above Mc are considered as complete data, while those below M_c are either undetected by the network or unavailable in the records [162]. In terms of time-based completeness, two methods are widely used: the decade-based approach proposed by Stepp [163] and the yearly-based cumulative visual method introduced by Mulargia and Tinti [164].

In this study, the Stepp method was employed to assess the completeness of data within a specific time period. This method involves dividing the events into different magnitude classes with a designated time interval and determining the number of events per year in each magnitude class. The process takes into account the Poisson distribution, which is calculated using the following formula:

$$\lambda = \frac{1}{n}\sum_{i=1}^{n} x_i, \tag{4.7}$$

$$\sigma_\lambda = \sqrt{\frac{\lambda}{T}}, \tag{4.8}$$

where, λ is the mean rate ($\lambda = \sqrt{\frac{N}{T}}$), x_i is the number of events in each magnitude range per year, T is the duration, and σ_λ is the standard deviation. The EC is divided into four magnitude classes, and the distribution of seismic events by magnitude and time and standard deviation calculations are shown in Tables 4.6 and 4.7, respectively.

Table 4.6 Distribution of earthquake events by time and magnitude.

Time period	(T)	$4 \le M_w \le 4.9$		$5 \le M_w \le 5.9$		$6 \le M_w \le 6.9$		$M_w \ge 7.0$	
		N	λ =N/T	N	λ =N/T	N	λ =N/T	N	λ =N/T
2015–2021	6	39	6.5	21	3.5	3	0.5	1	0.16667
2010–2021	11	73	6.63636	26	2.36364	4	0.36364	2	0.18182
2005–2021	16	105	6.5625	39	2.4375	4	0.25	2	0.125
2000–2021	21	136	6.47619	52	2.47619	4	0.19048	2	0.09524
1995–2021	26	161	6.19231	67	2.57692	5	0.19231	2	0.07692
1990–2021	31	164	5.29032	75	2.41935	7	0.22581	2	0.06452
1980–2021	41	166	4.04878	89	2.17073	9	0.21951	3	0.07317
1970–2021	51	167	3.27451	108	2.11765	10	0.19608	3	0.05882
1960–2021	61	167	2.7377	118	1.93443	11	0.18033	3	0.04918
1950–2021	71	167	2.35211	122	1.71831	12	0.16901	3	0.04225
1930–2021	91	167	1.83516	123	1.35165	13	0.14286	6	0.06593
1900–2021	121	167	1.38017	124	1.02479	13	0.10744	6	0.04959
1850–2021	171	167	0.97661	126	0.73684	13	0.07602	7	0.04094
1800–2021	221	167	0.75566	127	0.57466	14	0.06335	8	0.0362

Table 4.7 Calculation of the completeness check by Stepp [166] method.

Time period	√T	$4 \le M_w \le 4.9$		$5 \le M_w \le 5.9$		$6 \le M_w \le 6.9$		$M_w \ge 7.0$	
		λ	σ_λ	λ	σ_λ	λ	σ_λ	λ	σ_λ
2015–2021	2.449	2.5495	1.04083	1.8708	0.76376	0.7071	0.28868	0.4082	0.16667
2010–2021	3.317	2.5761	0.77673	1.5374	0.46355	0.603	0.18182	0.4264	0.12856
2005–2021	4	2.5617	0.64043	1.5612	0.39031	0.5	0.125	0.3536	0.08839
2000–2021	4.583	2.5448	0.55533	1.5736	0.34339	0.4364	0.09524	0.3086	0.06734
1995–2021	5.099	2.4884	0.48802	1.6053	0.31482	0.4385	0.086	0.2774	0.05439
1990–2021	5.568	2.3001	0.4131	1.5554	0.27936	0.4752	0.08535	0.254	0.04562
1980–2021	6.403	2.0122	0.31425	1.4733	0.2301	0.4685	0.07317	0.2705	0.04225
1970–2021	7.141	1.8096	0.25339	1.4552	0.20377	0.4428	0.06201	0.2425	0.03396
1960–2021	7.81	1.6546	0.21185	1.3908	0.17808	0.4247	0.05437	0.2218	0.02839
1950–2021	8.426	1.5337	0.18201	1.3108	0.15557	0.4111	0.04879	0.2056	0.0244
1930–2021	9.539	1.3547	0.14201	1.1626	0.12187	0.378	0.03962	0.2568	0.02692
1900–2021	11	1.1748	0.1068	1.0123	0.09203	0.3278	0.0298	0.2227	0.02024
1850–2021	13.08	0.9882	0.07557	0.8584	0.06564	0.2757	0.02109	0.2023	0.01547
1800–2021	14.87	0.8693	0.05847	0.7581	0.05099	0.2517	0.01693	0.1903	0.0128

From Figure 4.6, the analysis shows that the collected data are complete for all magnitude ranges.

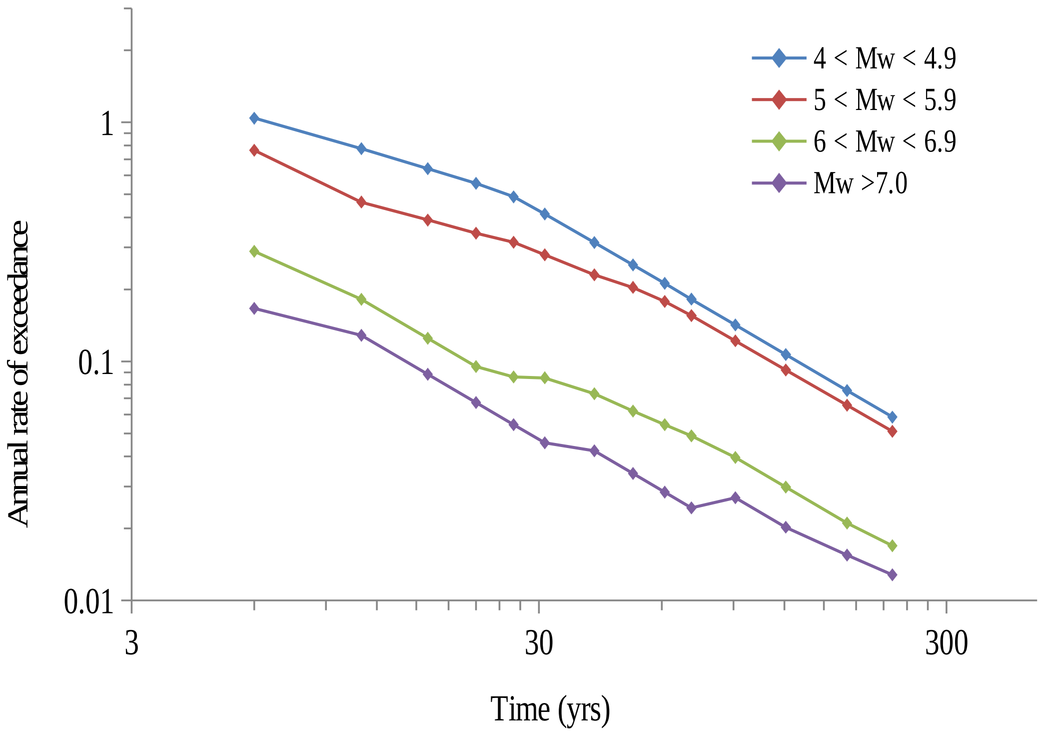

Figure 4.6. Data completeness using the method from Stepp [163].

Given that the dataset used in this study is deemed complete, the seismicity parameters are estimated using the Gutenberg and Richter [165] recurrence law. These seismicity parameters play a crucial role in both PSHA and FPSHA approaches. A comprehensive explanation of the estimation process for seismicity parameters can be found in Chapter 5.

4.3.5 Final Catalogue

Figure 4.7 presents the final catalogue, which has undergone homogenization, de-clustering, and completeness assessments. This catalogue encompasses a total of 316 seismic events spanning from 1800 to 2021, covering a period of 212 years. Within the final catalogue, there are 166 seismic sources with moment magnitudes ranging from 4.0 to 4.9, 127 events with magnitudes between 5.0 and 5.9, and 23 events of magnitude greater than 6.0. Notably, Figure 4.7 illustrates a notable increase in earthquake events of Mw 4.0 starting from the 19th century, with a continuous upward trend over time. Additionally, Figure 4.8 depicts the cumulative distribution of magnitudes over time, emphasizing events of $M_w \geq 7.0$.

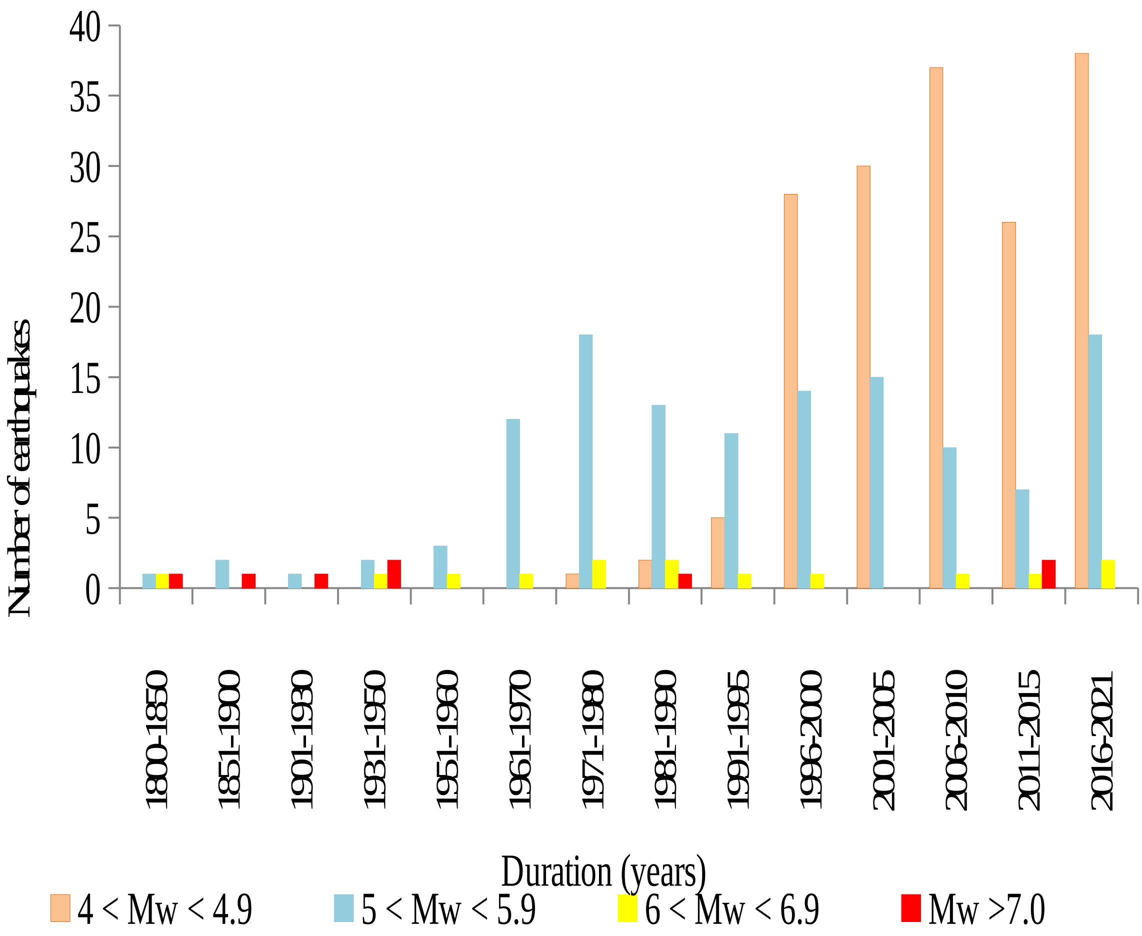

Figure 4.7 The final catalogue earthquake records will be distributed over time (from 1800–2019 with magnitudes ranging from 4.0 to 7.0).

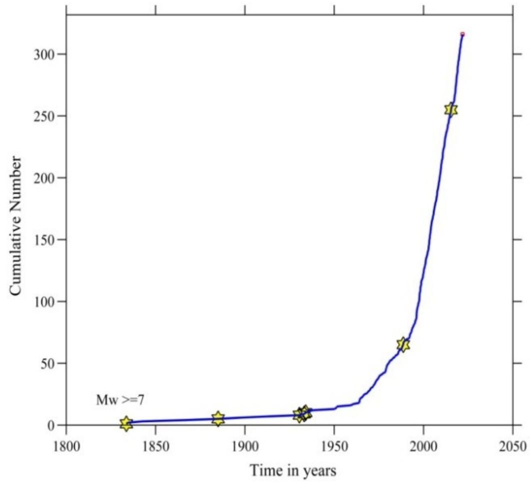

Figure 4.8 The cumulative distribution curve of the final catalogue.

4.4 Preparation of a seismo-tectonic map

Numerous researchers have dedicated their efforts to developing seismo-tectonic maps, each employing distinct temporal ranges, radial distances, and other considerations. In this study, a seismo-tectonic map encompassing a radius of 300km has been created using QGIS software. The map incorporates 20 prominent linear tectonic features and depicts 316 earthquake events as point sources, spanning the time period from 1800 to 2021. Figure 4.9 provides a visual representation of the seismo-tectonic map, illustrating the integration of all seismo-tectonic features alongside significant earthquakes measuring 4.0 magnitude and higher.

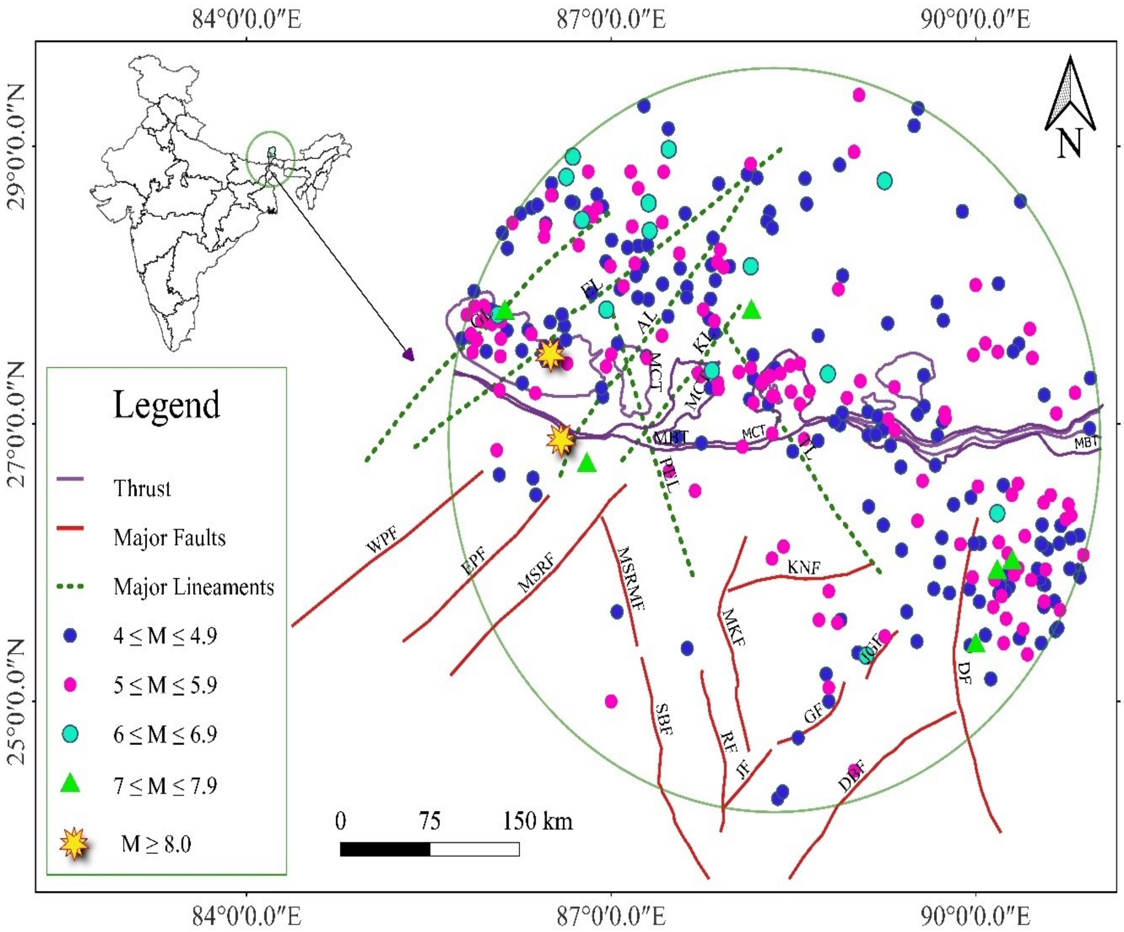

Figure 4.9 Seismo-tectonic map of the study area.

4.5 Selection of attenuation relation

The estimation of accurate SA or PGA is important in SHA. Non-availability of hypo central distances and lack of recorded data are observed in the Himalayan region due to a lack of strong-motion data for a wide range of magnitudes making the hazard estimation more challenging [167]. Computation of a ground motion for all possible fault ruptures incorporating many uncertain parameters is impossible. Given the various uncertainties and complexity problems, the regression equations help theoretically resolve this issue. The equations are also called GMPEs, ground motion models, attenuation relations, or engineering models developed by statistical analysis. The GMPEs helps to estimate the amplitude change when an earthquake occurs away from the fault with a certain magnitude at a given distance. The GMPEs are developed based on records of either the observed or the synthetic data [168].

Due to the scarcity of strong-motion data, the stochastic method is commonly used to simulate synthetic ground motions. Since the installation of 300 strong-motion seismographs by IIT Roorkee in 2004, most researchers have developed GMPEs based on these actual ground motion datasets in the Himalayan region. Some GMPEs have been developed using recorded and synthetic earthquake data. Synthetic data is generated without recorded data, relying on different models. A few GMPEs have been developed based on simulated data [169][170]. The Next Generation Attenuation Relations have been designed to improve the estimation and prediction of ground motions [171] by modifying or updating previously published equations [172][173]. These GMPEs are widely used in seismic hazard studies to develop hazard maps.

The GMPE is a crucial equation that estimates the conditional distribution of ground motion at a specific site, considering earthquake ground motion parameters. The dependent parameters include amplitude, frequency, and duration, while the independent parameters consist of magnitude, source-to-site distance, depth, and faulting style. Selecting reliable parameters with minimum standard quality is essential for unbiased predictions [174]. The equation incorporates several factors, such as logarithm peak ground parameter (Y), earthquake magnitude (m), source-to-site distance (R), type of faulting, damping ratio, site classification (A , B and C), and coefficients (C1 and C2) derived from regression analysis. The difference between observed and predicted values is denoted as ε, and the standard deviation σlnY represents the level of uncertainty [27].

As discussed in previous chapters, India encompasses various tectonic regions with different attenuation factors based on its diverse tectonic framework. Consequently, different GMPE’s should be employed according to specific regions or areas. The proper selection of GMPE’s is a critical step in SHA and rapid hazard assessment. Moreover, the accuracy of GMPE’s relies on observed and available datasets, the size of the database, and regular updates as the database grows annually. Although different GMPE’s have been developed for various parts of India, the availability of region-specific GMPE’s is limited when considering local site effects [67][175]. GMPE’s have their limitations and advantages, encompassing a restricted range of regional source data, magnitudes, and distances.

For our study area in the Eastern Himalayas of the Darjeeling-Sikkim region, several GMPE’s developed specifically for the Himalayan region, Eastern Himalayan region, Sikkim region, Darjeeling region, and West Bengal region have been thoroughly studied. Suitable GMPE’s have been selected based on their applicability to the site. Many researchers have developed specific GMPE’s for the Himalayan regions at both the bedrock and surface levels, utilizing simulated and recorded earthquake data. The region-specific GMPE’s are developed by Singh et al. [167] for the Himalayan region, Sharma [176] for the Himalayan region, Jain et al. [177] for the Central Himalayan, Saini et al. [178] for the Himalayan region, Nath et al. [179] for the Sikkim Himalayas, Sharma and Bungum [180] for the Himalayan region, Das et al. [181] for Northeast India, Sharma et al. [182] for the Himalayan region, Baruah et al. [183] for Northeast India, Nath et al. [170] for Guwhati, Gupta [184] Indo-Burmese sub-duction zone, NDMA [169] for India, Nath et al. [185] for the Shillong region, Northeast India, Anbazhagan et al. [186] for the Himalayan region, Kumar et al. [187] for Northeast India, Rebecca et al. [188] for Northeast India, Bajaj and Anbazhagan et al. [189] for the Himalayan region, and Kundu [190] for the Himalayan region.

Several GMPE’s developed for other regions worldwide, considering similar tectonic conditions, have been applied to the Himalayan region and utilized in seismic hazard studies. These include GMPE’s by Youngs et al. [191], Ambraseys et al. [192], Kanno et al. [193], Zhao et al. [194], Campbell and Bozorgnia [195], Idriss and An [196], Akkar and Bommer [197], among others. However, selecting appropriate region-specific equations for hazard analysis in the Himalayan region is challenging. Therefore, the limitations, advantages, and disadvantages of each equation are carefully examined to identify the most applicable GMPE for the present study. Four GMPEs developed by Toro [200], NDMA [67], Anbazhagan et al. [186], and Kanno et al. [193] are considered suitable for the Eastern Himalayan region [201].

Among the regional GMPE’s mentioned above, only Das et al. [65], NDMA [67], Anbazhagan et al. [186], and Bajaj and Anbazhagan et al. [189] are capable of predicting PGA values up to a distance of 300 km. However, Anbazhagan et al. [205] is specific to a shear wave velocity of 2000 m/s. Furthermore, an efficacy test proposed by Delavaud et al. [198] was conducted by Nath and Thinbaijam [199] for 16 GMPE’s from different tectonic provinces, including regional and global GMPE’s. They identified the top-ranked and most suitable five GMPE’s for the Himalayan region: Kanno et al. [193], Campbell and Bozorgnia [195], Sharma et al. [182], Akkar and Bommer [197], and Idriss and An [196].

Anbazhagan et al. [186] compared 13 GMPEs, including the five highly ranked GMPE's listed by Nath and Thingbaijam [199], as well as eight regional GMPE's. They also considered GMPEs by Nath et al. [179], Das et al. [181], Sharma and Bungum [180], Nath et al. [170], Sharma et al. [182], Gupta [184], NDMA [67], and Iyenger and Ghosh [202] for Delhi in their analysis. GMPEs by Sharma et al. [176] and Singh et al. [167] were excluded from the study due to the absence of a standard error term in the earthquake dataset. The GMPE by Baruah et al. [183] was also not considered because it is only valid up to 5.0 Md. The comparison revealed that the regional GMPEs cannot predict hazard values as accurately as the highly ranked GMPE's, leading to the development of a new regional GMPE, ANBU13, for the Himalayan region.

The ANBU13 GMPE is developed based on simulated and recorded data from 14 or 13 earthquakes occurring at different segments of the Himalayan belt at the bedrock level. Synthetic ground motions are generated for each earthquake to fill the gaps in recorded data, based on the FINISM model. ANBU13, along with the five highly ranked GMPEs listed by Nath and Thingbaijam [199], is validated and compared with PGA values from three recorded earthquake events at rock and soil sites (2008 Pithoragarh EQ [Mw 4.3], 2011 India–Nepal EQ [Mw 5.7], and Sikkim EQ [Mw 6.8]). The comparison shows that ANBU13 GMPE and the first-ranked Kanno et al. [193] GMPE match well with the recorded PGA data, while the other GMPEs either underestimate or overestimate the values. ANBU13 is capable of predicting PGA values close to the recorded data and exhibits compatibility with a magnitude range of Mw 4.3 to 8.7, even though it is developed for Mw 5.3–8.7.

In addition, a quantitative analysis is performed on two regional GMPE's, Das et al. [65] and NDMA [67], as they are the only equations capable of predicting PGA values up to 300 km. The analysis concludes that ANBU13 GMPE provides better predictions for spectral acceleration (up to 2 s) and PGA values compared to any other region-specific equations. ANBU13 is considered the primary choice for the present study, covering a magnitude range of M_w 4–8.7 up to a distance of 300 km. The ANBU13 equation at the bedrock level is expressed as follows:

$$logY = c_1 + c_2 M - b\,log\left(X + e^{c3M}\right) + \sigma, \tag{4.9}$$

$$X = \sqrt{\left(R^2 + h^2\right)},$$

Where Y is the SA (g); c1, c2, and c3 are the regression coefficients shown in Table 4.8; M is the moment magnitude; R is the closest distance to rupture (km); h is focal depth (km); σ is the standard error, and b is the decay parameter.

Table 4.8 Coefficients used in GMPE for the different periods proposed by Anbazhagan et al. [186]

Period (s)	c_1 (std.err.)	C_2 (std.err.)	C_3 (std.err.)	b	σ
0	−1.283(0.093)	0.544(0.015)	0.381 (0.030)	1.792	0.283
0.1	−1.475(0.098)	0.544(0.015)	0.544 (0.015)	1.585	0.307
0.2	−1.366(0.107)	0.546(0.017)	0.546 (0.017)	1.641	0.318
0.3	−1.982(0.097)	0.542(0.016)	0.542 (0.016)	1.385	0.298
0.4	−2.602(0.096)	0.555(0.015)	0.555 (0.015)	1.178	0.298
0.5	−2.980(0.095)	0.606(0.015)	0.606 (0.015)	1.206	0.292
0.6	−3.00(0.10)	0.623(0.016)	0.623 (0.016)	1.258	0.299
0.8	−3.812(0.096)	0.670(0.015)	0.670 (0.015)	1.080	0.296
1	−4.357(0.099)	0.731(0.016)	0.731 (0.016)	1.114	0.300
1.2	−4.750(0.099)	0.766(0.016)	0.766 (0.016)	1.082	0.298
1.4	−5.018(0.099)	0.779(0.016)	0.779 (0.016)	1.032	0.303
1.6	−5.219(0.102)	0.824(0.016)	0.824 (0.016)	1.123	0.306
1.8	−5.327(0.105)	0.840(0.017)	0.840 (0.017)	1.139	0.313
2	−4.920(0.122)	0.953(0.022)	0.953 (0.022)	1.617	0.310

This comprehensive review and analysis of various GMPE’s in the Himalayan region establishes the significance of selecting appropriate equations for seismic hazard assessment and emphasizes the compatibility of ANBU13 GMPE for the study area. The ANBU13 GMPE, developed by Anbazhagan et al. [186], is used in DSHA, PSHA, and FPSHA to estimate PGA and 5% damped elastic pseudo response SAs (0-2 s period) in the Himalayan region. It is a reliable and compatible equation for seismic hazard assessment in the further study area.

4.5.1 Distance measure (R)

The distance parameter (R) plays a crucial role in the attenuation equation, and it is important to use the appropriate distance for each specific GMPE. Different distance measures have been developed to account for rupture extension over several kilometers. These include epicenter distance (R_{epi}), hypo-central distance (R_{hyp}), Joyner-Boore distance (R_{jb}) (closest distance to the surface projection of rupture), closest distance to the rupture surface (R_{rup}), and distance to the zone of energy release, as depicted in Figure 4.10. The choice of distance parameter depends on the specific GMPE selected. Generally, for point sources, R_{hyp} and R_{epi} are used, while R_{jb} and R_{rup} are employed for measuring distances to the rupture plane.

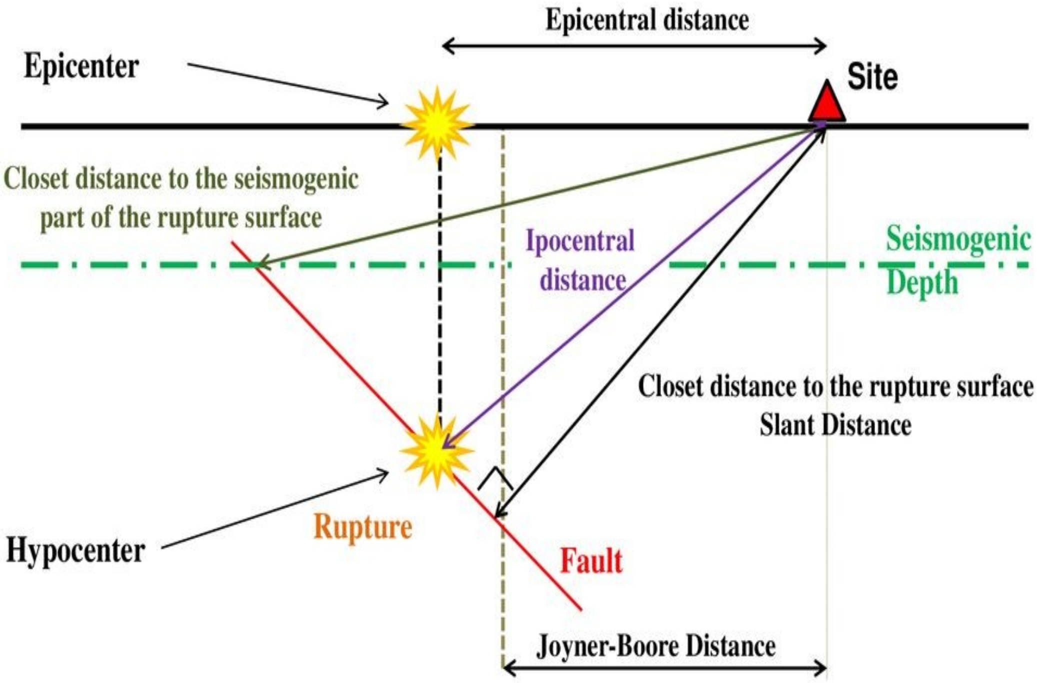

Figure 4.10 Earthquake characteristics [206].

According to the ANBU 13 GMPE (Equation 4.9), the distance parameter utilized in the equation is the closest distance to the rupture surface, denoted as R_{rup}. To calculate this distance, various physical equations are employed. In this study, the QGIS vector analysis-distance matrix module is utilized to compute the nearest distances from the site to the seismic sources. The relationship between earthquake magnitudes and the corresponding distances is illustrated in Figure 4.11.

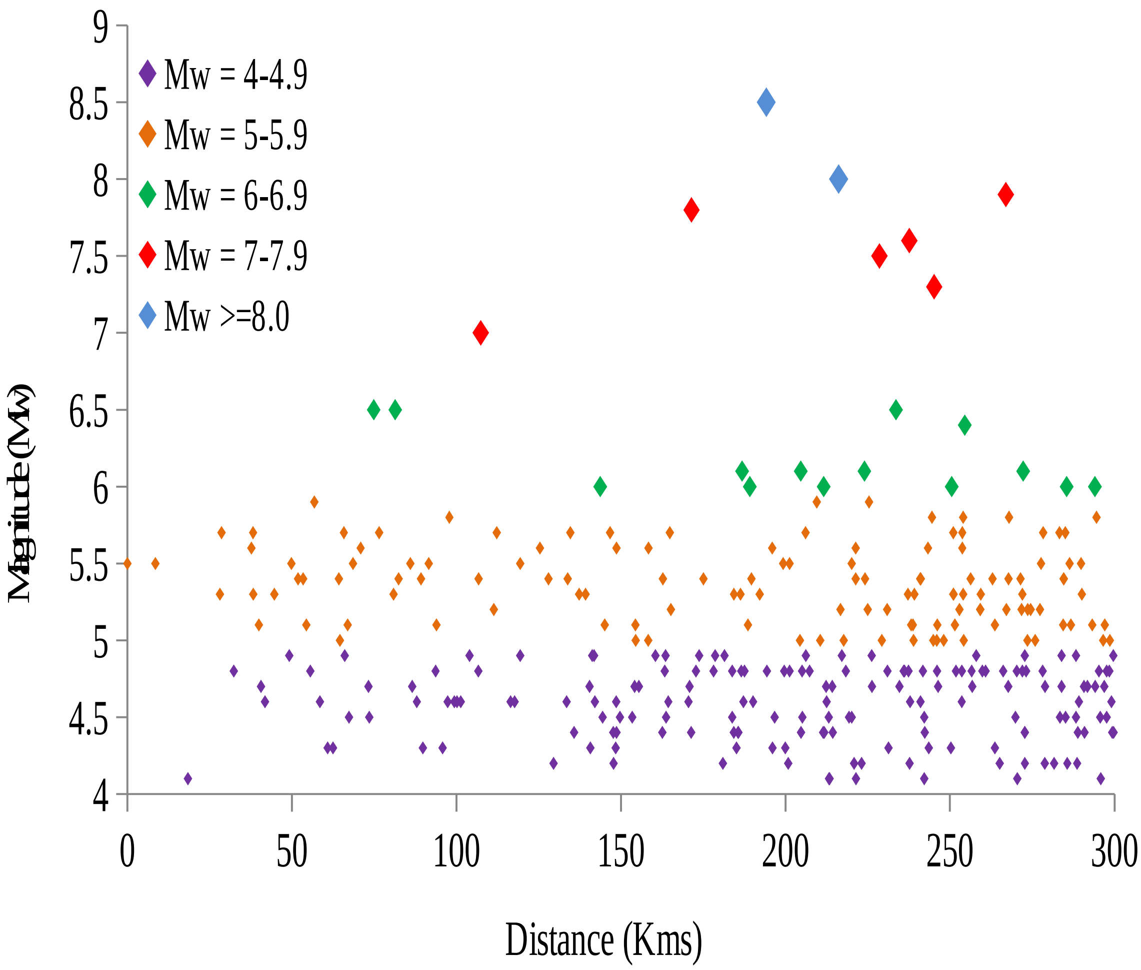

Figure 4.11 Distribution of earthquake magnitudes with distance.

4.5.2 Local site effects

The seismic hazard assessment is influenced not only by parameters such as distance, magnitude, and depth, but also by the local geology and subsurface lithology, which introduce significant variations in site conditions. These variations result in different spectral acceleration values from the surface to the bedrock level. Shear wave velocity (V_s) is commonly used to define local site effects and is a crucial parameter for assessing the dynamic properties of subsurface layers, including shear strength and stiffness. The average shear wave velocity within the top 30 meters of a site, known as V_{s30}, is widely adopted as a descriptive variable for site effects in various GMPE studies [203][189] and others. Consequently, the selection of a suitable GMPE requires consideration of the V_s value.

Numerous empirical studies and geotechnical and geophysical investigation techniques exist to measure V_s. The standard penetration test and multichannel surface wave analysis are commonly employed geotechnical methods for generating V_s profiles. V_s can be estimated either at the bedrock depth (V_{sR}) or at the top 30-meter depth (V_{s30}). The V_s values vary from soil strata to bedrock based on the stiffness of the materials. V_{s30} is an internationally recognized parameter widely used in seismic site classification, microzonation, and site response studies [207]. Notable codes and organizations such as Eurocode 8, the American Society of Civil Engineers (ASCE), the National Earthquake Hazard Reduction Program (NEHRP), and the Electrical Power Research Institute (EPRI) incorporate V_{s30} for site classification. These seismic design codes classify sites into different classes based on site factors estimated through empirical and analytical studies utilizing available strong motion data, with ongoing improvements as new data becomes available.

In this study, the average crustal shear wave velocity (V_s) beneath the sediment layers of the Darjeeling–Sikkim Himalaya region was analyzed using data from temporary seismic stations and available seismographs, yielding a value of 3.59 km/s (Acton et al., 2011). The V_{s30} value for Darjeeling falls into site class C, as determined by an empirical equation based on peak parameters of the horizontal-to-vertical spectral ratio (HVSR) [205]. Site class C aligns with the provisions of the NEHRP building code [208], which categorizes sites into five classes: A, B, C, D, and E, corresponding to V_{s30} value ranges of V_{s30} >1500 m/s (hard rock), 1500 m/s > V_{s30} > 760 m/s (rock with moderate weathering), 760 m/s > V_{s30} > 360 m/s (very dense soil and soft rock), 360 m/s > V_{s30} > 180 m/s (stiff soil), and V_{s30} < 180 m/s (soft clay soil). Therefore, this study falls within the V_{s30} range of 360 m/s to 760 m/s. The comparison of the GMPE with recorded data from site class C shows good agreement [186].

4.5.3 Depth measures

The selection of earthquake focal depth is a crucial aspect of seismic hazard assessment (SHA). Focal depths are categorized into three types: shallow (< 70 km), intermediate (70–300 km), and deep (> 300 km). In SHA, the preferred approach is to consider the least possible focal depth [186] or to account for different depth ranges.

In the provided seismic hazard analysis, the earthquake catalog has been classified based on depth ranges, as presented in Table 4.9. Shallow focal depths contain earthquakes with magnitudes greater than 5, while a few earthquakes with magnitudes above six are found in the intermediate focal depth. No earthquakes have been observed in the deep focal depth category.

Table 4.9 Details of earthquake records with focal depths.

Magnitude classes	Depth ranges of earthquake		
	Shallow (0–70km)	Intermediate (71–300 km)	Deep (>300 km)
$4 \leq M_w \leq 4.9$	162	4	0
$5 \leq M_w \leq 5.9$	123	4	0
$6 \leq M_w \leq 6.9$	12	2	0
$7 \leq M_w \leq 7.9$	6	0	0
$M_w \geq 8.0$	2	0	0

Figure 4.12 illustrates the distribution of earthquake magnitudes according to focal depth, ranging from 0 km to 150 km. Approximately 80% of the earthquake magnitudes occur at shallow focal depths, with 50% occurring below 20 km and 30% within the depth range of 40–70 km. The remaining 20% of earthquake magnitudes are associated with intermediate focal depths. The average depth for the study area was determined to be 30 km.

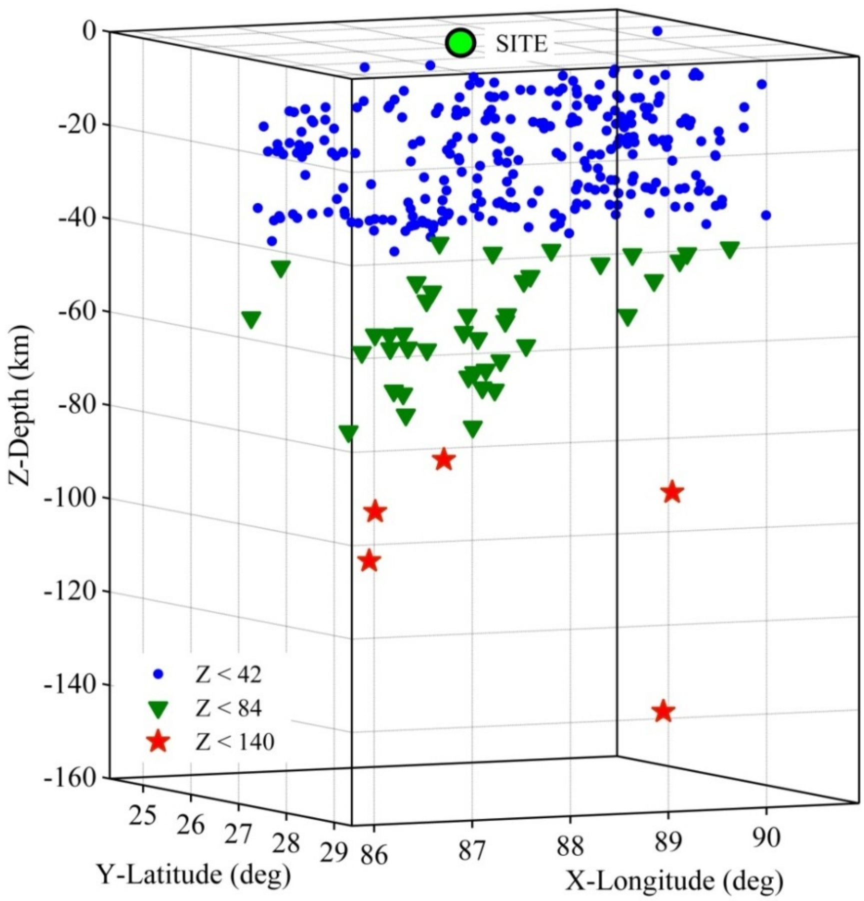

Figure 4.12 3D view of the distribution of earthquakes beneath the earth's surface.

Therefore, in this study, the depth for each earthquake event is considered based on the appropriate focal depth as obtained from seismological databases (refer to Annexure-A), with a specific focus on fault depths within the range of 30 km. This approach is adopted to ensure accurate estimation of seismic hazard and to mitigate the risk of incorrect hazard assessment.

4.6. Summary and Conclusion

This chapter presents a comprehensive seismic hazard analysis (SHA) that encompasses the framework and methodologies employed. The key inputs in SHA include the earthquake catalog (EC), local site effects, depth range, distance, and the selection of a suitable Ground Motion Prediction Equation (GMPE). The preparation of a refined EC involves meticulous data collection, homogenization, de-clustering, and completeness verification.

The seismic point sources are gathered from instrumental and historical databases, spanning a data period of 212 years (1800-2021), resulting in a collection of 2308 raw earthquakes. Additionally, 30 significant tectonic sources are compiled from the SEISAT database of India to form linear seismic sources. The completeness of the earthquake catalog is evaluated using Stepp's method, confirming the data's completeness within each magnitude class. Consequently, the final EC comprises 316 earthquakes and 20 active tectonic sources.

Moreover, a thorough examination of previous attenuation relationships is conducted to select the most suitable GMPE for the study area. The ANBU-13 equation is chosen as it demonstrates optimal performance for earthquake magnitudes ranging from 4 to 8.7 at distances up to 300 km. The analysis in this chapter also includes the assessment of the shortest distance between the rupture and the site.

The final EC, selected GMPE, distance to the site, and focal depths constitute crucial input data utilized in the subsequent chapters dedicated to deterministic seismic hazard analysis (DSHA), probabilistic seismic hazard analysis (PSHA), and finite-fault seismic hazard analysis (FPSHA). These chapters, namely Chapters 5, 6, and 7, provide detailed information regarding the utilization of these input data in the respective analyses.

Chapter 5

Deterministic Seismic Hazard Analysis

5.1 Introduction

In response to the significant earthquake events and the resulting loss of human life and property in India, seismic hazard studies have become essential over the past decade. Deterministic seismic hazard maps for the Indian region have been prepared using the deterministic seismic hazard analysis (DSHA) approach. However, broad zoning studies have been deemed unscientific and have underestimated the design peak ground acceleration in high seismicity regions (Naik and Choudharuy, 2015; Iyengar and Ghosh, 2004). Therefore, it is imperative to develop regional hazard maps that consider local seismo-tectonic settings.

DSHA provides a simplified framework that requires minimal information to estimate site-specific seismic hazard, primarily influenced by the maximum hazard posed by the nearest controlling seismic source. This approach ensures that each seismic source is assigned the maximum earthquake potential by considering critical scenarios at the closest possible distance to the site. The fundamental concept in DSHA involves determining the worst-case ground motion associated with the highest maximum magnitude (M_{max}) at the shortest distance (R_{min}) from the seismic source to the site, considering various earthquakes (Kramer, 1996).

A comprehensive review of previous deterministic studies is presented in Chapter 2, Section 2.3.1.1.1. While some seismic studies in the present study area have utilized a probabilistic approach, fewer attempts have been made using a deterministic approach. Therefore, this chapter aims to develop hazard maps for deterministic seismic hazard (DSH) analysis in the study area and its surrounding regions within a distance of 300 km.

For this purpose, 15 active seismo-genic sources with observed magnitudes greater than 5.0 have been carefully selected. The maximum magnitude has been determined through different deterministic and probabilistic methods. The seismic data collected from various sources spanning the period from 1800 to 2021, as explained in detail in Chapter 3, have been utilized. The shortest distance from each seismic source to the site has been estimated, and the ANBU-13 GMPE has been employed to predict strong motion characteristics. The DSHA approach has been utilized to estimate the peak ground acceleration (PGA) hazard and response spectrum maps for the study area.

Overall, this chapter focuses on the development of hazard maps using the DSHA approach, considering the specific characteristics of the study area and incorporating essential seismic data, source-to-site distances, and ground motion predictions provided by the ANBU-13 GMPE.

5.2 Methodology and procedure of DSHA

The deterministic seismic hazard analysis (DSHA) is an approach commonly used in seismic hazard studies. This approach involves assessing the peak ground acceleration (PGA) parameters by considering the knowledge of seismic sources and attenuation equations.

As outlined by Kramer [27], the DSHA methodology consists of four main steps, which are illustrated in Figure 5.1:

1. Identification of all potential seismo-tectonic sources located in the vicinity of the site.
2. Determination of the distance (R) from the site to each seismic source and estimation of the maximum possible earthquake magnitude ($M_{max)}$ associated with each source.
3. Calculation of ground motion values, such as PGA, at a given magnitude and distance using selected ground motion prediction equations (GMPE's). This step involves determining the earthquake scenario that controls the ground motion at the site.
4. Presentation of the hazard results in the form of PGA and spectral acceleration hazard maps, as well as PGA curves.

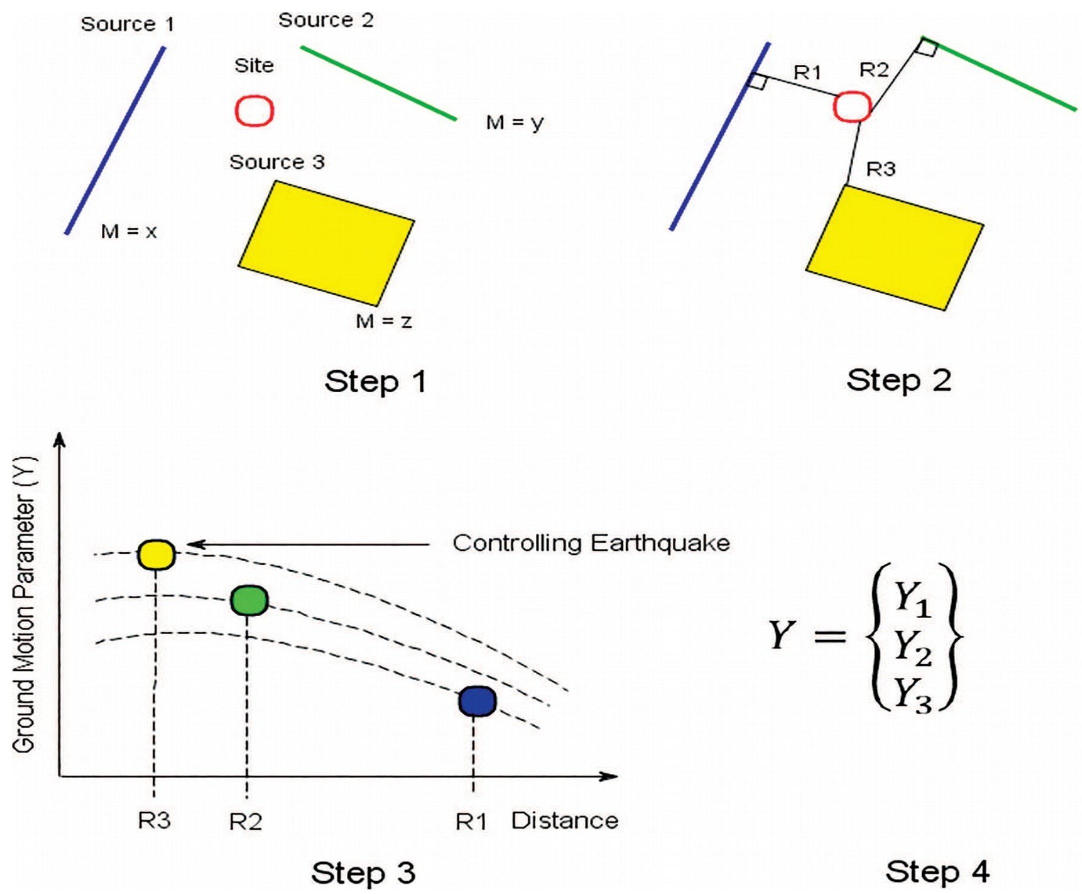

Figure 5.1 Steps involved in DSHA (Source: Nitish Puri, 2020).

The DSHA procedure, while relatively straightforward to implement, involves subjective decisions and relies on collective knowledge for estimating the Maximum Expected Earthquake (MEE). In some regions, it is referred to as the Maximum Credible Earthquake (MCE) due to the use of deterministic methods to limit excessively high values associated with the 2475-year return period in probabilistic approaches. The implementation of this mechanism varies across different researchers and geographic locations, and there is limited documentation in the literature regarding its application.

In this study, the DSHA calculations were performed using Microsoft Excel and QGIS tools, enabling detailed analysis and evaluation. These software tools facilitated the necessary computations and spatial analysis required for the seismic hazard assessment.

5.3 Application of DSHA on the study area

5.3.1 Identification of Seismo-tectonics

The first step in the Dynamic Seismic Hazard Analysis (DSHA) is to identify and select potential seismic sources within the study area, which spans 300 kilometers. We obtained this information from the Seismo-tectonic Atlas of India [125], and you can find more details in Chapter 4, section 4.3.1.1. We selected a total of 15 active linear sources with magnitudes greater than 5.0 for further analysis. You can refer to Table 4.1, S. No:1-15 for the specific details of these sources. After selecting the seismic sources, we evaluated the maximum magnitudes for each tectonic fault. These maximum magnitudes play an important role in the analysis.

5.3.2 Estimation of Maximum earthquake magnitude (M_{max})

The determination of the maximum possible magnitude (M_{max}) is crucial in assessing the seismic potential of a source zone or area, as it represents the highest magnitude earthquake that the source is capable of generating. It serves as a threshold beyond which earthquakes are not expected to occur with greater magnitude [186][211]. Accurate estimation of M_{max} is essential in various seismic and engineering applications to ensure realistic assessments and avoid overestimation of earthquake magnitudes [212].

Initially, M_{max} is often evaluated using historical earthquake records. The largest observed earthquake within a specific source zone is considered as the maximum earthquake magnitude (M_{max}) [3]. However, this method provides a conservative lower bound for M_{max} [212]. Another approach, known as the incremental method, involves incrementing the maximum observed magnitude (M_{obs}) by a certain factor (ranging from 0 to 3.2) based on seismicity values [213]. However, results obtained through this method are inconsistent, often leading to M_{max} estimates exceeding M_{obs} [212].

Recognizing the significance of determining the maximum magnitude for engineering applications, new methods have been developed, falling into two categories: deterministic and probabilistic. These approaches aim to provide more refined estimations of M_{max}.

5.3.2.1 Deterministic approaches

The deterministic approach in estimating the maximum magnitude (M_{max}) is commonly employed and relies on empirical relations. These relations establish correlations between magnitude and various fault rupture parameters, which are based on key geometric characteristics of faults such as rupture length, rupture area, rupture width, slip rate, and surface displacement [214] [215] [216] [217] [218] [219] [220] [221] [222]. Among these parameters, rupture length is frequently used as a fundamental feature for calculating M_{max}. It is important to note that these empirical relations vary depending on fault parameters and seismic regions.

In some cases, researchers have also established relationships between M_{max} and strain rate or the rate of seismic moment release [223][224][225] [226][227]. This particular approach has been utilized to assess M_{max} for seismic events induced by mining activities. Additionally, a relationship has been developed between the logarithm of coda (Q_o) and the largest observed magnitude of earthquakes in China by [228] but this method has shown inconsistencies in estimating M_{max} [212].

While there are several empirical relations available for estimation, it is important to acknowledge that no single method is universally applicable due to the inherent uncertainty in accurately predicting M_{max}. In this study, the deterministic approaches considered for analysis include the incremental method and empirical relations proposed by [220] [221][229][222]. These widely used approaches are selected to account for the variability in estimating M_{max}.

5.3.2.1.1 Deterministic estimation of M_{max} for the study region

The Wells and Coppersmith [222] method is a widely used empirical relation. This approach is used to compute the relations of strike-slip, reverse, and normal faults. The equations are expressed as follows:

$$M_w = 5.16 + 1.12 \log_{10}(RLD) \text{ for strike-slip fault,} \quad 5.1$$

$$M_w = 5.00 + 1.22 \log_{10}(RLD) \text{ for reverse fault,} \quad 5.2$$

$$M_w = 4.86 + 1.32 \log_{10}(RLD) \text{ for normal fault,} \quad 5.3$$

$$M_w = 5.08 + 1.16 \log_{10}(RLD) \text{ for all faults.} \quad 5.4$$

The rupture length distance (RLD) is calculated using the relation given by Wells and Coppersmith [222]. The relation is expressed as follows:

$$\log(RLD) = 0.59\, M_w^{obs} - 2.44, \quad 5.5$$

where M_w^{obs} is the observed earthquake moment magnitude. This relation is valid for magnitudes ranging from 4.8 to 8.1 and length/width range of 1.1–350 km and applicable for all faults, shallow earthquakes, and inter/intra plate earthquakes.

The Nowroozi (1985) equation is expressed as follows:

$$M_s = 1.259 + 1.244 * \log(RLD), \quad 5.6$$

where the RLD is estimated using Equation 5.5, and $M_s$is converted to moment magnitude using Equation 4.2.

The equation proposed by Bonilla et al. [220] is as follows:

$$M_s = 6.24 + 0.62 \log_{10}(RLD) \text{for strike-slip fault,} \quad 5.7$$

$$M_s = 6.24 + 0.62 \log_{10}(RLD) \text{for reverse fault,} \quad 5.8$$

$$M_s = 6.04 + 0.71 \log_{10}(RLD) \text{for all faults.} \quad 5.9$$

The rupture length with magnitude relationship from Slemmons [229] equation is:

$$M_s = 1.404 + 1.169 \log_{10}(L) \text{for strike-slip fault,} \quad 5.10$$

$$M_s = 2.021 + 1.142 \log_{10}(L) \text{for reverse fault,} \quad 5.11$$

$$M_s = 0.809 + 1.341 \log_{10}(L) \text{for normal faults,} \quad 5.12$$

where L is rupture length in (m).

Half of the total length of the fault would rupture during a maximum earthquake. Accordingly, many studies assume that the RLD might be half or one-third of the TFL [215][41]. In this study, the RLD is calculated using Wells and Coppersmith equation 5.5. The TFL, maximum observed earthquake, RLA, M_{max} calculated using the five deterministic methods, and maximum probable earthquake for each tectonic fault within a 300km radius from the site as per its fault mechanism is estimated and listed in Table 5.2.

5.3.2.2 Probabilistic approaches

Probabilistic approaches in estimating the maximum magnitude (M_{max}) rely on statistical procedures that utilize the seismological history of the study area. The extrapolation method, which is widely applicable, estimates M_{max} based on a magnitude-frequency relation initially proposed by Gutenberg and Richter (1944). However, the results obtained from this method exhibit consistency with the size of the study area while displaying inconsistency with the recurrence intervals of large earthquakes [212].

Analytical methods have also been developed, such as those utilizing the strain energy released, as suggested by Markropoulos and Burton (1983, 1985). Additionally, Mark [215] proposed a relationship between magnitude and total fault length. Kijko and Singh [232] put forth 12 statistical procedures for estimating maximum magnitude, encompassing parametric, non-parametric, and data fitting approaches. These methods are particularly useful when the earthquake catalog (EC) is incomplete.

The aforementioned methods primarily rely on observed magnitudes, seismicity data, and frequency-magnitude distribution, often without considering regional rupture characteristics. An alternative approach, developed by Anbazhagan et al. [233], focuses on regional rupture characteristics to estimate M_{max}. This unique method considers the rupture length from past earthquakes and associated source/fault length. It provides consistency and uniqueness, especially for active regions, and is independent of the seismic study area.

In the present study, the evaluation of M_{max} utilizes regional rupture characteristics by considering the observed maximum magnitude (M_w^{obs}) for the selected potential seismic sources. This approach ensures robustness and reliability.

5.3.2.2.1 Regional rupture character (RRC)

The estimation of the maximum magnitude for each seismogenic source within the study area was evaluated by considering the regional rupture characteristics developed by Anbazhagan, as described in Anbazhagan et al. [234, 235] Anbazhagan et al. (2013b, 2014). Anbazhagan et al. (2013b, 2014). Anbazhagan et al. (2013b, 2014). Previous methods did not account for regional rupture phenomena, but this approach takes into consideration the seismo-tectonic features where future seismicity is expected to occur [236].

The maximum magnitude depends on the density and shear wave velocity at the rupture location for each source that influences the fault rupture. These parameters are typically uniform in many seismological models. However, in this approach, the rupture characteristics of the region are derived by considering damaging earthquakes with magnitudes (M_w) of 5.0 and above, along with their associated subsurface rupture lengths (RLD). This method remains consistent regardless of the seismic study area [186].

The rupture character of the region is determined considering damaging earthquakes of magnitude (M_w) of 5.0 and associated subsurface rupture length (RLD). The RLD if each damaging earthquake is evaluated using Wells and Coppersmith (1994), which is applicable to all types of faults as shown in equation 5.5. The RLD obtained from past earthquakes is divided by total fault length of the associated seismo-tectonic source expressed in percentage defined as percentage fault rupture (PFR). For the radius of 300km, based on seismicity and seismo-tectonics of 5.0 to 8.5 M_w are selected and the respective percentage of PFR values are calculated. Then the PFR values are plotted against TFL, the graph of PFR follows a unique trend line referred as rupture as character of the region as shown in Figure 5.2. From the graph, it is observed that percentage of fault rupture for shorter faults is higher compared to that of longer faults and shows the increase in trend line with decrease in fault length and most of the earthquakes in the study region follow the same trend.

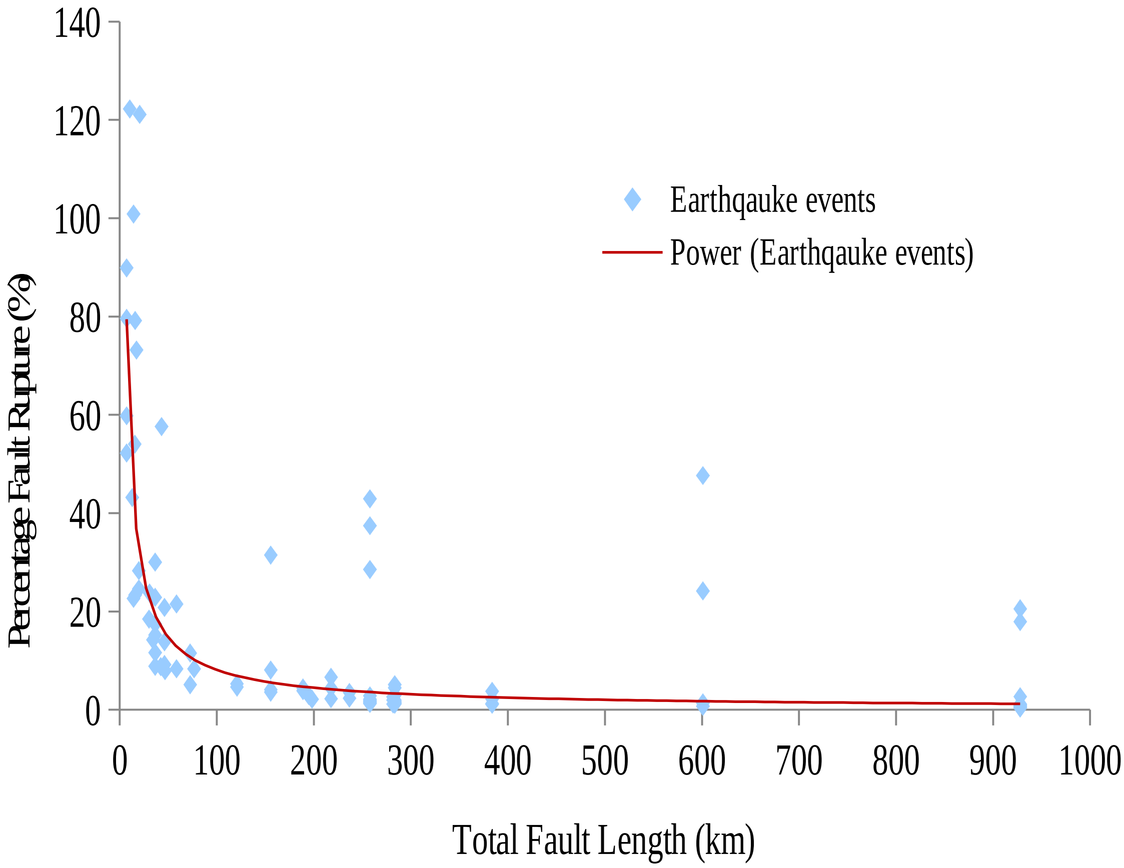

Figure 5.2 Regional rupture characters for the 300 km study area.

To determine the worst-case scenario for PFR, the maximum, minimum, and average PFR values are confirmed within four bins for the study area, as outlined in Table 5.1. For each bin, the PFR for the worst-case scenario earthquakes is taken as five times the average PFR (%TFL). The worst-case scenario indicates earthquakes with magnitudes higher than the maximum reported PFR.

Table 5.1 Regional rupture character for various length bins

Length bins	PFR (%TFL)			PFR (% TFL) for worst scenario (WS)	Ratio of PFR for WS to maximum PFR to maximum PFR
	Maximum	Minimum	Average		
<50	122.23	7.94	42.84	128.51	1.05
50-200	31.46	2.14	8.35	41.74	1.33
200-500	42.91	1.11	5.96	29.79	0.69
>500	47.66	0.35	7.18	35.88	0.75

The maximum magnitudes obtained from the aforementioned approaches are calculated and presented in Table 5.2. The maximum magnitude (M_{max}) for each source is derived using these probabilistic approaches and is provided in the last column of Table 5.2.

Table 5.2 Maximum magnitude values from deterministic and probabilistic approaches and assigned M_{max} value for each source.

Fault code	Observed Mw	TFL	Deterministic method (M_{max})						Probabilistic method (M_{max})		M_{max}		
			RLD	By incremental +0.5	Slemmons (1982)	Bonilla et al. (1984)	Nowroozi (1985)	(1994)Wells and Coppersmith	RLD (% TFL)	Regional rupture character	Deterministic	Probabilistic	**Final**
JGF	6	44.9	12.6	6.5	6.58	7.02	6.63	6.36	24.43	6.49	7.02	6.49	**6.49**
GF	5.5	76.7	6.4	6.0	6.18	6.81	6.26	6.01	32.03	6.69	6.81	6.69	**6.69**
KNF	5.5	120.8	6.4	6.0	6.18	6.81	6.26	6.01	50.42	7.02	6.81	7.02	**7.02**

KL	7	155.7	49.0	7.5	7.38	7.44	7.37	7.04	64.97	7.21	7.50	7.21	**7.21**
SBF	5.7	188.9	8.4	6.2	6.34	6.90	6.41	6.15	78.86	7.35	6.90	7.35	**7.35**
DBF	5.4	194.9	5.6	5.9	6.05	6.70	6.19	6.00	81.35	7.37	6.70	7.37	**7.37**
WPF	5.2	198.3	4.2	5.7	5.91	6.63	6.04	5.86	82.76	7.39	6.63	7.39	**7.39**
PEL	6.1	217.8	14.4	6.6	7.05	6.96	6.71	6.41	64.87	7.21	7.05	7.21	**7.21**
TL	5.7	236.8	8.4	6.2	6.34	6.90	6.41	6.15	70.54	7.27	6.90	7.27	**7.27**
DF	7.6	257.9	110.7	8.1	7.86	7.69	7.82	7.45	76.82	7.33	8.10	7.33	**8.10**
AL	5.6	281.7	7.3	6.1	6.26	6.85	6.34	6.08	83.92	7.40	6.85	7.40	**7.40**
GSL	6.1	283.4	14.4	6.6	6.54	6.96	6.71	6.46	84.42	7.40	6.96	7.40	**7.40**
EL	6.1	383.8	14.4	6.6	6.54	6.96	6.71	6.46	114.31	7.62	6.96	7.62	**7.62**
MCT	8	928.0	190.5	8.5	8.34	7.65	8.12	7.78	332.93	8.41	8.50	8.41	**8.41**
MBT	8.3	601.0	286.4	8.8	8.42	7.98	8.34	7.93	215.62	8.09	8.80	8.09	**8.09**

In the next section, the combination of the maximum magnitude at the closest distance from the selected site will be utilized to determine the maximum ground motion, using an empirical attenuation relation.

5.3.3 Estimation of the shortest distance

In the development of deterministic hazard maps, the traditional approach involves considering the center of the study area as the location for earthquake occurrence. However, in this particular approach, earthquakes are assumed to potentially occur at any location within the study area. To facilitate this analysis, the study area is divided into grids with dimensions of 0.0050 * 0.0050 along the latitude and longitude, respectively, as shown in Annexure C.

To determine the distance from the center of each grid to the fault, a virtual layer is created in QGIS software. This layer allows for the estimation of distances between the grid centers and the fault. From all these distances, the minimum hypocentral distance is selected for each grid. This minimum hypocentral distance is then used to calculate the Peak Ground Acceleration (PGA) for that specific grid. The same procedure is applied to all the grids within the study area, resulting in the estimation of PGA values for each location. These PGA values are used to create a deterministic hazard map for the study area. An illustrative example of this process for one center grid is provided in Figure 5.3.

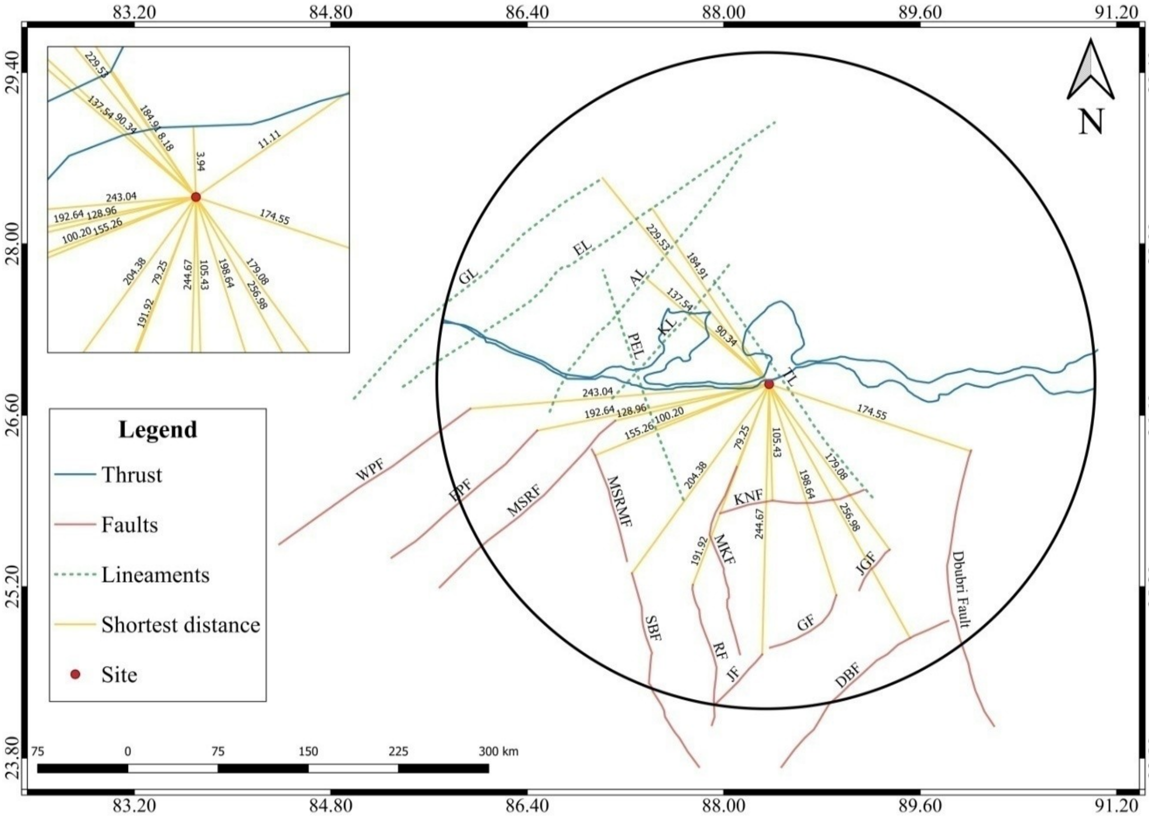

Figure 5.3 Virtual distribution of shortest distance from site to all tectonic features

5.4 DSHA hazard assessment

5.4.1 Hazard maps

In this study, a worst-case scenario hazard map was developed using Deterministic Seismic Hazard Analysis (DSHA) for a 300 km study area in the QGIS software. The estimation of intermediate values of Peak Ground Acceleration (PGA) required for the development of the hazard map was performed using the inverse distance weighting (IDW) interpolation technique within QGIS.

For this analysis, the average depth of the study area was 30 km, corresponding to the upper crust region. The hazard maps for the 300 km study area were evaluated using statistical analysis based on the empirical relation ANBU-13, which incorporates earthquake magnitude and site-to-source distance.

The resulting DSHA PGA hazard map at a zero-time period for the study region is presented in Figure 5.4. Within the study area, the PGAs range from 0.28 g to 0.90 g. The highest ground motions are observed in the central part of the study area, ranging from 0.66 g to 0.90 g, followed by the surrounding areas. These high hazard values are primarily attributed to the presence of the Main Central Thrust (MCT) and Main Boundary Thrust (MBT) thrust faults, which traverse the study region from east to west and have the potential to generate devastating earthquakes.

The site with the maximum credible earthquake (MCE), representing the most severe/largest earthquake expected to occur on a nearby fault based on geologic and seismological evidence, was identified at coordinates 89^{0} 39^{1} 47.88^{11} longitude and 25^{0} 33^{1} 45.82^{11} latitude, with a PGA value of 0.903 g. This location exhibited the highest PGA value due to its close proximity of 1 km to the seismically active MCT thrust fault.

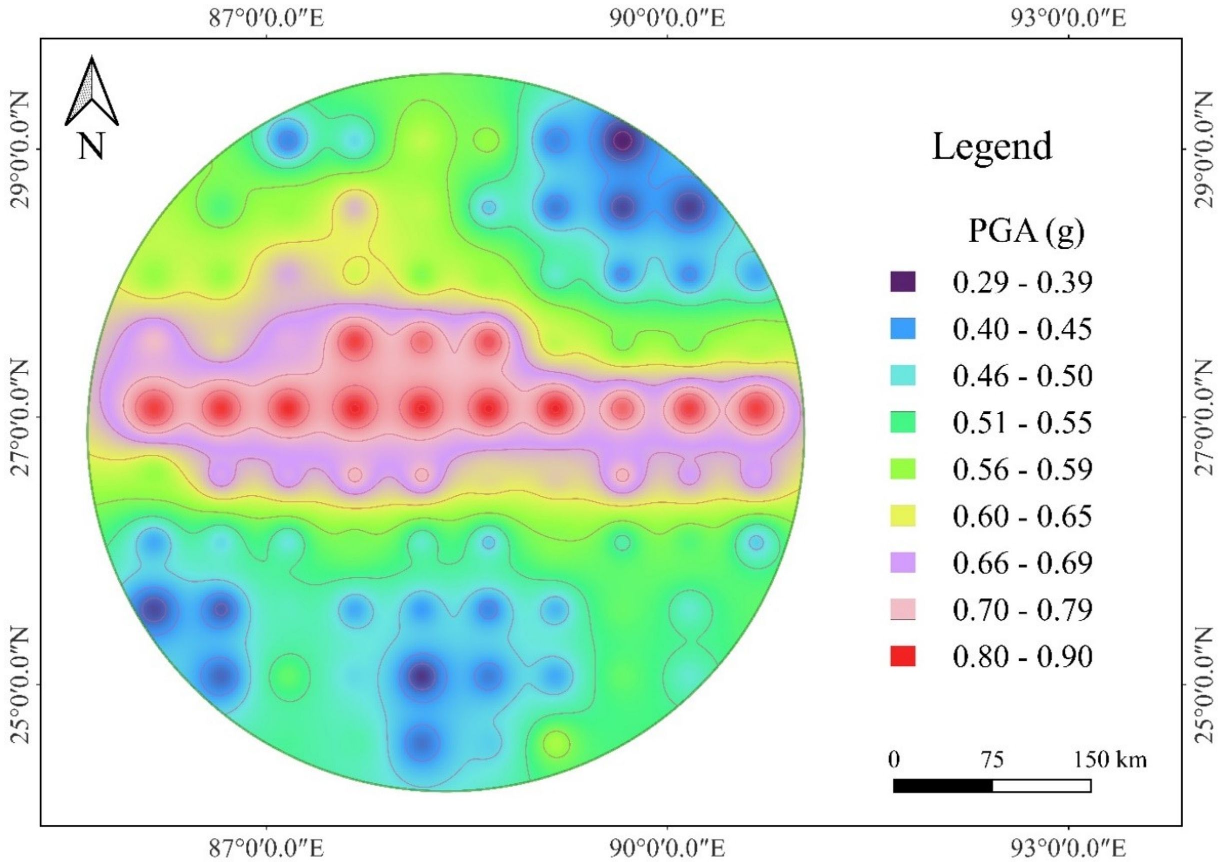

Figure 5.4 PGA hazard map from DSHA for the study area.

Furthermore, in this study, spectral acceleration (SA) maps were developed at various time periods (0.1, 0.2, 0.3, 0.4, 0.5, 0.6, 0.8, and 1.0 seconds) based on the ANBU-13

Ground Motion Prediction Equation (GMPE). It is customary in seismic design to evaluate structures based on normalized response spectral accelerations. Therefore, the ANBU-13 attenuation relation was utilized to calculate the spectral acceleration values for different response spectra. The SA maps were generated considering a damping factor of 5% and are presented in Figures 5.5 to 5.12. These maps provide spatial representations of the spectral acceleration at different time periods, allowing for a comprehensive understanding of the ground motion characteristics within the study area.

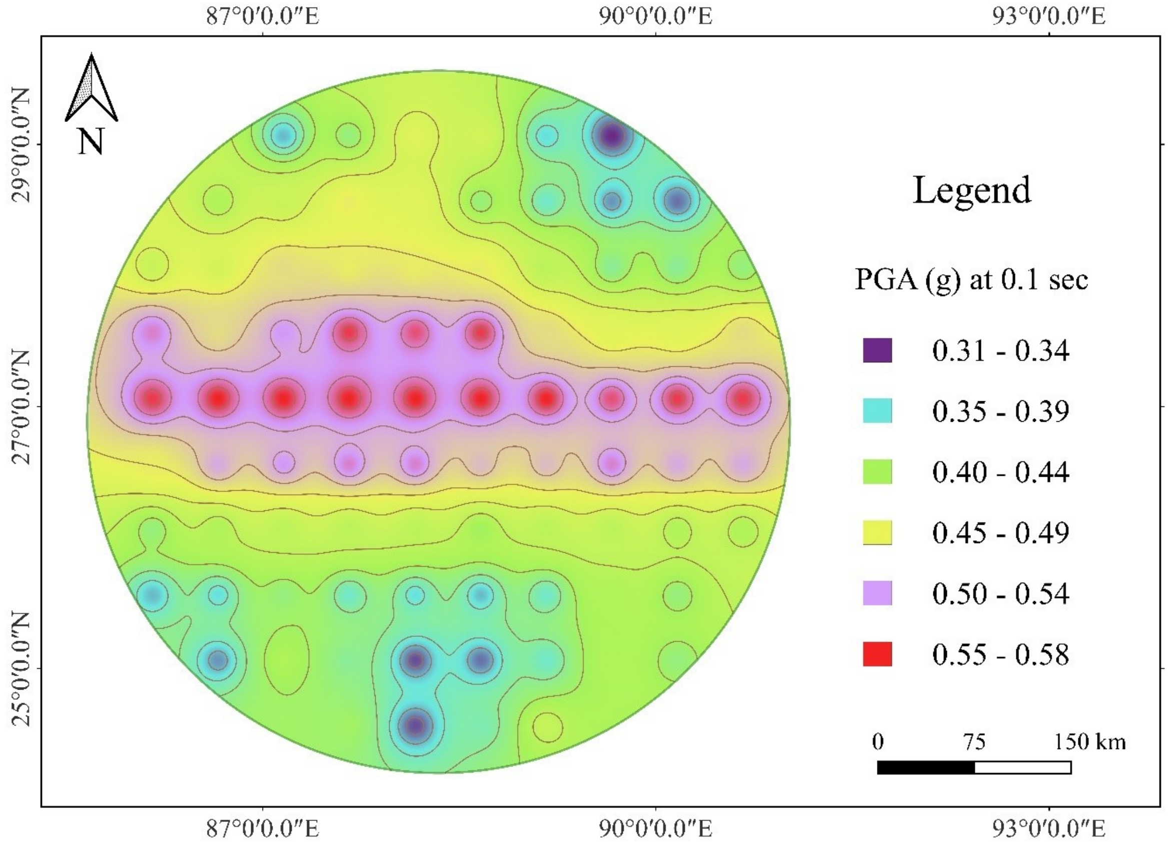

Figure 5.5 DSHA spectral acceleration at 0.1 s of the study area

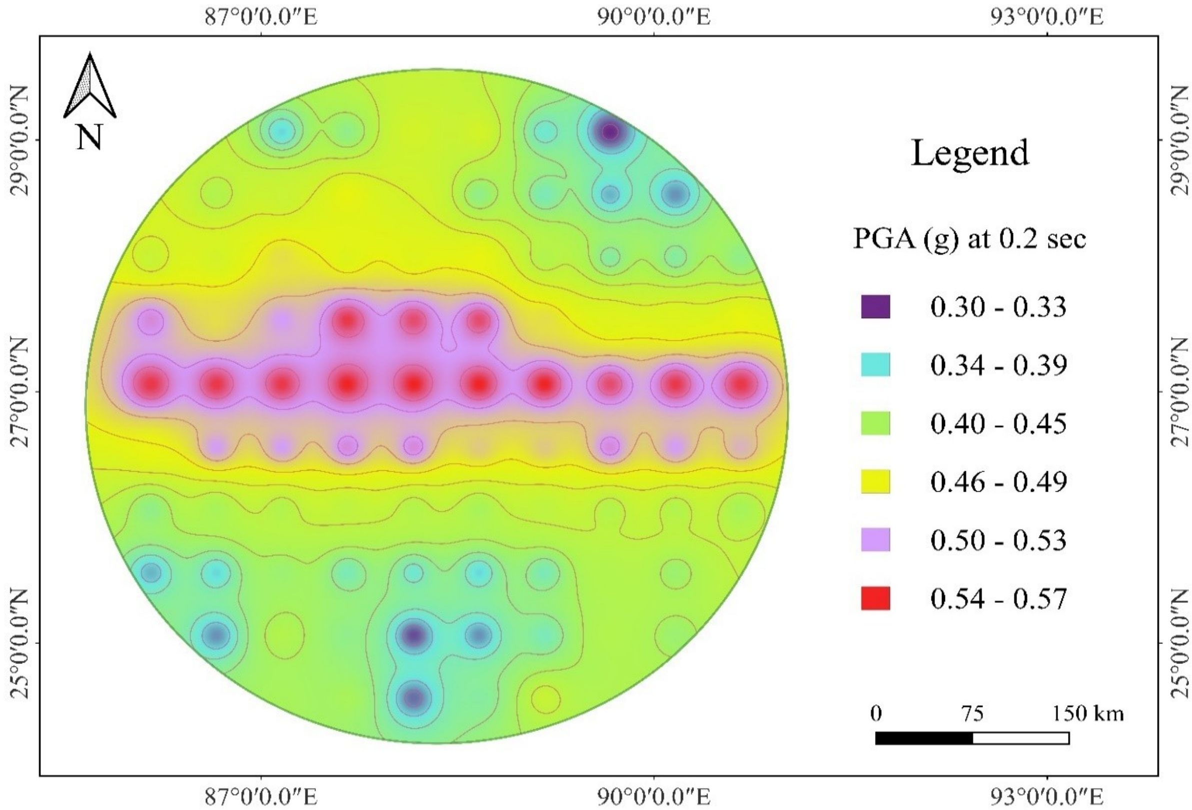

Figure 5.6 DSHA spectral acceleration at 0.2 s of the study area

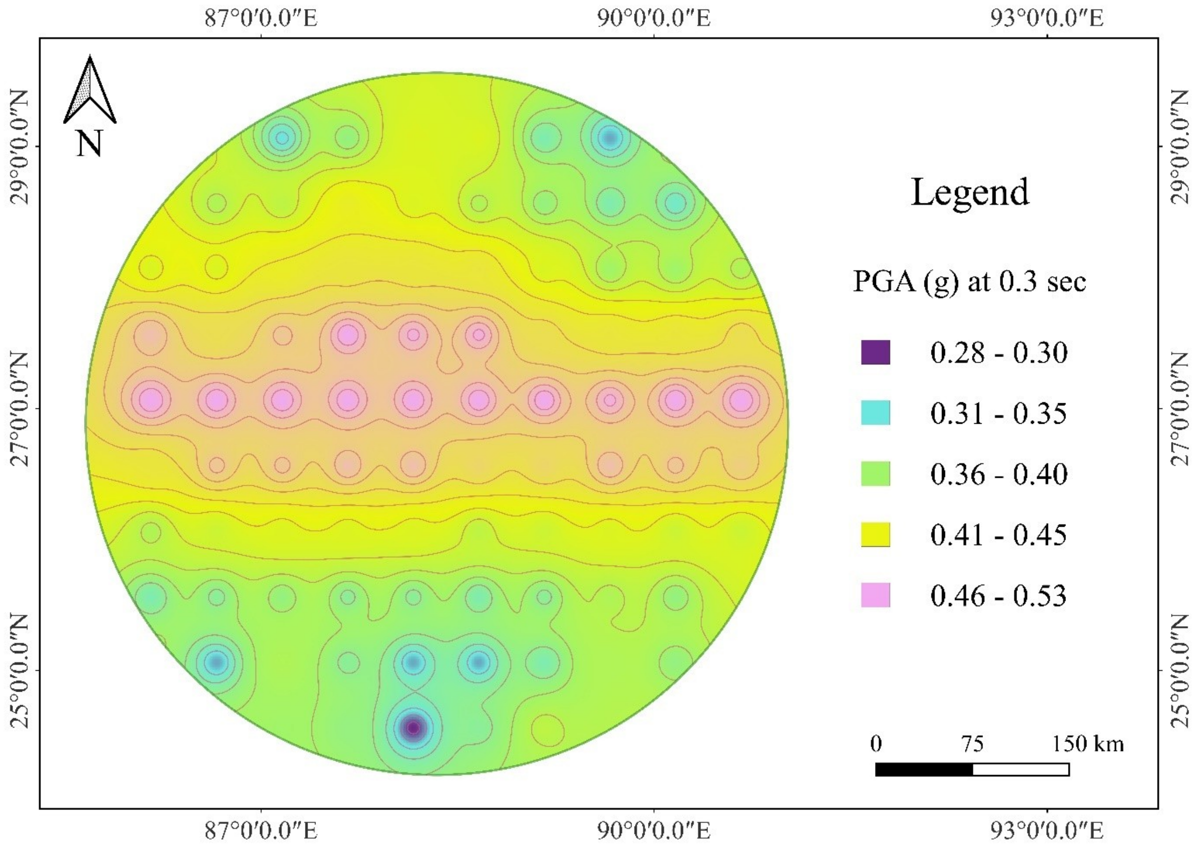

Figure 5.7 DSHA spectral acceleration at 0.3 s of the study area

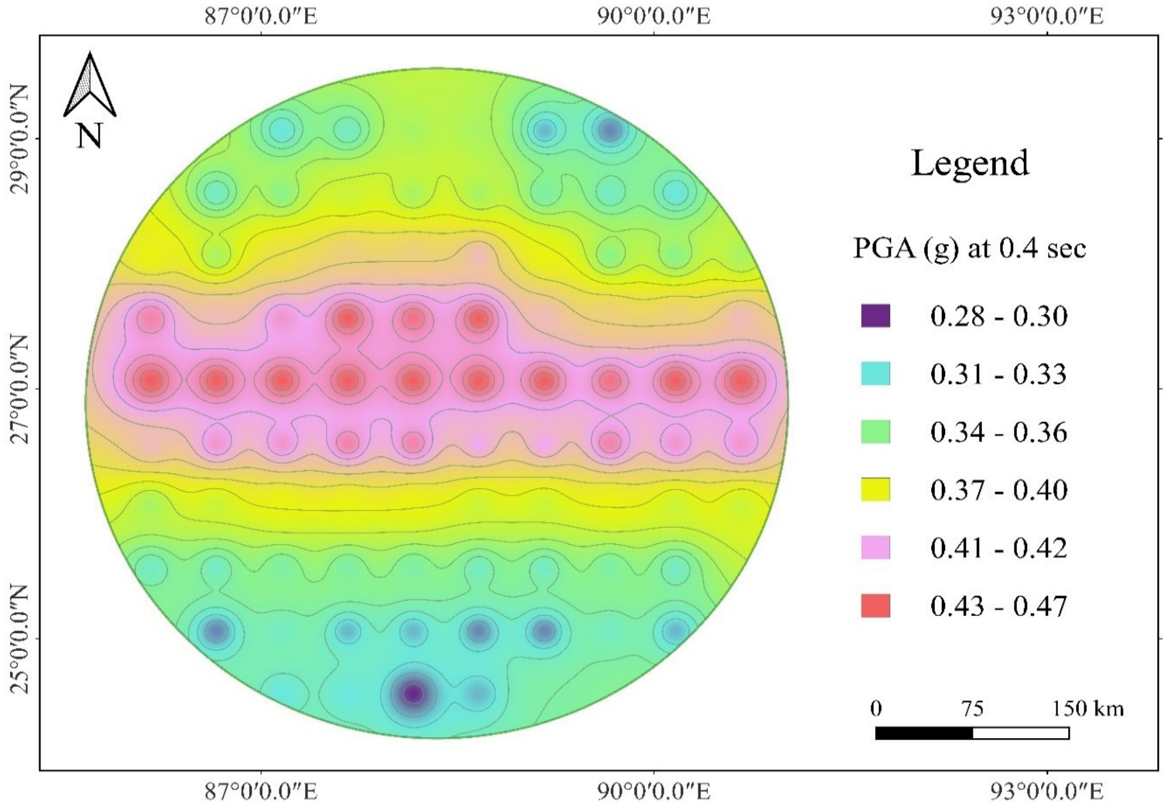

Figure 5.8 DSHA spectral acceleration at 0.4 s of the study area

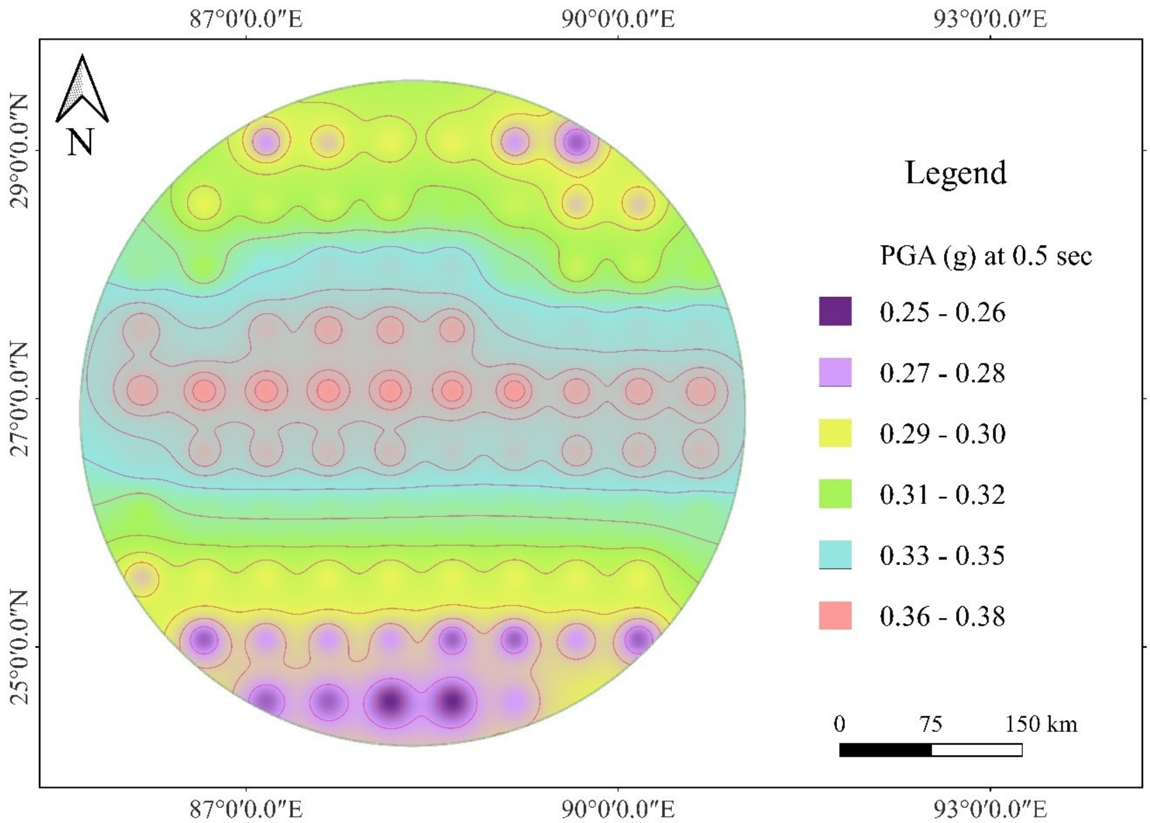

Figure 5.9 DSHA spectral acceleration at 0.5 s of the study area

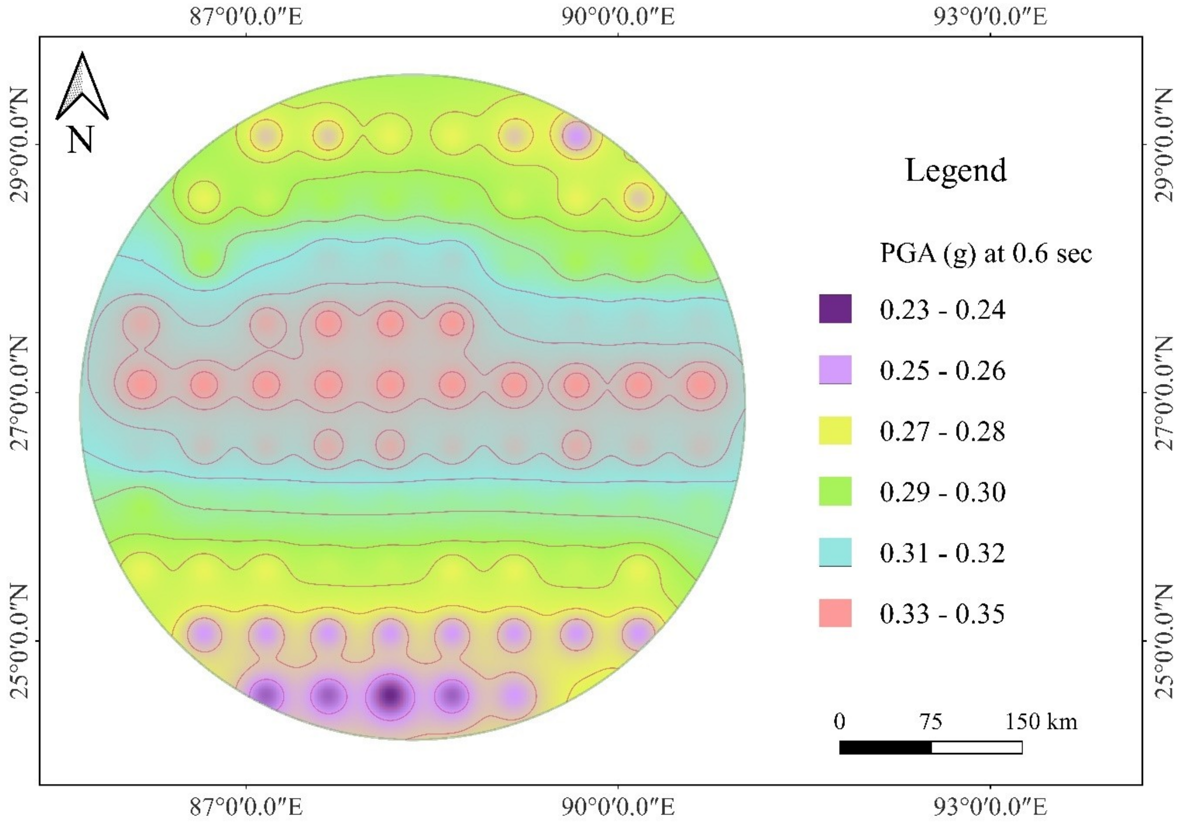

Figure 5.10 DSHA spectral acceleration at 0.6 s of the study area

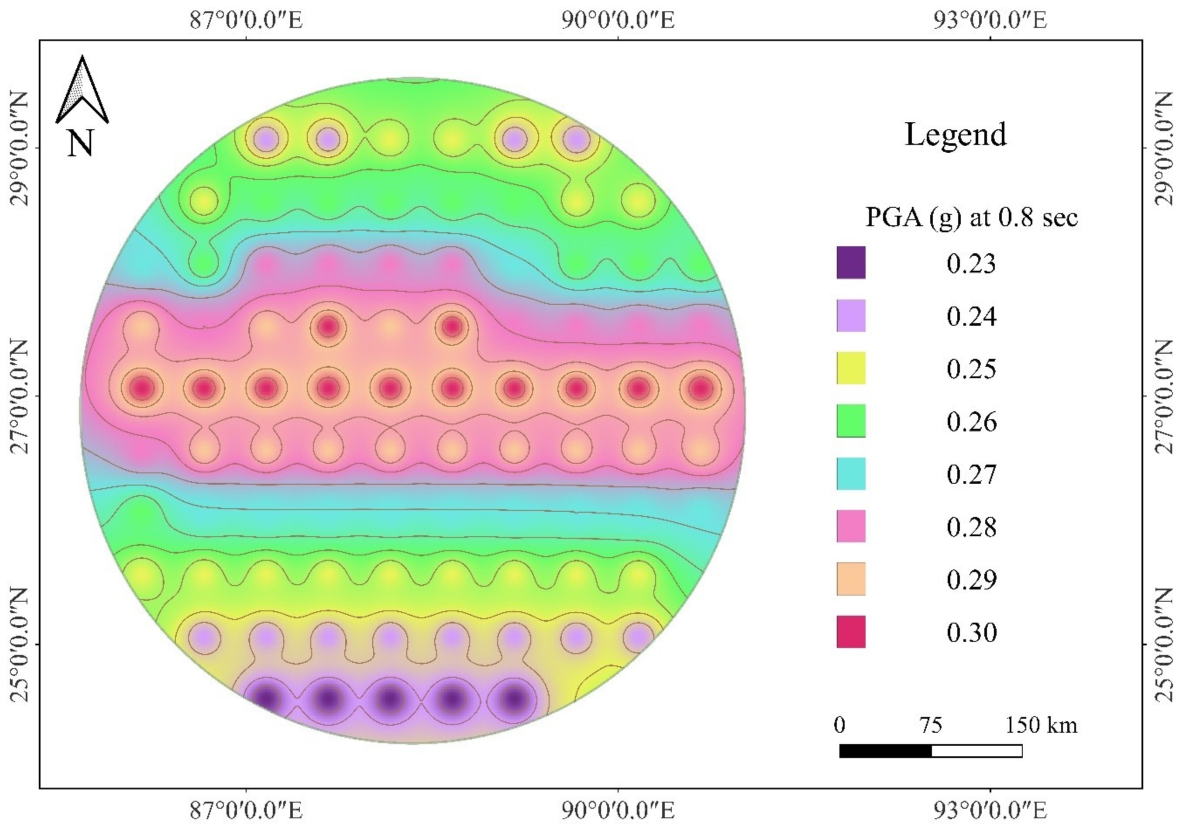

Figure 5.11 DSHA spectral acceleration at 0.8 s of the study area

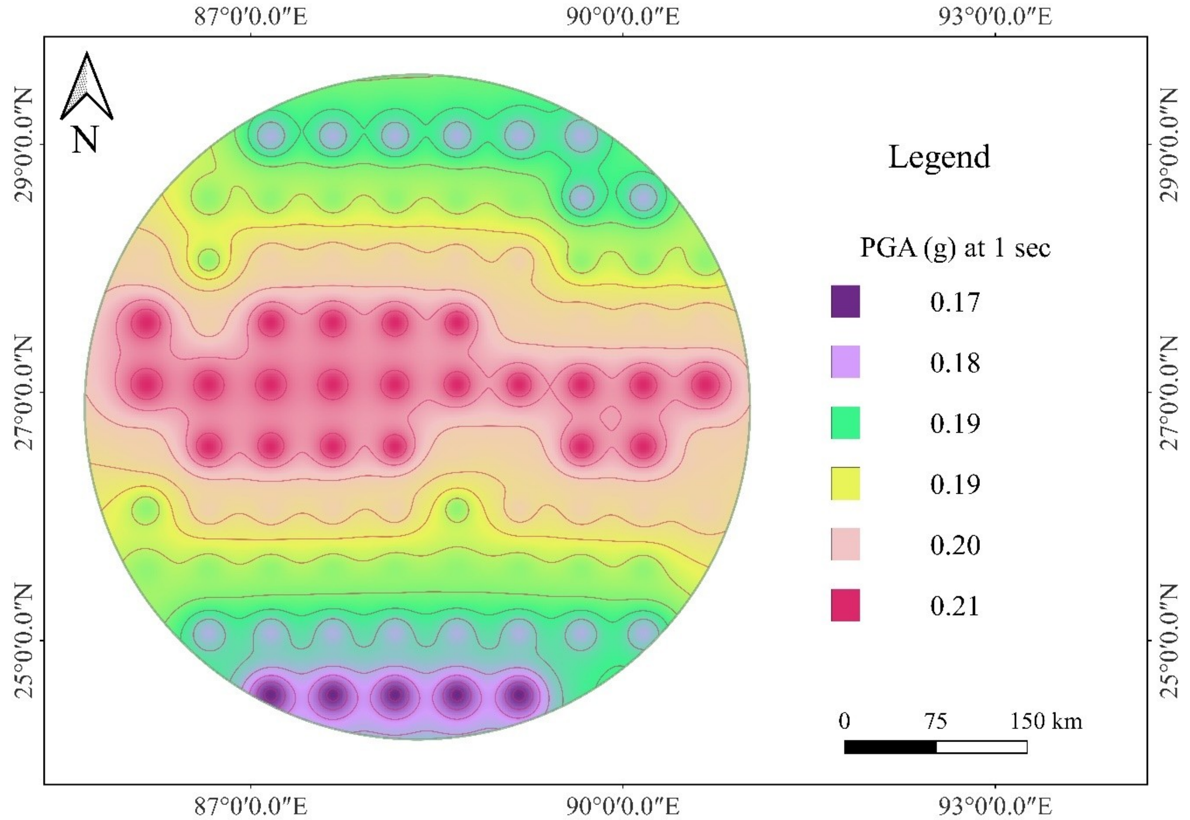

Figure 5.12 DSHA spectral acceleration at 1 s of the study area

Upon analysis, it is evident that the response spectra at the same location within the study area exhibit notable differences, yet they follow a similar pattern. Specifically, the spectral acceleration (SA) values gradually decrease from the central region towards the surrounding areas. Figures 5.5 and 5.6 demonstrate that the highest SA values, ranging from 0.30 to 0.56g, are observed at time periods of 0.1 and 0.2 seconds.

It is worth noting that the regions along the Main Central Thrust (MCT) and Main Boundary Thrust (MBT) active fault zones exhibit elevated seismic hazard. These areas display a decreasing trend of SA values as one moves away from the central part. In particular, the central part extending from west to east within the study area, where the active faults are present, is particularly susceptible to higher seismic hazard.

5.4.2 Uniform Hazard Response spectrum (UHRS)

The Unified Hazard Response Spectrum (UHRS) was developed in order to better understand the amplification characteristics specific to the study region. The UHRS plays a vital role in the seismic design of structures within the selected area. To derive the UHRS, spectral acceleration graphs were plotted at the center of the study region.

Figure 5.13 (a & b) illustrates the selection of 15 faults for deriving the Site-Specific Acceleration (SSA). Among these faults, particular attention was given to the three vulnerable faults: TL, MCT, and MBT. A comparison was made between these vulnerable faults and the remaining sources.

Upon analyzing the graphs in Figure 5.13 (a & b), it can be observed that the spectral accelerations associated with the vulnerable faults gradually decrease over the time period. However, the remaining faults exhibit an increasing trend at 0.1 seconds, followed by a moderate decrease over the time period.

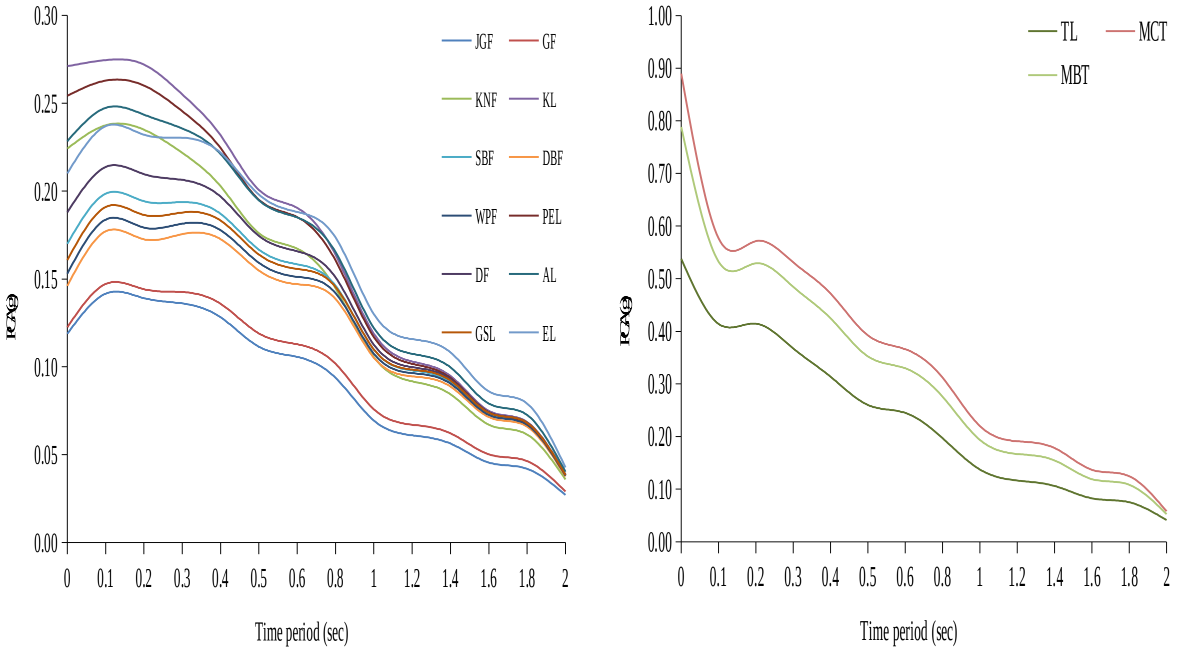

(a) (b)

Figure 5.13 Hazard response spectrum of **(a)** 12 faults **(b)** three vulnerable faults

5.5 Conclusion

In this chapter, a Deterministic Seismic Hazard Analysis (DSHA) was conducted for the study area, which involved dividing the site into 86 grids along the latitude and longitude within a 300 km area. Data specific to the region, including the most active 15 linear active fault thrusts and lineaments, were collected for analysis. Maximum earthquake magnitudes for each fault were determined using five deterministic methods, namely the incremental method and empirical relations proposed by [220][221][229][222], as well as the probabilistic method of regional rupture characteristics.

To assess the ground motions, the average focal depth of 30 km for the study area was considered. The distances from each grid to various faults were evaluated using a virtual layer in the QGIS software, and the minimum distance was selected for PGA assessment. The ANBU-13 Ground Motion Prediction Equation (GMPE) was employed to evaluate ground motions for DSHA. Hazard maps and spectral acceleration maps at various time periods (0.1, 0.2, 0.3, 0.4, 0.5, 0.6, 0.8, and 1 sec) for the 300 km study area were developed using IDW interpolation in the QGIS software. The PGA values ranged from 0.29 to 0.90g, with the maximum credible earthquake observed at a specific location.

The cumulative deterministic PGA for the entire study area was determined to be 0.55g. Spectral acceleration varied from 0.01 to 0.56g, with higher values obtained at shorter time periods (0.1 and 0.2 sec) and gradually decreasing with longer time periods. The analysis revealed that the MCT and MBT sources, located from west to east in the central part of the study area, contributed to high PGA values.

The worst-case scenario PGA values obtained from DSHA for different grid points ranged from 0.29 to 0.90g, and a deterministic hazard map was generated based on these values. However, the deterministic approach only provides one fixed high hazard value without considering the probability of exceedance or accounting for uncertainties in earthquake size, magnitude, distance, location, ground motion intensities, and GMPE. This approach lacks the ability to account for the occurrence of new earthquakes, and the results tend to provide conservative estimates of future PGA.

Considering the limitations of the deterministic approach, the next chapter will employ a Probabilistic Seismic Hazard Analysis (PSHA) framework, which integrates a wide range of information and uncertainties to provide exceedance probability information for future earthquakes and evaluate the seismic hazard of the study area.

Chapter 6

Probabilistic Seismic Hazard Analysis

6.1 Introduction

The selection of ground shaking for analysis poses challenges because the precise prediction of earthquake parameters, such as location, size, and severity of future earthquakes, is not possible. The ground motion assessment conducted using the deterministic approach is based on a single magnitude at a fixed distance from the site [45][116]. In contrast, the probabilistic approach considers the effects of all earthquakes with varying magnitudes around the site and quantifies uncertainties [45][237].

The Probabilistic Seismic Hazard Analysis (PSHA) incorporates uncertainties and evaluates the rate of exceedance of future ground motion at a specific location during a specific time period by combining mathematical models [237]. This study presents a comprehensive assessment of seismic hazards using analytical expressions [45] and seismicity models while addressing uncertainties [27].

PSHA has been widely used since 1984 to evaluate the risk of earthquakes in specific cities or regions in India with a historical seismic vulnerability [164]. The methodology of PSHA, including the prediction of future recurrence rates, estimation of the maximum magnitude, and computation of the Peak Ground Acceleration (PGA) at different time periods, is explained in this chapter. The main outputs of PSHA include hazard curves representing the annual rate of exceedance versus ground motion intensity, hazard maps describing the ground motion over time, and response Spectral Acceleration (SA) curves and maps for specific periods [238].

The probabilistic procedures offered by PSHA enable the computation of various hazard statistics [238], address engineering safety concerns [237], and determine security criteria for dams, nuclear, and hydroelectric plants [239]. The inclusion of uncertainties in the analysis adds complexity but facilitates risk reduction for engineers. The combination of different mathematical models helps overcome data limitations and provides a more comprehensive understanding of seismic hazards.

6.2 Methodology and framework of PSHA

In this study, the seismic hazard evaluation for 300 km study area is performed using the Probabilistic Seismic Hazard Analysis (PSHA) methodology proposed by Cornell [45]. The PSHA framework follows a four-step approach as outlined by Reiter [122]. A schematic representation of the PSHA procedure is presented in Figure 6.1.

1. Identification and characterization of earthquake sources that can produce significant ground motion.
2. Determining Gutenberg–Ritcher parameters a and b via recurrence relationship.
3. Prediction of a ground motion using GMPE’s.
4. Generation of hazard curves and maps.

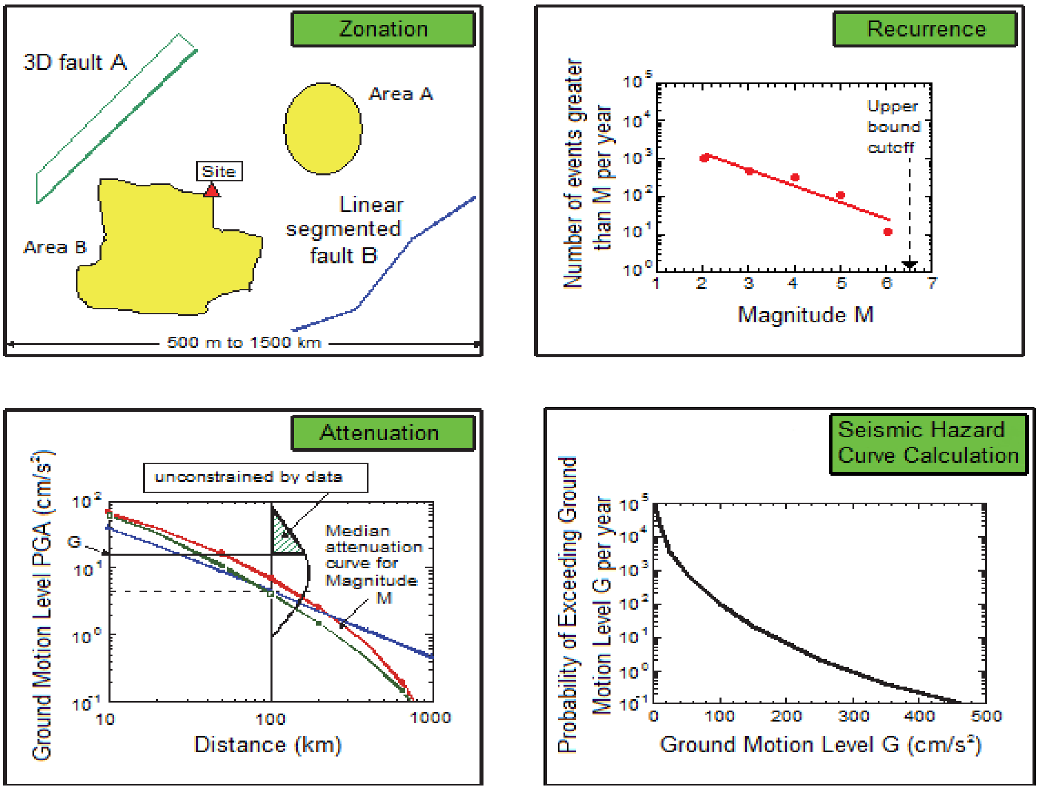

Figure 6.1 Schematic of the four steps of PSHA (Hutchings, L. and Gisela Viega, 2012).

The specific steps of the PSHA procedure are elucidated in Figure 6.2. The collection of earthquake sources, preparation of the final Earthquake Catalog (EC), and selection of appropriate GMPE's are discussed in detail in Chapter 4. This chapter focuses on the remaining steps (four, five, and six), providing a comprehensive description of each.

1. Collection of earthquake sources

Collection of seismic sources around the 300 km radius from previous literature, historical, and instrumental data

Collection of seismotectonic data of the study area from SEISAT-2000

2. Preparation of an refined earthquake catalogue, followed by homogenization, de-clustering, and completeness check.

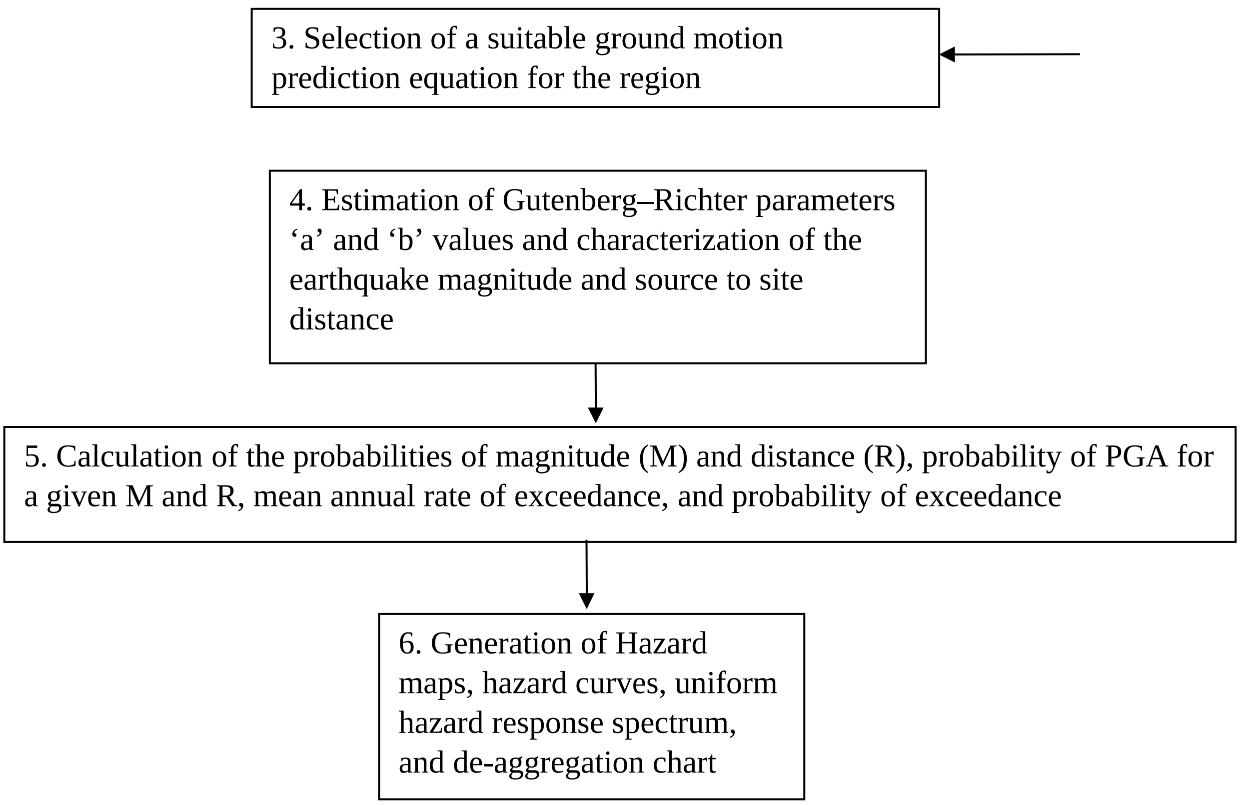

Figure 6.2 The theoretical framework of PSHA.

6.3 PSHA theorem

PSHA involves several critical elements, including earthquake source parameters such as size, location, and timing, as well as the selection of appropriate Ground Motion Prediction Equation (GMPE) models. It is important to recognize that these elements are subject to certain degrees of uncertainty. In PSHA, these uncertainties are systematically identified, quantified, and appropriately combined to provide a comprehensive understanding of seismic hazards.

To effectively address uncertainties in PSHA, various approaches are utilized. One common method is the modeling and description of uncertainties using probability distributions, specifically the Cumulative Density Function (CDF) and Probability Density Function (PDF). The CDF represents the cumulative probability of a variable falling within a certain range, while the PDF is the derivative of the CDF, providing a measure of the likelihood of specific values occurring.

By incorporating the CDF and PDF within the PSHA framework, uncertainties associated with earthquake parameters and GMPE models can be effectively characterized and integrated into the hazard assessment process. This enables a more robust and comprehensive evaluation of seismic hazards, taking into account the inherent uncertainties in the input parameters.

6.3.1 Distance/spatial uncertainty

The geometry of earthquake sources in PSHA is influenced by the underlying tectonic processes involved in their formation. These sources can exhibit different geometries, including point, linear, areal, and volumetric sources [27]. Linear sources, such as fault planes, can give rise to earthquakes occurring at various locations along their length. For short faults with limited impact on the site, they can be approximated as point sources. However, for longer faults, the distance from the site to the fault becomes a significant factor, making them better characterized as linear sources.

In PSHA, accurate modeling of the distance from the site to the earthquake source is essential for predicting seismic events associated with linear sources. Given that an earthquake can potentially occur at any point along the fault, the probability density function (PDF) is utilized to account for the uncertainties in the source-to-site distance. The PDF for a linear source is as follows:

$$f_R(r) = \frac{r}{L_f \sqrt{r^2 - r_{min}^2}}, \tag{6.1}$$

Where, f_R (r) is the PDF, r is the distance, L_f is the fault length, and r_{min} is the minimum distance.

6.3.2 Size uncertainty (magnitude probability)

Gutenberg-Richter [165] conducted pioneering research on the observation of earthquake magnitudes and their frequency of occurrence. It was observed that earthquakes occur across a range of magnitudes, with larger earthquakes being less frequent compared to smaller ones. The recurrence law formulated by Gutenberg-Richter [165] describes the statistical distribution of earthquake sizes within a specific region over a given time period.

6.3.2.1 Gutenberg–Richter (G-R) recurrence law

The Gutenberg-Richter recurrence law is derived from the analysis of earthquake data collected over multiple years, encompassing earthquakes of various magnitudes. It provides a mathematical relationship that expresses the annual distribution of earthquakes with magnitudes greater than a specified value (M_w) in a particular region. The formulation of the recurrence law is expressed as follows:

$$\log \lambda_m = a - b\, M_w, \tag{6.2}$$

where:

λ_m =cumulative number of earthquakes with magnitudes greater than or equal to M_w.

a = Mean yearly number of earthquakes in a region.

b = Relative ratio of larger to smaller magnitude events.

M_w = Earthquake moment magnitude.

The mean annual rate of exceedance, λ_m, for an earthquake magnitude Mw is determined by dividing the number of observed earthquakes that exceed that magnitude by the length of the time period considered. The reciprocal of the annual rate of exceedance for each magnitude corresponds to the return period, representing the average time interval between occurrences of earthquakes of that magnitude.

The estimation of the 'a' and 'b' constants in the Gutenberg-Richter relationship involves statistical analysis of historical earthquake data. By plotting the logarithm of the annual rate of exceedance against the corresponding magnitudes, these constants can be determined. Figure 6.3 illustrates this relationship between the annual rate of exceedance and earthquake magnitudes.

Accurate seismicity parameters are crucial for reliable seismic hazard evaluation. Two commonly employed methods for estimating these parameters from available earthquake catalogs are the least square method (LSM) and the maximum likelihood method (MLM). These approaches minimize the differences between observed earthquake data and the Gutenberg-Richter relationship, and the choice between them depends on factors specific to the earthquake catalog being analyzed [240]. The resulting probability distribution of earthquakes whose magnitudes are greater than the minimum magnitude M_{min} is computed as follows [241]

$$\lambda_M = v \exp ¿, \tag{6.3}$$

$v = 10^{a - b M_{min}}$. (6.4)

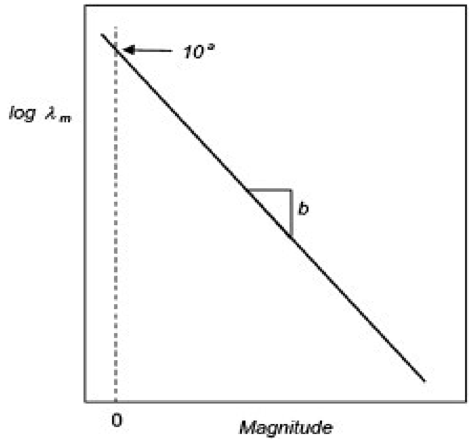

Figure 6.3 Gutenberg–Richter recurrence law, representing *a* and *b* parameters [237].
Equation 6.2 is expressed in CDF as follows:

$$F_M(m) = 1 - 10^{-b(m - m_{min})}, m > m_{min}. \quad (6.5)$$

Equation 6.5 is expressed in PDF as follows:

$$f_M(m) = b \ln(10) 10^{-b(m - m_{min})}, m > m_{min}. \quad (6.6)$$

In PSHA analysis, the probability distribution of earthquakes with magnitudes greater than a minimum magnitude M_{min} is computed. The general form of the Gutenberg-Richter equation covers an infinite range of magnitudes; however, for practical purposes, small earthquakes are often excluded due to their minimal engineering significance. To make the PSHA analysis realistic, an upper bound earthquake magnitude (m_{max}) associated with source zones is considered. Additionally, a lower magnitude threshold (m_{min}) of 4.0 is typically chosen since magnitudes below this value do not cause significant structural damage. Once m_{max} and m_{min} are determined, Equation 6.2 can be expressed as follows:

$\lambda_M = v \exp$ ¿¿. (6.7)

The CDF for the upper and lower bounds are expressed as follows:

$$F_M(m)=\frac{1-10^{-b(m-m_{min})}}{1-10^{-b(m_{max}-m_{min})}}, m_{min}<m<m_{max}. \quad (6.8)$$

Equation 6.7 is expressed in PDF as follows:

$$f_M(m)=\frac{b\ln(10)10^{-b(m-m_{min})}}{1-10^{-b(m_{max}-m_{min})}}, m_{min}<m<m_{max}. \quad (6.9)$$

Further for the PSHA calculations, we will convert the continuous distribution of magnitudes into a discrete set of magnitudes computed as follows:

$$P(M=m)=F_M(m_{j+1})-F_M(m_j), \quad (6.10)$$

where m_j is a discrete set of magnitudes.

To perform PSHA calculations, the continuous distribution of magnitudes is discretized into a set of discrete magnitudes. This is achieved by assigning probabilities to each magnitude using magnitude spacing of 0.1 or less, commonly used in PSHA analyses.

The Gutenberg-Ritcher relationship allows for the estimation of earthquake occurrence probabilities based on magnitude, providing valuable insights into the seismic activity of a region. By applying the Gutenberg-Richter recurrence law, seismic hazard analysts can assess the likelihood of earthquakes of different magnitudes and incorporate this information into the probabilistic seismic hazard analysis.

6.3.3 GMPE uncertainty

Predictive relationships for ground motion intensities are established through statistical regression analysis, which allows for the examination of the probability distribution of these intensities based on strong motion data. The inherent variability in the data arises from factors such as the travel path of seismic waves, site conditions, rupture mechanisms, and other relevant information. While this scatter in the data cannot be eliminated, it can be quantified through measures such as the standard deviation of the predicted parameters or confidence limits [242].

To account for the probabilistic nature of ground motion, the probability of occurrence is computed using the mean and standard deviation. In particular, since the logarithm of peak ground acceleration (PGA) typically exhibits a normal distribution, this probabilistic factor can be expressed as follows:

$$P(PGA>a|\quad m,r)=1-\phi\left(\frac{\ln(a)-\ln\,(PGA)}{\sigma_{lnPGA}}\right),$$

(6.11)

where $\varnothing()$ = standard normal cumulative distribution function, and σ_{lnPGA} is the standard deviation.

This formulation acknowledges the probabilistic nature of ground motion and enables a quantitative assessment of the probability associated with different levels of intensity. By considering the mean and standard deviation, the analysis incorporates the inherent uncertainties and variability in the data, providing a more comprehensive understanding of the seismic hazard.

6.3.4 Combined probability

Probabilistic Seismic Hazard Analysis (PSHA) plays a crucial role in assessing safety and risk levels associated with seismic events [243]. It involves the development of seismic hazard curves, which represent the annual probability of exceeding a specific peak ground acceleration (PGA) within a defined time period. These calculations take into account all potential seismic sources in the region, considering various earthquake magnitudes, site-to-source distances, and a ground motion prediction model as described in Equation 6.13. The total probability theorem [45] is utilized to calculate the cumulative probabilities for all sources that exceed a certain acceleration threshold "a," as illustrated in Equation 6.12.

$$P(PGA>a)=\int_{m_{min}}^{m_{max}}\int_{o}^{r_{max}} P(PGA>a|\quad m,r).f_M(m).f_R(r).dm.dr \qquad (6.12)$$

Where a is the seismic intensity level; $f_M(m)\wedge f_R(r)$ indicate the probability density distribution of magnitude and source to site distance, respectively; $P(PGA>a|\quad m,r)$ indicates that the conditional probability comes from the ground motion model; and m_{max} and m_{min} are maximum and minimum magnitudes, respectively.

For "n" number of sources ($n_{sources}$), the seismic intensity greater than the "a" value can be estimated using the formula:

$$\lambda\left(PGA>a\right)=\sum_{i=1}^{n_{sources}}\lambda\left(M_i\text{¿¿}m_{min}\right)\sum_{j=1}^{n_M}\sum_{k=1}^{n_R}P\left(PGA>a\middle|\quad m_j,r_j\right).P\left(M_i=m_k\right).P\left(R_i=r_k\right)\text{¿},\tag{6.13}$$

Where n_M and n_R are the numbers of possible magnitudes and distances for source i, respectively; and $P(M_i = m_k)$ and $P(R_i = r_k)$ is the probability of magnitudes and distances in source i, respectively.

By employing this PSHA formulation, hazard curves, maps, and Uniform Hazard Response Spectra (UHRS) can be determined for a specific site. These outputs provide valuable insights into the seismic hazard characteristics, enabling a comprehensive assessment of potential risks and aiding in the formulation of appropriate safety measures.

6.3.5 Hazard De-aggregation

De-aggregation analysis represents an extension of Probabilistic Seismic Hazard Analysis (PSHA) and addresses the question of identifying the earthquake scenario most likely to cause a peak ground acceleration (PGA) exceeding a specified threshold (a) from potential earthquakes of varying magnitudes and distances [244] [27]. While PSHA calculates the rate of exceedance without associating it with specific distances or magnitudes, de-aggregation analysis expresses the mean annual rate of exceedance as a function of both earthquake magnitude and source-to-site distance.

The de-aggregation process is valuable for various purposes, including the selection of a ground motion/design earthquake and understanding the contribution of different magnitudes and distances to the overall seismic hazard. This procedure involves considering incremental changes in magnitude (Δ_m) and distance (Δ_r). By performing hazard de-aggregation, the mean annual rate of exceedance can be computed, providing insights into the relationship between earthquake magnitude, source-to-site distance, and the resulting hazard using equation 6.14.

$$\lambda\left(PGA>a,M=m,R=r\right)=\sum_{i=1}^{n_{sources}}\lambda\left(M_i\text{¿¿}m_{min}\right).P\left(PGA>a\middle|\quad m_j,r_j\right).P\left(M_i=m\right).P\left(R_i=r\right)\text{¿}$$

6.14

De-aggregation analysis enhances the understanding of the specific earthquake scenarios that are most likely to contribute significantly to the hazard at a given site.

6.4 Application of PSHA on the study area

6.4.1 Identification and characterization of sources

In accordance with the methodology outlined in Chapter 4, the process of identifying and selecting earthquake sources has been conducted for the current study. A total of 20 significant faults and a refined selection of 316 earthquake events have been chosen for the purpose of conducting a Probabilistic Seismic Hazard Analysis (PSHA). The details of the 20 major faults can be found in Table 4.1, which provides a comprehensive overview of their characteristics and relevance to the study. Additionally, Annexure-A contains a summary of the selected 316 earthquake events, providing essential information regarding their occurrence and pertinent attributes.

6.4.2. Probability distribution of magnitude and distance

In the context of Probabilistic Seismic Hazard Analysis (PSHA), it is assumed that all seismic sources possess the potential to generate earthquakes of varying magnitudes at any distance. To incorporate this consideration, magnitude and distance distributions have been assigned to each source, employing equations 6.8 and 6.9 as elucidated in the preceding sections.

To facilitate the PSHA calculations, a set of site-to-source distances are required, evenly distributed along the fault's length. Manually generating such distances can be challenging and time-consuming. Consequently, the utilization of RCRISIS software has been employed to generate the necessary distance calculations.

On the other hand, the magnitude distribution can be determined manually. Figures 6.4(a and b) illustrate the Probability Density Function (PDF) and Cumulative Distribution Function (CDF) for a study area spanning 300km, encompassing magnitudes ranging from 4 to 8.5. Moreover, Figure 6.5 presents a discrete representation of the probability distribution for each fault's magnitude occurrence.

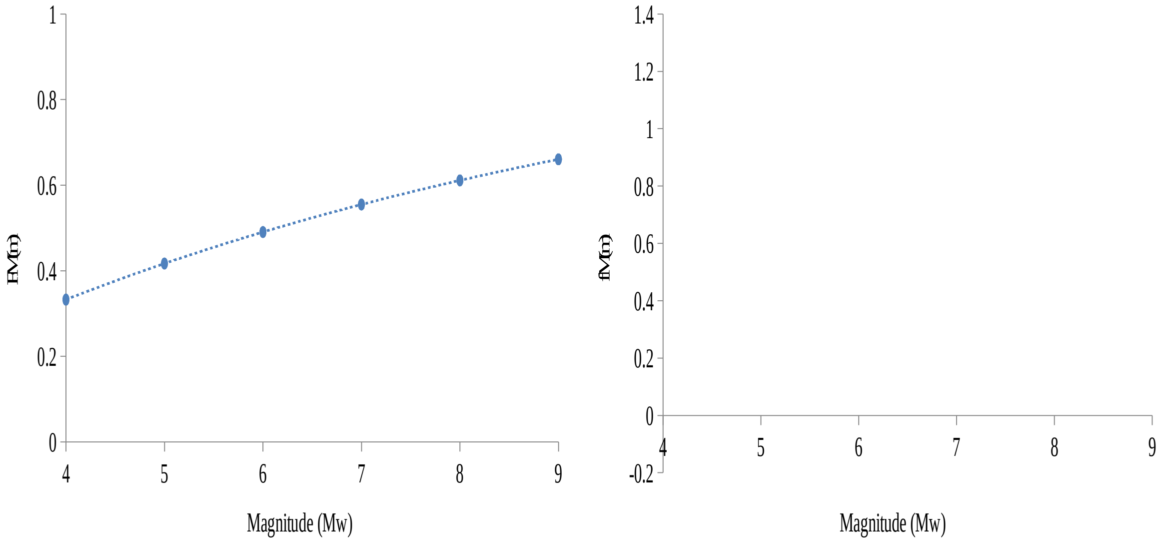

(a) (b)

Figure 6.4 (a) CDF and **(b)** PDF of magnitude.

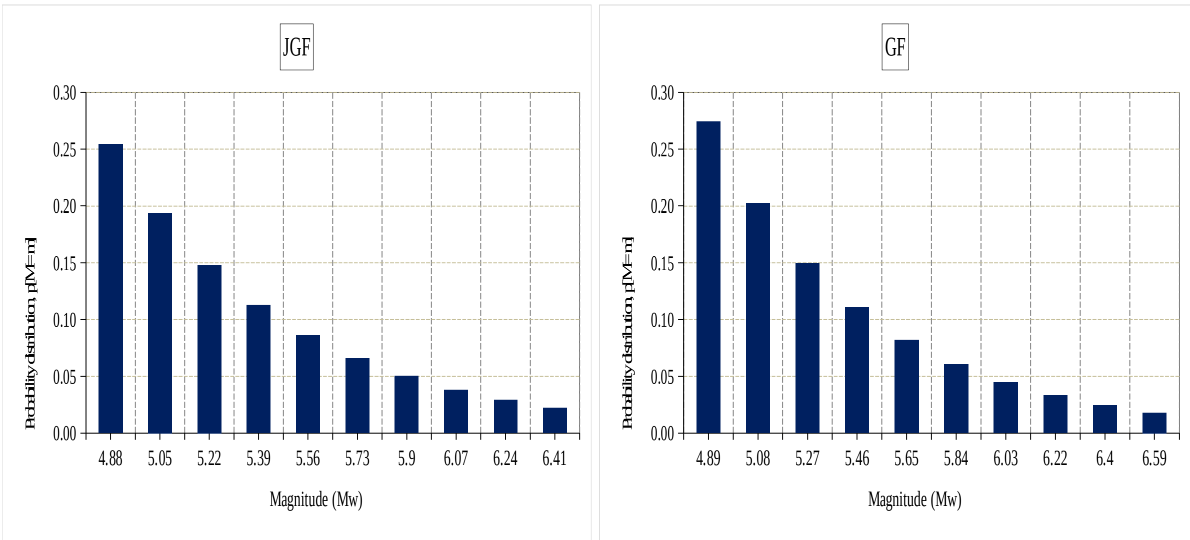

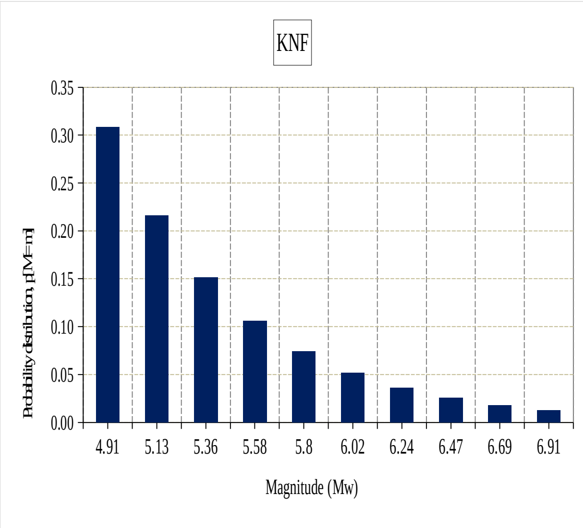
KNF
Probability distribution p[M=m]
0.00 0.05 0.10 0.15 0.20 0.25 0.30 0.35
4.91 5.13 5.36 5.58 5.8 6.02 6.24 6.47 6.69 6.91
Magnitude (Mw)

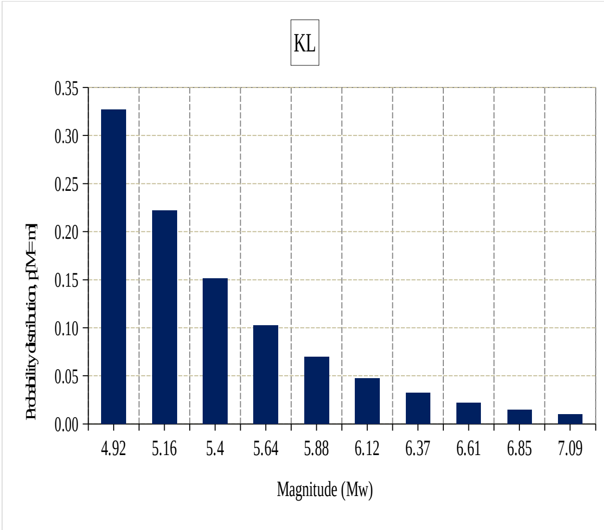
KL
Probability distribution p[M=m]
0.00 0.05 0.10 0.15 0.20 0.25 0.30 0.35
4.92 5.16 5.4 5.64 5.88 6.12 6.37 6.61 6.85 7.09
Magnitude (Mw)

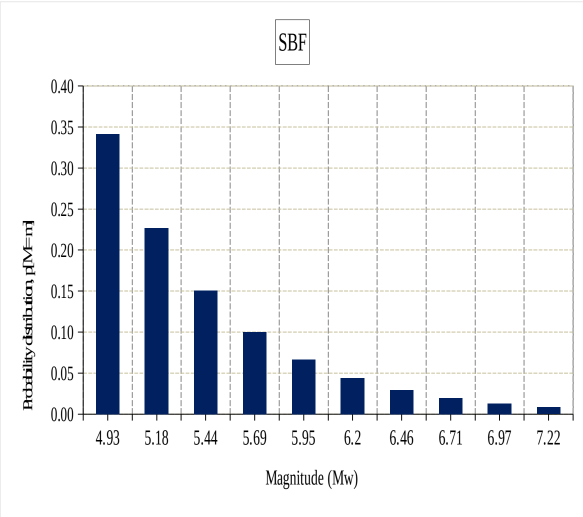
SBF
Probability distribution p[M=m]
0.00 0.05 0.10 0.15 0.20 0.25 0.30 0.35 0.40
4.93 5.18 5.44 5.69 5.95 6.2 6.46 6.71 6.97 7.22
Magnitude (Mw)

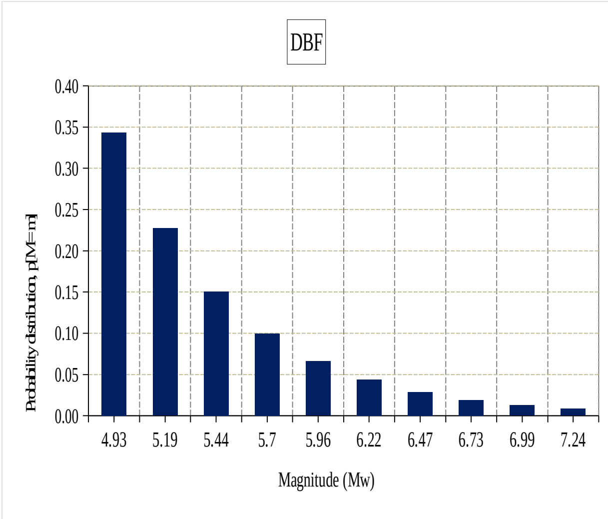
DBF
Probability distribution p[M=m]
0.00 0.05 0.10 0.15 0.20 0.25 0.30 0.35 0.40
4.93 5.19 5.44 5.7 5.96 6.22 6.47 6.73 6.99 7.24
Magnitude (Mw)

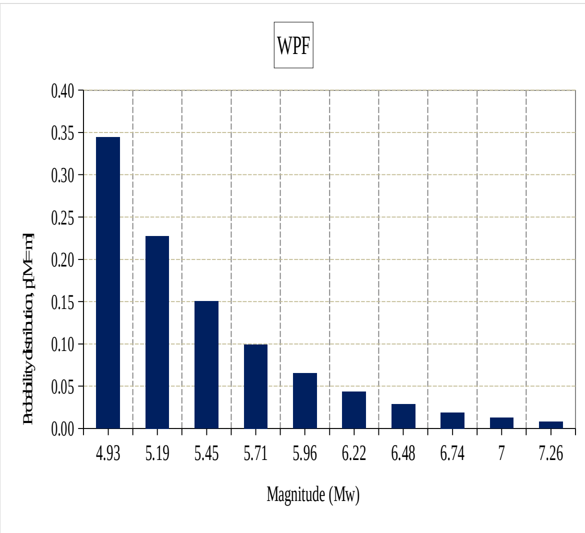
WPF
Probability distribution p[M=m]
0.00 0.05 0.10 0.15 0.20 0.25 0.30 0.35 0.40
4.93 5.19 5.45 5.71 5.96 6.22 6.48 6.74 7 7.26
Magnitude (Mw)

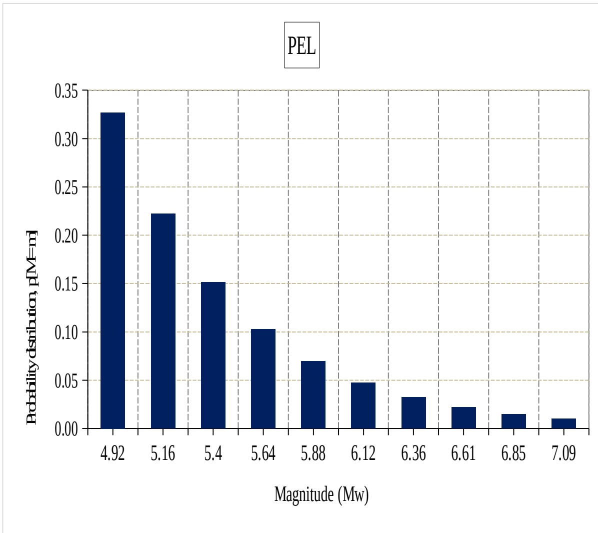
PEL
Probability distribution p[M=m]
0.00 0.05 0.10 0.15 0.20 0.25 0.30 0.35
4.92 5.16 5.4 5.64 5.88 6.12 6.36 6.61 6.85 7.09
Magnitude (Mw)

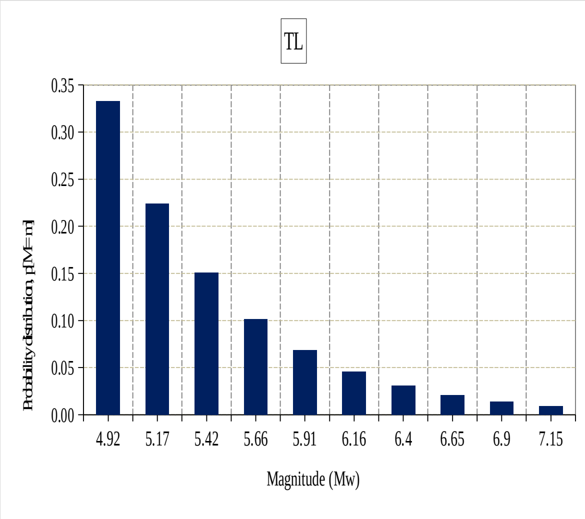
TL
Probability distribution p[M=m]
0.00 0.05 0.10 0.15 0.20 0.25 0.30 0.35
4.92 5.17 5.42 5.66 5.91 6.16 6.4 6.65 6.9 7.15
Magnitude (Mw)

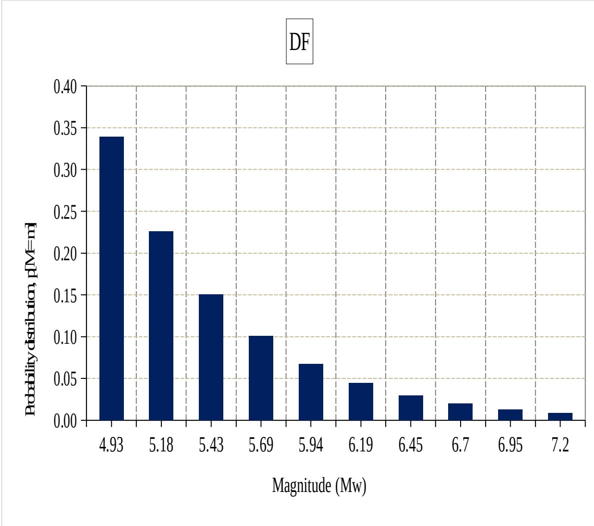
DF
Probability distribution p[M=m]
0.00 0.05 0.10 0.15 0.20 0.25 0.30 0.35 0.40
4.93 5.18 5.43 5.69 5.94 6.19 6.45 6.7 6.95 7.2
Magnitude (Mw)

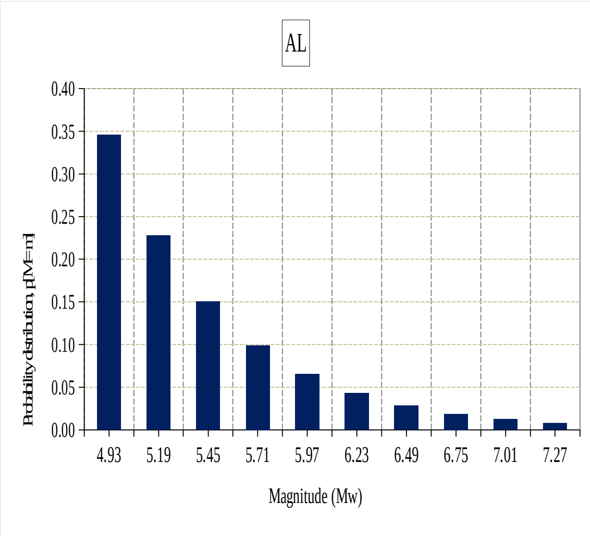
AL
Probability distribution p[M=m]
0.00 0.05 0.10 0.15 0.20 0.25 0.30 0.35 0.40
4.93 5.19 5.45 5.71 5.97 6.23 6.49 6.75 7.01 7.27
Magnitude (Mw)

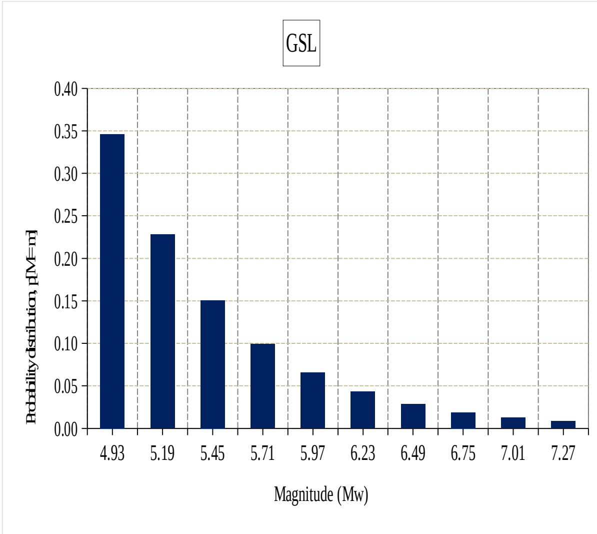
GSL
Probability distribution p[M=m]
0.00 0.05 0.10 0.15 0.20 0.25 0.30 0.35 0.40
4.93 5.19 5.45 5.71 5.97 6.23 6.49 6.75 7.01 7.27
Magnitude (Mw)

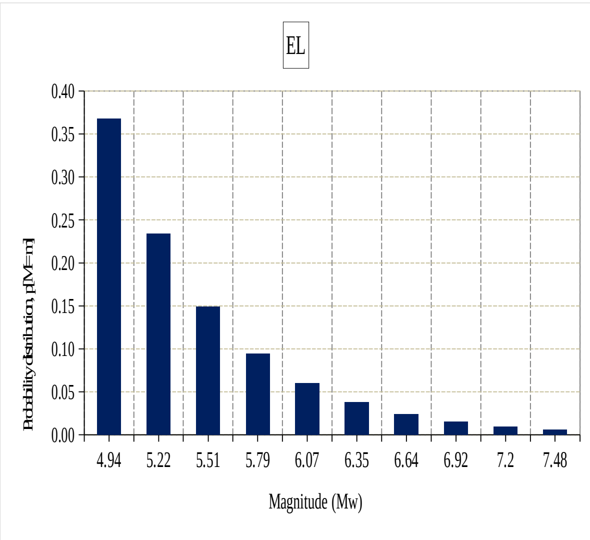
EL
Probability distribution p[M=m]
0.00 0.05 0.10 0.15 0.20 0.25 0.30 0.35 0.40
4.94 5.22 5.51 5.79 6.07 6.35 6.64 6.92 7.2 7.48
Magnitude (Mw)

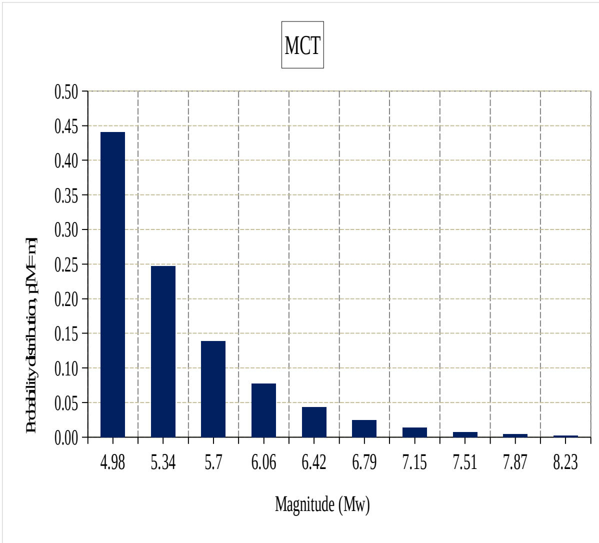
MCT
Probability distribution p[M=m]
0.00 0.05 0.10 0.15 0.20 0.25 0.30 0.35 0.40 0.45 0.50
4.98 5.34 5.7 6.06 6.42 6.79 7.15 7.51 7.87 8.23
Magnitude (Mw)

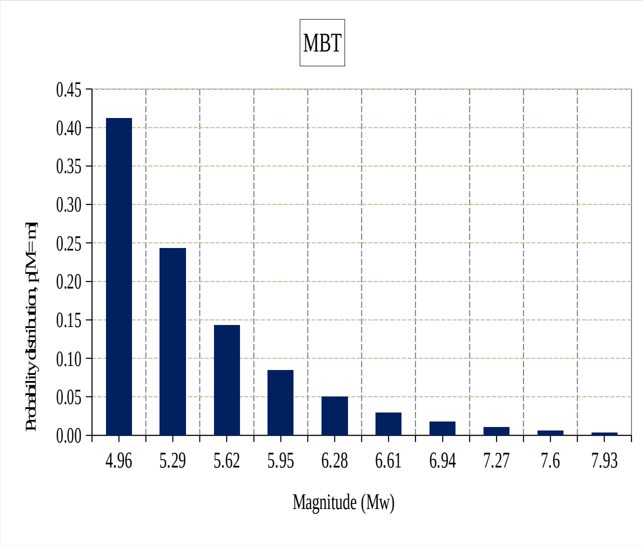

Figure 6.5 Probability distribution of magnitude for each fault.

6.4.3 Estimation of the seismicity parameters

The determination of the mean annual rate of earthquake exceedance, considering various magnitudes and locations over a period of 221 years, involves dividing the number of occurrences for each magnitude by the length of the time span. In this study, the seismic hazard parameters, denoted as "a" and "b," are derived from the Guttenberg-Richter recurrence law (equation 6.2). Figure 6.6 displays the values of these parameters for the study region, with "a" calculated as 3.16 and "b" as 0.656.

$$\log \lambda_m = 3.16 - 0.656\, M_w. \quad (6.15)$$

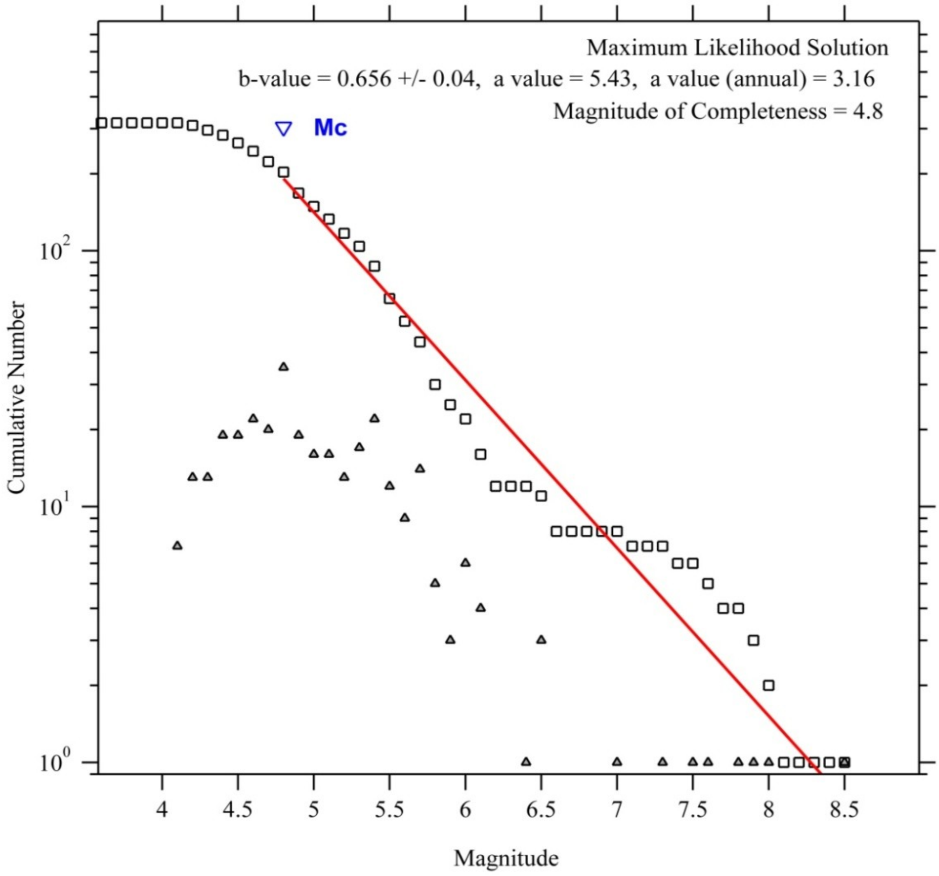

Figure 6.6 Application of Gutenberg–Richter law to Sikkim seismicity data.

The obtained values for "a" and "b" align with previous research conducted in Northeast India, the Darjeeling-Sikkim Himalayas, and adjacent areas. Nath et al. (2014) performed a Probabilistic Seismic Hazard Analysis (PSHA) for West Bengal's polygonal seismogenic sources with a hypocentral depth of 0-25 km, yielding "a" and "b" parameters of 1.96 (±0.36) and 0.54 (±0.07), respectively. For hypocentral depths of 25-70 km, the corresponding values were determined as 3.95 (±0.36) for "a" and 0.93 (±0.07) for "b." Additionally, Nayak and Sitharam [245] established "a" and "b" values of 6.0 and 0.7 (±0.2) for the Western and Central Himalayas and the Indo-Gangetic plain, respectively. The National Disaster Management Authority [169] recommended "a" and "b" values of 2.30 and 0.78 (±0.04), while Sreevalsa et al. [246] reported "a" and "b" as 6 and 0.8. Shankar and Sharma [247] proposed a value of 0.82 (±0.12) for "b".

6.4.3.1 Spatial distribution of the seismicity parameters

The spatial distribution of the seismic hazard parameters "a," "b," and the magnitude of completeness "M_c" is estimated using the ZMAP seismic tool developed by Wiemer

[161]. The study area, spanning 300km, is divided into a grid with a grid spacing of 0.1° × 0.1°. At each grid point, the "a" and "b" values are calculated based on the magnitude of completeness "M_c."

The determination of "M_c" relies on the power-law fit to the frequency-magnitude distribution relationship proposed by Wiemer and Wyss [248] within the ZMAP seismic tool [161]. To assess the uncertainties associated with "a," "b," and "M_c," the bootstrap method, as described by Chernick [249], is employed.

Figure 6.7 presents the spatial variation of the parameter "a," which exhibits a range of values from 5.4 to 5.6 across the study area. Similarly, Figure 6.8(a and b) illustrates the variation of parameter "b" with a range of 0.66 to 0.69, along with corresponding uncertainty ranges of 0.050 to 0.054.

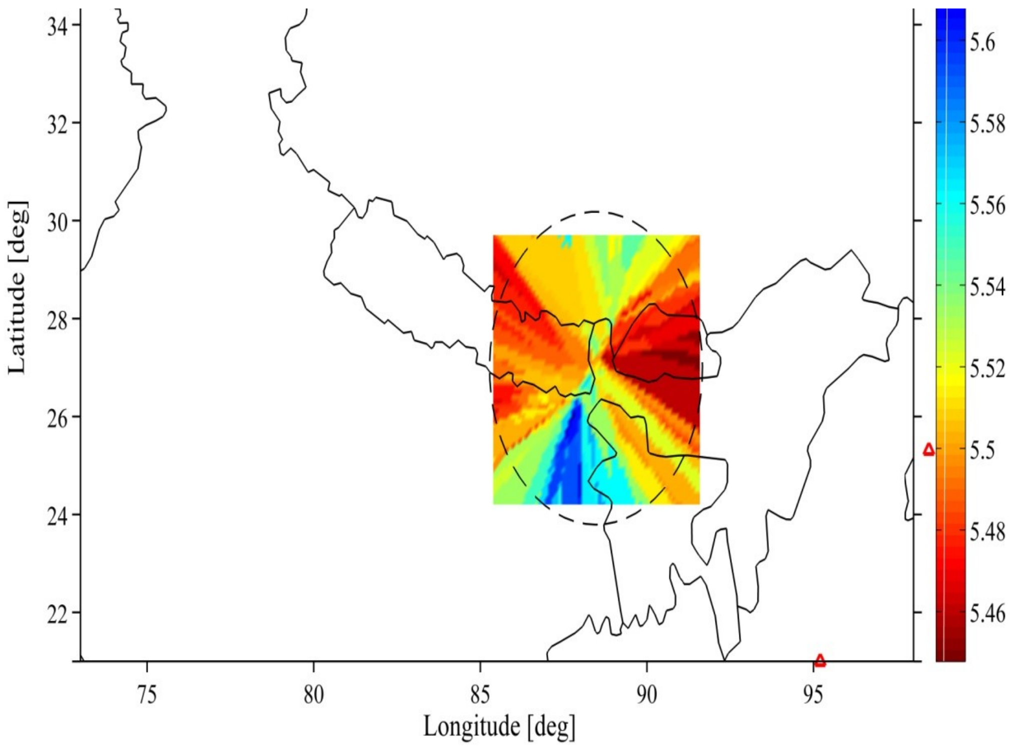

Figure 6.7 Spatial variation of *a*.

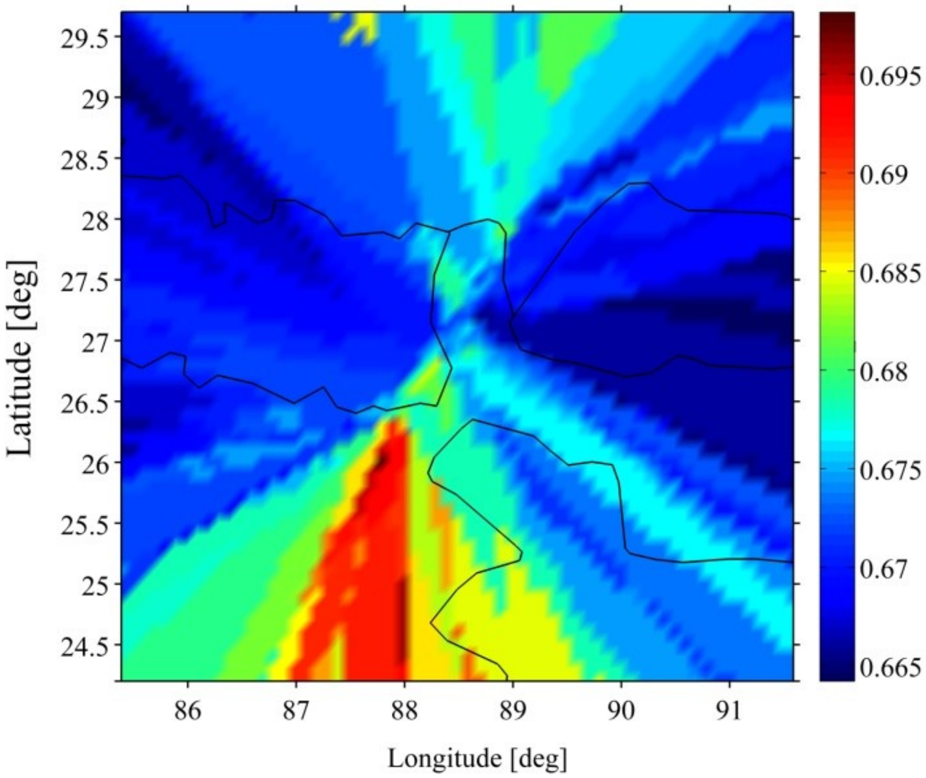

(a)

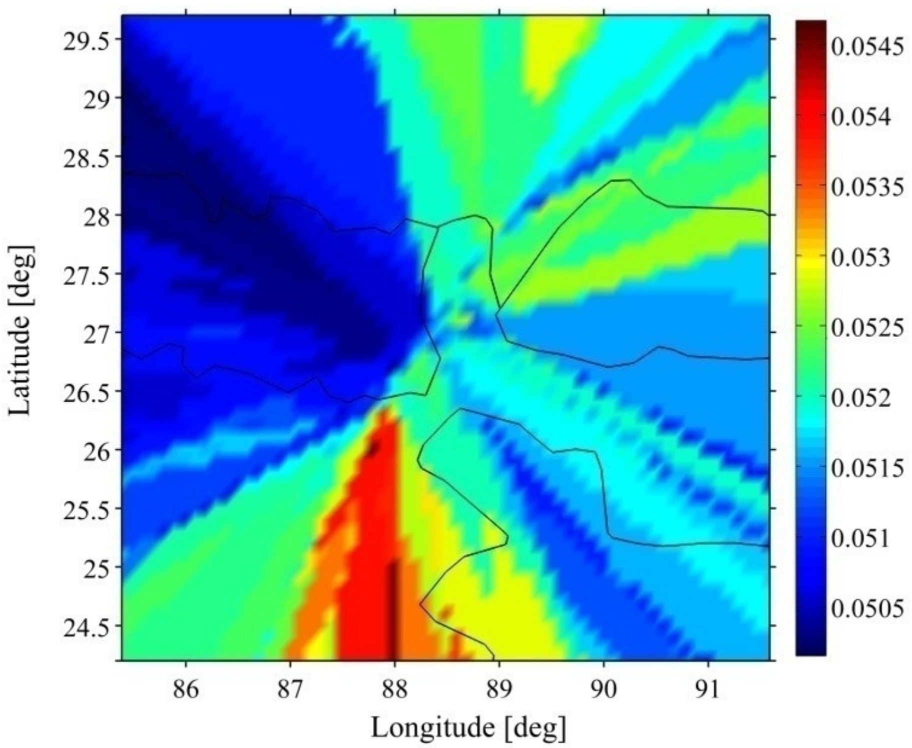

(b)

Figure 6.8 Spatial variations of the **(a)** *b* value and **(b)** standard deviation.

6.5 Hazard assessment

The Probabilistic Seismic Hazard Analysis (PSHA) in this study follows the classical approach presented by Cornell [45]. The evaluation process involves several key steps, including the identification of seismic sources, determination of seismicity parameters, selection of appropriate attenuation relationships, and consideration of uncertainties. Using the RCRISIS software, the PSHA calculates the frequency of exceedance for various levels of ground motions, corresponding to the mean return period, within the designated study area. The outcomes of the analysis are then presented as hazard maps and curves. By adhering to this established methodology, the study provides valuable insights into the seismic hazard characteristics of the region. The PSHA results, obtained through the utilization of RCRISIS software, are presented below in the subsequent sections.

6.5.1 Hazard maps

To assess the seismic hazard in the 300 km study area, hazard distribution maps were generated for Peak Ground Acceleration (PGA) and Peak Spectral Acceleration (PSA) corresponding to 10% and 2% probability of exceedance in 50 years. The analysis considered both point and linear seismic sources.

The study area was divided into a grid with a spacing of 0.1° × 0.1°, covering the entire 300 km region. Geometric and seismicity parameters of all sources were incorporated, and the depth information for each source was obtained from seismological databases. The tectonic depth range was limited to 30 km. An attribute table of ANBU-13 GMPE (Ground Motion Prediction Equation) along with 14 spectral ordinates was developed and utilized within the RCRISIS software.

By combining all input parameters, including uncertainties, the frequency of exceedance of ground motions was estimated for each source at every grid point, leading to the development of hazard maps. These hazard curves were further combined to estimate the seismic hazard distribution maps for the entire study area. The resulting hazard maps included PGA and PSA values for 10% and 2% probability of exceedance in 50 years.

Additionally, Spectral Acceleration (SA) maps were evaluated at various time periods (0.1, 0.2, 0.3, 0.4, 0.5, 0.6, 0.8, 1, 1.2, 1.4, 1.6, 1.8, and 2 seconds) using the ANBU-13 GMPE.

Figure 6.9 presents the PGA hazard map for a 475-year return period within the 300 km study region. Furthermore, Figures 6.10 to 6.12 illustrate the PSA maps at 0.1, 0.5, and 1-second time periods for a 10% probability of exceedance in 50 years. Notably, the PGA values range from 0.21 to 0.32 g across the study area, while the highest ground intensity is observed in the 0.1-second PSA map, ranging from 0.28 to 0.40 g. The eastern and central parts of the study region exhibit the maximum hazard distribution, while other areas demonstrate comparatively lower levels of hazards that vary with the time period, as depicted in Figures 6.11 and 6.12. It is important to note that the 10% probability of exceedance in 50 years corresponds to a 475-year return period, which serves as the design basis earthquake (DBE) for seismic designs.

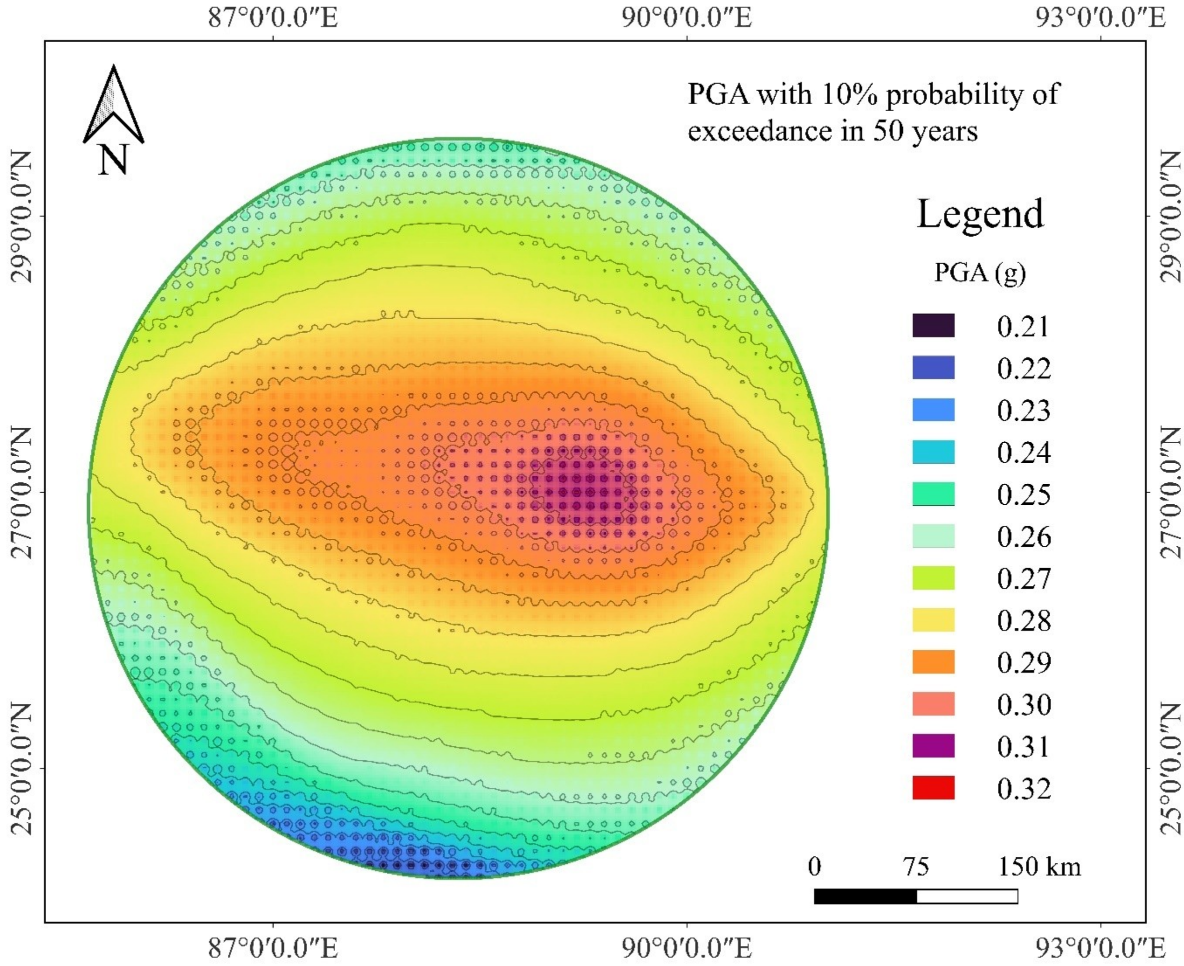

Figure 6.9 PGA hazard map for 10% probability of exceedance in 50 years

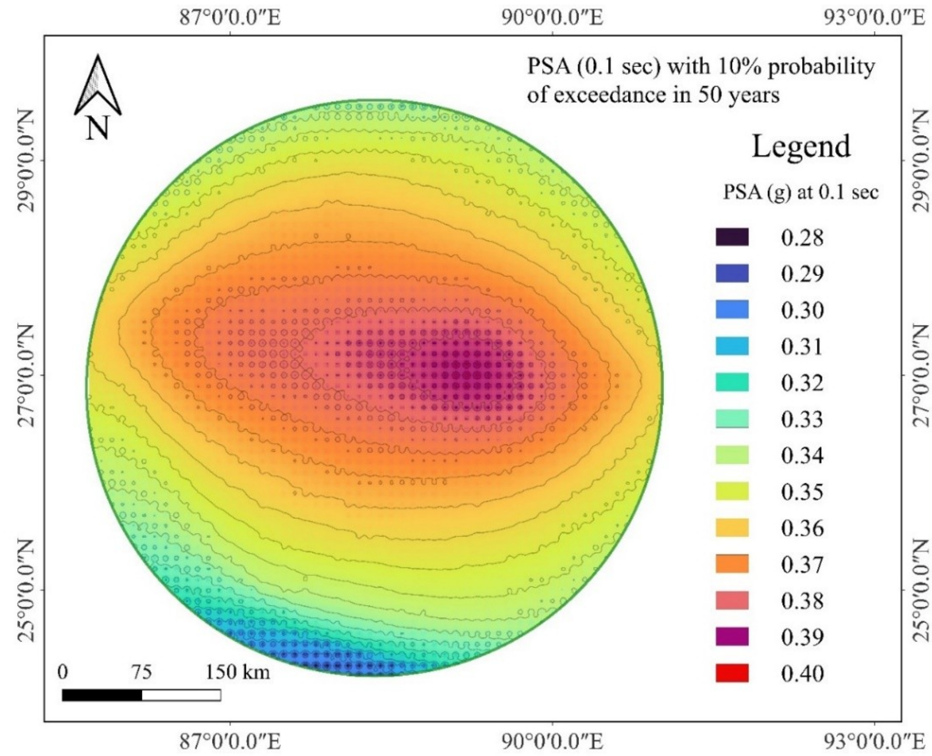

Figure 6.10 Seismic hazard distribution in terms of PSA at 0.1 sec for 475 years return period.

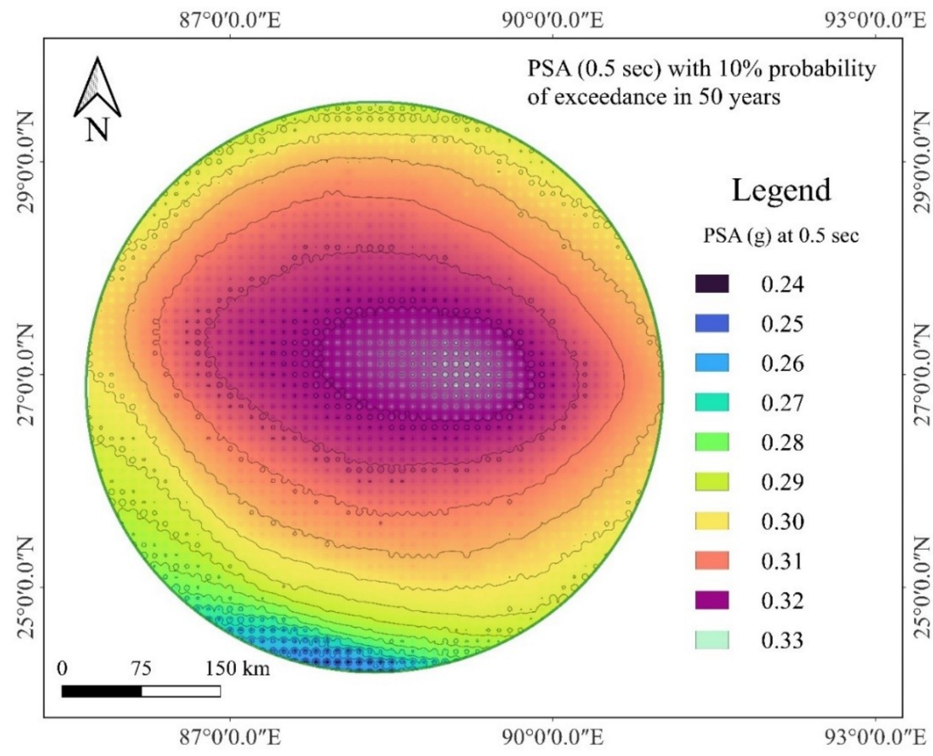

Figure 6.11 Seismic hazard distribution in terms of PSA at 0.5 sec for 475 years return period

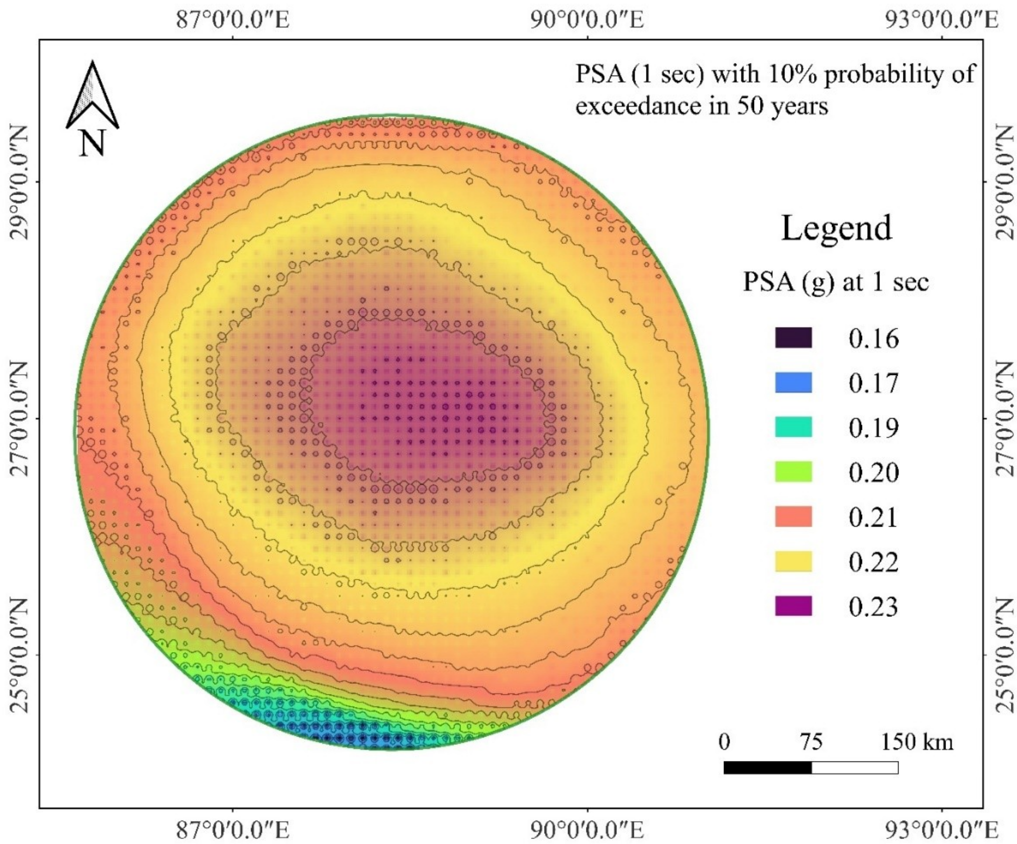

Figure 6.12 Seismic hazard distribution in terms of PSA at 1 sec for 475 years return period.

Similarly, hazard maps were developed for a 2% probability of exceedance in 50 years, corresponding to a return period of 2475 years. These maps provide the Maximum Considered Earthquake (MCE) values, which are crucial for ultimate checking and performance evaluation in seismic design.

Figure 6.13 displays the PGA hazard map for the 2475-year return period. It is evident from the figure that ground motions ranging from 0.20g to 0.26g have a higher occurrence rate compared to the 475-year return period. These ground motions exhibit higher intensity compared to the 475-year return period.

In addition to PGA, Spectral Acceleration (SA) maps were developed at various time periods. However, the focus was primarily on predominant time periods, namely 0.1, 0.5, and 1 second. The corresponding SA maps are depicted in Figures 6.14 to 6.16. Among these, the maximum hazard is observed at 0.1 second, with PGA values ranging from 0.26g to 0.33g.

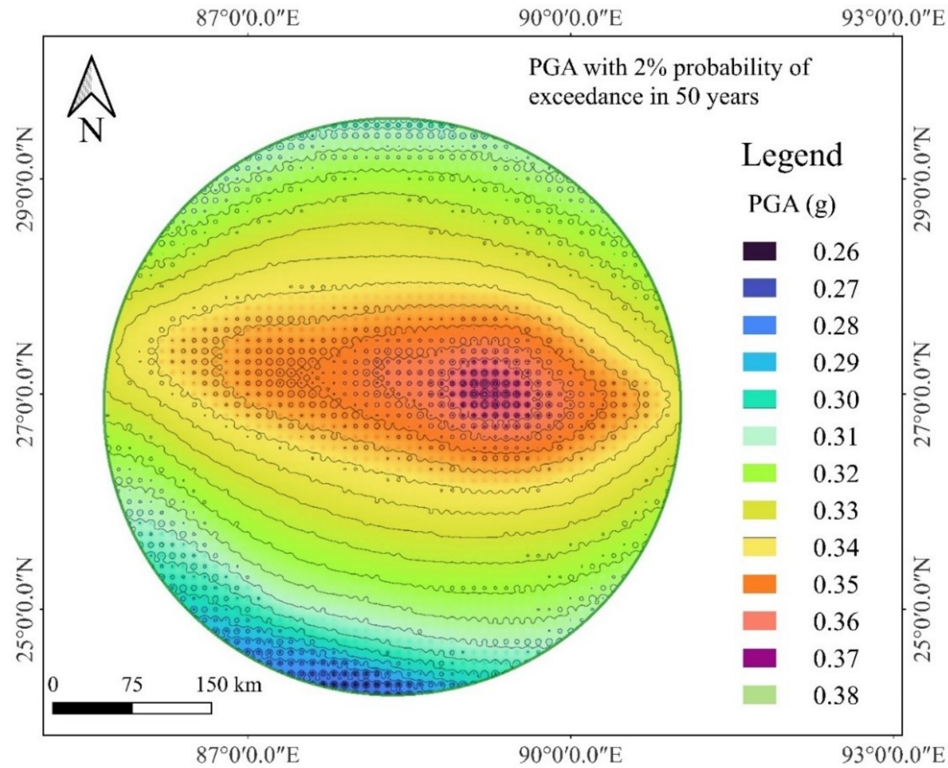

Figure 6.13 PGA hazard map for 2% probability of exceedance in 50 years for bed rock level.

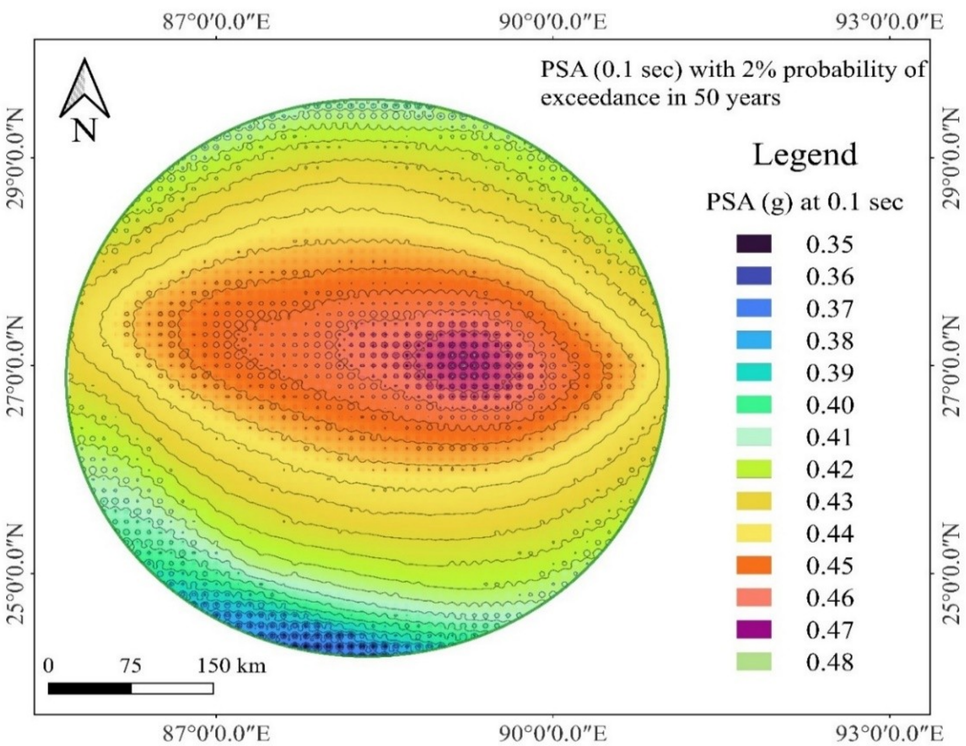

Figure 6.14 Seismic hazard distribution in terms of PSA at 0.1 sec for 2475 years return period.

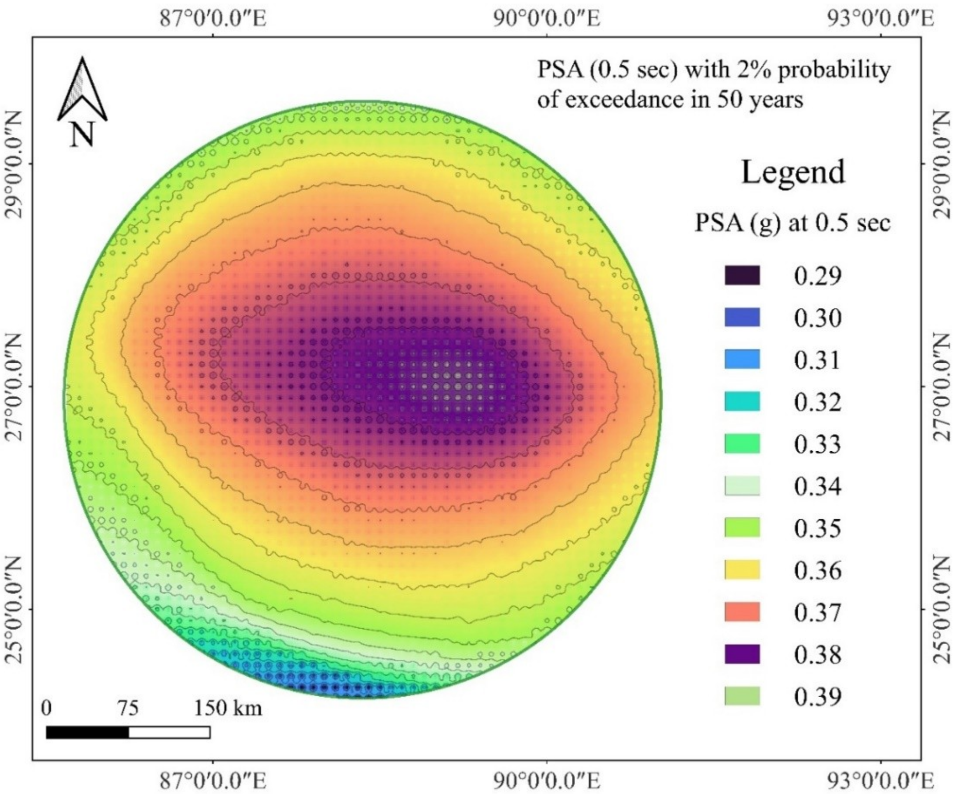

Figure 6.15 Seismic hazard distribution in terms of PSA at 0.5 sec for 2475 years return period.

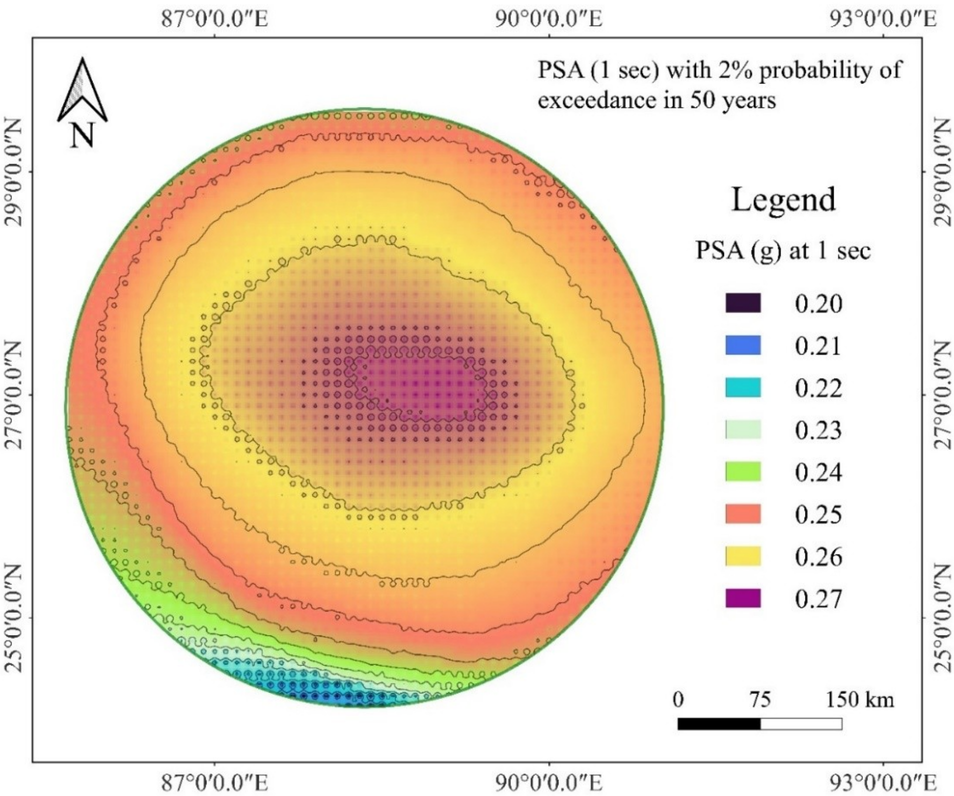

Figure 6.16 Seismic hazard distribution in terms of PSA at 1 sec for 2475 years return period.

6.5.2 Hazard curves

The hazard curves are a fundamental tool for comparing and assessing the probability of exceedance at specific sites. These curves provide valuable insights into the variation of hazards across different areas. They are plotted as a function of the annual rate of exceedance, cumulative rate of exceedance, or probability of exceedance (Y-axis), against the corresponding peak ground acceleration (X-axis).

For the study area, the hazard curve is derived by combining the hazard curves obtained from all active sources at each grid point. This cumulative hazard curve represents both the 2% and 10% probability of exceedance levels for a 50-year time frame, indicated by the red and green dotted lines in Figure 6.17.

Analysis of the cumulative hazard curve reveals important information. For example, at zero seconds, the frequency of exceedance probability is 0.28g for a return period of 475 years and 0.34g for a return period of 2475 years. This implies that a peak ground acceleration of 0.28g has a 10% probability of being exceeded within a 50-year period, while a peak ground acceleration of 0.34g has a 2% probability of exceedance within the same time frame.

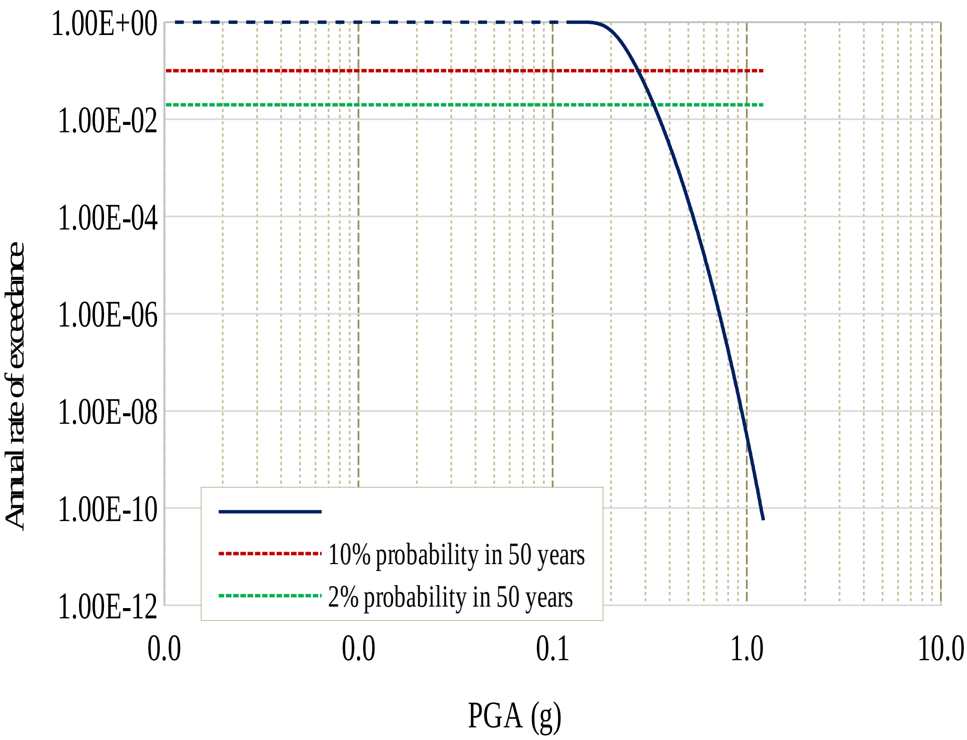

Figure 6.17 Cumulative Hazard curve of the study area

The maximum hazard level is observed in the eastern-central part of the study area, specifically located at latitude 27° 0' 7. 27" N and longitude 89° 12' 18. 68" E. The hazard curve for this location is depicted in Figure 6.18. At this point, the design peak ground motion is recorded as high, reaching 0.32g, while the effective peak ground acceleration measures 0.38g. The hazard curves exhibit variations across different locations, influenced by the surrounding seismicity characteristics. These hazard curves specific to various locations are presented in Annexure-C.

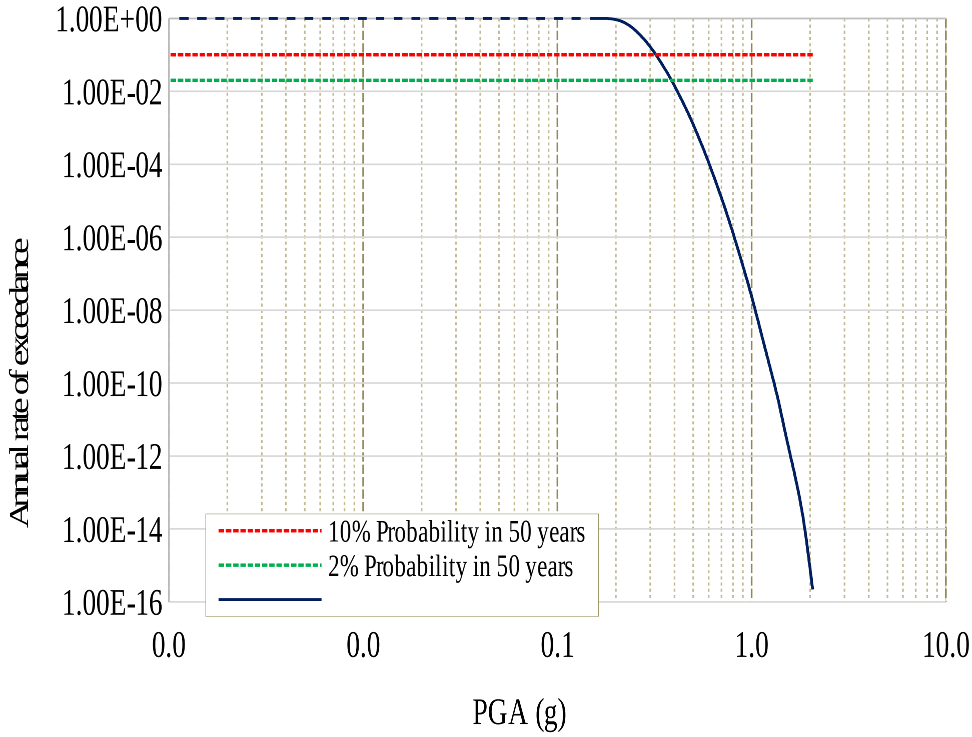

Figure 6.18 Hazard center of the site that produced highest design ground motion within the site.

To compare the findings of the present study with previous data, Table 6.1 provides a comprehensive overview. The results obtained in this study are compared with the PGA hazard maps generated by earlier researchers for the same study region. However, it should be noted that variations in results may arise due to differences in factors such as hypo-central depth range and the Ground Motion Prediction Equation (GMPE) employed. In the present study, the choice of GMPE, depth range, and distance considered for the study area aligns closely with the findings of Maiti et al. [75], where a hypo-central depth of 0-25km was utilized. Nevertheless, it is important to acknowledge that different GMPE's, depths, and distances may yield varying results in hazard assessments.

Table 6.1 PSHA Previous studies related to the study area.

Researcher	**Area**	**PGA(g)**
Present study	Darjeeling Sikkim Himalayas (Tectonic seismogenic source of hypocentral depth: 30km and earthquake events depth is considered according to the collected data from seismological database.	0.28
Manik and Nath [69]	Darjeeling–Sikkim Himalaya (surface level)	0.579
Nath et al. [74]	Entire West Bengal (Rock level)	0.42
Maiti et al. [75]	Entire West Bengal	
	Rock level	0.42
	Tectonic seismogenic source (hypocentral depth: 0–25km)	0.325
	Tectonic seismogenic source (hypocentral depth: 25–70km)	0.175
	Layered polygonal seismogenic source (hypocentral depth: 0–25km)	0.25
	Layered polygonal seismogenic source (hypocentral depth: 25–70km)	0.11
	At the firm rock site condition conforming to B/C site class (Vs: 620–760 m/s)	0.445
	Surface consistent	0.714

6.5.3 Uniform hazard response spectrum

The Uniform Hazard Response Spectrum (UHRS) is a design tool used to assess the maximum acceleration as a function of time period, considering a specific damping ratio. It represents the seismic hazard due to ground shaking levels and is commonly employed to analyze the structural performance under earthquake loading. The UHRS is derived from probabilistic analysis, ensuring an equal exceedance probability at each vibration period. It is developed based on hazard curves for various periods to generate an equivalent hazard response spectrum.

In the present study, the 5% damping uniform hazard response spectra are generated for the study area. Figures 6.19 illustrate the response spectra corresponding to a 10% and 2% probability of exceedance in a 50-year time frame. These response spectra are crucial in identifying potential risks associated with the study region. Notably, at a 10%

probability of exceedance in 50 years, the PSA at 0.1 sec exhibits the highest ground intensity, measuring 0.36g. As the time period increases, the ground intensity gradually decreases from 0.36g to 0.07g.

Similarly, the hazard distribution at a 2% probability of exceedance in 50 years shows a maximum ground intensity of 0.43g, which then decreases gradually from 0.43g to 0.092g across the time periods. It is important to note that significant changes in return periods are observed as the period of interest increases. Furthermore, the study indicates that the spectral acceleration at zero period amounts to 0.28g for a return period of 475 years.

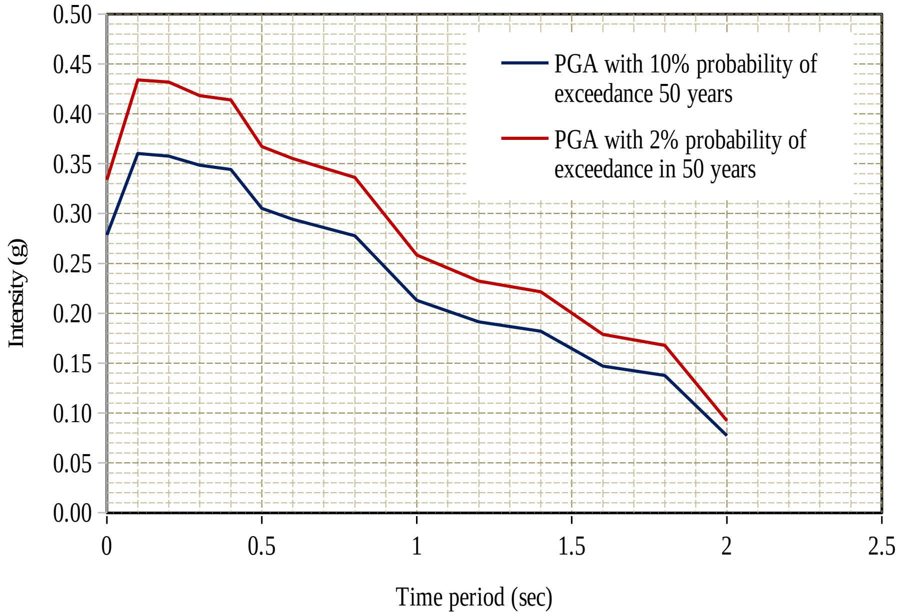

Figure 6.19 UHRS generated for the study area at 2% and 10% probability of exceedance in 50 years.

The uniform hazard response spectrum at the latitude and longitude of 27° 0' 7. 27" N - 89° 12' 18.648" E shows highest response and is shown in Figure 6.20. The PSA at 0.1 sec exhibits the highest ground intensity of 0.40g and 0.48g for 10% and 2% probability of exceedance in 50 years.

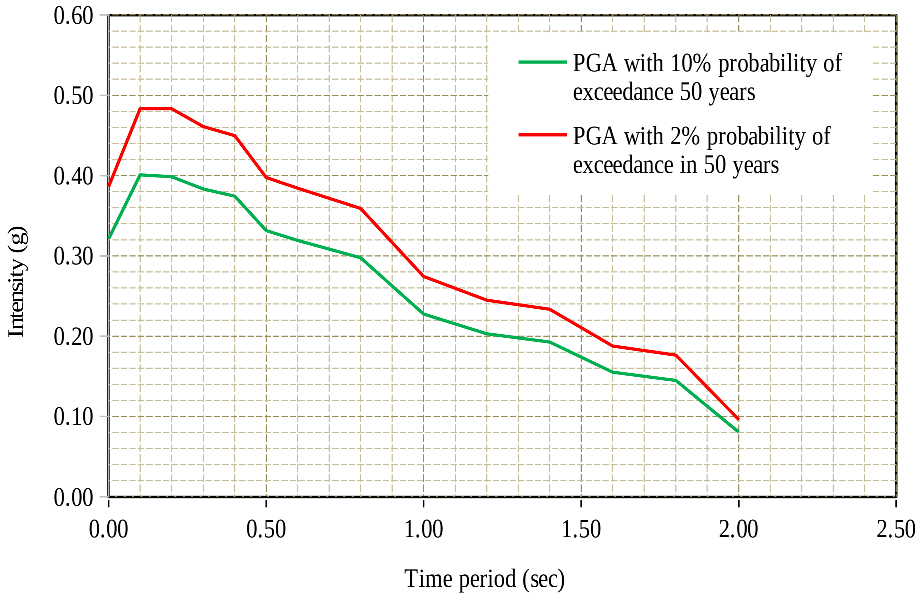

Figure 6.20 UHRS generated for the site that produced highest within the study area for 2% and 10% probability of exceedance in 50 years.

The UHRS results vary from site to site and are presented in Annexure-C for different grid points.

6.5.3.1 Comparison of MCE with IS:1892-2002 zone factor

In the context of PSHA analysis, the Design Basis Earthquake (DBE) and Maximum Credible Earthquake (MCE), also known as the Maximum Considered Earthquake, are essential design parameters that define the peak horizontal accelerations with specific probabilities of exceedance over a 50-year time period. The MCE represents the most severe earthquake effects that can be anticipated, while the DBE is considered a reasonable estimate of the earthquake effect expected to occur at least once during the design life of a structure [250].

In this study, the PSHA analysis yielded a DBE of 0.28g for the 300 km study area, indicating the peak ground acceleration with a 10% probability of exceedance in 50 years. Additionally, the MCE for the study area was determined to be 0.34g, representing the peak ground acceleration with a 2% probability of exceedance in 50 years.

It is worth noting that according to IS:1893-2002, the seismic zone factor (Z) is influenced by the maximum considered earthquake in the respective zone, which provides a reasonable estimate of the effective peak ground acceleration. In the case of the study area, the seismic zone factor prescribed by the IS code for Zone IV is 0.24g. However, the analysis conducted in this study indicates a value of 0.33g for the study area, suggesting a higher seismic loading than what is accounted for in the code. It is important to acknowledge that certain regions in India, situated in high seismicity areas along the Himalayan plate boundary, exhibit zone factors similar to those designated for Zone V. Consequently, the current Indian code might be overly optimistic and could potentially underestimate the seismic loading in such high seismicity regions.

These findings highlight the significance of comprehensive and accurate seismic hazard assessments to ensure the appropriate design and construction of structures in areas prone to seismic activity. They also emphasize the need for periodic updates and revisions to building codes to align with the latest scientific understanding and reflect the true seismic hazards faced in different regions.

6.5.4 De-aggregation

To assess the hazard contribution from different combinations of magnitude, distance, and epsilon values, a de-aggregation plot was generated. De-aggregation provides insights into the probability of exceedance for a specific intensity measure (such as PGA>x) based on various factors. In this study, the de-aggregation was conducted using R-Crisis software for a 10% probability of exceedance in 50 years. The de-aggregation plot was generated at a critical site within the study area, located at latitude 27° 0' 7.27" N and longitude 89° 12' 18.68" E. Figure 6.21 presents the de-aggregation plot for this site, showing that within the next 50 years, there is a 10% probability of exceedance of 0.28g at a distance of 21 km, associated with a magnitude of 7.3. It is important to note that the de-aggregation results may vary for different sites, and the detailed de-aggregation results for various grid points are provided in Annexure-C.

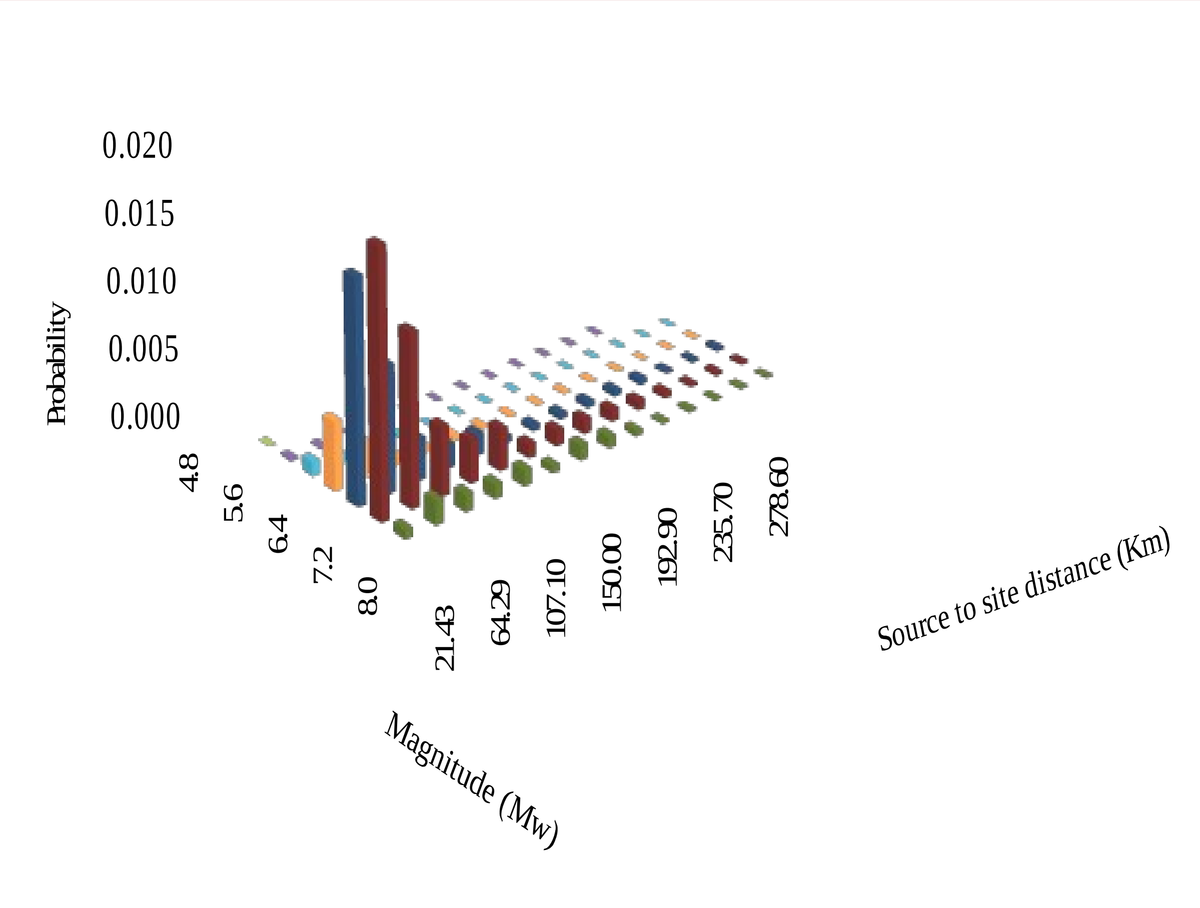

Figure 6.21 De-aggregation chart at center of the study area

6.6 Summary and conclusion

A comprehensive seismic hazard assessment using Probabilistic Seismic Hazard Analysis (PSHA) has been conducted for the study area of DSH and its surrounding 300 km radius. The assessment involved the development of a refined earthquake catalog spanning the period from 1800 to 2021, encompassing moment magnitudes ranging from 4.0 to 8.5. Depth information for the earthquakes was obtained from seismological databases, with 30 km focal depth assigned to 20 active seismotectonic features identified in the region. The ANBU-13 Ground Motion Prediction Equation (GMPE) was selected to estimate ground motions for the study area. PSHA computations were performed using RCRISIS software, utilizing fine grids to account for uncertainties and generate hazard curves, hazard maps, uniform hazard response spectra, and de-aggregation analysis for a 2% and 10% probability of exceedance in 50 years.

The Gutenberg-Richter relationship provided recurrence parameters a (3.16) and b (0.65) from the PSHA calculations. The hazard curves indicated a design-specific ground intensity of 0.28g for the study area and a maximum considered ground intensity of 0.33g. Spectral accelerations were generated for 14 natural periods ranging from 0 to 2 seconds at 5% damping, with ground intensities ranging from 0.06g to 0.40g and 0.07g to 0.48g for 475 and 2475-year return periods, respectively. Seismic hazard maps provided detailed information about the hazard distribution within the study area, with the site located at latitude 27° 0' 7.272" N and longitude 89° 12' 18.648" E showing the maximum hazard, likely due to its proximity to major tectonic features. Uniform hazard response spectra (UHRS) were generated for the study area and the major hazard site at different time periods. De-aggregation analysis revealed a 10% probability of occurrence for a PGA of 0.31g with a magnitude of 7.3 at a distance of 21 km from the site within the next 50 years. Extensive hazard curves, UHRS, and de-aggregation results for different grid points are provided in Annexure-C.

The findings of this PSHA assessment contribute valuable insights to engineering practices and infrastructure development, aiding in the development of future mitigation measures for the study area's various hazards. This study provides updated seismic hazard information compared to previous studies, offering detailed hazard maps and curves for earthquake-resistant analysis and design. The design shaking intensity and spectrum derived from this analysis are beneficial for dynamic landslide analysis and other seismic designs, contributing to reducing damage from future earthquakes and slope failures.

While PSHA is a widely accepted approach for seismic hazard assessment, it does not account for topography and soil properties. Therefore, the next chapter of this study will explore a fully probabilistic technique that incorporates topography and slope parameters into the seismic hazard assessment.

Fully Probabilistic Seismic Hazard Analysis

7.1 Introduction

Earthquake-induced landslides pose significant natural hazards in the Himalayan terrain. While active seismicity plays a crucial role in triggering landslides, passive factors such as slope geology and hilly terrain also contribute to slope instability. While it may not be possible to eliminate the risk of landslides, early prediction of potential problems can help mitigate the impact of significant ground shaking or other triggering factors.

Designing appropriate ground motion is vital for minimizing the impact of landslides in seismically active regions. Many researchers utilize probabilistic seismic hazard maps to determine design ground motion for slope stability analysis. However, these approaches often overlook uncertainties associated with the selection of ground motion levels and slope parameters in both probabilistic and deterministic seismic hazard analyses. To address this, researchers have integrated mathematical relationships between seismic hazard assessment and landslide-causing factors such as topography and geology. This combined study provides valuable insights into the most probable ground motion that could trigger landslides, thereby aiding in earthquake-induced landslide mitigation.

Given the high vulnerability of the study area to earthquakes and landslides, this study adopts an improved fully probabilistic approach for seismic hazard assessment. The approach incorporates the history of earthquakes, slope terrain, and geotechnical properties. It combines probabilistic assessment with a dynamic slope stability model based on Newmark's approach to estimate consistent earthquake scenarios for landslides. Moreover, this approach effectively addresses data uncertainties and provides reliable hazard management for landslides. The framework aims to calculate the total probability of slope failure under various levels of ground shaking.

The objective of this chapter is to develop different slope models based on varying slope properties and integrate them with probabilistic assessment to determine design ground motions for each slope model. The resulting design charts represent the most probable ground motions capable of triggering landslides.

7.2 Methodology of FPSHA

The fully probabilistic approach encompasses the complete probability framework for seismically induced landslides, considering the entire chain of events from strong motion prediction to deformation mode. This approach involves two key calculation stages: (1) assessing the probability of occurrence for different Peak Ground Acceleration (PGA) values (y_i) over a specific period, and (2) determining the conditional probability at which a landslide is triggered by a given PGA. The total probability of slope failure within a specified time period (T) is computed using the following equation:

$$P_T(slope\,failure)=\sum_j \sum_i w_j P_T(PGA=y_i).P(slope\,failure|\quad y_i, model\ j)=\sum_j \sum_i w_j p_{ij}, \quad (7.1)$$

where P_T (PGA = y_i) occurrence probability of PGA (y_i) in a specific time interval and P (slope failure | y_i, model j) is the probability of the slope failure under seismic loading (y_i) for slope model j. Geo-mechanical models of the slope were ranked by weight w_j, where $\sum_j w_j = 1$.

7.2.1 Probability of occurrence of PGA

Probabilistic Seismic Hazard Analysis (PSHA) plays a crucial role in the development of seismic hazard curves, which are essential for addressing engineering safety concerns at specific levels of hazard [243]. The primary objective of this analysis is to determine the probability of exceeding a particular Peak Ground Acceleration (PGA) within specified time intervals, as depicted in seismic hazard curves [110]. The study incorporates all potential seismic sources in the vicinity, considering a range of earthquake magnitudes, site-to-source distances, and Ground Motion Prediction Equations (GMPE's). The calculation involves assessing the contributions from all relevant seismic sources that exceed a certain acceleration is:

$$\lambda(PGA>y)=\sum_{i=1}^{n_{sources}} v(M_i ¿¿ m_{min}) \sum_{j=1}^{n_M} \sum_{j=1}^{n_R} P(PGA>y_i \vee m_j, r_j).P(M_i=m_k).P(R_i=r_k)¿ \quad (7.2)$$

where, $n_{sources}$ represent the potential earthquake sources, and n_M and n_R represent the

number of possible earthquakes and distances. P(M_i = m_k) and P(R_i = r_k) are the probability

of magnitudes and distances in source i. *v*, the average rate of the threshold magnitude greater than the minimum magnitude, can be expressed as

$$v = 10^{a - b m_o} \tag{7.3}$$

where a and b parameters are constants and m_o are the constant mean annual exceedance rate. These three parameters are obtained from the EC using Gutenberg–Richter distribution.

The probability of magnitude is

$$F_M(m) = \frac{1 - 10^{-b(m - m_0)}}{1 - 10^{-b(m_{max} - m_0)}}, \tag{7.4}$$

where $F_M(m)$ is the cumulative distribution function and m_{max} is the maximum magnitude that the source produces.

The (PGA>y_i | m_j, r_k) is the probability of exceedance of the PGA for acceleration y_i for m_j and r_k. The probability of exceedance of any PGA value is derived as follows:

$$P(PGA > y| \quad m, r) = 1 - \phi\left(\frac{\ln(y) - \ln\,(PGA)}{\sigma_{lnPGA}}\right) \tag{7.5}$$

Where σ_{lnPGA} is the standard deviation.

The probability of exceeding the PGA value (y_i) in the next T years is

$$P_T(PGA > y) = 1 - e^{-\lambda(PGA > y).T} (7.6)$$

The probability of occurrence of a discrete set of ground motions is as follows:

$$P_T(PGA = y_i) = P_T(PGA > y_i) - P_T(PGA > y_{i+1}) (7.7)$$

Equation (7.7) is used to evaluate the total probability of slope failure in equation 7.1.

7.2.2 Conditional probability

The second step in calculating the fully probabilistic analysis is to know the probability of slope failure under seismic loading. The analysis is evaluated using Jibson probabilistic model [251], which corresponds to the Weibull distribution shown in equation 7.8. The model was calibrated with predicted sliding displacement (D_N) in cm, critical acceleration (a_c) and peak ground acceleration (y) based on the Newmark approach [10]. Newmark's approach assesses the probability of slope triggering given the critical slope acceleration (a_c) and PGA value (y).

$$P\left(slopefailure \middle| D_N\right) = 0.335 ¿$$

Where,

$$\log D_N(y) = 0.215 + ¿ \qquad (7.9)$$

7.2.2.1 Newmark's critical acceleration and cases considered

Many empirical relations are combined with Newmark's displacement (D_N) and intensity. However, in the present study, the predicted Newmark's slope displacement is evaluated with PGA using the above equation 7.9 [252].

The critical acceleration (a_c) is a function of slope geometry and static factor of safety (F_s) and is given as [10]

$$a_c = \left(F_s - 1\right) g sin\alpha \left(7.10\right)$$

Where F_s and g are the static factor of safety and factor of gravity, and α is the dip angle of the sliding surface.

The calculation of the static safety factor involves the use of a simplified limit equilibrium model for an infinite slope, based on the Newmark approach [10]. According to Newmark's approach, the initiation of landslide failure occurs when internal deformation accumulates within the sliding mass due to seismic forces exceeding a critical value.

The model assumes that the landslide mass slides along a planar surface and incorporates the following assumptions: the slope is homogeneous, the influence of pore pressure is negligible, the static safety factor is stress-independent and constant, the sliding mass of the slope behaves as a rigid solid, and the coefficients of static and dynamic friction remain constant and equal. The static factor of safety (F_s) is determined based on the principles of limit equilibrium theory [251]:

$$F_s = \frac{c'}{yzsin\alpha} + \frac{tan\varphi}{tan\alpha} + \frac{m y_w tan\varphi}{ytan\alpha}$$

(7.11)

where c’ is cohesion, φ is friction angle, z is slope normal thickness, γ and γ_w are the unit weight of material and groundwater, α is dip angle of the sliding surface, and m is the saturated sliding mass thickness. The soils in the area are saturated most of the year, so pore pressures are neglected from equation 7.11 and paid great attention to a third term of the equation.

In the next T years, the total probability of seismically induced landslide is obtained by substituting equations (7.8) and (7.7) in equation (7.1).

7.3 Material properties of the study area

The determination of the ground motion that triggers slope failure involves considering both the geotechnical parameters of the slopes and the characteristics of earthquake events. In this study, a total of 316 earthquake events and 20 major tectonic sources were selected for the initial step of the analysis, as detailed in Chapter 4.

Subsequently, the geotechnical parameters required for the Fully Probabilistic Seismic Hazard Analysis (FPSHA) were incorporated based on the limit equilibrium approach described in Equation (7.11). Various slope models were prepared, considering different slope angles (α) and soil parameters specific to the study region, including cohesion (c), friction angle (φ), and unit weight of the material (γ). The consideration of soil properties is crucial for conducting site-specific analyses. To obtain these geotechnical parameters, information from various research papers was gathered. According to Mandal [253], the friction angle (φ) ranges from 18 to 36 degrees for dry and wet conditions, while the cohesion varies from 0.01 to 0.90 kg/cm^3. The slope angle in the lesser Himalayas was reported to range from 30 to 75 degrees [254], and the unit weight of the materials (γ) in the study area was considered to be between 18 and 26 kN/m^3. Throughout the analysis, a constant thickness (z) of 5m and a saturated sliding mass thickness (m=1) were assumed. The choice of a 5m thickness for the slides is based on the observation that most earthquake and rainfall-induced landslides in the region are shallow and generally have a thickness within this range. Furthermore, it has been observed that even deep-seated landslides can be triggered by these shallow slides.

Based on these geotechnical properties, a total of 3120 slope models were developed. Each slope model was then linked to the PSHA analysis to evaluate the most probable triggering ground motion for that particular slope model. The FPSHA analysis was performed for all the slope models, following the two critical steps outlined in the preceding section.

7.4 FPSHA Results (Design charts)

Design charts have been developed to determine the most probable ground motion that would trigger the slope models. These charts provide a convenient and efficient method for assessing slope stability in terms of the anticipated ground motion. They offer a rapid means of evaluating different solutions to prevent slope failure, allowing for quick comparisons and consideration of the advantages and disadvantages of each solution. Previous studies have also provided design charts for slope stability based on the limit equilibrium method, such as those by Taylor [255], Bishop [256], and Morgenstern [257], which expressed slope stability in terms of factors of safety.

In the present study, design charts have been produced specifically for the triggering ground motion of slopes, incorporating the combination of Newmark's model and seismic hazard analysis. The analysis was conducted by considering various values of slope parameters at different slope angles, while keeping the unit weight and friction angle constant within each chart but varying them across different charts. Each slope model was prepared based on its specific slope angle and characteristics, resulting in a total of 3160 slope models within the study area.

The design-based earthquake (DBE), obtained from the 10% probability of occurrence in 50 years, is widely utilized as the design ground motion in seismic design practices worldwide. In this study, the DBE or the most probable ground motion scenario that would trigger the slopes within the next 50 years has been estimated and presented in the form of design charts. These design charts consider various slope angles ranging from 10^0 to 70^0, friction angles (φ) ranging from 18^0 to 36^0 degrees, cohesion (c) ranging from 0 to 80 kPa, and unit weight (γ) of 18 kN/m³. Figures 7.1 (a to j) depict the calculated DBE values for the different slope angles and geotechnical parameters.

The figures reveal that the most probable ground motion scenario for triggering landslides is higher for slopes with angles ranging from 10^0 to 40^0, whereas slopes with angles from 45^0 to 70^0 are triggered by lower Peak Ground Acceleration (PGA) values. Significant variations in ground motions are observed between deterministic and probabilistic analyses.

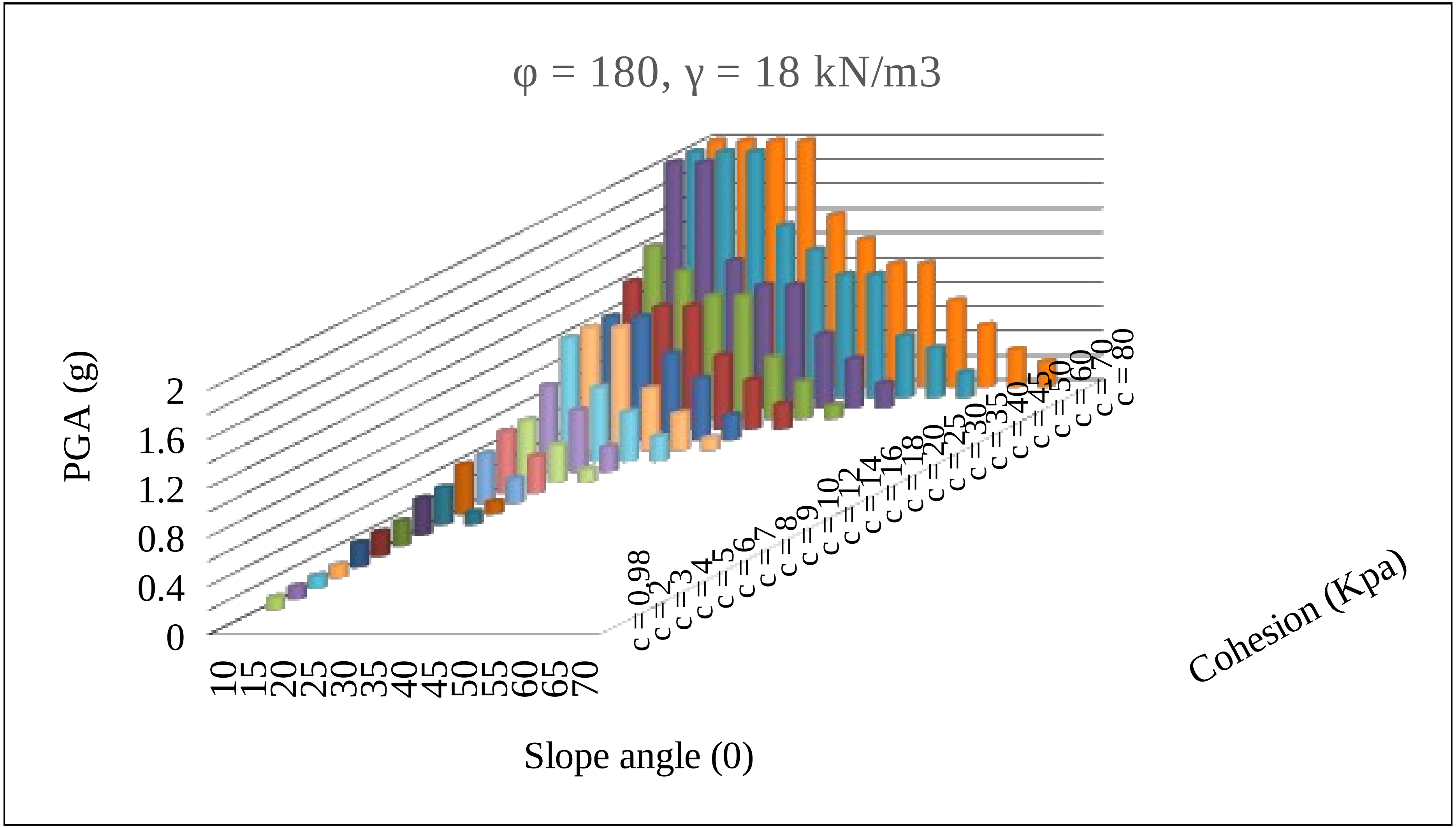

Figure 7.1 DBE design charts at various slope angle, Cohesion and γ = 18 kN/m^3 for (a) φ=18^0

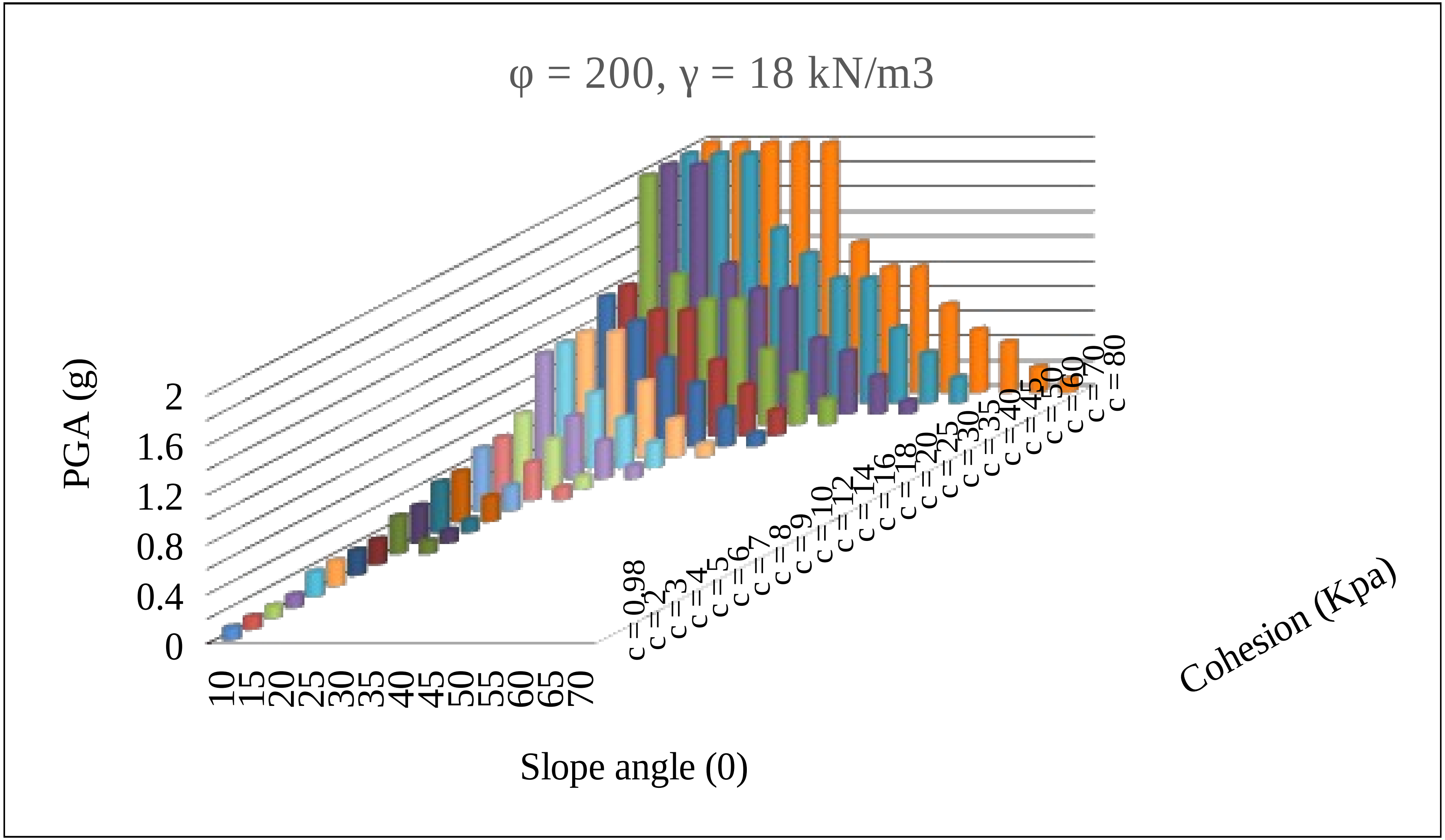

Figure 7.1 (b) φ=20^0

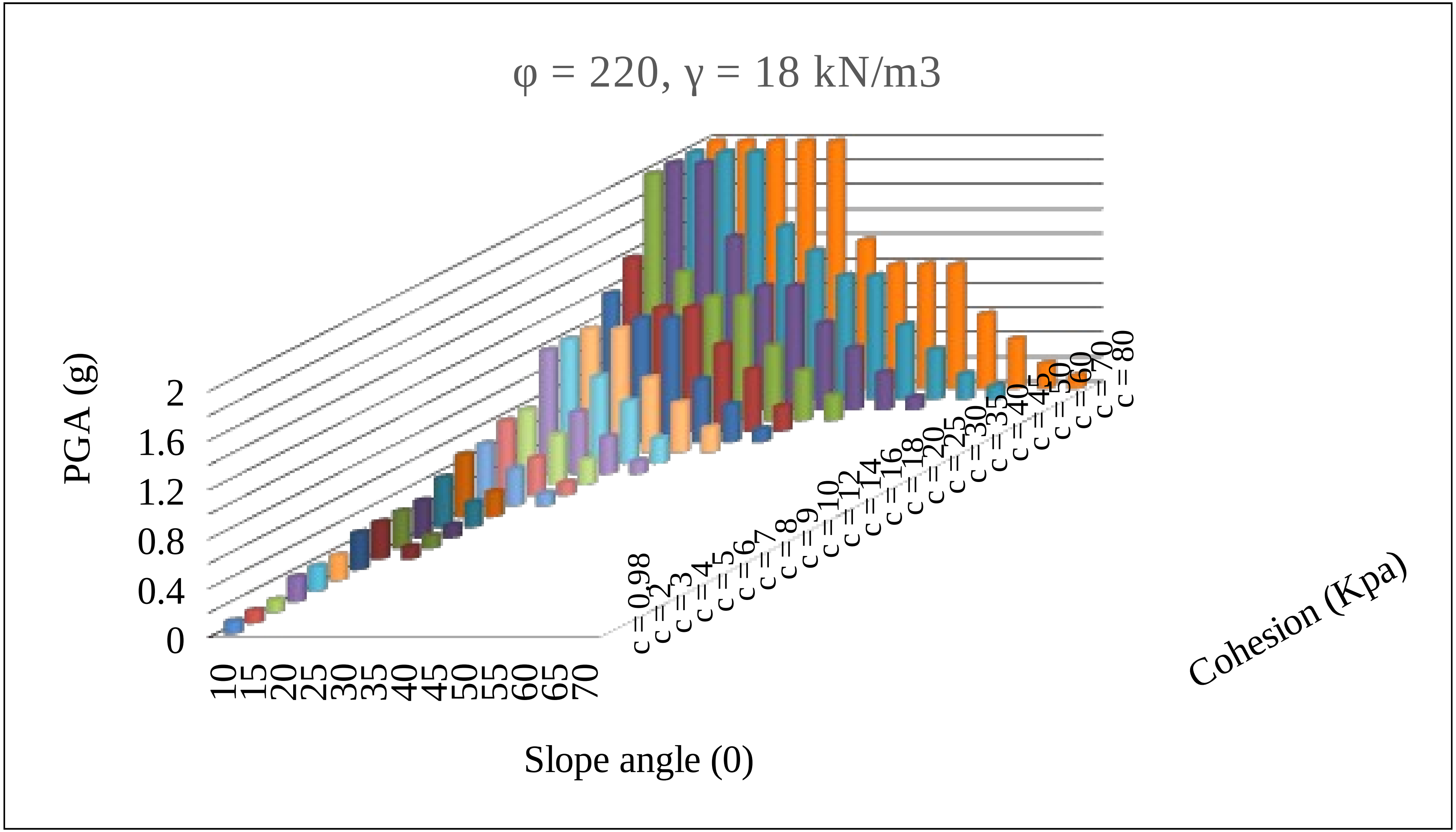

Figure 7.1 (c) $\varphi=22^0$

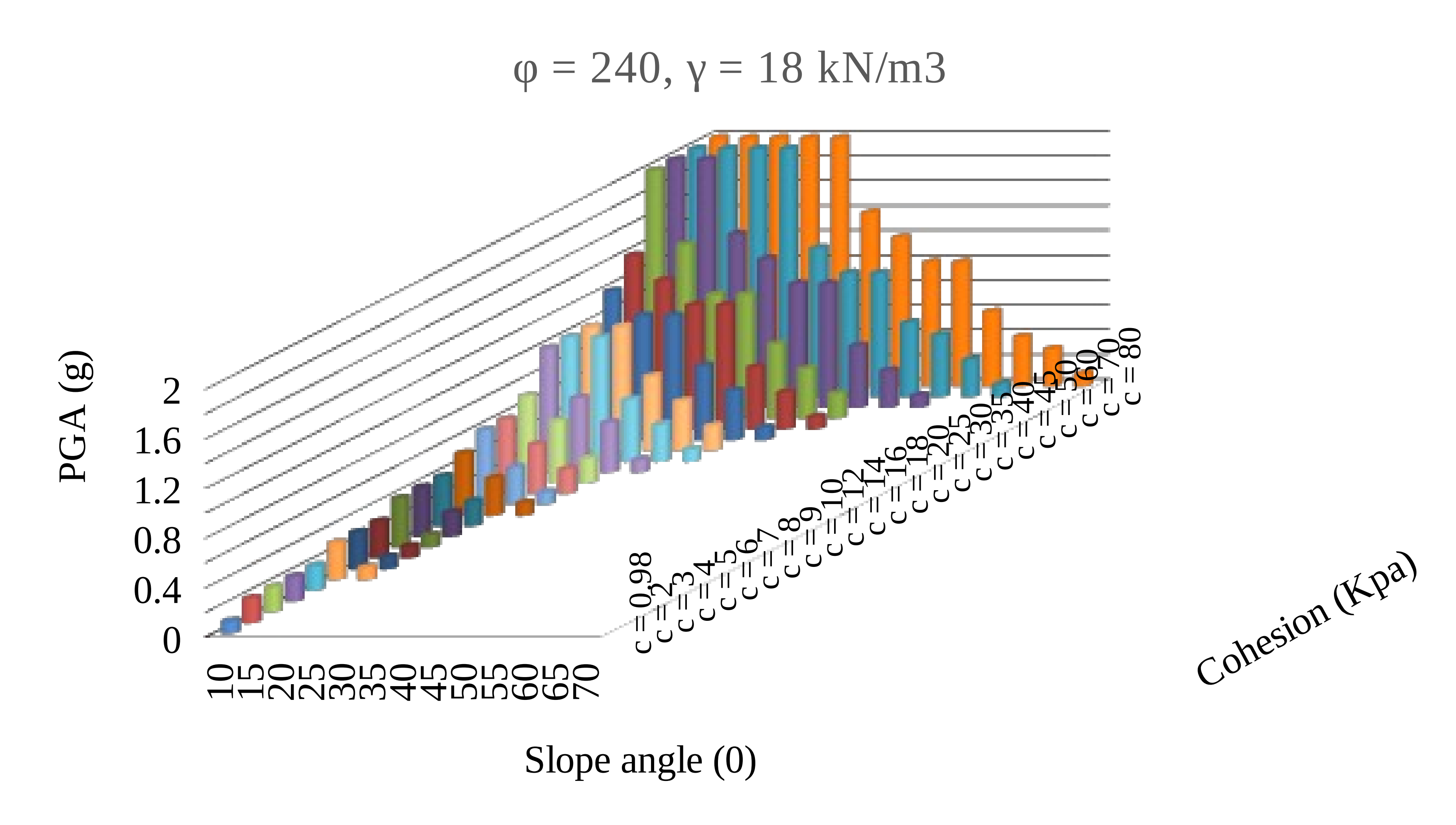

Figure 7.1 (d) φ=24^0

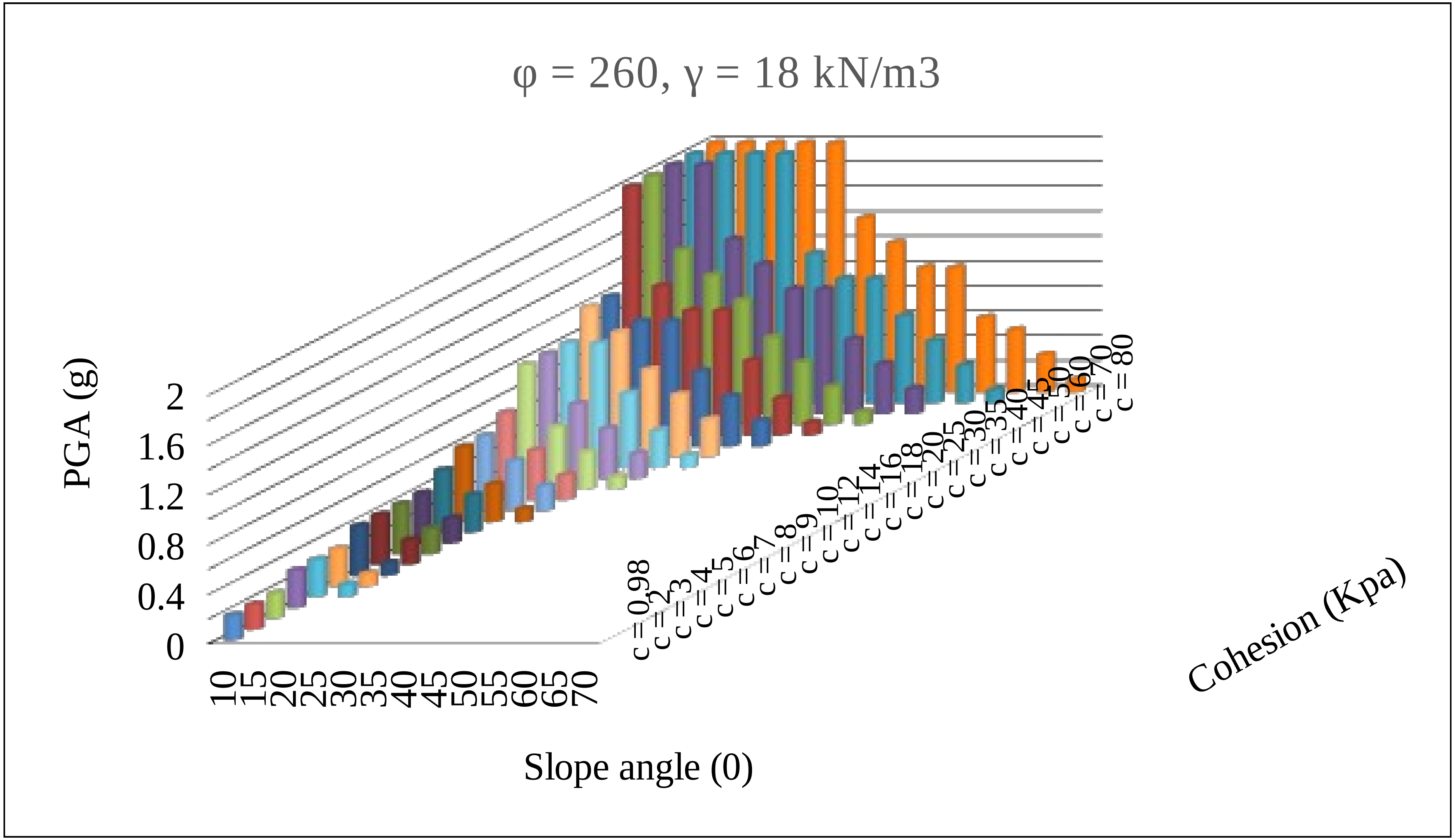

Figure 7.1 (e) φ=26^0

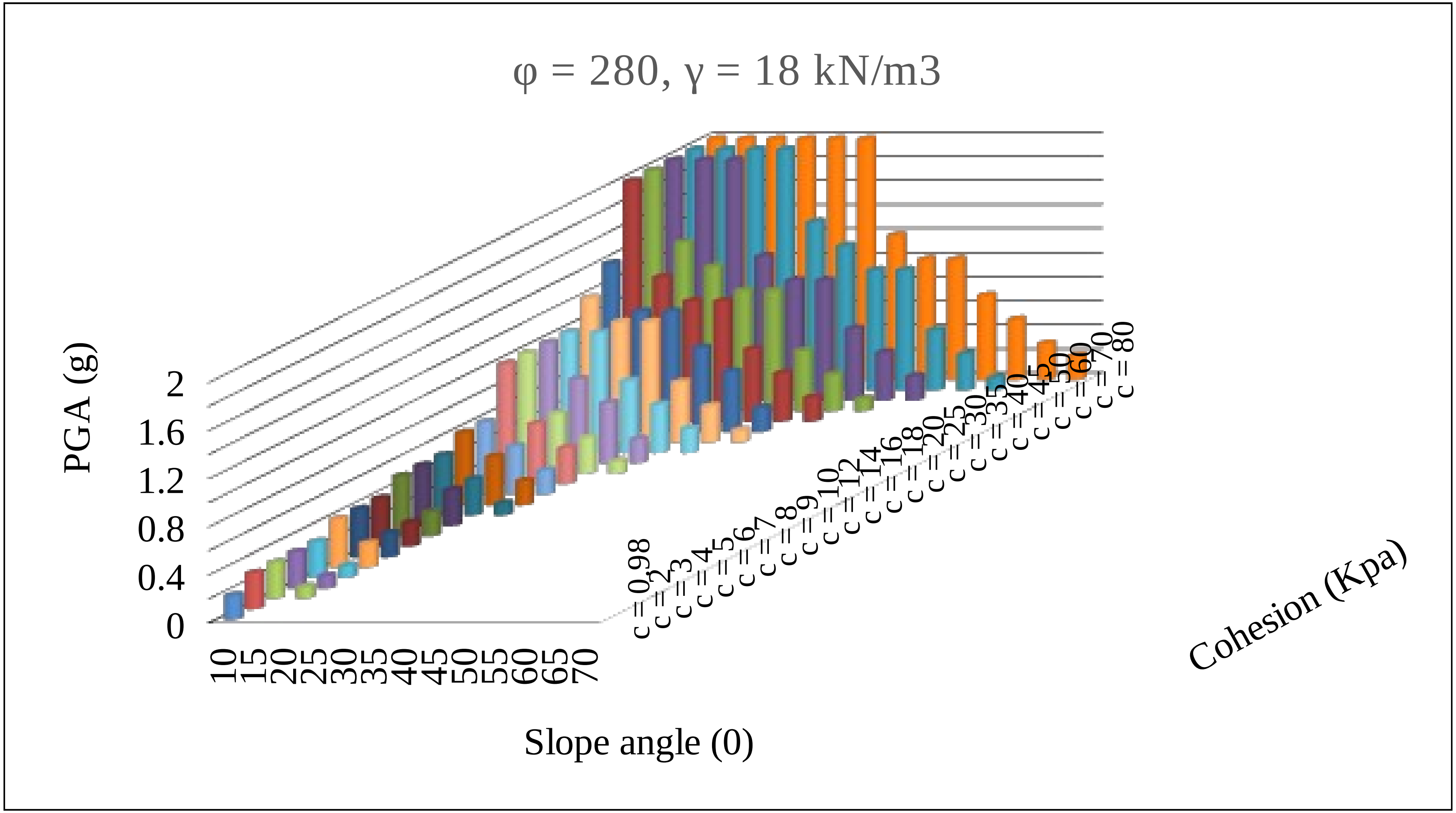

Figure 7.1 (f) $\varphi=28^0$

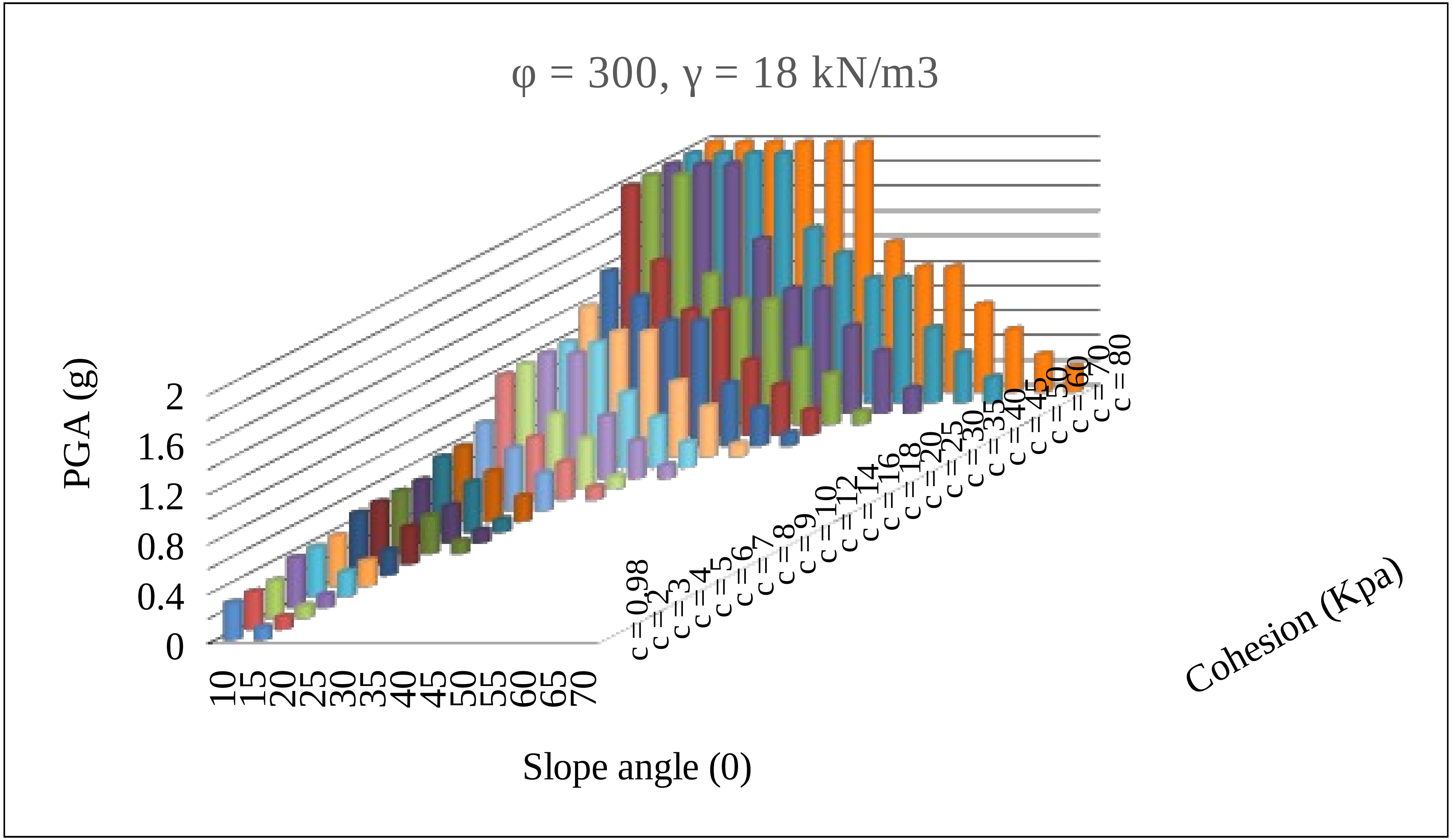

Figure 7.1 (g) φ=30^0

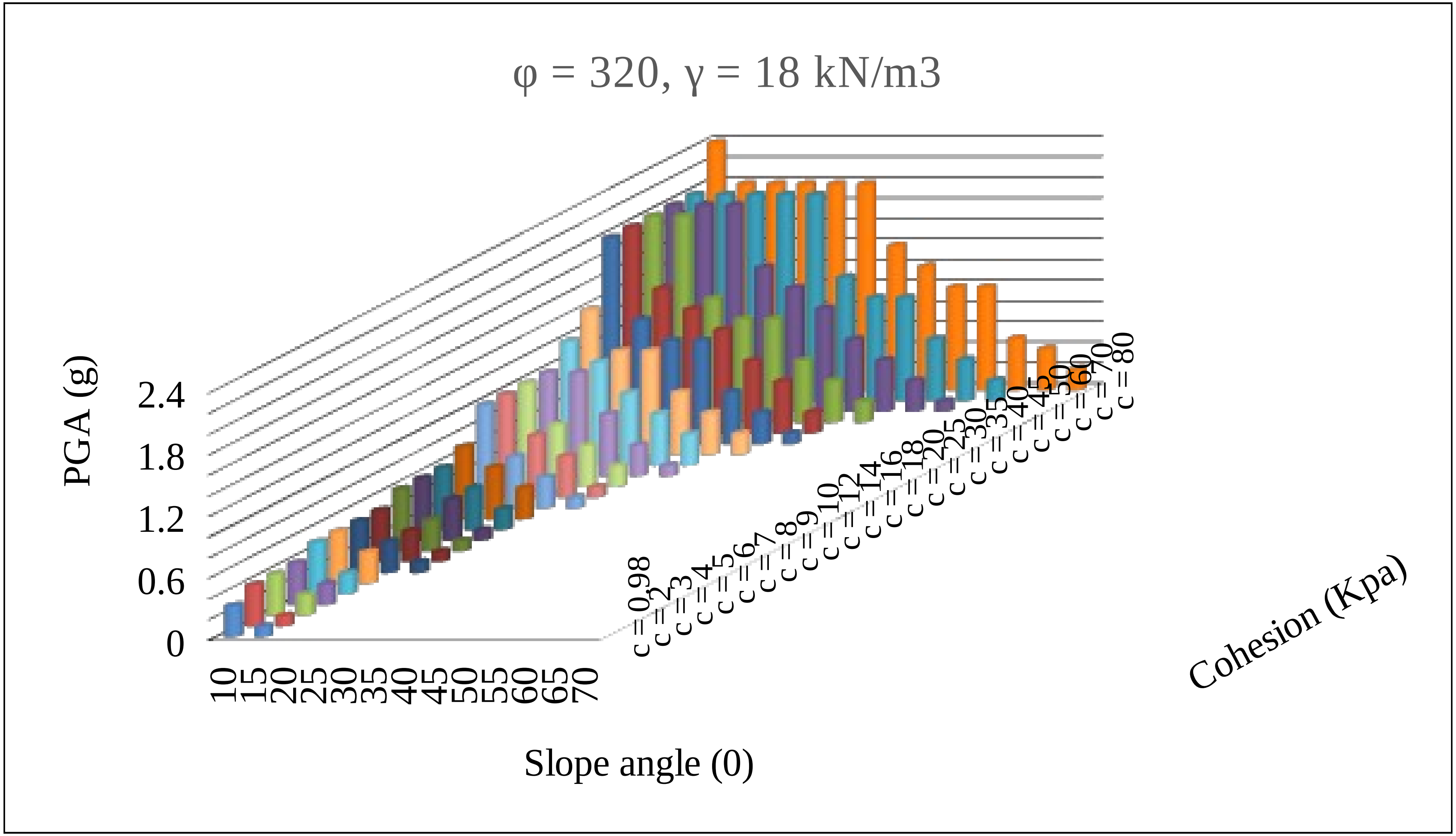

Figure 7.1 (h) $\varphi=32^0$

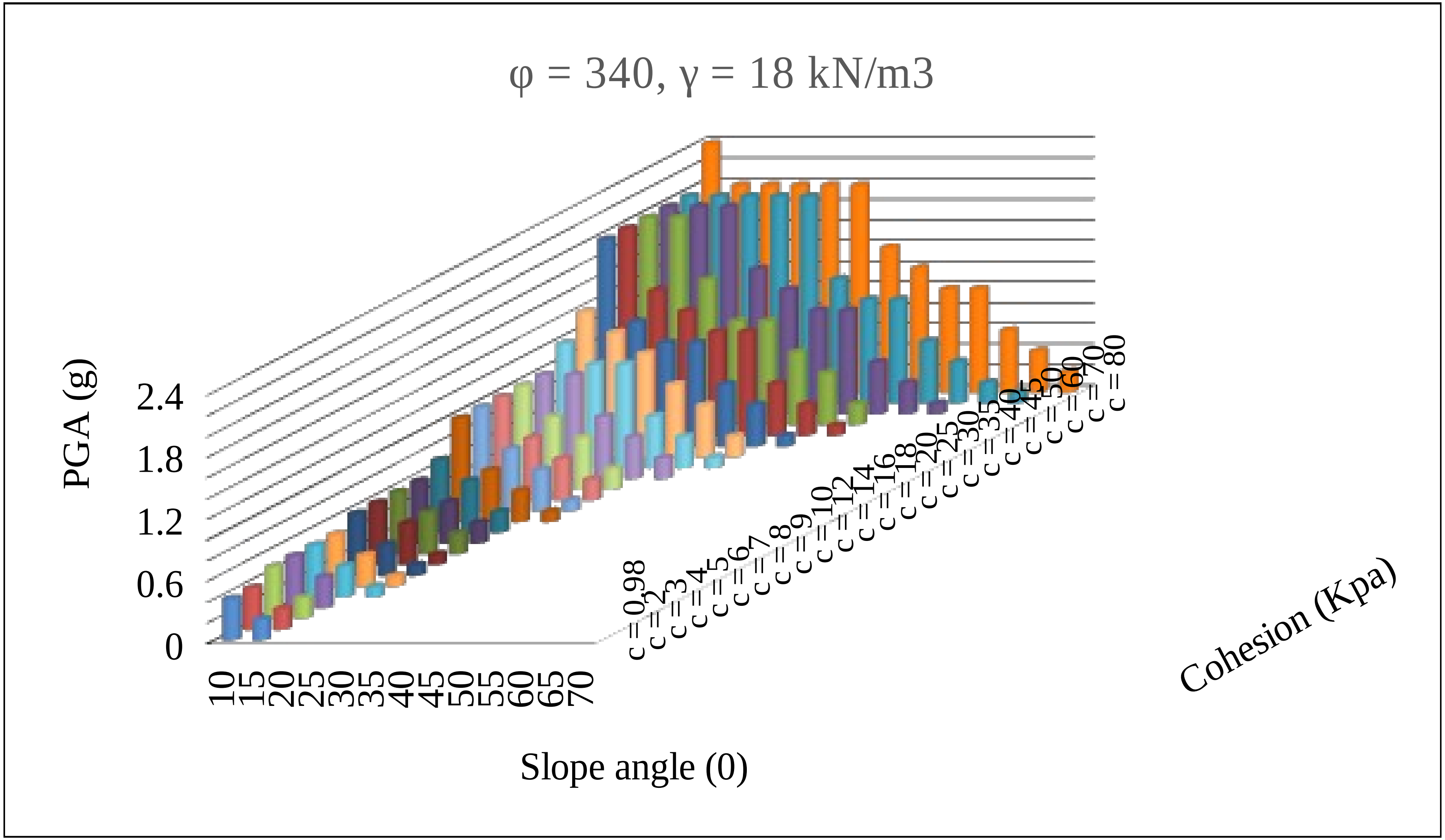

Figure 7.1 (i) φ=34^0

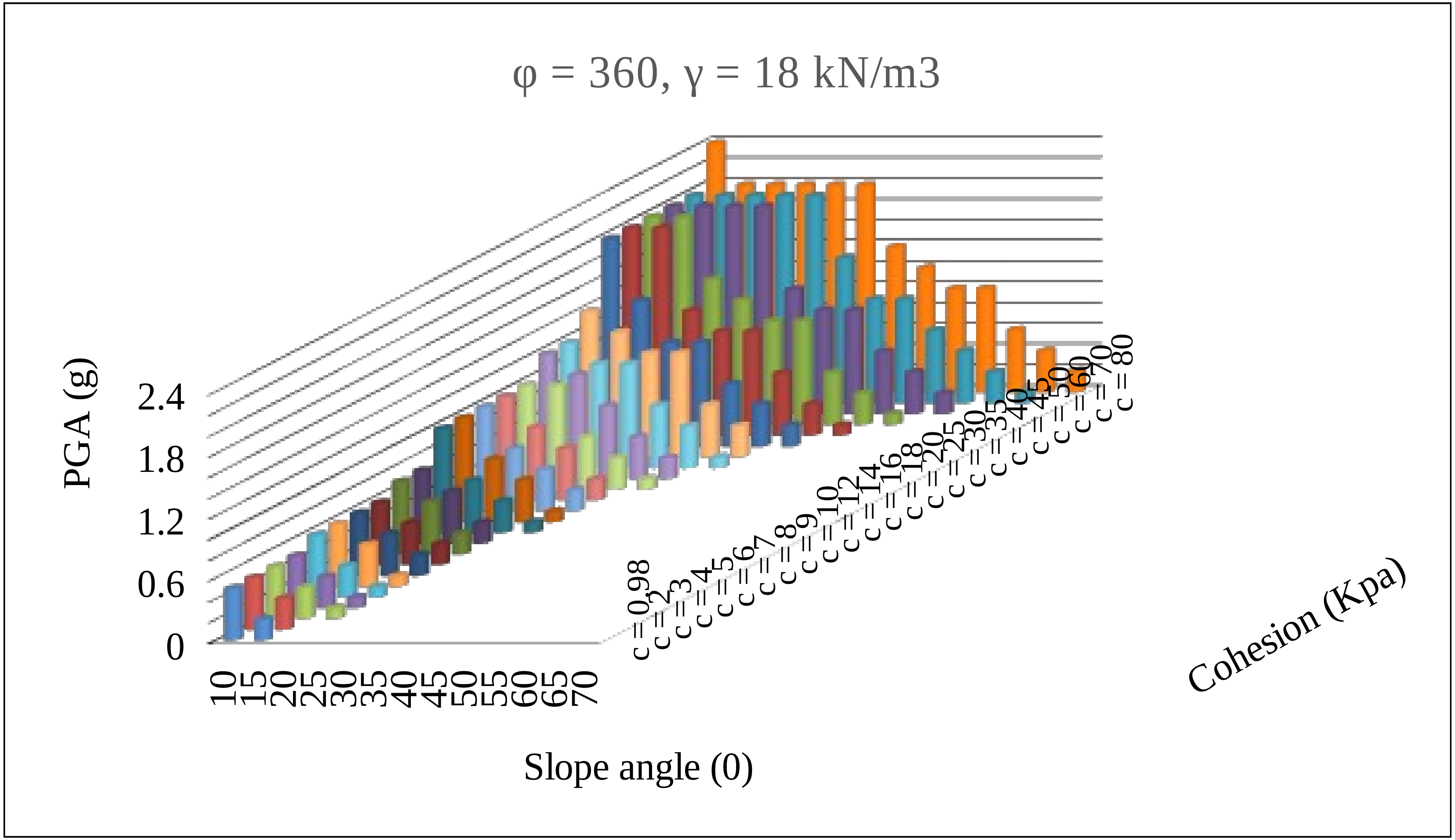

Figure 7.1 (j) φ=36^{0}

The design charts of DBE calculated for slope angles 10 to70^0, φ=18^0 - 36^0, c = 0 to 80 Kpa, at γ = 19 kN/m^3 are calculated and presented in Figures 7.2 (a to j).

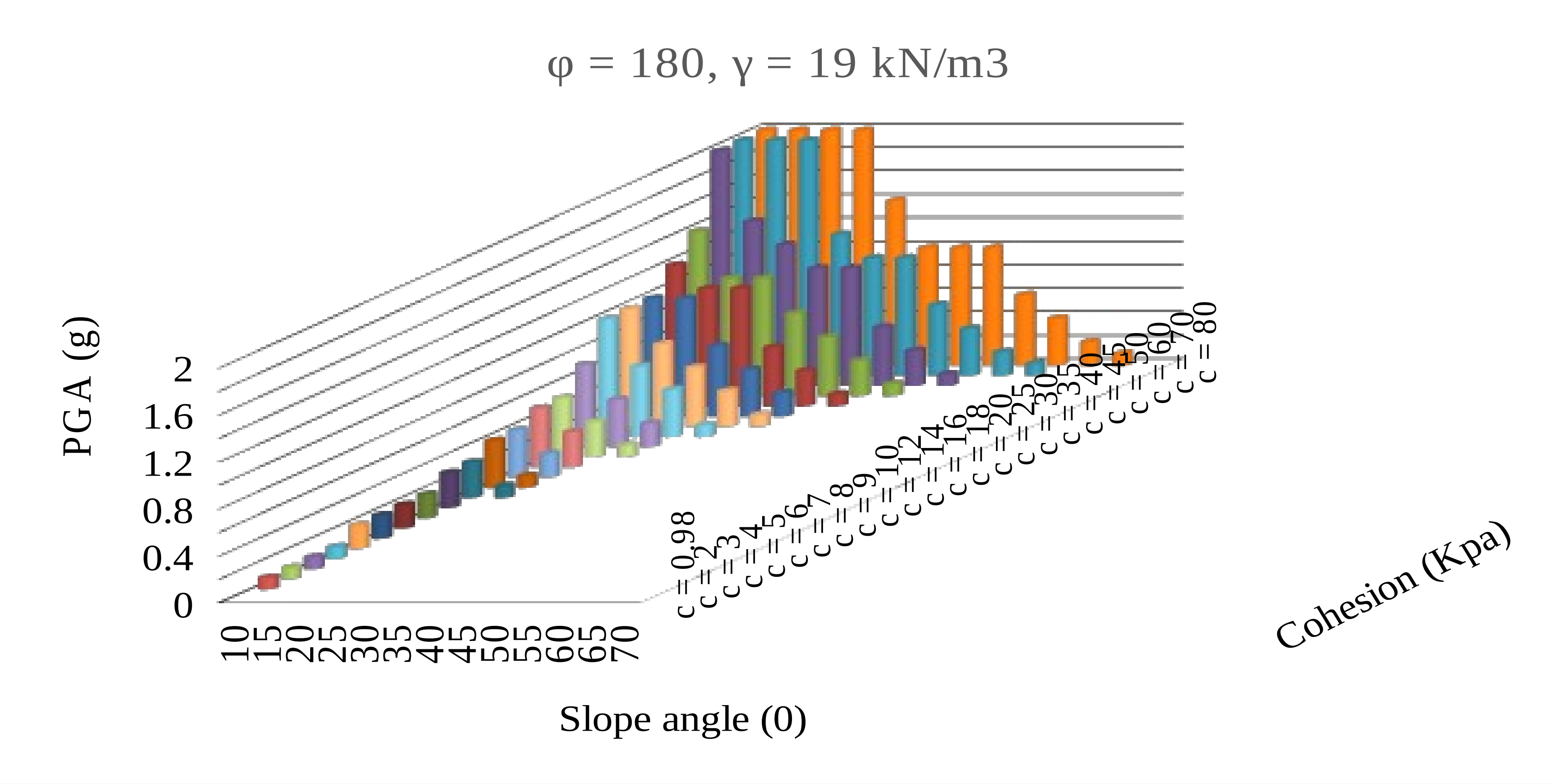

Figure 7.2 DBE design charts at various slope angle, Cohesion and γ = 19 kN/m^3 for (a) φ=18^0

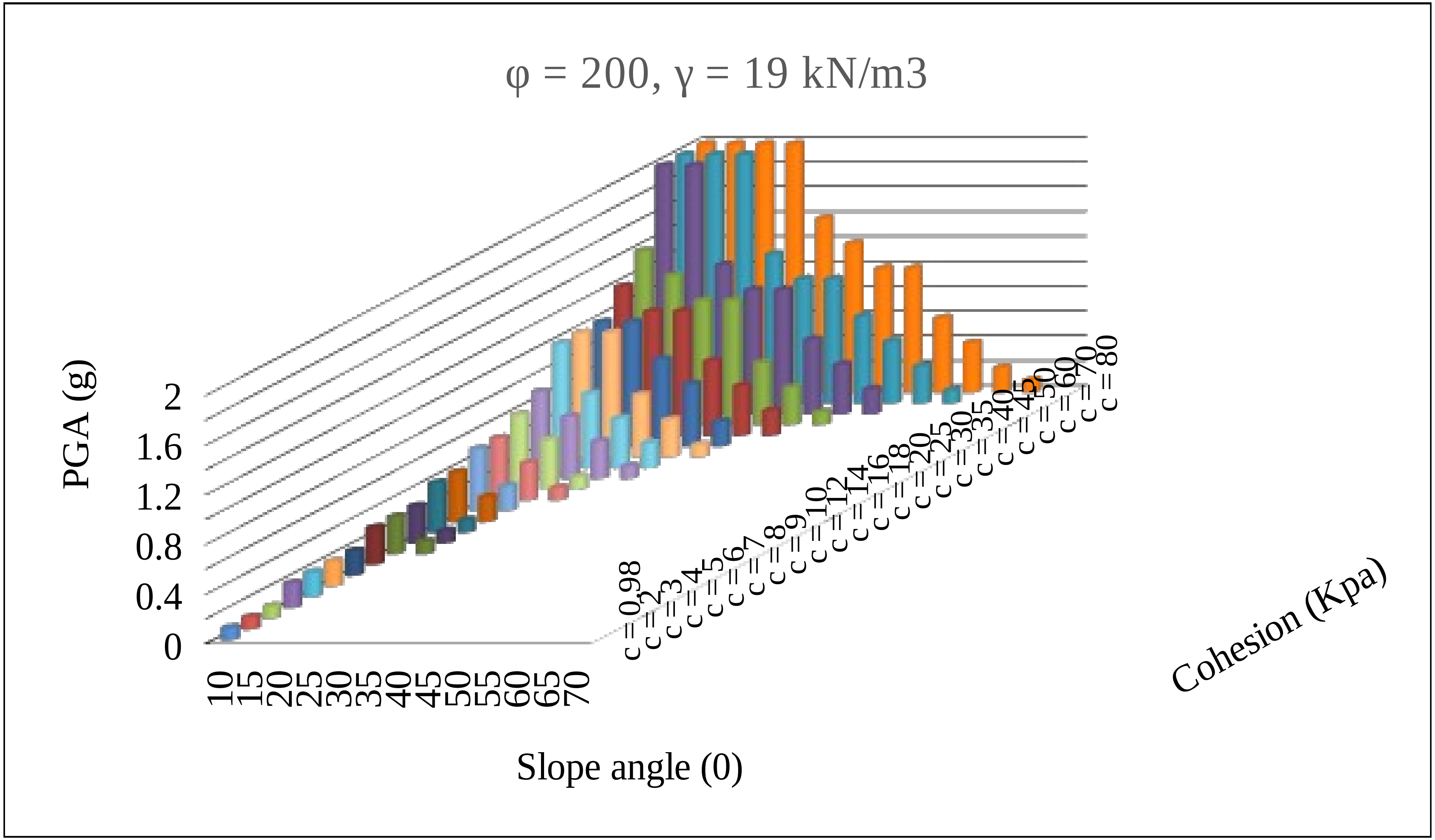

Figure 7.2 (b) φ=20^0

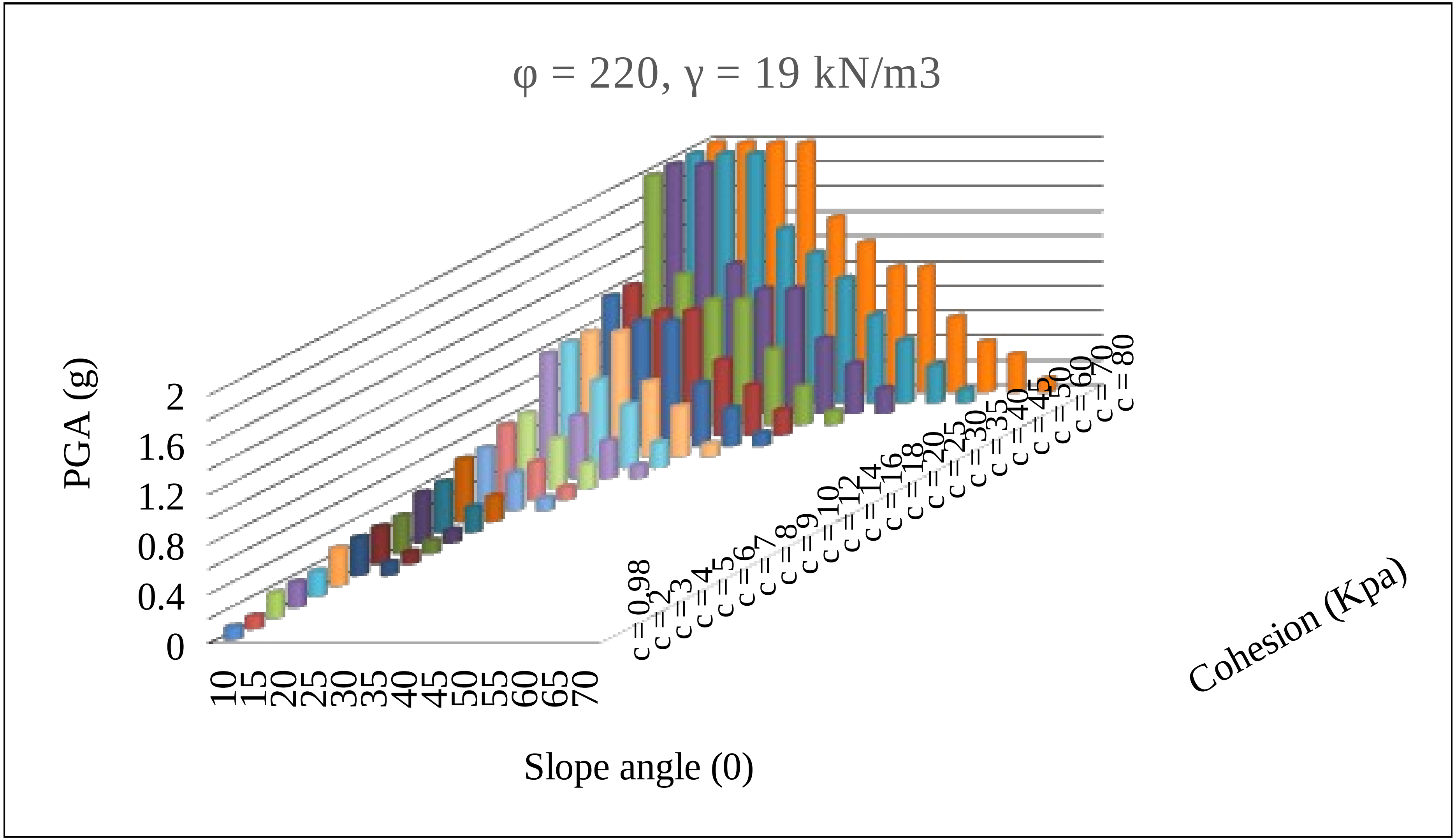

Figure 7.2 (c) $\varphi=22^0$

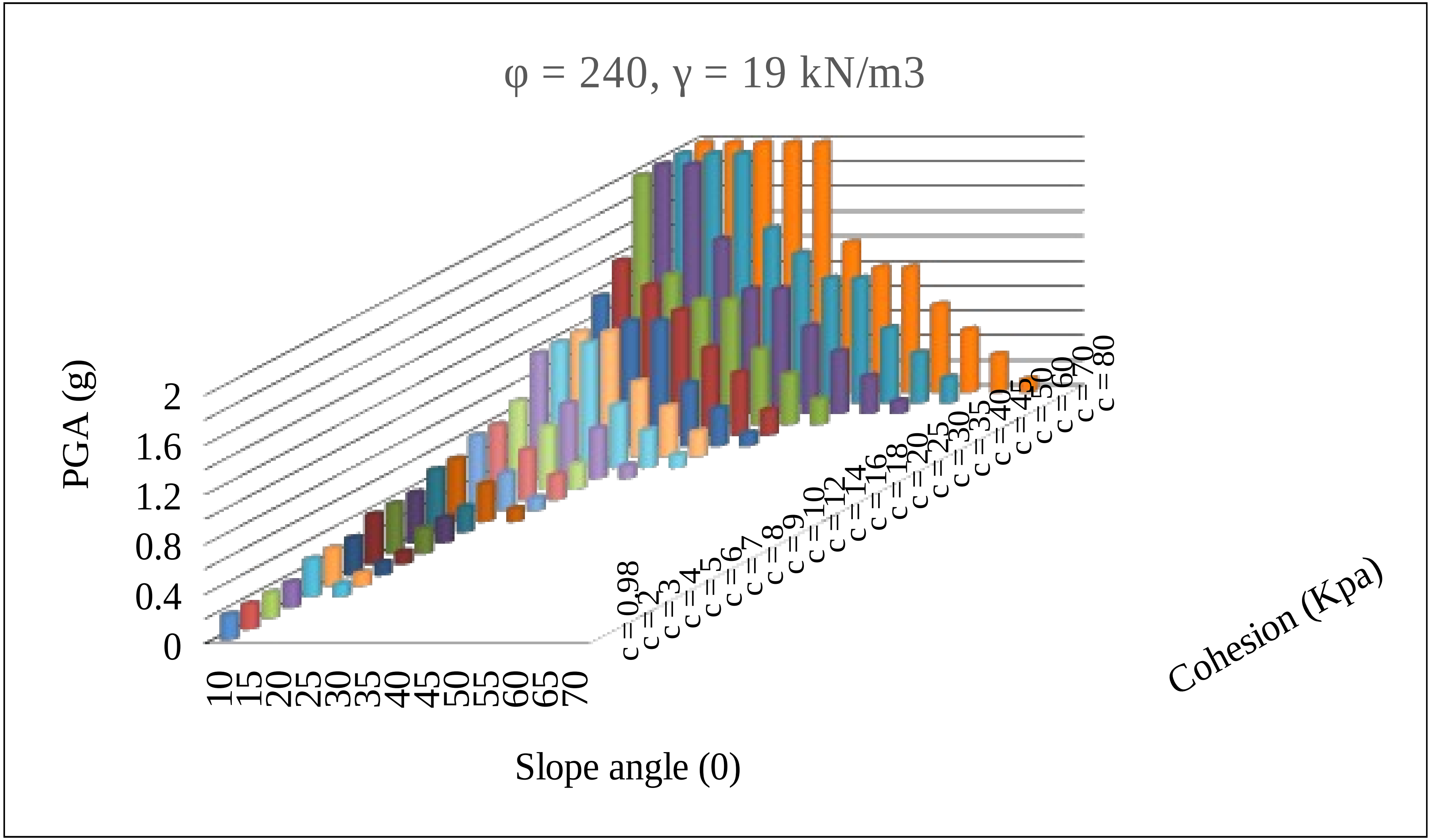

Figure 7.2 (d) φ=24^0

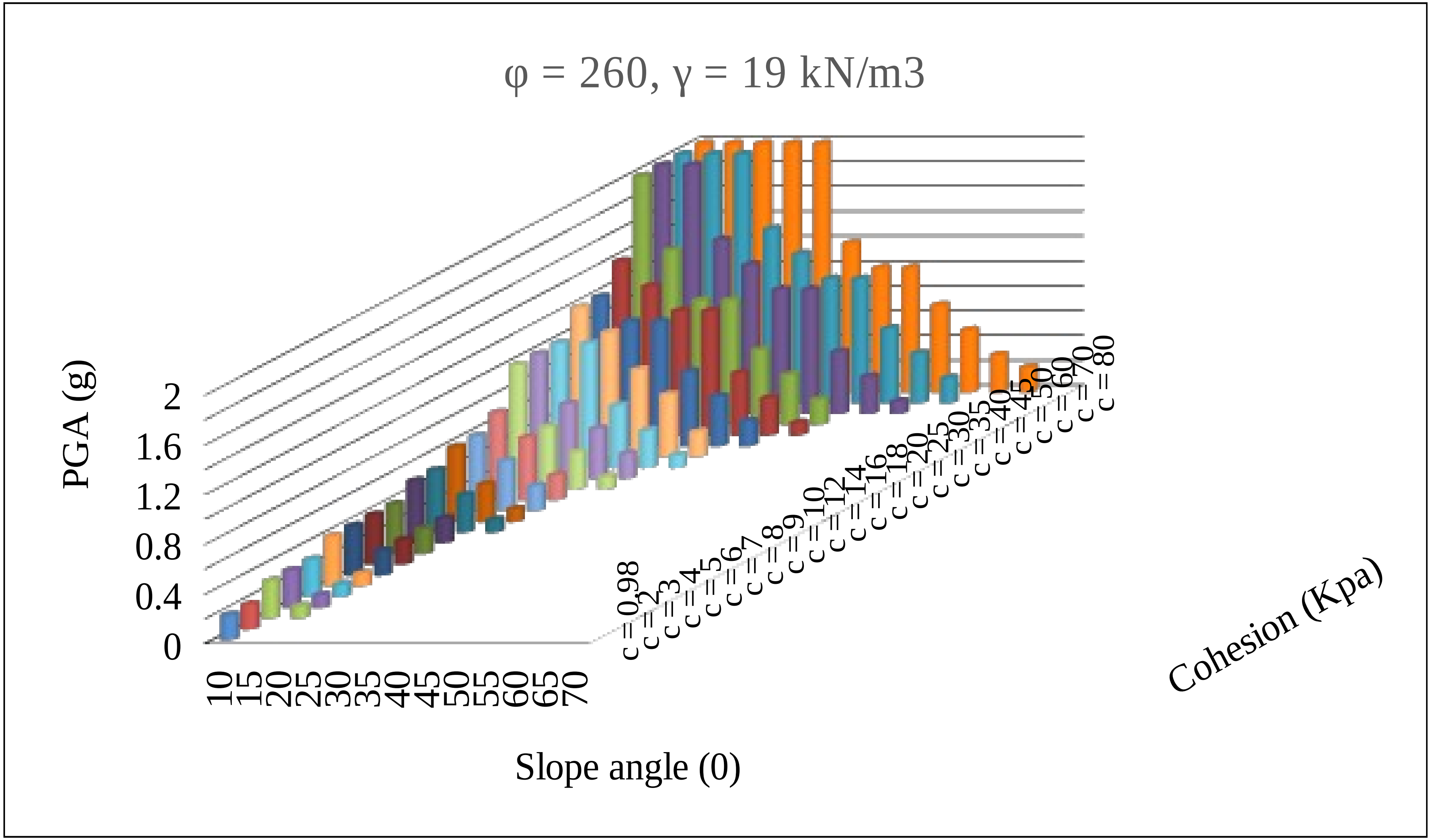

Figure 7.2 (e) φ=26^0

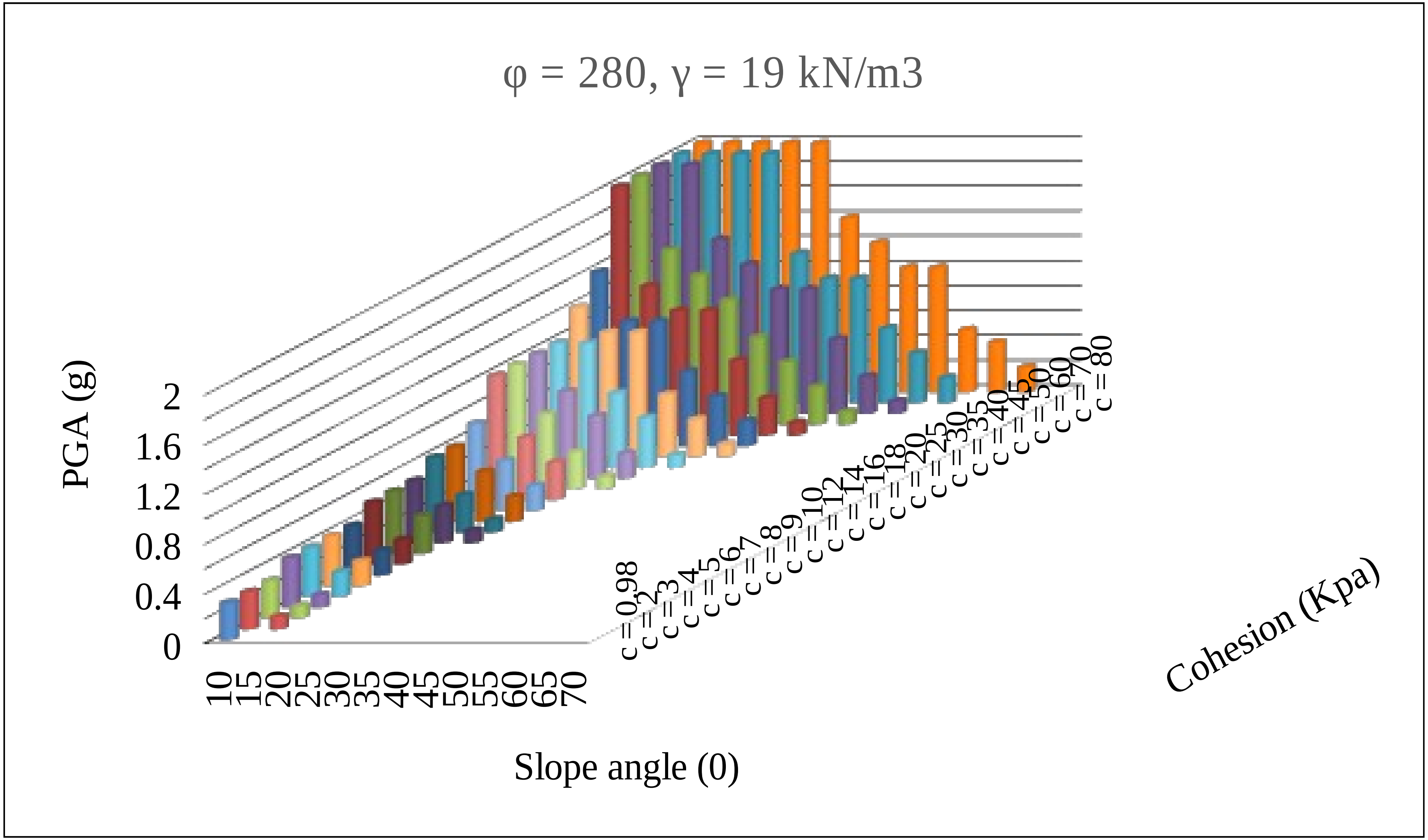

Figure 7.2 (f) φ=28^0

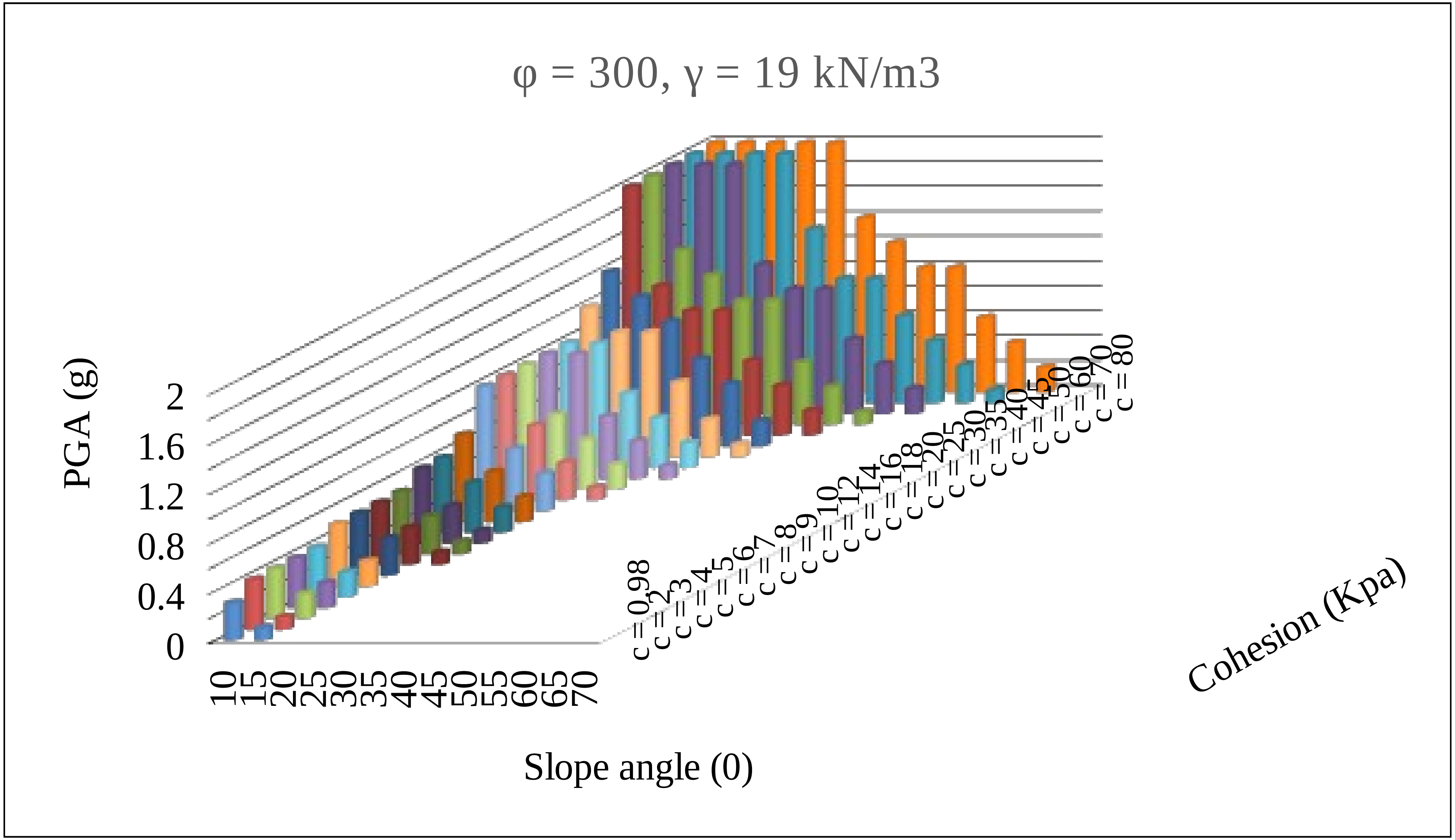

Figure 7.2 (g) φ=30^0

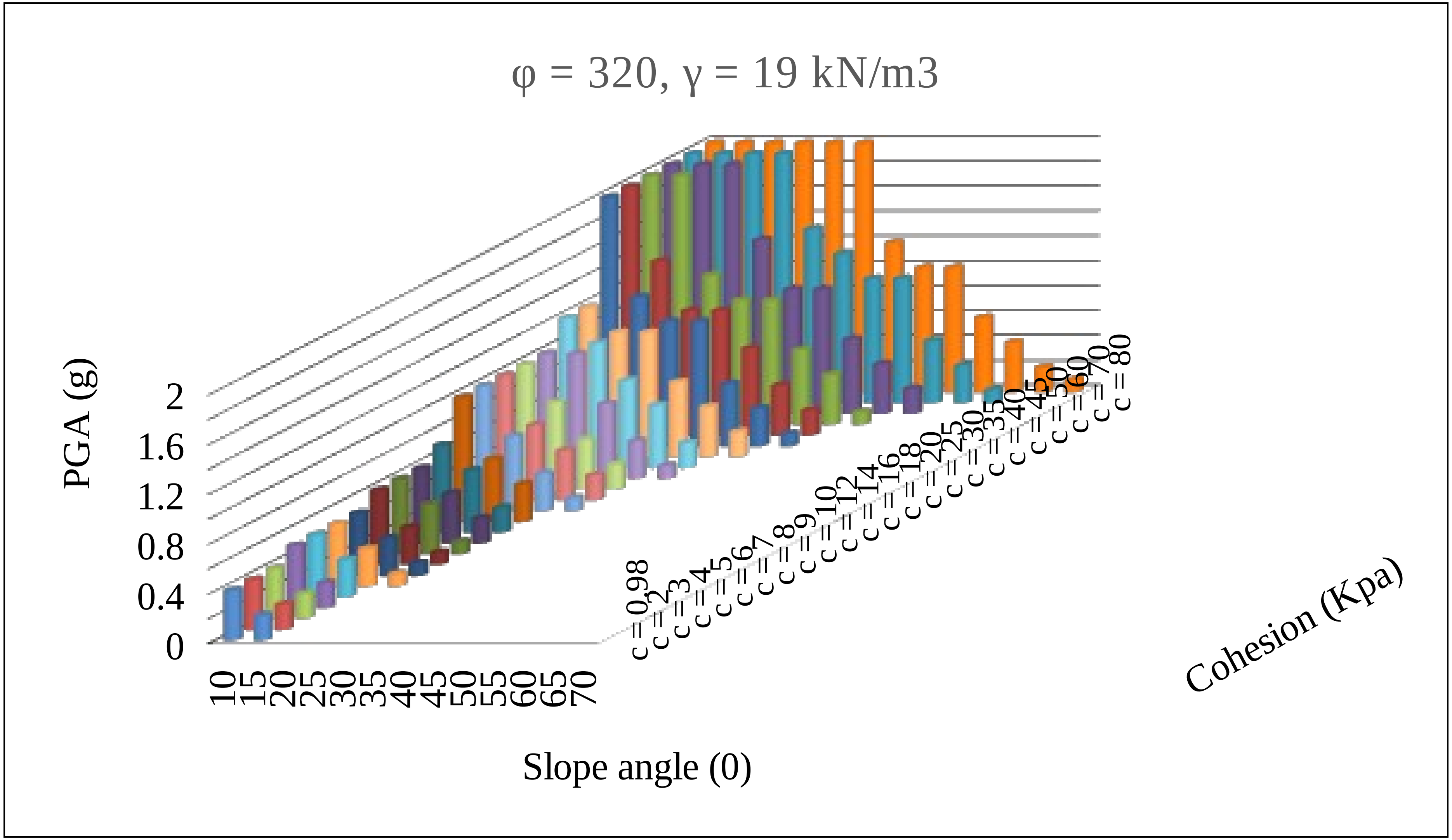

Figure 7.2 (h) $\varphi=32^0$

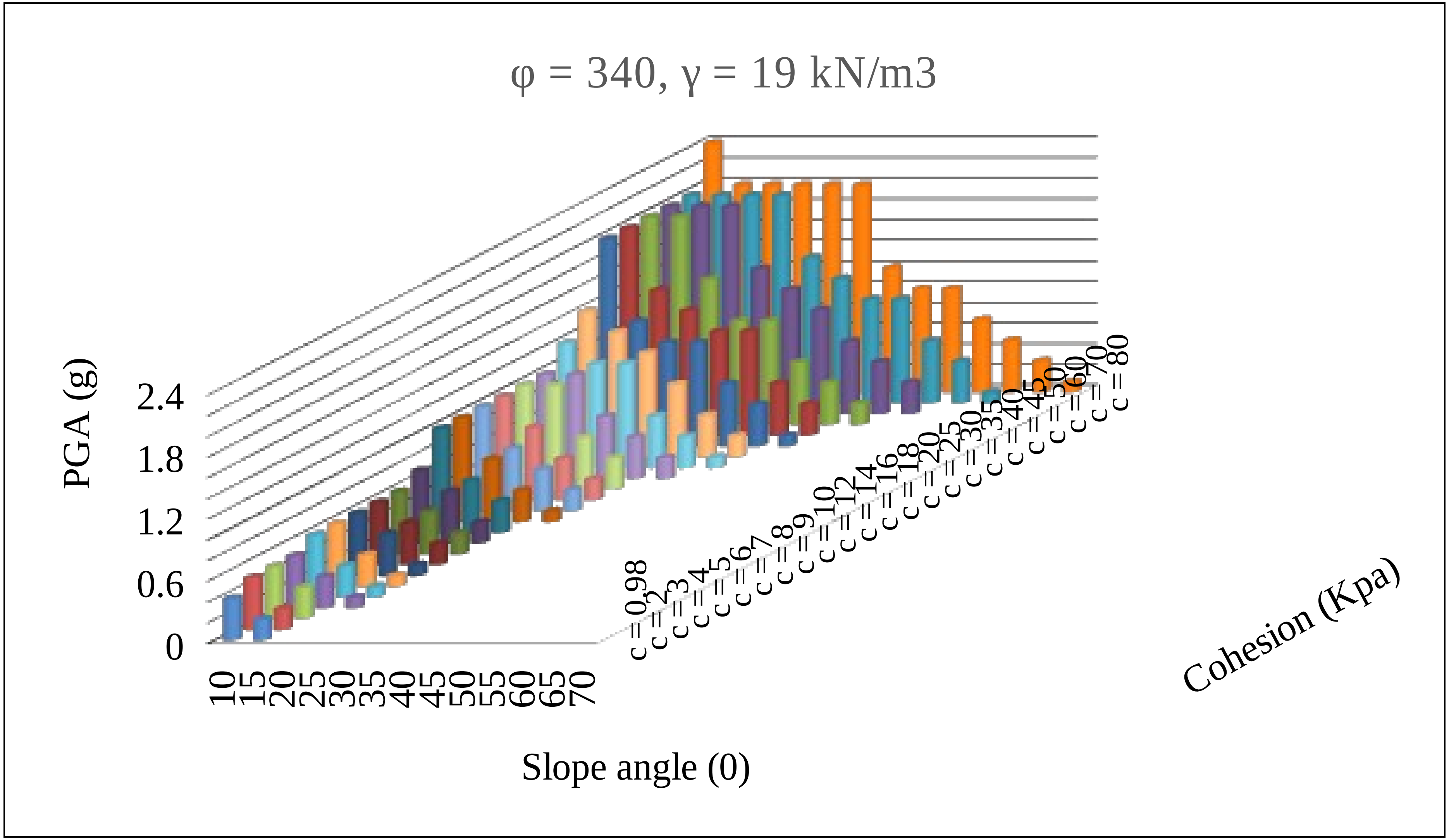

Figure 7.2 (i) φ=34^0

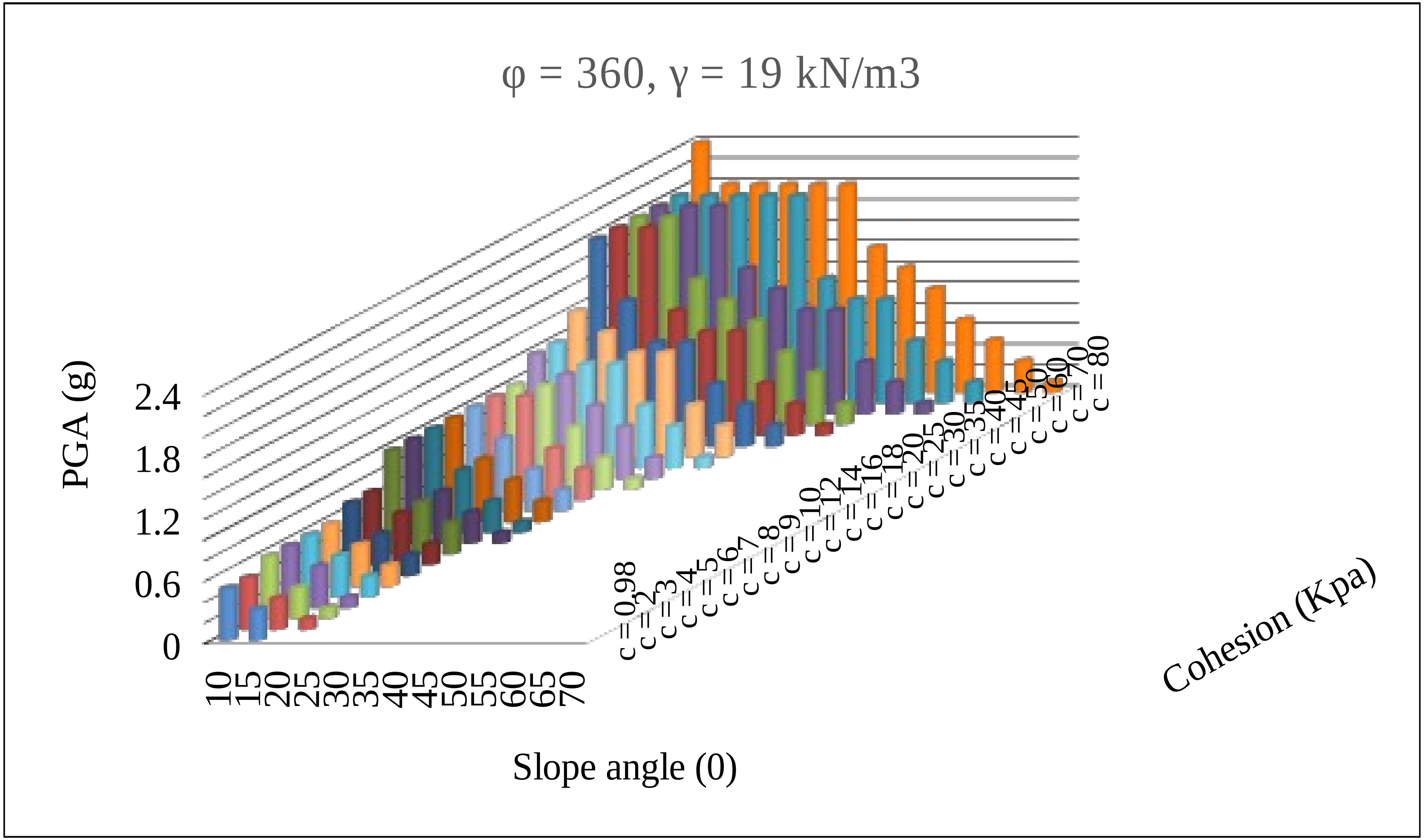

Figure 7.2 (j) φ=36^0

The design charts of DBE calculated for slope angles 10 to70^0, φ=18^0 - 36^0, c = 0 to 80 Kpa, at γ = 20 kN/m^3 are calculated and presented in Figures 7.3 (a to j).

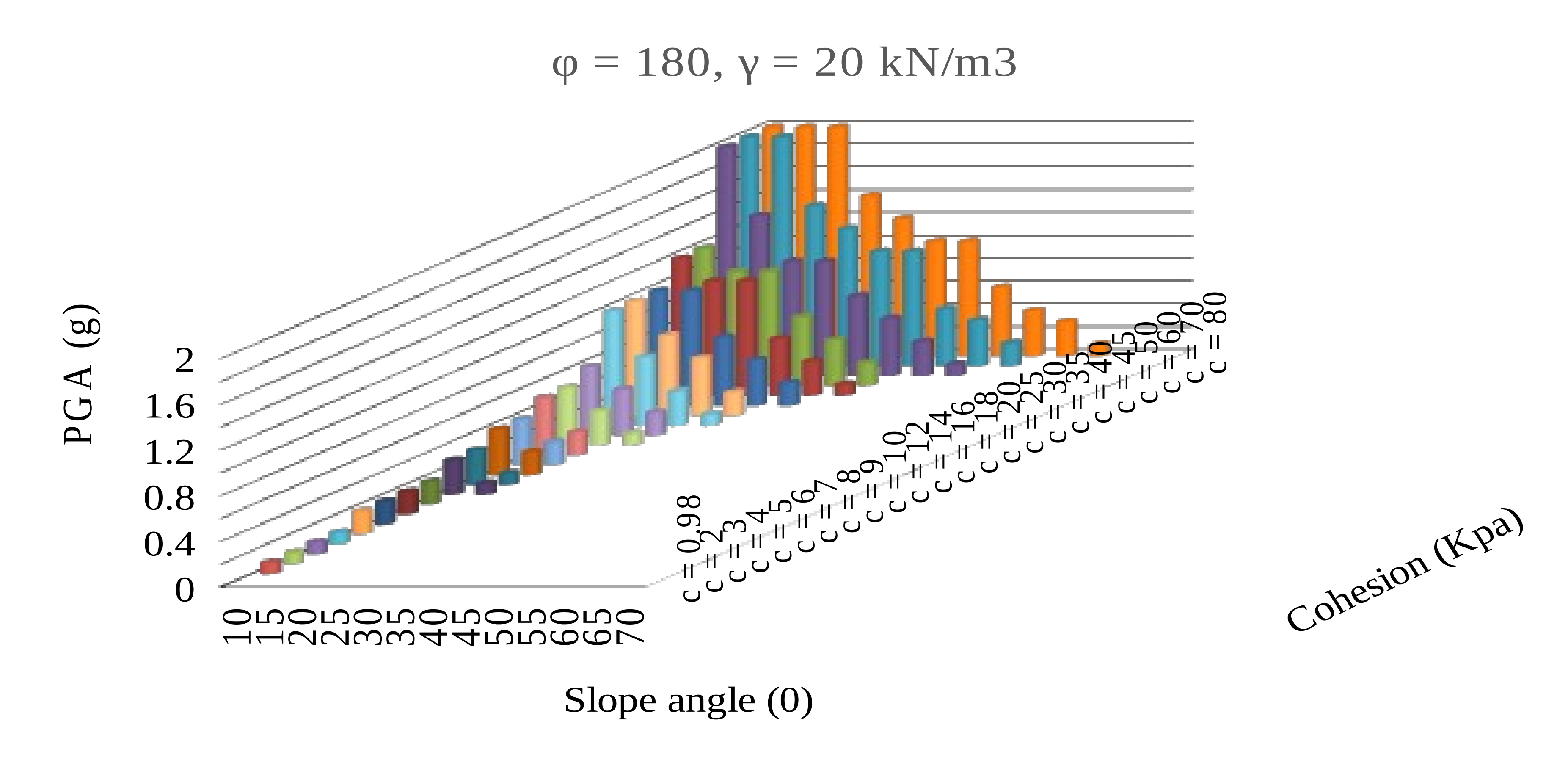

Figure 7.3 DBE design charts at various slope angle, Cohesion and γ = 20 kN/m^3 for (a) φ=18^0

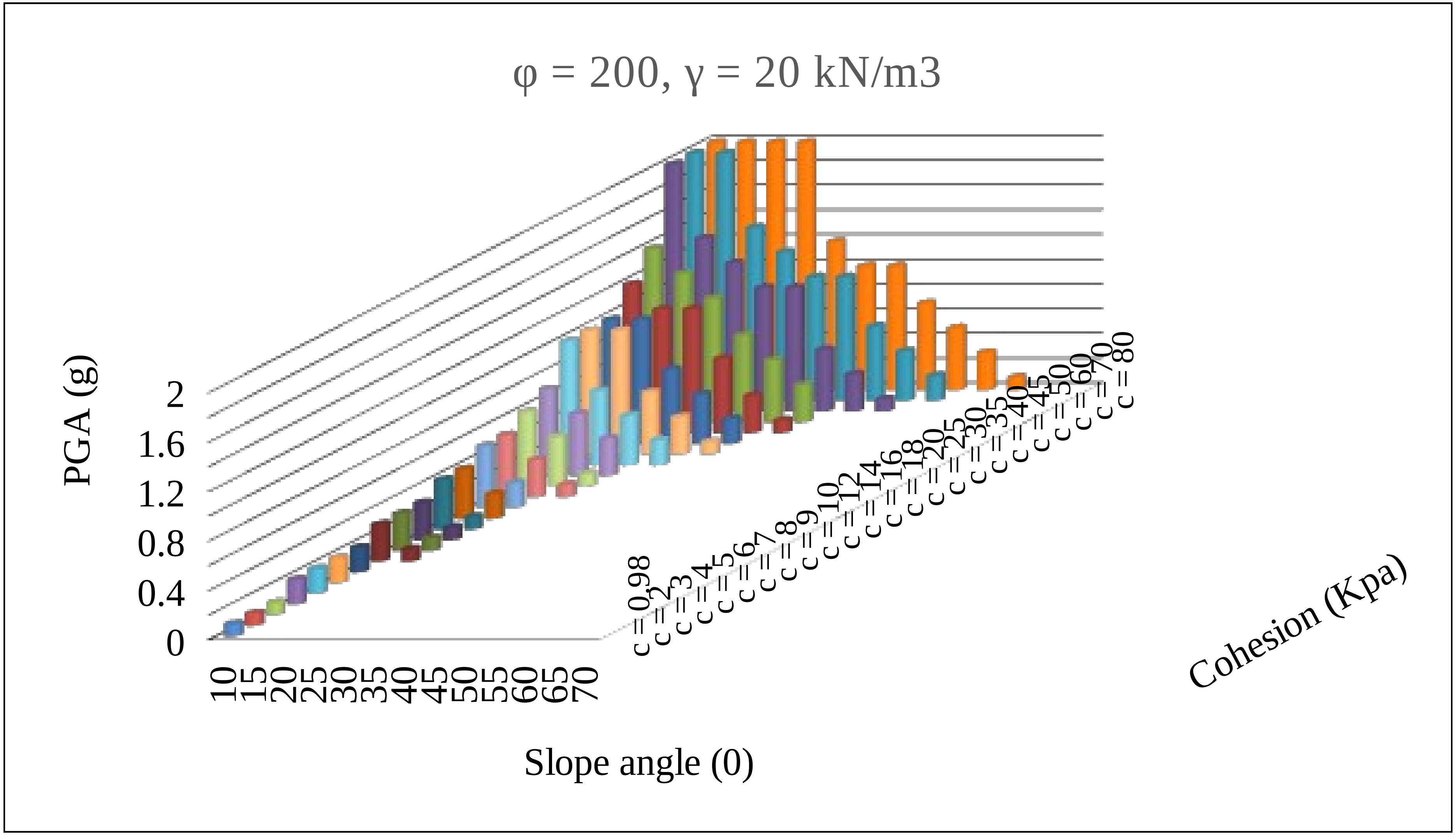

Figure 7.3 (b) $\varphi=20^0$

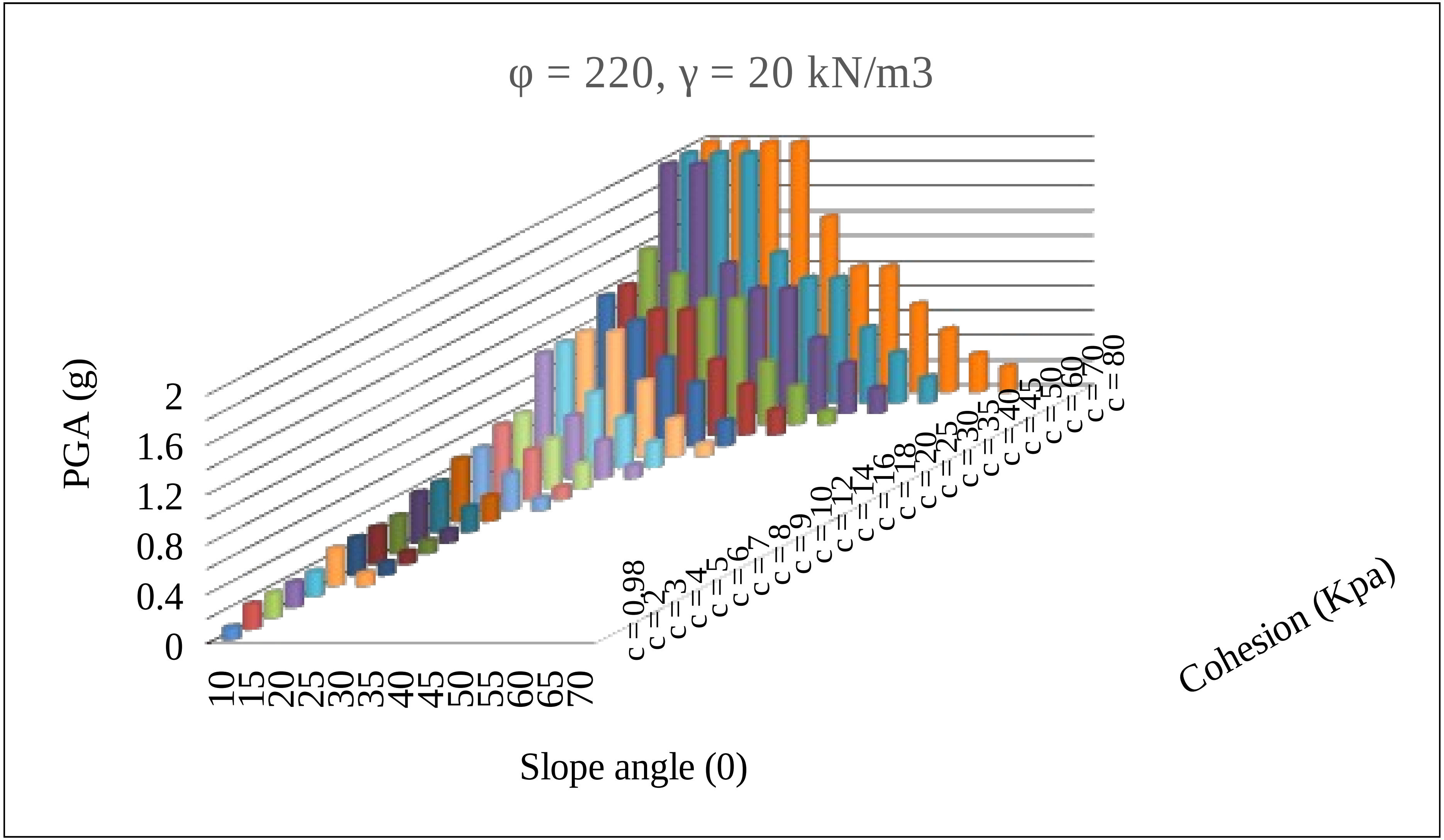

Figure 7.3 (c) φ=22^0

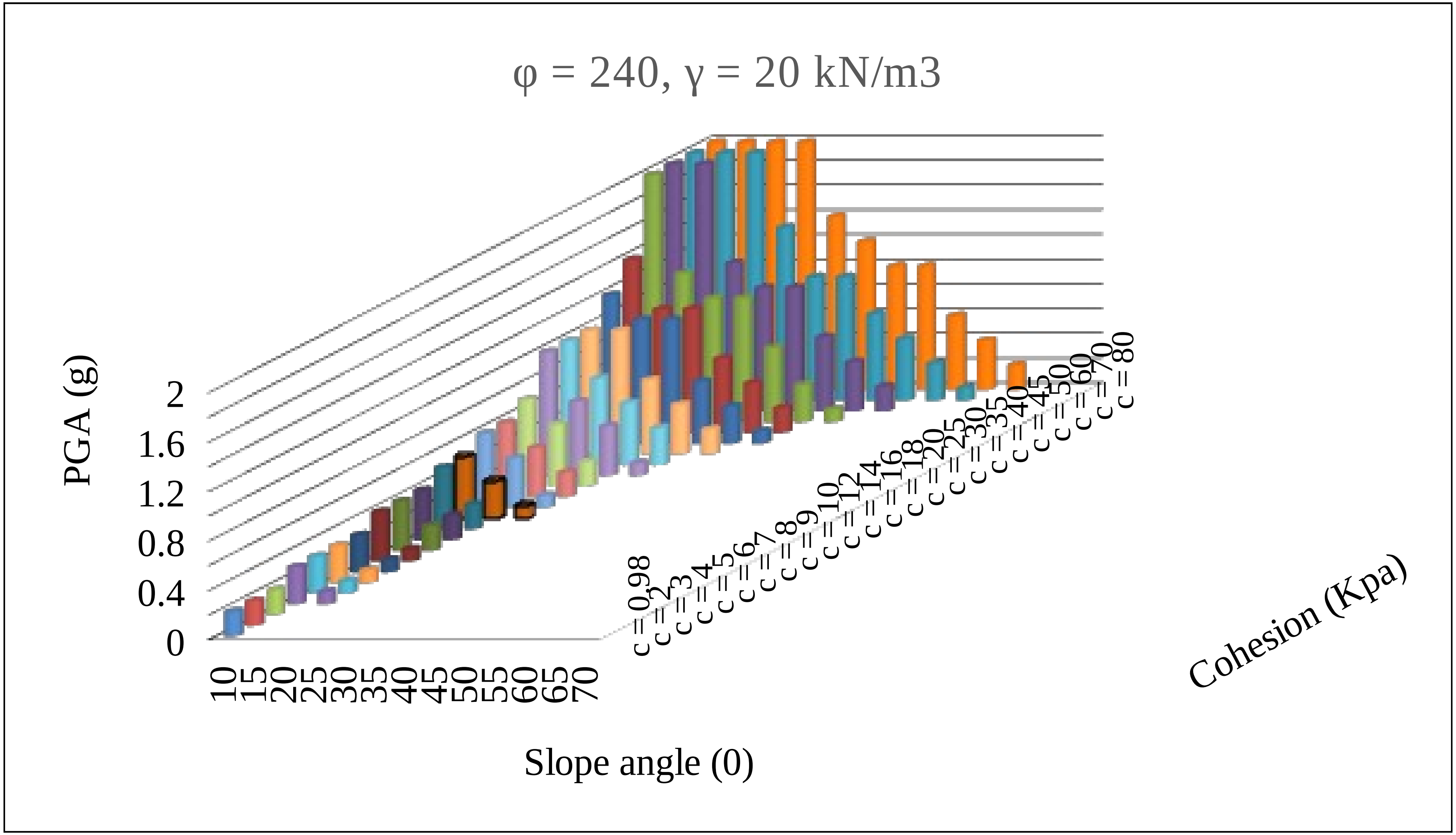

Figure 7.3 (d) $\varphi=24^0$

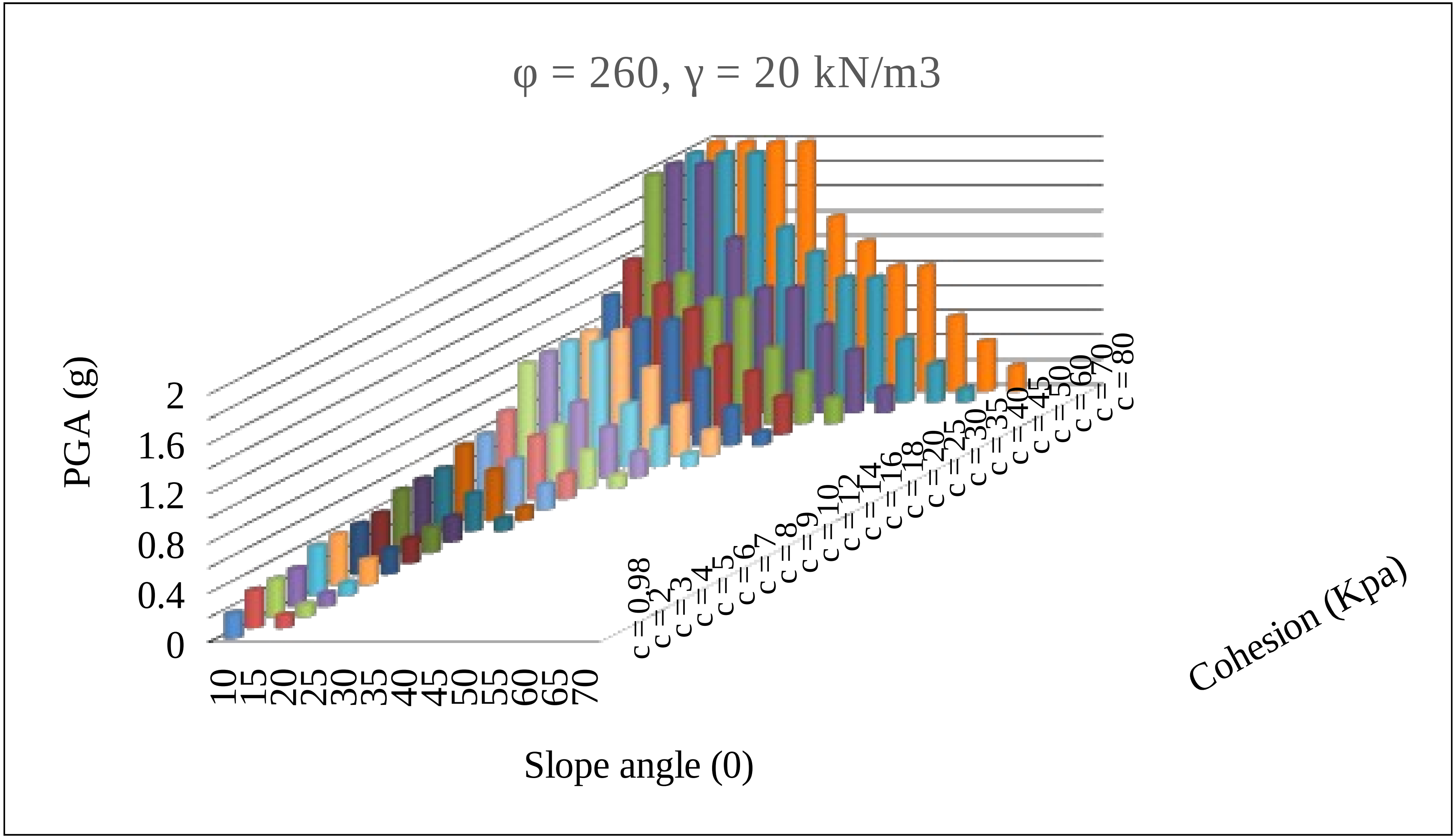

Figure 7.3 (e) $\varphi=26^0$

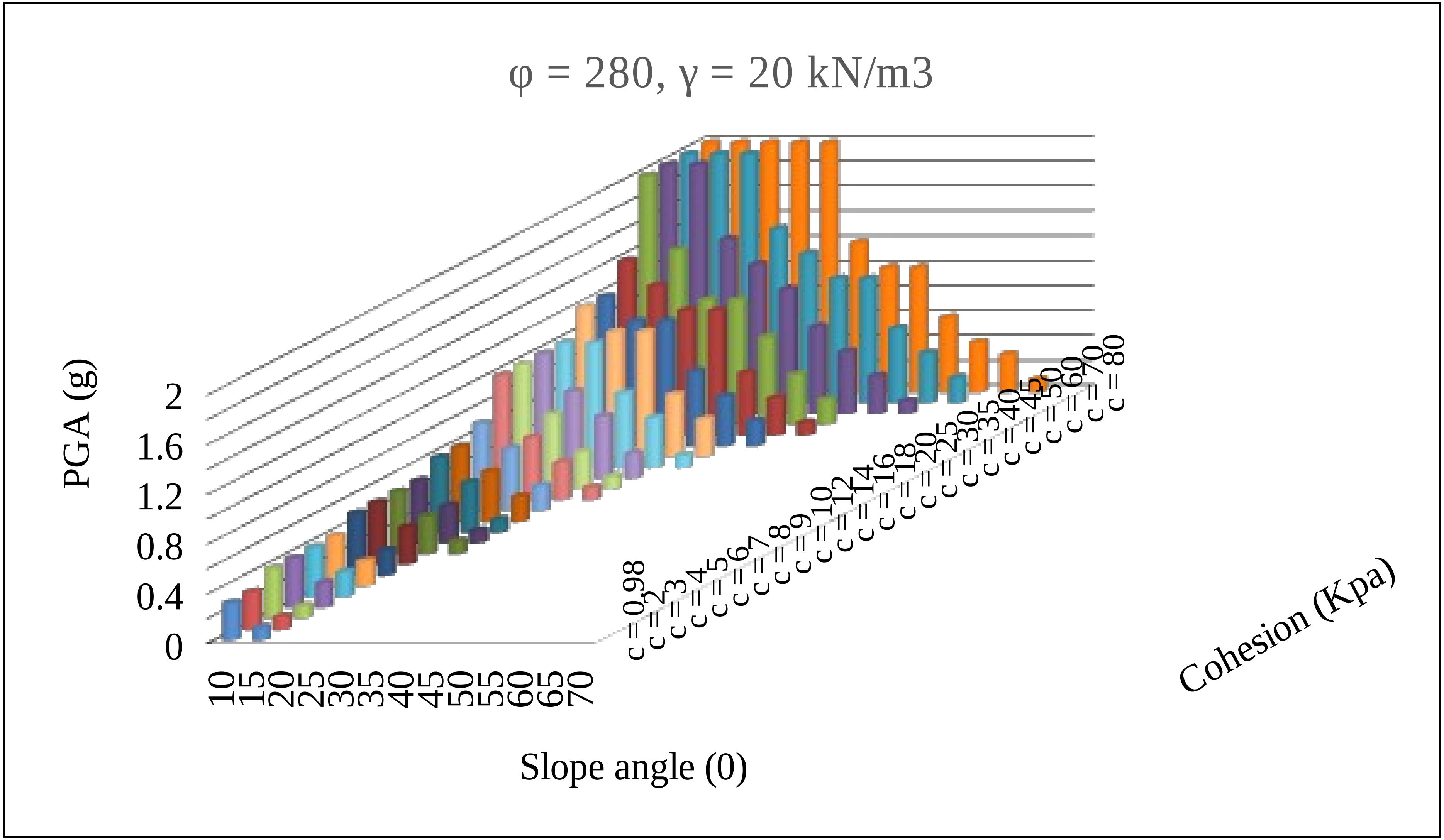

Figure 7.3 (f) φ=28^0

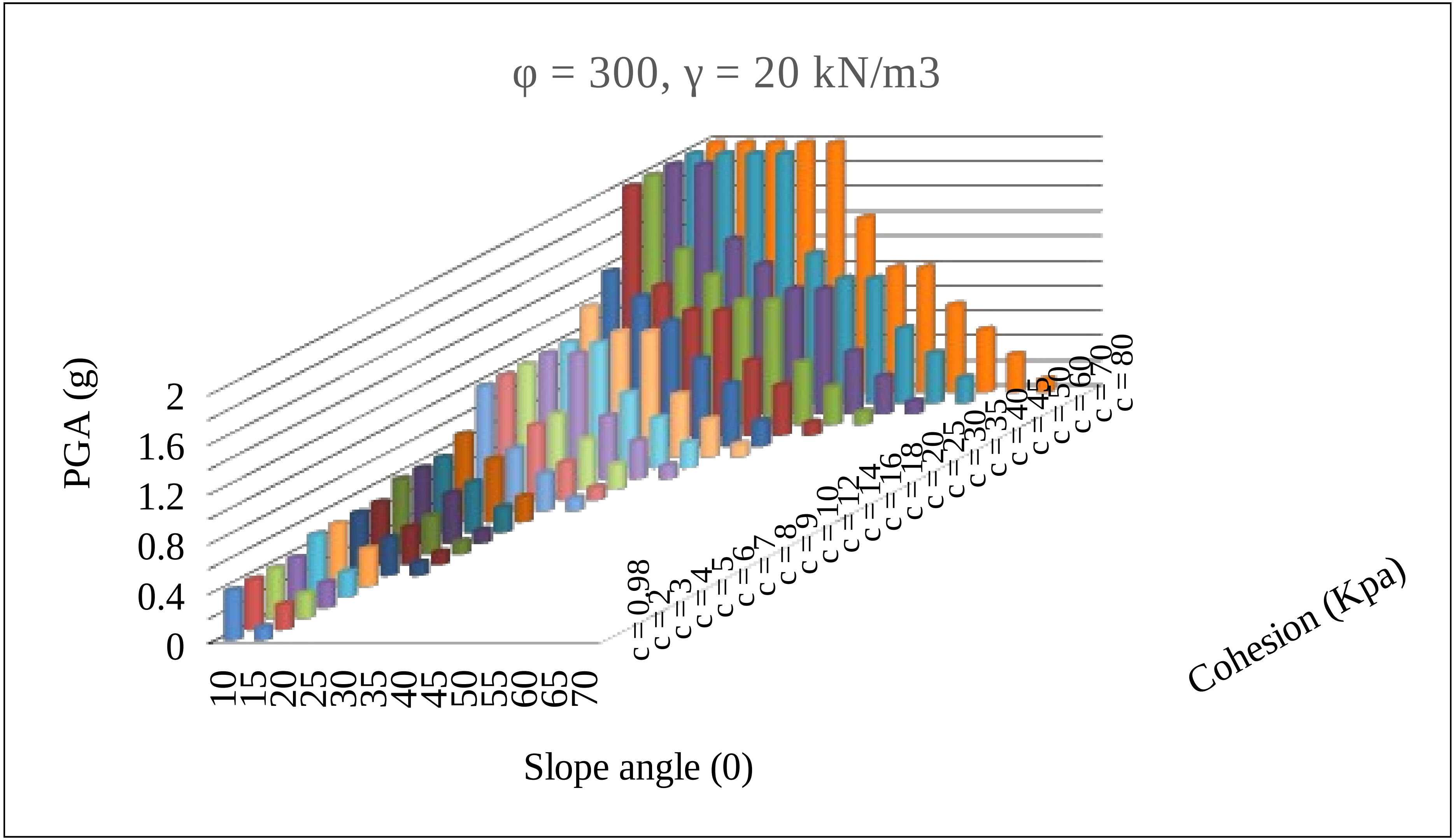

Figure 7.3 (g) $\varphi=30^0$

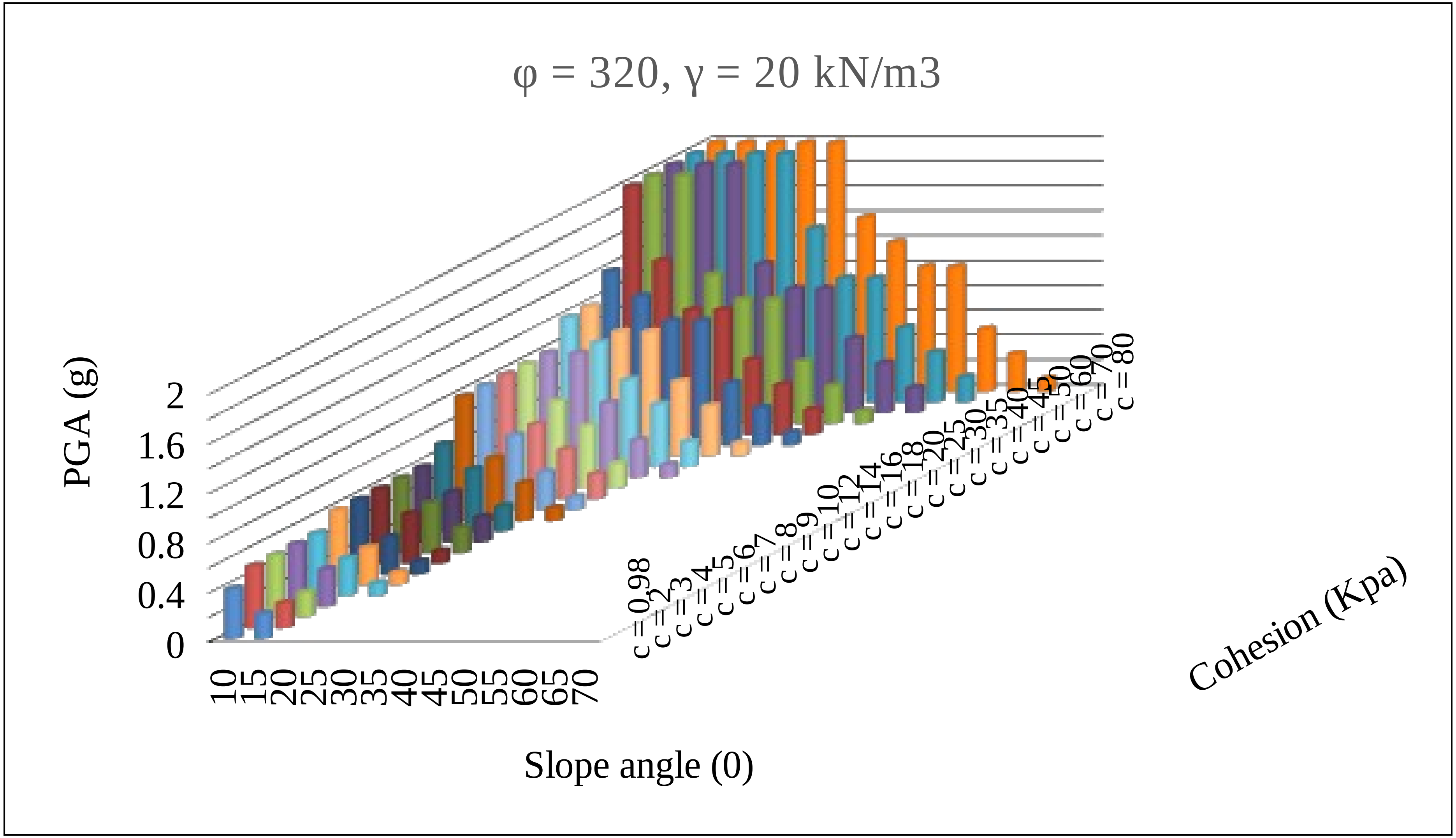

Figure 7.3 (h) $\varphi=32^0$

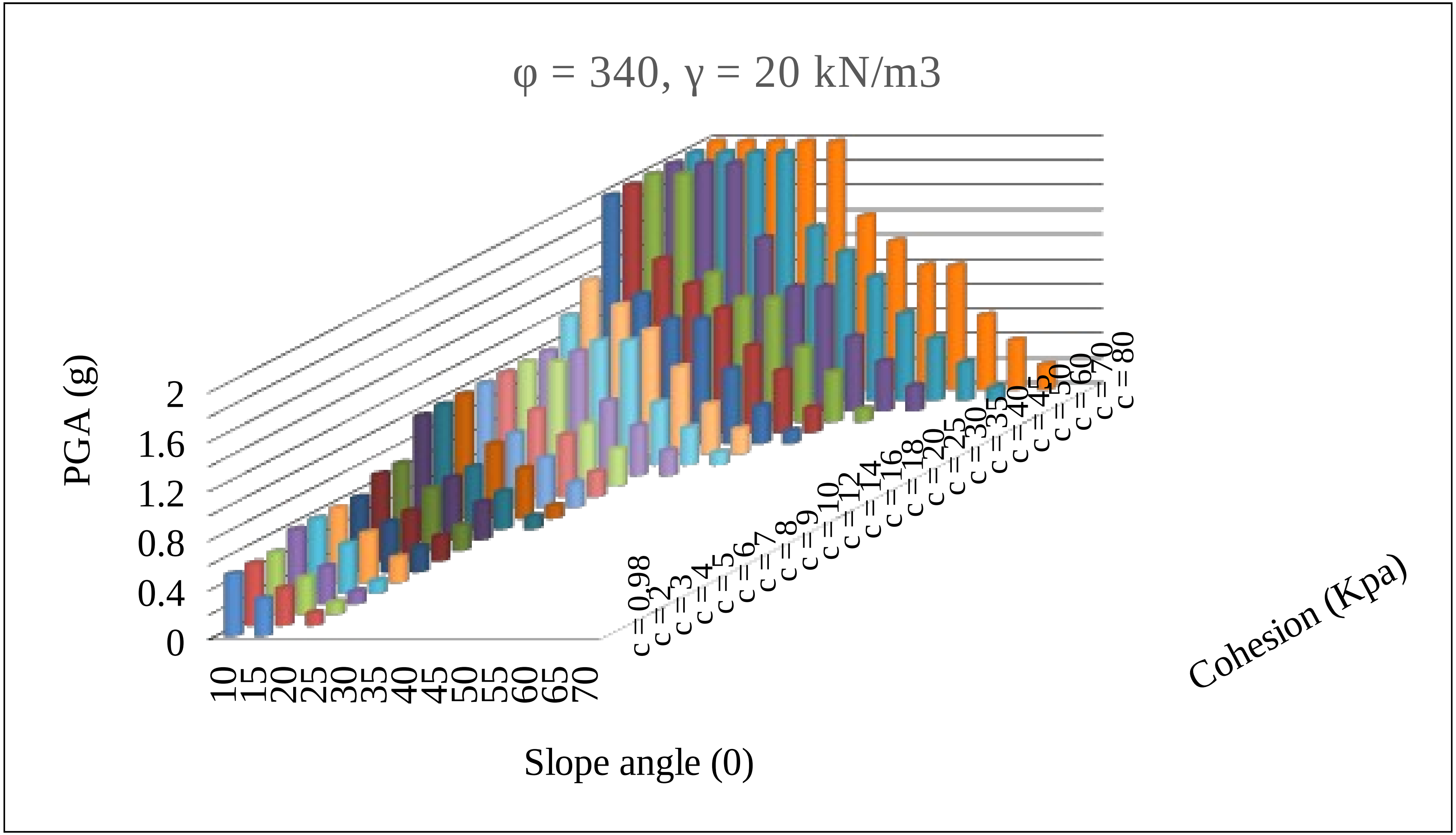

Figure 7.3 (i) φ=34^0

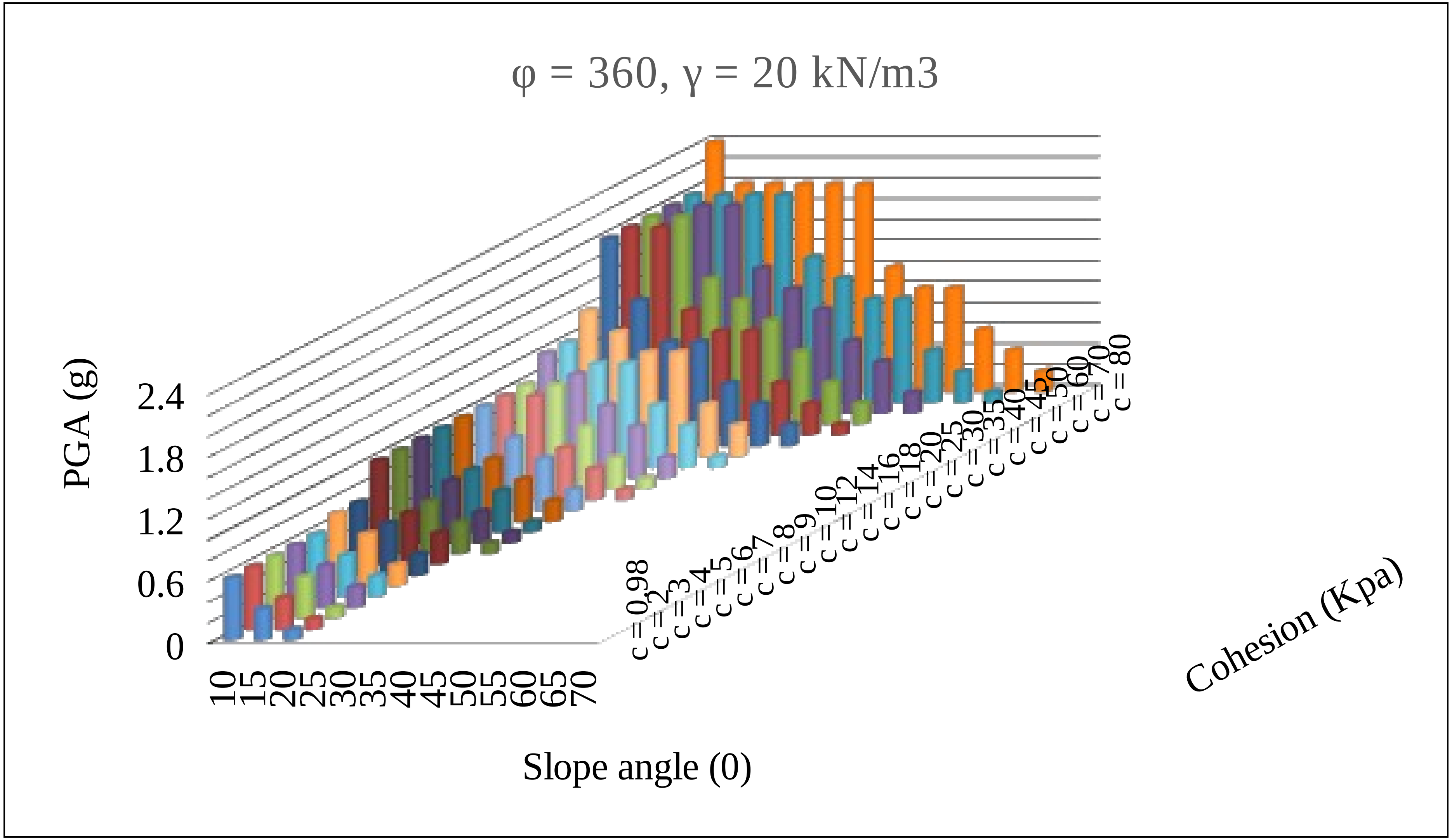

Figure 7.3 (j) φ=36^0

The design charts of DBE calculated for slope angles 10 to70^0, φ=18^0 - 36^0, c = 0 to 80 Kpa, at γ = 21 kN/m^3 are calculated and presented in Figures 7.4 (a to j).

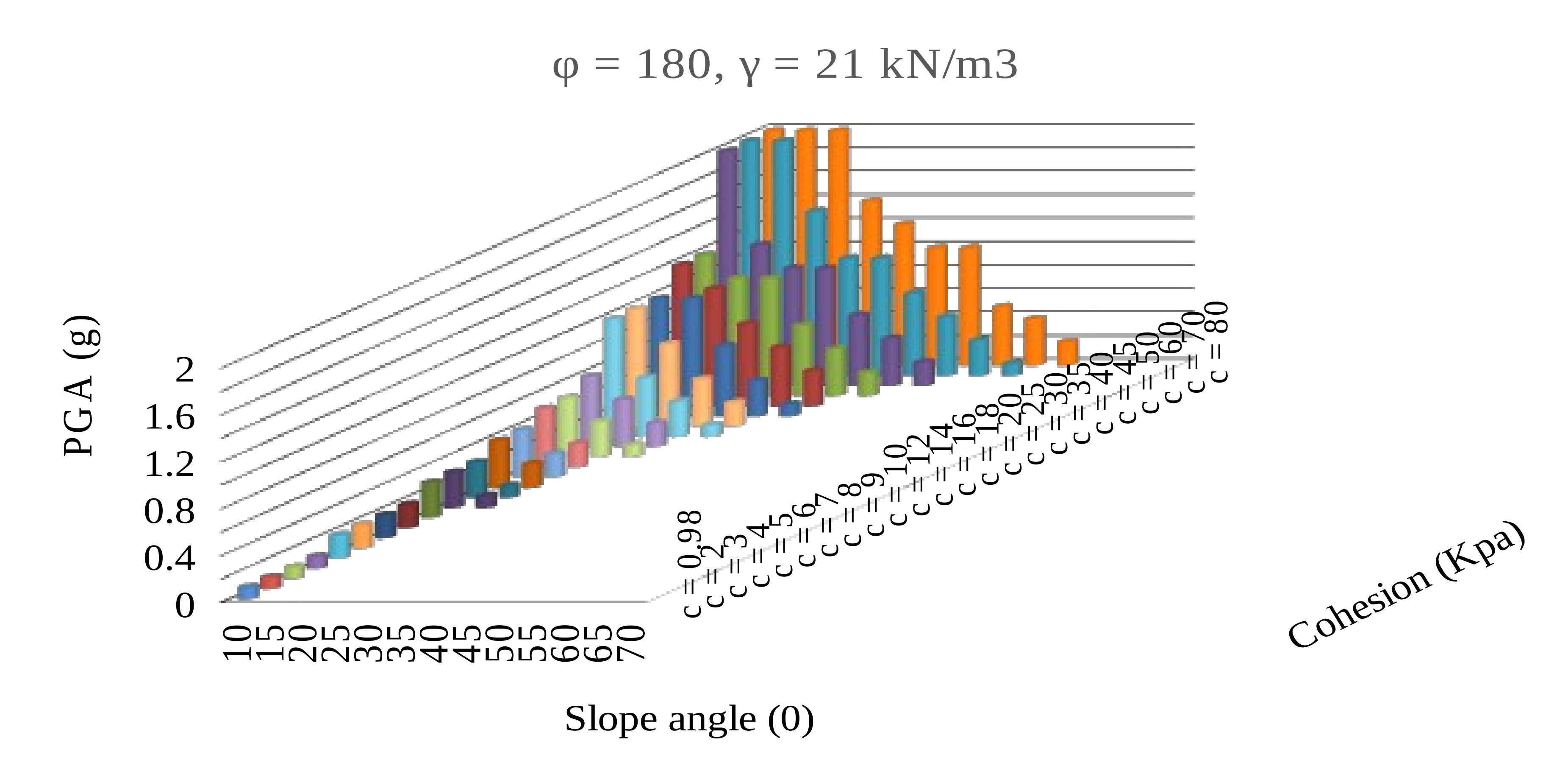

Figure 7.4 DBE design charts at various slope angle, Cohesion and γ = 21 kN/m^3 for (a) φ=18^0

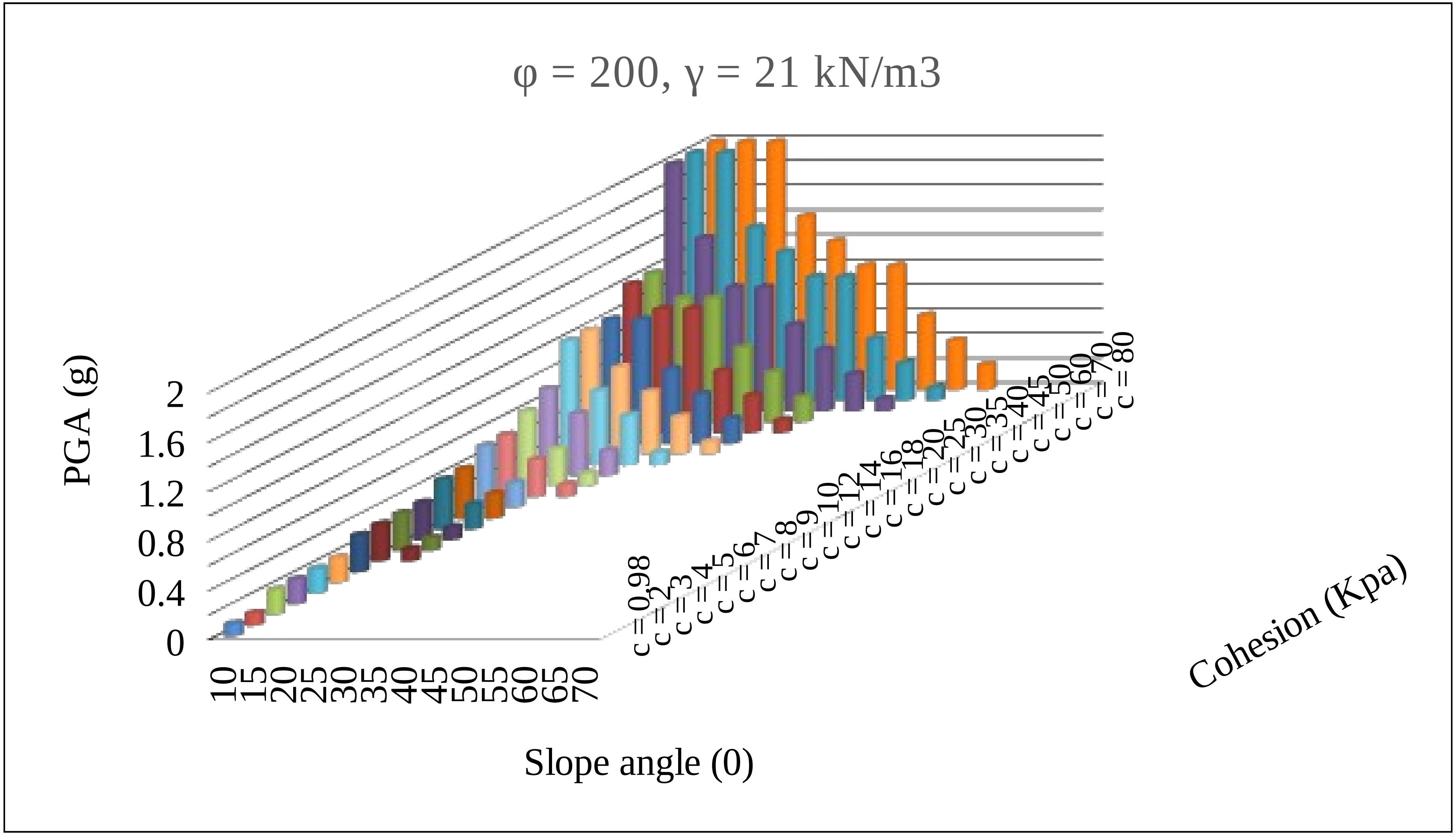

Figure 7.4 (b) φ=20^0

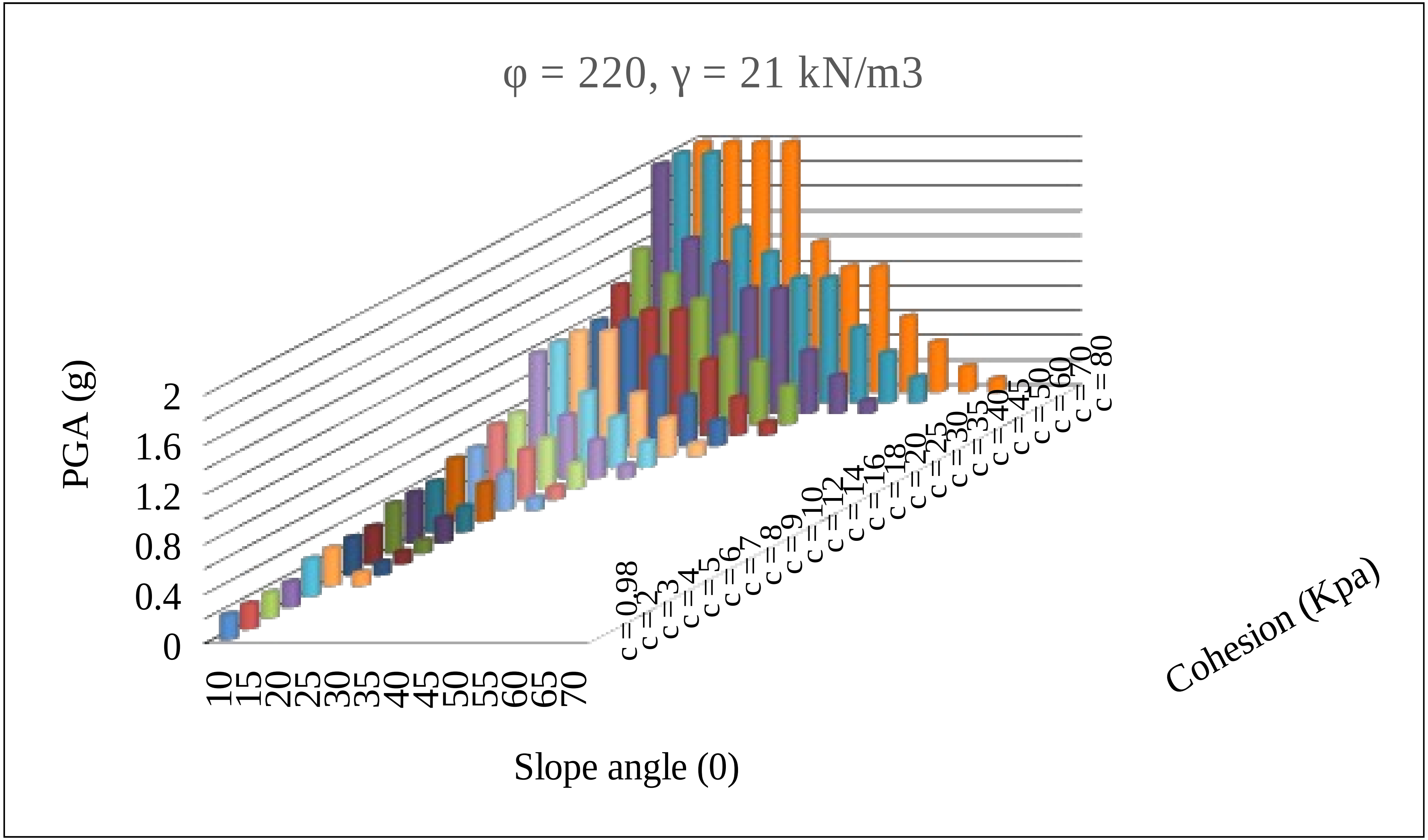

Figure 7.4 (c) φ=22^{0}

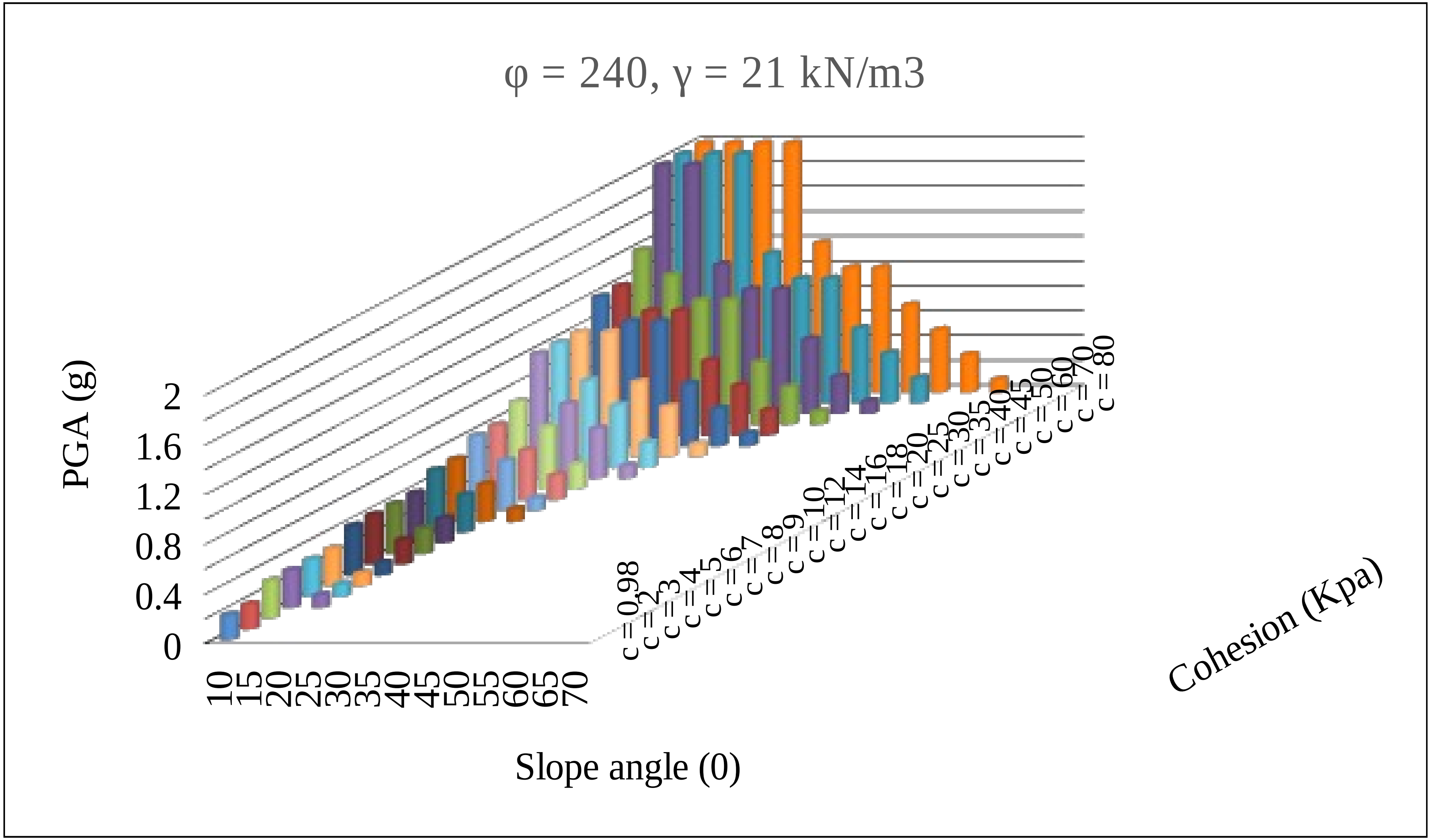

Figure 7.4 (d) φ=24^0

.

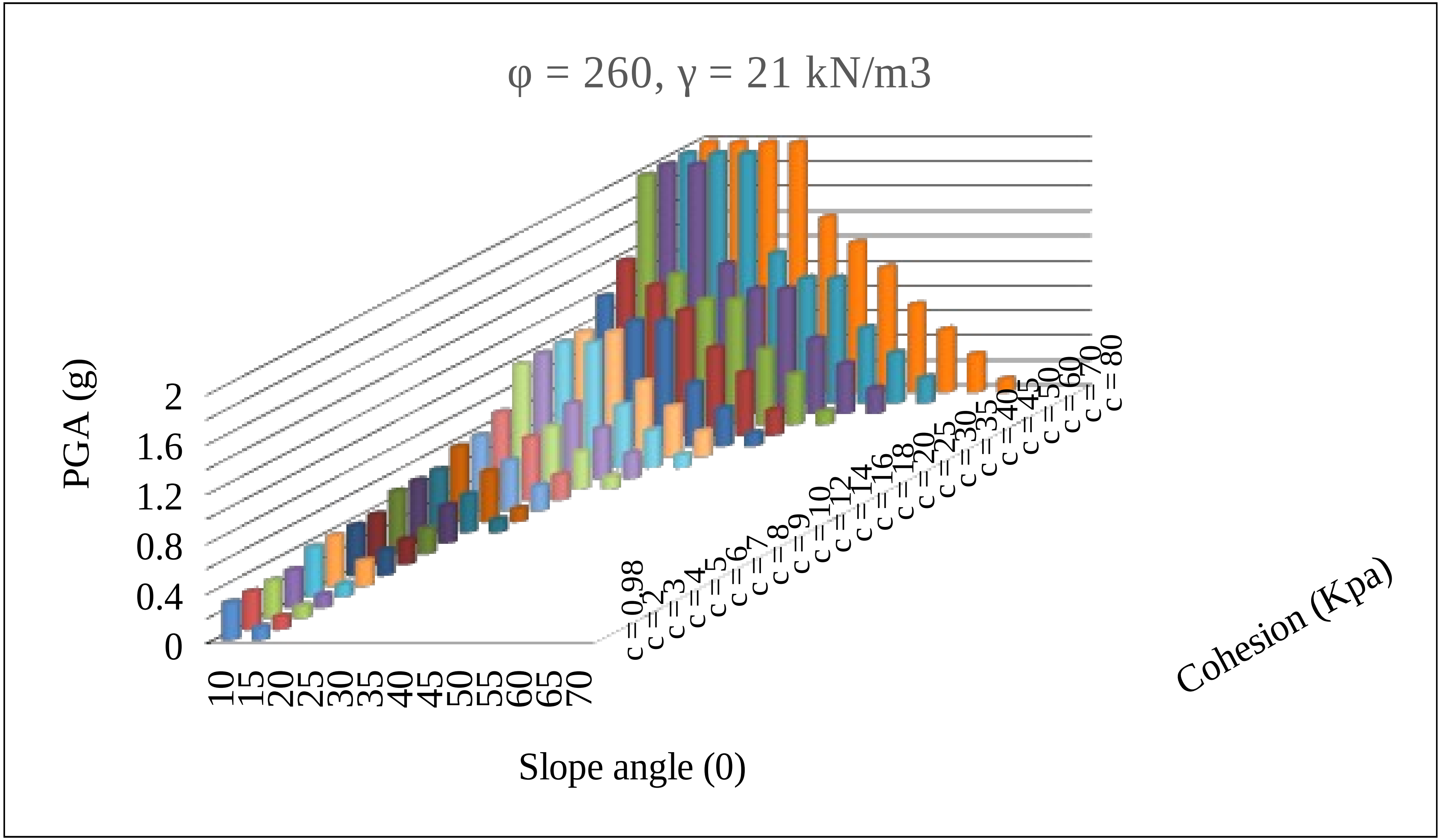

Figure 7.4 (e) φ=26^0

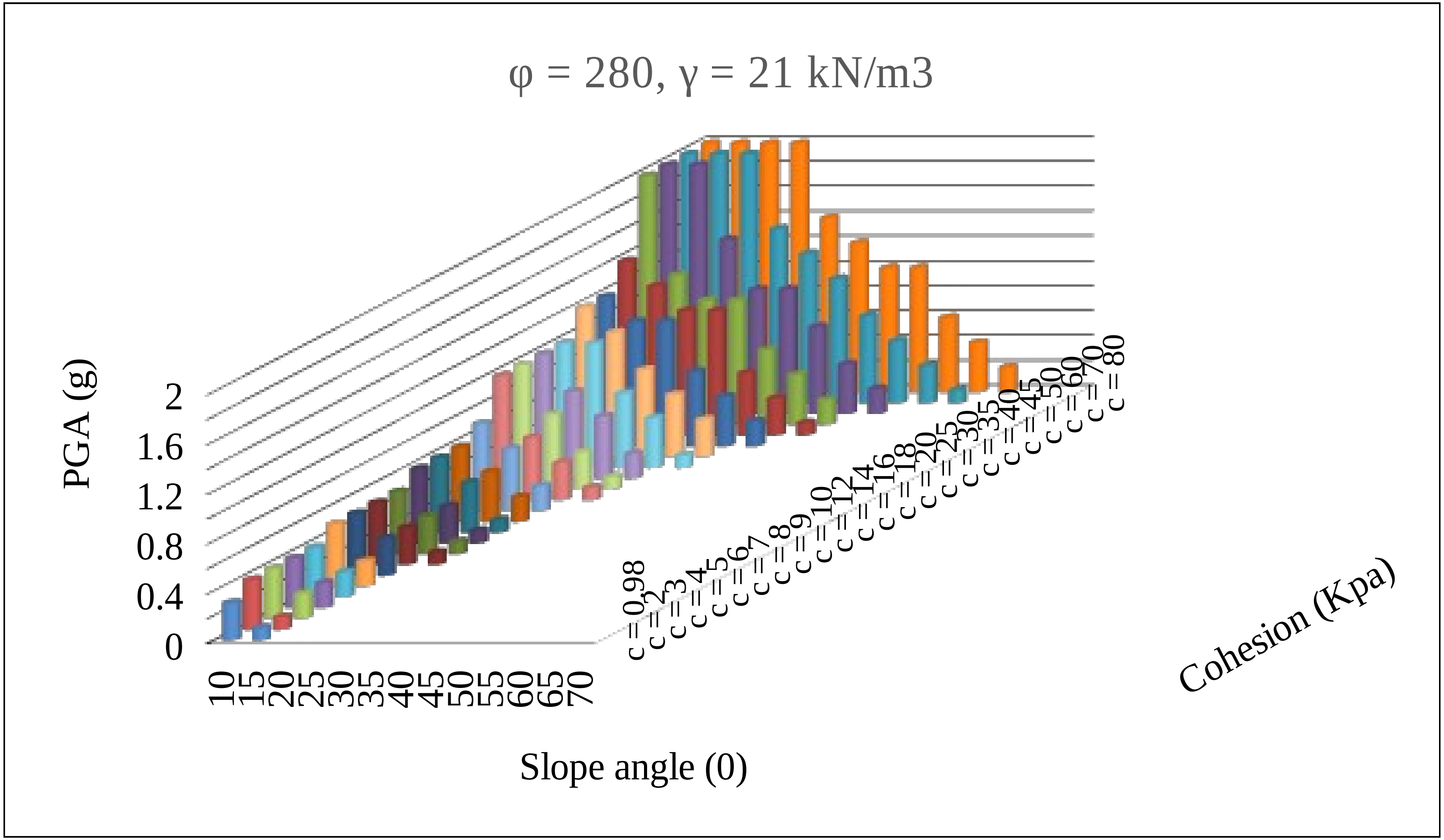

Figure 7.4 (f) φ=28^0

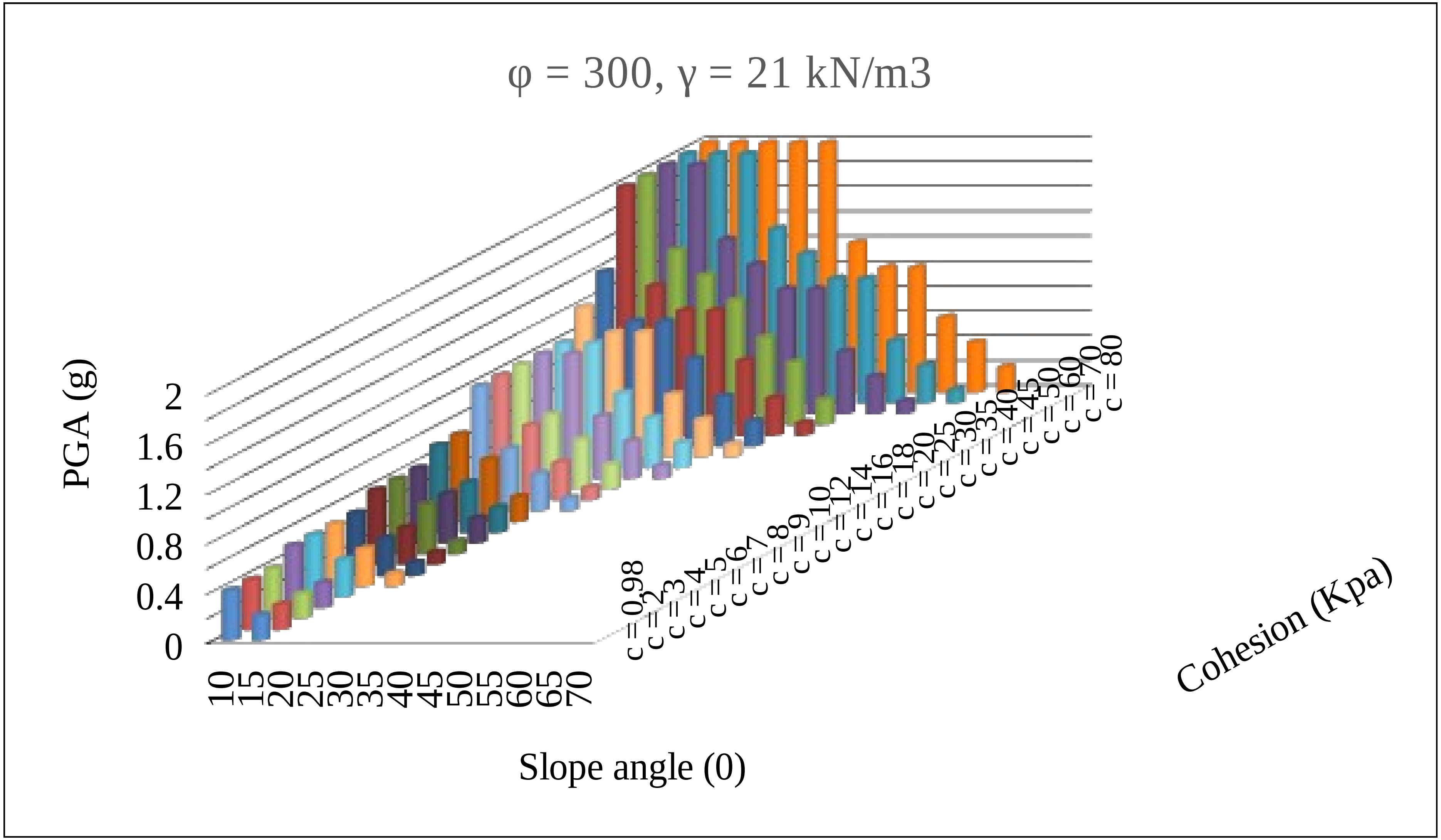

Figure 7.4 (g) φ=30^0

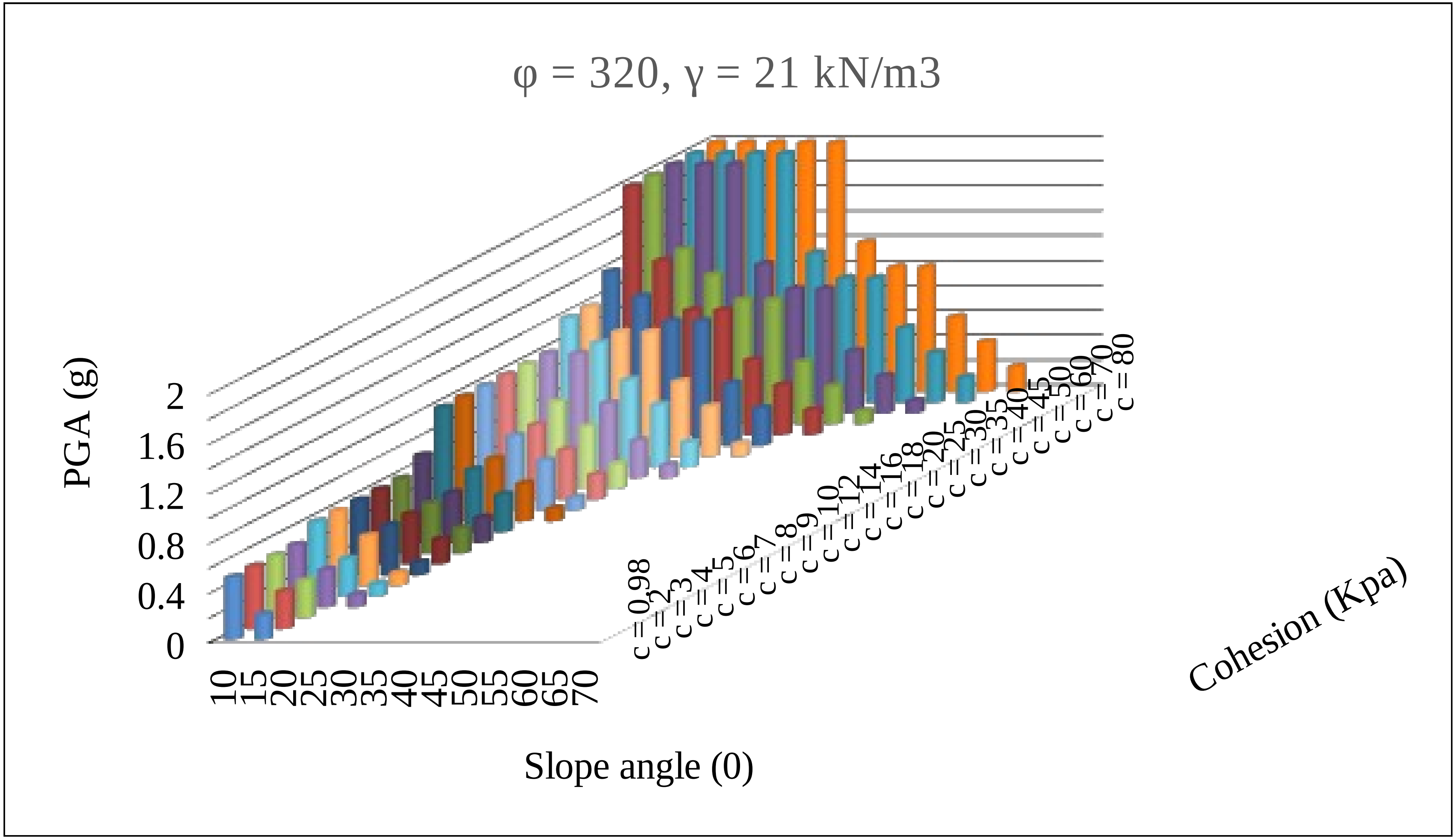

Figure 7.4 (h) φ=32^0

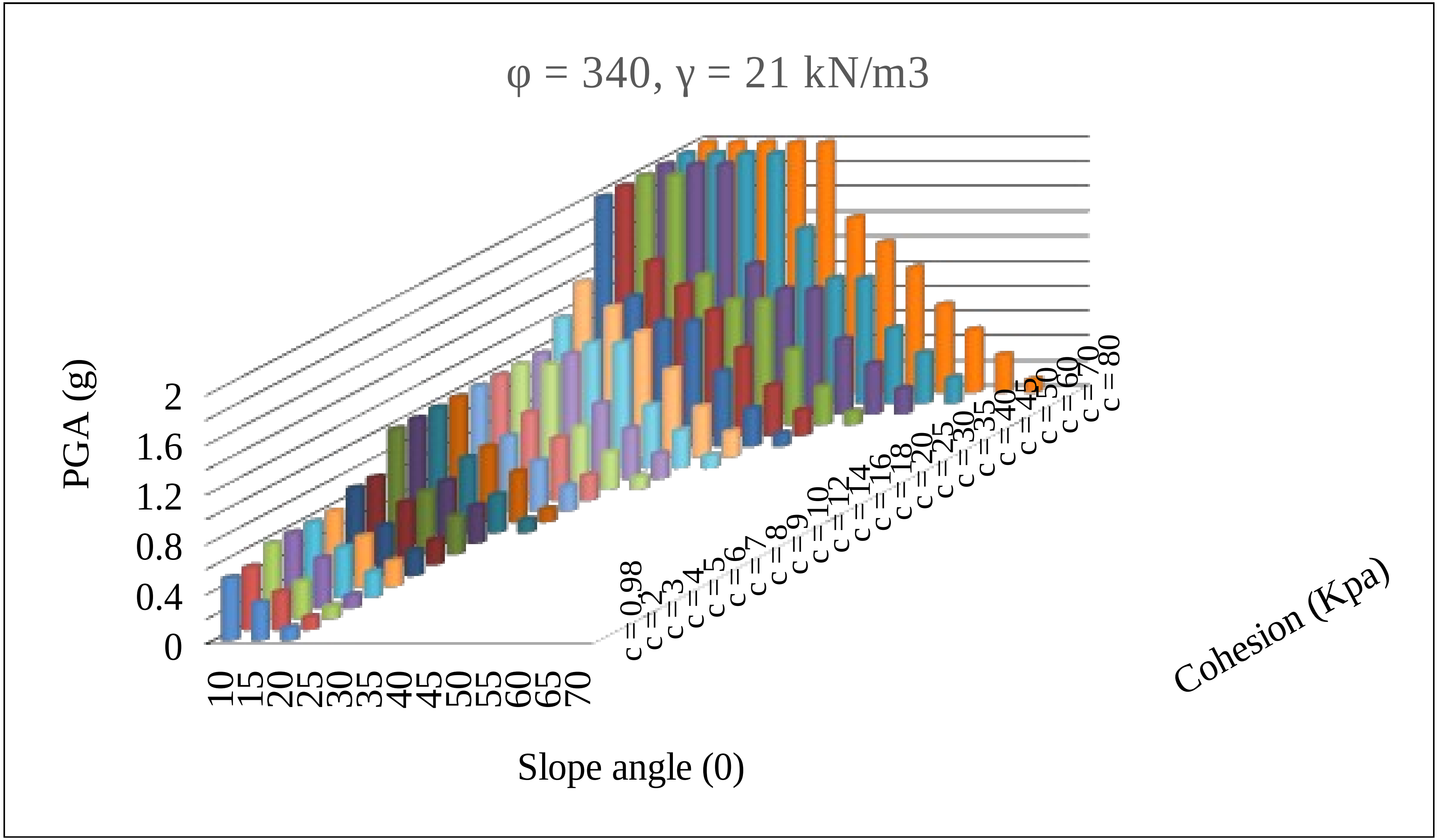

Figure 7.4 (i) φ=34^0

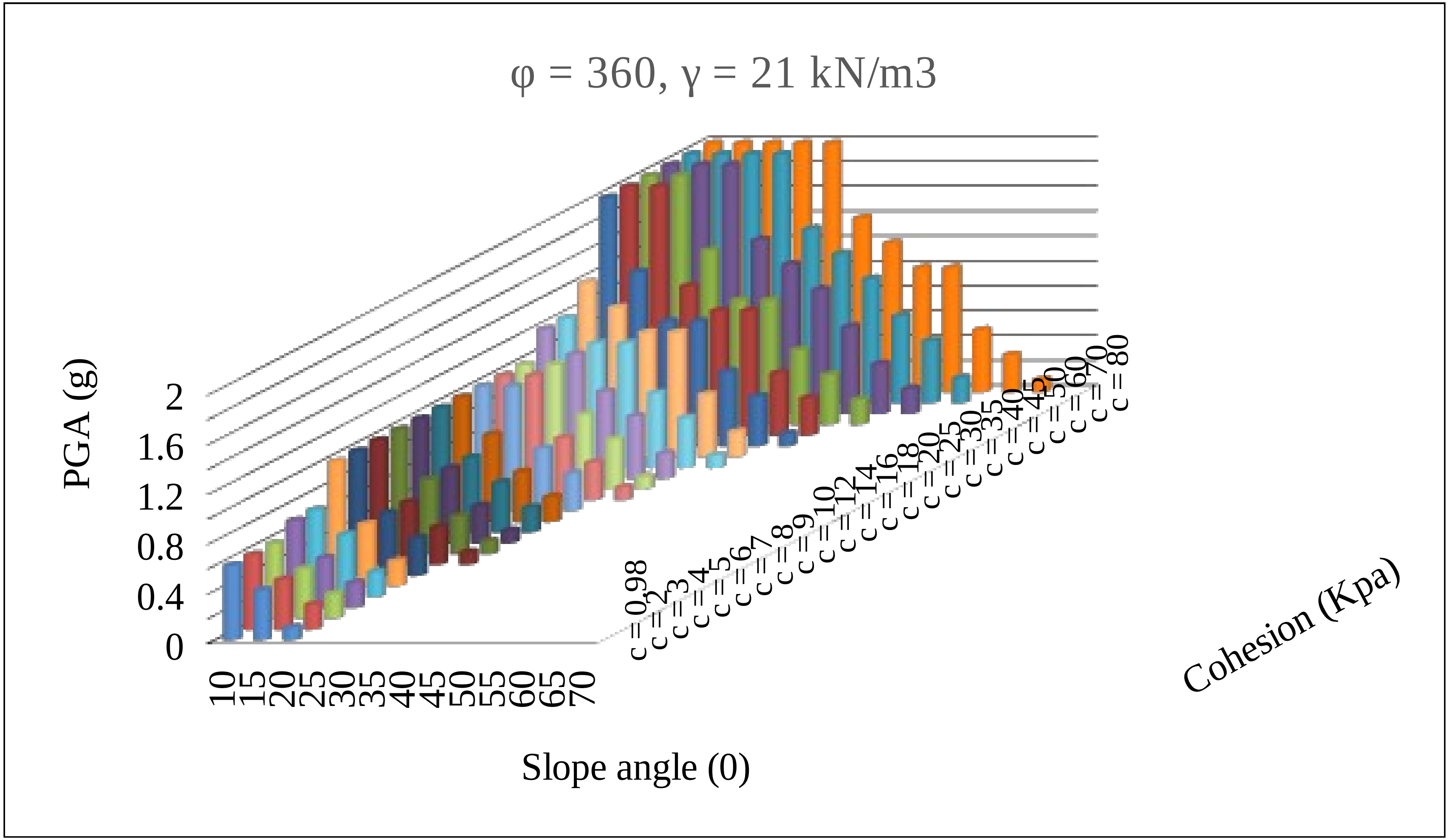

Figure 7.4 (j) φ=36^0

The design charts of DBE calculated for slope angles 10 to70^0, φ=18^0 - 36^0, c = 0 to 80 Kpa, at γ = 22 kN/m^3 are calculated and presented in Figures 7.5 (a to j).

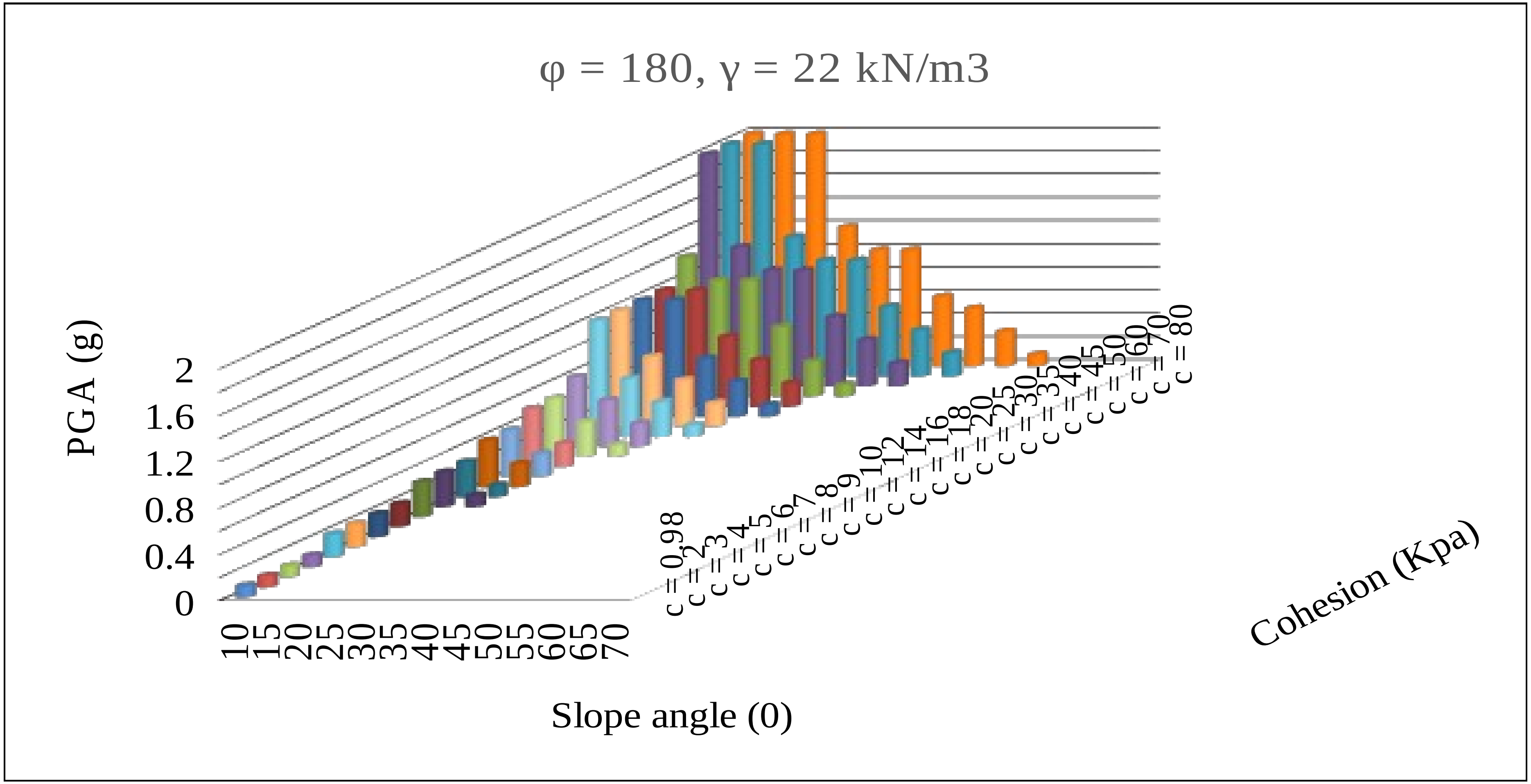

Figure 7.5 DBE design charts at various slope angle, Cohesion and γ = 22 kN/m^3 for (a) φ=18^0

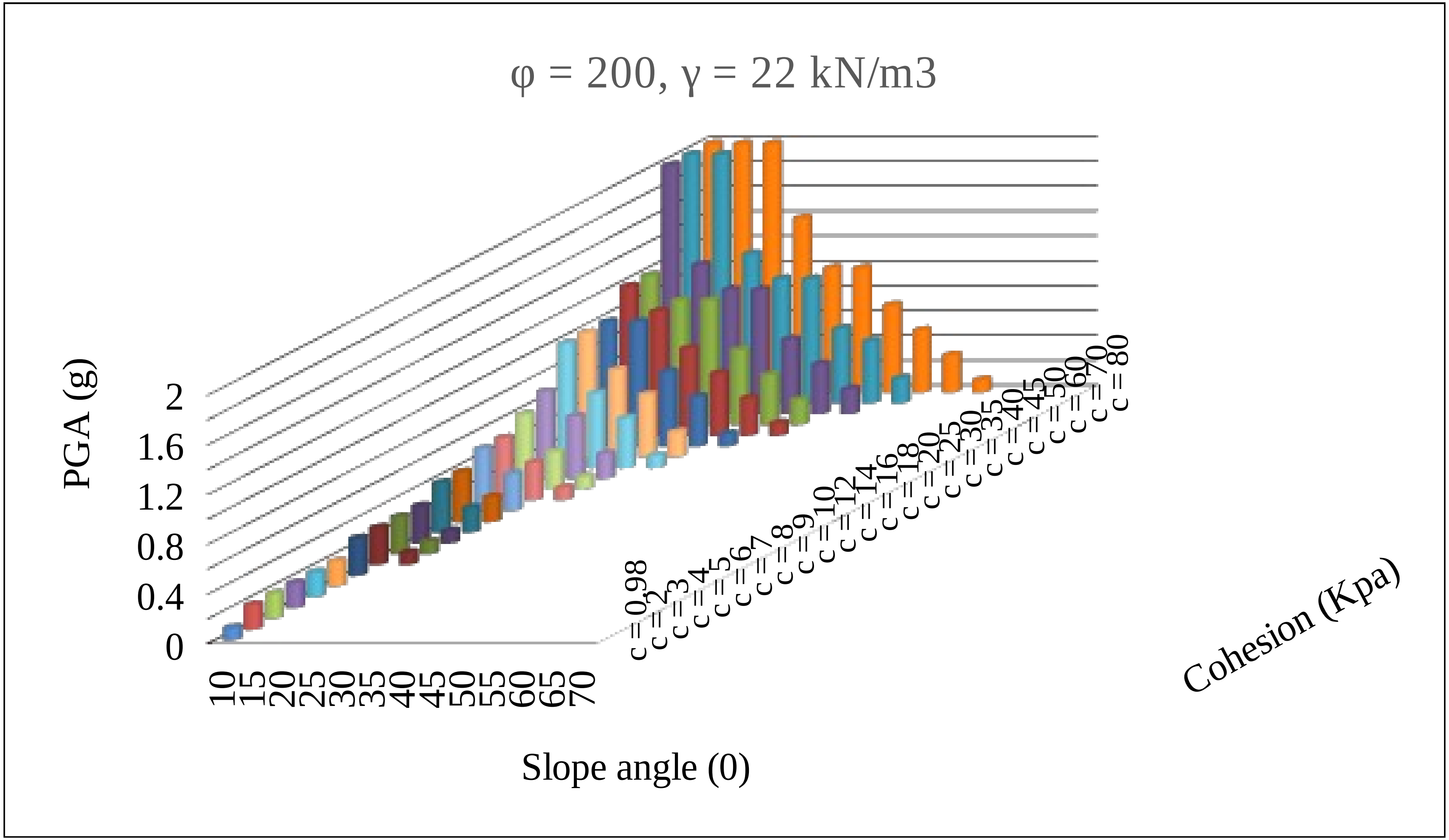

Figure 7.5 (b) φ=20^0

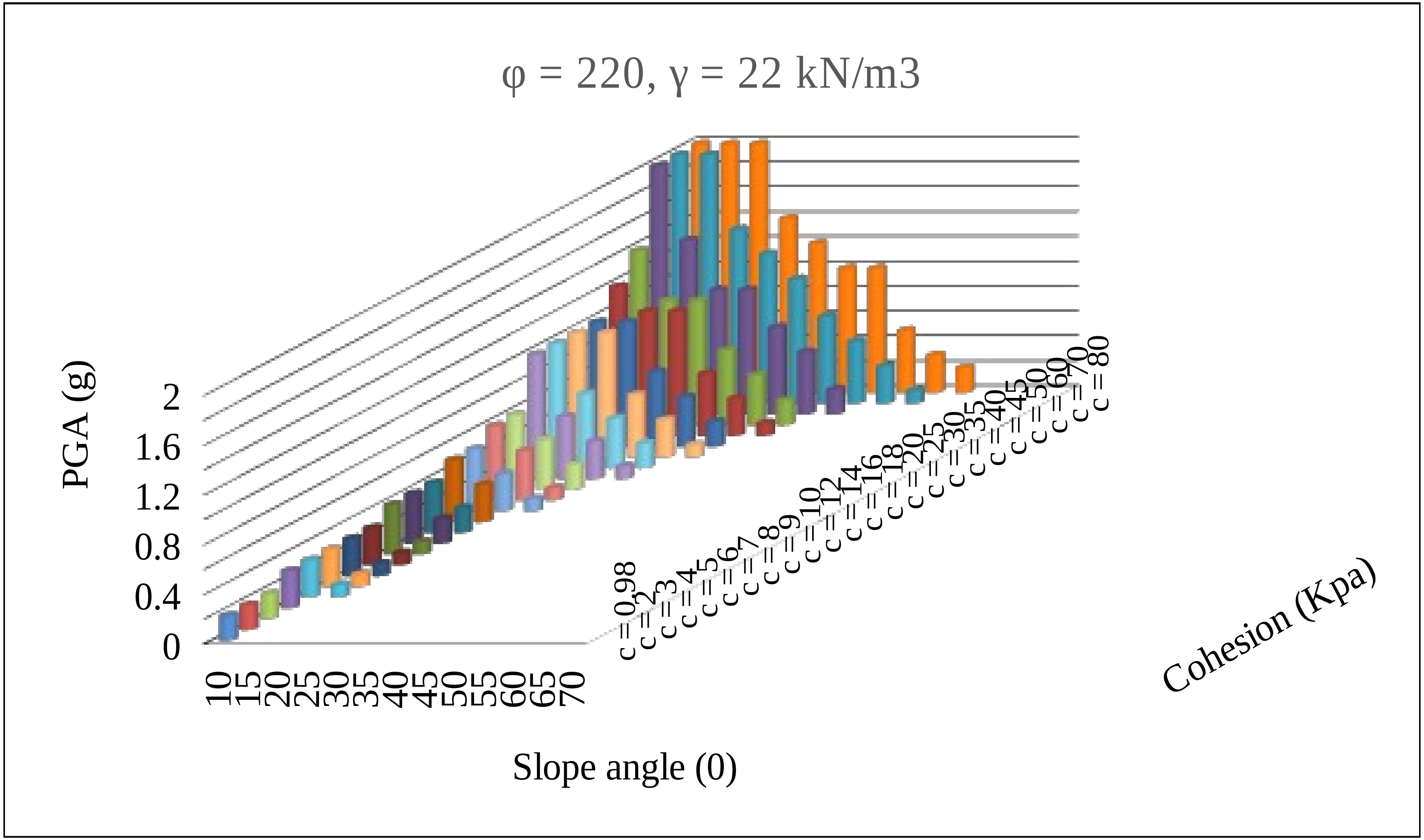

Figure 7.5 (c) φ=22^0

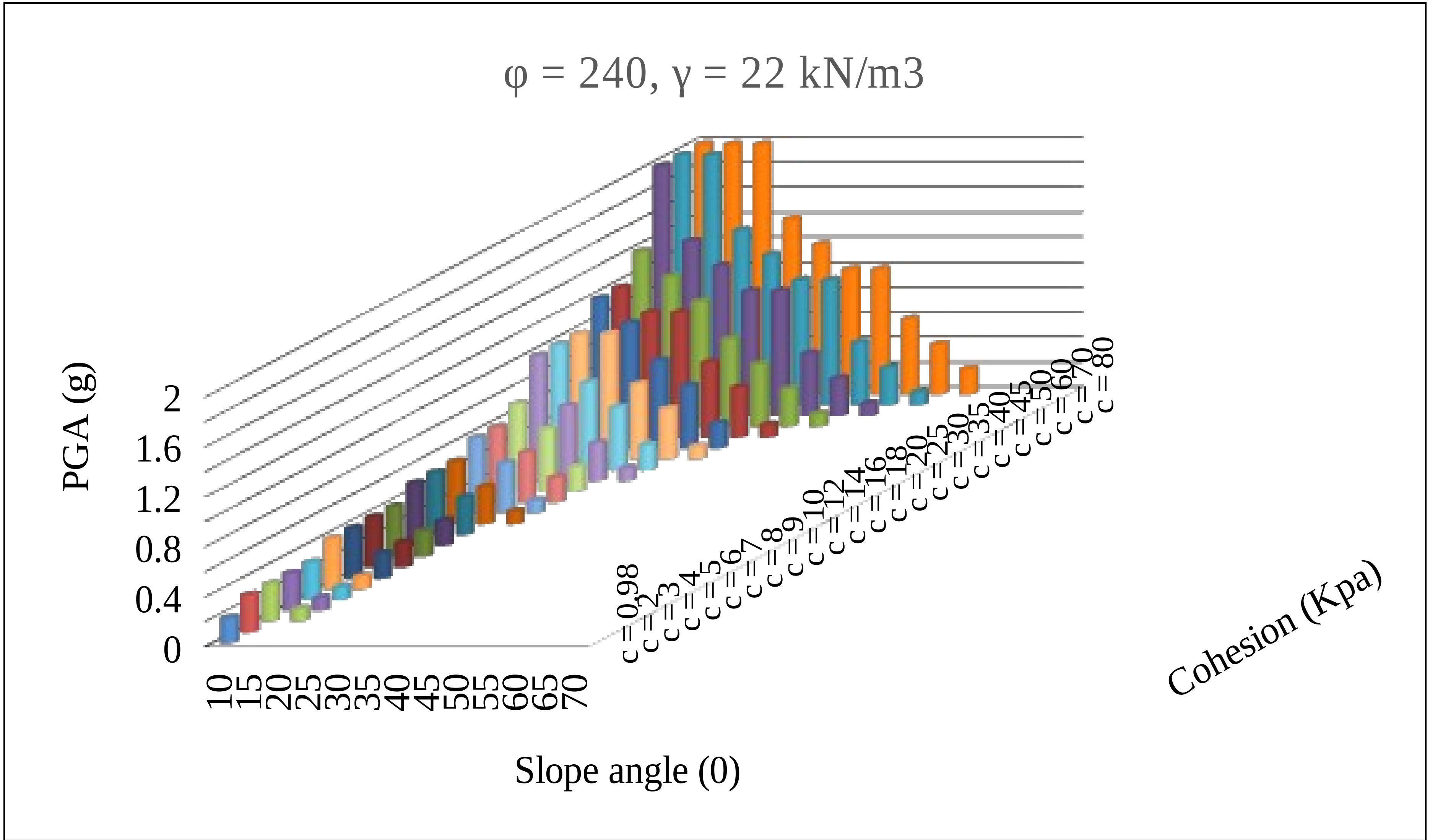

Figure 7.5 (d) φ=24^0

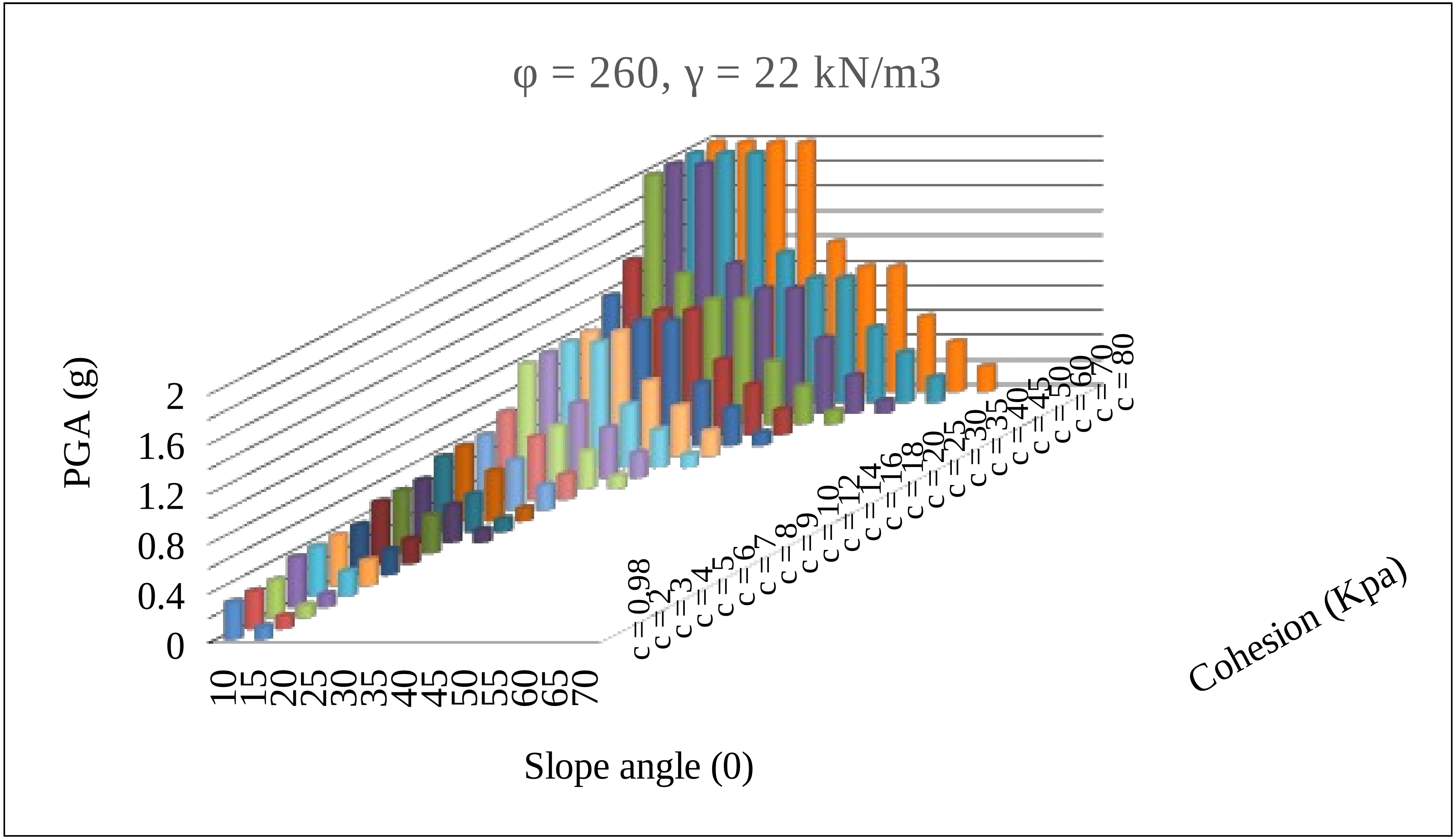

Figure 7.5 (e) $\varphi=26^0$

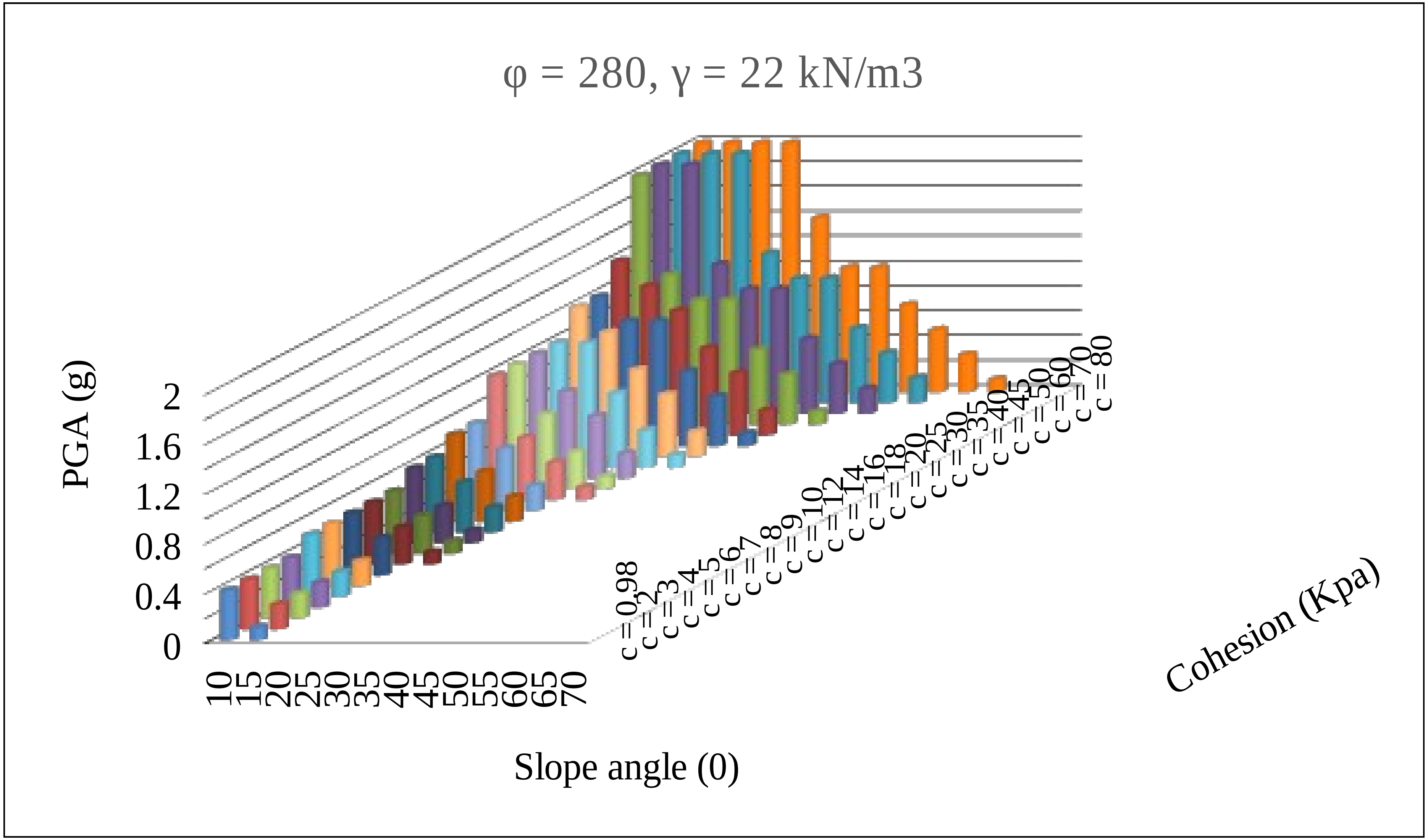

Figure 7.5 (f) $\varphi=28^0$

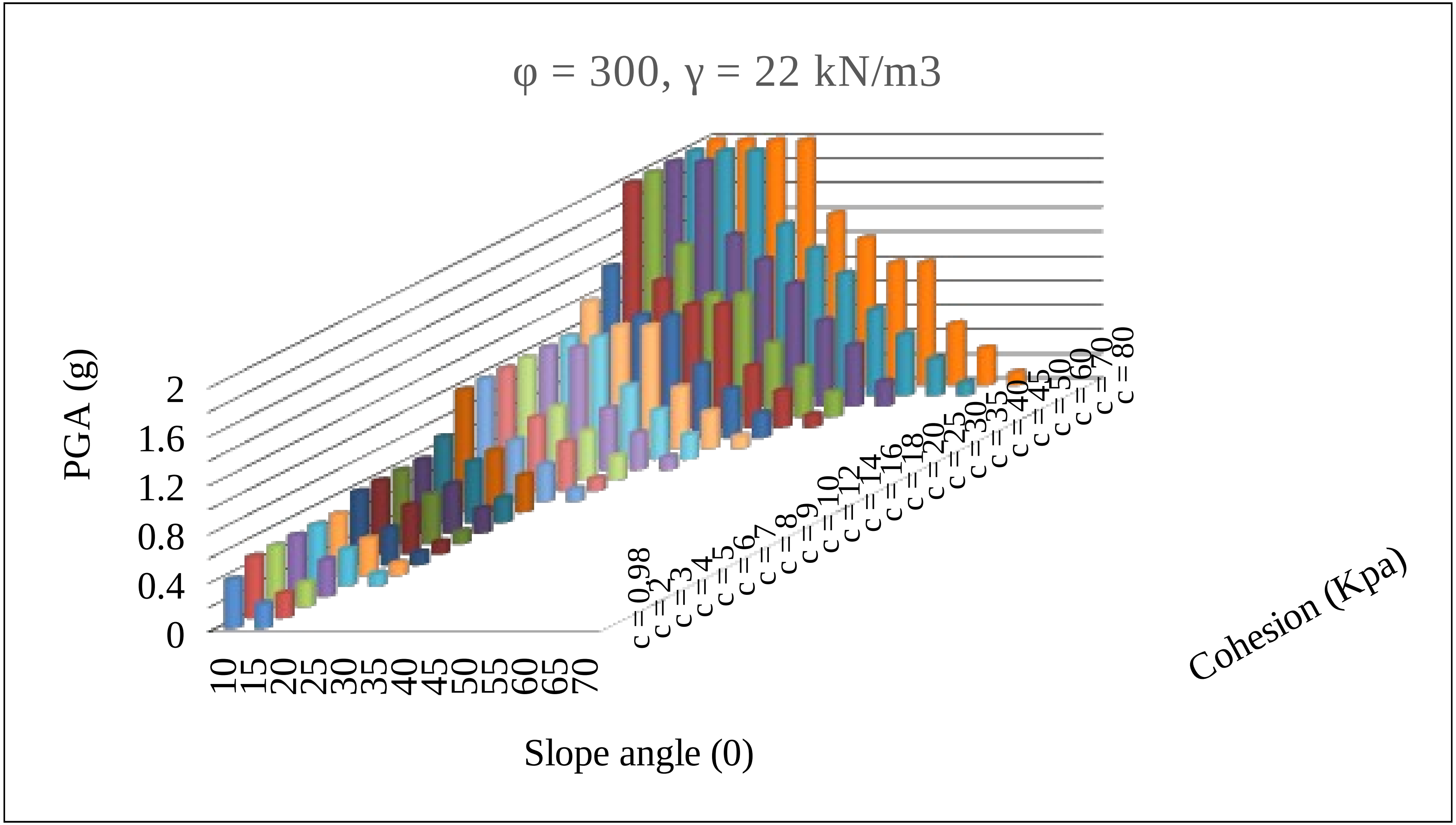

Figure 7.5 (g) φ=30^0

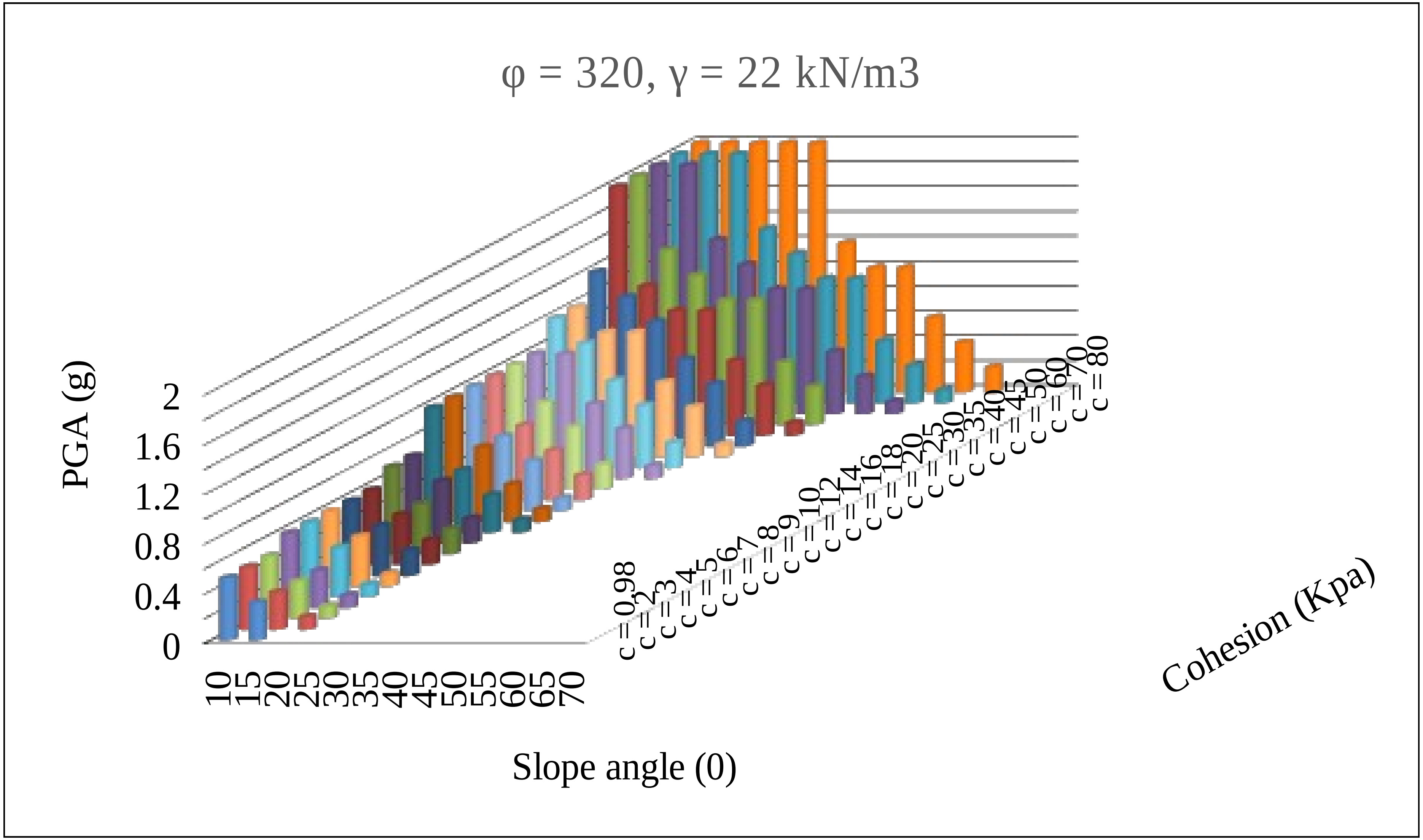

Figure 7.5 (h) φ=32^0

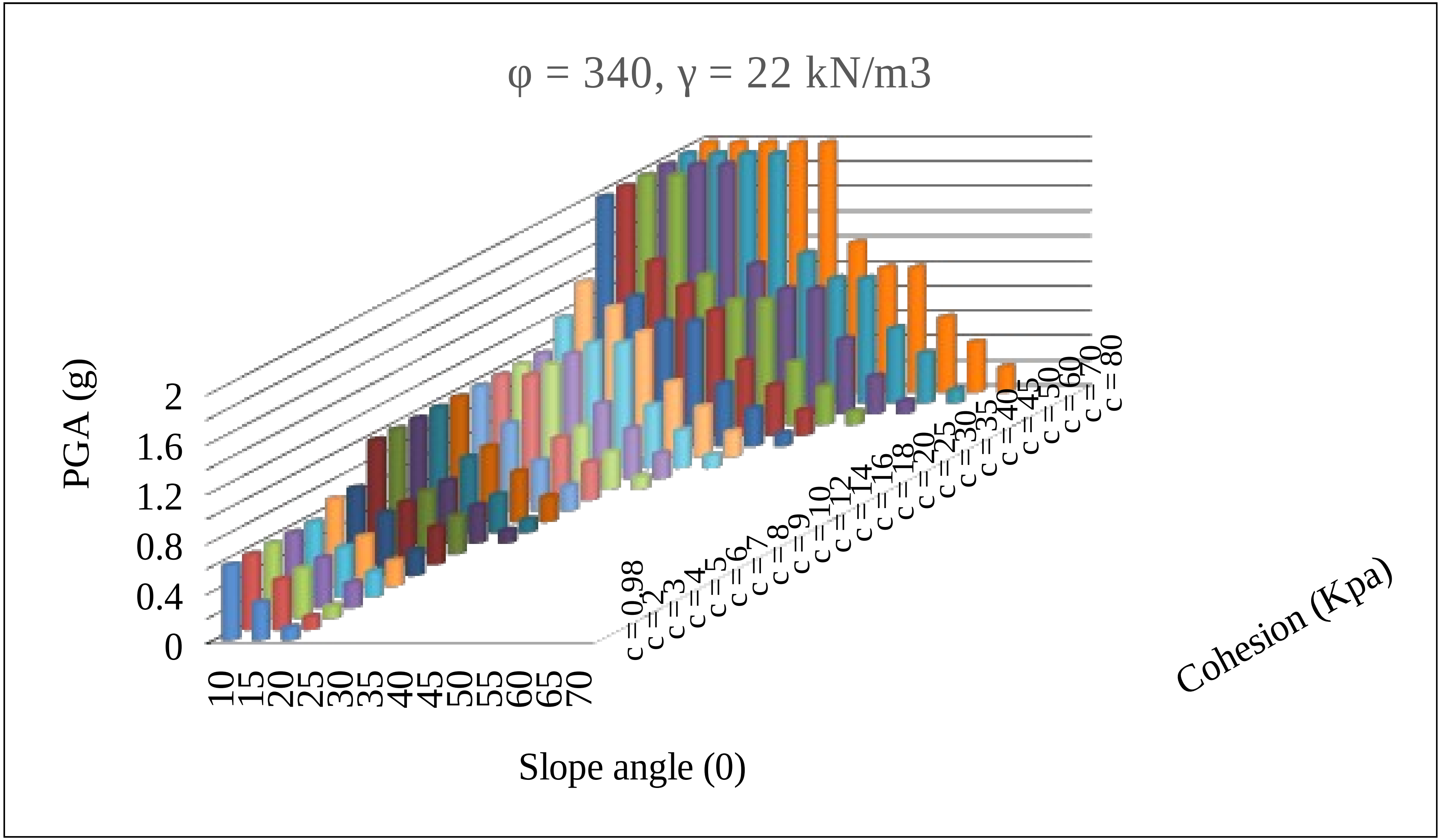

Figure 7.5 (i) φ=34^0

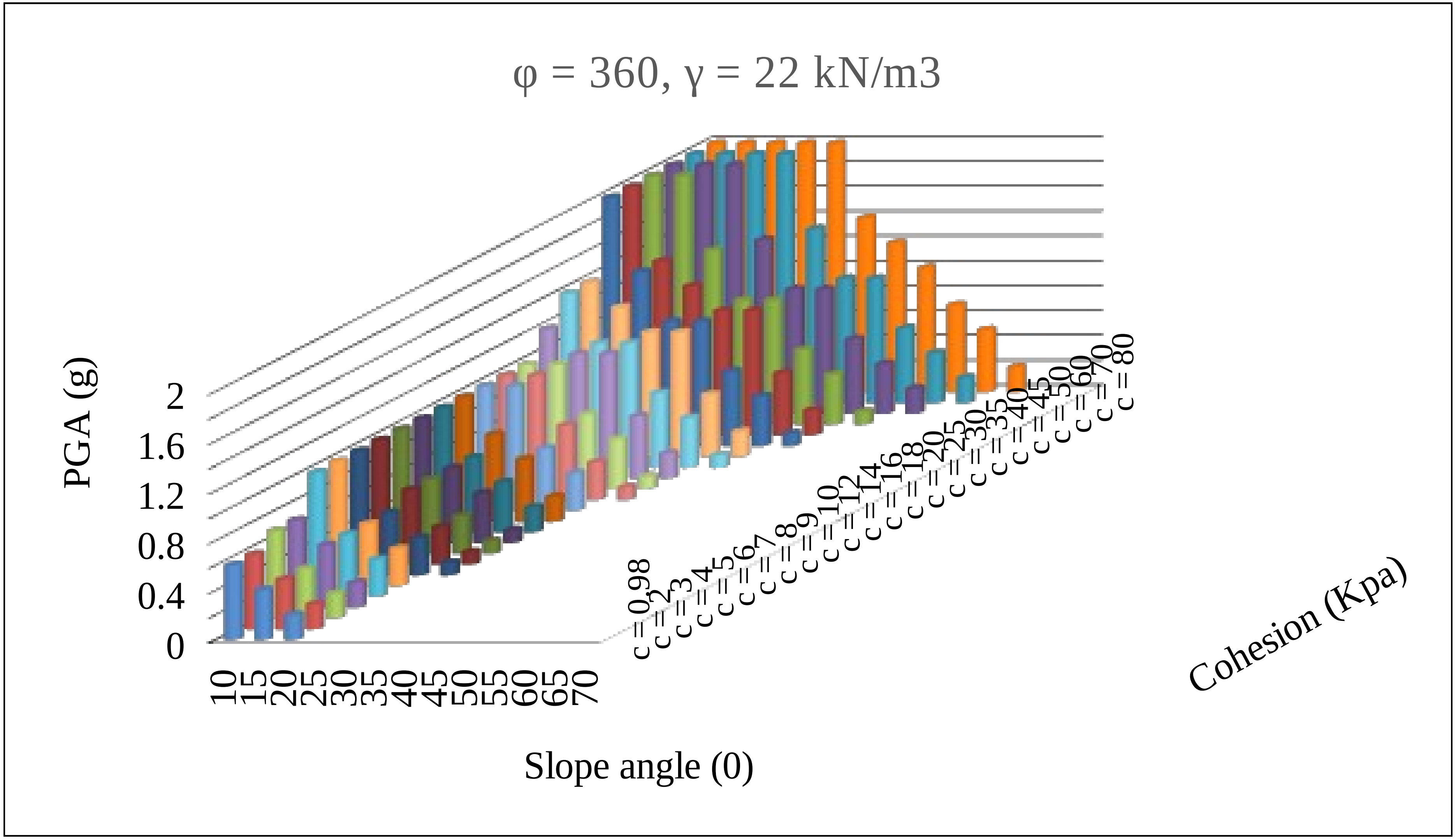

Figure 7.5 (j) φ=36^{0}

The design charts of DBE calculated for slope angles 10 to70^0, φ=18^0 - 36^0, c = 0 to 80 Kpa, at γ = 23 kN/m^3 are calculated and presented in Figures 7.6 (a to j).

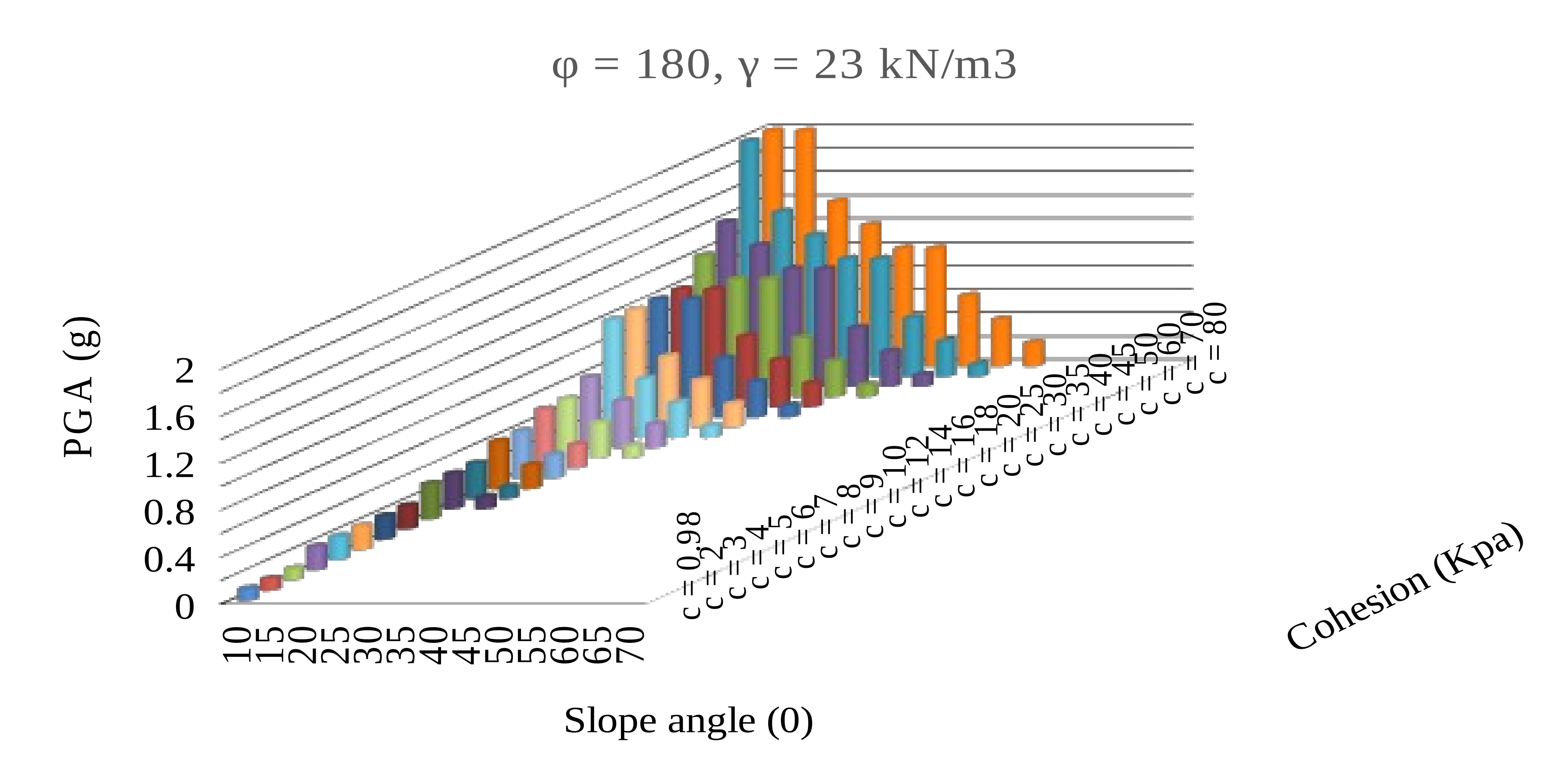

Figure 7.6 DBE design charts at various slope angle, Cohesion and γ = 23 kN/m^3 for (a) φ=18^0

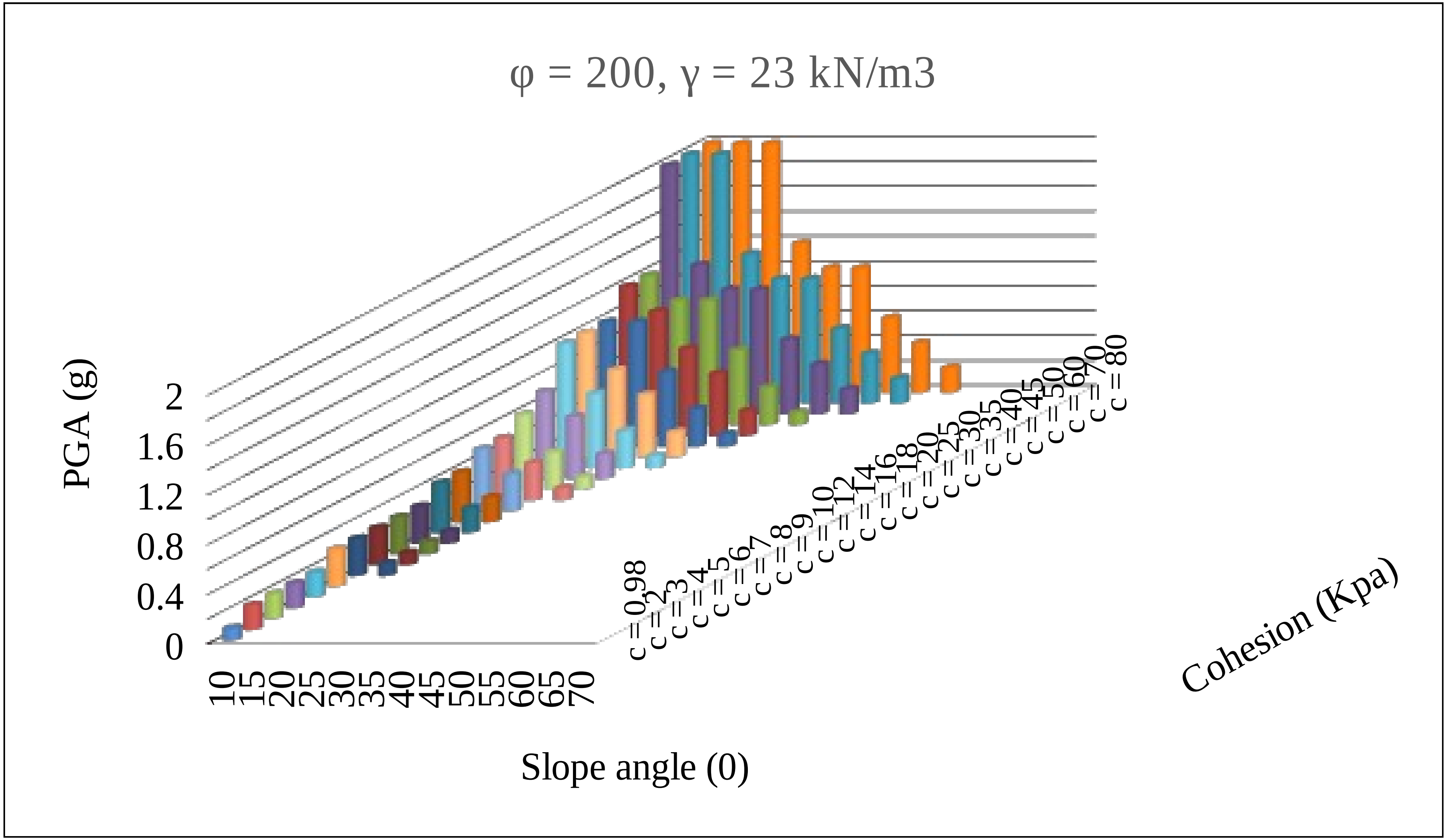

Figure 7.6 (b) $\varphi=20^0$

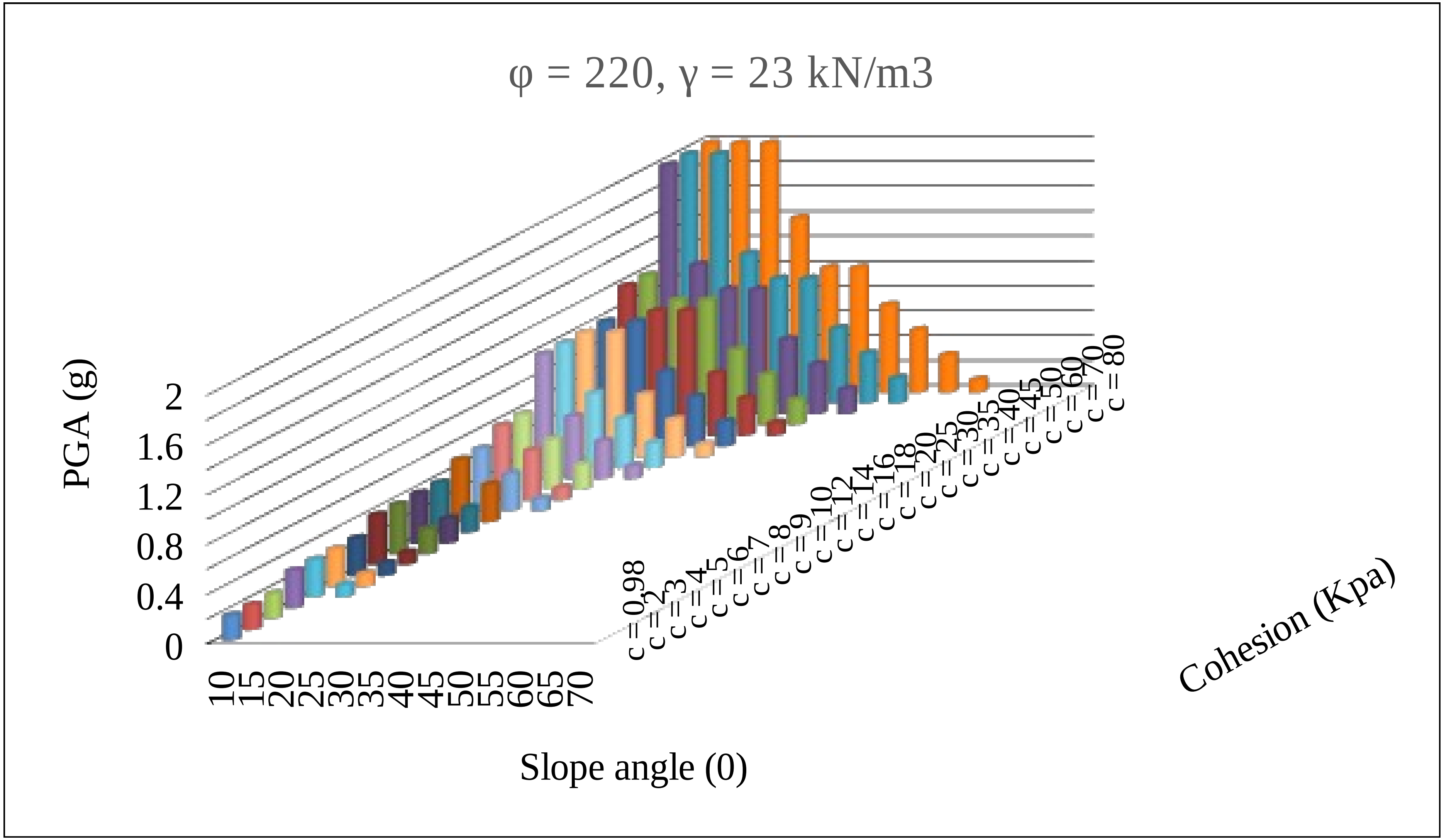

Figure 7.6 (c) φ=22^0

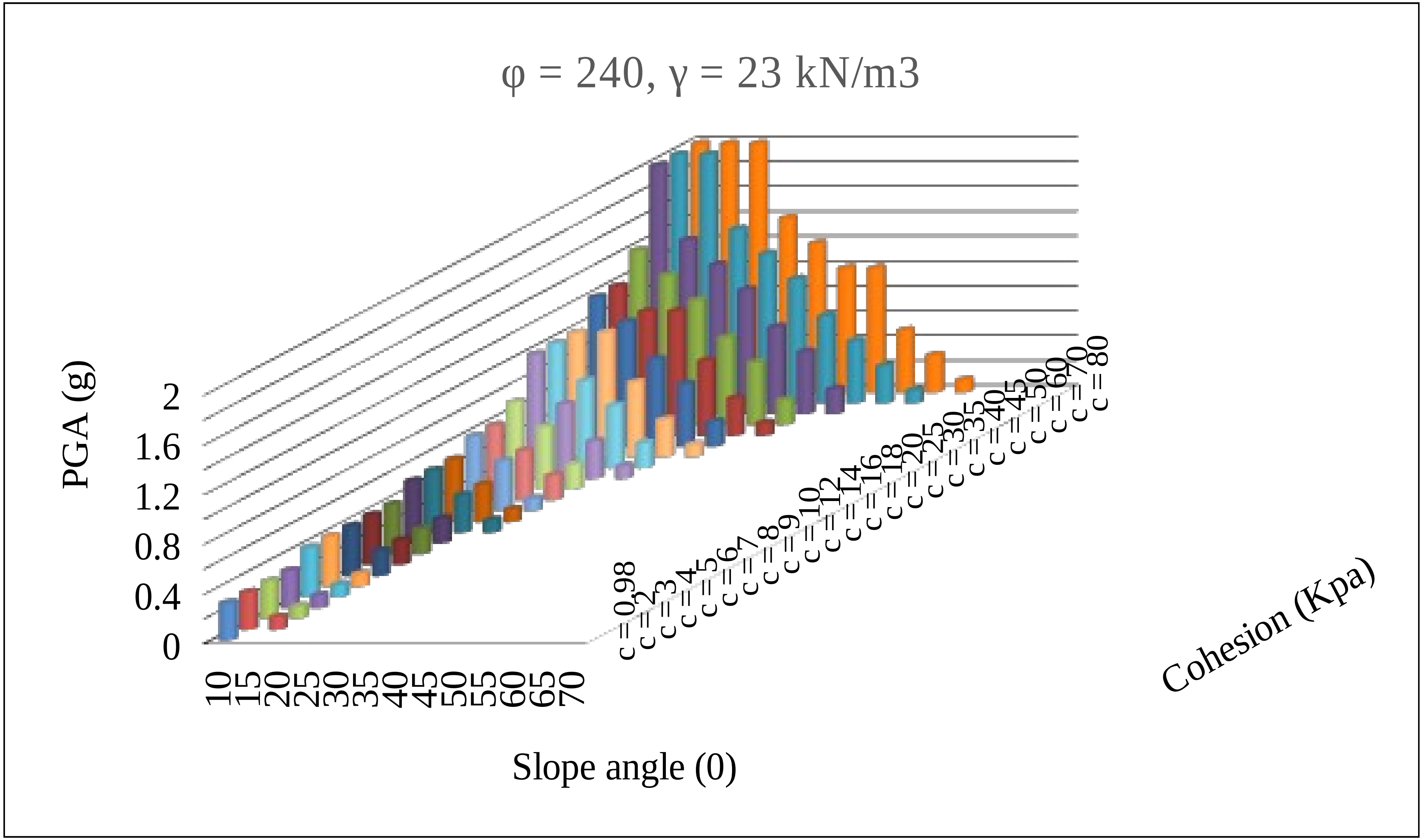

Figure 7.6 (d) $\varphi=24^0$

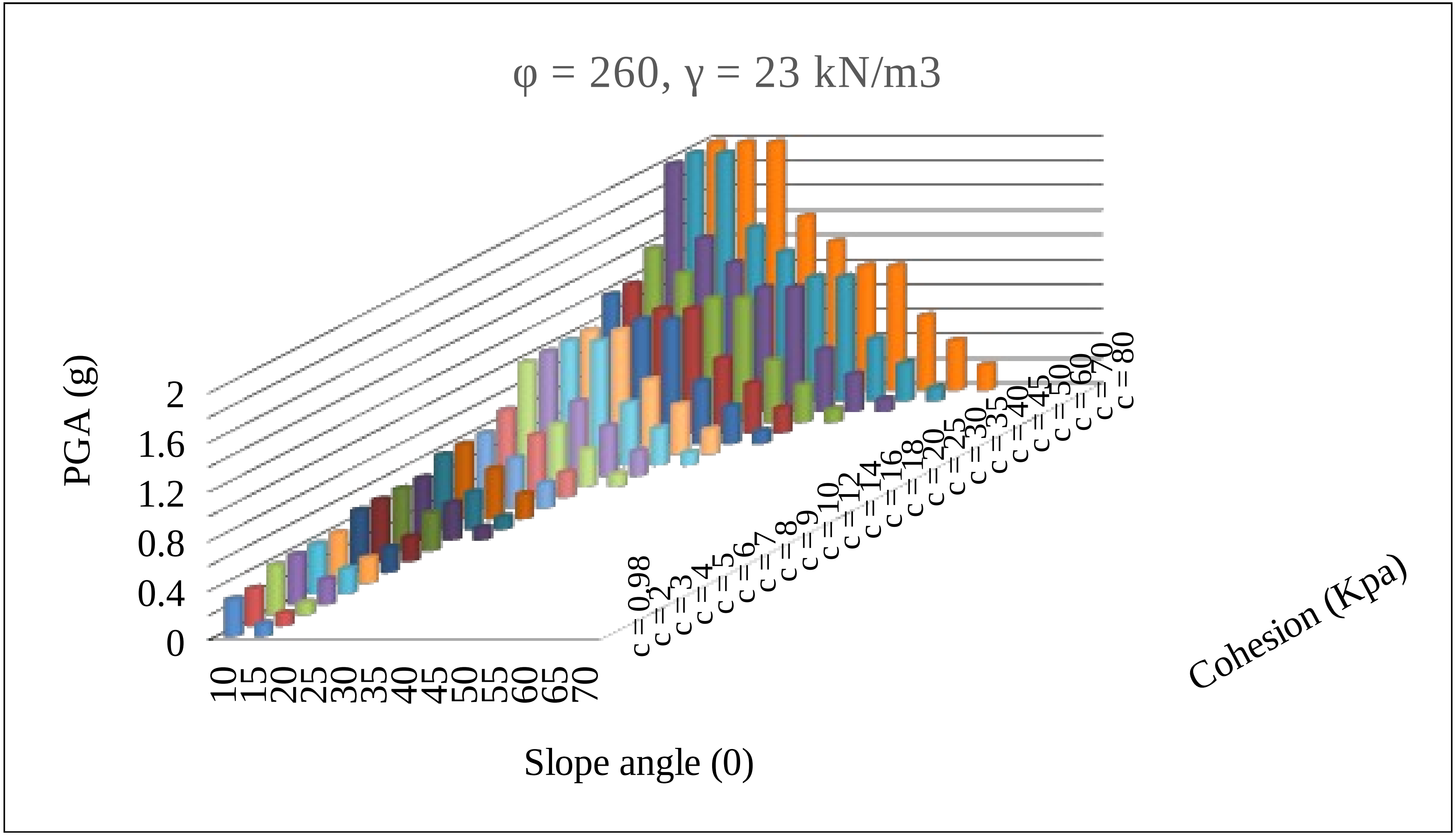

Figure 7.6 (e) φ=26⁰

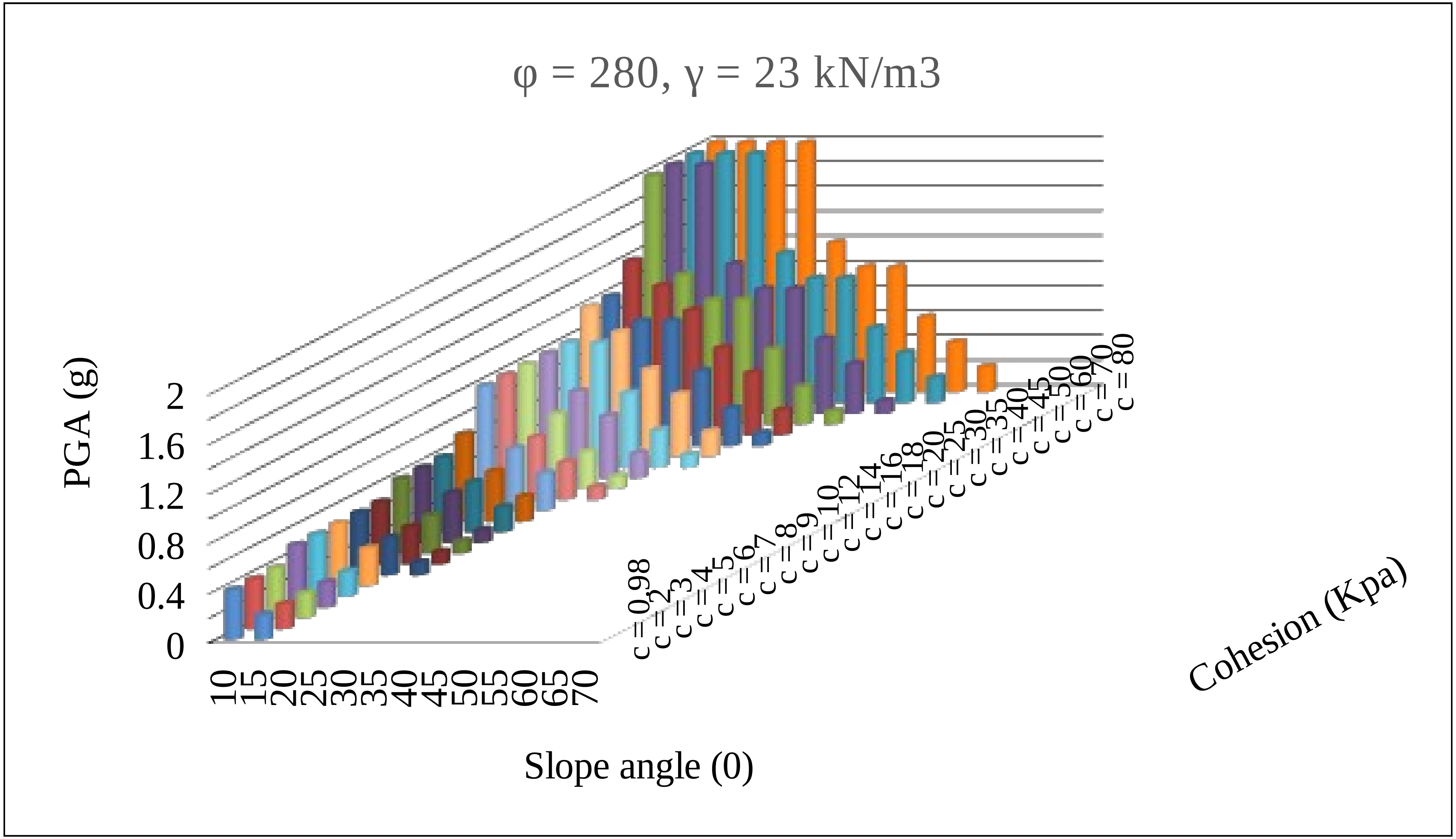

Figure 7.6 (f) φ=28^0

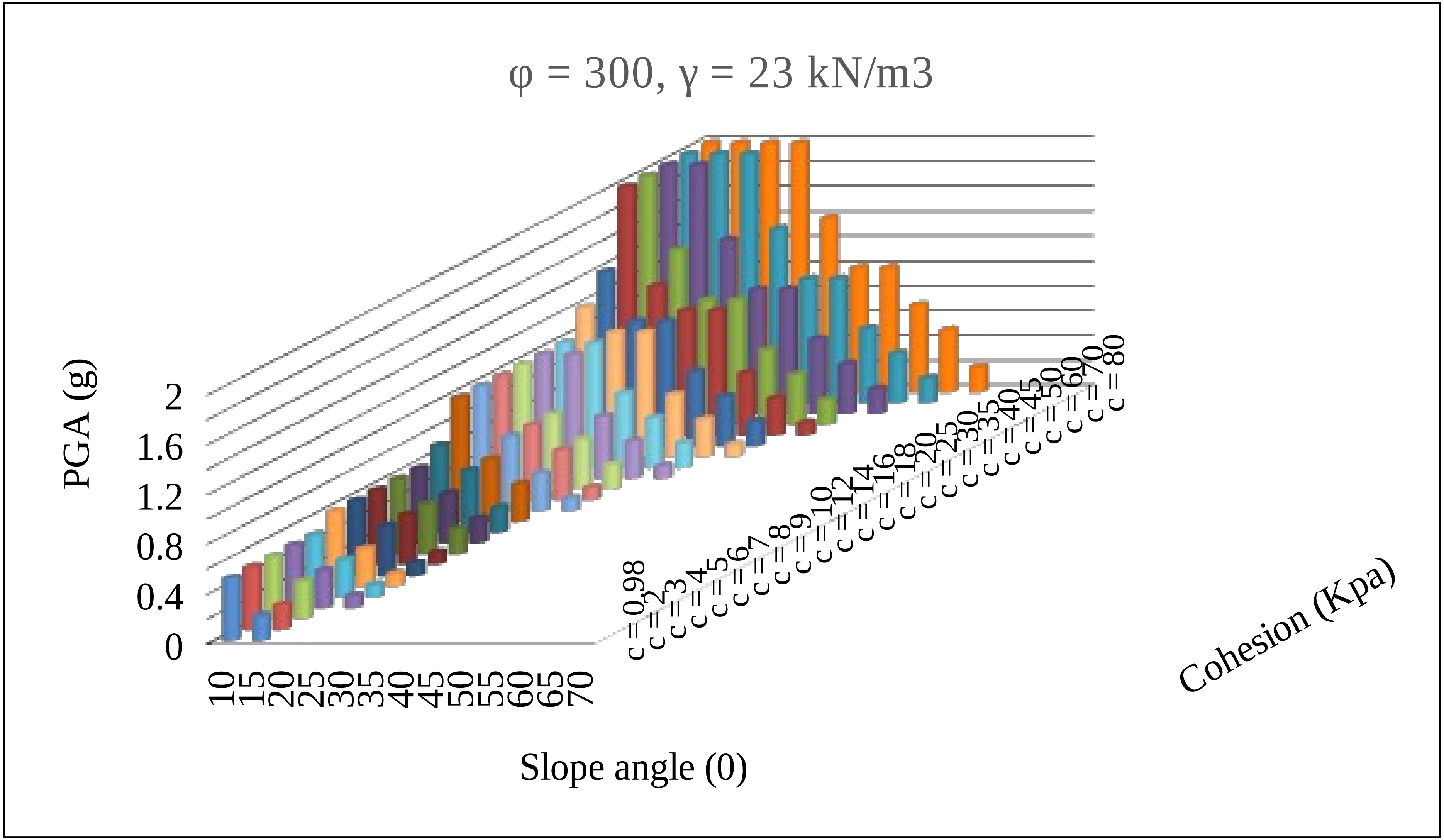

Figure 7.6 (g) φ=30^0

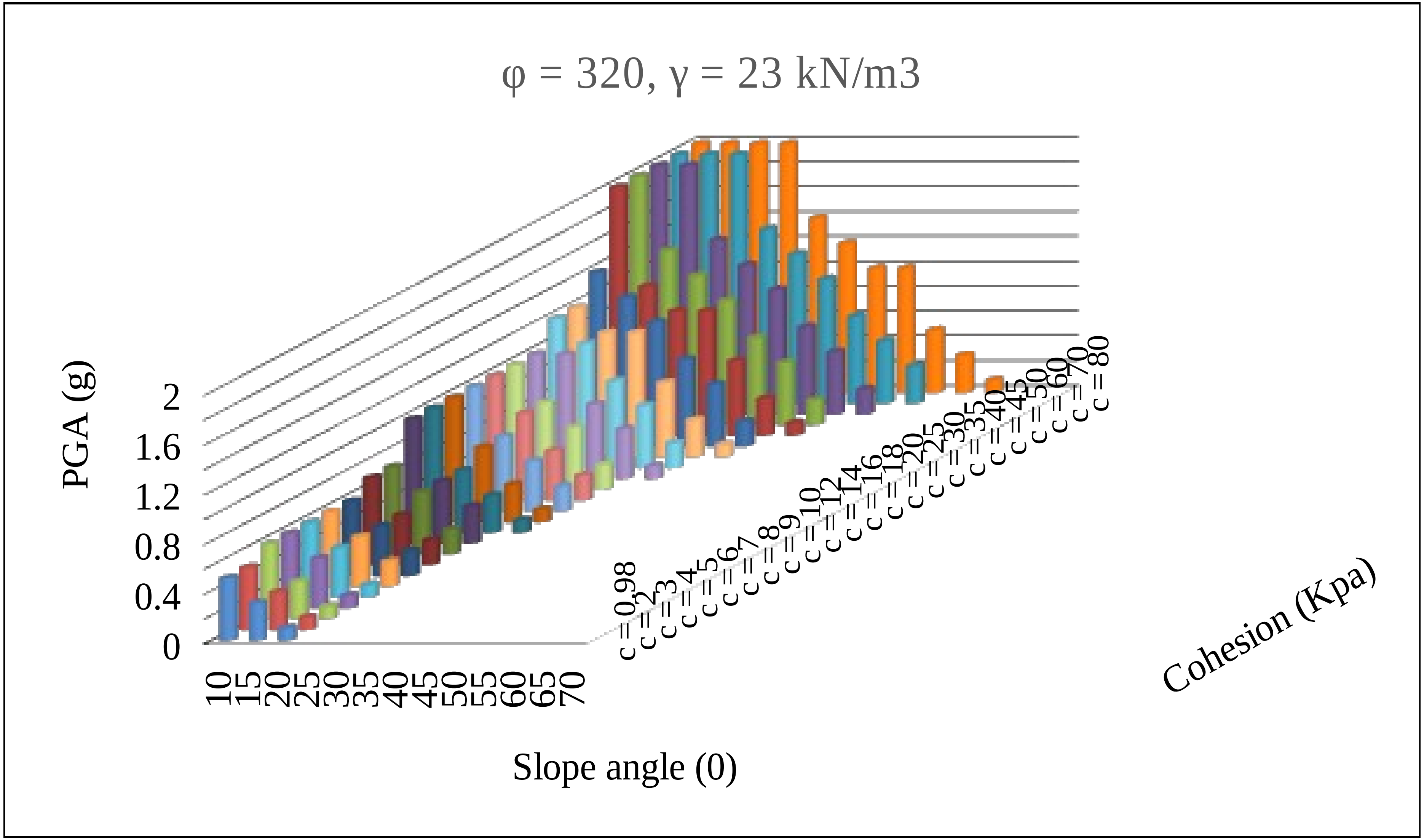

Figure 7.6 (h) $\varphi=32^0$

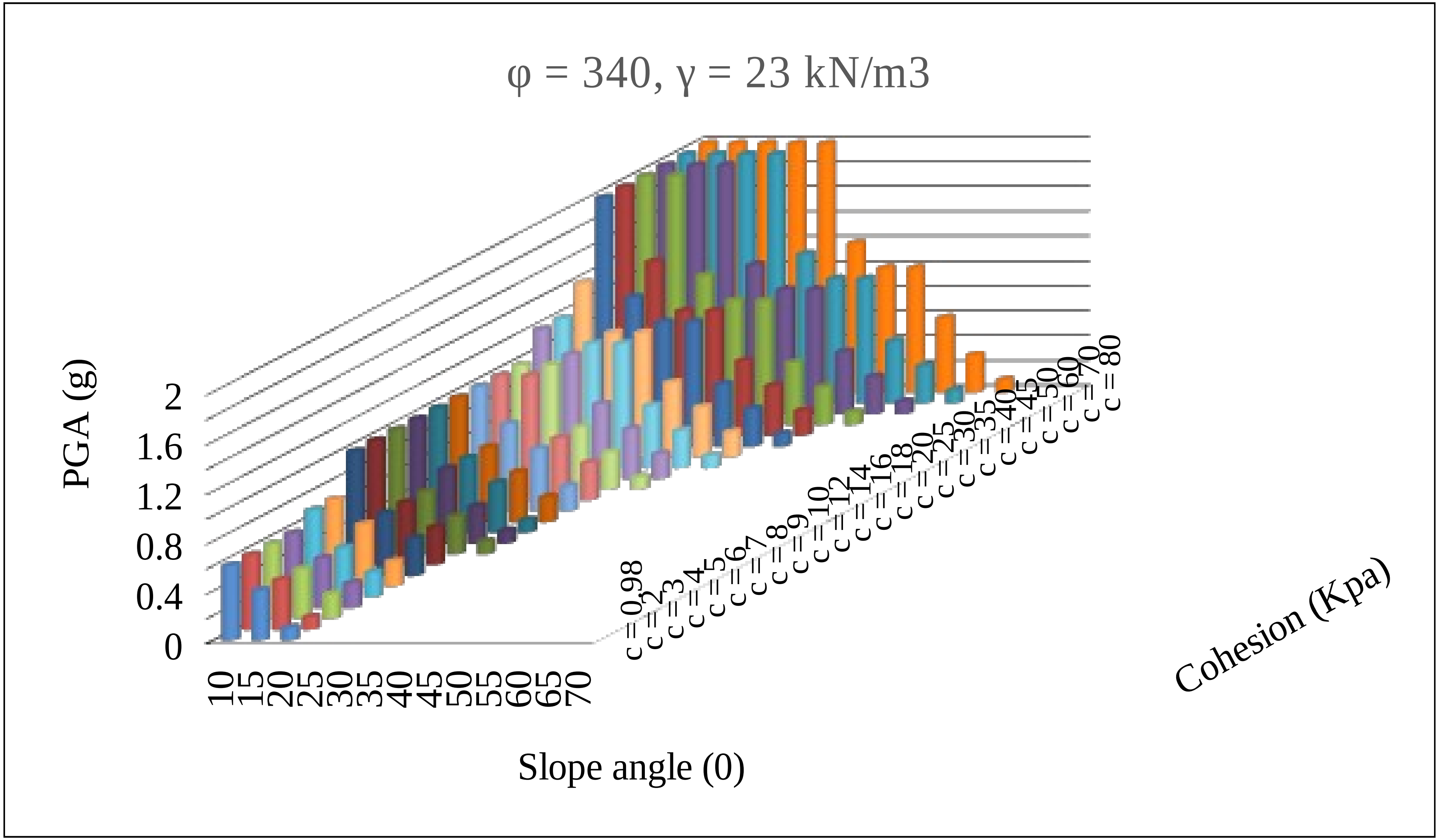

Figure 7.6 (i) φ=34^0

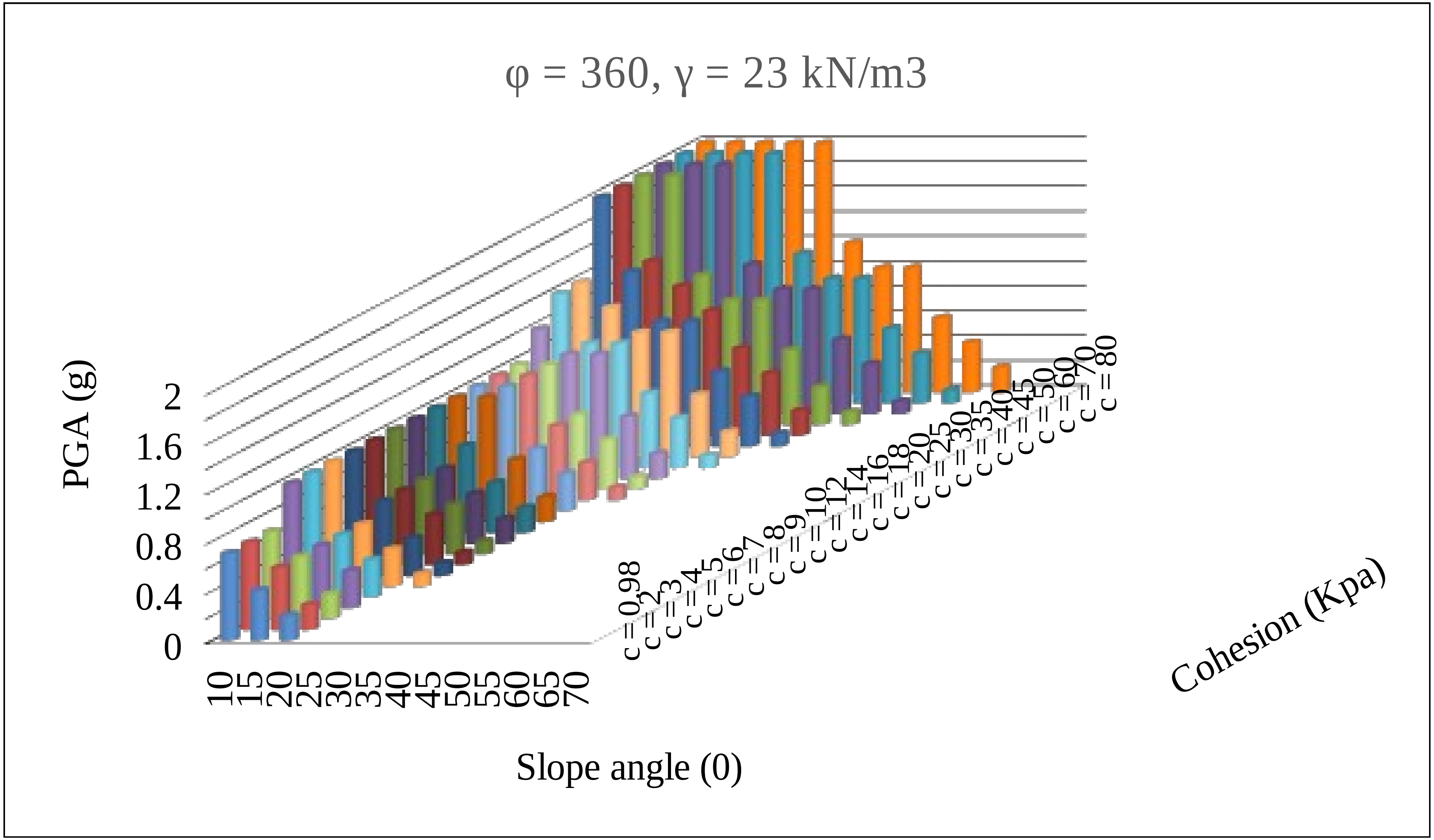

Figure 7.6 (j) φ=36^{0}

The design charts of DBE calculated for slope angles 10 to70^0, φ=18^0 - 36^0, c = 0 to 80 Kpa, at γ = 24 kN/m^3 are calculated and presented in Figures 7.7 (a to j).

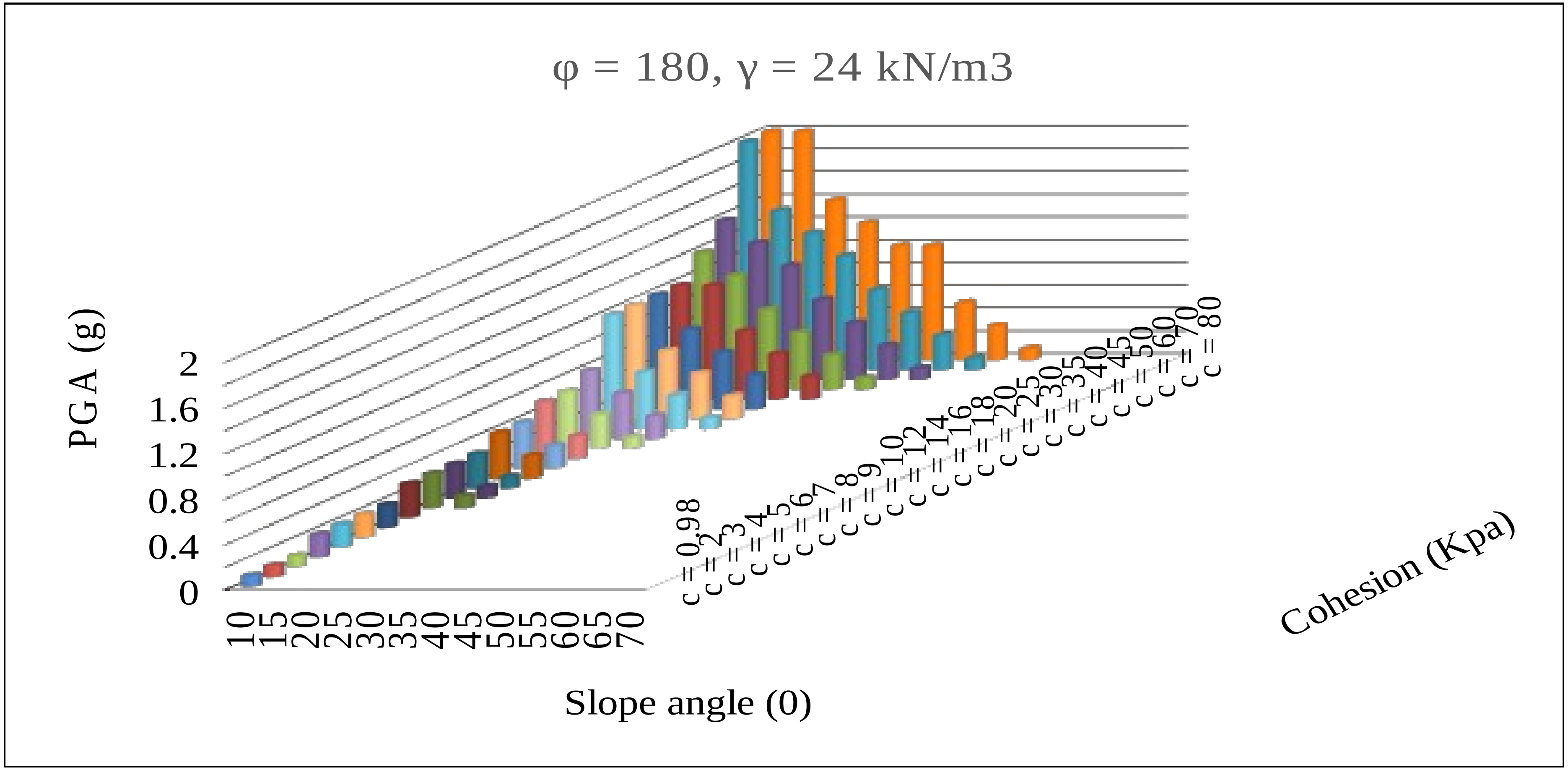

Figure 7.7 DBE design charts at various slope angle, Cohesion and γ = 24 kN/m^3 for (a) φ=18^0

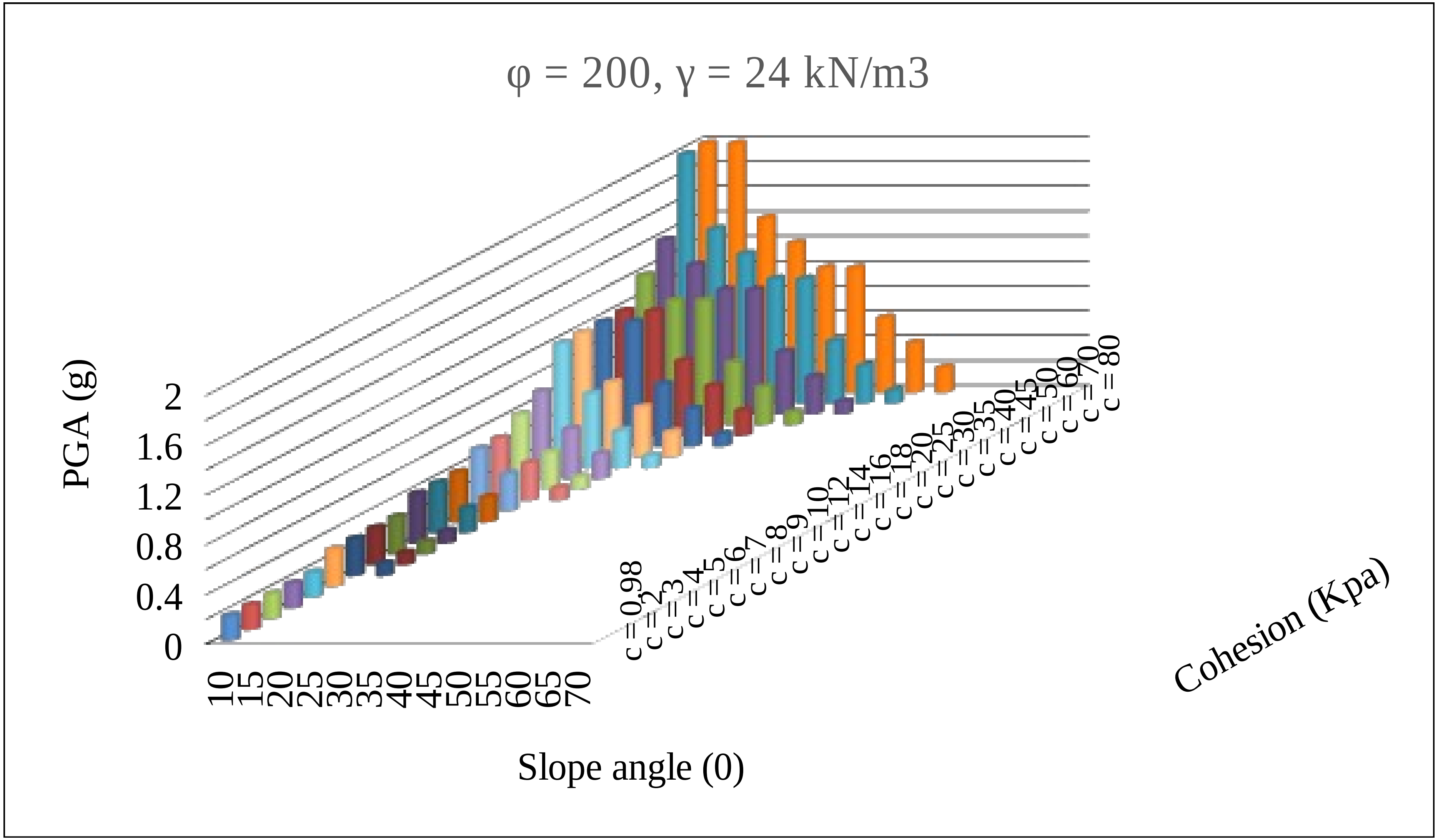

Figure 7.7 (b) φ=20^0

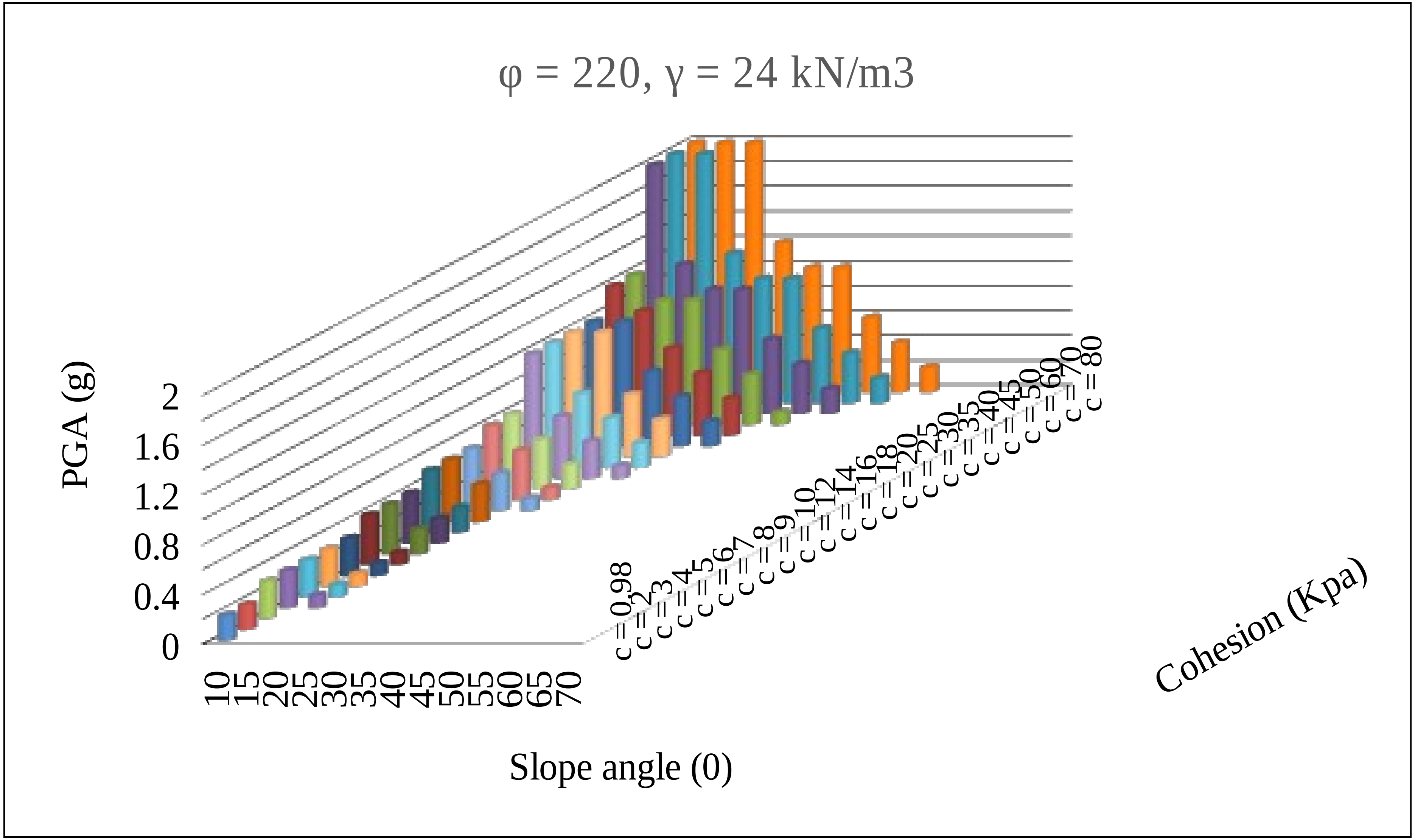

Figure 7.7 (c) $\varphi=22^0$

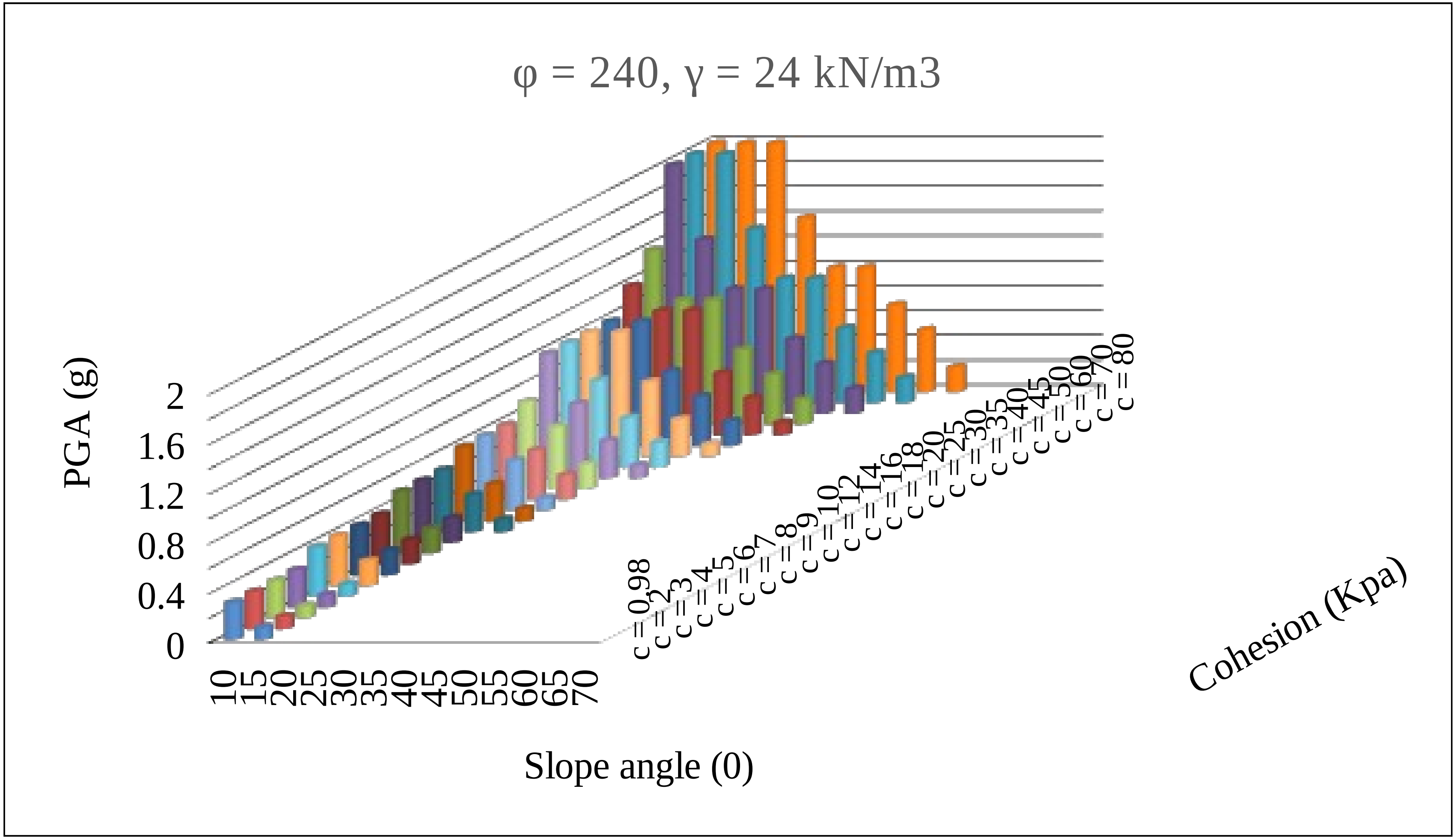

Figure 7.7 (d) $\varphi=24^0$

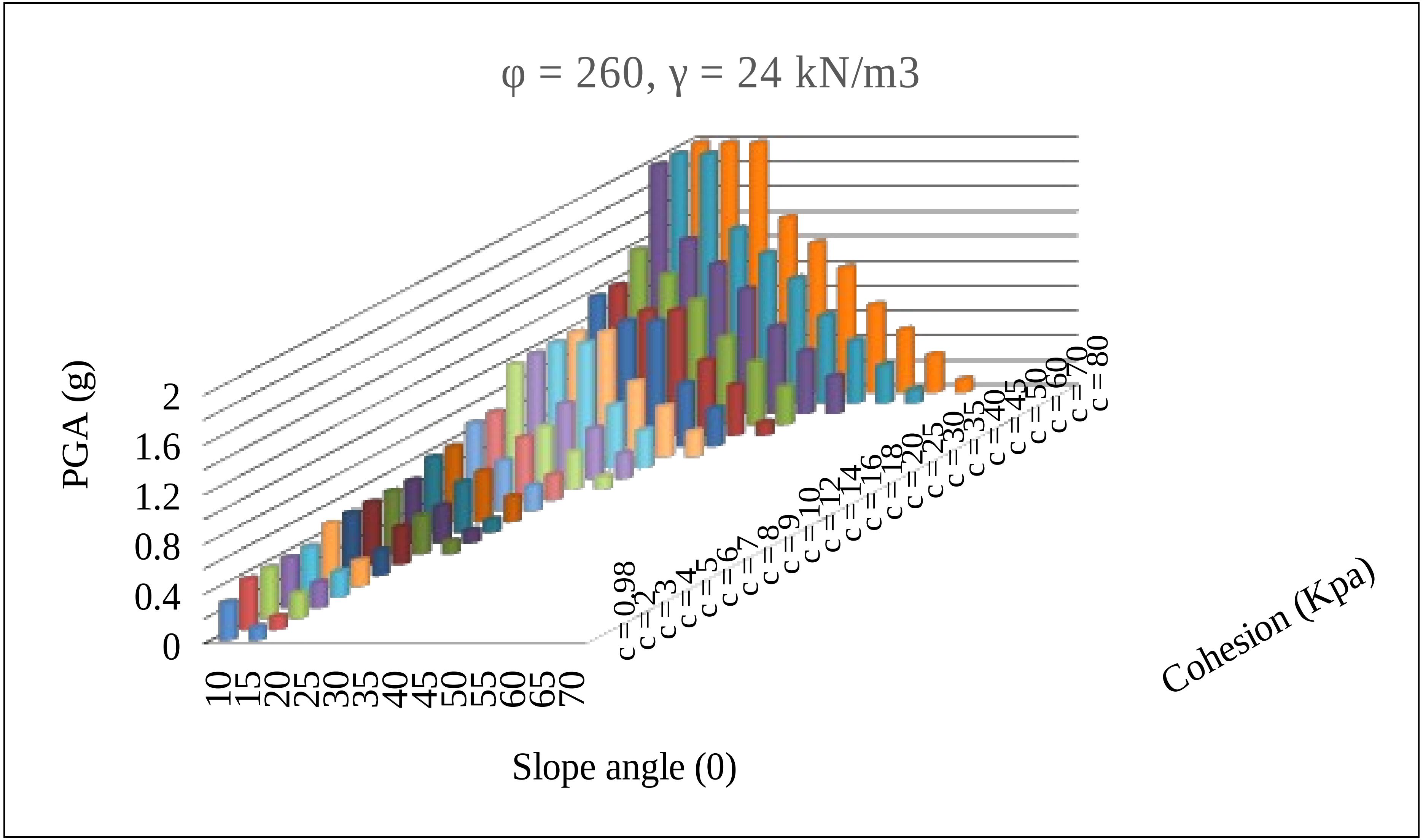

Figure 7.7 (e) φ=26^0

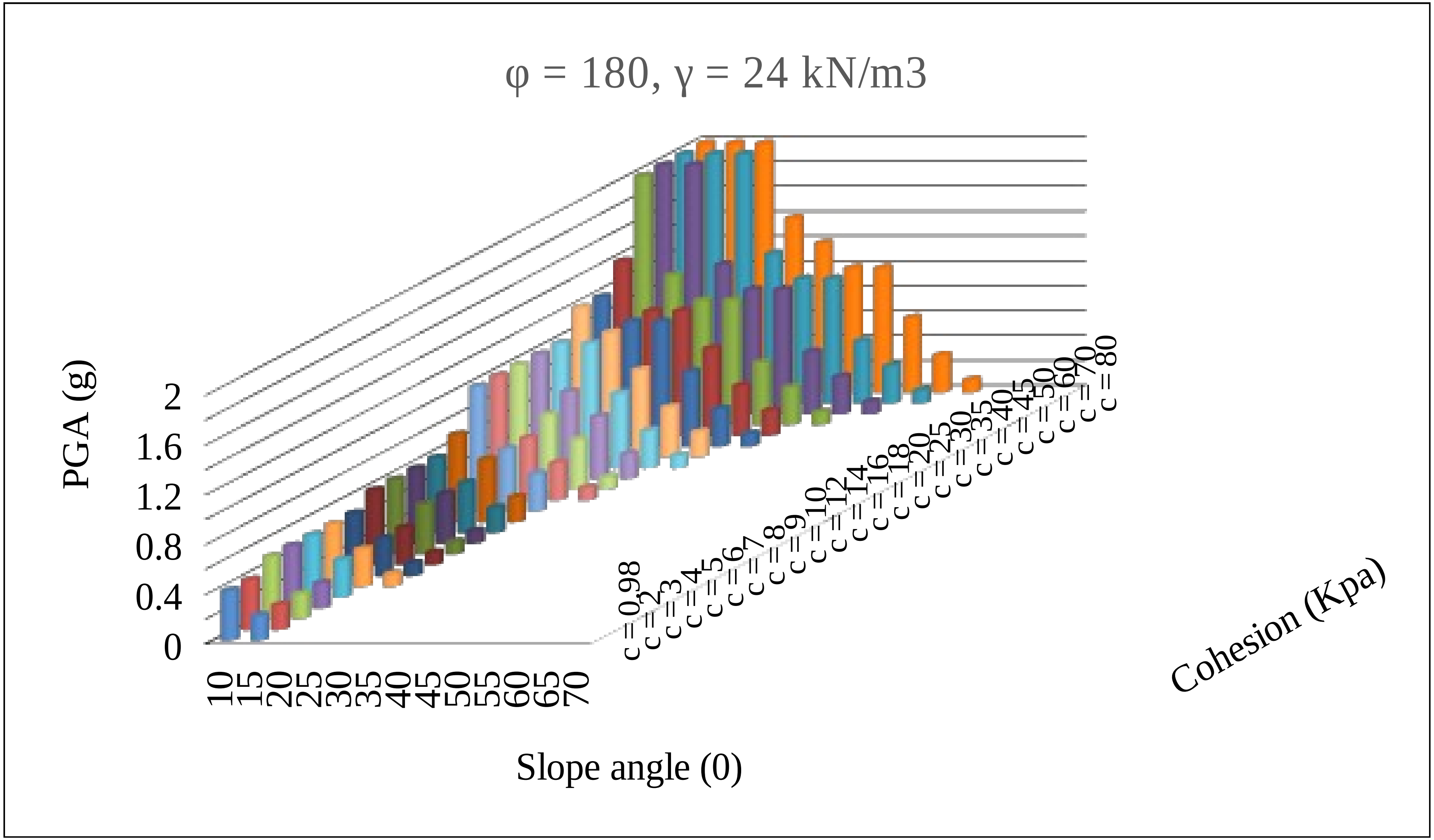

Figure 7.7 (f) φ=28^0

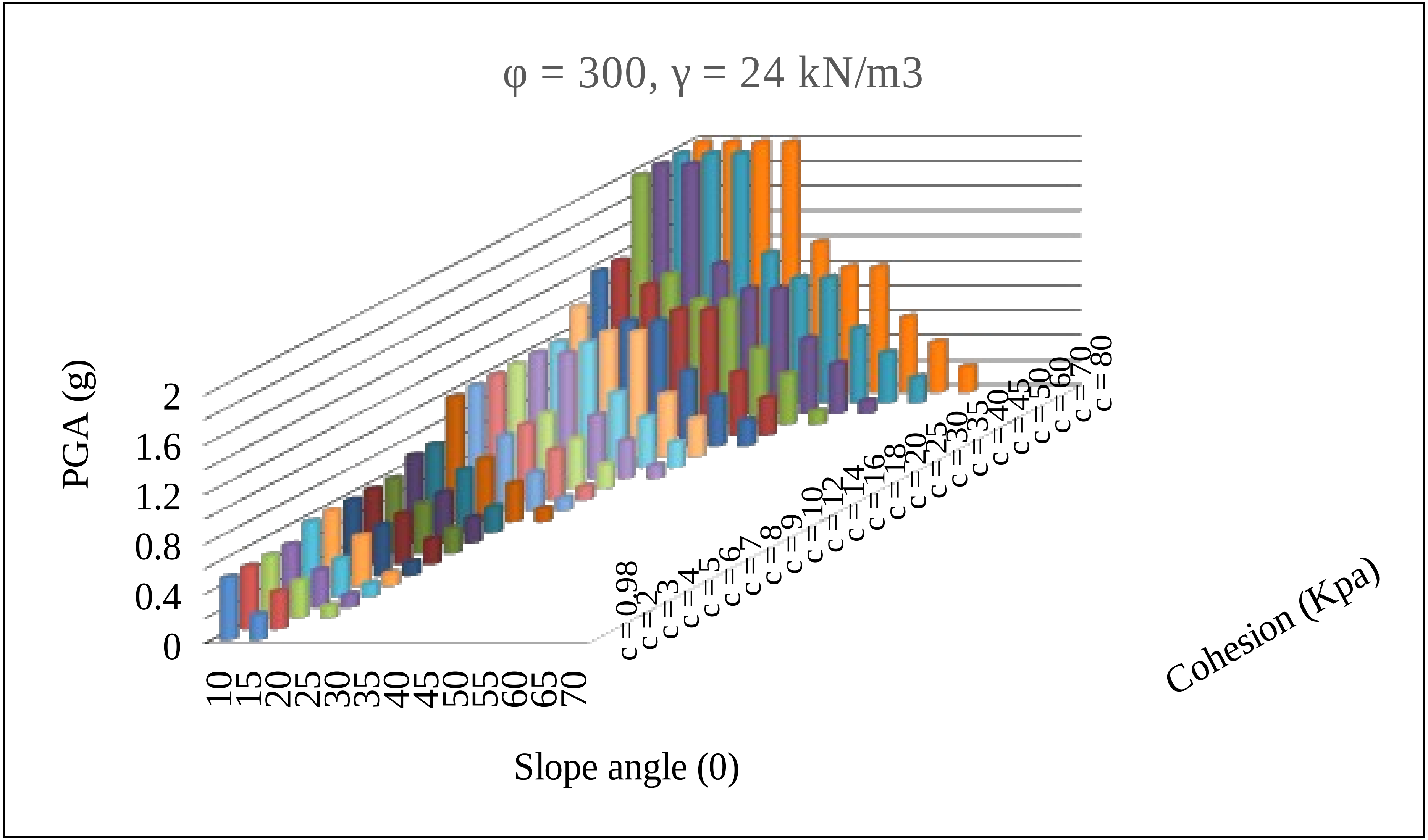

Figure 7.7 (g) $\varphi=30^0$

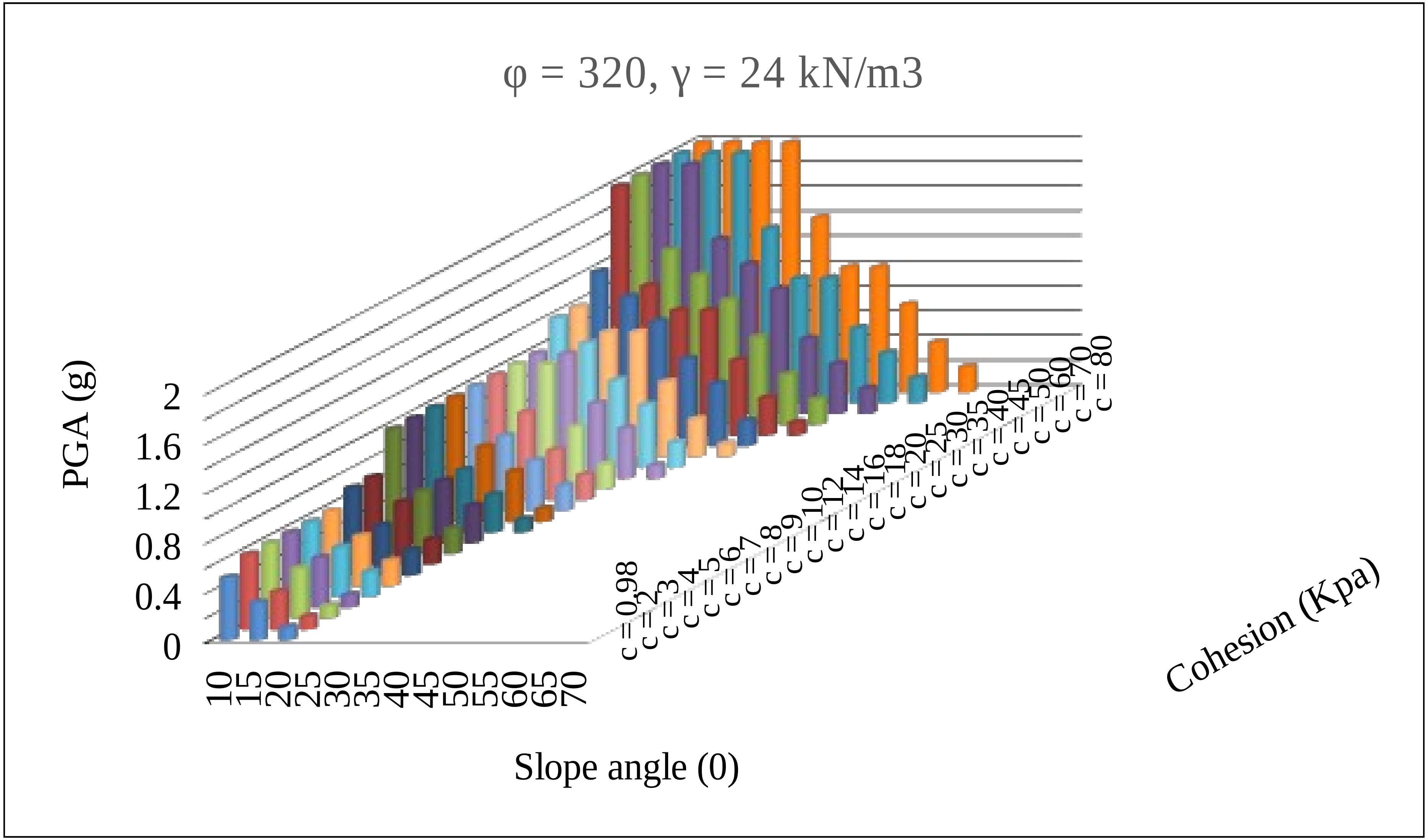

Figure 7.7 (h) $\varphi=32^0$

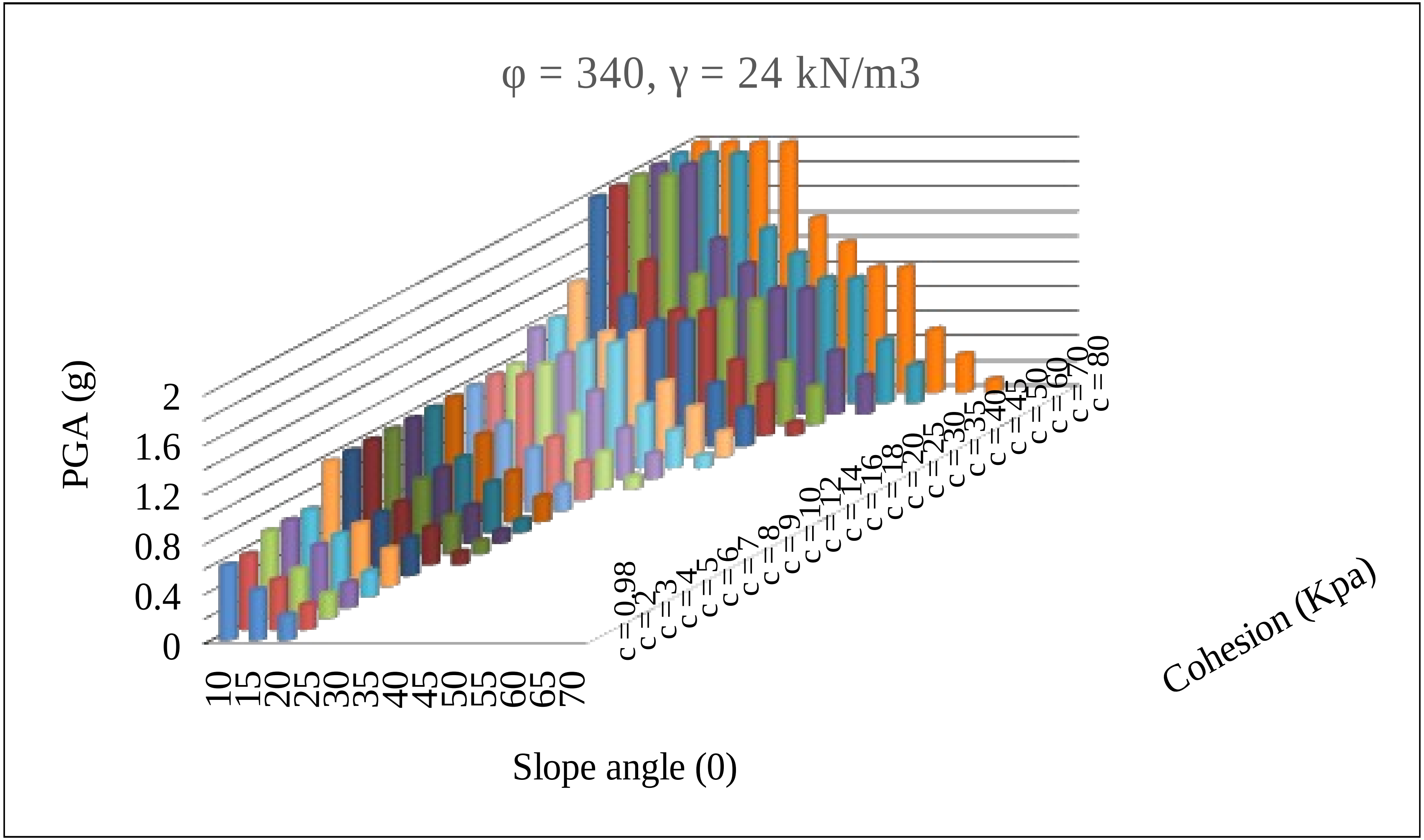

Figure 7.7 (i) $\varphi=34^0$

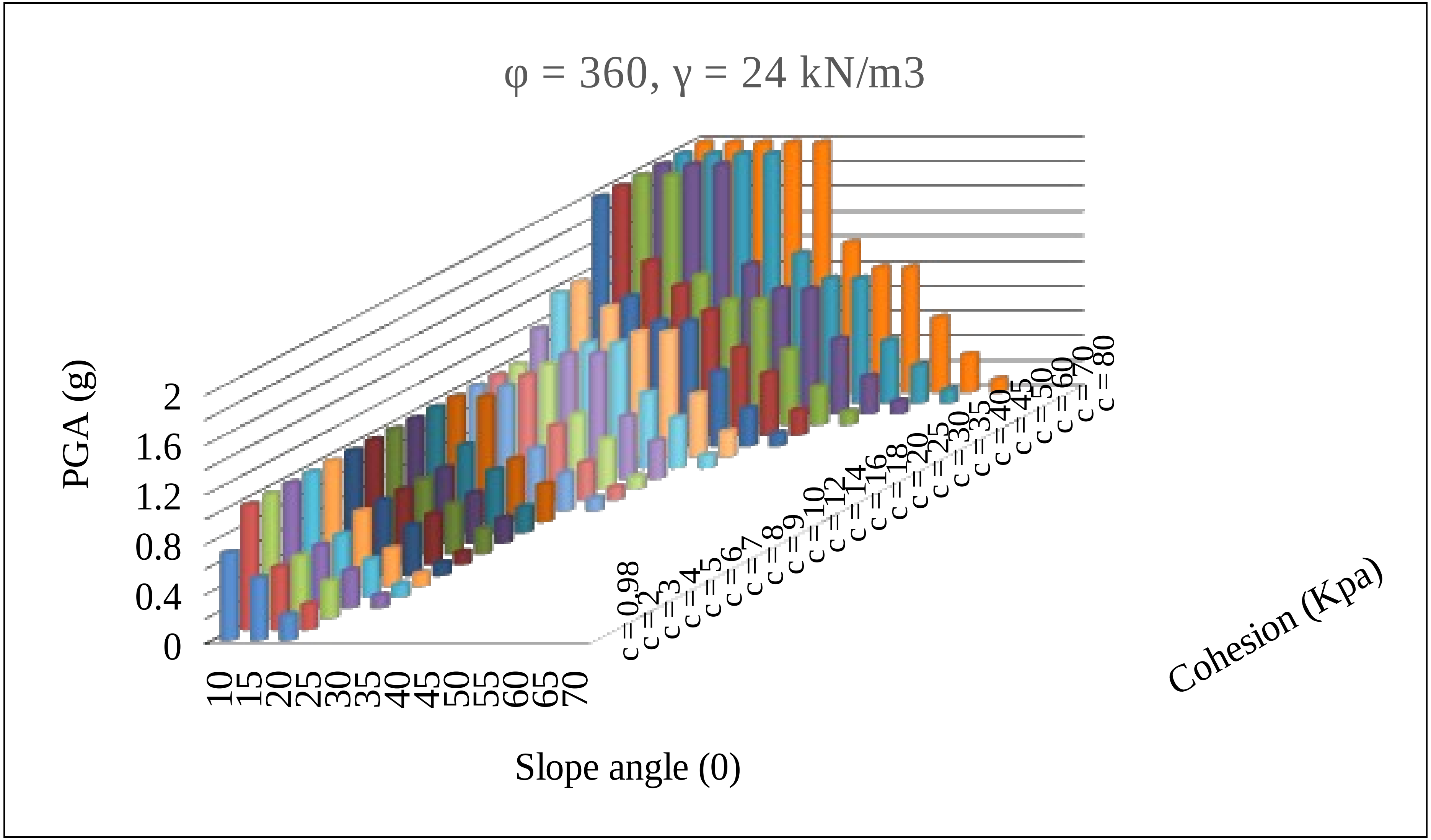

Figure 7.7 (j) φ=36^0

The design charts of DBE calculated for slope angles 10 to70^{0}, φ=18^{0} - 36^{0}, c = 0 to 80 Kpa, at γ = 25 kN/m^{3} are calculated and presented in Figures 7.8 (a to j).

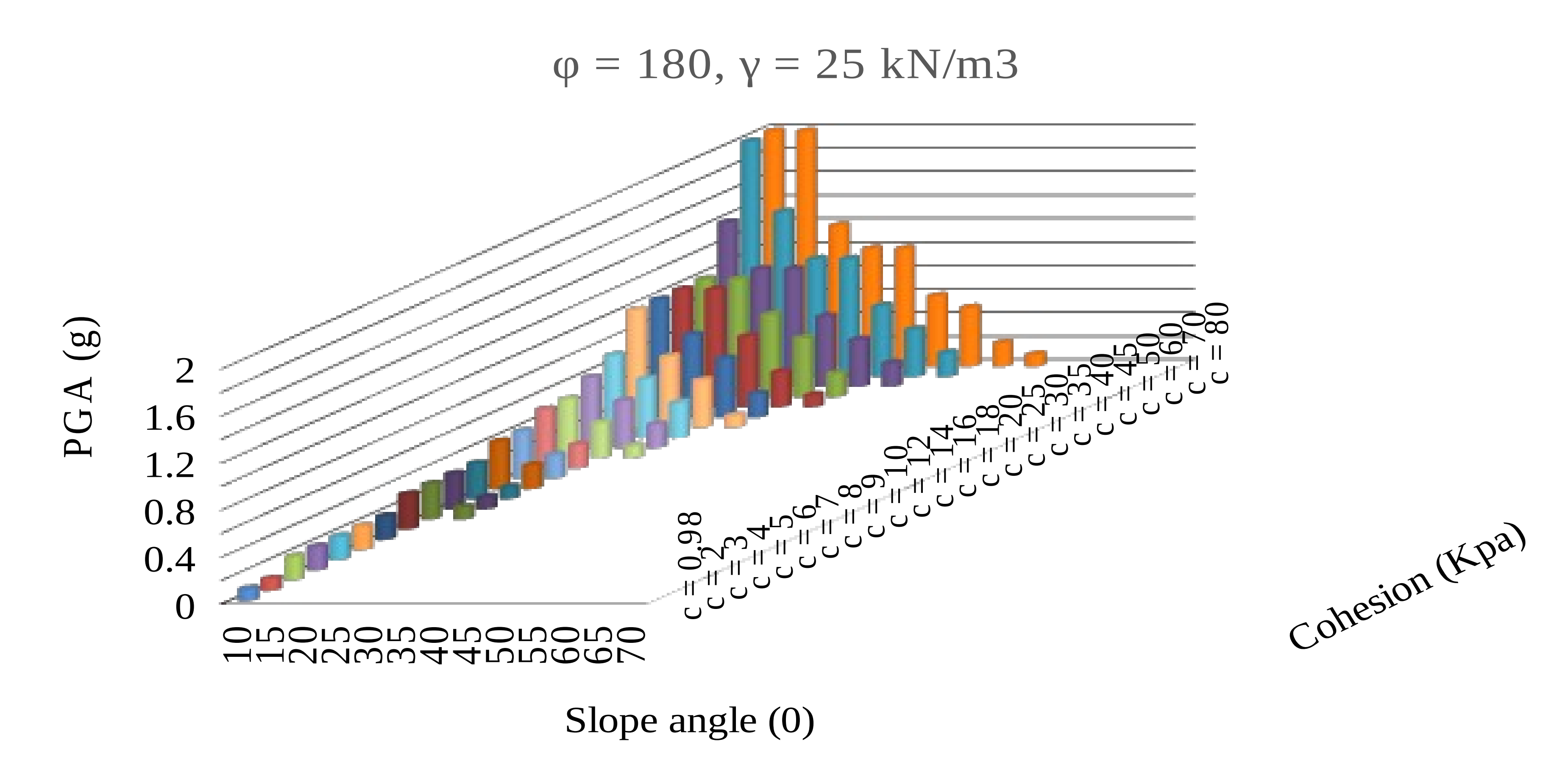

Figure 7.8 DBE design charts at various slope angle, Cohesion and γ = 25 kN/m^{3} for (a) φ=18^{0}

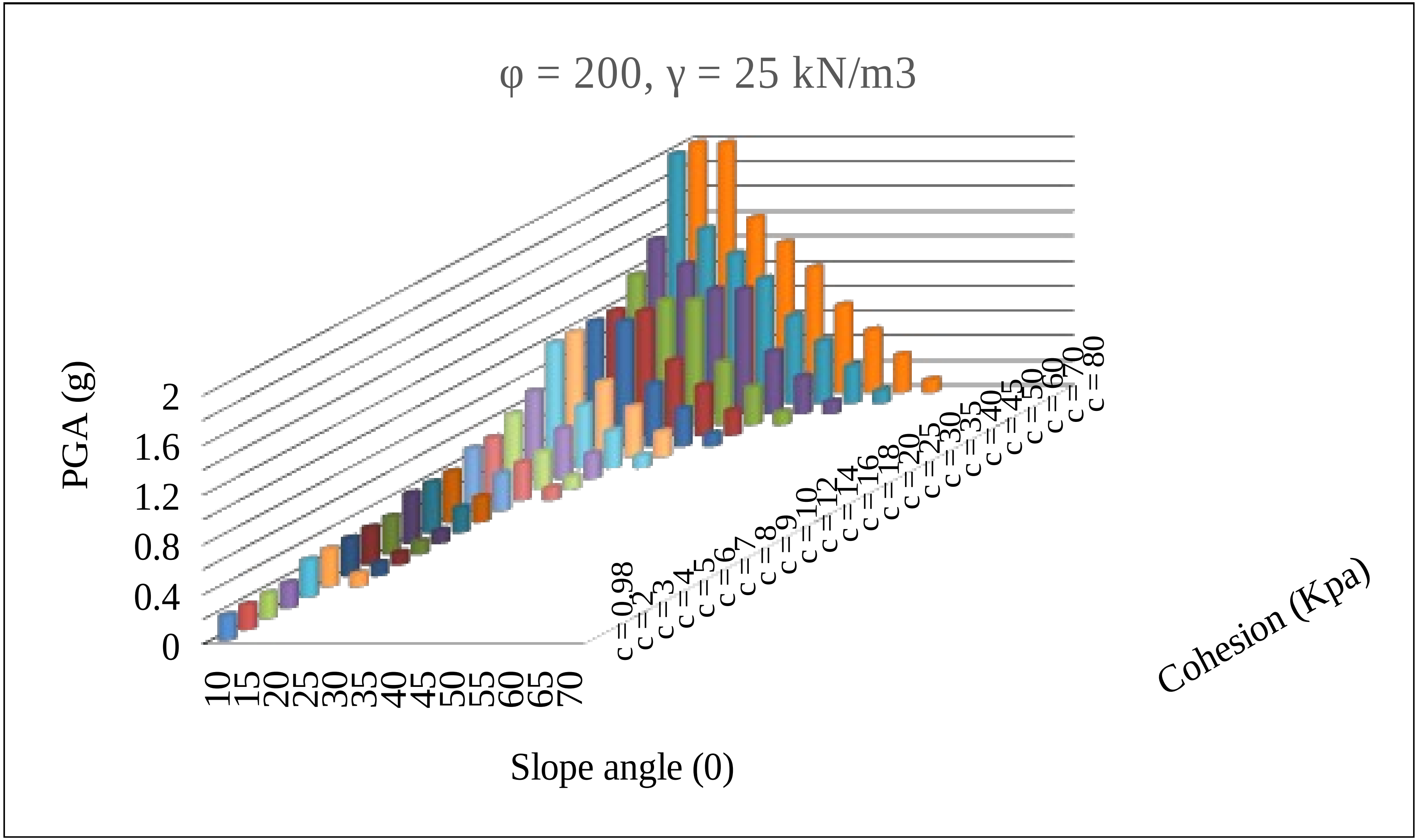

Figure 7.8 (b) φ=20^0

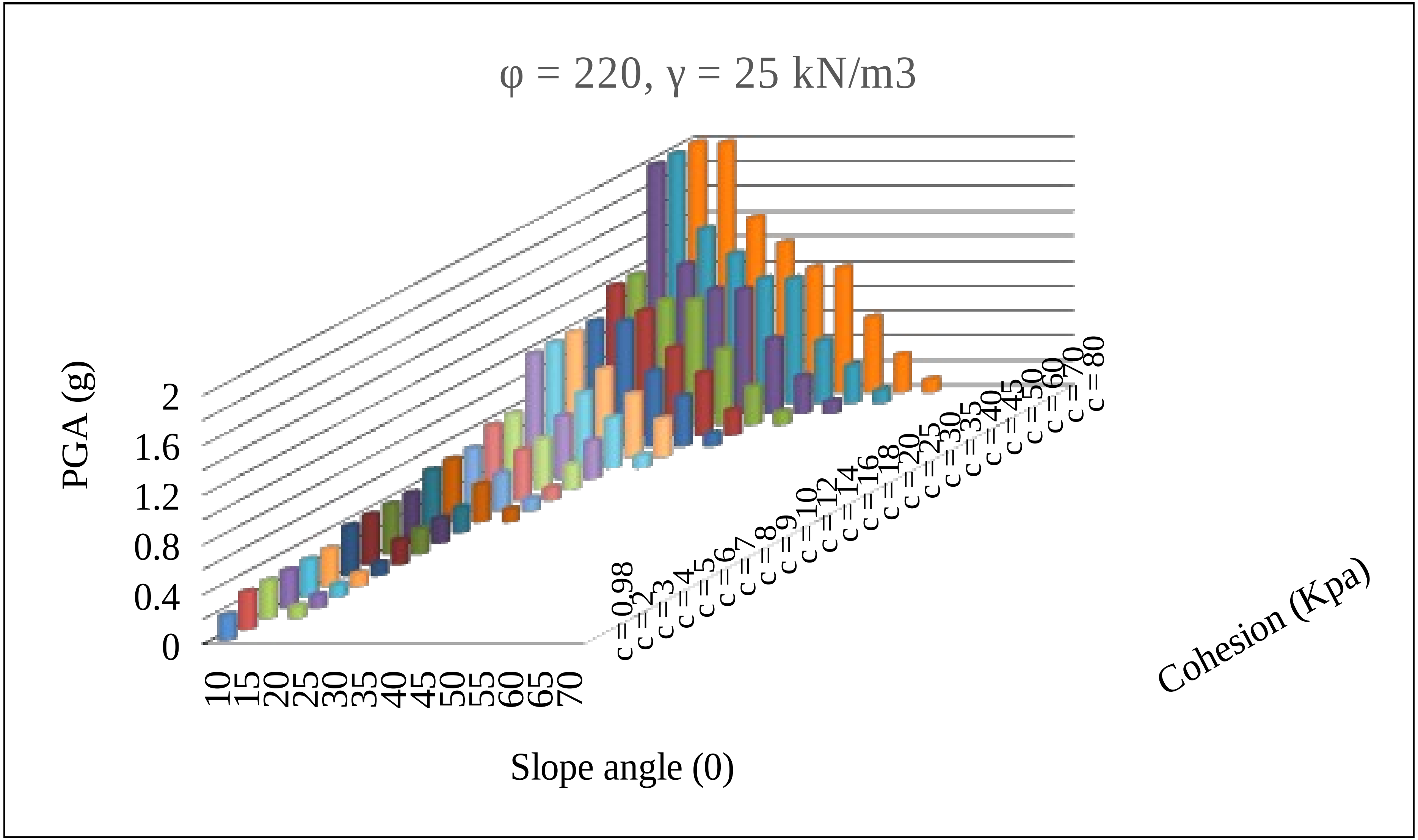

Figure 7.8 (c) φ=22^0

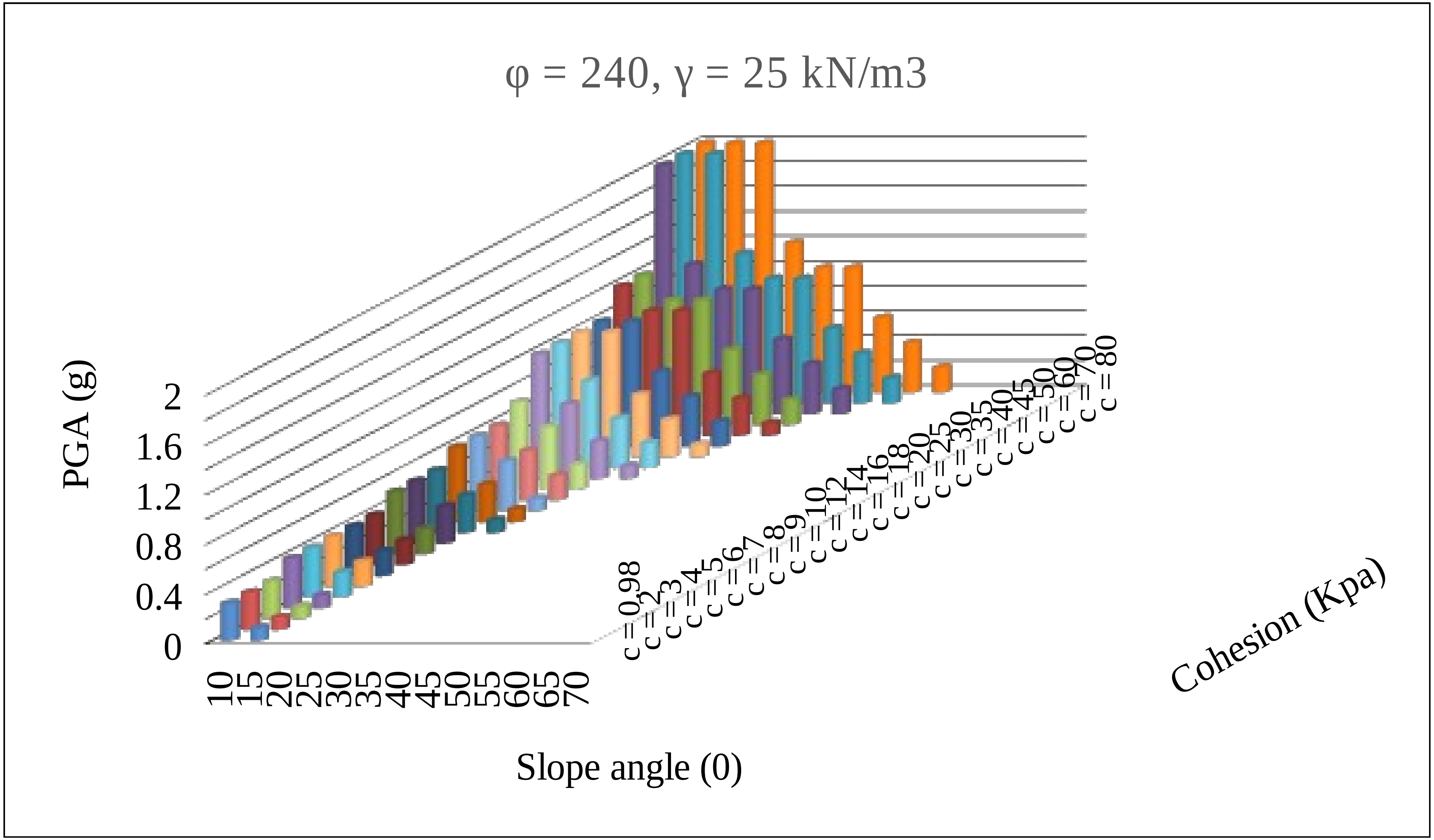

Figure 7.8 (d) φ=24^{0}

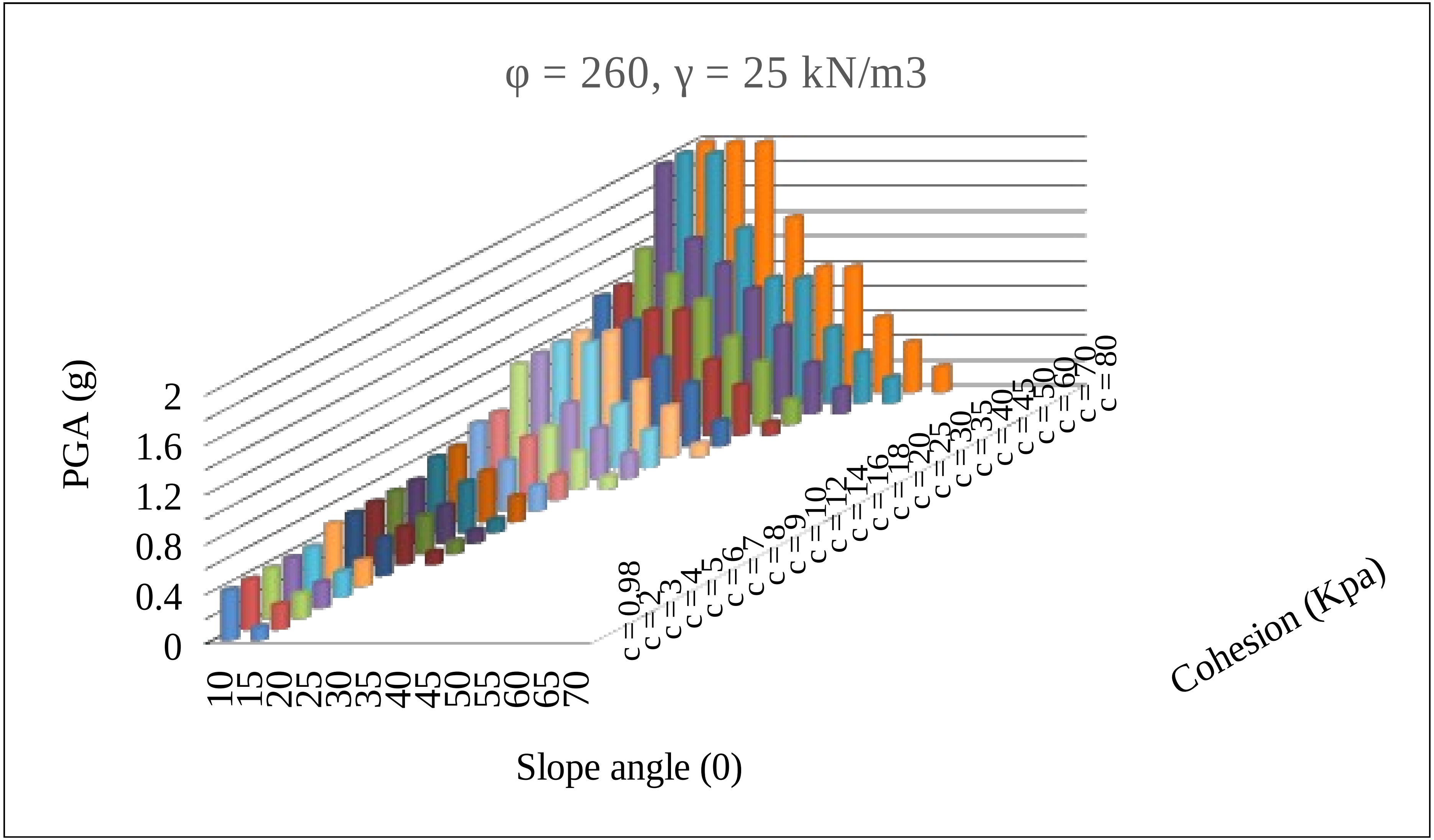

Figure 7.8 (e) φ=26^0

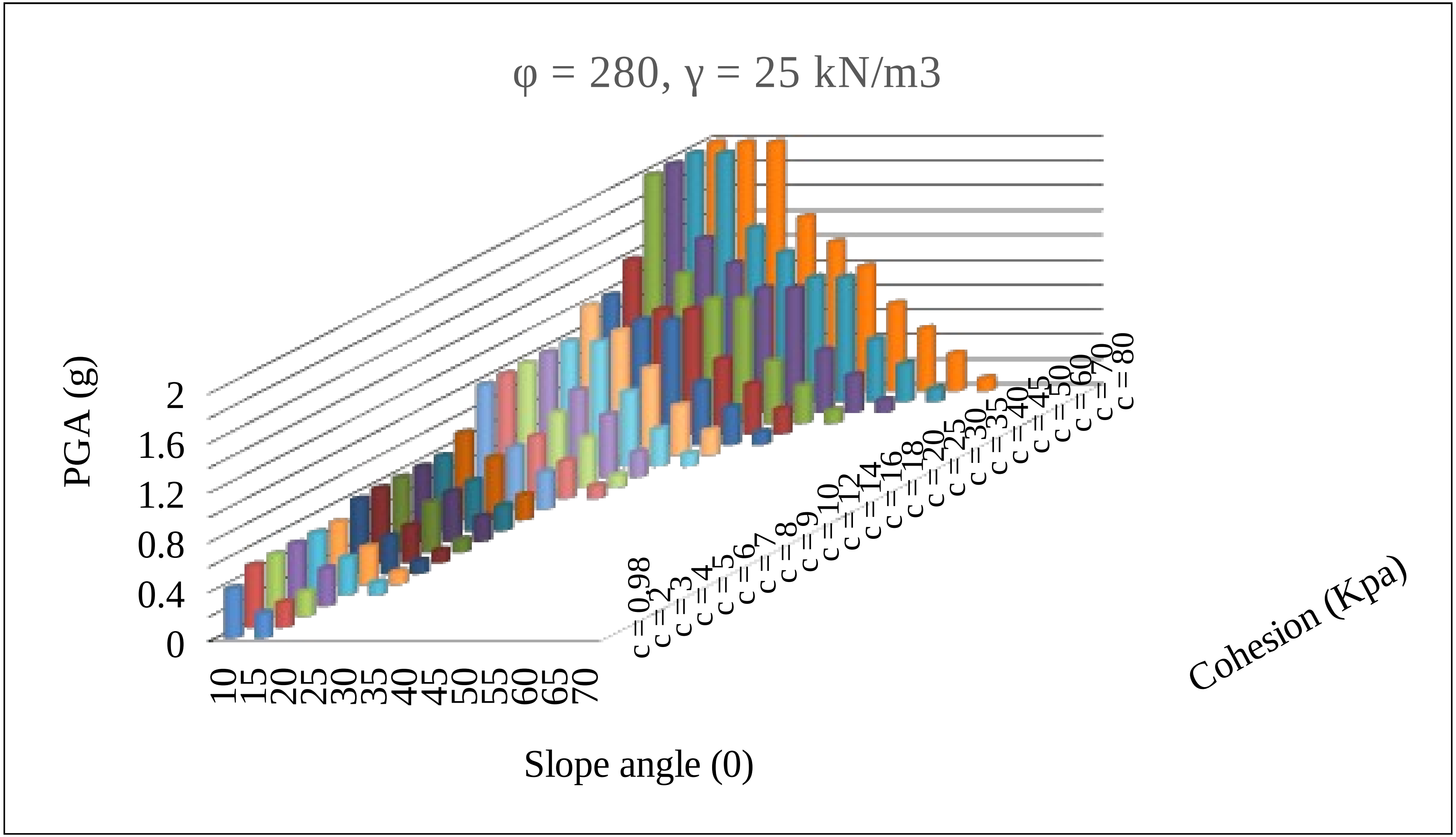

Figure 7.8 (f) φ=28^0

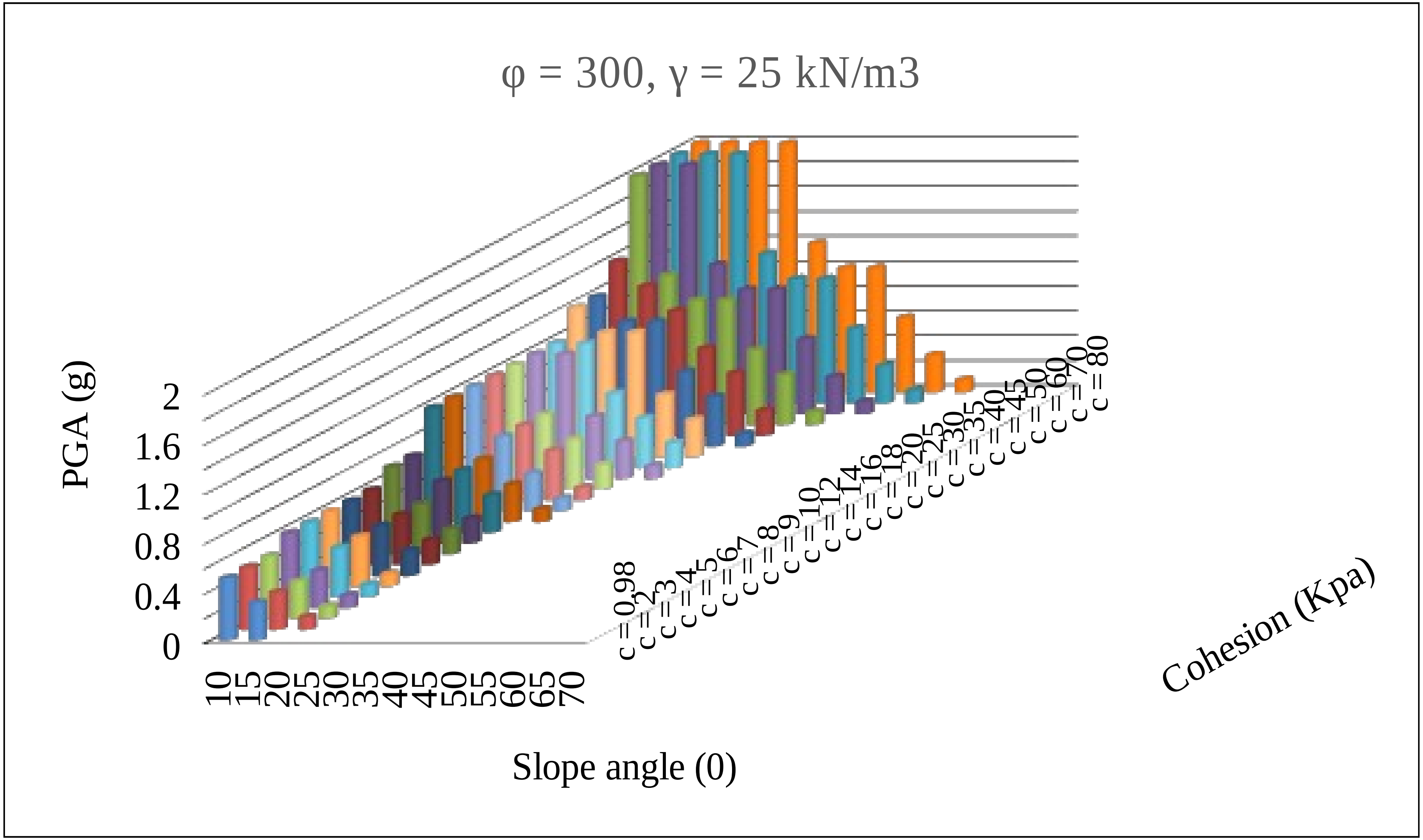

Figure 7.8 (g) $\varphi=30^0$

.

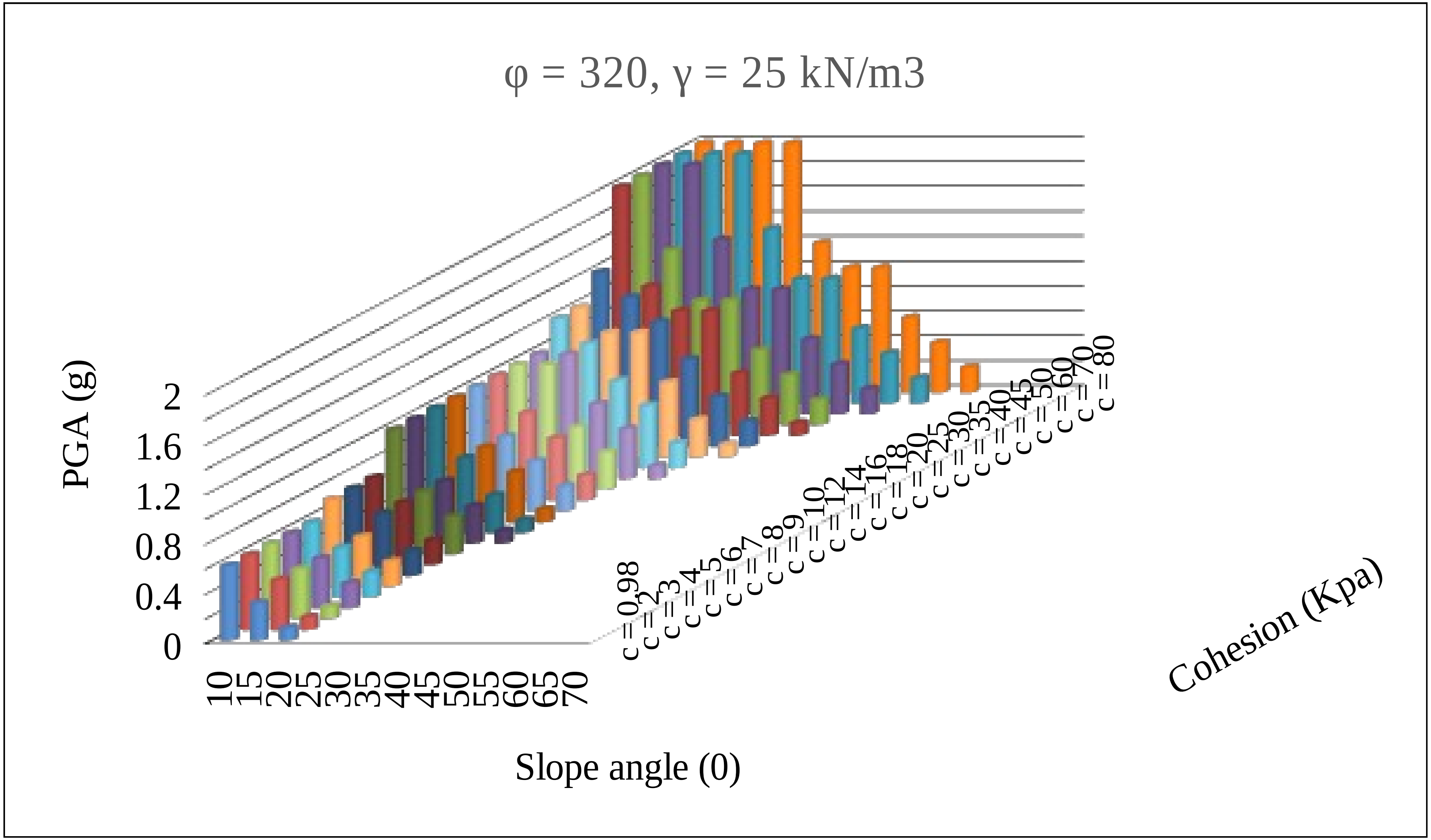

Figure 7.8 (h) φ=32^0

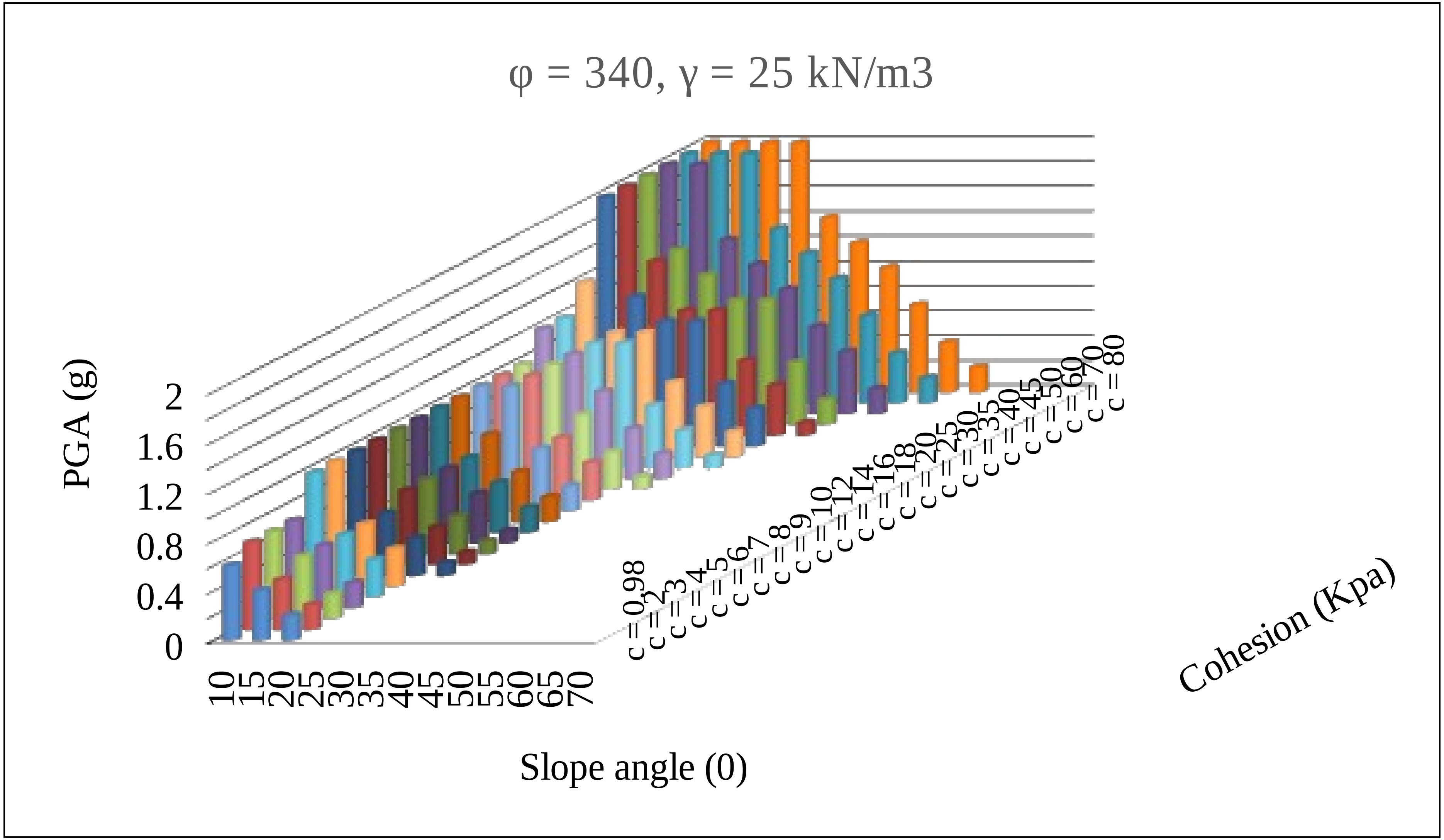

Figure 7.8 (i) φ=34^{0}

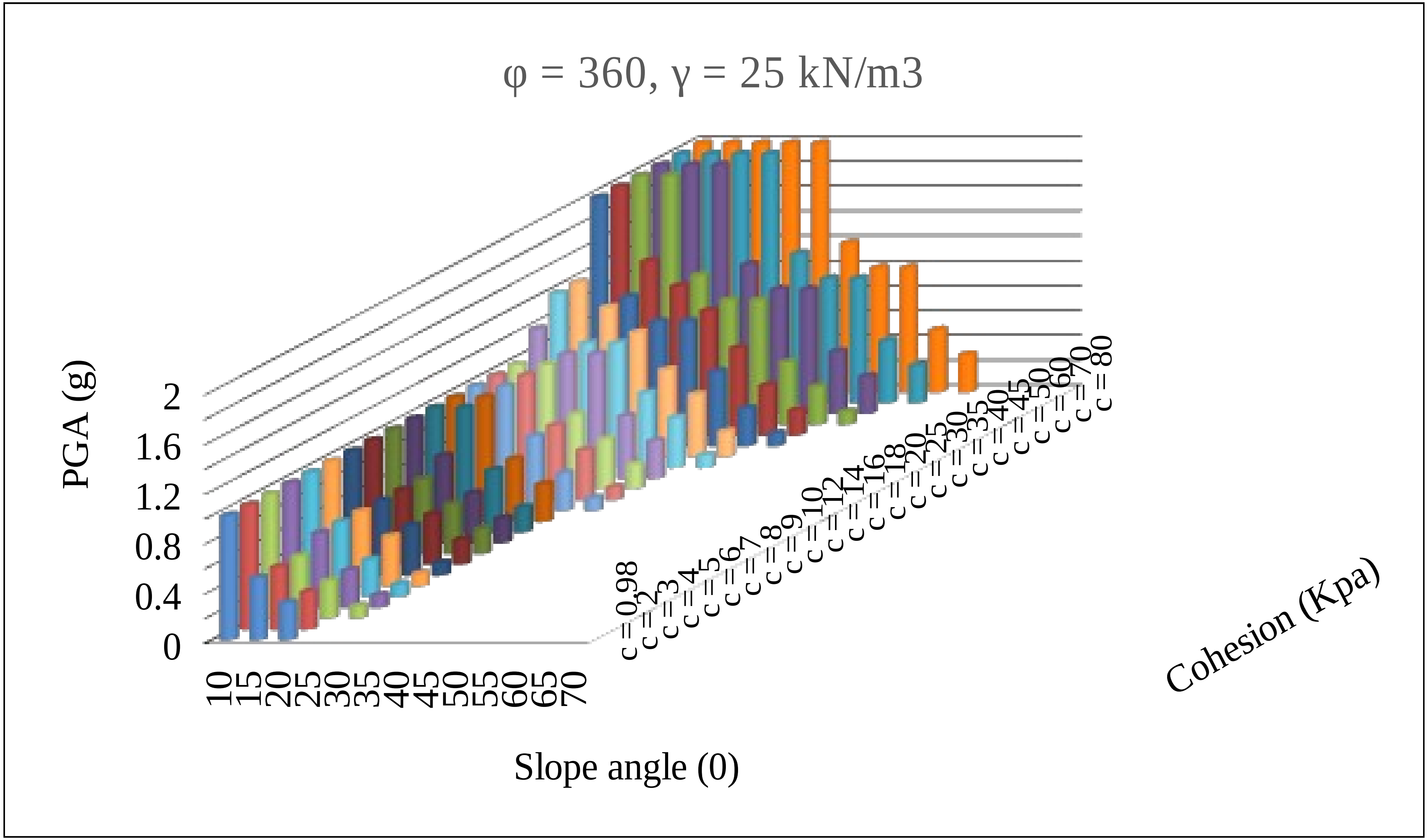

Figure 7.8 (j) φ=36^0

The design charts of DBE calculated for slope angles 10 to70^0, φ=18^0 - 36^0, c = 0 to 80 Kpa, at γ = 27 kN/m^3 are calculated and presented in Figures 7.9 (a to j).

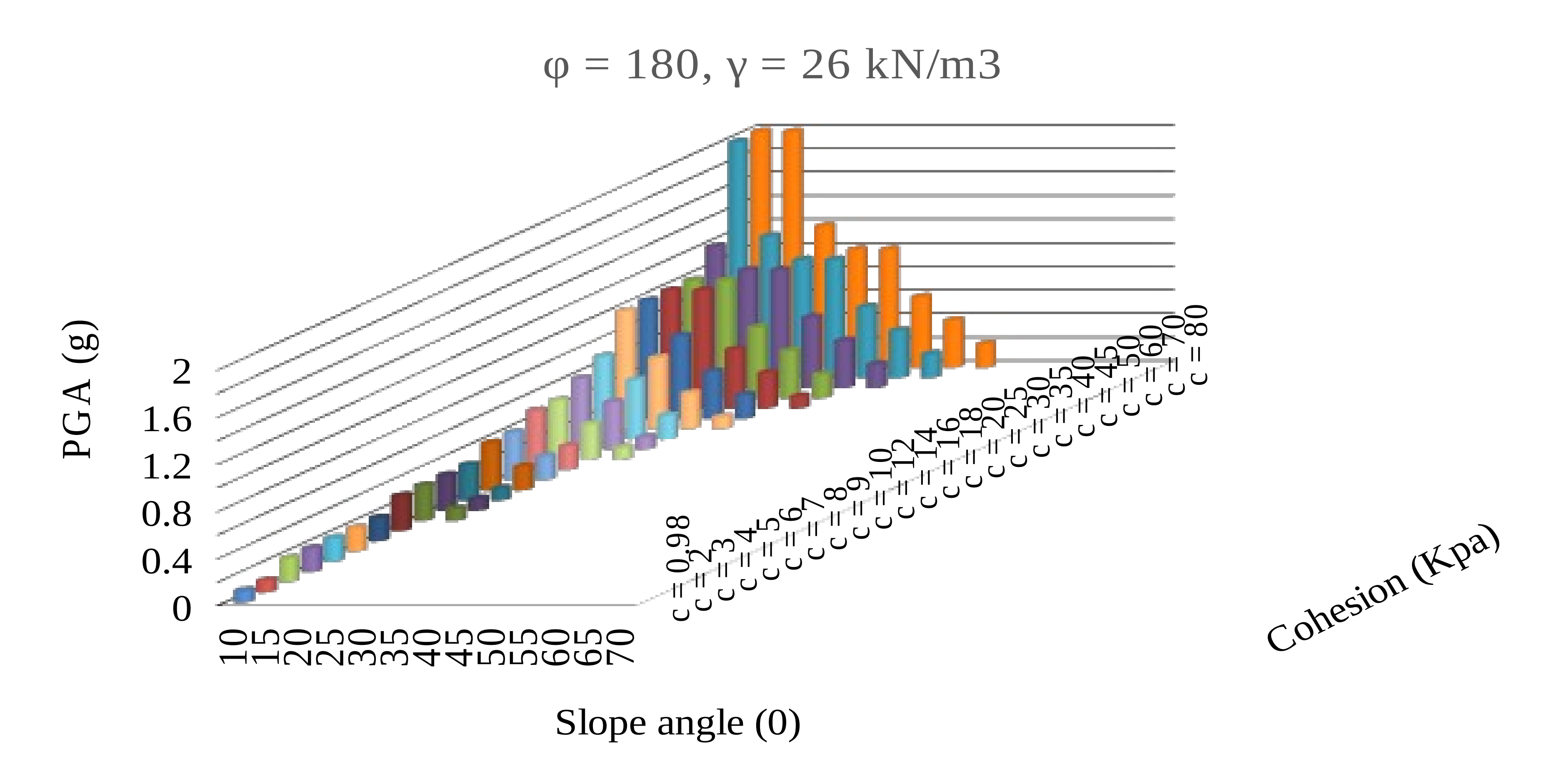

Figure 7.9 DBE design charts at various slope angle, Cohesion and γ = 26 kN/m^3 for (a) φ=18^0

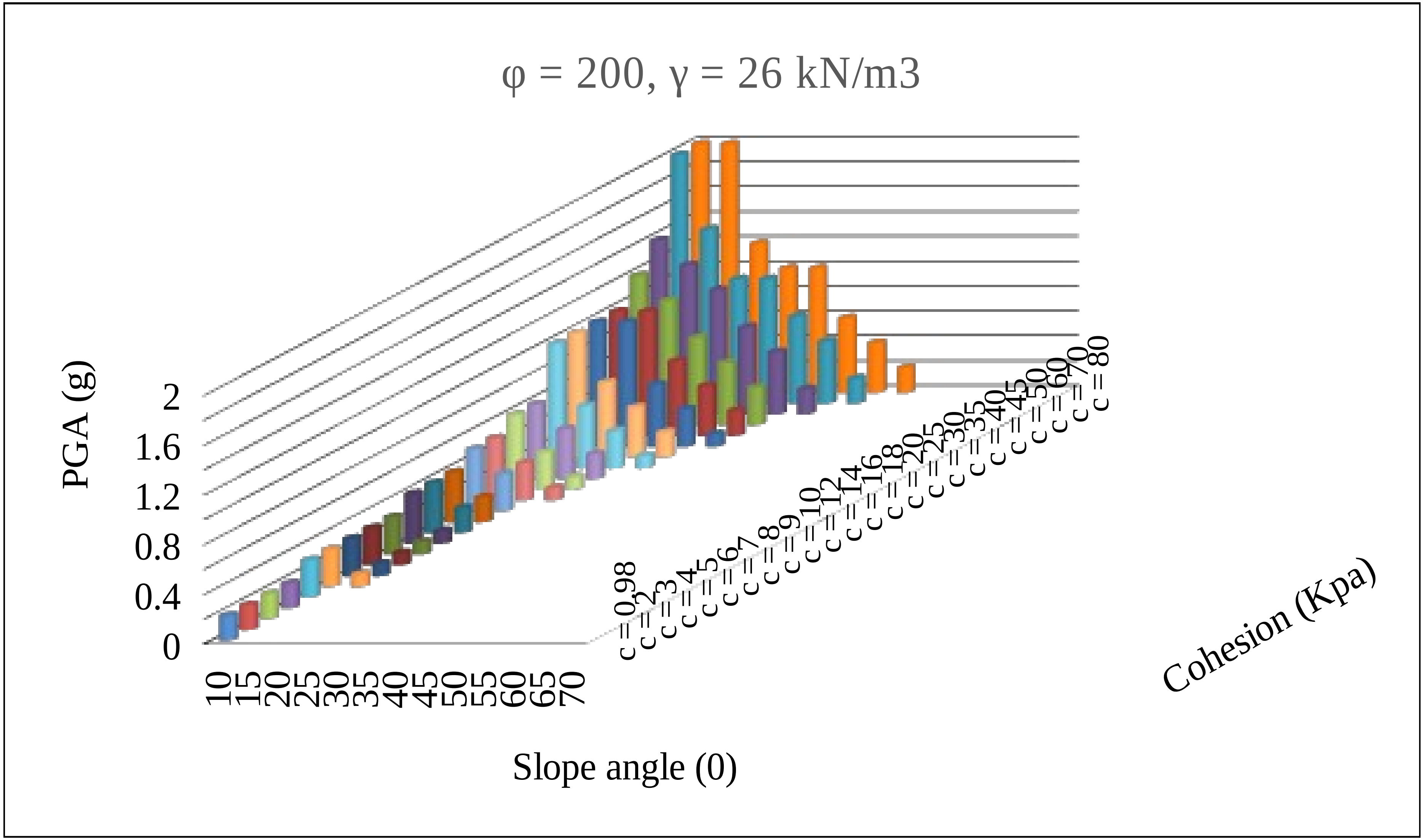

Figure 7.9 (b) φ=20^0

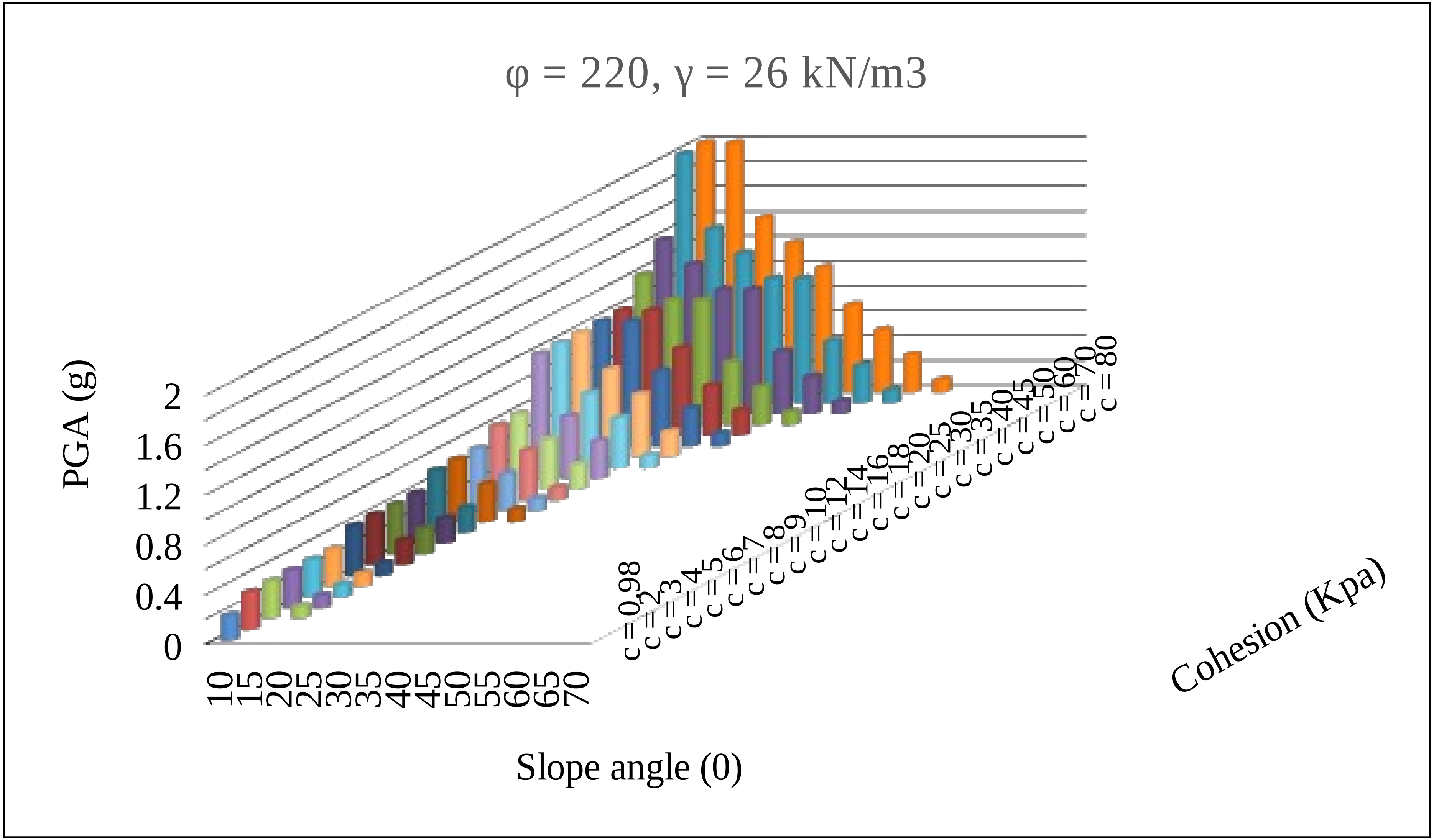

Figure 7.9 (c) φ=22^0

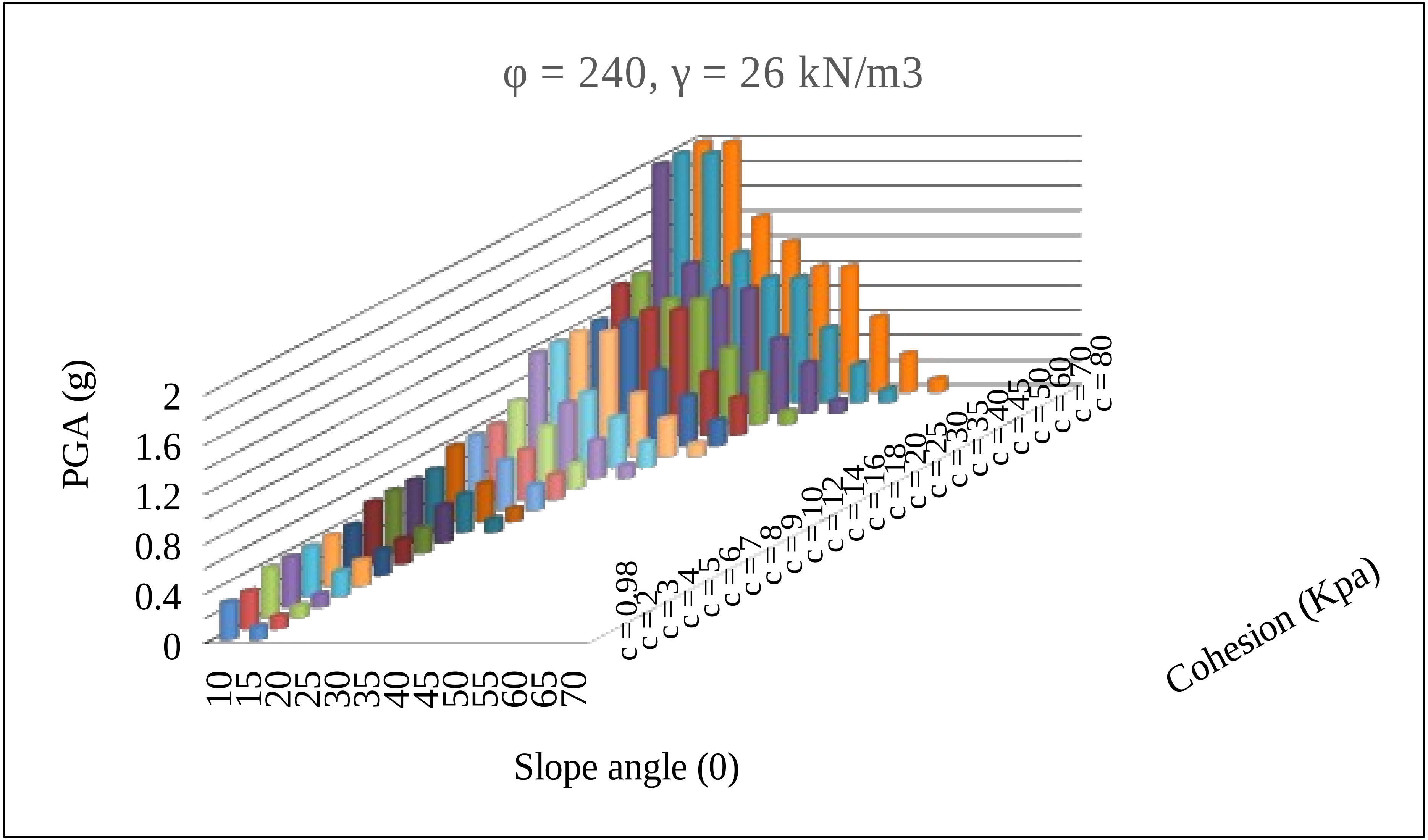

Figure 7.9 (d) φ=24^0

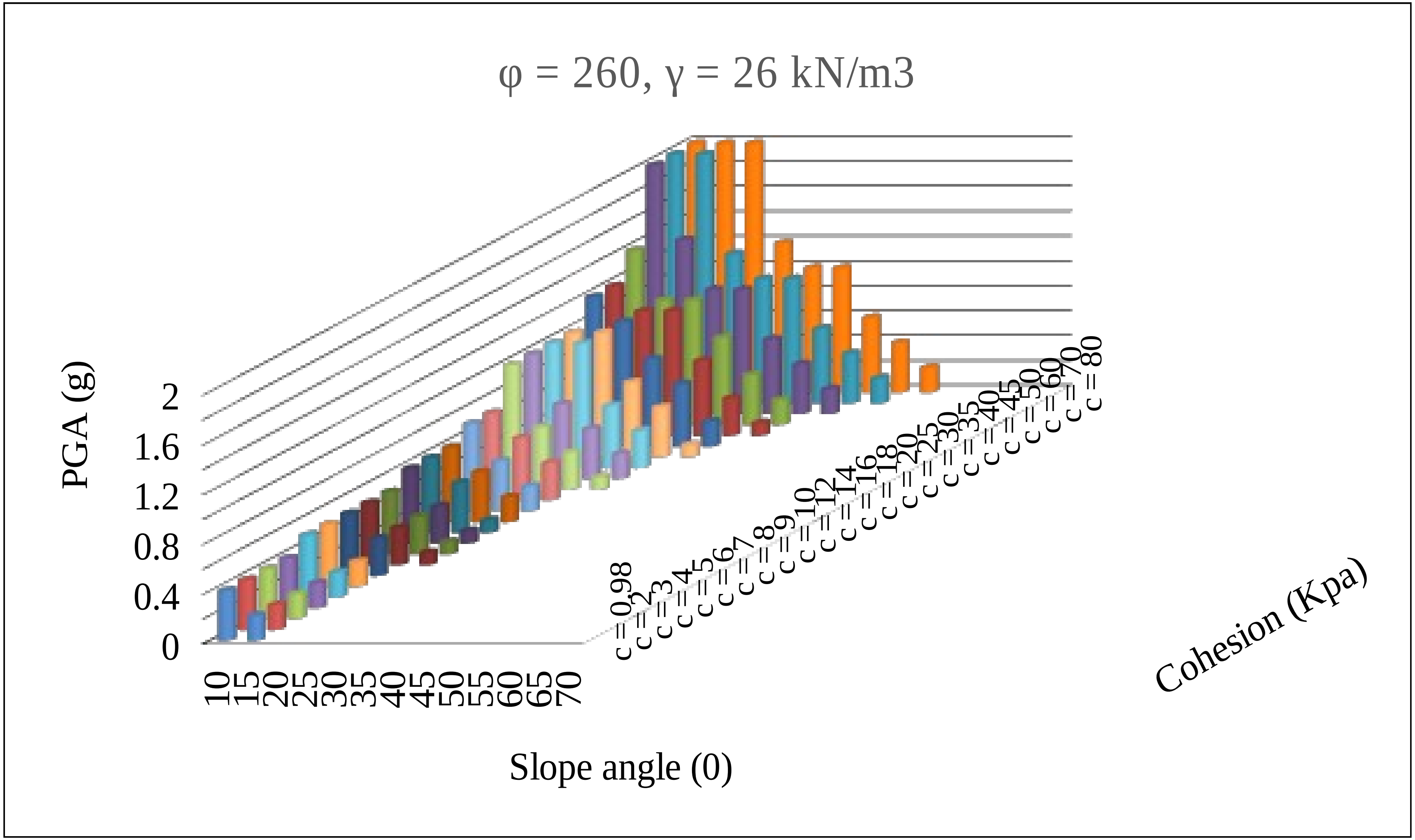

Figure 7.9 (e) φ=26^0

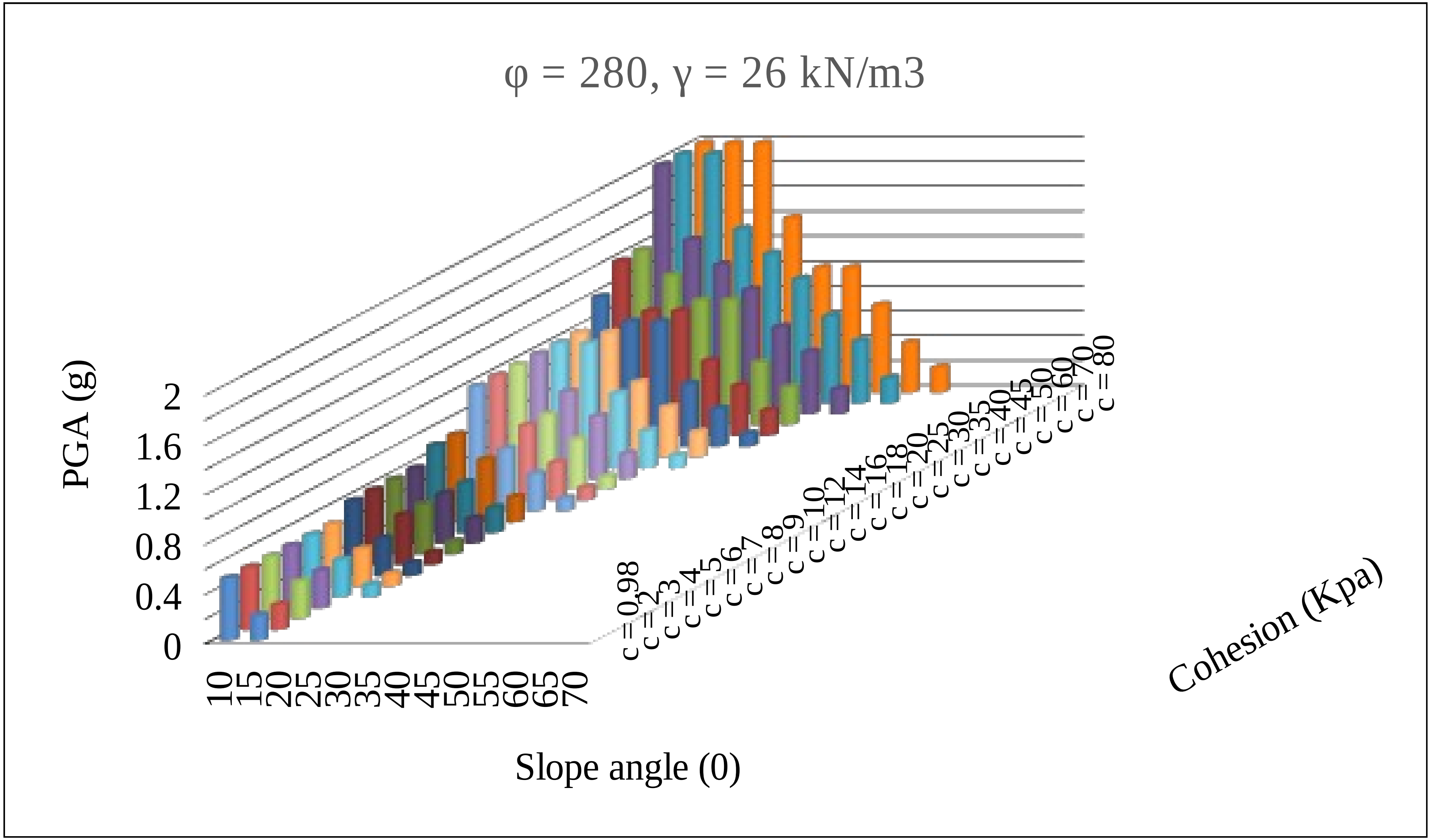

Figure 7.9 (f) φ=28^0

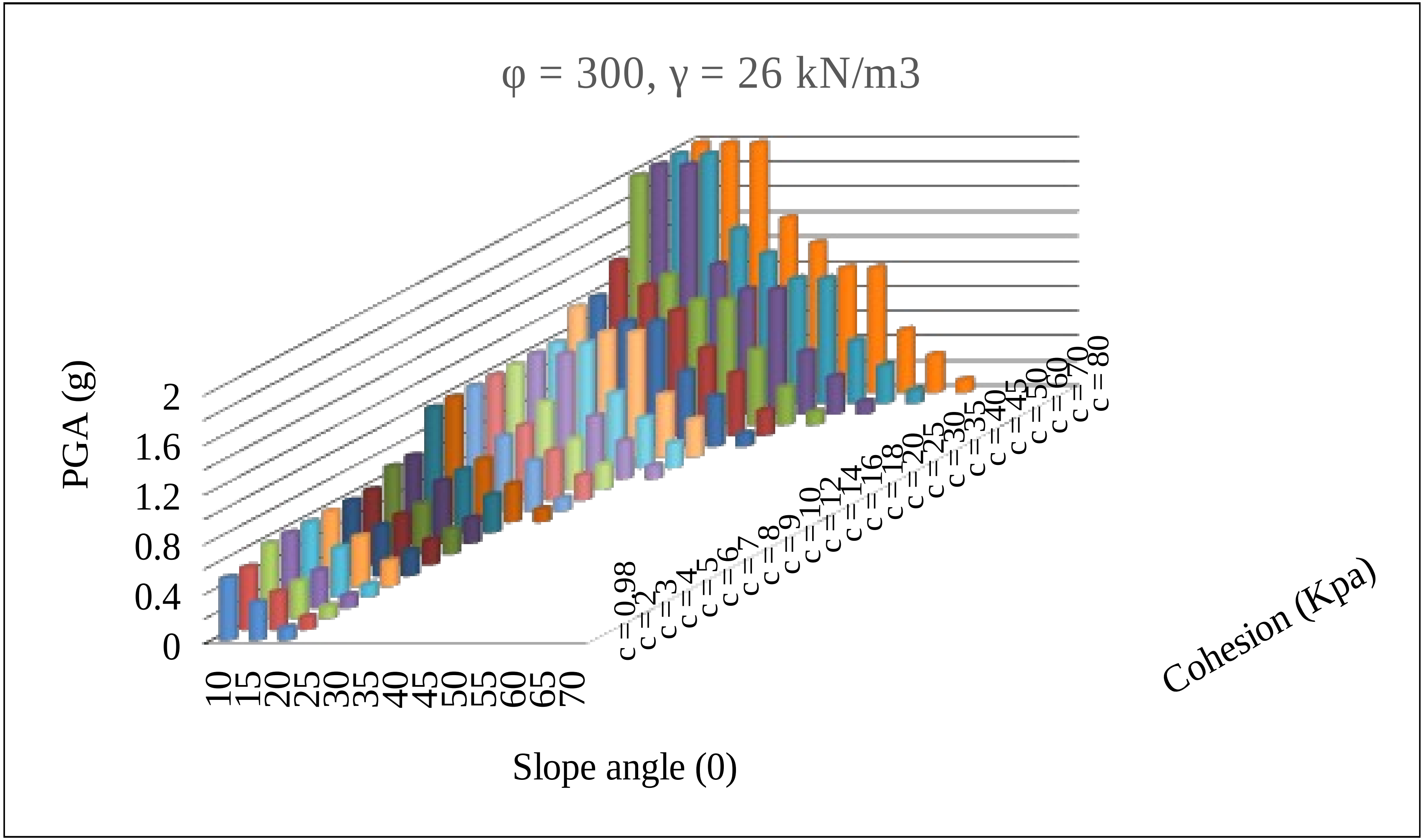

Figure 7.9 (g) φ=30^0

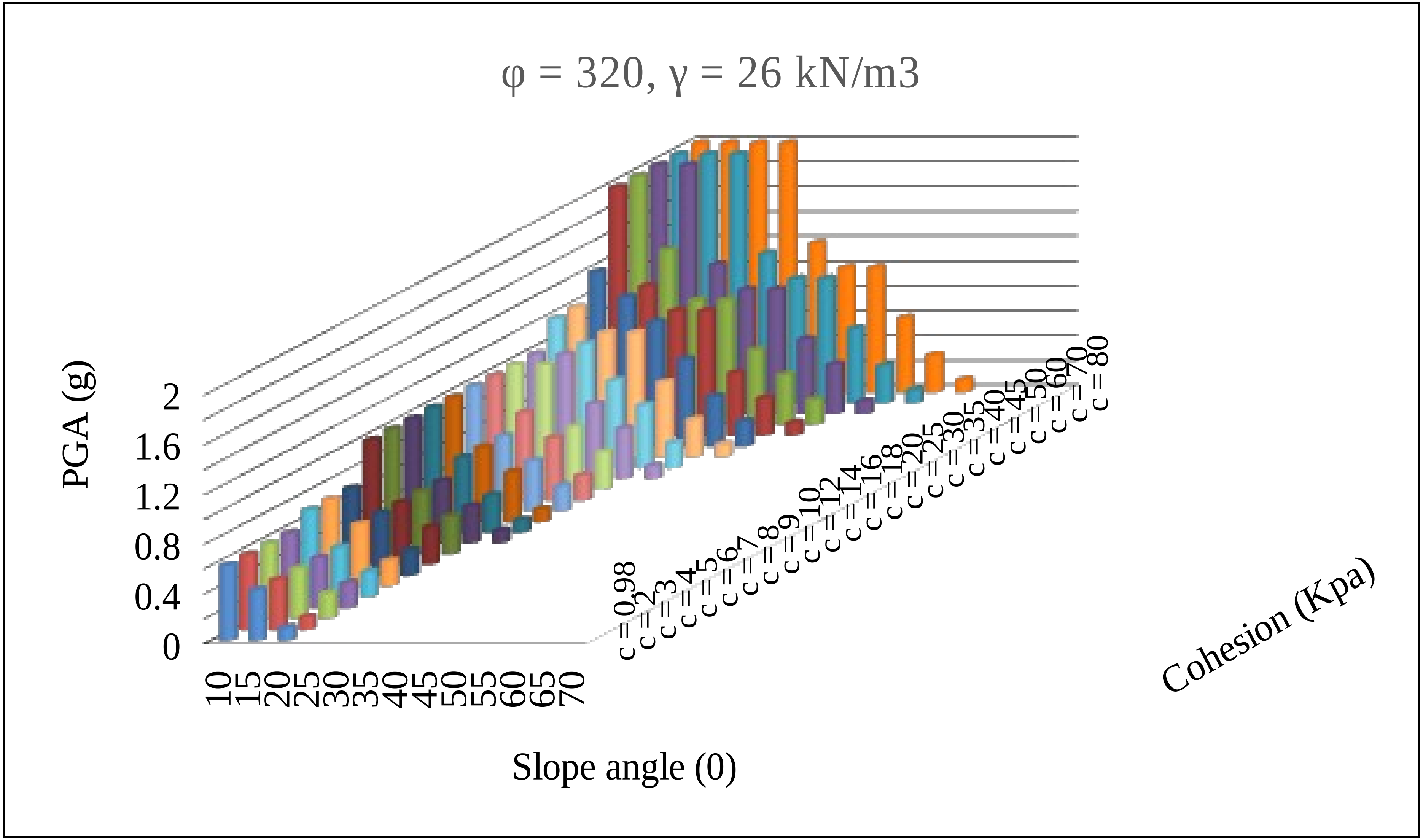

Figure 7.9 (h) φ=32^0

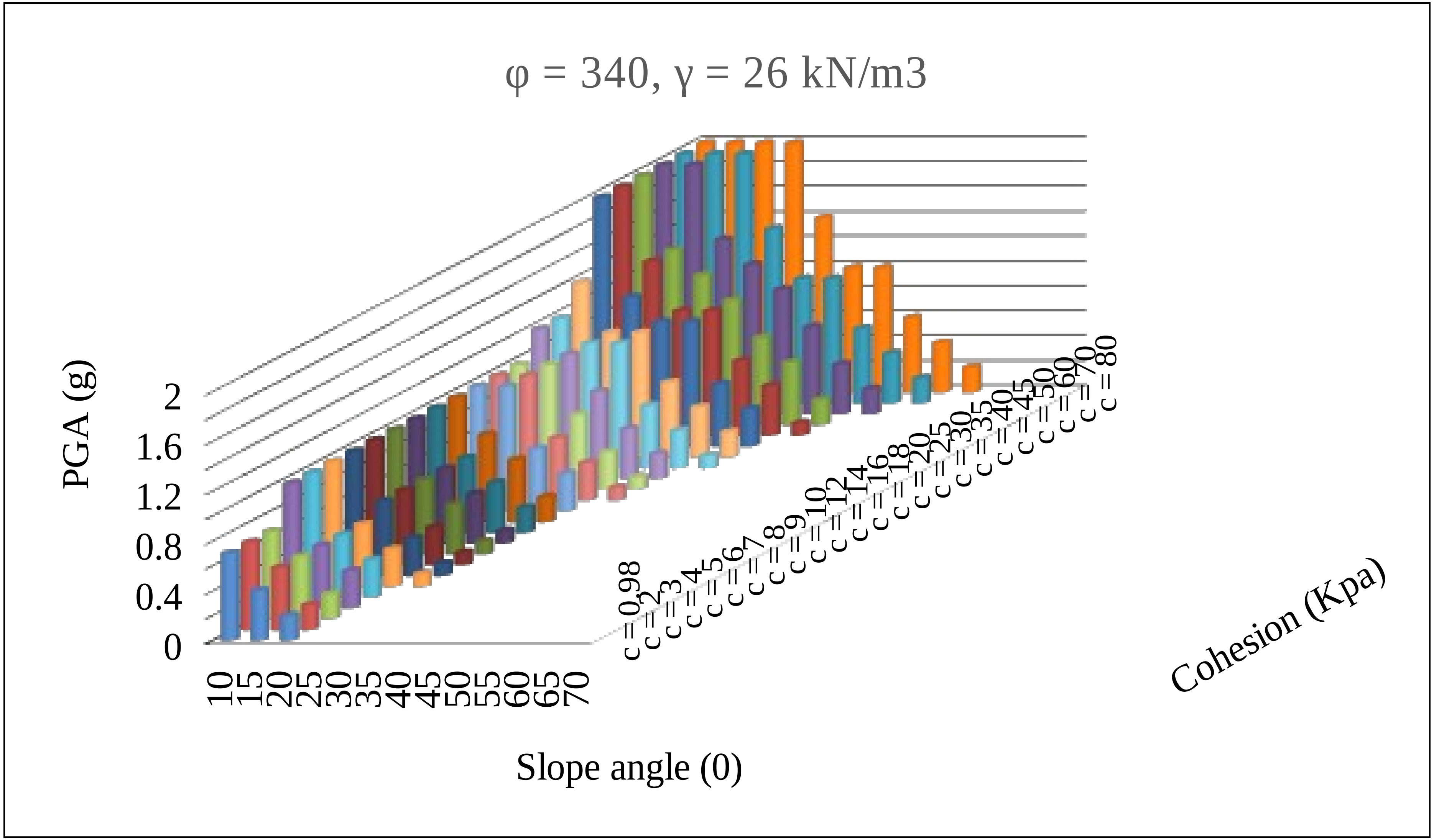

Figure 7.9 (i) φ=34^{0}

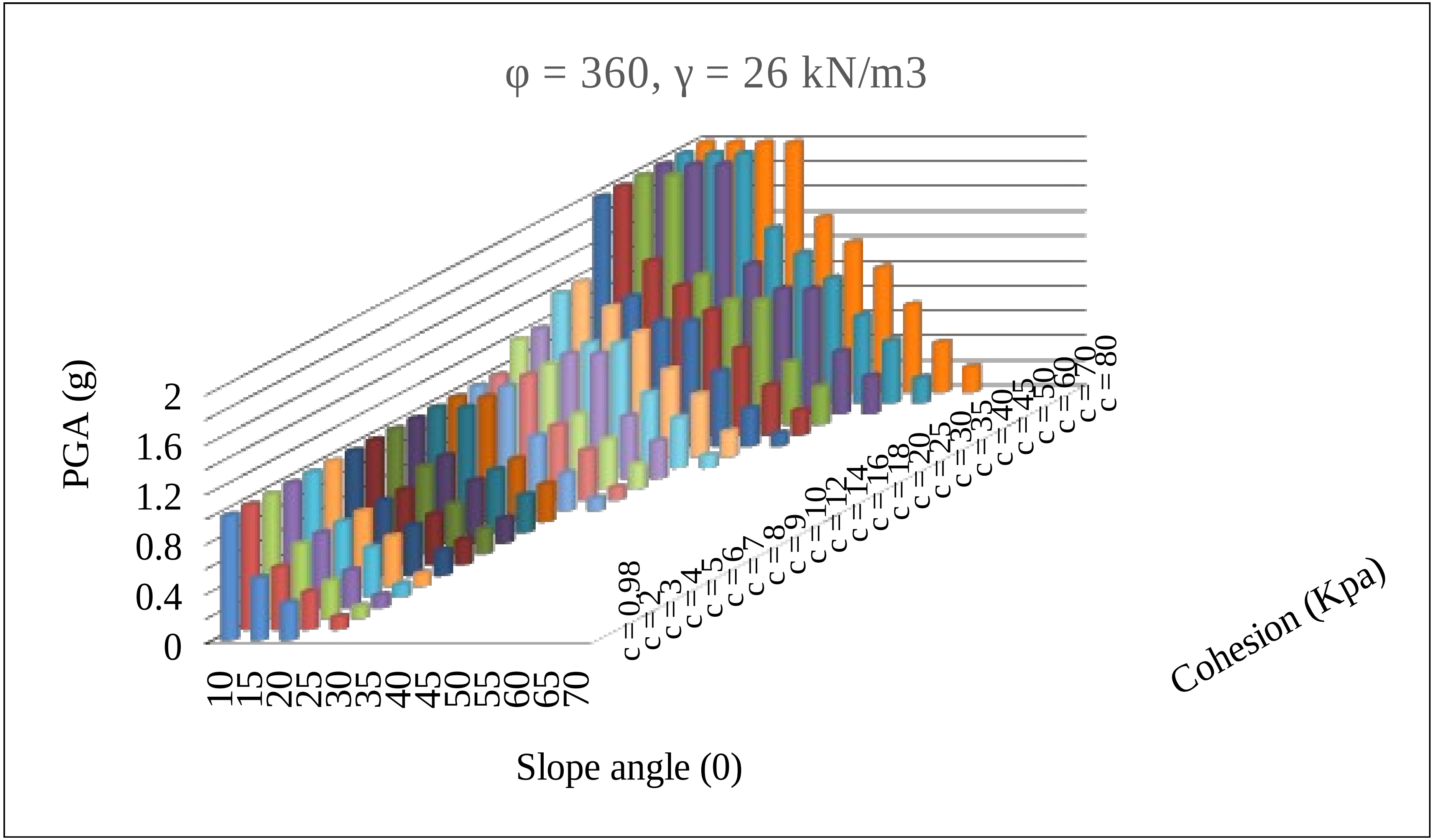

Figure 7.9 (j) φ=36^0

The design charts of DBE calculated for slope angles 10 to70^0, φ=18^0 - 36^0, c = 0 to 80 Kpa, at γ = 27 kN/m^3 are calculated and presented in Figures 7.10 (a to j).

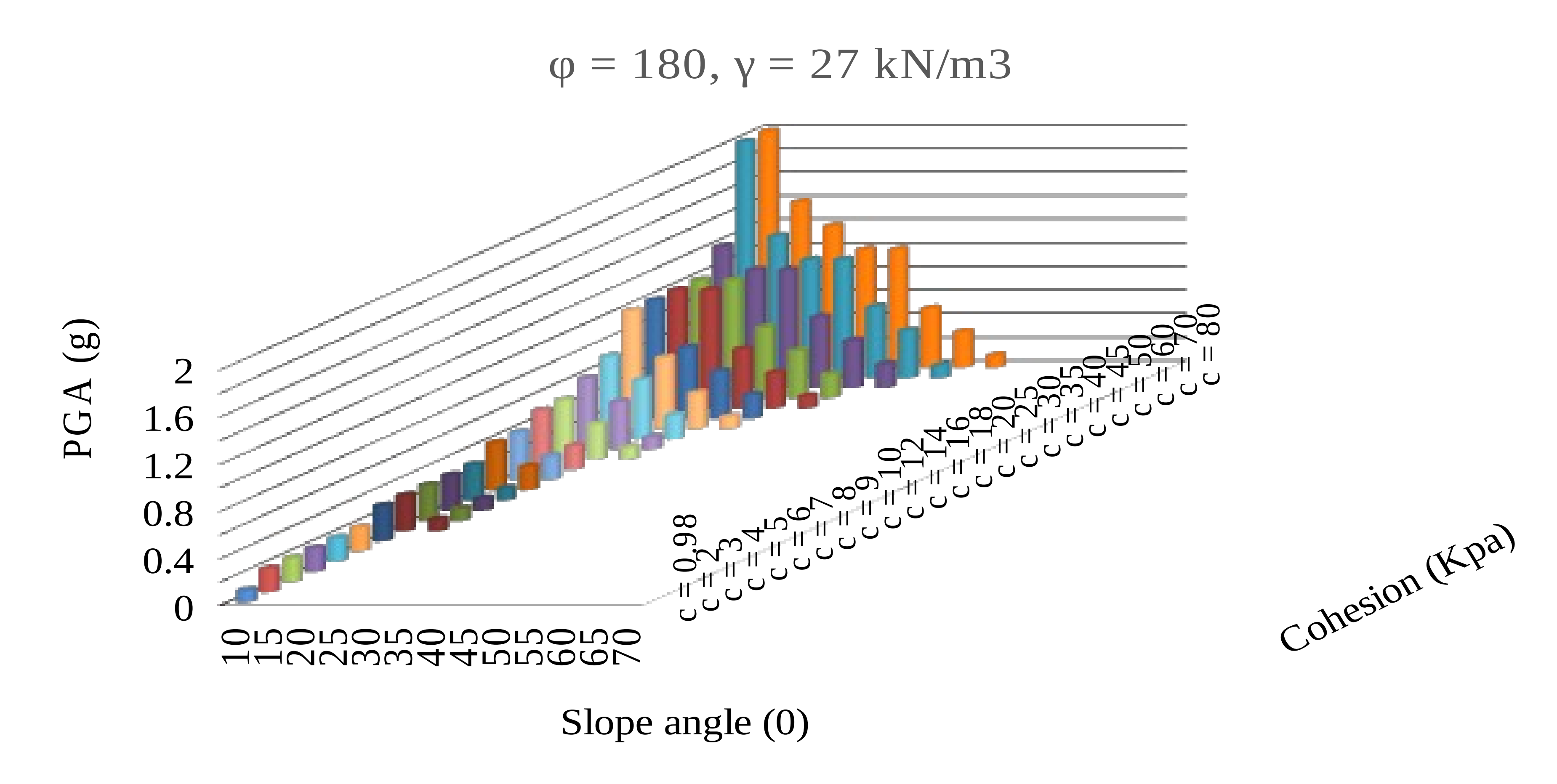

Figure 7.10 DBE design charts at various slope angle, Cohesion and γ = 27 kN/m^3 for (a) φ=18^0

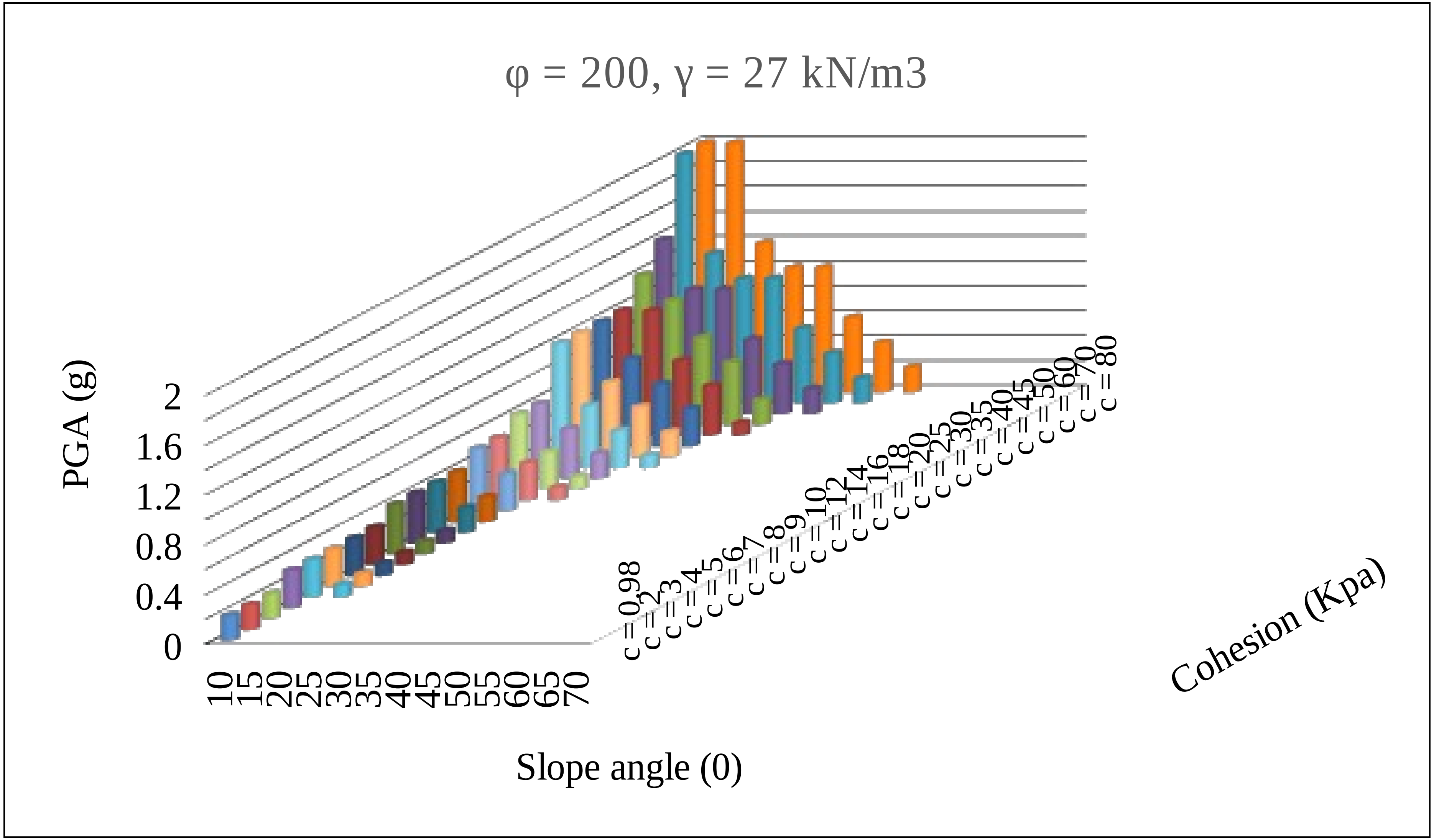

Figure 7.10 (b) φ=20^0

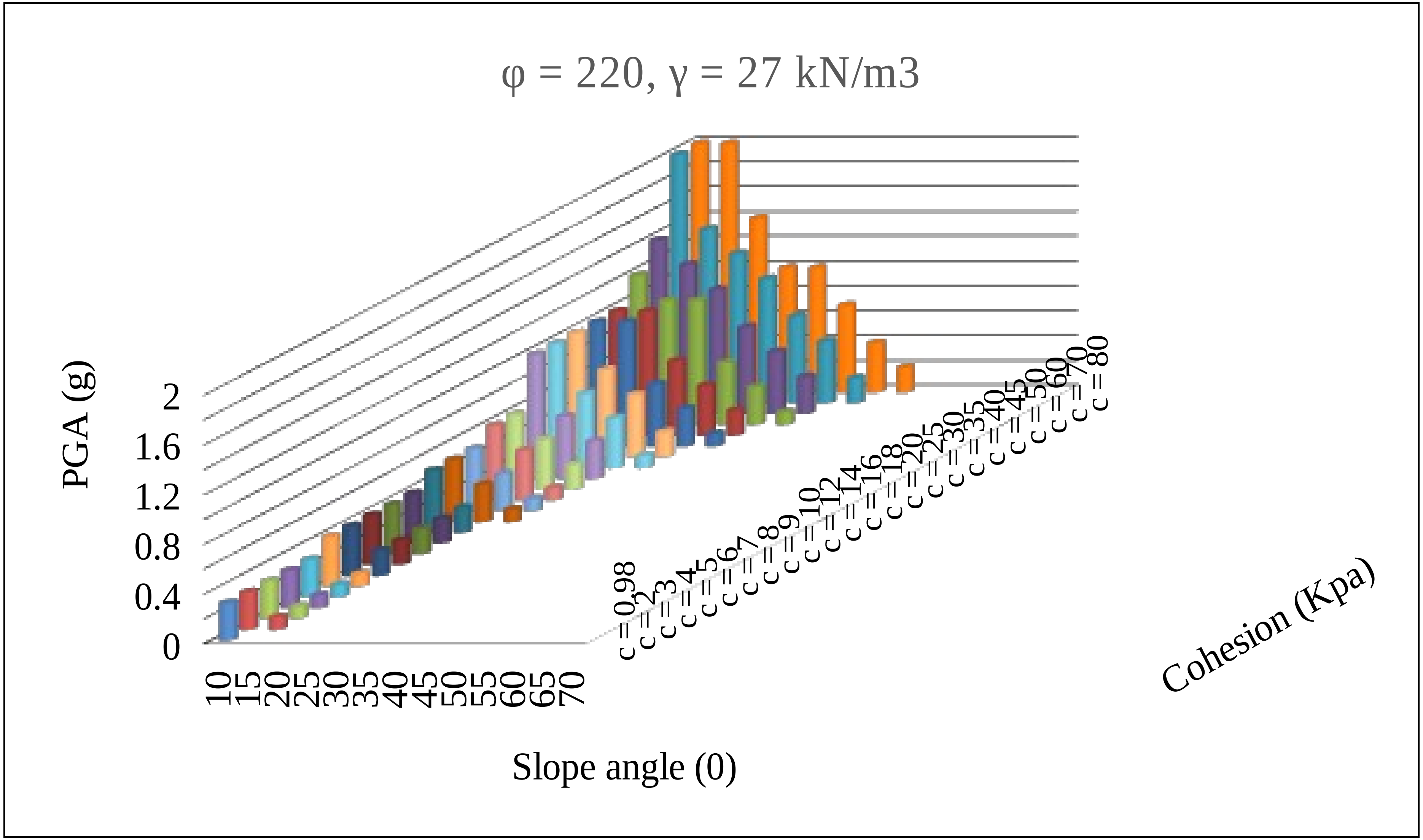

Figure 7.10 (c) $\varphi=22^0$

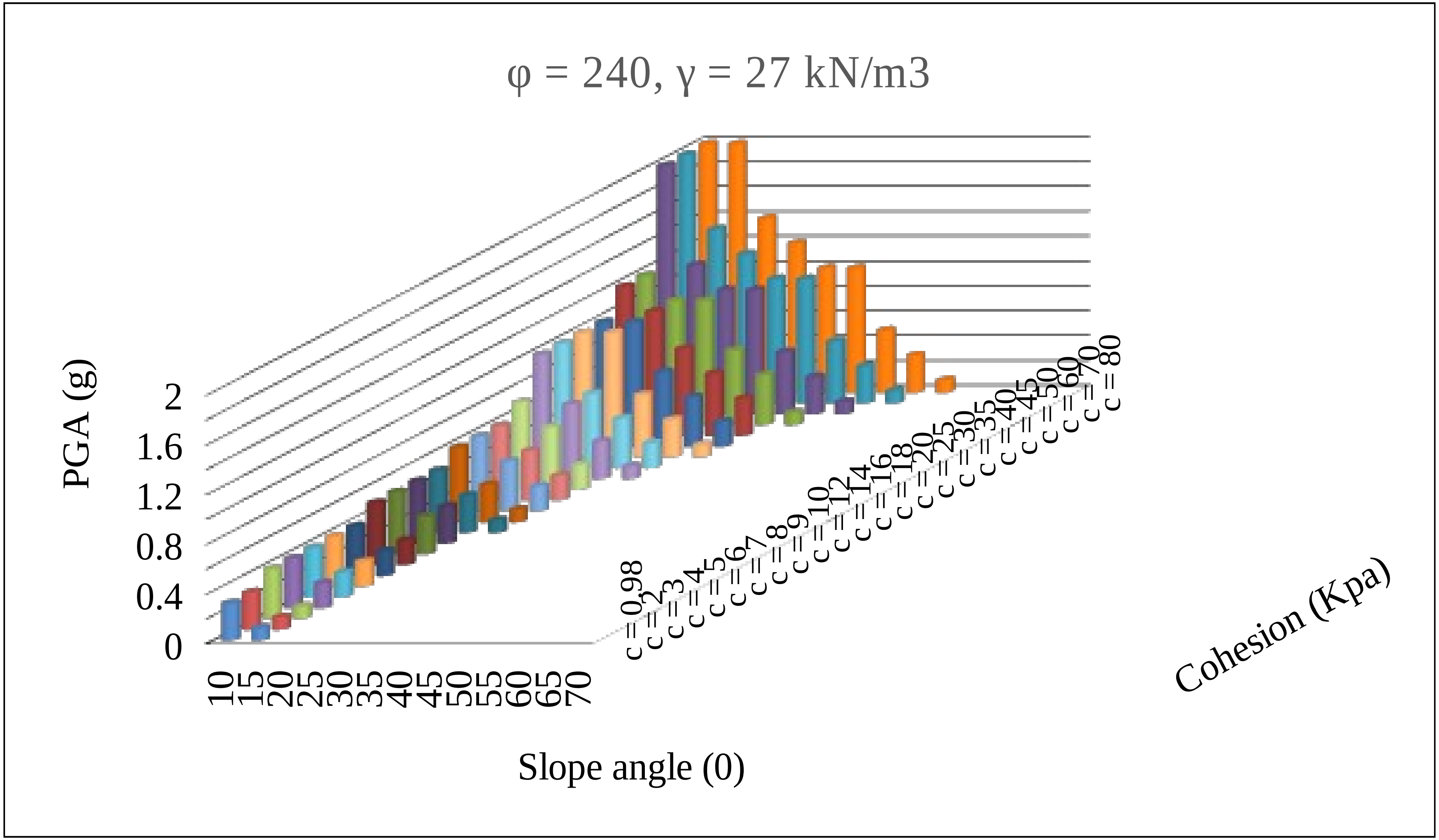

Figure 7.10 (d) $\varphi=24^0$

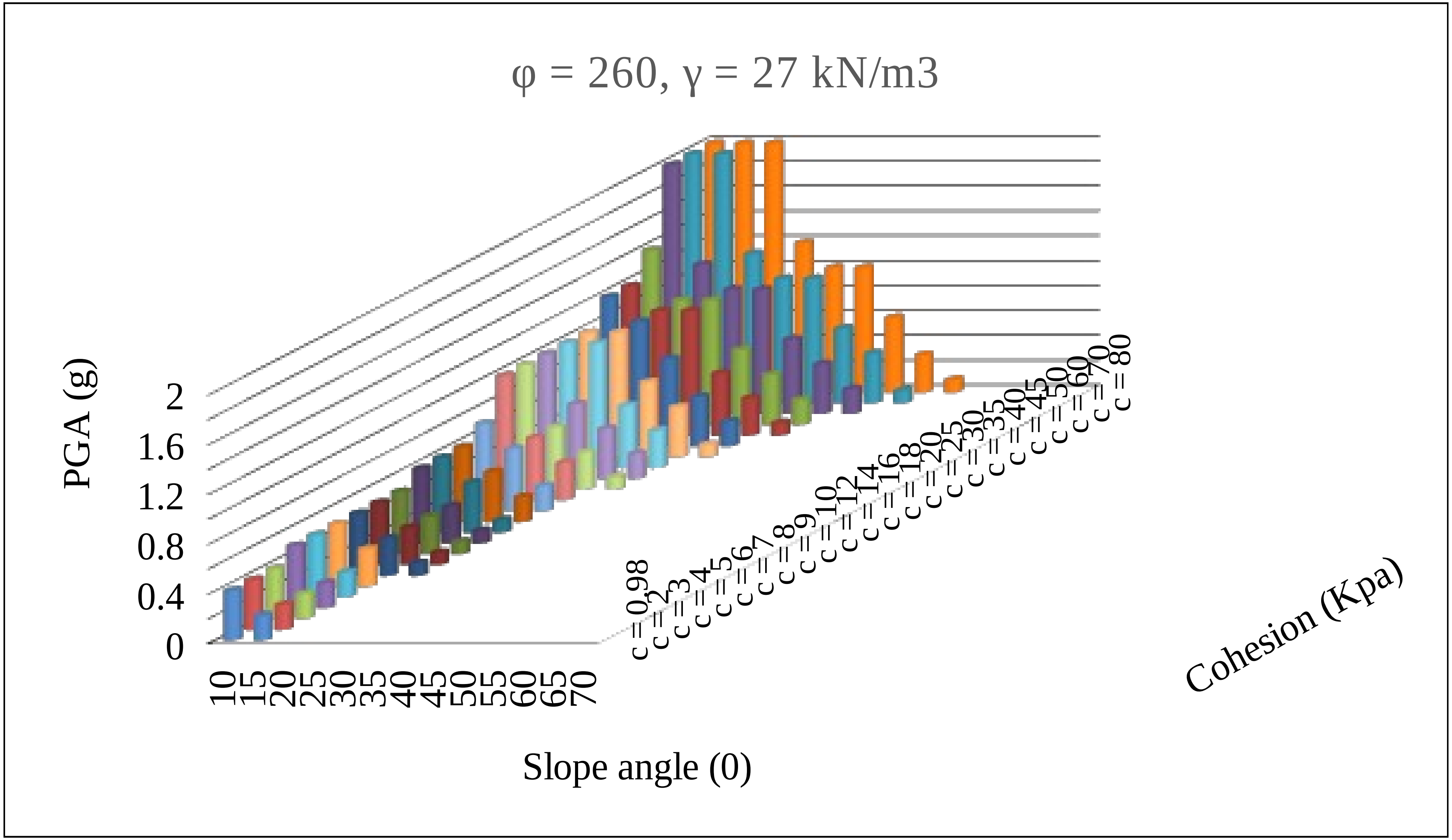

Figure 7.10 (e) $\varphi=26^0$

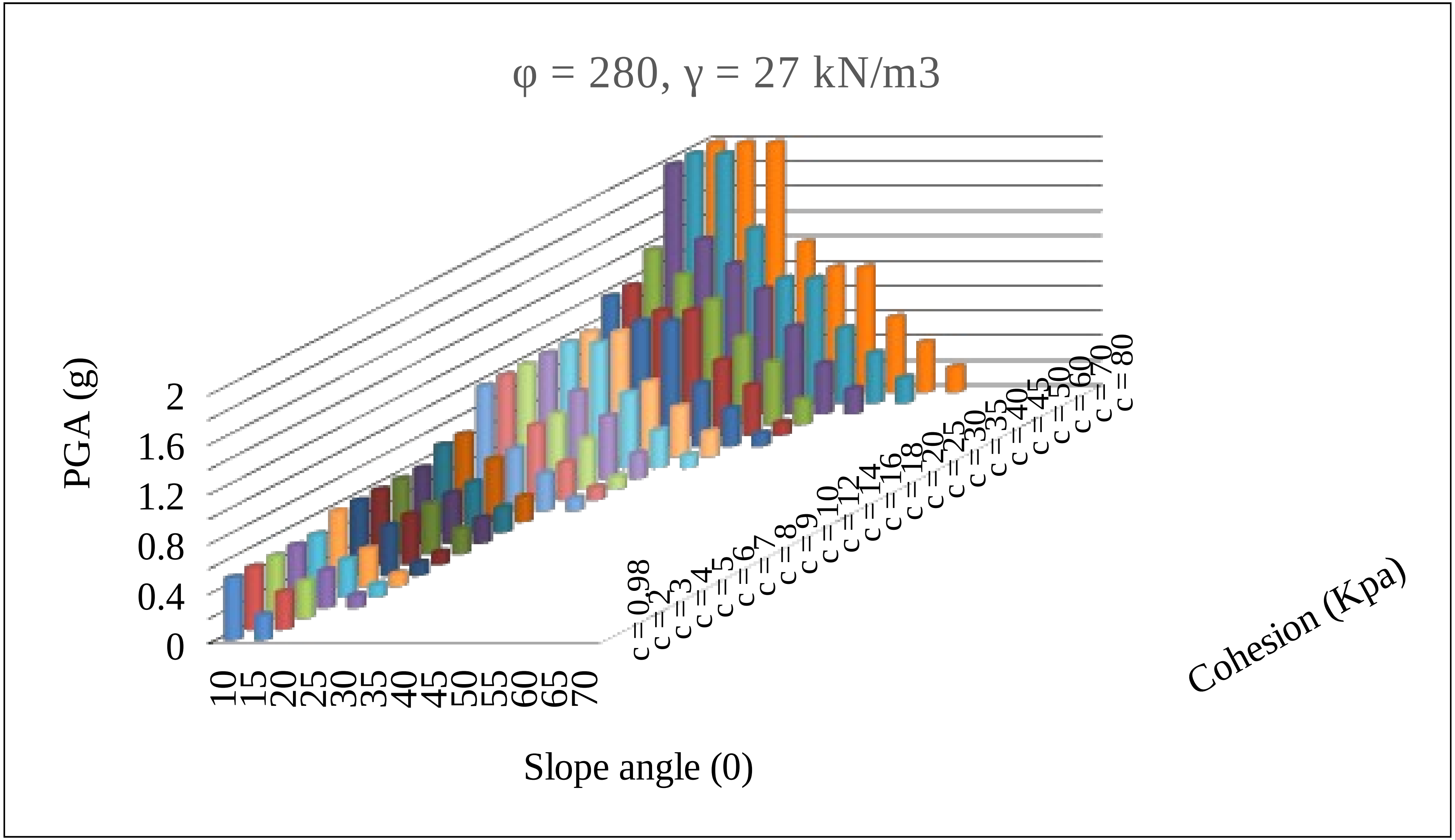

Figure 7.10 (f) $\varphi=28^0$

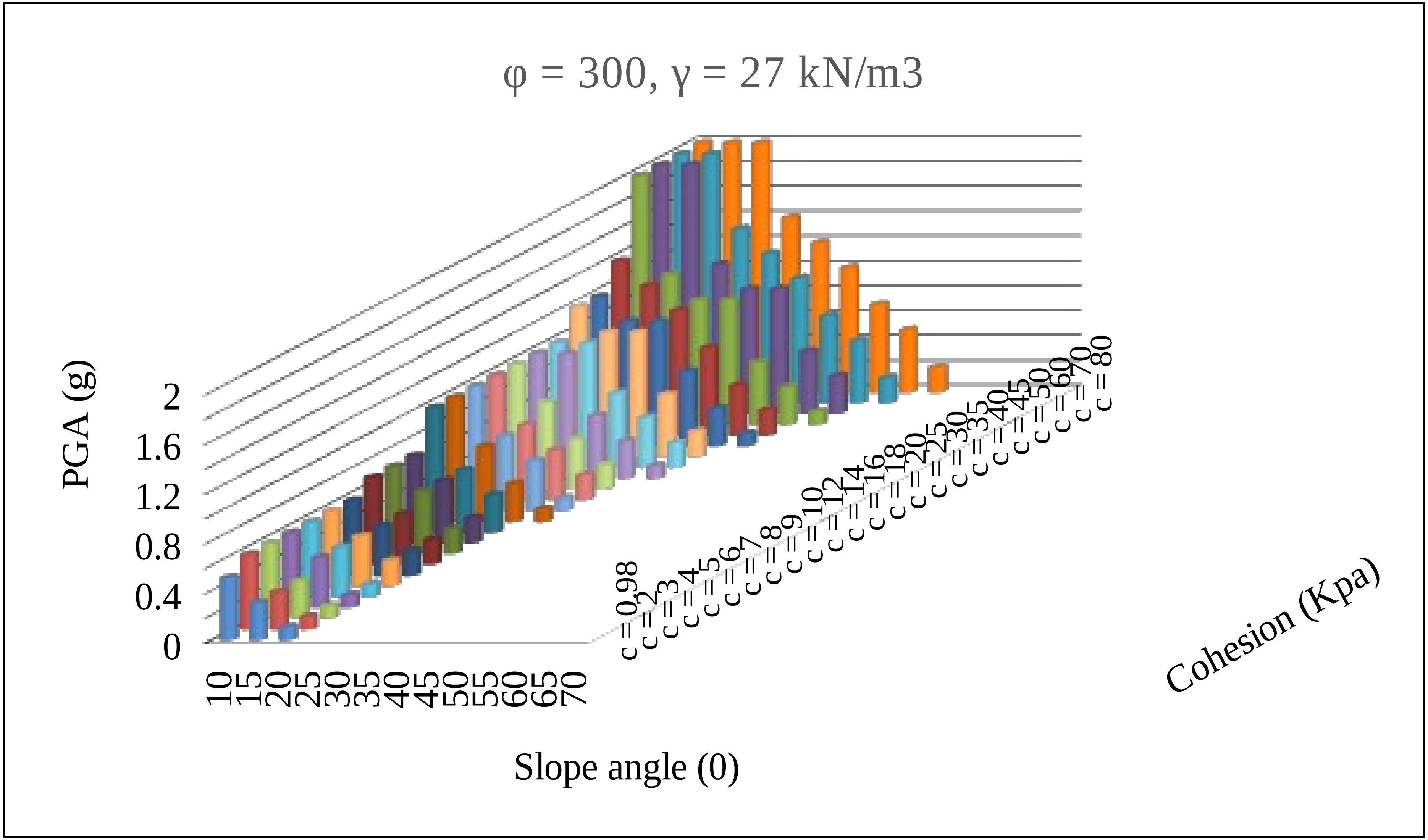

Figure 7.10 (g) φ=30^0

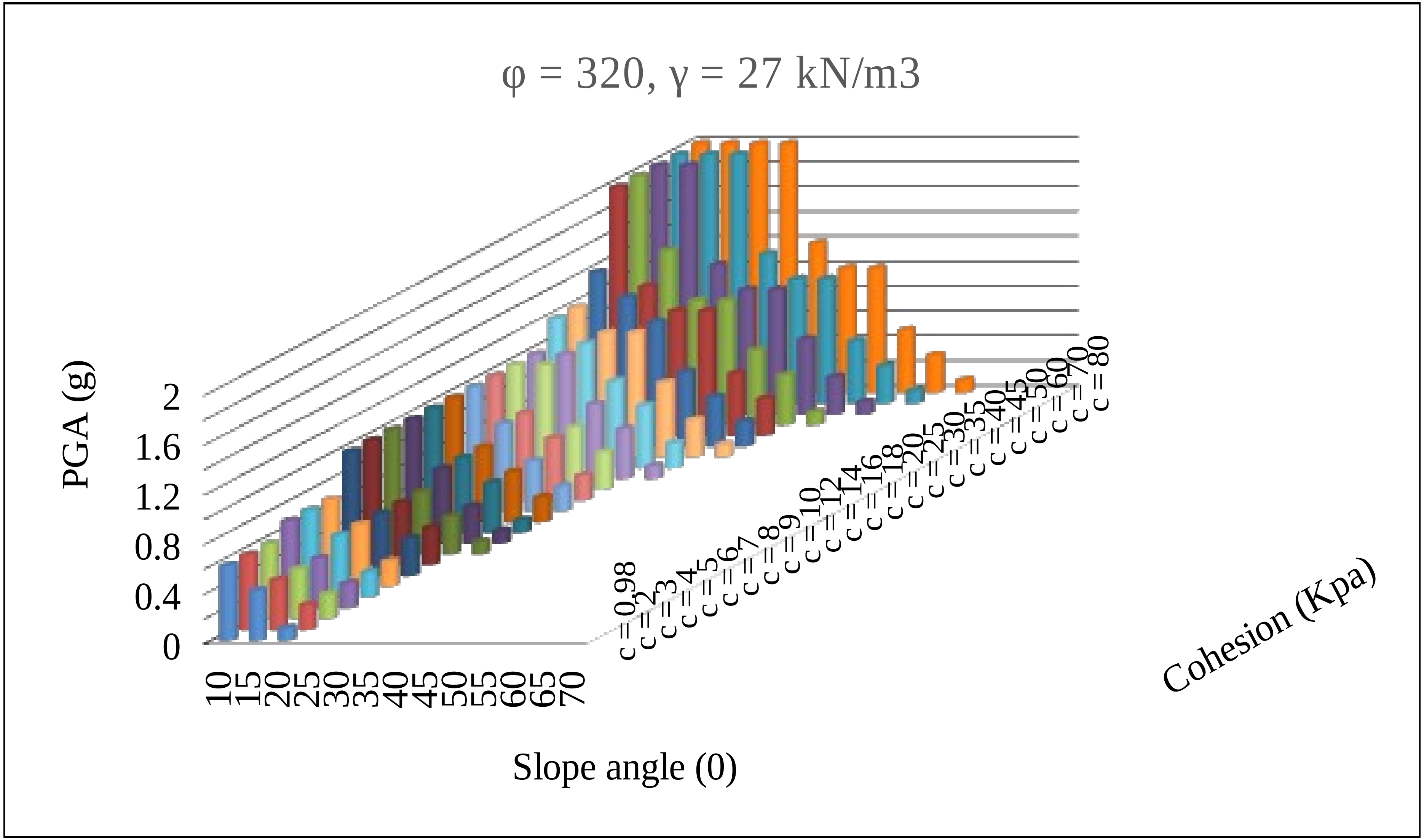

Figure 7.10 (h) φ=32^0

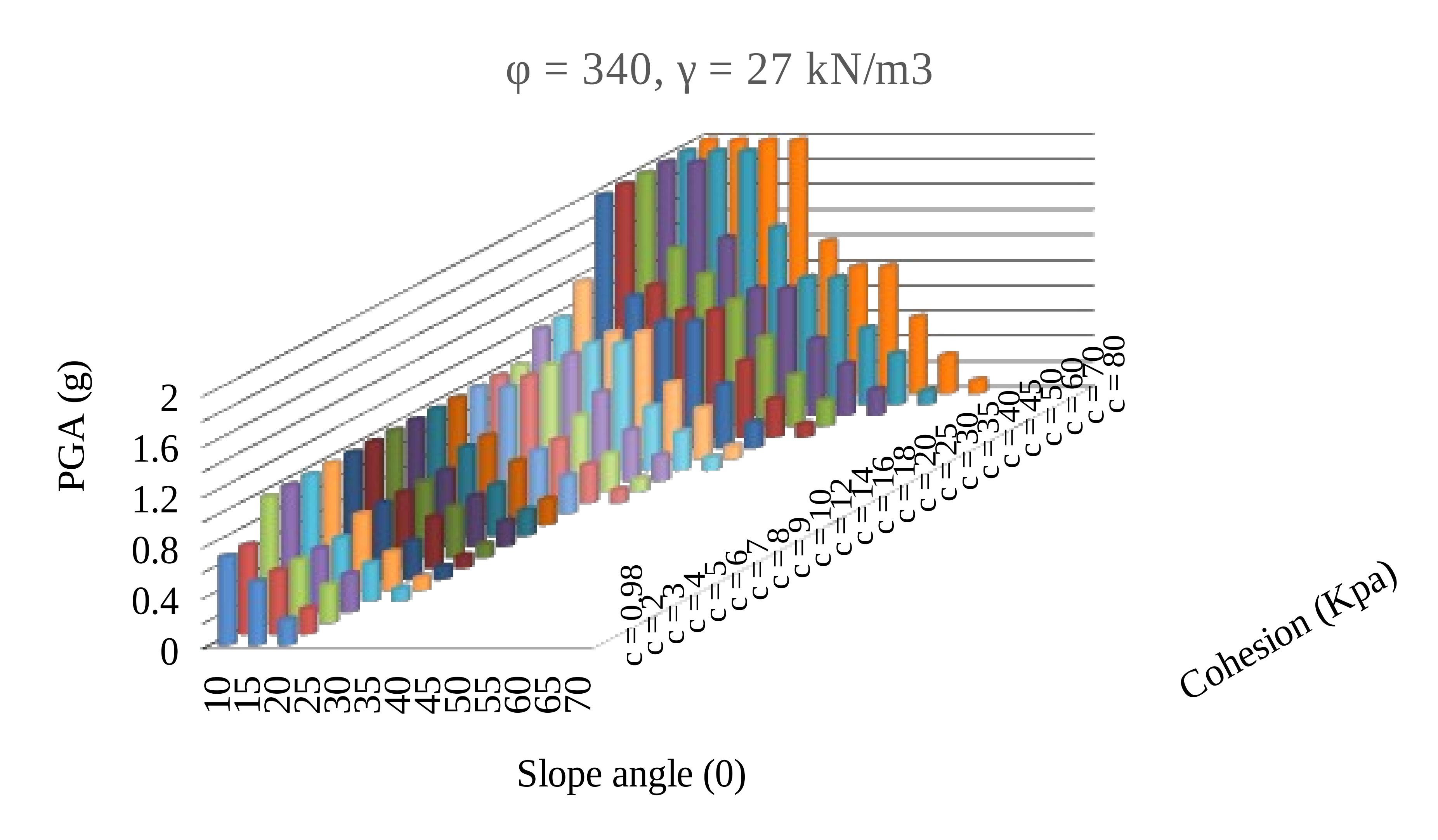

Figure 7.10 (i) $\varphi=34^0$

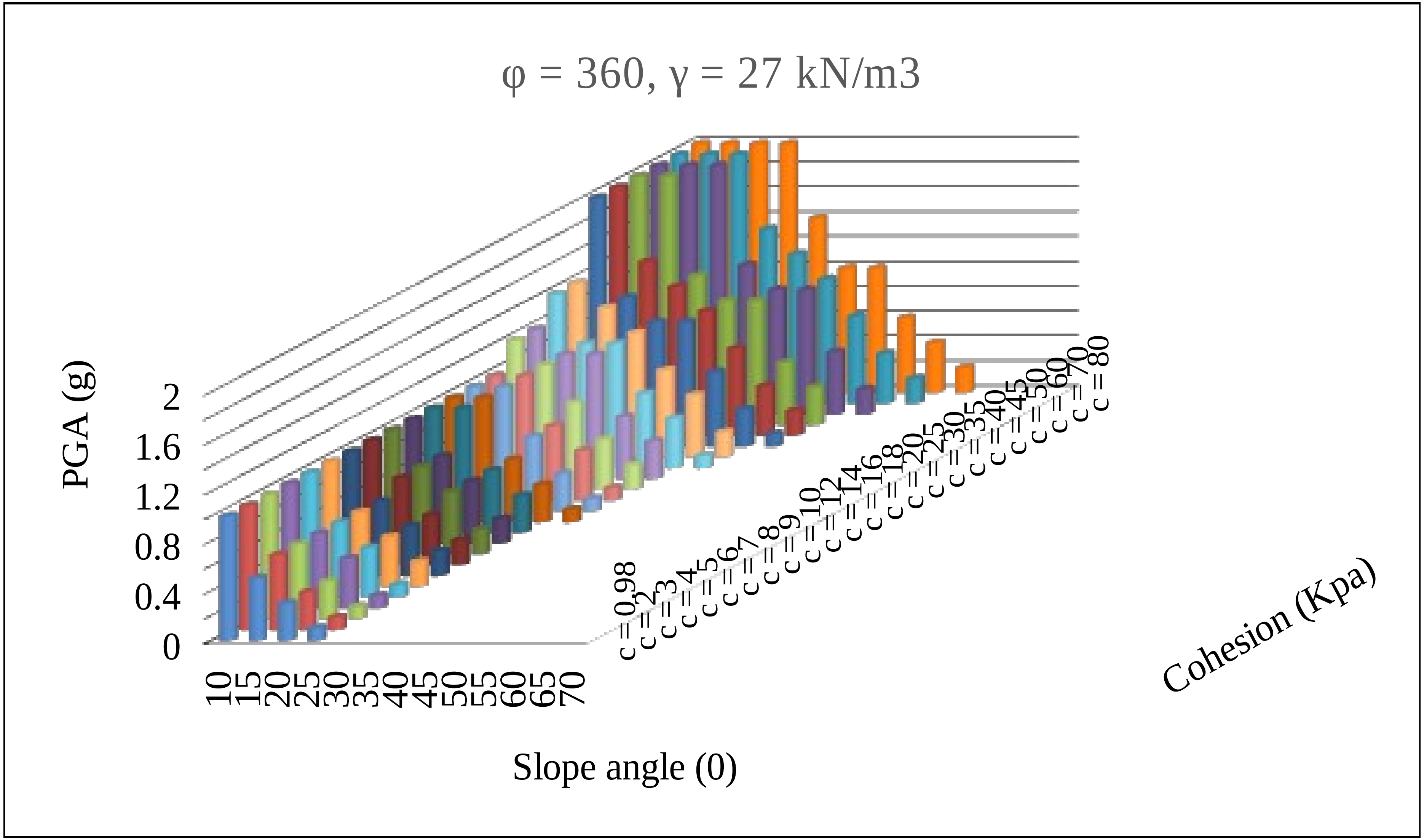

Figure 7.10 (j) φ=36^0

7.5 Summary and conclusion

The study utilizes an improvised fully probabilistic technique to assess the most probable seismic hazard that would trigger landslides. This method involves three stages of data processing, namely the selection of seismic sources, the generation of slope models based on slope parameters, and the choice of a ground motion prediction equation. A total of 20 tectonic sources and 316 seismic sources are selected, leading to the generation of 3160 slope models based on various slope parameters and angles. The ANBU-13 Ground Motion Prediction Equation (GMPE) is employed for evaluating the hazard of seismically induced landslides.

The fully probabilistic assessment is carried out through a multistage hazard assessment process. Firstly, the probability of a specific ground intensity value occurring within a given time interval in the study area is evaluated. Subsequently, the conditional probability of the ground motion parameters triggering a particular slope model is determined.

Design charts are developed to express the most probable ground motion that would trigger each slope model within the next 50 years. These design charts are based on different slope angles and properties. Notably, the results obtained from the Fully Probabilistic Seismic Hazard Analysis (FPSHA) show significant variations compared to those obtained from Deterministic Seismic Hazard Analysis (DSHA) and Probabilistic Seismic Hazard Analysis (PSHA). The most probable ground motion for triggering slope models varies depending on each individual model. It is observed that some slope models are triggered by very low ground motion, while others require higher ground motions, highlighting the influence of slope-specific characteristics in handling all possible ground-motion scenarios.

The comparison of ground motions at the same location between FPSHA, DSHA, and PSHA reveals discrepancies, indicating potential overestimation or underestimation of landslide hazard when relying solely on design ground motions from PSHA and DSHA. These assessments do not consider slope topography and parameters. Detailed examples demonstrating the variations in ground motion at the same location are presented in the subsequent chapter.

In conclusion, designers and researchers equipped with soil parameters can utilize the design charts provided in this study for quick assessments of the dynamic stability of slopes in the study region. Alternatively, they can rely on the PSHA maps. The design charts offer a valuable resource for assessing slope stability and can be applied by professionals for efficient evaluations in the study area.

Chapter 8

Case study: SHA for Tindharia Landslide

8.1 General overview

The primary objective of seismic hazard analysis is to determine the site-specific design ground motion for a particular location. Although various methods exist for seismic hazard analysis, there are significant differences in the determination of factors, leading to uncertainties. Factors such as seismo-tectonics, distance from fault, fault depth, hypo central distance, local site effects, ground motion prediction equations, and soil properties influence the design of ground motion. This chapter focuses on analyzing the influence of Deterministic Seismic Hazard Analysis (DSHA), Probabilistic Seismic Hazard Analysis (PSHA), and Fully Probabilistic Seismic Hazard Analysis (FPSHA) methods on the Tindharia site. The comparison of Peak Ground Accelerations (PGAs) obtained from these methods is conducted for the case study, and an economically optimized methodology for landslide assessment is proposed.

8.2 Brief description of the Tindharia landslide

8.2.1 Overview of landslide

The Tindharia landslide, which occurred on September 18, 2011, with a moment magnitude (M_w) of 6.9, is the central focus within the 300 km study area. Located in the Tindharia village, along the hill cart road between Siliguri and Kurseong in the Kurseong subdivision of the Darjeeling district, West Bengal state, the landslide's location is depicted in Figure 8.1.

The district is situated in the northwestern part of the state, bordering Nepal, Bhutan, and Bangladesh, as well as the states of Sikkim and Bihar. Known as the "Queen of Hills," the district attracts numerous tourists annually due to its magnificent landscapes, but it also faces frequent earthquakes and landslides, causing concern among the local population. Tindharia village is renowned as a railway settlement town, primarily developed for tourism purposes and hosting the "Darjeeling–Himalayan Railways (DHR)," also known as the toy train. The construction of the railway track dates back to 1879, and its operation commenced in 1880. The area is designated as a UNESCO World Heritage site. The landslide site is particularly significant as it intersects with the tourist destination of the DHR and NH-55. The region falls within the Shiva Khola catchment, which is a tributary of the Ganga River.

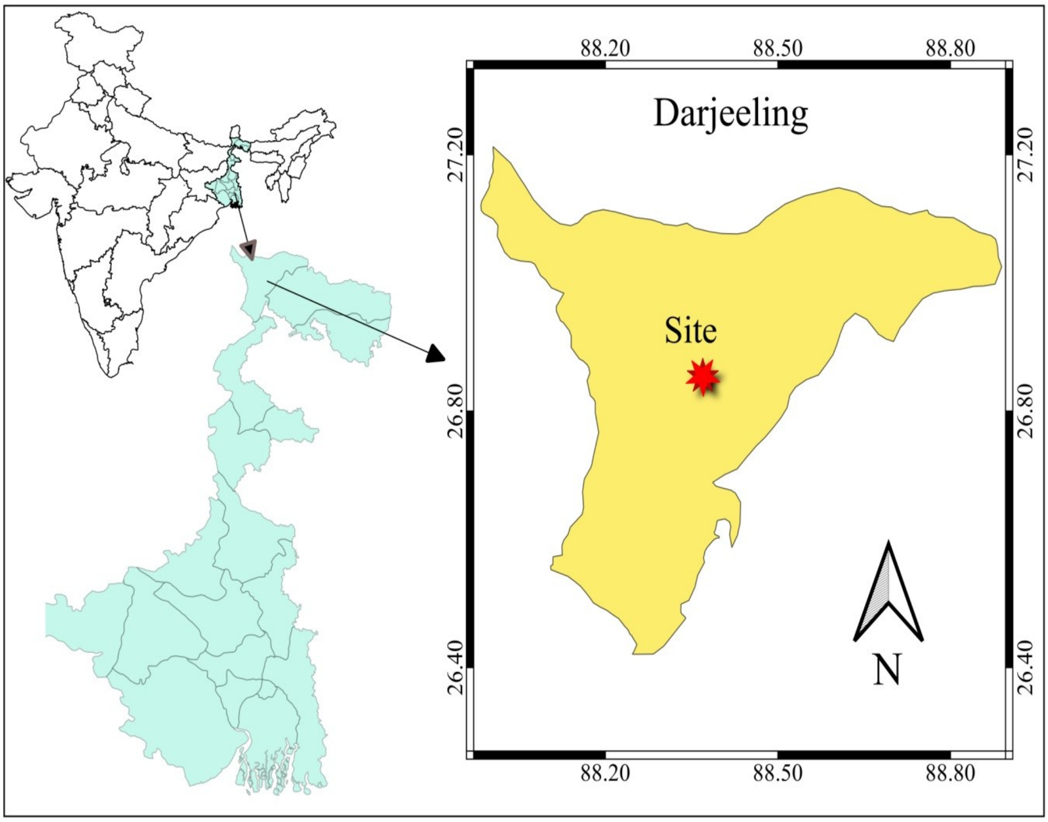

Figure 8.1 Location of the Tindharia landslide, West Bengal, India.

The Tindharia landslide occurred along the hill cart road at geographical coordinates $26^{0}51^{1}14.55^{11}$ North latitude and $88^{0}20^{1}13.12^{11}$ East longitude. It resulted from the settlement of NH-55, which runs parallel to the Darjeeling toy train track, a world heritage site used for tourism. The Tindharia slope is characterized by a narrow, deep valley and steep terrain. Above the landslide site lies the Darjeeling Himalayan railway workshop, constructed between 1909 and 1913, which is nearly a century old. The slope failure and collapse on September 18, 2011, caused damage to NH-55, as depicted in

Figure 8.2 (a). The triangular debris slide, initially triggered by the earthquake, had a crown width of 130m and a length of 180m from crown to toe. The debris was scattered extensively across the site and accumulated at the lower part of the slope. The occurrence of several cracks on NH-55 within the landslide area due to earthquake-induced landslides is illustrated in Figure 8.2 (b).

(a) (b)

Figure 8.2 Tindharia landslide failed during the 2011 earthquake: **(a)** Front view; **(b)** side view (https://savethehills.blogspot.com/2011/)

Subsequent to the initial earthquake-induced slope failure, further destabilization and a series of failures were observed in the study area following heavy rainfall on September 28, 2011. The heavy rains caused the ground to weaken, leading to the complete removal of the toy railway section that followed the road, as shown in Figure 8.3 (b). Although the Darjeeling Himalayan railway workshop remained undamaged, extensive cracks threatened its structural integrity, as depicted in Figure 8.3 (a). The debris was eroded and washed away due to surface runoff, exposing highly weathered sandstone in some areas and revealing open cracks, particularly at the top. Additionally, destabilization and failure occurred at the toe of the hill due to stream erosion. A stream of water flowed towards the base of the slide, playing a significant role in mass wasting and further exacerbating slope instability. The road and railway infrastructure in the area are vital transportation lifelines, and the landslide had a severe socio-economic impact on residents, causing shortages of essential supplies and disruptions in transportation.

(a)

(b) (c)

Figure 8.3 Tindharia landslide reactivated during 2011 monsoon season: **(a)** Closer view; **(b)** side view; **(c)** front view.

(https://blogs.agu.org/landslideblog/2012/07/28/a-landslide-is-rapidly-destroying-a-world-heritage-site-in-india/)

8.2.2 Previous landslides in Tindharia

The Tindharia district has a history of being severely impacted by seismic events and landslides. During the Bihar-Nepal earthquake on January 15th, 1934, the district experienced significant damage, with the Tindharia railway station being the most severely affected area. The seismic motion during this earthquake influenced the slope, leading to the development of failure surfaces that failed either during or after the earthquake, often exacerbated by heavy rainfall. In June 1950, heavy rainfall measuring 834.10 mm over a three-day period resulted in landslides in and around the Kurseong subdivision, claiming the lives of 127 individuals. Tindharia itself was struck by another devastating landslide in September 1980, triggered by heavy rainfall totaling 229.1 mm over the course of the 3rd and 4th of that month. Landslide events have been a recurring occurrence in Tindharia, with notable incidents documented in 1993, 1995, 1998, 2001, 2002, 2003, 2006, and 2007. The Hill cart road of Tindharia has been particularly susceptible to these landslides. The NH-55 route from Darjeeling to Siliguri experienced failures on August 4th and July 14th, 2007. The destructive landslides witnessed in Tindharia and other areas were also triggered by the 2011 Sikkim-Nepal earthquake. This earthquake-initiated failure paths for numerous landslides, which were further exacerbated by rainfall.

8.2.3 Details of the study area

Based on the topographic surveys conducted by Rao [258] and Kundu [190] on the Tindharia slope, it has been determined that the elevation of the slope ranges from 600 m to 800 m, while the slope gradient varies between 30° and 45°. Additionally, the slide scar on the slope is observed to have a very steep inclination of 50° to 60°.

To illustrate the changes in the ground profile resulting from the earthquake-induced failure, two profiles were developed. The "Before" ground profile was constructed using elevation data from the Survey of India (SOI) topographic sheet, while the "After" profile was created using field-based elevation measurements. These profiles are depicted in Figure 8.4, highlighting the alterations in the slope configuration following the occurrence of the earthquake.

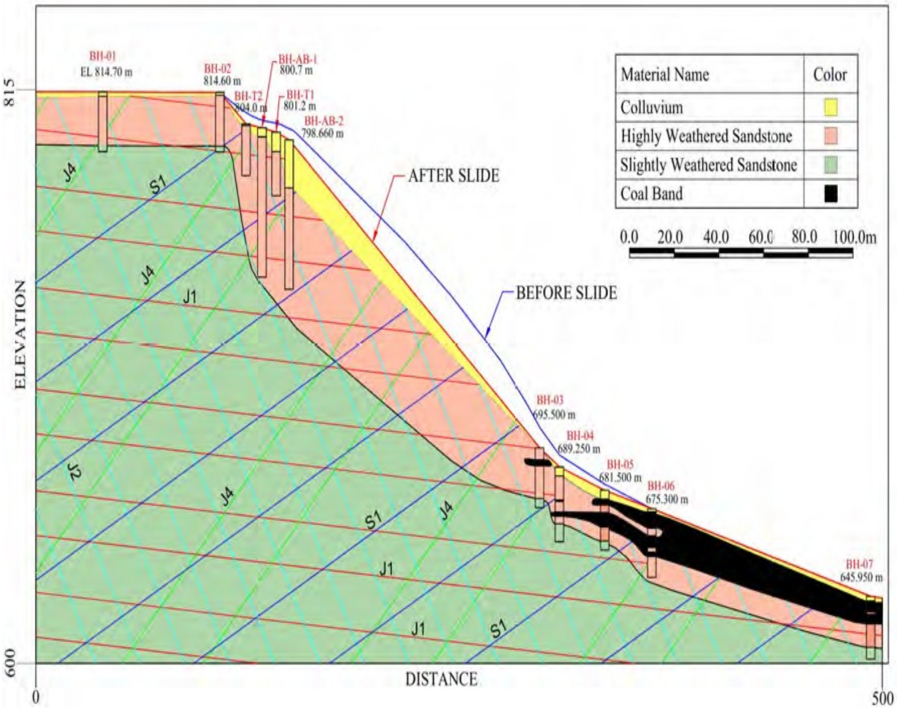

Figure 8.4 Geological profile of the Tindharia landslide [190].

The Tindharia site exhibits a distinct geological composition, characterized by the presence of different domains separated by various thrusts. The Siwalik group is separated from the Gondwana sediments by the Main Boundary Thrust (MBT), while the Daling group is separated by the Main Central Thrust (MCT) [259].

Based on the site survey conducted by Kundu [190], it was observed that a significant portion of the debris on the Tindharia slope had been washed away due to surface runoff. The remaining material predominantly comprised highly weathered sandstone, as depicted in Figure 8.4. During the site visit conducted by Rao [258] and Kundu [190], it was noted that the slide primarily consists of sandstone, quartzite, coaly shale, and slide debris. The exposed slide scar comprises sandstone, shale, and coaly shale. The uppermost layer consists of quartzite, followed by sandstone, coaly shale, and shale, which in certain areas can be easily crumbled by hand.

The debris resulting from the landslide is widely distributed across the entire site, with a substantial portion being washed away by surface runoff. The exposed rocks have undergone weathering processes, leading to a degradation in the quality of the rock mass. In some areas of the slope, shale and coaly shale can be easily crumbled by hand. Additionally, open cracks have been observed at various locations, attributed to the Sikkim–Nepal earthquake. Seepage through open joints is also observed at the base of the slide. Above the slide, the upper part of the slope consists of colluviums and residual soils, with variable thickness ranging from 0 to 8 meters following the earthquake.

8.2.4 Geotechnical characteristics

In order to assess the slope characteristics prior to failure, a significant challenge arises due to the limited availability of data on pre-failure soil properties. Many studies have primarily focused on analyzing soil properties after the occurrence of slope failure. To address this challenge, a back analysis approach was employed by Nishant Roy et al. [260] to evaluate the probable range of geomechanical parameters that lead to slope instability.

For the back analysis, the following parameters were utilized: a cohesion (c') of 50 kPa, a friction angle (φ) of 25°, a unit weight of material (γ) of 18 kN/m³, a unit weight of groundwater (γ_w) of 9.8 kN/m³, a slope normal thickness (z) of 5 m, and a dip angle (α) of 35°. The saturated sliding mass thickness (m) was considered as 1 in the present study. Based on these material parameters, the critical acceleration was determined using Equation 7.10, yielding a value of 0.163g.

8.3 SHA for Tindharia

8.3.1 DSHA analysis

8.3.1.1 Application of DSHA on Tindharia

The Deterministic Seismic Hazard Analysis (DSHA) is a widely used methodology in seismic hazard analysis that employs a simplified framework. It aims to determine the most severe ground motion expected from the nearest controlling seismic source. A comprehensive explanation of DSHA can be found in Chapter 5 of the study.

In the case of the Tindharia site, it is considered the central location within a radial influence zone spanning 300 km, as depicted in Figure 3.1. To conduct the DSHA analysis, seismic sources within this 300 km radius were carefully selected. The major linear seismic sources, including faults and lineaments, were compiled from India's seismotectonic Atlas (SEISAT) (GSI, 2000). For each fault, the maximum magnitude (M_{max}) was calculated using regional rupture characteristics, and these values are summarized in Table 5.1.

The shortest distance from the tectonic fault sources to the site (R_{rup}) was calculated using QGIS software, employing a virtual layer. The resulting distances are presented in Table 8.1. Additionally, based on observations, the average depth of the study area was determined to be 30 km. Therefore, for all linear sources within this depth range, the Peak Ground Acceleration (PGA) was calculated. In this study, the ANBU-13 attenuation equation proposed by Anbazhagan et al. [186] and presented as Equation 4.9 was selected as the most suitable method for calculating deterministic PGA. A detailed explanation of this equation can be found in Chapter 4. The PGA's for all active faults surrounding the Tindharia site were computed using the ANBU-13 GMPE, and the results are summarized in Table 8.1.

Table 8.1 DSHA PGA for Tindharia landslide

Fault code	JGF	GF	KNF	KL	SBF	DBF	WPF	PEL	TL	DF	AL	GSL	EL	MCT	MBT
M_{max}	6.49	6.69	7.02	7.21	7.35	7.37	7.39	7.21	7.27	7.33	7.4	7.4	7.62	8.09	8.41
R_{rup}	179.08	198.64	105.43	90.34	204.38	256.96	243.04	100.2	11.11	174.55	137.54	229.53	184.91	8.18	3.94
PGA(g)	0.1	0.1	0.2	0.3	0.2	0.2	0.2	0.3	0.5	0.2	0.2	0.2	0.2	0.8	0.9

8.3.1.2 DSHA Conclusion

The seismic hazard at the Tindharia site is determined using the Deterministic Seismic Hazard Analysis (DSHA) approach, which involves the selection of controlling earthquakes based on a comparison of their peak ground acceleration (PGA) levels. In this analysis, it was found that the MBT source event located at a distance of 3.94 km produces a PGA of 0.90g, making it the selected controlling earthquake for the site. Additionally, the MBT and Tista lineaments, located at distances of 8.18 km and 11.11 km respectively, were observed to generate PGAs of 0.80g and 0.5g.

8.3.2 PSHA analysis

The deterministic approach to ground motion assessment considers a single magnitude earthquake at a fixed distance from the site. On the other hand, the probabilistic approach takes into account the effects of all earthquakes with varying magnitudes in the vicinity of the site and incorporates uncertainties in the analysis. This study aims to provide a comprehensive understanding of seismic hazards by utilizing analytical expressions, seismicity models, and addressing uncertainties in a rational manner [27]. A detailed discussion on Probabilistic Seismic Hazard Analysis (PSHA) can be found in Chapter 6 of the study.

8.3.2.1 Application of PSHA on Tindharia site

For the seismic hazard analysis, earthquake sources that have the potential to generate significant ground motion, including linear sources and point sources, were selected (refer to Table 4.1 and Annexure-A). Instead of considering only the shortest distance, the distance to the site was consistently modeled for each source, as earthquakes can occur at various locations. To account for magnitude uncertainty, the Gutenberg-Richter recurrence law was adopted, and the seismicity parameters 'a' and 'b' obtained from the recurrence law were found to be 3.16 and 0.656, respectively. By combining all the relevant factors and using equation 6.13, the complete probability was calculated, resulting in the determination of the design ground motion for a 10% probability in 50 years, as depicted in Figure 8.5.

In seismic hazard analysis, the design ground motion is often assessed based on seismic hazard maps that provide information on the ground motion expected over a 475-year return period. This information serves as a crucial factor for evaluating the stability of seismic slopes. Specifically, the graph representing the 10% probability in 50 years (475-year return period) was evaluated, leading to the determination of the site-specific design ground motion for the Tindharia landslide, which was found to be 0.30g (refer to Figure 8.5).

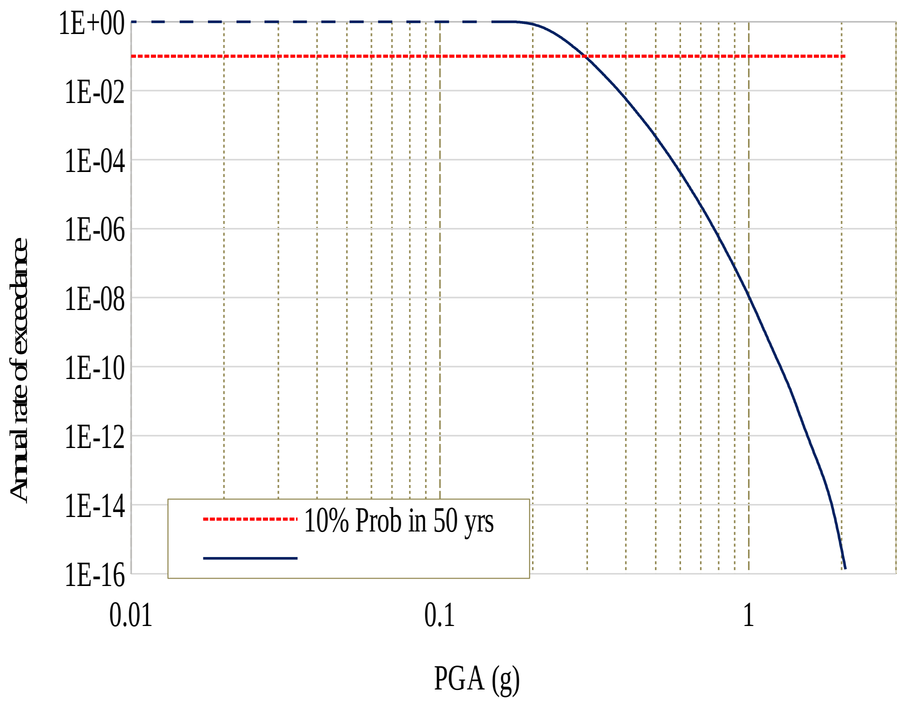

Figure 8.5 Cumulative hazard curve of Tindharia landslide site for 10% probability in 50 years.

8.3.2.2 Conclusion

A probabilistic seismic hazard analysis (PSHA) was conducted for the Tindharia site using the ANBU-13 Ground Motion Prediction Equation (GMPE) and a seismotectonic depth of 30km. The seismicity parameters 'a' (3.16) and 'b' (0.65) were determined through the maximum likelihood method for the study area. The site-specific design ground motion intensity for the Tindharia site was calculated to be 0.30g. The obtained peak ground acceleration (PGA) from the seismic hazard curve was compared with the results from previous research conducted in the same area, demonstrating a good agreement.

8.3.3 FPSHA analysis

In this study, an improved fully probabilistic approach [82] was employed to estimate a consistent earthquake scenario for assessing seismic slope stability. This approach, known as Fully Probabilistic Seismic Hazard Analysis (FPSHA), considers various ground shaking levels, as well as the geometric and mechanical parameters of the landslide, to determine the site-specific design ground motion that triggers slope failure. The detailed methodology for FPSHA was described in Chapter 7.

8.3.3.1 Application of FPSHA on Tindharia site

The FPSHA approach consists of two stages. The first stage involves evaluating the probability of ground motion occurrence within the study area over a specified time interval. In the second stage, the probability of ground motion parameters triggering a landslide is assessed. Combining these two stages yields the total probability of slope failure, as calculated using Equation 7.1. The slope failure probability for the next 50 years is determined based on the PGA obtained by combining these crucial stages.

Seismic hazard curves, which illustrate the PGA against the mean annual exceedance rate, were computed using the CRISIS (2007) software. All calculations were performed for accelerations exceeding the critical value of 0.163g. For the considered slope model and critical acceleration (a_c), the most probable ground motion that would trigger the Tindharia landslide in the next 50 years was determined to be 0.06g, as shown in Figure 8.6. The occurrence hazard, with a variance of ±0.05g, ranges from 0.01 to 0.11g [261]. These results are consistent with the fact that the landslide failed with a ground motion of 0.12g during the 2011 Sikkim Nepal earthquake. However, notable variations in PGA were observed when compared with the findings of the other two studies.

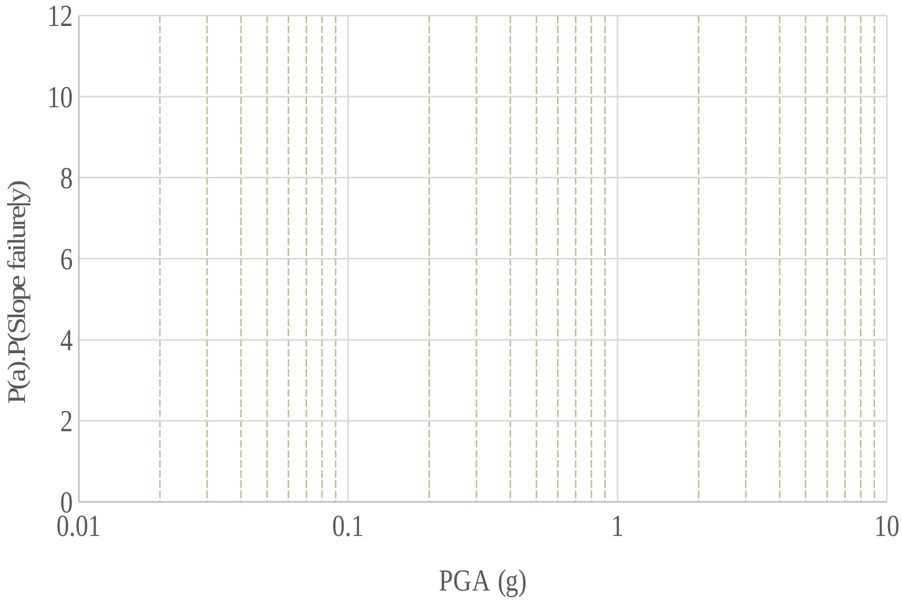

Figure 8.6 Probability distribution function of Tindharia slope failure in the next 50 years

For instance, if the critical acceleration is increased to 2.0g at the same location, the PGA required to trigger the landslide exceeds the value of 0.3g obtained from the PSHA analysis. This indicates that a higher PGA is necessary to induce slope failure compared to the ground motion estimated by the PSHA methodology.

8.3.3.2 FPSHA Conclusion

The multistage hazard assessment of the Tindharia landslide was conducted using an improved fully probabilistic approach. The analysis revealed that the most probable ground motion capable of triggering the Tindharia landslide within the next 50 years is estimated to be 0.06g. Notably, the site-specific design acceleration derived from the fully probabilistic approach is significantly lower than the PGA obtained from the PSHA analysis. This finding suggests that the ground motion estimated by the PSHA methodology may result in underestimation or overestimation of the landslide hazard assessment.

8.4 Summary and conclusion

Ground shaking plays a crucial role in earthquake disasters, and accurate assessment of ground motion is essential for implementing effective risk mitigation measures and slope design. The findings of the present study highlight significant differences in ground-shaking intensity among the three methods employed. The site-specific design ground motions obtained from DSHA, PSHA, and FPSHA are determined as 0.90g, 0.30g, and 0.06g, respectively. While DSHA and PSHA approaches indicate potential failure, FPSHA provides a more accurate evaluation of actual failure for the slopes. It is evident that the design ground motion estimated by DSHA and PSHA may result in overestimation or underestimation of the landslide hazard assessment. In contrast, the fully probabilistic approach (FPSHA) considers a wide range of possible ground-motion scenarios and offers a reasonable estimation of the most probable design ground motion for seismic slope stability assessment. Based on the conclusions drawn from these three assessments, it can be inferred that the fully probabilistic approach is a viable method for accurately assessing seismic slope stability.

Chapter 9

Conclusions

9.1 Summary of the thesis

The research focus of this study encompasses the Darjeeling Sikkim Himalayas and its surrounding area within a 300 km radius. The selection of this region is based on seismo-tectonic considerations specific to the area. A comprehensive data collection process is undertaken, involving the gathering of relevant information from previous research papers, various departments, and reputable websites. This includes seismicity data, climatic conditions, topographic details, as well as geological and geotechnical characteristics pertaining to the study area.

For the seismic hazard assessment, the ANBU-13 Ground Motion Prediction Equation (GMPE) is chosen as the appropriate model at the bedrock level. The analysis incorporates three different methodologies, namely Deterministic Seismic Hazard Analysis (DSHA), Probabilistic Seismic Hazard Analysis (PSHA), and Fully Probabilistic Seismic Hazard Analysis (FPSHA). These methodologies are applied across the 300 km study area to assess the seismic hazard.

9.2 Conclusions

In this study, several seismic hazard assessment approaches were applied to evaluate ground motion characteristics in the study area.

- The earthquake catalogue was refined to include 316 events spanning the time period from 1800 to 2021.
- Deterministic analysis revealed a range of peak ground acceleration (PGA) values from 0.29 to 0.90g, with corresponding peak spectral acceleration (PSA) values ranging from 0.05 to 0.58g. The worst-case scenario ground motion observed in this study was 0.90g, as determined through deterministic seismic hazard assessment.

- Probabilistic seismic hazard analysis (PSHA) provided seismic hazard parameters, with a regional recurrence defined by a value of 3.01 for parameter 'a' and 0.76 for parameter 'b'. The spatial variation of the 'b' value ranged from 0.66 to 0.69, with a standard deviation between 0.050 and 0.054.
- The probabilistic PGA for a 10% probability of exceedance in 50 years ranged from 0.21 to 0.32g, while PSA values ranged from 0.04 to 0.40g. The hazard maps indicated higher PGA values at a time period of 0.1 sec compared to other periods. Similarly, for a 2% probability of exceedance in 50 years, the PGA range was 0.26 to 0.38g, with PSA ranging from 0.07 to 0.48g. The maximum PGA was observed at a period of 0.1 sec, gradually decreasing beyond 0.5 sec.
- PSHA assessment yielded a cumulative design ground motion of 0.28g for a 475-year return period in the study area, with the maximum considered earthquake ground motion obtained from a 2475-year return period reaching 0.34g.
- A comparison with the Indian seismic design code (IS:1893-2002) revealed that the seismic zone factor (Z) in the study area was higher (0.33g) than the value specified for Zone IV (0.24g). This suggests that the code's provisions may underestimate seismic loading in high seismicity regions, and some areas within the Himalayan plate boundary may require higher zone factors.
- Using a fully probabilistic approach (FPSHA), the probability of slope failure under seismic loading was computed for 3160 slope models within the study area. The site-specific design ground motions triggering slope failure ranged from 0.01 to 2.1g for these models.
- The central part of the study area, characterized by the MCT and MBT faults, showed a higher seismic hazard due to a significant number of earthquakes occurring along the fault boundary region.

The study highlights the strengths and weaknesses of deterministic (DSHA) and probabilistic (PSHA) approaches. While DSHA lacks the ability to account for uncertainties and potential occurrence of new earthquakes, PSHA integrates uncertainties but does not consider topography adequately, which can lead to misleading accuracy, particularly in hilly terrain regions. The results of PSHA can be useful for general infrastructure assessments and when considering soil properties. On the other hand, the FPSHA approach developed in this study, incorporating slope topography, soil profile, material properties, and seismicity parameters, proved effective for dynamic landslide hazard assessment. The selection of scenario triggering conditions using DSHA or PSHA ground motion levels may lead to overestimation or underestimation in seismic landslide hazard assessment.

9.3 Practice recommendations

- The regional rupture character, established through the analysis of regional rupture phenomena, represents a unique trend line that remains consistent across different seismic study areas. This trend line can serve as a valuable tool for other researchers in determining the maximum magnitude for seismic faults in their respective regions.
- While there is support for deterministic seismic hazard analysis (DSHA) studies, the hazard maps derived from this approach have broader applicability for various future projects, including nuclear power plants and related facilities within the study area.
- The probabilistic seismic hazard analysis (PSHA) hazard maps, on the other hand, are suitable for seismic design in general planning purposes within the study area. These maps provide valuable insights for adopting mitigation measures and safeguarding future infrastructure from potential damage.
- The design charts developed in this study, specifically tailored for different slope models, offer practical guidance for seismic design considerations in the study region. These charts can be instrumental in ensuring the safety and stability of slopes.
- The site-specific hazard maps produced in this study serve as a valuable reference for comparison purposes. They play a crucial role in identifying areas with higher ground motions and are invaluable in the decision-making process related to site selection and planning.
- The seismic hazard maps generated from this study hold significant importance in the planning of upcoming projects and the development of pre- and post-disaster management plans. By incorporating these maps into practice, the seismic risk and potential damage resulting from future earthquakes can be effectively reduced.

9.4 Future scope

- To enhance the accuracy and refinement of the results, the implementation of a more advanced area-specific attenuation relation is recommended. This would provide a more precise characterization of the ground motion in the study area.

- The logic tree approach, incorporating multiple ground motion prediction equations (GMPE’s) with assigned weightage, can be utilized to calculate peak ground accelerations (PGA’s) in the study area. This approach allows for a comprehensive evaluation of different seismic scenarios and improves the robustness of the hazard assessments.
- Furthermore, the three hazard assessments can be expanded by considering various focal depths to better understand the influence of the focal depth on ground motions. This analysis would provide valuable insights into the variations of ground shaking patterns based on different focal depths.
- It should be noted that the design charts developed in this study are limited to slope thicknesses of up to 5. However, future research can focus on producing design charts for various slope thicknesses to cater to a wider range of slope configurations. This would enhance the applicability of the findings to a broader spectrum of slope designs.
- The improvised probabilistic technique applied in this study, which has demonstrated its efficacy within the study area's 300 km radius, holds potential for extension to other areas in the Himalayan terrain. Expanding the application of this technique would contribute to a more comprehensive understanding of seismic hazards in the region.

LIST OF PUBLICATIONS

Journals

- Neharika G.N.S. and Neelima Satyam (2022), "Deterministic and Probabilistic Seismic Hazard Analysis of Tindharia, Darjeeling Sikkim Himalaya, India", Journal of the Geological Society of India, Springer, https://doi.org/10.1007/s12594-022-2165-0, (I.F. 1.466).
- Neharika G.N.S. and Neelima Satyam (2021), "Earthquake scenario selection of Tindharia landslide in India", Journal of Engineering Geology, Indian Society of Engineering Geology (ISEG), 46(1), 91-105.
- Ganta, N.R.; Satyam, N. Investigation of Failure Mechanism of Lungchok Landslide, Sikkim (India). Preprints 2019, 2019080230 (doi:10.20944/preprints201908.0230.v1).
- G.N.S. Neharika Rao and Dr. Neelima Satyam (2021), "An updated earthquake catalogue of Tindharia, Darjeeling Sikkim Himalayas, India", Innovative Infrastructure Solutions (decision in process).

Conferences

- G.N.S. Neharika Rao and Dr. Neelima Satyam (2022), "Deterministic seismic hazard analysis of Tindharia, West Bengal, India", Indian Geotechnical Conference, GEOLEAP, Kochi, INDIA, TH11-03.
- Neharika Ganta and Neelima Satyam (2021) Landslide hazard management of Tindharia slope, West Bengal, India, NH35A-0464, AGU Fall Meeting 2021.
- Ganta N.R., Satyam N. (2021), "Probabilistic and Deterministic Analysis of Lungchok Landslide, South Sikkim, India", In: Patel S., Solanki C.H., Reddy K.R., Shukla S.K. (eds) Proceedings of the Indian Geotechnical Conference 2019. Lecture Notes in Civil Engineering, vol 133. Springer, Singapore. https://doi.org/10.1007/978-981-33-6346-5_53.
- G.N.S. Neharika Rao and Dr. Neelima Satyam (2018), "PSHA analysis at South Sikkim, Indian", Proceedings of Indian Geotechnical Conference, TH03_52.

- G.N.S. Neharika Rao and Dr. Neelima Satyam (2017), "Landslide hazard assessment of Mangan slope", Proceedings of Indian Geotechnical Conference.

References

1. Kumar, A., Anbazhagan, P., & Sitharam, T. G. (2013). Seismic hazard analysis of Lucknow considering local and active seismic gaps. Natural Hazards, 69(1), 327–350.
2. Valdiya, K. S. (1987). Himalayan Earthquakes and the Himalaya-Indian Tectonics. Tectonophysics, 134(1-2), 1-10.
3. EERI. (2012). Sikkim Earthquake of September 18, 2011: Reconnaissance Report. Retrieved from: https://www.eeri.org/images/archived/wp-content/uploads/Sikkim-EQ-report-FINAL_03-08.pdf.
4. Khattri, K. N. (1999). Earthquakes and Seismicity of the Himalayan Region. Journal of the Nepal Geological Society, 19, 175-190.
5. UNDRO (United Nations Disaster Relief Organization). (1991). Earthquake-Induced Landslides: A Report of an International Conference Held at the International Centre for Theoretical Physics, Trieste, Italy, 7-12 July 1991. UNDRO Publication Series, No. 55, Geneva.
6. Keefer, D. K. (1984). Landslides caused by earthquakes. Geological Society of America Bulletin, 95(4), 406-421.
7. Martino, S. (2017). Earthquake-induced landslides: A chain effect. Landslides and Engineered Slopes: Protecting Society through Improved Understanding, 345-353.
8. Martino, S., Battaglia, S., Delgado, J., Esposito, C., Martini, G., & Missori, C. (2018). Probabilistic Approach to Provide Scenarios of Earthquake-Induced Slope Failures (PARSIFAL) Applied to the Alcoy Basin (South Spain). Geosciences, 8, 57p.
9. Keefer, D. K. (2002). Investigating landslides caused by earthquakes—A historical review. Surveys in Geophysics, 23, 473-510.
10. Newmark, N. M. (1965). Effects of earthquakes on dams and embankments. Geotechnique, 15(2), 139-160.
11. Terzaghi, K. (1950). Mechanism of landslides. In Application of geology to engineering practice (pp. 83-123). Geological Society of America.
12. Malamud, B. D., Turcotte, D. L., Guzzetti, F., & Reichenbach, P. (2004). Landslide inventories and their statistical properties. Earth Surface Processes and Landforms, 29(6), 687-711.
13. Papadopoulos, G. A. (1999). Dynamic analysis of seismic slopes. In Proceedings of the 2nd International Conference on Earthquake Geotechnical Engineering (pp. 13-16).
14. Seed, H. B. (1979). Considerations in the earthquake resistant design of earth and rock fill dams. Geotechnique, 29(3), 213-263.
15. Bo, J., Xu, G., & Jing, L. (2001). Seismic response and dynamic stability analysis of soil slopes. Earthquake Engineering and Engineering Vibration, 21(2), 116–120.
16. Liu, C., Qi, S., Tong, L., & Zhao, F. (2004). Stability analysis of slope under earthquake with FLAC3D. Chinese Journal of Rock Mechanics and Engineering, 23(16), 2730-2733. (in Chinese).
17. Zhang, C., Liang, Q., & Chen, Z. (1997). Analysis of Slope Stability Based on Numerical Method. Rock and Soil Mechanics, 18(4), 41-46.
18. Griffiths, D. V., & Lane, P. A. (1999). Slope Stability Analysis by Finite Elements. Geotechnique, 49(3), 387-403.
19. Clough, G. W., & Chopra, A. K. (1966). Dynamic response of multidegree-of-freedom systems under random excitation. Journal of Engineering Mechanics Division, 92(EM4), 139-156.

20. Guzzetti, F., Carrara, A., Cardinali, M., & Reichenbach, P. (1999). Landslide hazard evaluation: a review of current techniques and their application in a multi-scale study, Central Italy. Geomorphology, 31, 181-216.
21. Fabbri, A. G. (2003). The challenge of the fourth dimension: data, representation, and processing issues in geomorphology. In A. G. Fabbri (Ed.), Geomorphological Processes and Landscape Change: Britain in the Last 1000 Years (pp. 47-67). Wiley.
22. Van Westen, C. J., Castellanos, E., & Kuriakose, S. L. (2008). Spatial data for landslide susceptibility, hazard, and vulnerability assessment: an overview. Engineering Geology, 102(3-4), 112-131.
23. Lee, C. T., Huang, C. C., Lee, J. F., Pan, K. L., Lin, M. L., & Dong, J. J. (2008). Statistical approach to earthquake-induced landslide susceptibility. Engineering Geology, 100, 43-58.
24. Wang, T., Liu, J., Shi, J., & Wu, S. (2017). The influence of DEM resolution on seismic landslide hazard assessment based upon the Newmark displacement method: A case study in the loess area of Tianshui, China. Environmental Earth Sciences, 76, 604.
25. Bureau of Indian Standards (BIS). (2002). IS 1893-2002 (Part 1) Indian Standard Criteria for Earthquake Resistant Design of Structures, Part 1-General Provisions and Buildings. New Delhi: Bureau of Indian Standards.
26. Reiter, L. (1990). Earthquake Hazard Analysis: Issues and Insights. Columbia University Press.
27. Kramer, S. L. (1996). Geotechnical Earthquake Engineering. Prentice-Hall.
28. Krinitzsky, E. L. (1995). Deterministic versus probabilistic seismic hazard analysis for critical structures. Engineering Geology, 40(1-2), 1-7.
29. Mualchin, L. (2011). History of modern earthquake hazard mapping and assessment in California using a deterministic or scenario approach. Pure and Applied Geophysics, 168(3-4), 383-407.
30. Wang, Z. (2011). Seismic hazard assessment: Issues and alternatives. Pure and Applied Geophysics, 168(1-2), 11-25.
31. Liu, L., Gao, Y., Liu, B., & Li, S. (2019). Preliminary seismic hazard assessment for the proposed Bohai Strait subsea tunnel based on scenario earthquake studies. Journal of Applied Geophysics, 163, 13-21.
32. Panza, G. F., Vaccari, F., & Zonno, G. (2011). Probabilistic seismic hazard assessment: A critical review of current methods and approaches. Geophysical Journal International, 186(3), 945-967.
33. Babayev, G., Khalilov, A., & Allahverdiyeva, S. (2010). Deterministic and probabilistic seismic hazard assessment for Azerbaijan. Natural Hazards, 55(2), 383-400.
34. Parvez, I. A., Vaccari, F., & Panza, G. F. (2003). A deterministic seismic hazard map of India and adjacent areas. Geophysical Journal International, 155(2), 489-508.
35. Kolathayar, S., Sitharam, T. G., & Vipin, K. S. (2012). Deterministic seismic hazard macrozonation of India. Journal of Earth System Science, 121(5), 1351-1364.
36. Sitharam, T. G., & Anbazhagan, P. (2007). Seismic hazard analysis for the Bangalore region. Natural Hazards, 40(2), 261-278.
37. Joshi, A., Rajendran, K., & Rajendran, C. P. (2007). Seismic hazard assessment for northeast India. Current Science, 93(11), 1579-1586.
38. Boominathan, A., Dodagoudar, G. R., Suganthi, A., & Maheswari, R. U. (2008). Seismic hazard assessment of Chennai city considering local site effects. Journal of Earth System Science, 117(2), 853-863.
39. Shiuly, A., & Narayan, J. P. (2012). Deterministic seismic microzonation of Kolkata city. Natural Hazards, 60, 223-240.
40. Desai, S. S., & Choudhury, D. (2014). Deterministic seismic hazard analysis for greater Mumbai, India. In Geo-congress 2014: Geotechnical special publication no. GSP 234 (pp. 389-398). ASCE.
41. Shukla, K. K., & Choudhury, D. (2012). Seismic hazard analysis for major cities of Gujarat using deterministic seismic hazard analysis (DSHA). Journal of Earth System Science, 121(2), 397-410.

42. Ramakrishnan, D., Sitharam, T. G., & Choudhury, D. (2021). Deterministic seismic hazard analysis of North and Central Himalayas. Journal of Earthquake Engineering, 25(3), 388-408.
43. Bureau of Indian Standards (BIS). (2016). IS 1893:2016 - Criteria for Earthquake Resistant Design of Structures. New Delhi, India: Bureau of Indian Standards.
44. Kanth, S. R., & Iyengar, R. N. (2007). Estimation of seismic spectral acceleration in peninsular India. Journal of Earth System Science, 116(3), 199-214.
45. Cornell, C. A. (1968). Engineering seismic risk analysis. Bulletin of the Seismological Society of America, 58(5), 1583–1606.
46. Krishna, J. (1959). Seismic zoning of India. In Proceedings of the Symposium on Earthquake Engineering (pp. 1-5).
47. West, W. D. (1937). Earthquakes in India (presidential address). Proceedings of the Indian Science Congress, 24th, Hyderabad, 189-227.
48. Tandon, A. N. (1956). Zones of India liable to earthquake damage. Indian Journal of Meteorology and Geophysics, 10, 137-146.
49. Auden, J. B. (1959). Earthquakes in relation to the Damodar Valley Project. Proc. Symp. Earthquake Eng., 1st, Univ. Roorkee, Roorkee.
50. Mithal, R. S., & Srivastava, L. S. (1959). Geotectonic position and earthquakes of Gango-Bramhaputra region. In Proc. Symp. Earthquake Eng., lst, Univ. Roorkee, Roorkee.
51. Guha, S. K. (1962). Seismic regionalization of India, Proc. Symp. Earthquake Eng., 2nd, Roorkee, 191–207.
52. Gubin, I.E. (1968). Seismic zoning of Indian peninsula. Bull. Int. Inst. Seismol. Earthquake Eng., 5, 109-139.
53. Kaila, K. L., Gaur, V. K., & Narain, H. (1972). Quantitative seismicity maps of India. Bulletin of the Seismological Society of America, 62, 1119-1132.
54. I.S.I. (1975). Indian standard recommendations for earthquake resistant design of structures. Indian Standards Institution, New Delhi, 15, 1893-1975.
55. Srivastava, L. S. (1976). Seismic zoning of India. In A. S. Arya et al. (Eds.), Earthquake Engineering (pp. 49-65). Sariska Prakashan.
56. Kaila, K. L. and Rao, M. (1979). Seismic zoning maps of Indian subcontinent. Geophys. Res. Bull., 17, 293–301.
57. Algermissen, S. T., & Perkins, D. M. (1976). A probabilistic estimate of maximum acceleration in rock in the contiguous United States. U.S. Geological Survey Open-File Report, 76-416, 45 pp.
58. Sinvhal, H., Singh, V. N., Mithal, D. K., Khattri, K. N., & Gaur, V. K. (1976). Seismic zoning of Uttar Pradesh for engineering purposes. In Symposium on Contribution of Earth Sciences towards Research and Developmental Activities in the Northern Region (pp. 1-12). Geological Survey of India.
59. Basu, S., & Nigam, N. C. (1977). Seismic risk analysis of Indian Peninsula. Proceedings of the World Conference on Earthquake Engineering, 6th, New Delhi, 2, 425–431.
60. Basu, S., & Nigam, N. C. (1978). On seismic zoning map of India. Proceedings of the Symposium on Earthquake Engineering, 4th, Roorkee, Roorkee, 1, 83–90.
61. Khattri, K. N., Rogers, A. M., Perkins, D. M., & Algermissen, S. T. (1984). A seismic hazard map of India and adjacent areas. Tectonophysics, 108, 93–134.
62. Basu, S., & Nigam, N. C. (1978). On seismic zoning map of India. Proceedings of the Symposium on Earthquake Engineering, 4th, Roorkee, Roorkee, 1, 83–90.
63. Bhatia, S. C., Kumar, M. R., & Gupta, H. K. (1999). A probabilistic seismic hazard map of India and adjoining regions. Annali di Geofisica, 42(6), 1153–1166.
64. Bureau of Indian Standards (BIS). (2002). IS 1893:2002 - Criteria for Earthquake Resistant Design of Structures (Fifth Revision). New Delhi, India: Bureau of Indian Standards.

65. Das, S., Gupta, I. D., & Gupta, V. K. (2006). A probabilistic seismic hazard analysis of Northeast India. Earthquake Spectra, 22, 1-27.
66. Joyner, W. B. and D. M. Boore (1981) Peak horizontal acceleration and velocity from strong motion records from 1979 Imperial Valley, California, earthquake, Bull. Seis. Soc. Am., 71, 2011-2038.
67. National Disaster Management Authority (NDMA) (2011) Development of probabilistic seismic hazard map of India. Technical Report, 16 March. New Delhi, India: National Disaster Management Authority.
68. Nath SK, Thingbaijam KKS, Maiti SK, Nayak A (2012) Ground-motion predictions in Shillong region, northeast India. Journal of Seismology, 16(3), 475–488.
69. Adhikari, M. D., & Nath, S. K. (2016). Site-specific Next Generation Ground Motion Prediction Models for Darjeeling-Sikkim Himalaya using Strong Motion Seismometry. In Proceedings of the International Conference on Earthquake Engineering and Disaster Mitigation (ICEEDM) (pp. 151-158).
70. Boore, D. M., & Atkinson, G. M. (2008). Ground-motion prediction equations for the average horizontal component of PGA, PGV, and 5% damped PSA at spectral periods between 0.01 s and 10.0 s. Earthquake Spectra, 24(1), 99–138.Campbell and Bozorgnia, 2003.
71. Campbell, K. W., & Bozorgnia, Y. (2003). Next generation attenuation (NGA) models for ground-motion prediction of PEER-NGA strong-motion database. Pacific Earthquake Engineering Research Center (PEER).
72. Giardini, D. (1999). The Global Seismic Hazard Assessment Program (GSHAP) - 1992/1999. Annals of Geophysics, 42(6).
73. Huo, Y., & Hu, J. (1992). Empirical attenuation relations for horizontal and vertical components of peak ground acceleration, peak ground velocity, and pseudo-relative velocity. Journal of Structural Engineering, 118(6), 1594-1608.
74. Nath, S. K., Adhikari, M. D., Maiti, S. K., Devaraj, N., Srivastava, N., & Mohapatra, L. D. (2014). Earthquake scenario in West Bengal with emphasis on seismic hazard microzonation of the city of Kolkata, India. Natural Hazards and Earth System Sciences, 14, 2549–2575. https://doi.org/10.5194/nhess-14-2549-2014.
75. Maiti, S. K., Nath, S. K., Adhikari, M. D., Srivastava, N., Sengupta, P., & Gupta, A. K. (2016). Probabilistic Seismic Hazard Model of West Bengal, India. Journal of Earthquake Engineering, DOI: 10.1080/13632469.2016.1210054.
76. Panza, G.F., La Mura, C., Peresan, A., Romanelli, F. and Vaccari, F. (2012) 'Seismic hazard scenarios as preventive tools for a disaster resilient society', Advances in Geophysics, Vol. 53, pp.93–165.
77. Magrin, A., Peresan, A., Kronrod, T., Vaccari, F., & Panza, G. (2017). Neo-deterministic seismic hazard assessment and earthquake occurrence rate. Engineering Geology, 229. doi: 10.1016/j.enggeo.2017.09.004.
78. Nayek, P.S., Gade, M. (2021). Seismic landslide hazard assessment of central seismic gap region of Himalaya for a Mw 8.5 scenario event. Acta Geophysica, 69, 747-759. doi: 10.1007/s11600-021-00572-y.
79. Ma, S., Xu, C. (2019). Assessment of co-seismic landslide hazard using the Newmark model and statistical analyses: a case study of the 2013 Lushan, China, Mw6.6 earthquake. Natural Hazards, 96, 389-412. doi: 10.1007/s11069-018-3548-9.
80. Del Gaudio, V., Wasowski, J., & Pierri, P. (2003). An Approach to Time-Probabilistic Evaluation of Seismically Induced Landslide Hazard. Bull. Seismol. Soc. Am., 93, 557–569.
81. Olsen, M.J., Ashford, S.A., Mahlingam, R., Sharifi-Mood, M., O'Banion, M., Gillins, D.T. (2015). Impacts of Potential Seismic Landslides on Lifeline Corridors; Final Report SPR 740. School of Civil and Construction Engineering, Oregon State University: Corvallis, OR, USA. p. 24.
82. Alexey, K., Yuriy, G., & Andrey, S. (2020). Hazard-Consistent Earthquake Scenario Selection for Seismic Slope Stability Assessment. Sustainability, 12, 4977.
83. Rathje, E.M., and Saygili, G. (2008). "Probabilistic seismic hazard analysis for the sliding displacement of slopes: Scalar and vector approaches." J. Geotech. Geoenviron. Eng., 134(6), 804-814.

84. Martino, S.; Battaglia, S.; D'Alessandro, F.; Della Seta, M.; Esposito, C.; Martini, G.; Pallone, F.; Troiani, F. (2019). Earthquake-induced landslide scenarios for seismic microzonation: Application to the Accumoli area (Rieti, Italy). Bull. Earthq. Eng. 2019, 1–19.
85. Medlicott, H. B. (1864). On the geological structure and relations of the southern portion of the Himalayan ranges between the Rivers Ganges and the Ravee. Memoir Geological Survey of India, 3, 102.
86. Jagabandhu Roy, Sunil Saha, Alireza Arabameri, Thomas Blaschke, & Dieu Tien Bui. (2019). A Novel Ensemble Approach for Landslide Susceptibility Mapping (LSM) in Darjeeling and Kalimpong Districts, West Bengal, India. MDPI. Remote sensing, 11, 2866.
87. Thakur, V., Mahajan, A.K., Gupta, V. (2012). "Seismotectonics of 18 September 2011 Sikkim earthquake: A component of transcurrent deformation in eastern Himalaya." Himalayan Geology, 33, 89-96.
88. Jangpangi, B. S. (1972). Some observations on the stratigraphy and reverse metamorphism in Darjeeling Hills. Himalayan Geology, 2, 356-370.
89. Mallet, F.R. (1875). On the Geology and Mineral Resources of the Darjeeling District and the Western Duars. Mem. G.S.I. 11(1): 1-72.
90. Dutta, K.K. (1950). Landslips in Darjeeling and neighbouring hillslopes, Bulletin G.S.I., 15 (1): 7-30.
91. Gansser, A. (1964). Geology of Himalayas, Inter Science Publishers, London.
92. Von, H.N. and Saxsena, A.C. (2005) Sustainable Development in Darjeeling Hills, India: Ecological and Socio-Economic Aspects for Small-Scale Farmers with Supportive Observations from Kanagawa, Japan. Dissertation, Johannes Gutenberg-Universität Mainz. [Online] Available: file:///C:/Users/DELL/Downloads/714.pdf.
93. Chakraborty, T., & Ghosh, P. (2010). Geomorphology and sedimentology of the Tista megafan, Darjeeling Himalaya: Implications for megafan building processes. Geomorphology, 115, 252-266.
94. Pal, R., Biswas, S. S., Mondal, B., & Pramanik, M. K. (2016). Landslides and floods in the Tista Basin (Darjeeling and Jalpaiguri Districts): Historical evidence, causes, and consequences.
95. Kalvoda, J. (1972). Geomorphological studies in the Himalaya with special reference to the landslides and allied phenomena. Himalayan Geology, 2, 301-316.
96. Wadia, D. N. (1975). Geology of India (5th ed.). New Delhi: Tata McGraw-Hill Publishing Company Limited.
97. Darjeeling District Survey Report. (2020). Work Order No. MDTC/PM-5/160/66.
98. Pawde, M. B., & Saha, S. S. (1982). Geology of the Darjeeling Himalayan. Geological Survey of India Miscellaneous Publications, 41(11), 50-54.
99. Bhattacharya, S. K. (2012). Landslide Disaster Perception of the AILA Cyclone in the Darjeeling Town, West Bengal, India. International Journal of Geomatics and Geosciences, 3(1), 13-29.
100. Krishnan, M. S. (1953). The structure and tectonic history of India. Memoir of the Geological Survey of India, 81.
101. Sharma, M. L., & Malik, S. (2006). Probabilistic seismic hazard analysis and estimation of spectral strong ground motion on Bedrock in North East India. In 4th International Conference on Earthquake Engineering, Taipei, Taiwan, Oct 12-13, 2006.
102. Sorkhabi, R. B., & Macfarlane, A. (1999). Himalaya and Tibet: Mountain roots to mountain top. In A. Macfarlane, R. B. Sorkhabi, & J. Quade (Eds.), Himalaya and Tibet: Mountain roots to mountain top (pp. 1-7). Geological Society of America Special paper 328.
103. Chakraborty, I., Ghosh, S., Bhattacharya, D., & Bora, A. (2011). Earthquake-induced landslides in the Sikkim-Darjeeling Himalayas - An aftermath of the 18th September 2011 Sikkim earthquake.
104. Kumar, A., Anbazhagan, P., & Sitharam, T. G. (2013). Seismic hazard analysis of Lucknow considering local and active seismic gaps. Natural Hazards, 69(1), 327-350.
105. District census handbook Darjeeling, West Bengal, Census of India 2011, Series 20, Part XII-A.
106. Yoshida, Y., Kuwano, J., & Kuwano, R. (1991). Rain-induced slope failures caused by reduction in soil strength. Soils and Foundations, 31(4), 187-193.

107. Fourie, A. B. (1996). Predicting rainfall-induced slope instability. Proceedings of the Institution of Civil Engineers - Geotechnical Engineering, 119(4), 211-218.
108. Hazra, N., & Ghosh (2001). Tea Cultivation: Comprehensive Treatise. International Book Distributing Company, Lucknow, 1-200.
109. Papazachos, B. C., Papaioannou, Ch. A., Margaris, V. N., & Theodulidis, N. P. (1992). Seismic hazard assessment in Greece based on strong motion duration. Proceedings 10WCEE, Madrid, 2, 425-430.
110. Cornell, C. A. (1968). Engineering seismic risk analysis. Bulletin of the Seismological Society of America, 58(5), 1583-1606.
111. Todorovska, M. I., & Trifunac, M. D. (1999). Liquefaction opportunity mapping via seismic wave energy. Journal of Geotechnical and Geoenvironmental Engineering, 125(12), 1032-1042.
112. Del Gaudio, V., & Wasowski, J. (2004). Time Probabilistic Evaluation of Seismically Induced Landslide Hazard in Irpinia (Southern Italy). Soil Dynamics and Earthquake Engineering, 24(12), 915-928.
113. McGuire, R. K. (1977). Seismic Design Spectra and Mapping Procedures Using Hazard Analysis Based Directly on Oscillator Response. Earthquake Engineering & Structural Dynamics, 5(3), 211-234.
114. Anderson, J. G., & Trifunac, M. D. (1977). On Uniform Risk Functionals Which Describe Strong Earthquake Ground Motion: Definition, Numerical Estimation, and an Application to the Fourier Amplitude Spectrum of Acceleration. Report CE 77-02, University of Southern California.
115. Anderson, J. G., & Trifunac, M. D. (1978). Uniform Risk Functionals for Characterization of Strong Earthquake Ground Motion. Bulletin of the Seismological Society of America, 68(1), 205-218.
116. Lee, V. W., & Trifunac, M. D. (1985). Uniform Risk Spectra of Strong Earthquake Ground Motion: NEQRISK. Report CE 85-05, University of Southern California, Los Angeles, U.S.A.
117. Todorovska, M. I., Trifunac, M. D., & Lee, V. W. (2005). Probabilistic assessment of permanent ground displacement across earthquake faults. Proceedings of the International Conference on Earthquake Engineering "Earthquake Engineering in the 21st Century—IZIIS 40 EE-21C", Skopje/Ohrid, Macedonia (on CD).
118. Stepp, J. C., Wong, I., Whitney, J., Quittmeyer, R., Abrahamson, N., Toro, G., Youngs, R., Coppersmith, K., Savy, J., & Sullivan, T. (2001). Probabilistic Seismic Hazard Analyses for Ground Motions and Fault Displacement at Yucca Mountain, Nevada. Earthquake Spectra, 17(1), 113-151.
119. American Society of Civil Engineers (ASCE). (2013). Minimum Design Loads for Buildings and Other Structures (ASCE/SEI 7-16). Reston, VA: American Society of Civil Engineers.
120. Chen, W. F., & Scawthorn, C. (2002). Earthquake Engineering Handbook. CRC Press.
121. Alexey, K., Yuriy, G., & Andrey, S. (2020). Hazard-Consistent Earthquake Scenario Selection for Seismic Slope Stability Assessment. Sustainability, 12, 4977.
122. Reiter, L. (1990). Earthquake Hazard Analysis: Issues and Insights. Columbia University Press.
123. Anderson, J. G. (1997). Benefits of Scenario Ground Motion Maps. Engineering Geology, 48(1), 43–57.
124. Krinitzsky, E. L. (2002). How to Obtain Earthquake Ground Motions for Engineering Design. Engineering Geology, 65(1), 1–16.
125. Geological Survey of India (GSI). (2000). Seismotectonic Atlas of India and its Environs.
126. Oldham, T. A. (1883). Catalogue of Indian earthquakes. Memoirs of the Geological Survey of India, 19, 163-215.
127. Oldham, R. D. (1926). The Cutch (Kachchh) earthquake of the 16th June, 1819 with a revision of the great earthquake of the 12th June, 1897, India. Geological Survey Memoir, 46, 71–147.
128. Abe, K. (1981). Magnitudes of large shallow earthquakes from 1904 to 1980. Physics of the Earth and Planetary Interiors, 27, 72–92.
129. Rao, B. R., & Rao, P. S. (1984). Historical seismicity of peninsular India. Bulletin of the Seismological Society of America, 74(6), 2519–2533.

130. Guha, S. K., & Basu, P. C. (1993). Catalogue of earthquakes (M≥3.0) in Peninsular India. Atomic Energy Regulatory Board, Tech. Document No. TD/CSE-1, 1–70.
131. Ambraseys, N. (2001). Assessment of surface-wave magnitudes of earthquakes in Greece. Journal of Seismology, 5(1), 103-116.
132. Ambraseys, N. N., & Douglas, J. (2004). Magnitude calibration of north Indian earthquakes. Geophysical Journal International, 159(1), 165–206.
133. Rajendran, C. P., Rajendran, K., Duarah, B. P., Baruah, S., & Earnest, A. (2004). Interpreting the style of faulting and paleoseismicity associated with the 1897 Shillong, northeast India, earthquake: Implications for regional tectonism. Tectonics, 23, TC4009. doi:10.1029/2003TC001605.
134. Bilham, R., & Ambraseys, N. (2005). Apparent Himalayan slip deficit from the summation of seismic moments for Himalayan earthquakes, 1500-2000. Current Science, 88, 1658–1663.
135. Das, B., Prasad, M., Shome, S., & Naskar, S. (2011). The 1897 Shillong earthquake: An analytical approach. Bulletin of the Seismological Society of America, 101(2), 847-862.
136. Kolathayar, S., Sitharam, T. G., & Vipin, K. S. (2012). Deterministic seismic hazard macrozonation of India. Journal of Earth System Science, 121(5), 1351–1364.
137. Alam, E., & Dominey-Howes, D. (2016). A catalogue of earthquakes between 810 BC and 2012 for the Bay of Bengal. Natural Hazards, 81, 2031–2102.
138. Chen, K. P., & Tsai, Y. B. (2008). A catalog of Taiwan earthquakes (1900–2006) with homogenized Mw magnitudes. Bulletin of the Seismological Society of America, 98(1), 483–489.
139. Das, R., & Wason, H. R. (2010). Comment on "A homogenous and complete earthquake catalog for Northeast India and the adjoining region" by RBS Yadav, P. Bormann, BK Rastogi, MC Das, and S.Chopra. Seismological Research Letters, 81(2), 232-234.
140. Kanamori, H. (1977). The energy release in great earthquakes. Journal of Geophysical Research, 82(20), 2981-2987.
141. Scordilis, E. M. (2006). Empirical global relations converting Ms and Mb to moment magnitude. Journal of Seismology, 10(2), 225-236.
142. Nuttli, O. W. (1983). Average seismic source parameter relations for mid-plate earthquakes. Bulletin of the Seismological Society of America, 73, 519–535.
143. Giardini D (1984). Systematic analysis of deep seismicity: 200 centroid-moment tensor solutions for earthquakes between 1977 and 1980. Journal of the Royal Astronomical Society, 77, 883–914.
144. Heaton, T. H., Tajima, T. F., & Mori, A. W. (1986). Estimating ground motions using recorded accelerograms. Survey of Geophysics, 8, 25–83.
145. Patton, H. J., & Walter, W. R. (1993). Regional moment-magnitude relations for earthquakes and explosions. Geophysical Research Letters, 20(4), 277–280.
146. Johnston, A. C. (1996). Seismic moment assessment of earthquakes in stable continental regions: Instrumental seismicity. Geophysical Journal International, 124, 381–414.
147. Papazachos, B. C., Kiratzi, A. A., & Karacostas, B. G. (1997). Toward a homogeneous moment-magnitude determination for earthquakes in Greece and the surrounding area. Bulletin of the Seismological Society of America, 87(2), 474-483.
148. Braunmiller, J., Deichmann, N., Giardini, D., Wiemer, S., & the SED Magnitude Working Group. (2005). Homogeneous moment magnitude calibration in Switzerland. Bulletin of the Seismological Society of America, 95(1), 58–74.
149. Thingbaijam, K. K. S., Nath, S. K., Yadav, A., Raj, A., Walling, M. Y., & Mohanty, W. K. (2008). Recent seismicity in northeast India and its adjoining region. Journal of Seismology, 12(1), 107-123.

150. Yadav, R. B. S., Bormann, P., Rastogi, B. K., Das, M. C., & Chopra, S. (2009). A homogeneous and complete earthquake catalog for Northeast India and the adjoining region. Seismological Research Letters, 80(4), 609-627.
151. Das, R., Wason, H. R., & Sharma, M. L. (2011). Global regression relations for conversion of surface wave and body wave magnitudes to moment magnitude. Natural Hazards, 59(2), 801–810.
152. Liu, R., Chen, Y., Ren, X., et al. (2007). Comparison between different earthquake magnitudes determined by China Seismograph Network. Acta Seismologica Sinica, 20, 497–506.
153. Deniz, A., & Yucemen, M. S. (2010). Magnitude conversion problem for the Turkish earthquake data. Natural Hazards, 55(2), 333-352.
154. Reasenberg, P. (1985). Second-order moment of central California seismicity, 1969–1982. Journal of Geophysical Research, 90(B7), 5479–5495.
155. Knopoff, L. (1964). The statistics of earthquakes in Southern California. Bulletin of the Seismological Society of America, 54(6), 1871–1873.
156. Gardner, J. K., & Knopoff, L. (1974). Is the sequence of earthquakes in Southern California, with aftershocks removed, Poissonian? Bulletin of the Seismological Society of America, 64(5), 1363-1367.
157. Uhrhammer, R. (1986). Characteristics of Northern and Central California Seismicity. Earthquake Notes, 57(1), 21.
158. Zhuang, J., Ogata, Y., & Vere-Jones, D. (2002). Stochastic declustering of space-time earthquake occurrences. Journal of the American Statistical Association, 97, 369-380.
159. Hainzl, S., Scherbaum, F., & Beauval, C. (2006). Estimating Background Activity Based on Interevent-Time Distribution. Bulletin of the Seismological Society of America, 96(1), 313–320, doi:10.1785/0120050053.
160. Marsan, D., & Lengline, O. (2008). Extending earthquake catalogues for the study of local seismicity and earthquake clustering. Bulletin of the Seismological Society of America, 98(2), 835-846.
161. Wiemer, S. (2001). A software package to analyze seismicity: ZMAP. Seismological Research Letters, 72(3), 373-382.
162. Rydelek, P. A., & Sacks, I. S. (1989). Testing the completeness of earthquake catalogues and the hypothesis of self-similarity. Nature, 337(6204), 251-253.
163. Stepp, J. C. (1972). Analysis of completeness in the earthquake sample in the Puget Sound area and its effect on statistical estimates of earthquake hazard. Proceedings of the International Conference on Microzonation, Seattle, Washington.
164. Mulargia, E., & Tinti, S. (1985). Seismic sample areas defined from incomplete catalogues: An application to the Italian territory. Physics of the Earth and Planetary Interiors, 40, 273-300.
165. Gutenberg, B., & Richter, C. F. (1944). Frequency of earthquakes in California. Bulletin of the Seismological Society of America, 34(4), 185-188.
166. Stepp, J. C. (1973). Analysis of completeness of the earthquake sample in the Puget Sound area. NOAA Tech. Report ERL 267-ESL30, Boulder, Colorado.
167. Singh, R. P., Aman, A., & Prasad, Y. J. J. (1996). Attenuation relations for strong seismic ground motion in the Himalayan region. Pure and Applied Geophysics, 147(1), 161–180.
168. Campbell, K. W., & Bozorgnia, Y. (2003). Next generation attenuation (NGA) models for ground-motion prediction of PEER-NGA strong-motion database. Pacific Earthquake Engineering Research Center (PEER).
169. NDMA. (2010). Development of probabilistic seismic hazard map of India. Technical report by National Disaster Management Authority, Government of India.
170. Nath, S. K., Raj, A., Thingbaijam, K. K. S., & Kumar, A. (2009). Ground motion synthesis and seismic scenario in Guwahati city; a stochastic approach. Seismological Research Letters, 80(2), 233–242.

171. Campbell, K. W., & Bozorgnia, Y. (2006). Campbell-Bozorgnia Next Generation Attenuation (NGA) relations for PGA, PGV and spectral acceleration: A progress report. Proceedings of the 8th U.S. National Conference on Earthquake Engineering, April 18-22, 2006, San Francisco, California, USA.
172. Zhao, J. X., Zhang, J., Asano, A., Ohno, Y., Oouchi, T., Takahashi, T., Ogawa, H., Irikura, K., Thio, H. K., Somerville, P. G., Fukushima, Y., & Fukushima, Y. (2006). Attenuation relations of strong ground motion in Japan using site classification based on predominant period. Bulletin of Seismological Society of America, 96, 898–913.
173. Atkinson, G. M., & Boore, D. M. (2011). Modifications to existing ground-motion prediction equations in light of new data. Bulletin of the Seismological Society of America, 101, 1121–1135.
174. Aki, K. (1970). Statistical analysis of seismicity. Handbook of Physical Constants, 1, 266-283.
175. Atkinson, G., & Boore, D. (2006). Ground motion prediction equations for earthquakes in eastern North America. Bulletin of Seismological Society of America, 96, 2181–2205.
176. Sharma, M. L. (1998). Attenuation relationship for estimation of peak ground horizontal acceleration using data from strong-motion arrays in India. Bulletin of the Seismological Society of America, 88(4), 1063-1069.
177. Jain, S. K., Roshan, A. D., Arlekar, J. N., & Basu, P. C. (2000). Empirical attenuation relationships for the Himalayan earthquakes based on Indian strong motion data. Proceedings of the Sixth International Conference on Seismic Zonation.
178. Jaiswal, K., & Sinha, R. (2007). Probabilistic seismic-hazard estimation for peninsular India. Bulletin of Seismological Society of America, 97(1B), 318–330.
179. Saini, S., Sharma, M. L., & Mukhopadhyay, S. (2002). Strong ground motion empirical attenuation relationship for seismic hazard estimation in the Himalaya region. In 12th Symposium on Earthquake Engineering, Roorkee, Dec. 16-18, Vol I, 143-150.
180. Nath, S. K., Vyas, M., Pal, I., & Sengupta, P. (2005). A hazard scenario in the Sikkim Himalaya from seismotectonics spectral amplification source parameterization and spectral attenuation laws using strong motion seismometry. Journal of Geophysical Research, 110, 1–24.
181. Sharma, M. L., & Bungum, H. (2006). New strong ground-motion spectral acceleration relations for the Himalayan region. In Proceedings, First European Conference on Earthquake Engineering and Seismology (ECEES), Paper 1312.
182. Das, S., Gupta, I. D., & Gupta, V. K. (2006). A probabilistic seismic hazard analysis of Northeast India. Earthquake Spectra, 22, 1-27.
183. Sharma, M. L., Douglas, J., Bungum, H., & Kotadia, J. (2009). Ground-motion prediction equations based on data from Himalayan and Zagros regions. Journal of Earthquake Engineering, 13, 1191–1210.
184. Baruah, S., Gogoi, N. K., Erteleva, Q., Aptikaev, F., & Kayal, J. R. (2009). Ground motion parameters of Shillong plateau: one of the most seismically active zones of North-eastern India. Earthquake Science, 22, 283–291.
185. Gupta, I. D. (2010). Response spectral attenuation relations for in-slab earthquakes in Indo-Burmese subduction zone. Soil Dynamics and Earthquake Engineering, 30(5), 368-377.
186. Nath, S. K., & Thingbaijam, K. K. S. (2011). Peak ground motion predictions in India: An appraisal for rock sites. Journal of Seismology, 15, 295–315.
187. Anbazhagan, P., Kumar, A., & Sitharam, T. G. (2013). Ground motion prediction equation considering combined dataset of recorded and simulated ground motions. Soil Dynamics and Earthquake Engineering, 53, 92-108.
188. Kumar, A., Suresh, G., Sitharam, T. G., & Hegde, A. V. (2017). Regional Ground Motion Prediction Equations (GMPEs) for the Himalayan Region using strong motion data. Journal of Earthquake Engineering, 21(4), 677-700. doi: 10.1080/13632469.2017.1382052.

189. Rebecca, R. (2017). Seismic Hazard and Structural Stability on Hill Slopes of North East India (Doctoral dissertation). IIT Delhi, India.
190. Bajaj, K., & Anbazhagan, P. (2019). Regional stochastic GMPE with available recorded data for active region – Application to the Himalayan region. Soil Dynamics and Earthquake Engineering, 126, 105825.
191. Kundu, P. K. (2019). Effect of rainfall and earthquake on landslides of Darjeeling Himalayas (Doctoral dissertation). IIT Delhi.
192. Youngs, R. R., Chiou, S. J., Silva, W. J., & Humphrey, J. R. (1997). Strong ground motion relationship for subduction earthquakes. Seismological Research Letters, 68, 58-73.
193. Ambraseys, N., Douglas, J. S., Sarma, K., & Smit, P. M. (2005). Equation for the estimation of strong ground motions from shallow crustal earthquakes using data from Europe and the Middle East: Horizontal peak ground acceleration and the spectral acceleration. Bulletin of Earthquake Engineering, 3, 1-53.
194. Kanno, T., Narita, A., Morikawa, N., Fujiwara, H., & Fukushima, Y. (2006). A new attenuation relation for strong ground motion in Japan based on recorded data. Bulletin of the Seismological Society of America, 96, 879–897.
195. Zhao, J. X., Zhang, J., Asano, A., Ohno, Y., Oouchi, T., Takahashi, T., Ogawa, H., Irikura, K., Thio, H. K., Somerville, P. G., & Fukushima, Y. (2006). Attenuation relations of strong ground motion in Japan using site classification based on predominant period. Bulletin of the Seismological Society of America, 96, 898-913.
196. Campbell, K. W., & Bozorgnia, Y. (2008). NGA ground motion model for the geometric mean horizontal component of PGA, PGV, PGD, and 5% damped linear elastic response spectra for periods ranging from 0.01 to 10 s. Earthquake Spectra, 24(1), 139–171.
197. Idriss, I. M., & An NGA. (2008). Empirical model for estimating the horizontal spectral values generated by shallow crustal earthquakes. Earthquake Spectra, 16, 363–372.
198. Akkar, S., & Bommer, J. J. (2010). Empirical equations for the prediction of PGA, PGV and spectral acceleration in Europe, the Mediterranean region and the Middle East. Seismological Research Letters, 81, 195–206.
199. Delavaud, E., Scherbaum, F., Kuehn, N., & Riggelsen, C. (2009). Information-theoretic selection of ground-motion prediction equations for seismic hazard analysis: An applicability study using Californian data. Bulletin of the Seismological Society of America, 99, 3248–3263.
200. Nath, S. K., & Thingbaijam, K. K. S. (2011). Peak ground motion predictions in India: An appraisal for rock sites. Journal of Seismology, 15, 295–315.
201. Toro, G. R. (2002). Modification of the Toro et al. (1997) attenuation equations for large magnitudes and short distances, Risk Engineering Inc. unpublished report. Available at: http://citeseerx.ist.psu.edu/viewdoc/download?doi=10.1.1.535.1566&rep=rep1&type=pdf.
202. Olympa Baro, Abhishek Kumar & Alik Ismail-Zadeh (2018). Seismic hazard assessment of the Shillong Plateau, India. Geomatics, Natural Hazards and Risk, 9(1), 841-861. DOI: 10.1080/19475705.2018.1494043.
203. Iyengar, R. N., Roshan, A. D., Arlekar, J. N., & Basu, P. C. (2004). Microzonation of Earthquake Hazard in Greater Delhi Area. Current Science, 87(9), 1193–1202.
204. Abrahamson, N. A., & Silva, W. J. (2008). Summary of the Abrahamson & Silva NGA ground-motion relations. Earthquake Spectra, 24(1), 67-97.
205. Acton, G., Anbazhagan, P., Raghukanth, S. T. G., & Sitharam, T. G. (2011). Empirical correlation of Vs30 with NEHRP site classes for the Darjeeling-Sikkim Himalayas, India. Journal of Earth System Science, 120(5), 901-912.
206. Bajaj, K., and Anbazhagan, P. (2019). Regional stochastic GMPE with available recorded data for active region - Application to the Himalayan region. Soil Dynamics and Earthquake Engineering, 126, 105825.
207. Jalayer, F. (2017, March 28). Climate change and Urban Vulnerability in Africa: Assessing vulnerability of urban systems, population and goods in relation to natural and man-made disasters in Africa [PowerPoint slides].

Training on the job course on Hazards, Risk and (Bayesian) multi-risk assessment. Retrieved from https://slideplayer.com/slide/746214/

208. Anbazhagan P, Aditya P and Rashmi HN. Amplification based on shear wave velocity for seismic zonation: comparison of empirical relations and site response results for shallow engineering bedrock sites. Geomechanics and Engineering, 3(3), 189–206. DOI: 10.12989/gae.2011.3.3.189.
209. Building Seismic Safety Council (BSSC; 2003). National earthquake hazards reduction program recommended provisions and commentary for seismic regulations for new buildings and other structures (FEMA450), part 1: Provisions, Federal Emergency Management Agency, Washington D.C., 356 p.
210. Naik, S. K., & Choudhury, D. (2014). Ground motion prediction equations for Goa, India, using probabilistic seismic hazard analysis. Natural Hazards, 70(3), 1877-1894. DOI: 10.1007/s11069-013-1007-y.
211. Iyengar, R.N. and Ghosh, S. (2004). Microzonation of Earthquake Hazard in Greater Delhi Area. Current Science, 87(9), 1193–1202.
212. Joshi, G. C., & Sharma, M. L. (2008). Uncertainties in the estimation of Mmax. Journal of Earth System Science, 117(Suppl 2), 671-682.
213. Wheeler, R. L. (2009). Methods of Mmax estimation east of the Rocky Mountains. U.S. Geological Survey Open-File Report 2009-1018. Retrieved from http://pubs.usgs.gov/of/2009/1018/pdf/OF09-1018.pdf.
214. Budnitz, R. J., Apostolakis, G., Boore, D. M., Cluff, L. S., Coppersmith, K. J., Cornell, C. A., & Morris, P. A. (1997). Recommendations for probabilistic seismic hazard analysis—guidance on uncertainty and use of experts. U.S. Nuclear Regulatory Commission NUREG/CR–6372, 1-109.
215. Tocher, D. (1958). Earthquake energy and ground breakage, Bulletin of the Seismological Society of America, 48, 147-153.
216. Mark, R. K. (1977). Application of linear statistical model of earthquake magnitude versus fault length in estimating maximum expectable earthquakes. Geology, 5, 464-466.
217. Slemmons, D.B. (1984). Dixie Valley-Fairview Peak earthquake areas, in Lintz, J., Jr., ed., Western Geological Excursions, Geological Society of America Field Trip Guidebook, 4, 418-420.
218. Slemmons, D. B., Bodin, P., & Zang, X. (1989). Determination of earthquake size from surface faulting events. In Proceedings of the International Seminar on Seismic Zonation (pp. 13). Guangzhou, China: State Seismological Bureau.
219. Hanks, T. C. and H. Kanamori (1979). A moment-magnitude scale, Journal of Geophysical Research, 84, 2348-2350.
220. Singh SK, Bazan E, Esteva L (1980) Expected earthquake magnitude from a fault. Bulletin of the Seismological Society of America, 70, 903–914.
221. Bonilla, M. G., Mark, R. K., & Lienkaemper, J. J. (1984). Statistical relations among earthquake magnitude, surface rupture length, surface rupture displacement. Bulletin of the Seismological Society of America, 74, 379–411.
222. Nowroozi, A. A. (1985). Empirical relations between magnitudes and fault parameters for earthquakes in Iran. Bulletin of the Seismological Society of America, 75, 1327-1338.
223. Wells D.L, Coppersmith KJ (1994) New empirical relationships among magnitude, rupture length, rupture width, rupture area, and surface displacement. Bulletin Seismology Society of America, 84(4), 975–1002.
224. Papastamatiou, D. (1980). Incorporation of Crustal Deformation to Seismic Hazard Analysis. Bulletin of the Seismological Society of America, 70, 1321-1335.
225. Anderson, J. G., and Luco, J. E. (1983). Consequences of Slip Rate Constraints on Earthquake Occurrence Relation. Bulletin of the Seismological Society of America, 73, 471-496.
226. WGCEP (Working Group on Central California Earthquake Probabilities). (1995). Seismic hazard in Southern California: probable earthquakes 1994 to 2024. Bulletin of the Seismological Society of America, 85, 379–439.

227. Stein, R. S., & Hanks, T. C. (1998). M 6 Earthquakes in Southern California During the Twentieth Century: No Evidence for a Seismicity or Moment Deficit. Bulletin of the Seismological Society of America, 88, 635-652.
228. Field, D. H., Jackson, D. D., & Dolan, J. F. (1999). A Mutually Consistent Seismic-Hazard Source Model for Southern California. Bulletin of the Seismological Society of America, 89, 559-578.
229. Jin, A., & Aki, K. (1988). Spatial and temporal correlation between coda Q and seismicity in China. Bulletin of the Seismological Society of America, 78, 741-769.
230. Slemmons, D. B. (1982). Determination of design earthquake magnitudes for microzonation. In Proceedings of the Third International Earthquake Microzonation Conference (Vol. 1, pp. 119-13). Washington, D.C.: U.S. National Science Foundation.
231. Markropoulos, K. C., & Burton, P. W. (1983). Seismic risk of circum-pacific earthquakes I. Strain energy release. PAGEOPH, 121(2), 247-267.
232. Markropoulos, K. C., & Burton, P. W. (1985). Seismic hazard in Greece I. Magnitude recurrence. Tectonophysics, 117, 205-257.
233. Kijko, A., & Singh, M. (2011). Statistical tool for maximum possible earthquake magnitude estimation. Acta Geophysica, 59, 674-700.
234. Anbazhagan, P., Bajaj, K., Moustafa, S. S. R., & Al-Arifi, N. S. N. (2015). Maximum magnitude estimation considering the regional rupture character. Bulletin of the Seismological Society of America, 105(3), 1547-1562.
235. Anbazhagan, P., Bajaj, K., Moustafa, S. S. R., & Al-Arifi, N. S. N. (2013). Estimation of maximum magnitude for seismogenic sources in the study area using regional rupture characteristics.
236. Anbazhagan, P., Smitha, C. V., & Kumar, A. (2014). Representative seismic hazard map of Coimbatore, India. Engineering Geology, 171, 81-95.
237. Anbazhagan, P., Bajaj, K., Moustafa, S. S. R., & Al-Arifi, N. S. (2014). Maximum magnitude estimation considering the regional rupture characteristics. Journal of Seismology.
238. Baker, J. W. (2008). An introduction to probabilistic seismic hazard analysis (PSHA). White Paper, Version 1.3, Stanford University.
239. Musson, R. M. W. (2000). The use of Monte Carlo simulations for seismic hazard assessment in the U.K. Annals of Geophysics, 43, 1-9.
240. Mulargia, F., Stark, P. B., & Geller, R. J. (2017). Why is Probabilistic Seismic Hazard Analysis (PSHA) still used? Physics of the Earth and Planetary Interiors, 264, 63-75.
241. Weichert, D. H. (1980). Estimation of the earthquake recurrence parameters for unequal observation periods for different magnitudes. Bulletin of the Seismological Society of America, 70(4), 1337-1346.
242. McGuire, R. K., & Arabasz, W. J. (1990). Earthquake recurrence and earthquake forecasting: A review. In T. D. Hanks (Ed.), Earthquake monitoring and seismic hazard mitigation in Balkan countries (pp. 31-58). Springer.
243. Campbell, K. W. (1985). Near-source attenuation of peak horizontal acceleration. Bulletin of the Seismological Society of America, 75(5), 1307-1335.
244. Raghukanth, S. T. G., & Iyengar, R. N. (2007). Estimation of seismic spectral acceleration in Peninsular India. Journal of Earth System Science, 116(3), 199–214.
245. Bazzurro, P., & Cornell, C. (1999). Disaggregation of seismic hazard. Bulletin of the Seismological Society of America, 89.
246. Nayak, M., & Sitharam, T. G. (2019). Estimation and spatial mapping of seismicity parameters in western Himalaya, central Himalaya and Indo-Gangetic plain. Journal of Earth System Science, 128, 45.
247. Sreevalsa, K., Sitharam, T. G., & Vipin, K. S. (2011). Spatial variation of seismicity parameters across India and adjoining area. Natural Hazards.
248. Shankar, D., & Sharma, M. L. (1998). Estimation of Seismic Hazard parameters in the Himalayas and its vicinity from its complete data files. Pure and Applied Geophysics, 152, 267–279.

249. Wiemer, S., & Wyss, M. (2000). Minimum magnitude of completeness in earthquake catalogs: Examples from Alaska, the western US, and Japan. Bulletin of the Seismological Society of America, 90, 859-869.

250. Chernick, M. R. (1999). Bootstrap methods: A practitioner's guide. Wiley.

251. Ghosh, B., Pappin, J. W., So, M. M. L., & Hicyilmaz, K. M. O. (2012). Seismic Hazard Assessment in India. Arup, United Kingdom, Arup, Hong Kong, Arup, Dubai.

252. Jibson, R. W., Harp, E. L., & Michael, J. A. (2000). A method for producing digital probabilistic seismic landslide hazard maps. Engineering Geology, 58, 271-289.

253. Romeo, R. (2000). Seismically induced landslide displacements: A predictive model. Engineering Geology, 58, 337-351.

254. Mandal, S. (2015). Assessing cohesion, friction angle, and slope instability in the Shivakhola watershed of Darjeeling Himalaya. International Research Journal of Earth Sciences, 3(8).

255. Vinay, K. P., & Naval, K. T. (2022). Angle of repose and slope stabilization in Himalaya. International Research Journal of Modernization in Engineering, Technology, and Science, 3(9).

256. Taylor, D. W. (1937). Stability of earth slopes. Journal of the Boston Society of Civil Engineers, 24, 197-246.

257. Bishop, A. W. (1955). The use of slip circle in the stability analysis of slopes. Geotechnique, 5(1), 7-17.

258. Morgenstern, N. R. (1963). Stability of slopes in cohesive materials. Canadian Geotechnical Journal, 1(4), 163-173.

259. Rao, K. S. (2020). Characterization, Modeling and Engineering of Rocks and Rockmasses. Indian Geotechnical Journal, 50(1), 1-95.

260. Ghosh, B. (2011). Seismic Hazard Assessment in India. In Proceedings of the 15th World Conference on Earthquake Engineering (15WCEE), Lisbon, Portugal.

261. Roy, N., Kumar, A., & Rao, S. (2021). Stability Analysis of Failed Slope in Tindharia Region, West Bengal, India — A Case Study. Journal of the Geological Society of India, 97, 887-892.

262. Bojadjieva, J., Sheshov, V., & Bonnard, C. (2018). Hazard and risk assessment of earthquake-induced landslides - case study. Landslides, 15, 161-171.

1.
2.
3. mon DB (1977) State of the art for assessing earthquake hazard in
4. the United States, Report 6; faults and earthquake magnitude:
5. U.S. Army Corps of Engineers, Waterways Experiment Station,
6. Vicksburg, Mississippi, Miscellaneous Paper S-73-1, 129 p
7. Slemmon DB (1977) State of the art for assessing earthquake hazard in
8. the United States, Report 6; faults and earthquake magnitude:
9. U.S. Army Corps of Engineers, Waterways Experiment Station,
10. Vicksburg, Mississippi, Miscellaneous Paper S-73-1, 129 p
11. Slemmon DB (1977) State of the art for assessing earthquake hazard in
12. the United States, Report 6; faults and earthquake magnitude:
13. U.S. Army Corps of Engineers, Waterways Experiment Station,
14. Vicksburg, Mississippi, Miscellaneous Paper S-73-1, 129 p

Annexure-A

Refined earthquake catalogue of Darjeeling Sikkim Himalayas

S.No	longitude	latitude	year	month	day	magnitude	Depth
1	86.616	27.707	2008	1	17	4.1	20
2	90.554	25.844	2014	2	5	4.1	20
3	86.357	26.609	2014	2	8	4.1	20
4	88.199	28.772	2017	10	10	4.1	20
5	90.187	28.01	2017	10	28	4.1	20
6	88.494	26.801	2019	1	17	4.1	20
7	90.842	25.943	2019	10	30	4.1	20
8	87.818	27.899	2010	9	28	4.2	71
9	86.381	26.488	2012	1	18	4.2	36.6
10	90.853	26.197	2007	9	7	4.2	35
11	86.697	28.591	2013	6	24	4.2	35
12	90.648	25.722	2007	11	5	4.2	34
13	87.225	28.281	2014	3	18	4.2	34
14	90.782	26.176	2010	8	29	4.2	20
15	86.018	27.82	2010	11	30	4.2	20
16	86.453	27.555	2019	1	10	4.2	20

17	89.432	25.646	2019	5	22	4.2	20
18	89.573	27.348	2020	4	26	4.2	20
19	90.189	25.778	2011	10	4	4.2	10
20	90.358	25.456	2018	7	21	4.2	10
21	87.624	27.985	2006	4	11	4.3	55.1
22	89.575	27.125	2001	2	9	4.3	35
23	90.589	26.098	2014	7	27	4.3	24
24	87.049	25.645	2017	6	21	4.3	22.7
25	88.704	27.635	2004	3	14	4.3	22
26	89.96	26.47	1996	5	28	4.3	20
27	90.564	27.207	2003	6	26	4.3	20
28	88.88	28.866	2007	3	22	4.3	20
29	89.784	25.781	2017	9	18	4.3	20
30	90.275	25.826	2020	9	19	4.3	20
31	89.112	27.086	2008	11	9	4.3	17
32	88.882	26.994	2014	11	25	4.3	17
33	88.348	27.402	2019	4	12	4.3	14.9
34	86.345	28.557	2000	9	6	4.4	105.4
35	86.462	28.442	2007	4	6	4.4	95.2
36	87.307	27.895	2011	4	15	4.4	50
37	88.791	25.001	2011	7	28	4.4	46.7
38	88.304	28.526	1999	9	8	4.4	35
39	86.958	28.168	2003	9	10	4.4	35
40	90.858	25.897	2010	6	13	4.4	35
41	86.105	28.374	2018	5	25	4.4	28
42	90.245	25.793	2009	7	6	4.4	24
43	87.29	27.486	2009	5	14	4.4	22.8
44	90.037	26.139	1998	2	15	4.4	20
45	87.974	28.134	2004	6	17	4.4	20
46	90.937	26.966	2009	9	22	4.4	20
47	88.595	28.768	2010	9	25	4.4	20
48	85.972	27.522	2019	2	26	4.4	20
49	89.818	26.418	2009	6	1	4.4	17.7
50	88.905	28.067	2005	11	25	4.4	10
51	87.26	28.134	2013	2	5	4.4	10
52	87.205	28.069	2012	1	28	4.4	1
53	86.393	28.576	1998	3	21	4.5	57
54	89.493	29.148	1997	8	10	4.5	35
55	87.052	27.578	2005	7	27	4.5	35
56	88.89	25.587	2018	4	26	4.5	35
57	87.004	28.323	2003	3	28	4.5	34
58	89.684	26.916	1998	3	16	4.5	33
59	86.254	28.515	1999	6	13	4.5	33
60	89.948	25.809	2003	7	5	4.5	27.1
61	88.167	27.494	2000	1	25	4.5	22
62	90.656	25.509	2004	8	12	4.5	20

63	89.39	26.09	2009	7	13	4.5	20
64	89.733	27.745	2010	12	3	4.5	20
65	87.47	29.126	2019	12	29	4.5	20
66	87.298	28.29	2017	11	20	4.5	19.6
67	86.316	27.676	2018	3	2	4.5	17
68	86.595	27.787	2005	10	14	4.5	10
69	86.841	27.939	2012	3	18	4.5	10
70	88.901	27.077	2019	1	16	4.5	10
71	88.371	24.301	2019	9	3	4.5	10
72	87.568	28.12	1997	8	17	4.6	68
73	87.805	27.758	2010	3	27	4.6	68
74	88.139	27.175	2010	10	5	4.6	36
75	88.769	25.196	1999	9	21	4.6	35
76	89.52	27.069	2004	2	17	4.6	35
77	90.355	27.575	2008	2	23	4.6	35
78	89.119	26.403	1994	1	16	4.6	33
79	87.546	26.905	2003	7	8	4.6	33
80	89.225	26.968	2001	7	3	4.6	31.7
81	90.546	26.272	2011	11	8	4.6	28.1
82	87.22	27.909	2009	9	9	4.6	25.3
83	89.384	26.689	2011	11	11	4.6	23.2
84	89.952	25.402	1997	7	20	4.6	20
85	89.525	29.272	2002	11	16	4.6	20
86	86.56	27.567	2020	4	15	4.6	20
87	89.667	26.702	2020	12	15	4.6	20
88	86.146	28.264	2010	2	27	4.6	19
89	87.074	27.972	2017	3	19	4.6	18
90	88.838	27.017	2012	5	23	4.6	17
91	89.243	26.961	2016	3	12	4.6	17
92	89.276	27.724	2013	6	6	4.6	10
93	89.191	27.053	2020	4	26	4.6	10
94	87.825	28.145	1998	7	31	4.7	71
95	86.51	28.731	2009	2	24	4.7	68.8
96	86.514	28.648	2008	9	19	4.7	59.9
97	86.672	28.599	2018	3	25	4.7	57
98	90.079	25.478	1997	1	22	4.7	35
99	90.536	26.137	1997	9	13	4.7	35
100	90.03	25.719	2001	1	16	4.7	35
101	90.56	25.683	2002	3	24	4.7	35
102	87.885	28.73	2002	11	17	4.7	35
103	87.468	27.774	2002	7	16	4.7	33
104	89.721	26.18	2006	8	31	4.7	29
105	89.728	27.015	2008	7	6	4.7	22.3
106	90.54	25.42	1974	9	21	4.7	20
107	87.816	27.259	2020	9	11	4.7	20
108	85.772	27.613	1997	11	26	4.7	19

109	86.269	27.293	2011	8	15	4.7	15.9
110	88.702	26.878	1996	3	23	4.7	10
111	90.944	27.329	2004	11	24	4.7	10
112	90.227	26.557	2014	5	30	4.7	10
113	89.114	26.916	2017	3	7	4.7	10
114	90.262	25.923	2004	8	4	4.8	61.7
115	86.929	28.566	2008	4	1	4.8	60.7
116	86.079	26.633	1995	1	29	4.8	56.9
117	90.569	25.842	1992	4	20	4.8	54.7
118	86.883	28.651	2000	9	6	4.8	50
119	90.7	26.267	2013	7	12	4.8	48.2
120	88.293	27.142	2011	2	10	4.8	44.1
121	89.178	26.922	2009	11	7	4.8	41.1
122	90.676	25.529	2006	6	19	4.8	40.9
123	90.368	28.604	1998	5	13	4.8	35
124	86.627	27.605	2002	5	2	4.8	35
125	90.529	25.881	2005	9	12	4.8	35
126	89.298	26.843	2006	7	17	4.8	35
127	90.124	25.162	2006	12	20	4.8	35
128	88.411	24.349	2008	7	5	4.8	35
129	86.265	27.527	1995	12	24	4.8	33
130	88.282	28.458	1996	2	12	4.8	33
131	86.464	27.455	1998	9	4	4.8	33
132	87.423	28.007	2002	10	29	4.8	33
133	89.986	26.137	2002	10	24	4.8	32
134	90.308	27.522	2014	11	17	4.8	31.87
135	90.202	25.83	2009	2	15	4.8	25.1
136	90.507	25.953	2003	2	15	4.8	24
137	89.89	28.53	1999	9	10	4.8	22
138	88.539	24.738	1999	4	14	4.8	20
139	89.682	27.877	2019	10	29	4.8	20
140	86.144	27.673	1997	10	11	4.8	19
141	89.516	25.432	2015	8	28	4.8	13.7
142	89.03	25.35	2013	2	19	4.8	11.8
143	89.655	25.811	2000	6	20	4.8	10
144	87.609	28.515	2003	2	25	4.8	10
145	88.609	28.584	2003	9	22	4.8	10
146	88.171	27.327	2017	5	16	4.8	10
147	87.27	29.291	2019	2	7	4.8	10
148	88.326	28.411	2020	7	29	4.8	10
149	86.932	27.196	2007	8	3	4.9	64
150	87.622	27.913	2007	2	6	4.9	58.9
151	87.838	28.338	2016	4	19	4.9	55.92
152	90.687	26.138	1996	2	17	4.9	50
153	87.135	28.27	2013	8	4	4.9	35.51
154	90.774	25.956	1987	12	11	4.9	35

155	88.119	28.798	2003	11	30	4.9	35
156	87.857	28.033	2021	2	9	4.9	35
157	87.626	25.382	1983	12	23	4.9	33
158	85.891	27.603	1994	6	25	4.9	33
159	86.498	27.733	1997	10	11	4.9	33
160	87.852	27.656	2000	3	13	4.9	33
161	87.742	26.861	2001	9	27	4.9	32.5
162	89.24	26.27	2007	8	11	4.9	20
163	89.703	26.003	2014	7	22	4.9	16.03
164	86.92	27.258	2019	1	22	4.9	10
165	90.545	26.129	2020	12	10	4.9	10
166	85.872	27.955	2021	10	18	4.9	10
167	88.237	27.286	2017	12	2	4.9	7.2
168	87.873	28.166	2019	11	27	5	64.7
169	88.474	27.42	2018	6	17	5	49.76
170	89.745	27.082	1985	10	2	5	45.9
171	86.846	28.494	1996	1	25	5	34
172	86.812	28.817	1978	10	23	5	33
173	87.223	28.696	1996	1	25	5	33
174	86.886	28.554	1998	3	15	5	33
175	85.813	27.785	2000	1	20	5	33
176	89.973	25.894	1995	8	8	5	30
177	90.182	27.519	2017	5	24	5	28.39
178	90.25	25.596	2003	12	6	5	26.7
179	90.156	25.875	1996	8	18	5	17.8
180	90.741	26.313	1979	4	2	5	10
181	88.999	28.959	2008	5	25	5	10
182	90.886	26.055	2018	9	25	5	10
183	87.421	28.452	2018	5	10	5	4.66
184	86.187	28.447	2012	11	5	5.1	77.8
185	86.507	28.647	1992	8	9	5.1	57
186	90.446	27.683	2009	11	18	5.1	43.9
187	86.733	28.287	1964	1	25	5.1	40
188	89.051	27.308	1987	10	22	5.1	35
189	90.466	27.474	2005	3	11	5.1	35
190	90.23	25.419	1993	3	3	5.1	33
191	88.553	27.142	2017	3	26	5.1	24.39
192	85.953	27.849	1966	1	11	5.1	19
193	87.882	27.25	2018	6	20	5.1	13.9
194	89.875	26.132	2018	1	20	5.1	11.47
195	89.521	26.301	2004	5	27	5.1	10
196	88.863	25.566	2015	10	13	5.1	10
197	86.343	27.647	2019	5	25	5.1	10
198	88.309	27.343	2021	7	25	5.1	10
199	90.693	25.659	2017	12	11	5.1	1.7
200	87.173	28.422	2019	6	17	5.2	84.75

201	89.335	26.956	1982	8	18	5.2	35
202	86.958	27.413	1992	4	1	5.2	35
203	90.563	25.719	1995	5	9	5.2	35
204	86.089	27.486	1984	1	25	5.2	33
205	90.763	26.419	1989	6	11	5.2	33
206	86.059	26.81	1993	7	9	5.2	33
207	88.148	28.872	1997	9	18	5.2	33
208	86.449	28.347	2003	2	26	5.2	33
209	90.262	26.066	2016	10	23	5.2	24.31
210	90.39	25.52	2010	9	11	5.2	20
211	86.02	27.719	2001	4	3	5.2	19.3
212	90.457	25.875	1994	4	15	5.2	17.4
213	86.74	28.456	2012	8	9	5.3	70.2
214	87.102	27.991	1987	4	23	5.3	47.6
215	86.082	27.244	1997	3	3	5.3	44.8
216	87.195	28.155	1971	10	24	5.3	35
217	88.588	26.89	1972	11	6	5.3	35
218	90.144	25.68	1985	6	17	5.3	35
219	86.457	28.426	1995	3	29	5.3	35
220	90.663	27.074	2012	7	10	5.3	35
221	88.48	27.23	2000	3	10	5.3	34.27
222	86.811	28.523	1993	7	3	5.3	34
223	89.252	25.468	1996	1	3	5.3	33
224	88.341	27.199	1998	9	10	5.3	33
225	90.29	25.987	1966	4	23	5.3	23.3
226	85.847	27.647	1976	9	12	5.3	19
227	89.563	26.589	2013	12	4	5.3	13.6
228	87.691	26.517	1988	8	29	5.3	10
229	88.87	27.97	2002	2	5	5.3	10
230	87.561	28.227	2004	2	27	5.4	78.5
231	87.897	28.253	2005	3	26	5.4	54.7
232	88.631	27.235	2008	12	25	5.4	49.2
233	87.419	27.636	2005	8	28	5.4	38.8
234	85.86	27.516	1988	4	11	5.4	38.5
235	88.255	27.314	1975	1	23	5.4	33
236	90.213	25.759	1980	6	11	5.4	33
237	88.791	25.794	1979	4	11	5.4	31.2
238	90.018	26.548	2009	10	29	5.4	30.4
239	89.282	27.032	1964	3	27	5.4	25.5
240	90.404	26.192	1971	10	31	5.4	24
241	87.717	27.366	1964	2	1	5.4	21
242	90.616	26.486	2001	2	27	5.4	20.2
243	89	24.5	1897	6	13	5.4	20
244	90	28	1912	11	1	5.4	20
245	86.377	27.221	2006	2	3	5.4	19.3
246	86.093	27.613	1968	10	28	5.4	19

247	85.931	27.739	2004	1	3	5.4	17.1
248	88.418	26.116	1977	6	5	5.4	16.7
249	88.15	27.402	1979	11	16	5.4	10
250	86.092	27.738	2005	2	8	5.4	10
251	89.04	29.369	1973	8	1	5.5	91.6
252	88.325	26.93	1986	1	7	5.5	69.6
253	89.331	27.264	2003	3	25	5.5	47.1
254	90.425	25.339	1967	1	30	5.5	41.4
255	88.324	26.029	1978	10	14	5.5	35
256	87.737	27.344	2007	8	11	5.5	35
257	88.791	25.099	1991	8	7	5.5	33
258	88.552	27.433	1996	9	25	5.5	33
259	86.638	27.435	1996	12	30	5.5	33
260	90.19	26.147	1959	5	24	5.5	20
261	88.238	27.292	2007	5	20	5.5	10.3
262	90.785	26.339	2020	2	8	5.5	10
263	87.433	28.815	2021	11	5	5.5	10
264	89.981	27.497	1969	11	5	5.6	35
265	89.752	27.038	1981	2	9	5.6	33
266	90.315	25.91	1982	7	6	5.6	33
267	88.171	27.15	2001	12	2	5.6	33
268	87.924	28.128	1992	4	4	5.6	31.4
269	87	25	1866	5	23	5.6	20
270	87.757	27.823	1996	4	26	5.6	17.6
271	90.297	26.488	1960	7	29	5.6	15
272	87.878	27.298	1972	8	21	5.6	10
273	87.85	27.74	1998	11	26	5.7	60.8
274	87	27.5	1938	1	29	5.7	35
275	86.993	28.135	1973	3	22	5.7	33
276	87.294	27.473	1975	6	24	5.7	33
277	85.963	27.834	1978	10	4	5.7	33
278	88.71	25.586	1970	7	25	5.7	27.7
279	88.051	27.373	2008	12	2	5.7	24.7
280	88.324	27.198	1988	9	27	5.7	24.2
281	87	25	1842	5	21	5.7	20
282	90.559	26.432	1968	8	18	5.7	19.7
283	88.08	26.835	2015	4	27	5.7	19.6
284	85.897	27.603	1970	2	26	5.7	19
285	90.817	27.223	1950	2	26	5.7	15
286	88.941	27.186	2021	4	5	5.7	10
287	87.161	28.817	2001	4	28	5.8	22.3
288	90.575	25.949	1951	4	7	5.8	15
289	87.477	26.659	1979	6	19	5.8	12.7
290	85.876	27.846	2020	9	15	5.8	10
291	90.35	25.96	2021	7	7	5.8	10
292	90.08	27.579	1964	4	13	5.9	35

293	88.393	27.363	2006	2	14	5.9	26.8
294	90.347	26.568	2015	6	28	5.9	24.4
295	86.761	28.47	2010	2	26	6	74.7
296	88.149	28.135	1990	1	9	6	61.8
297	86.631	28.778	1986	1	10	6	59.6
298	89.1	25.33	1834	7	8	6	20
299	86.685	28.925	1951	5	28	6	15
300	90.177	26.355	2018	9	12	6	14.1
301	86.068	27.785	1974	3	24	6.1	24
302	87.317	28.39	2015	4	25	6.1	10
303	87.308	28.59	2020	3	20	6.1	10
304	86.961	27.823	1998	9	3	6.1	8.6
305	87.474	28.978	1993	3	20	6.4	15.1
306	89.25	28.75	1935	5	21	6.5	140
307	88.783	27.36	1980	11	19	6.5	43.5
308	87.829	27.383	1965	1	12	6.5	22.8
309	88.154	27.804	2011	9	18	7	29.6
310	90	25.4	1885	1	1	7.3	15
311	90.177	25.929	1930	7	2	7.5	15
312	90.3	26	1933	3	6	7.6	15
313	86.8	26.7	1988	8	21	7.8	15
314	86.126	27.801	2015	5	12	7.9	12.3
315	86.5	27.5	1833	8	26	8	15
316	86.588	26.885	1934	1	15	8.5	15

Annexure-B

Prepared ANBU-13 GMPE Attenuation table. atn file (used in RCRISIS Software)

4	8.5	11							
0.5	300	11	4						
0	0.28	0	0						
114.81	89.952	64.881	50.342	41.331	35.240	30.844	27.515	24.901	22.788
54	53	36	99	45	36	7	72	14	85
143.88	113.30	82.116	63.879	52.522	44.825	39.259	35.039	31.721	29.039
97	61	51	1	64	16	96	74	93	49
179.79	142.39	103.76	80.959	66.682	56.973	49.938	44.596	40.391	36.988
03	54	55	72	36	53	92	19	08	25
223.89	178.48	130.88	102.46	84.568	72.349	63.474	56.721	51.399	47.088
94	58	22	76	07	83	55	68	51	24
277.79	223.06	164.73	129.48	107.11	91.780	80.607	72.088	65.363	59.909
7	34	88	42	63	33	39	33	56	41
343.26	277.85	206.85	163.32	135.47	116.28	102.25	91.535	83.054	76.166
31	17	6	54	83	79	85	18	7	68
422.27	344.82	259.03	205.57	171.06	147.13	129.56	116.10	105.43	96.753
2	31	35	93	04	17	84	52	5	89
516.97	426.20	323.37	258.14	215.56	185.85	163.94	147.08	133.69	122.78
96	15	62	49	76	23	11	91	94	43
629.70	524.45	402.31	323.26	271.04	234.32	207.09	186.07	169.32	155.63
46	63	47	96	9	1	49	45	42	84
762.90	642.28	498.61	403.58	339.94	294.79	261.11	235.00	214.12	197.01
62	65	64	24	37	14	71	3	36	91
919.16	782.59	615.38	502.11	425.12	369.95	328.52	296.23	270.31	249.01
28	78	58	94	35	26	23	05	18	42
0.1	0.31	0	0						
116.82	96.087	73.396	59.273	50.098	43.686	38.940	35.271	32.341	29.940
34	37	14	21	28	37	13	81	7	22

143.0842	118.8876	91.73973	74.51279	63.19555	55.23137	49.30847	44.71536	41.03731	38.01694
173.8213	146.1003	114.0888	93.30518	79.46568	69.64342	62.29641	56.57519	51.9794	48.19616
209.2651	178.1532	141.0367	116.2881	99.54076	87.53176	78.48547	71.40484	65.69495	60.98032
249.5054	215.365	173.1441	144.1233	124.1098	109.581	98.54278	89.84889	82.80463	76.96639
294.4842	257.9086	210.8898	177.4561	153.8905	136.5335	123.2112	112.639	104.0232	96.8497
344.0142	305.7918	254.6203	216.8637	189.5871	169.1568	153.2865	140.5787	130.1504	121.4197
397.8214	358.8655	304.5092	262.7986	231.8344	208.1969	189.5789	174.5136	162.0485	151.5436
455.603	416.8597	360.5397	315.5367	281.1364	254.3169	232.8585	215.284	200.603	188.1343
517.0874	479.442	422.5173	375.1461	337.8097	308.0313	283.7889	263.6626	246.6654	232.0999
582.0852	546.2858	490.1167	441.4868	401.9466	369.6476	342.8574	320.2814	300.982	284.2755
0.2	0.318	0	0						
119.0307	97.26044	73.61174	59.01055	49.58601	43.03389	38.20481	34.48623	31.52548	29.10578
145.6386	120.2698	91.99846	74.19347	62.56851	54.42884	48.40085	43.74306	40.02493	36.98015
176.6755	147.6652	114.3685	92.90069	78.6887	68.65048	61.17232	55.36927	50.72201	46.90681
212.313	179.8317	141.2886	115.7507	98.56252	86.29326	77.08658	69.90454	64.12999	59.37453
252.5656	217.0277	173.2789	143.3754	122.8547	108.0203	96.79084	87.97443	80.85106	74.96223
297.2866	259.3481	210.7606	176.3766	152.2473	134.543	120.9998	110.2843	101.5749	94.34103
346.192	306.7078	254.0038	215.2704	187.3938	166.5852	150.47	137.6015	127.0673	118.2678
398.9099	358.8542	303.0875	260.4289	228.8606	204.8326	185.9576	170.7219	158.1441	147.566
455.044	415.4102	357.8853	312.0279	277.0625	249.8686	228.1605	210.4193	195.6286	183.0899
514.2382	475.9399	418.0849	370.0191	332.2069	302.107	277.6487	257.3795	240.2909	225.6706
576.2287	540.0213	483.2421	434.1353	394.26	361.7339	334.7946	312.1256	292.7739	276.0448
0.3	0.298	0	0						
97.17884	81.90293	64.70734	53.67674	46.33702	41.10847	37.17645	34.09633	31.60716	29.54595
119.5928	101.684	81.04524	67.56351	58.49832	51.99843	47.08886	43.23087	40.10571	37.51312
146.1407	125.5034	101.0663	84.75711	73.65099	65.62406	59.5282	54.71931	50.81243	47.5639
177.1948	153.8677	125.3855	105.8958	92.42191	82.58934	75.07269	69.11448	64.25626	60.2052
213.053	187.2367	154.6288	131.6704	115.5144	103.5879	94.39728	87.06944	81.06778	76.0457

253.929	225.9946	189.3987	162.7981	143.6921	129.3949	118.2717	109.3402	101.9854	95.80462
299.9589	270.4313	230.2364	199.9865	177.7507	160.8478	147.5486	136.7799	127.8543	120.3147
351.2258	320.7416	277.5888	243.8908	218.479	198.8141	183.1394	170.3217	159.6158	150.5162
407.797	377.0441	331.7883	295.0723	266.6117	244.1472	225.9757	210.9469	198.2813	187.4376
469.7671	439.4184	393.0547	353.9679	322.7825	297.6348	276.9587	259.6391	244.8929	232.1616
537.2982	507.9533	461.5213	420.8813	387.4893	359.9487	336.9038	317.3272	300.4679	285.7736
0.4	0.298	0	0						
76.03471	65.84085	53.9627	46.07008	40.67434	36.74815	33.74398	31.3561	29.40192	27.76575
94.43821	82.42538	68.09462	58.39741	51.69758	46.79029	43.01868	40.01124	37.54413	35.47464
116.5406	102.6302	85.5798	73.79107	65.5414	59.44996	54.74246	50.97381	47.873	45.26585
142.7975	127.0024	107.0412	92.88986	82.83465	75.33698	69.50359	64.81068	60.93504	57.66691
173.6455	156.0893	133.1439	116.4065	104.2989	95.16455	87.99957	82.20084	77.39003	73.31873
209.4977	190.4205	164.5734	145.1119	130.7406	119.748	111.041	103.9433	98.02201	92.98882
250.7512	230.4986	202.0111	179.8114	163.0336	149.9945	139.5477	130.9583	123.7446	117.5802
297.8077	276.8013	246.1134	221.3164	202.0927	186.8821	174.5339	164.2787	155.5979	148.1325
351.1031	329.8002	297.5017	270.4173	248.8418	231.4293	217.0823	205.0294	194.7332	185.8124
411.1421	389.9915	356.7698	327.8655	304.1818	284.6587	268.3083	254.3945	242.3847	231.8899
478.5321	457.9361	424.5088	394.3737	368.9707	347.5633	329.3199	313.5763	299.8296	287.7013
0.5	0.292	0	0						
59.82701	51.96695	42.66928	36.42625	32.13616	29.00632	26.60822	24.70078	23.13933	21.83191
75.27003	66.02775	54.77012	47.03364	41.64381	37.6775	34.62058	32.17878	30.1735	28.49025
93.88796	83.27103	69.89897	60.45418	53.76363	48.78723	44.92352	41.82076	39.26234	37.10796
116.0302	104.143	88.60479	77.27813	69.09364	62.92644	58.09463	54.18856	50.95139	48.21452
142.0177	129.0667	111.4487	98.14374	88.30528	80.77605	74.81202	69.95121	65.89743	62.45306
172.1518	158.4316	138.9778	123.7114	112.1237	103.0943	95.84816	89.88417	84.87222	80.58763
206.7363	192.5994	171.7046	154.6332	141.2979	130.6923	122.0517	114.8572	108.7558	103.5013
246.1098	231.9252	210.1003	191.5253	176.5667	164.3995	154.3164	145.8085	138.5161	132.1811
290.6807	276.793	254.6072	234.9554	218.6272	205.0251	193.5409	183.7062	175.1741	167.6875

340.9592	327.6574	305.6732	285.4509	268.1215	253.3271	240.5886	229.5033	219.7576	211.11
397.5826	385.0829	363.7985	343.5328	325.6468	310.0024	296.2597	284.0989	273.2553	263.5163
0.6	0.299	0	0						
56.71389	49.08404	40.06063	34.01523	29.87312	26.86004	24.55768	22.73094	21.23896	19.99231
71.50929	62.56736	51.65137	44.15021	38.93246	35.10048	32.15323	29.80381	27.8781	26.26456
89.29264	79.07961	66.1538	57.00218	50.51852	45.70019	41.96396	38.96782	36.50091	34.42656
110.3466	99.00543	84.06953	73.12613	65.2022	59.22828	54.54909	50.76886	47.63864	44.99473
134.9151	122.689	105.8915	93.10613	83.61187	76.33067	70.5576	65.85106	61.92633	58.59276
163.2174	150.4279	132.0764	117.524	106.4068	97.7106	90.71544	84.94996	80.10096	75.95401
195.4761	182.4846	163.0257	146.9258	134.2416	124.0964	115.7991	108.8722	102.987	97.9122
231.9523	219.1156	199.0863	181.7969	167.7286	156.2009	146.5966	138.4607	131.4665	125.3768
272.9804	260.6113	240.5732	222.5561	207.4103	194.6814	183.862	174.5481	166.4345	159.2919
318.9962	307.3384	287.8113	269.5767	253.7553	240.1144	228.2765	217.9095	208.748	200.584
370.5564	359.7747	341.187	323.2306	307.1824	292.9985	280.4309	269.2296	259.181	250.1094
0.8	0.296	0	0						
39.60923	35.2044	29.76009	25.95702	23.27152	21.27331	19.71887	18.46728	17.43224	16.55801
50.87964	45.7164	39.10312	34.34693	30.92832	28.35554	26.33844	24.70506	23.34846	22.19875
64.69565	58.82419	50.99745	45.17374	40.89696	37.63265	35.04805	32.93996	31.17938	29.6808
81.39736	74.93304	65.93747	58.98213	53.74357	49.67638	46.41678	43.73401	41.47781	39.5467
101.3379	94.4522	84.43544	76.36106	70.1023	65.14469	61.11315	57.75824	54.91235	52.45962
124.9048	117.8036	107.0099	97.92373	90.65552	84.76591	79.89446	75.78717	72.26666	69.2068
152.5506	145.4453	134.1875	124.2921	116.1107	109.3146	103.585	98.68094	94.42611	90.69084
184.8251	177.9068	166.5234	156.0963	147.1843	139.5865	133.0478	127.3572	122.3518	117.9068
222.4077	215.8284	204.6393	193.9956	184.6035	176.3855	169.1607	162.761	157.0475	151.909
266.1342	260.0002	249.2722	238.7218	229.1341	220.5335	212.8114	205.8473	199.533	193.7775
317.0226	311.3957	301.3252	291.1364	281.6328	272.9106	264.9218	257.5903	250.8402	244.6031
1	0.3	0	0						
26.47289	23.65361	20.08326	17.54239	15.72957	14.37265	13.31324	12.45827	11.75017	11.15151
34.391	31.138	26.834	23.657	21.338	19.575	18.184	17.053	16.111	15.311

79		78	74	16	53	84	84	6	28
44.104	40.491	35.482	31.625	28.730	26.489	24.697	23.226	21.990	20.935
22	48	52	56	67	53	75	14	79	18
55.833	51.978	46.365	41.839	38.333	35.557	33.302	31.427	29.838	28.470
17	03	11	63	18	67	51	51	4	02
69.822	65.864	59.818	54.704	50.601	47.269	44.510	42.182	40.186	38.451
17	44	24	42	08	57	65	78	64	33
86.360	82.440	76.176	70.621	65.998	62.139	58.873	56.071	53.635	51.493
36	23	08	31	12	04	91	68	39	18
105.80	102.04	95.789	89.989		80.682	76.958	73.702	70.826	68.265
92	72	92	27	84.983	24	62	32	86	15
128.62	125.11	119.06	113.22	108.01	103.40	99.326	95.685	92.415	89.461
66	16	19	62	46	89	51	44	98	13
155.38	152.17	146.48	140.80	135.58	130.83	126.53	122.62	119.05	115.77
66	34	53	86	1	74	63	41	08	27
186.79	183.91	178.68	173.31	168.24	163.53	159.17	155.13	151.37	147.88
72	03	4	97	78	61	39	22	9	45
223.71	221.15	216.44	211.49	206.71	202.18	197.90	193.88	190.08	186.50
87	95	5	61	42	2	86	28	74	42
1.2	0.298	0	0						
21.174	19.082	16.375	14.411	12.992	11.920	11.078	10.395	9.8272	9.3453
79	65	19	24	15	52	39	31	62	68
27.748	25.355	22.109	19.657	17.839	16.441	15.330	14.420	13.658	13.009
25	55	97	8	1	79	3	64	94	26
35.860	33.239	29.500	26.542	24.279	22.504	21.069	19.882	18.879	18.018
78	18	04	23	62	01	94	76	84	32
45.724	42.972	38.844	35.413	32.696	30.509	28.711	27.200	25.910	24.792
84	95	18	81	3	9	19	99	9	69
57.586	54.812	50.444	46.631	43.494	40.899	38.718	36.856	35.244	33.832
44	45	75	21	72	75	91	97	85	01
71.749	69.053	64.617	60.557	57.088	54.132	51.588	49.375	47.429	45.701
72	01	89	45	55	24	81	84	76	93
88.601	86.059	81.719	77.572	73.897	70.671	67.828	65.303	63.044	61.010
04	25	41	02	67	94	26	43	88	21
108.63	106.29	102.18	98.102	94.367	90.995	87.951	85.192	82.680	80.381
02	42	09	09	55	66	27	3	21	91
132.44	130.34	126.54	122.66	119.00	115.62	112.49	109.61	106.93	104.44
96	53	79	58	93	38	87	08	53	94
160.81	158.94	155.51	151.91	148.45	145.17	142.08	139.18	136.44	133.87
36	68	37	79	1	16	5	19	9	24
194.64	193.00	189.95	186.69	183.48	180.40		174.64	171.95	169.39
12	41	01	09	96	8	177.46	5	76	05
1.4	0.303	0	0						
18.311	16.613	14.389	12.755	11.564	10.659	9.9441	9.3614	8.8750	8.4611
21	71	12	66	77	42	55	56	92	85
24.138	22.199	19.534	17.493	15.965	14.782	13.836	13.058	12.404	11.844
65	8	46	98	77	95	6	4	18	25
31.388	29.268	26.203	23.745	21.844	20.340	19.118	18.101	17.237	16.493
15	63	75	16	37	58	24	04	92	7
40.282	38.063	34.689	31.845	29.566	27.717	26.184	24.890	23.779	22.813
38	77	48	33	62	05	71	7	88	04
51.085	48.855	45.298	42.148	39.527	37.338	35.484	33.891	32.505	31.284
7	59	67	54	31	31	61	95	57	92
64.127	61.964	58.365	55.026	52.140	49.657	47.503	45.617	43.949	42.460

59	79	97	5	47	31	85	5		12
79.826	77.791	74.280	70.884	67.843		62.752	60.611	58.684	56.938
29	06	64	76	25	65.148	83	39	11	53
98.710	96.841	93.522	90.195	87.119	84.318	81.768	79.442	77.312	75.351
76	64	21	61	7	09	98	99	15	92
121.44	119.75	116.69	113.54	110.54	107.74	105.14	102.72	100.46	98.363
24	82	77	12	27	47	35	42	97	66
148.83	147.34	144.57	141.65	138.82	136.12	133.57	131.15	128.86	126.69
9	3	69	88	52	68	13	39	58	79
181.90	180.58	178.12	175.48	172.87	170.34	167.91	165.58	163.34	161.19
27	83	57	28	18	45	41	18	46	82
1.6	0.306	0	0						
14.692	13.315	11.485	10.129	9.1364	8.3809	7.7843	7.2987	6.8941	6.5503
1	51	76	28	92	71	23	93	35	35
19.376	17.842	15.689	14.014	12.748	11.763	10.973	10.323	9.7764	9.3083
88	41	83	66	49	66	7	34	02	84
25.140	23.513	21.102	19.124	17.572	16.333	15.319	14.472	13.752	13.130
19	86	82	53	52	16	63	82	38	11
32.128	30.485	27.917	25.693	23.875	22.380	21.129	20.065	19.146	18.344
41	61	52	18	88	46	3	12	71	1
40.524	38.934	36.328	33.950	31.925	30.204	28.728	27.446	26.321	25.324
2	63	1	34	61	99	37	47	41	32
50.565	49.082	46.549	44.128	41.983	40.101	38.442	36.970	35.654	34.469
55	4	43	5	88	57	79	62	32	09
62.561	61.217	58.845	56.486	54.322	52.363	50.592	48.985		46.178
68	75	69	98	15	62	41	1	47.52	36
76.906	75.715	73.559	71.346	69.253	67.308	65.507	63.837	62.287	60.844
11	62	86	5	26	21	08	97	83	36
94.089	93.052	91.138	89.124	87.172	85.317	83.565	81.910	80.347	78.869
53	72	71	08	23	67	03	4	42	19
114.71	113.82	112.15	110.36	108.59	106.88	105.24	103.66	102.15	100.71
48	3	32	25	48	52	24	72	76	03
139.51	138.75	137.31	135.75	134.18	132.65	131.16	129.71	128.30	126.94
59	57	77	41	9	45	07	05	41	06
1.8	0.313	0	0						
13.369	12.133	10.477	9.2429	8.3361	7.6445	7.0977	6.6523	6.2809	5.9653
37	07	65	86	41	75	23	52	69	36
17.647	16.281	14.347	12.829	11.675	10.775	10.051	9.4550	8.9525	8.5220
7	4	08	32	98	76	97	81	17	87
22.900	21.467	19.321	17.542	16.137	15.009	14.083	13.308	12.646	12.074
51	67	44	65	2	27	54	02	87	92
29.258	27.828	25.568	23.589	21.958	20.607	19.471	18.502	17.663	16.928
79	39	41	02	03	35	82	35	16	02
36.889	35.522	33.257	31.167	29.371	27.833	26.506	25.348	24.328	23.421
61	3	31	57	48	88	55	75	62	56
46.013	44.752	42.579	40.481	38.604	36.944	35.471	34.157	32.976	31.909
3	64	97	04	22	04	44	31	81	59
56.917	55.787	53.778	51.761	49.894	48.191	46.642	45.227	43.931	42.739
1	57	49	63	32	99	2	63	62	47
69.966	68.976	67.171	65.304	63.524	61.859	60.307	58.861	57.511	56.248
3	13	83	4	73	45	64	38	31	29
85.615	84.761	83.177	81.498	79.861	78.296	76.809	75.398	74.059	72.787
65	56	02	34	52	88	93	85	52	18
104.42	103.69	102.32	100.85	99.387	97.964	96.591	95.268	93.995	92.769

31	5	64	12	45	77	27	4	18	69
127.06	126.45	125.28	124.00	122.72	121.46	120.23	119.03	117.86	116.72
77	21	42	95	82	71	48	41	55	88
2	0.31	0	0						
11.426	10.238	8.6053	7.3723	6.4675	5.7829	5.2471	4.8160	4.4607	4.1625
86	03	93	16	9	03	95	1	98	35
14.422	13.252	11.524	10.123	9.0403	8.1896	7.5052	6.9424	6.4708	6.0693
73	2	57	17	26	58	79	69	56	43
17.717	16.642	14.947	13.472	12.268	11.282	10.462	9.7710	9.1790	8.6661
41	37	38	4	5	35	73	08	31	67
21.288	20.357	18.805	17.366	16.127	15.067	14.156	13.364	12.669	12.055
6	57	3	04	21	92	2	22	85	78
25.149	24.379	23.038	21.726	20.543	19.489	18.551	17.711	16.956	16.273
57	73	28	8	33	74	23	6	44	61
29.345	28.730	27.622	26.494	25.435	24.459	23.562	22.738	21.977	21.275
26	32	8	24	41	37	64	03	93	32
33.943	33.464	32.580	31.652	30.754	29.903	29.100	28.345	27.633	26.962
66	44	69	05	2	09	77	35	77	74
39.028	38.661	37.972	37.233	36.503	35.795	35.115	34.462	33.836	33.236
28	18	98	8	19	79	48	75	9	77
44.693	44.415	43.888	43.314	42.737	42.170	41.616	41.077	40.554	40.045
67	73	8	2	31	15	59	88	28	59
51.043	50.835	50.436	49.996	49.550	49.107	48.670		47.819	47.405
84	05	22	81	88	76	7	48.241	17	38
58.192	58.036	57.736	57.404	57.064	56.724	56.387	56.052	55.721	55.395
55	51	96	66	95	91	09	58	89	26

Annexure-C

Seismic hazard curves, Uniform hazard response spectrum and De-aggregation charts at each grid point within the study area

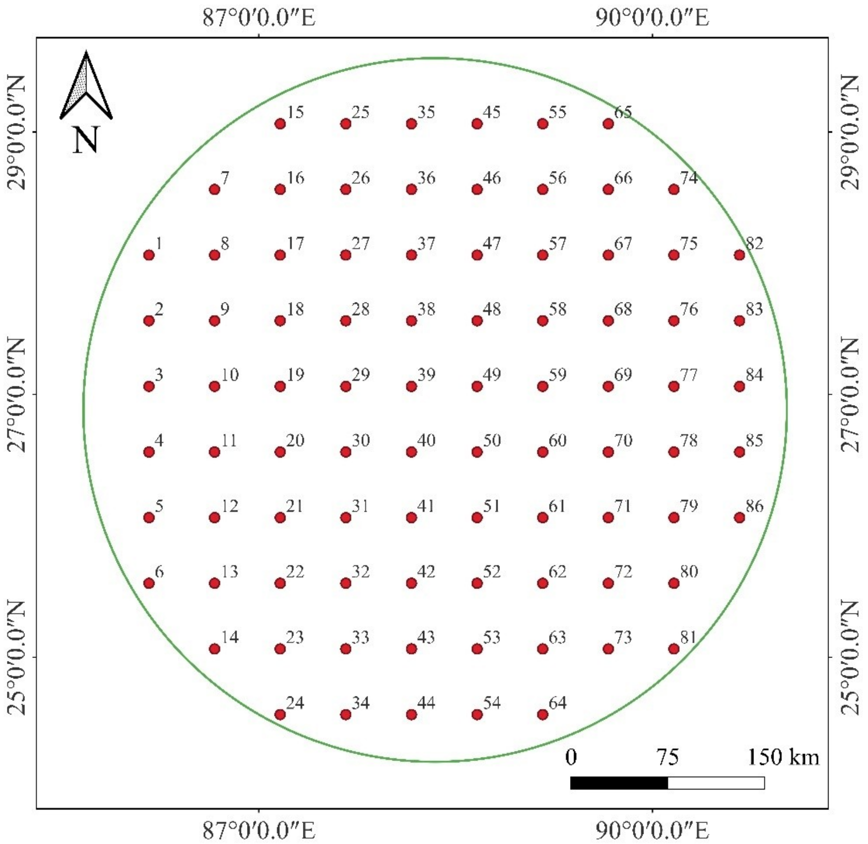
87°0′0.0″E
90°0′0.0″E
29°0′0.0″N
27°0′0.0″N
25°0′0.0″N
N
15 25 35 45 55 65
7 16 26 36 46 56 66 74
1 8 17 27 37 47 57 67 75 82
2 9 18 28 38 48 58 68 76 83
3 10 19 29 39 49 59 69 77 84
4 11 20 30 40 50 60 70 78 85
5 12 21 31 41 51 61 71 79 86
6 13 22 32 42 52 62 72 80
14 23 33 43 53 63 73 81
24 34 44 54 64
0 75 150 km

Grid 1

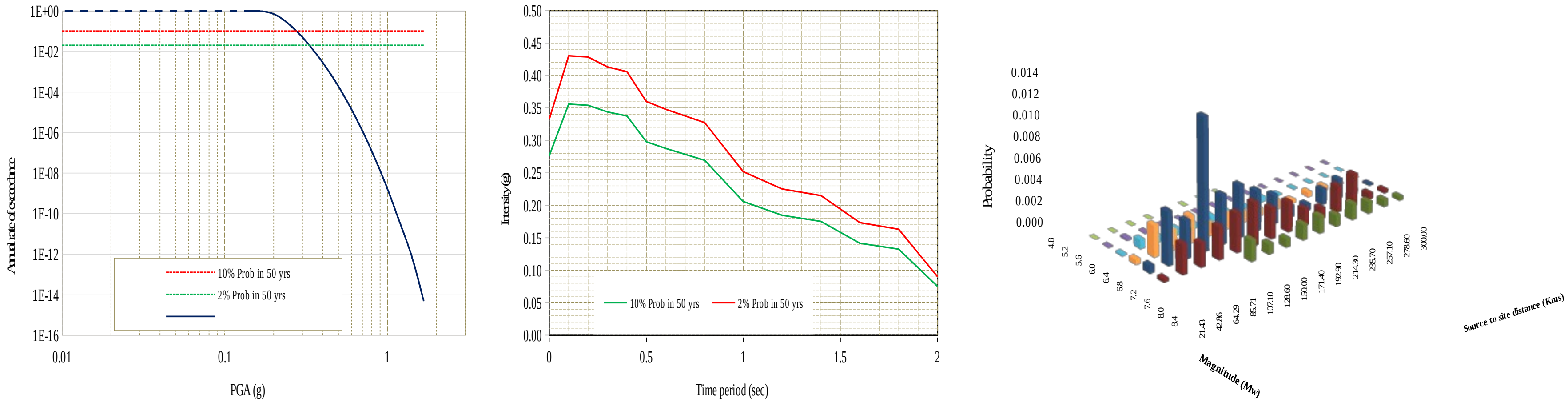
1E+00
1E-02
1E-04
1E-06
1E-08
1E-10
1E-12
1E-14
1E-16
0.01
0.1
1
PGA (g)
10% Prob in 50 yrs
2% Prob in 50 yrs
0.50
0.45
0.40
0.35
0.30
0.25
0.20
0.15
0.10
0.05
0.00
0
0.5
1
1.5
2
Intensity (g)
Time period (sec)
10% Prob in 50 yrs
2% Prob in 50 yrs
0.014
0.012
0.010
0.008
0.006
0.004
0.002
0.000
Probability
Magnitude (Mw)
Source to site distance (Kms)

Grid 2

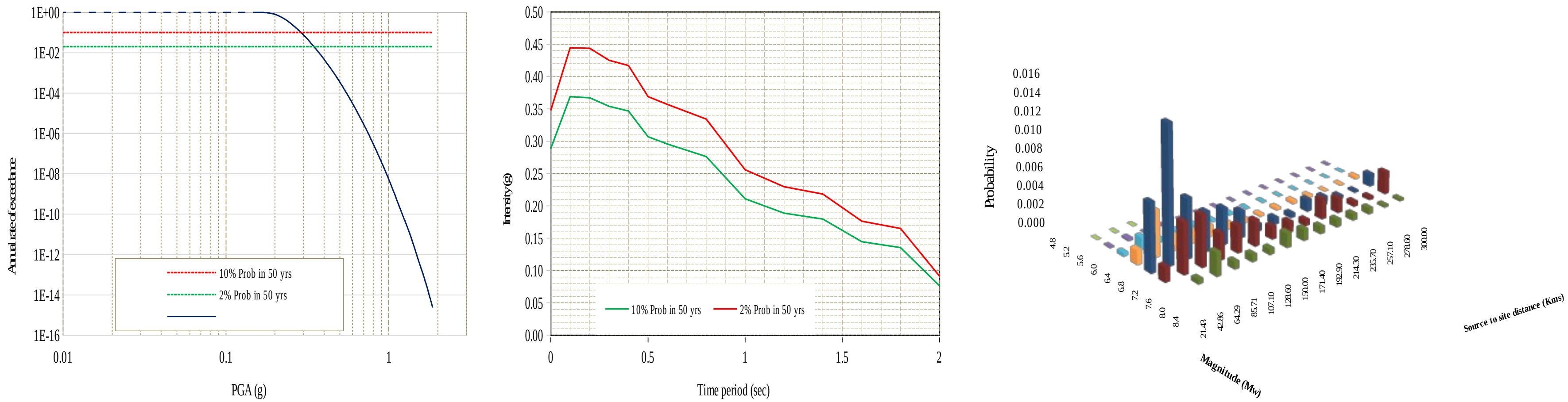
1E+00
1E-02
1E-04
1E-06
1E-08
1E-10
1E-12
1E-14
1E-16
0.01
0.1
1
PGA (g)
10% Prob in 50 yrs
2% Prob in 50 yrs
0.50
0.45
0.40
0.35
0.30
0.25
0.20
0.15
0.10
0.05
0.00
0
0.5
1
1.5
2
Intensity (g)
Time period (sec)
10% Prob in 50 yrs
2% Prob in 50 yrs
0.016
0.014
0.012
0.010
0.008
0.006
0.004
0.002
0.000
Probability
Magnitude (Mw)
Source to site distance (Kms)

Grid 3

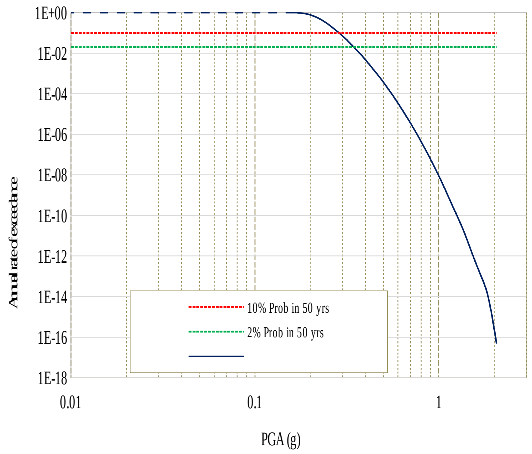

1E+00
1E-02
1E-04
1E-06
1E-08
1E-10
1E-12
1E-14
1E-16
1E-18
0.01
0.1
1
PGA (g)
10% Prob in 50 yrs
2% Prob in 50 yrs

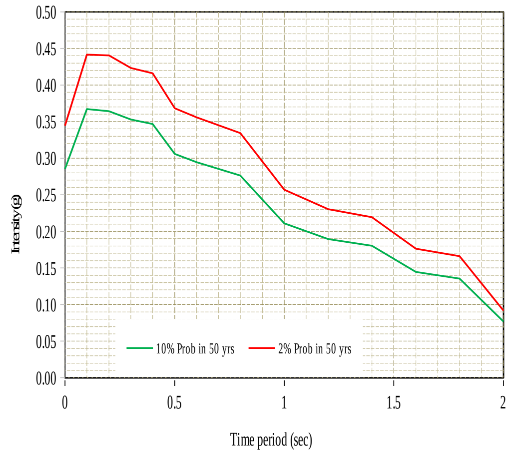

0.50
0.45
0.40
0.35
0.30
0.25
0.20
0.15
0.10
0.05
0.00
0
0.5
1
1.5
2
Intensity (g)
Time period (sec)
10% Prob in 50 yrs
2% Prob in 50 yrs

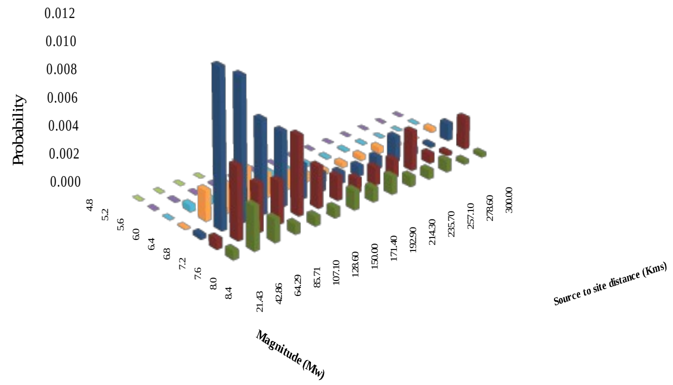

Probability
0.012
0.010
0.008
0.006
0.004
0.002
0.000
Magnitude (Mw)
Source to site distance (Kms)

Grid 4

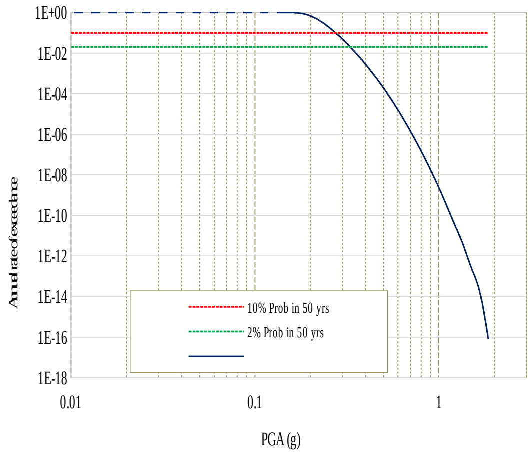

1E+00
1E-02
1E-04
1E-06
1E-08
1E-10
1E-12
1E-14
1E-16
1E-18
0.01
0.1
1
PGA (g)
10% Prob in 50 yrs
2% Prob in 50 yrs

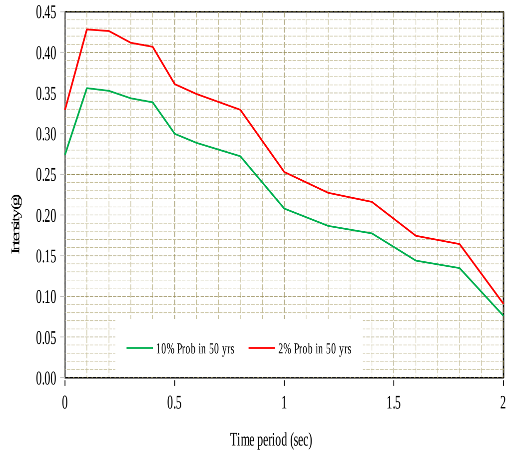

0.45
0.40
0.35
0.30
0.25
0.20
0.15
0.10
0.05
0.00
0
0.5
1
1.5
2
Intensity (g)
Time period (sec)
10% Prob in 50 yrs
2% Prob in 50 yrs

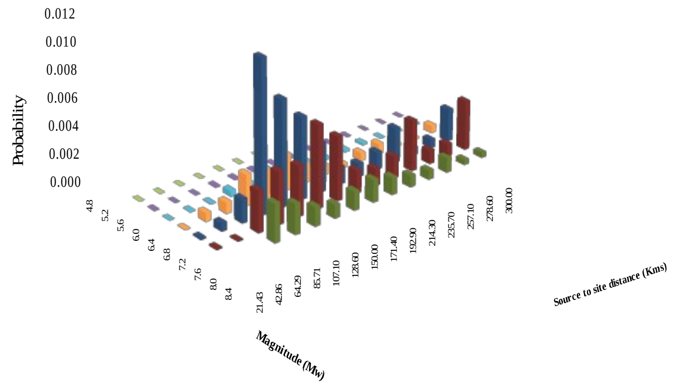

Probability
0.012
0.010
0.008
0.006
0.004
0.002
0.000
Magnitude (Mw)
Source to site distance (Kms)

Grid 5

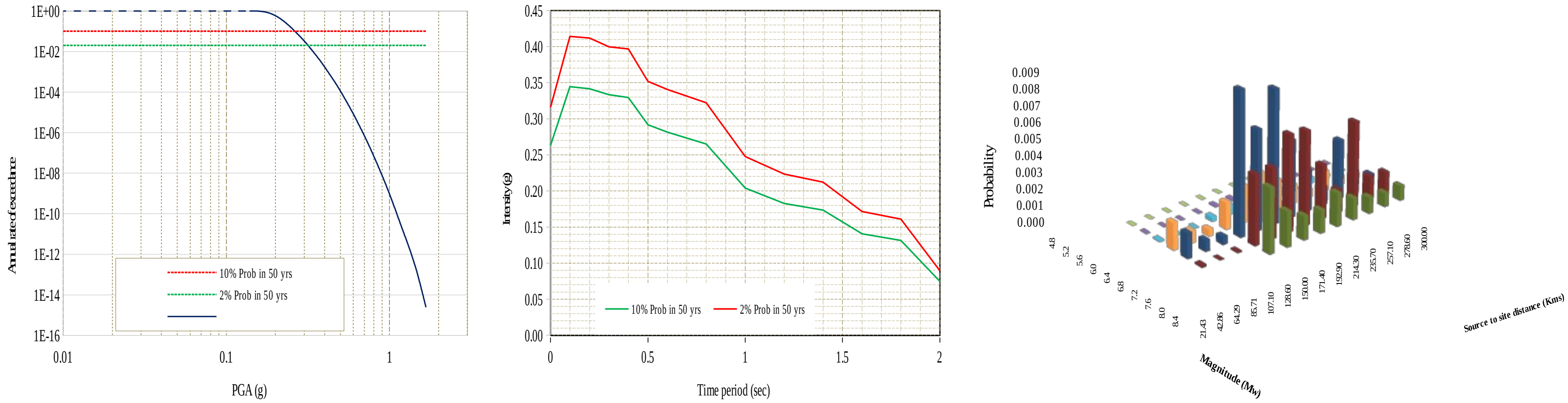

1E+00
1E-02
1E-04
1E-06
1E-08
1E-10
1E-12
1E-14
1E-16
0.01
0.1
1
PGA (g)
10% Prob in 50 yrs
2% Prob in 50 yrs
Intensity (g)
Time period (sec)
Probability
Magnitude (Mw)
Source to site distance (Kms)

Grid 6

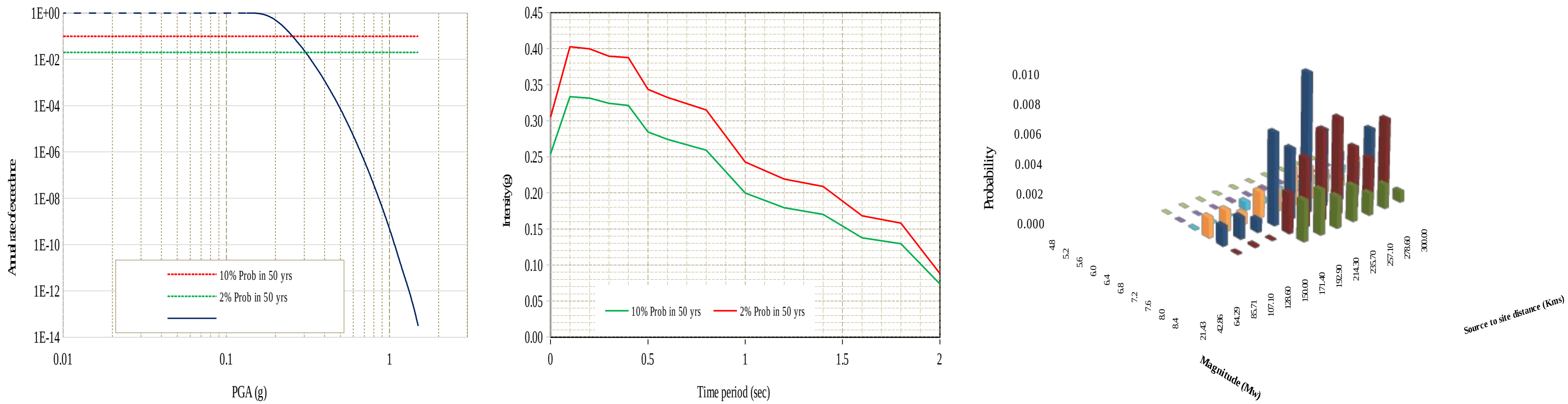

1E+00
1E-02
1E-04
1E-06
1E-08
1E-10
1E-12
1E-14
0.01
0.1
1
PGA (g)
10% Prob in 50 yrs
2% Prob in 50 yrs
Intensity (g)
Time period (sec)
Probability
Magnitude (Mw)
Source to site distance (Kms)

Grid 7

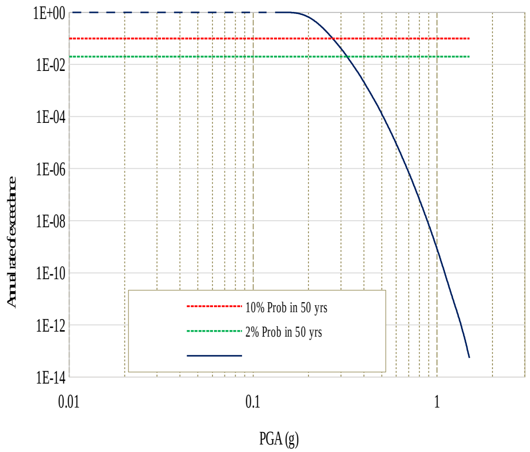
10% Prob in 50 yrs
2% Prob in 50 yrs
PGA (g)

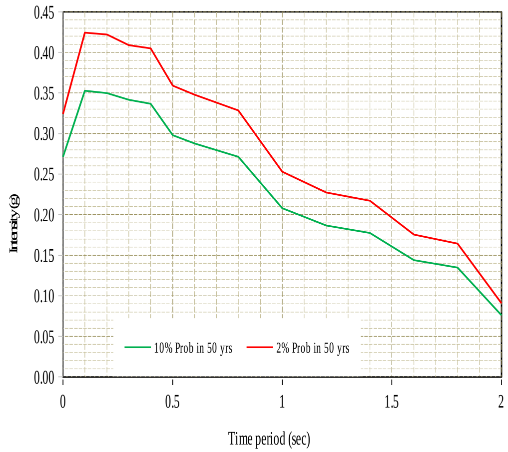
Intensity (g)
10% Prob in 50 yrs
2% Prob in 50 yrs
Time period (sec)

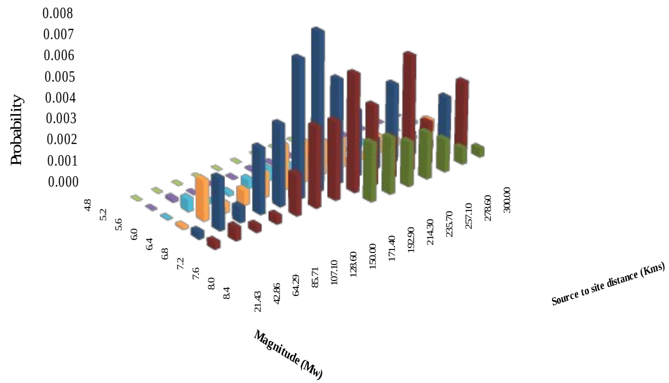
Probability
Source to site distance (Kms)
Magnitude (Mw)

Grid 8

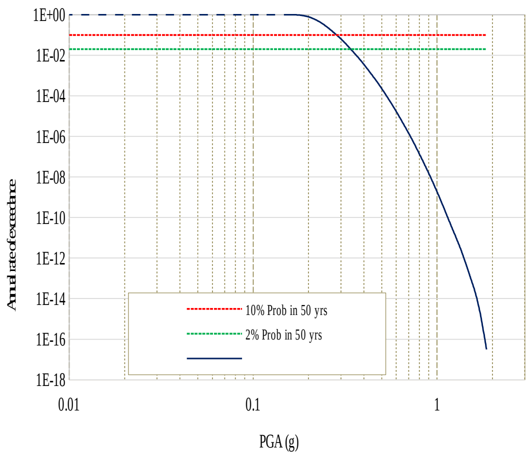
10% Prob in 50 yrs
2% Prob in 50 yrs
PGA (g)

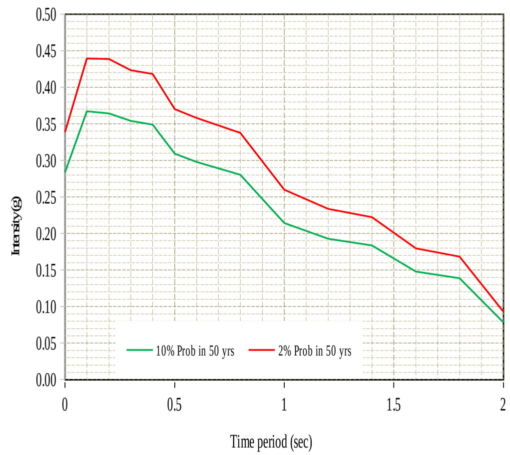
Intensity (g)
10% Prob in 50 yrs
2% Prob in 50 yrs
Time period (sec)

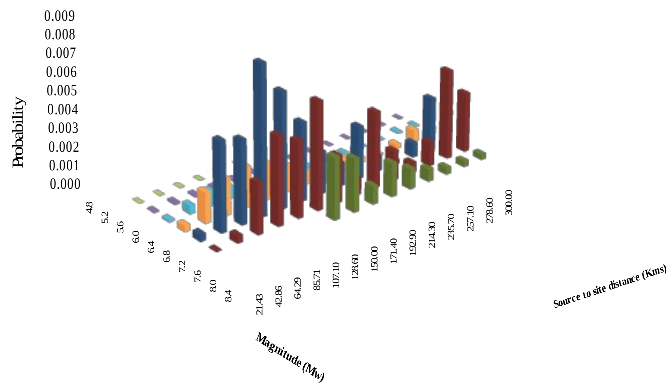
Probability
Source to site distance (Kms)
Magnitude (Mw)

Grid 9

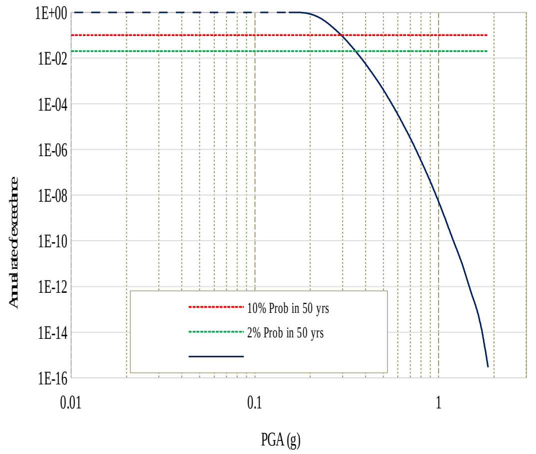

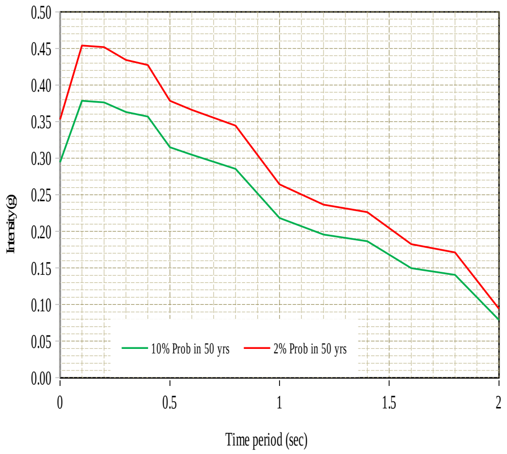

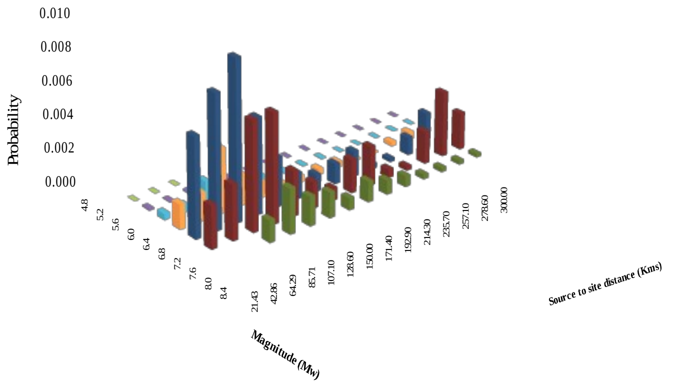

Grid 10

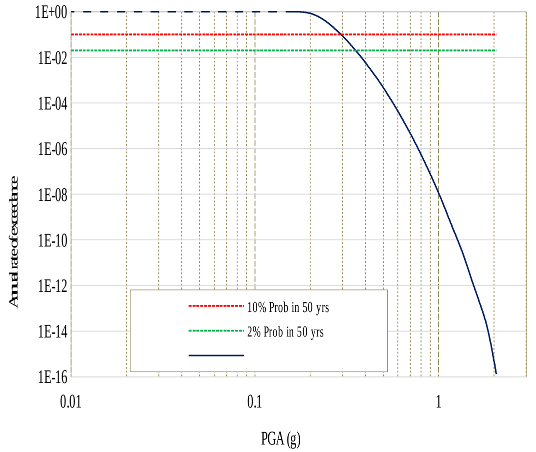

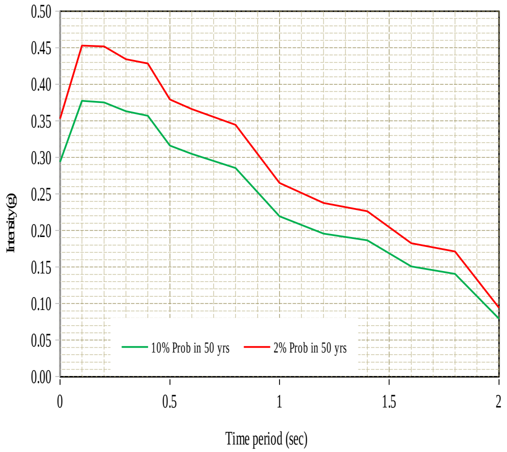

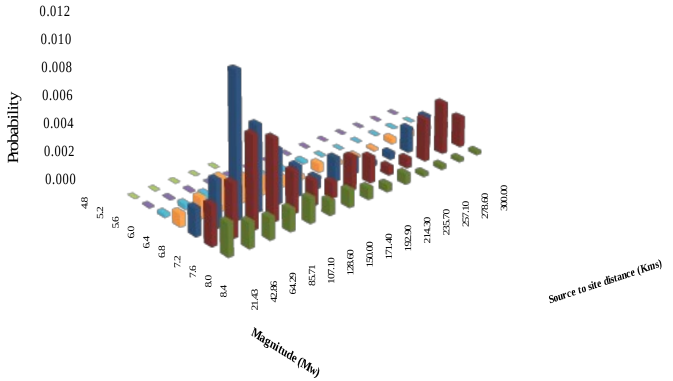

Grid 11

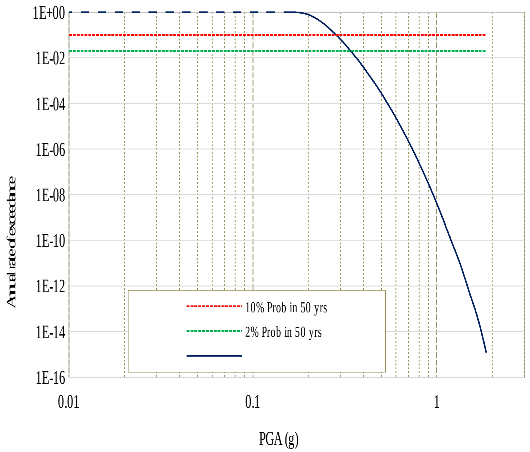

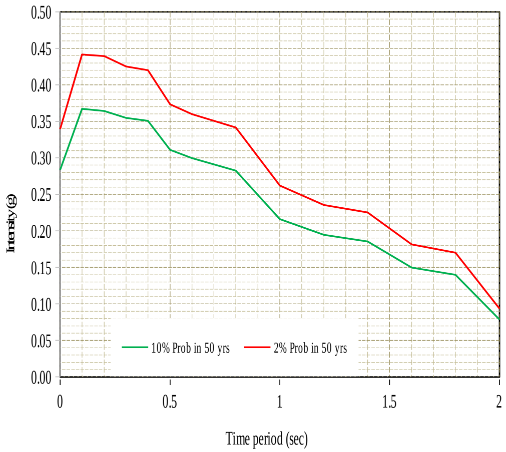

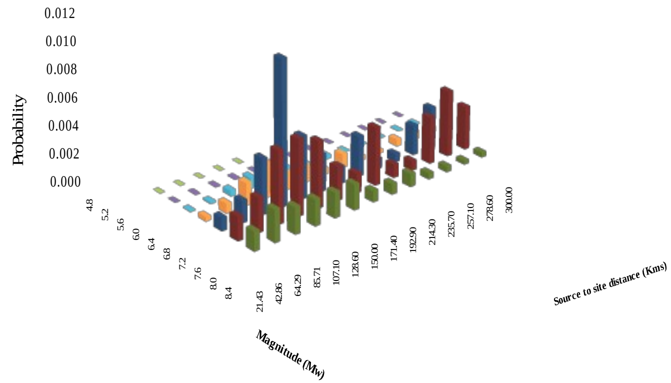

Grid 12

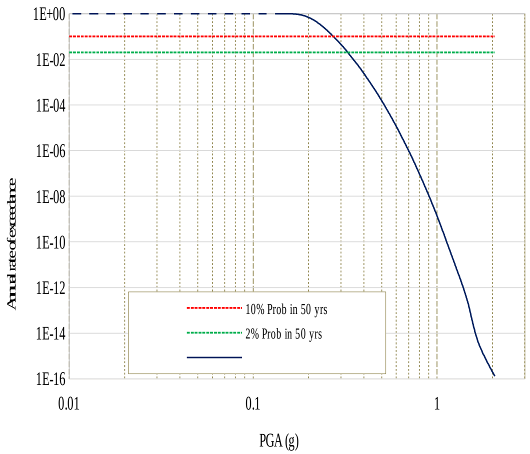

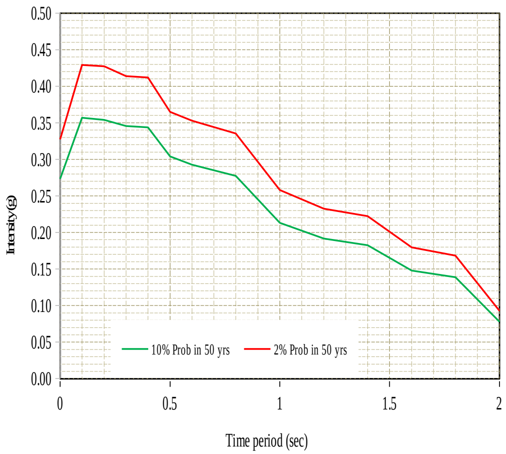

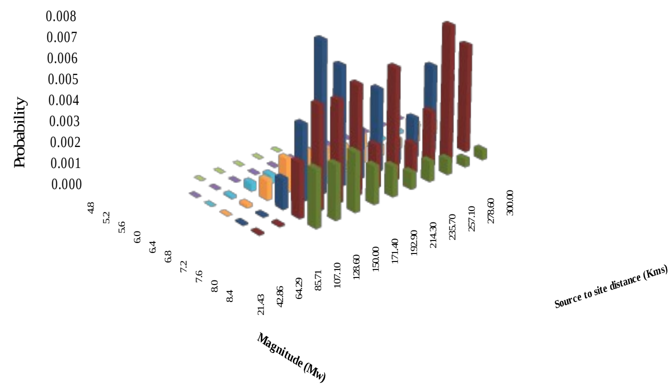

Grid 13

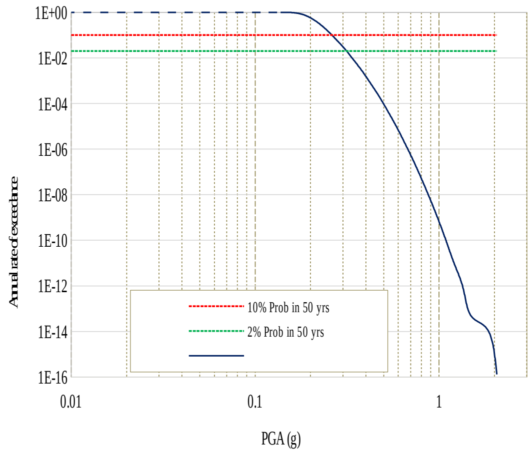

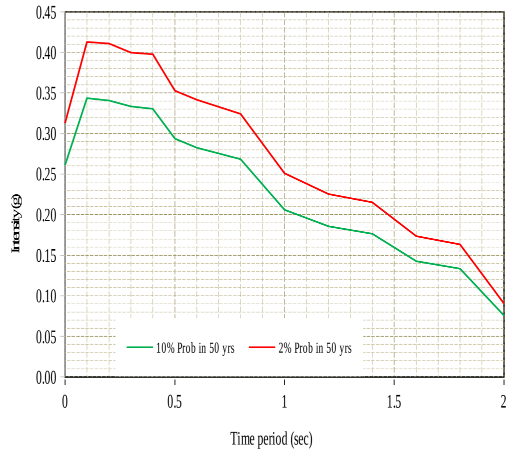

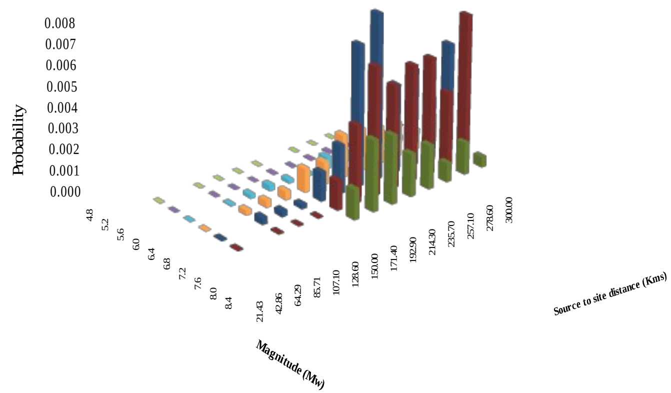

Grid 14

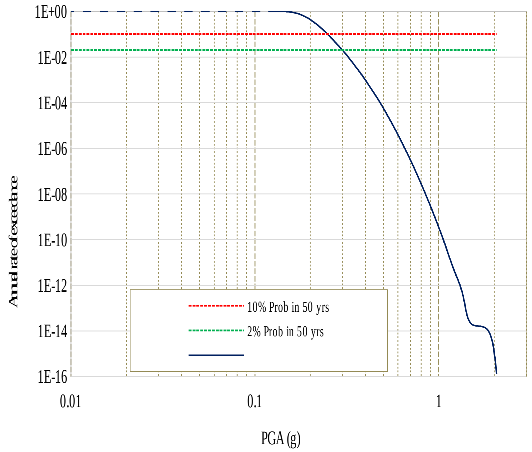

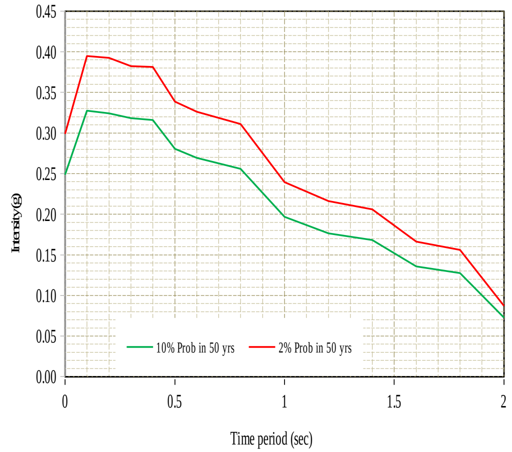

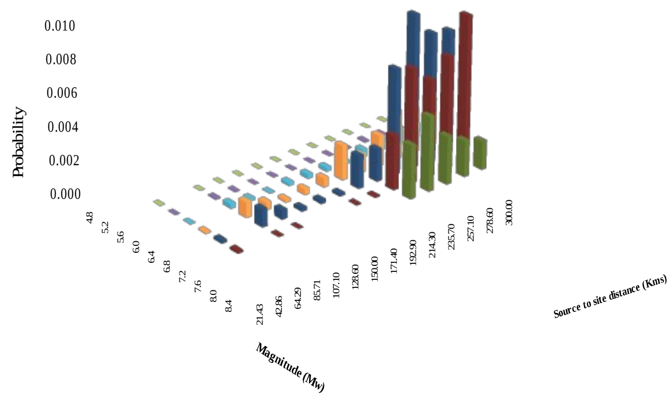

Grid 15

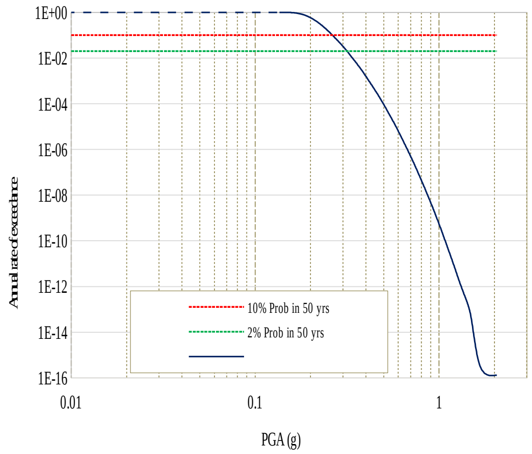

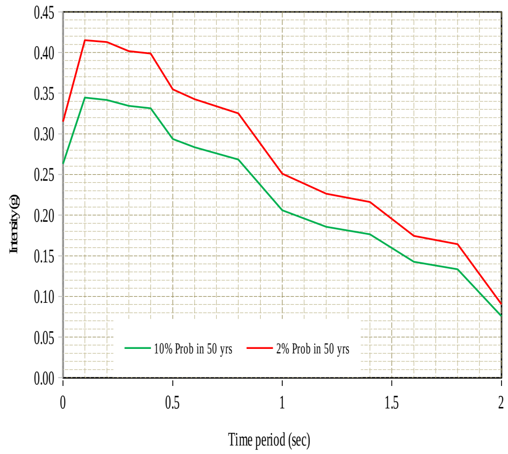

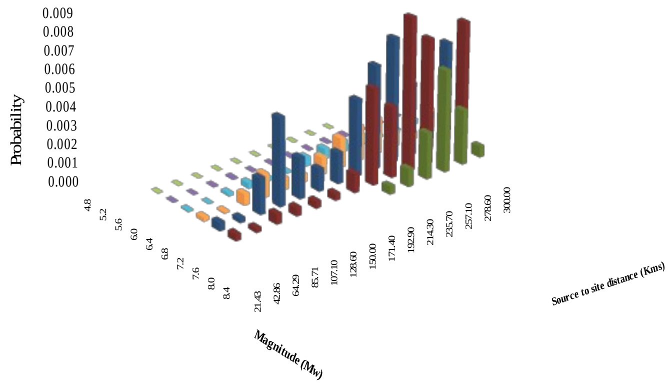

Grid 16

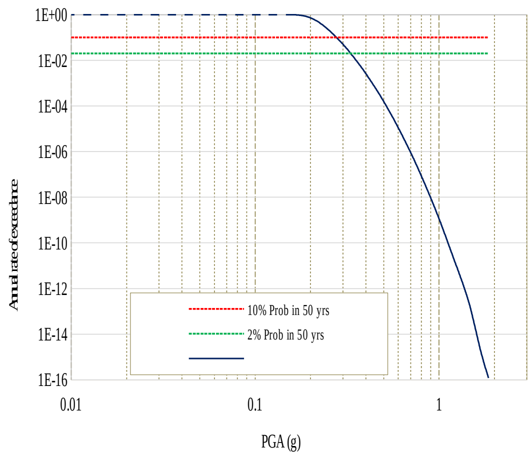

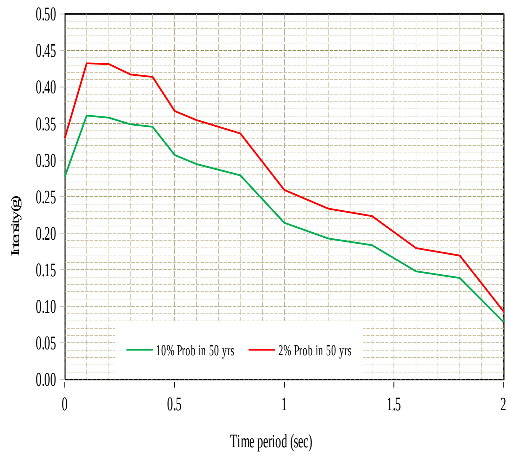

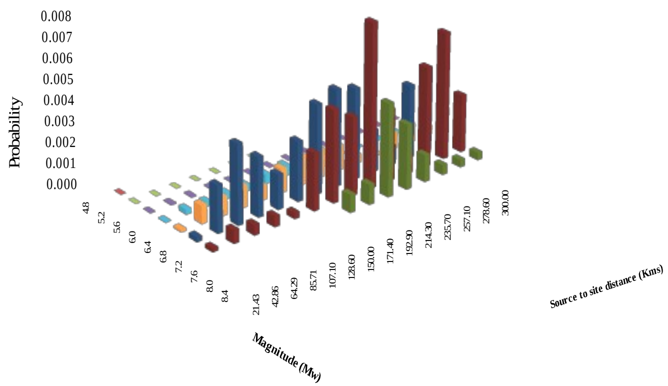

Grid 17

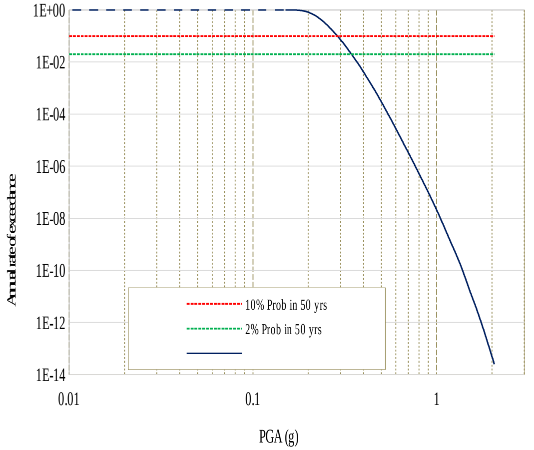

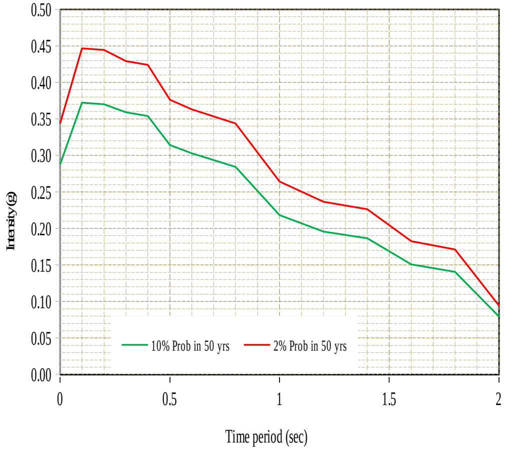

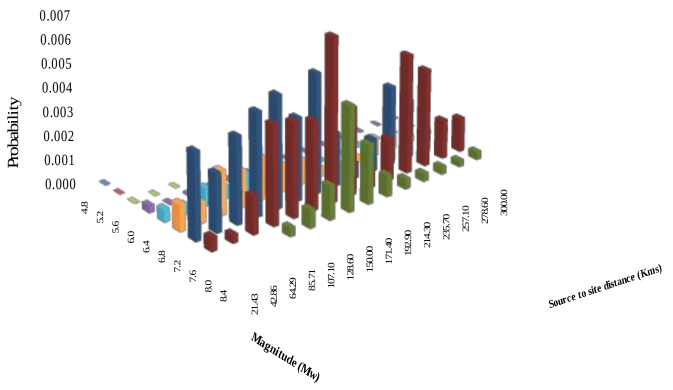

Grid 18

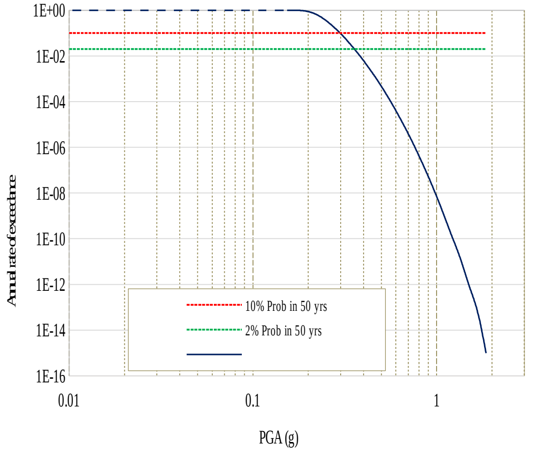

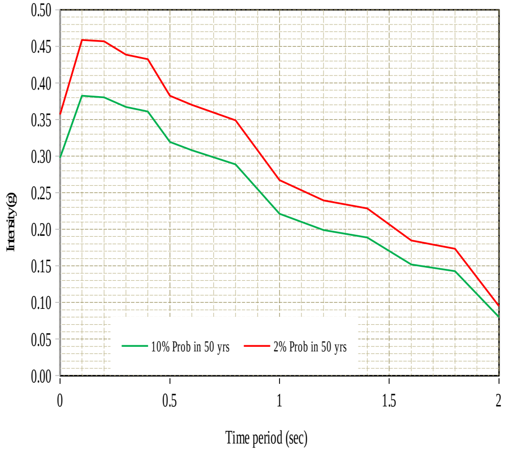

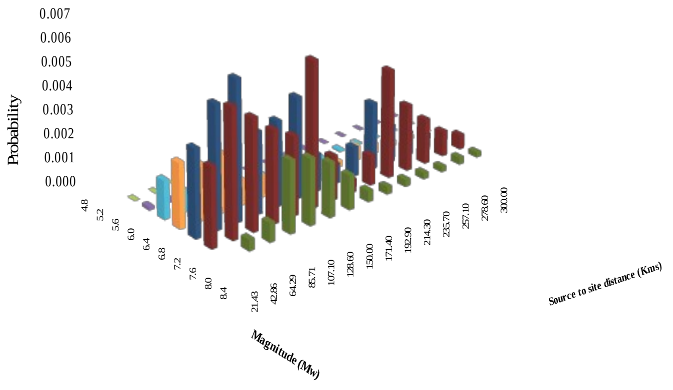

Grid 19

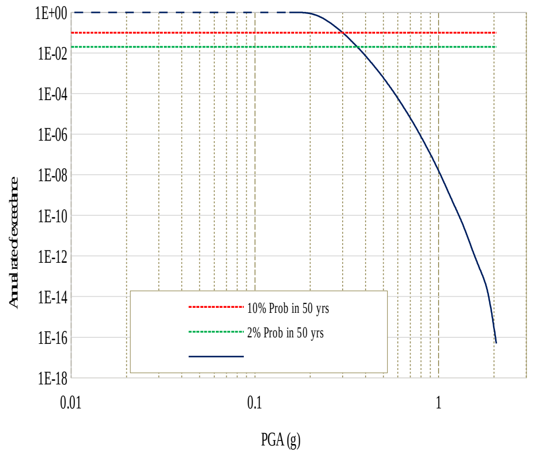

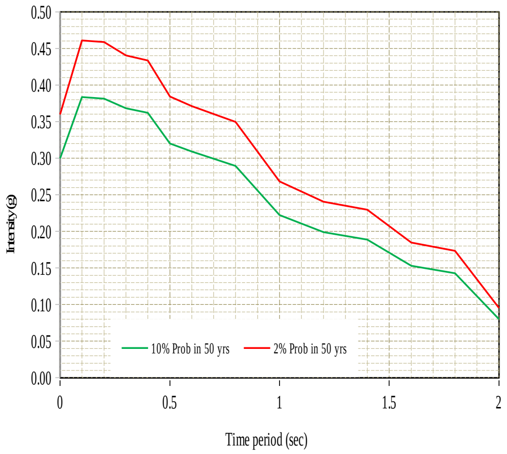

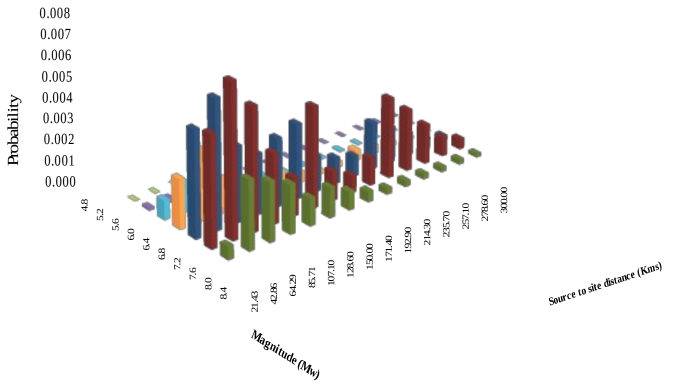

Grid 20

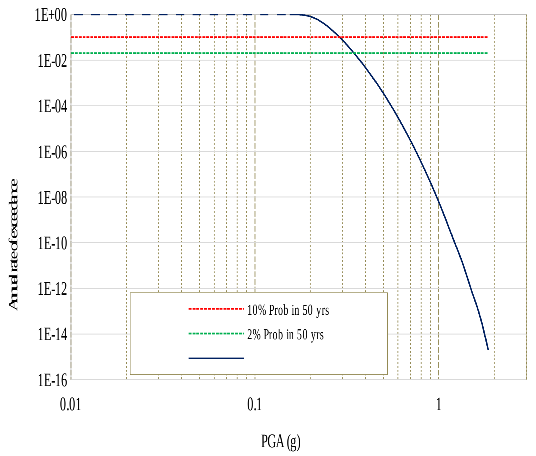

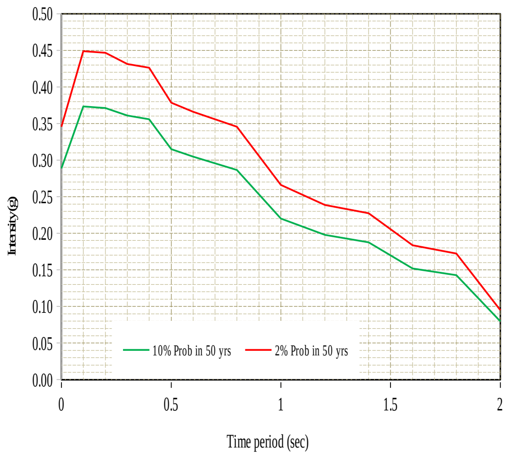

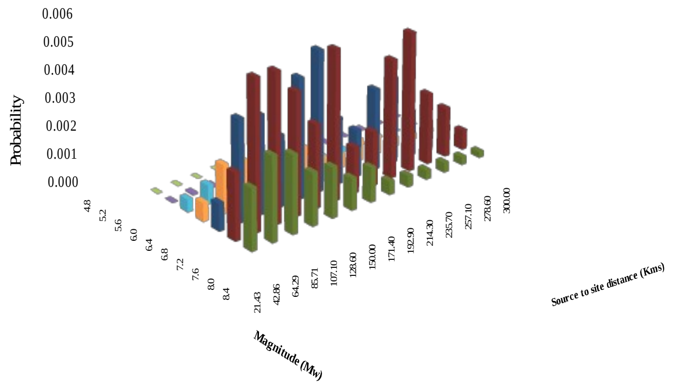

Grid 21

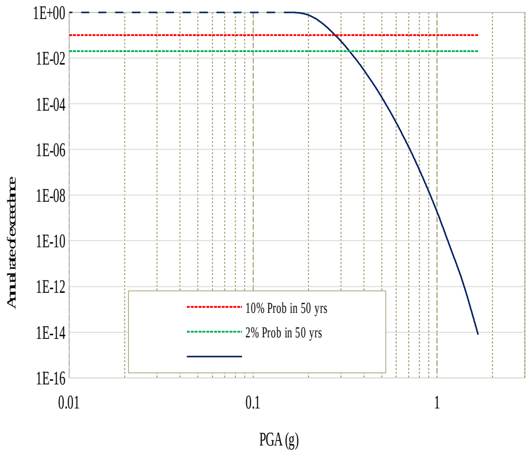

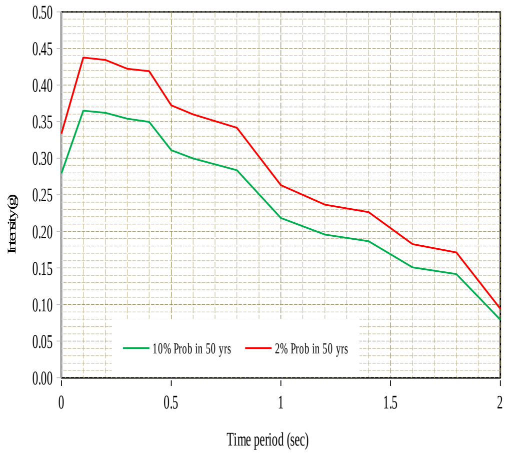

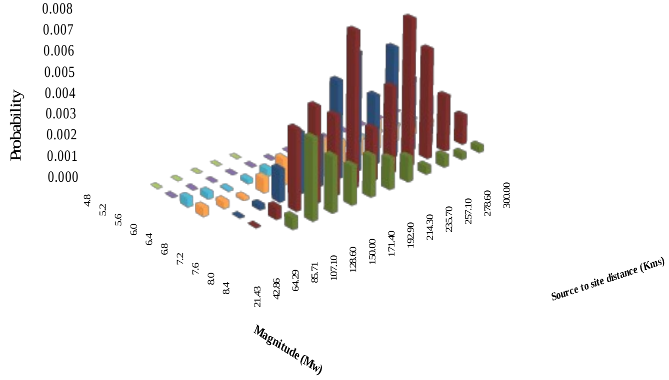

Grid 22

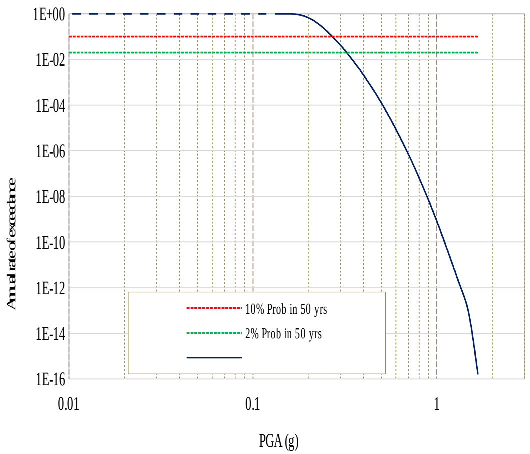

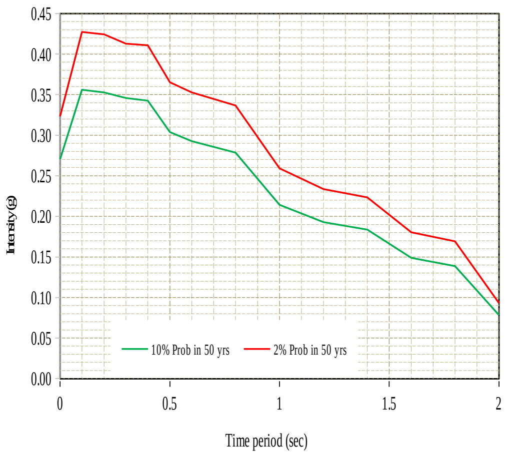

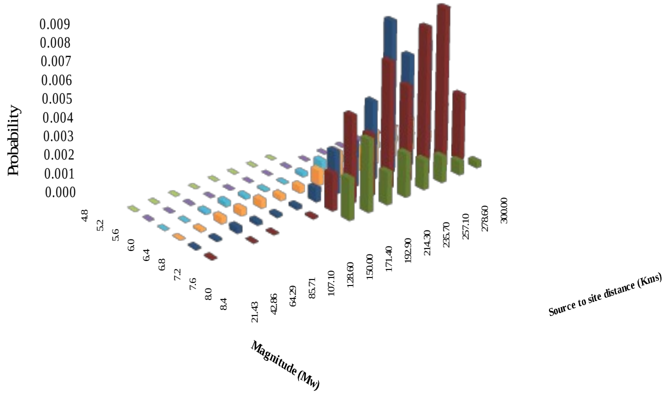

Grid 23

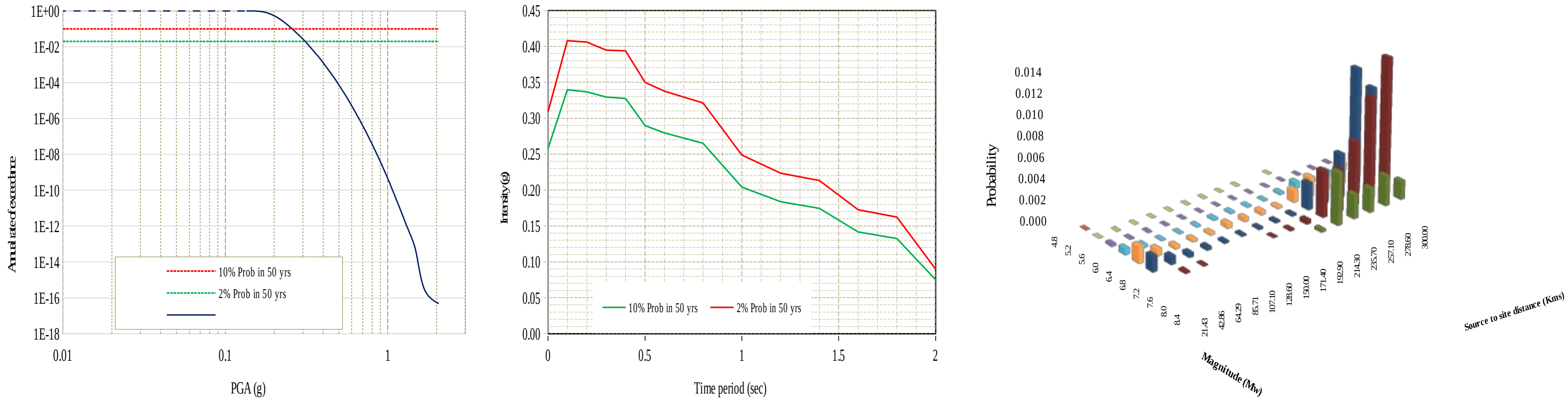

Grid 24

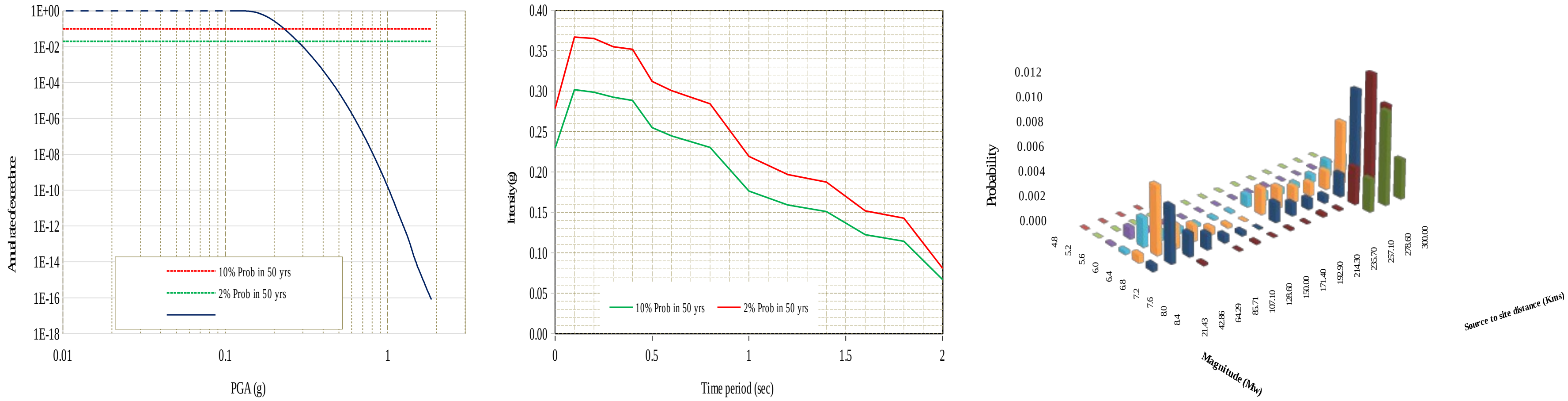

Grid 25

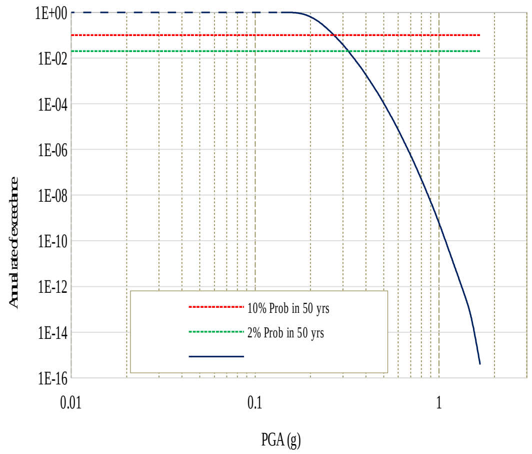

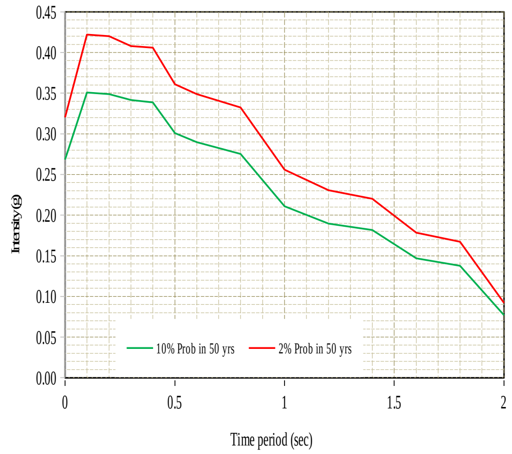

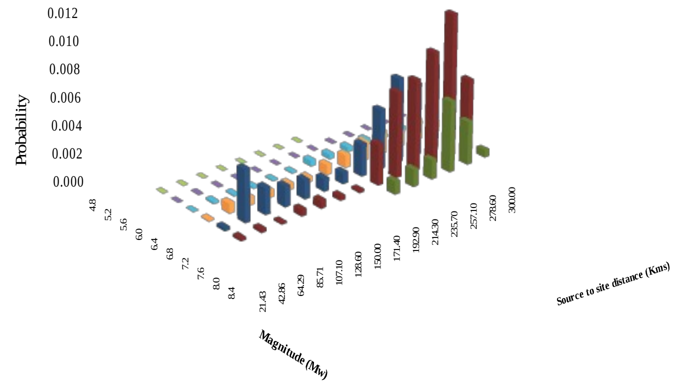

Grid 26

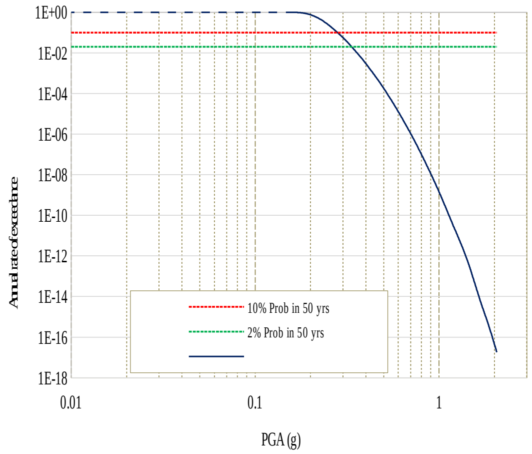

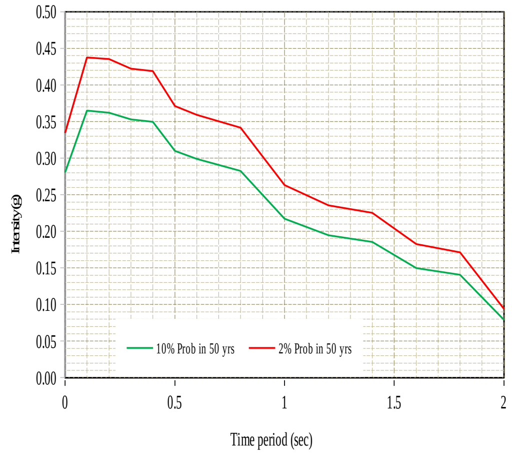

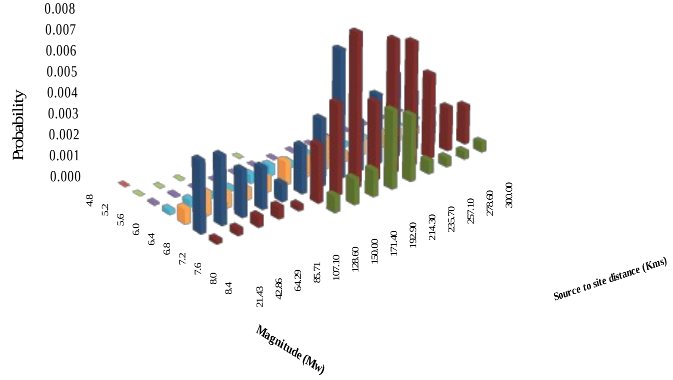

Grid 27

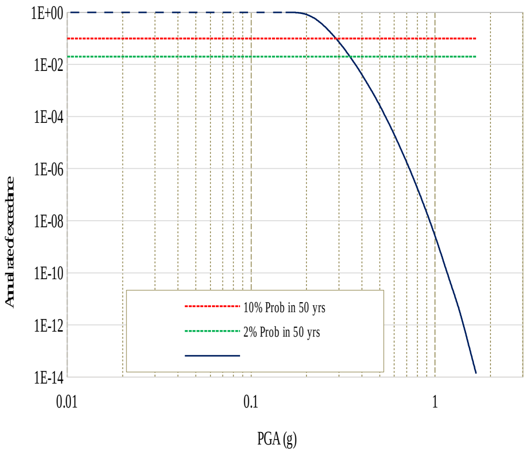

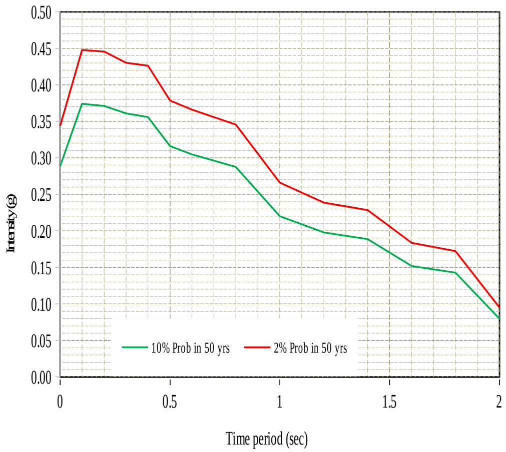

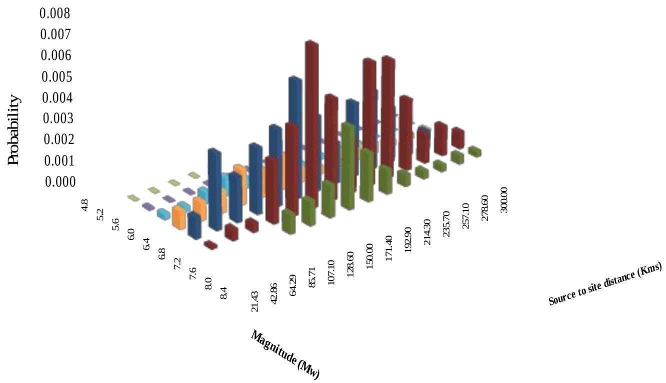

Grid 28

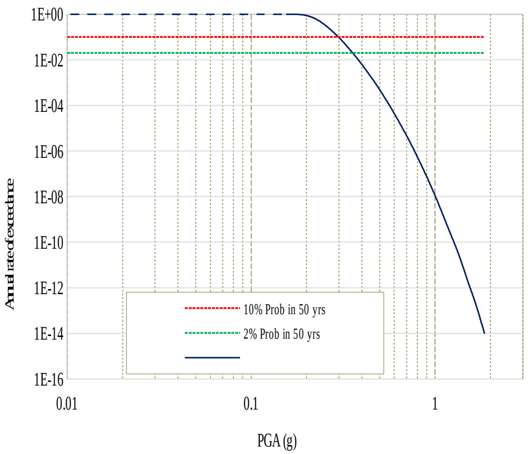

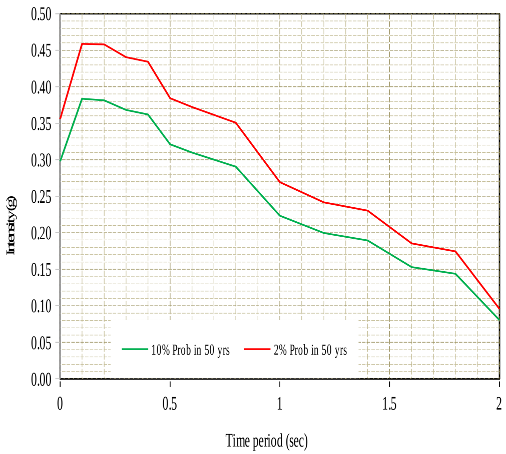

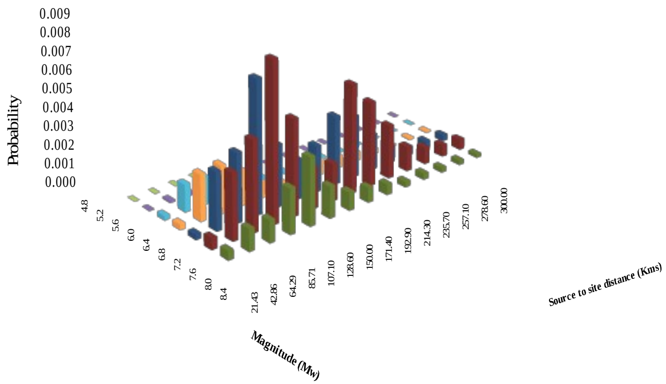

Grid 29

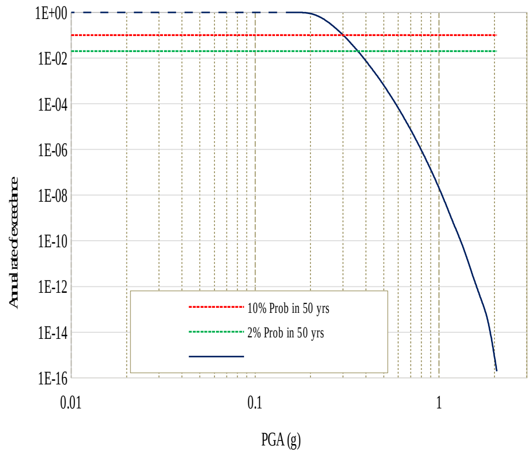

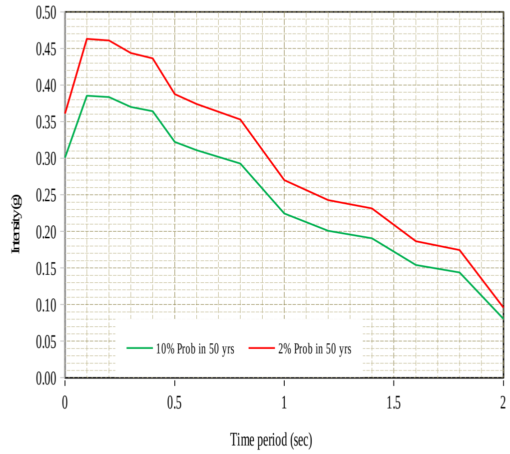

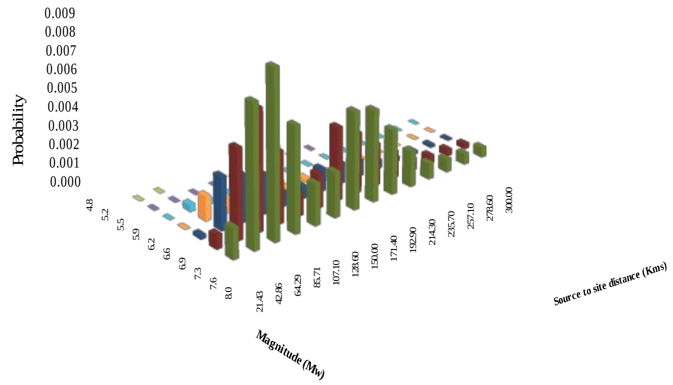

Grid 30

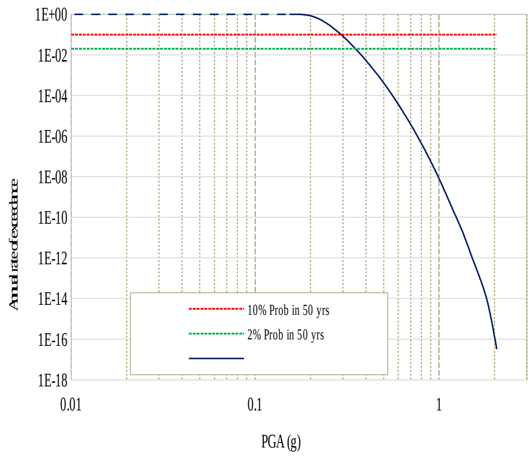

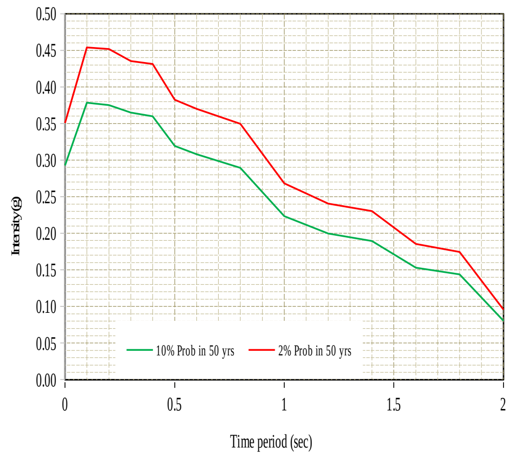

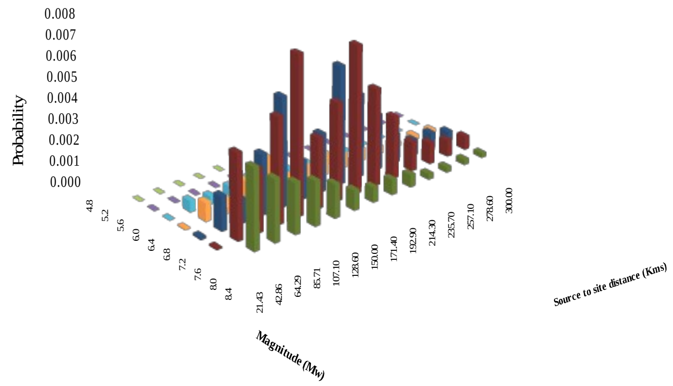

Grid 31

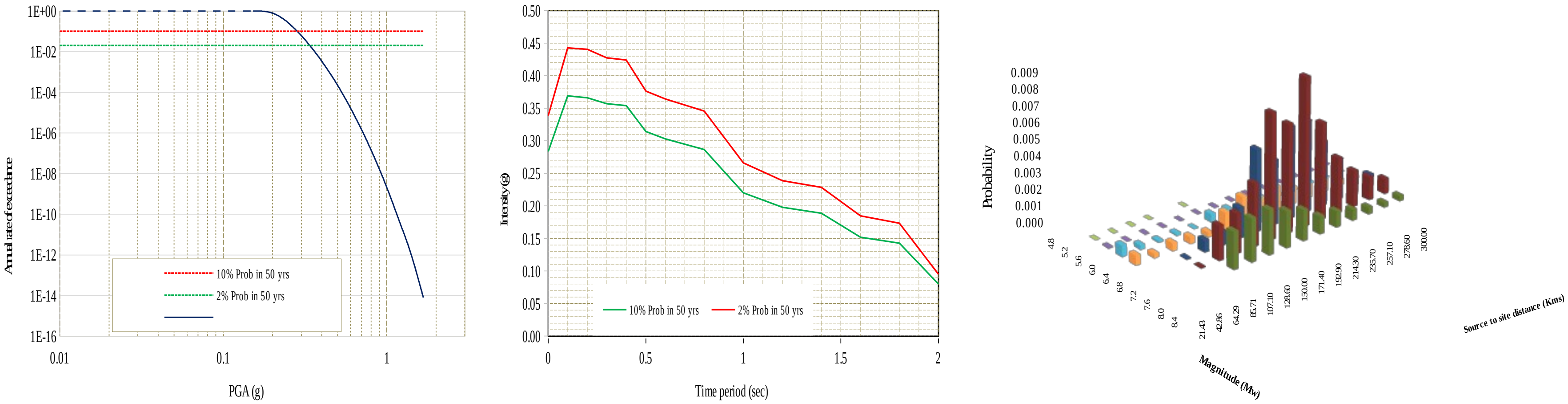

Grid 32

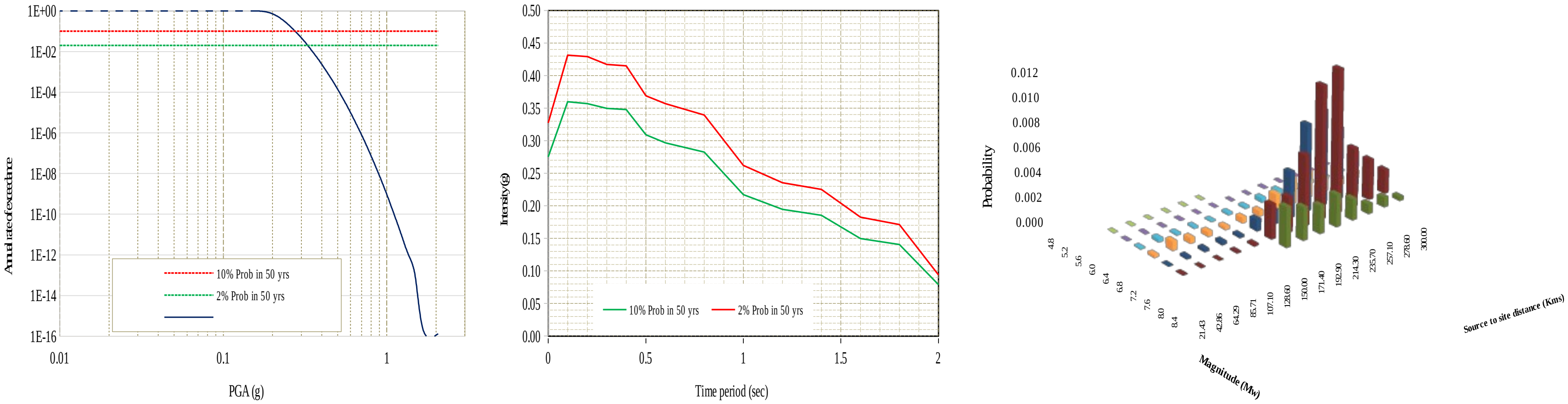

Grid 33

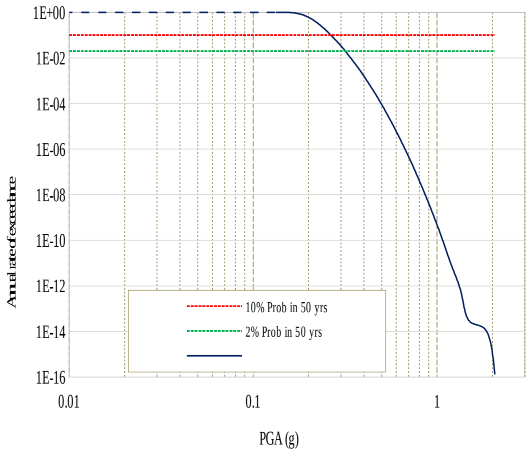

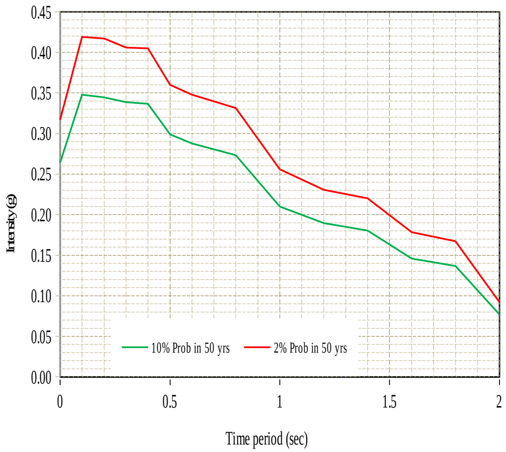

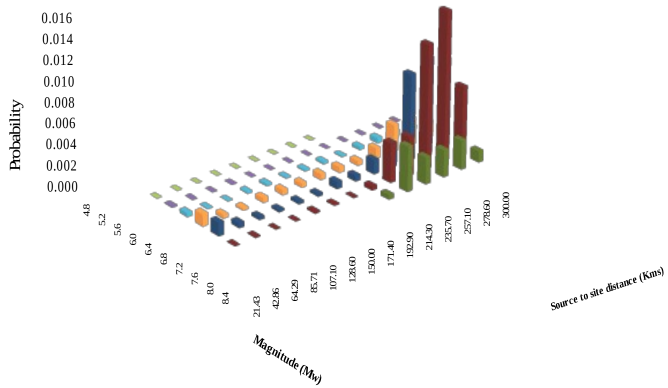

Grid 34

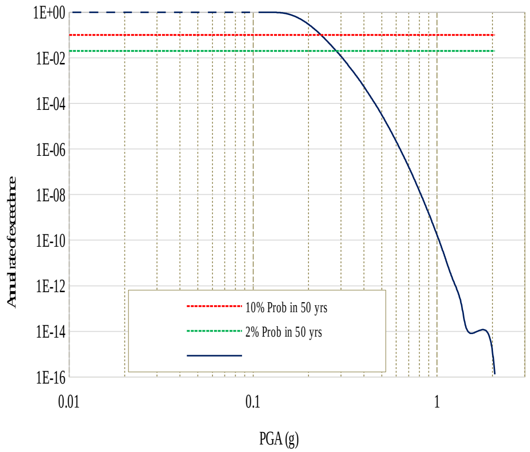

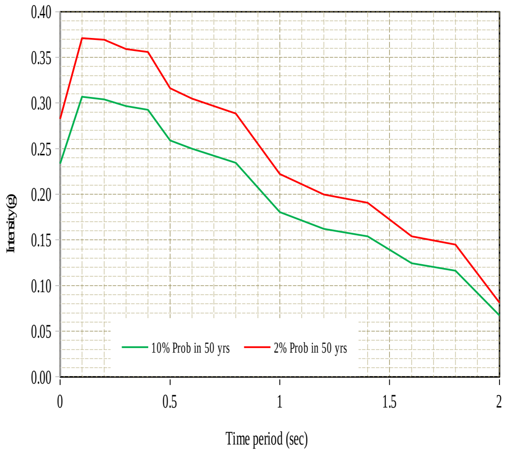

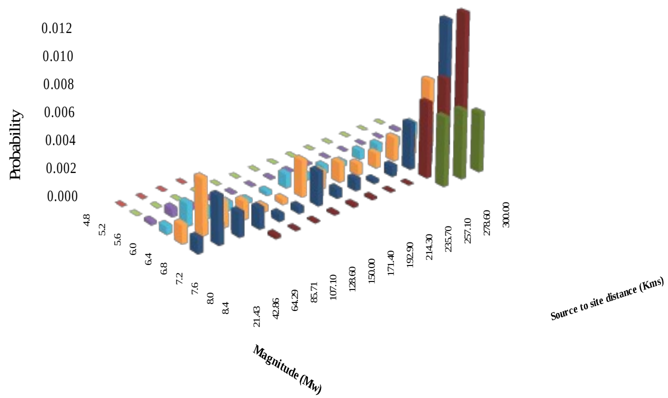

Grid 35

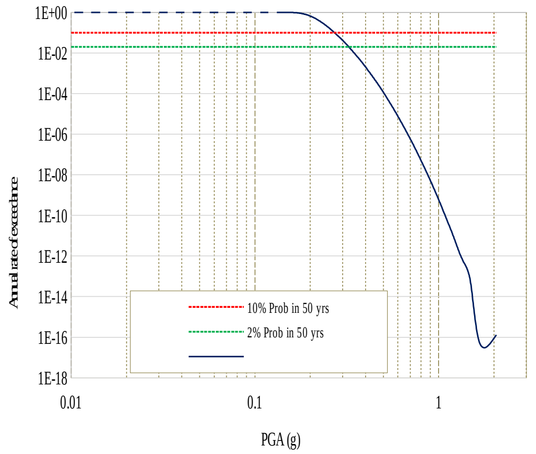

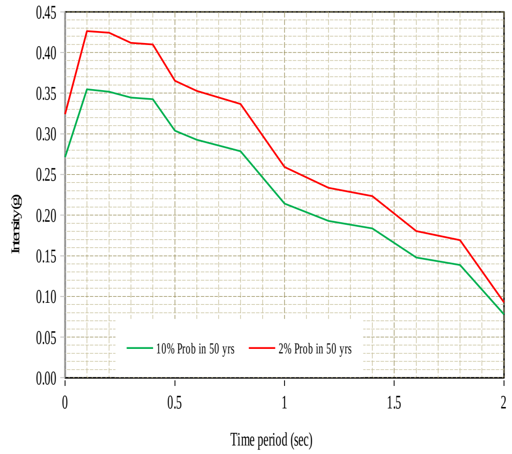

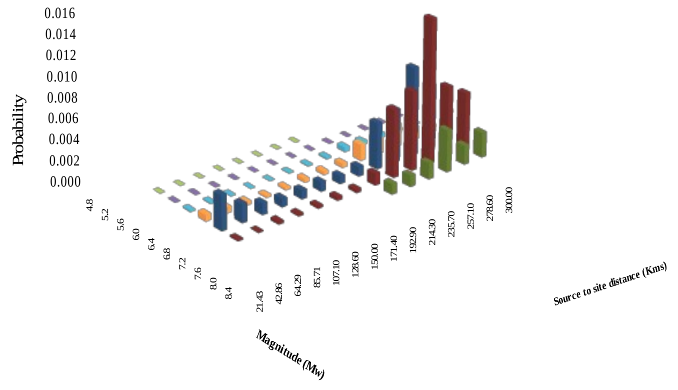

Grid 36

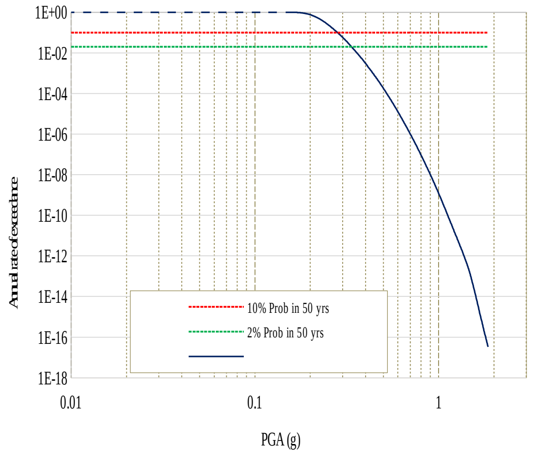

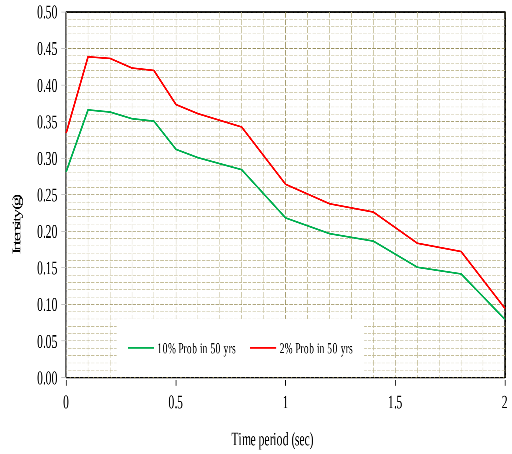

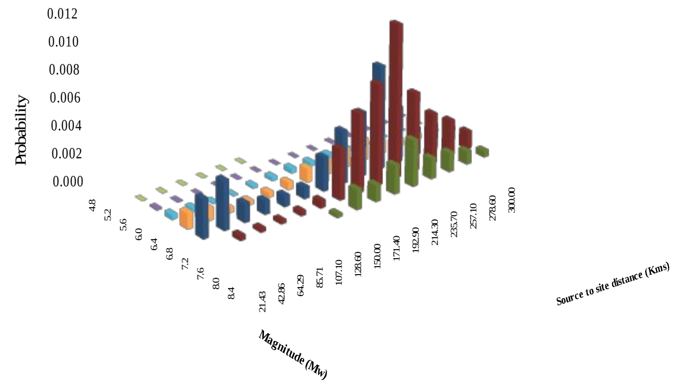

Grid 37

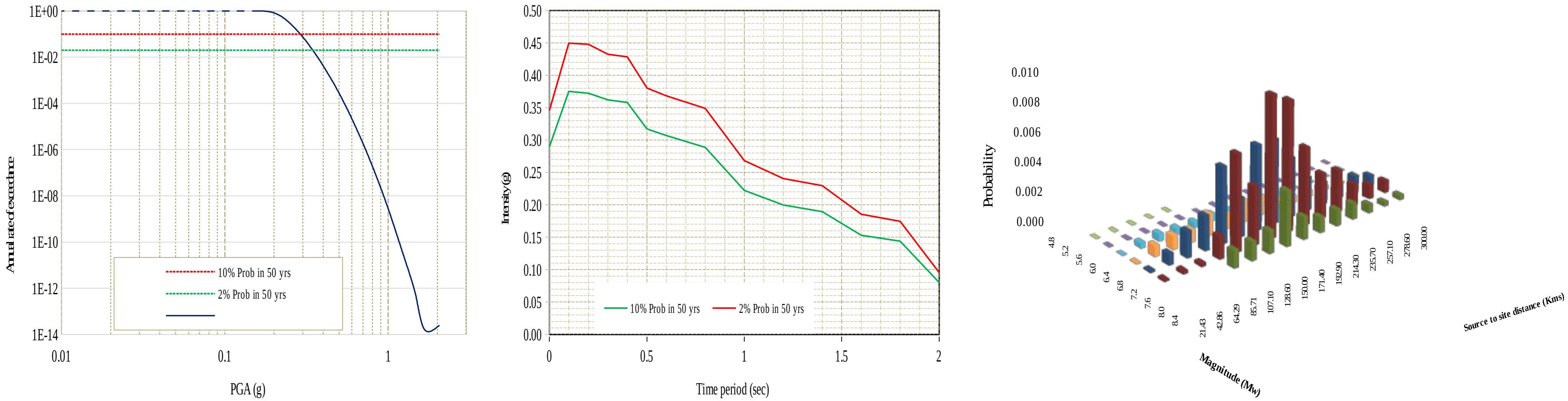

Grid 38

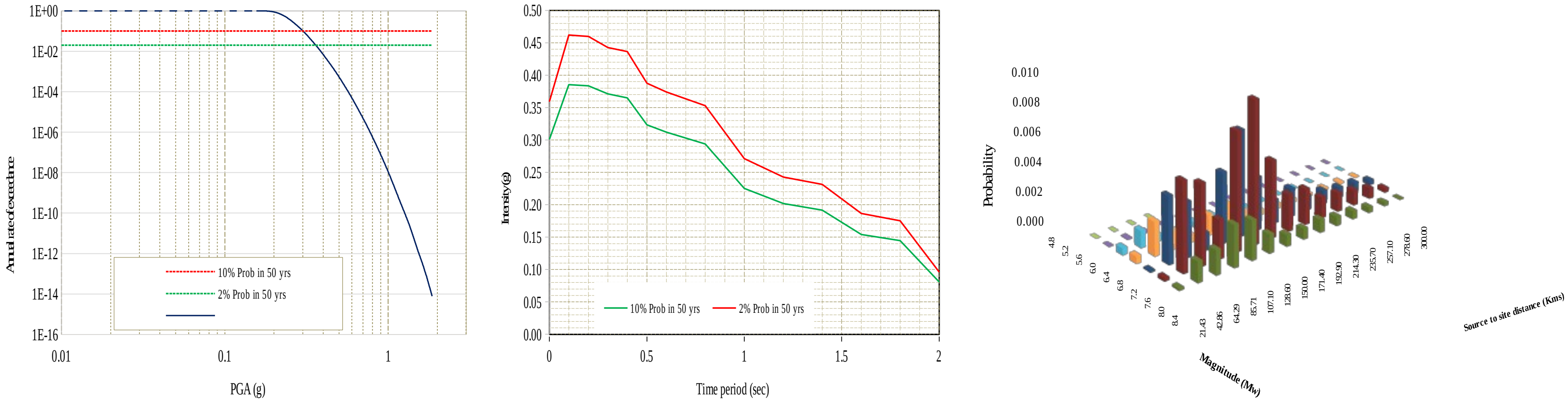

Grid 39

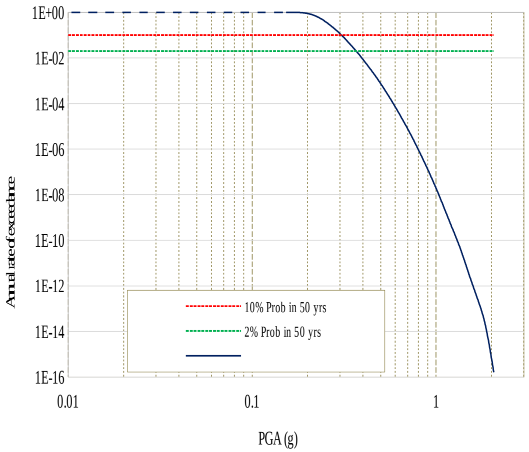

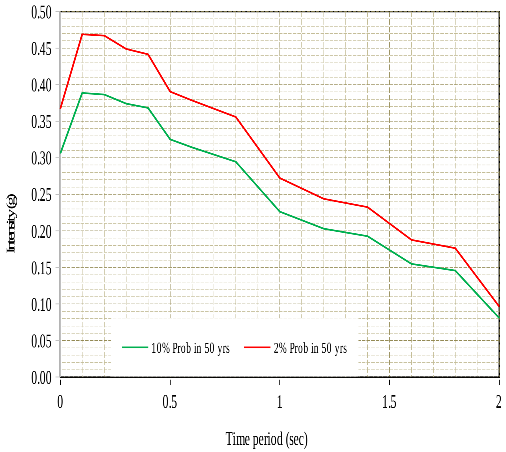

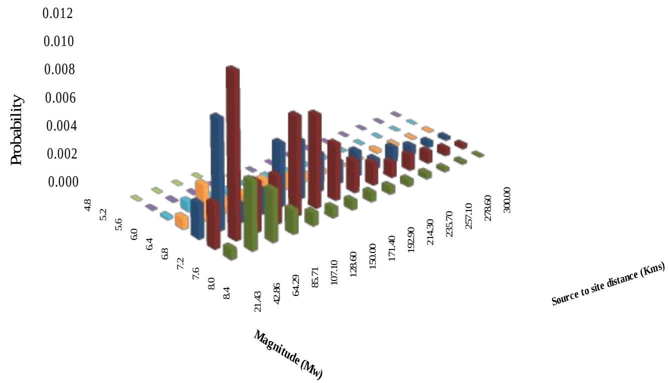

Grid 40

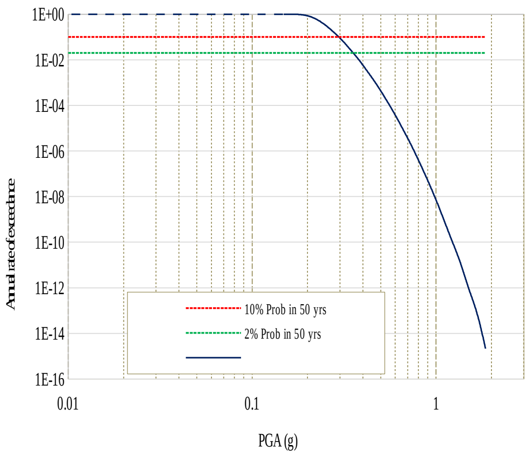

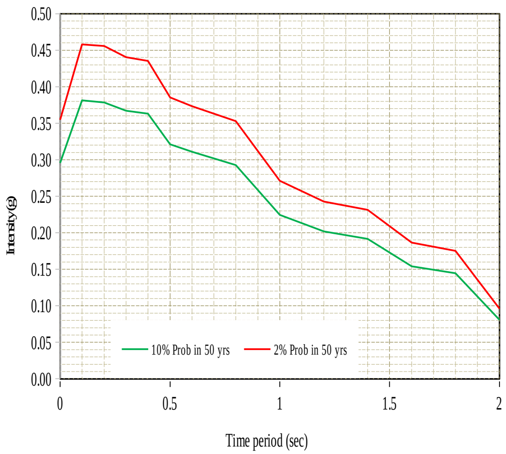

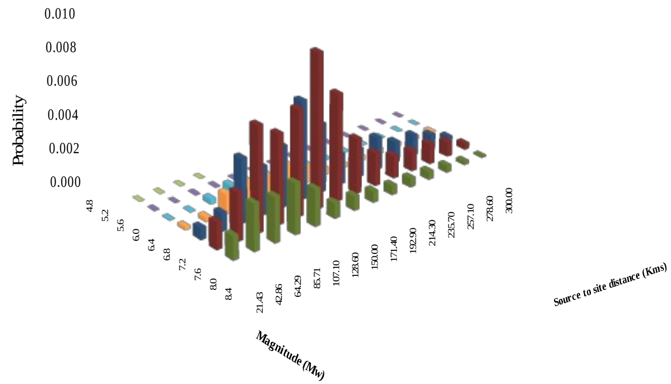

Grid 41

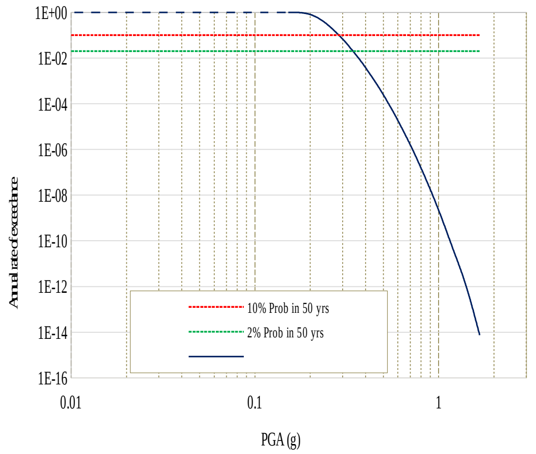

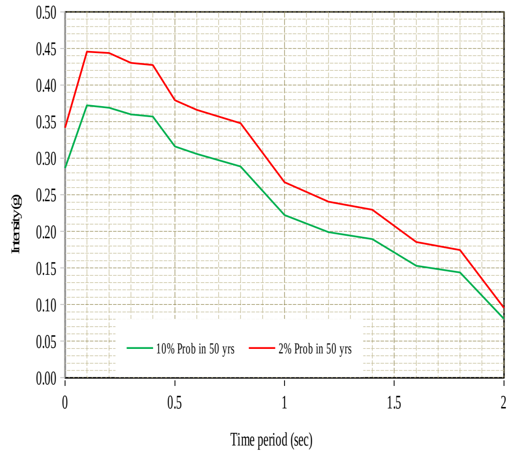

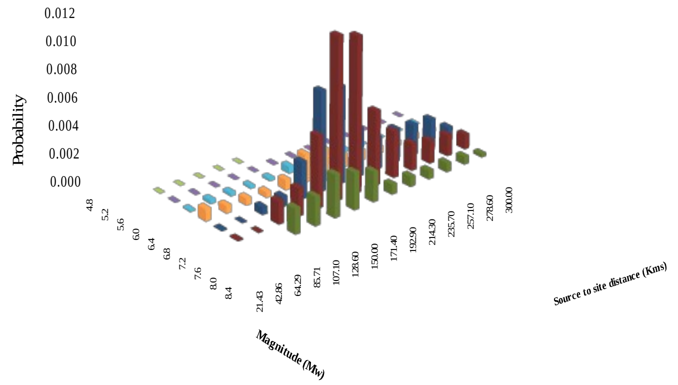

Grid 42

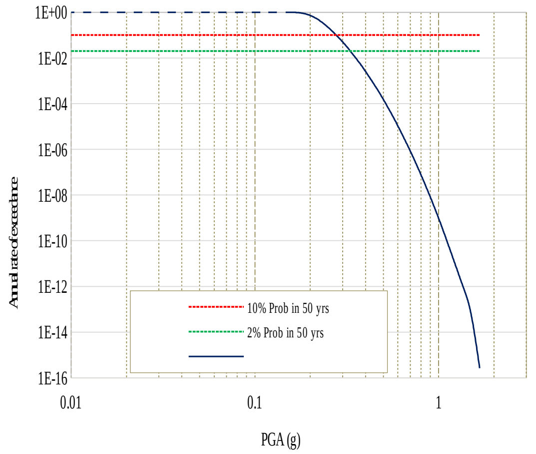

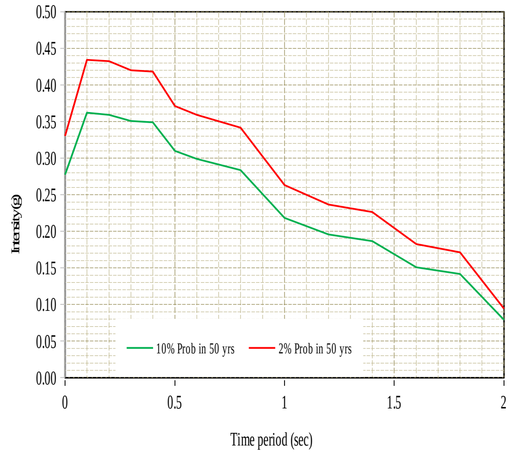

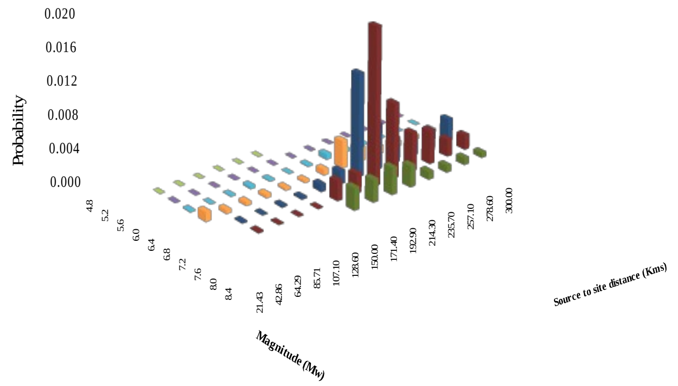

Grid 43

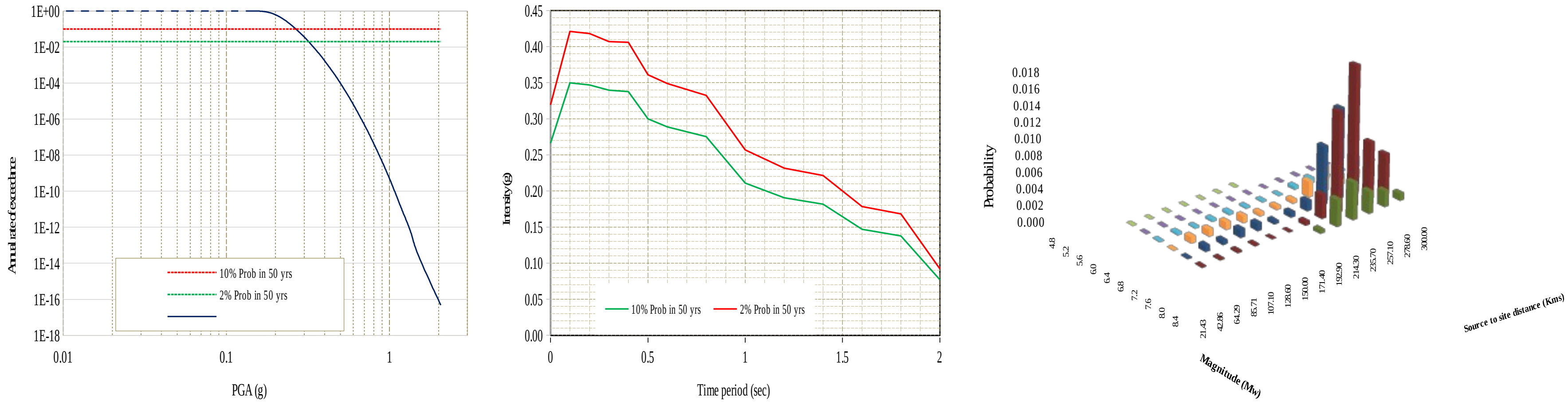

Grid 44

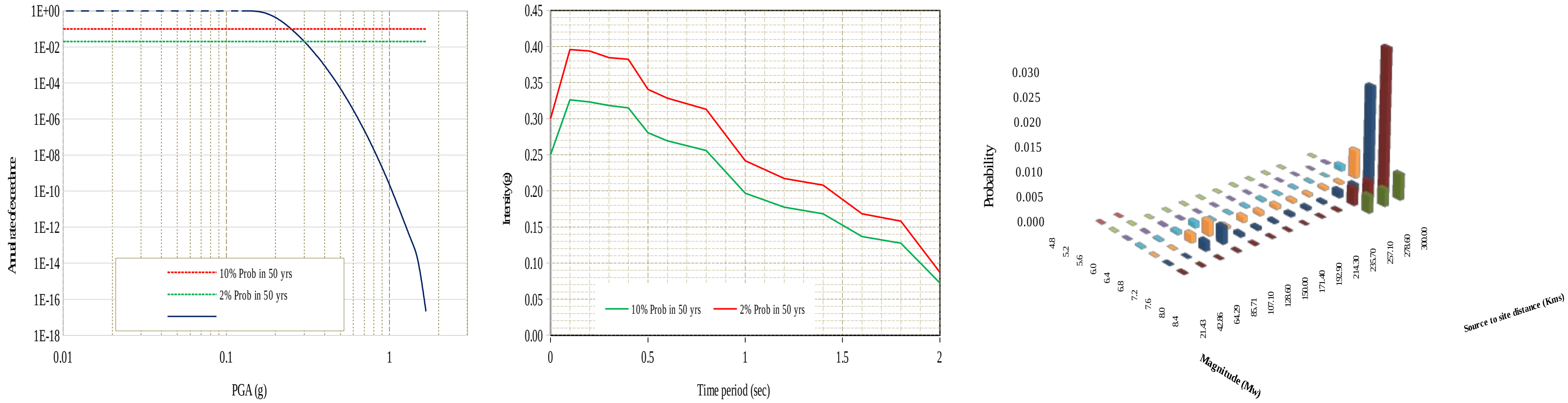

Grid 45

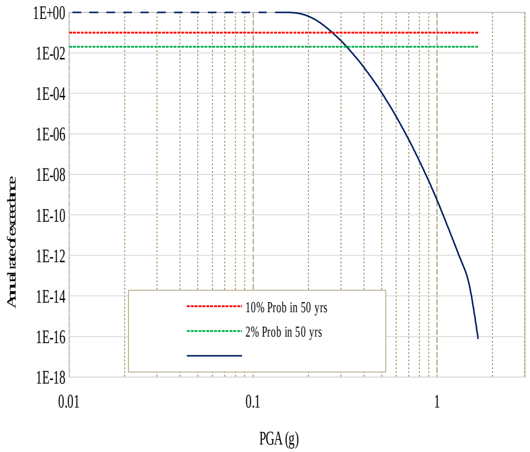

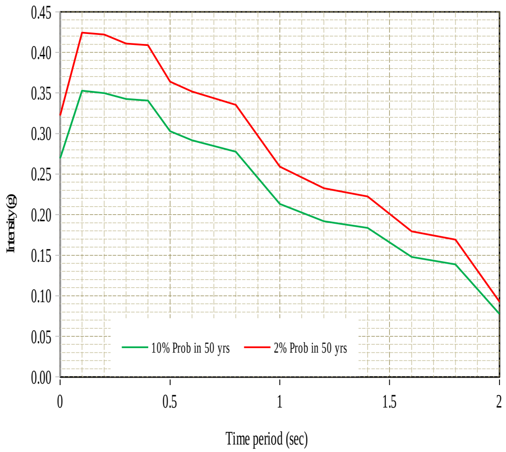

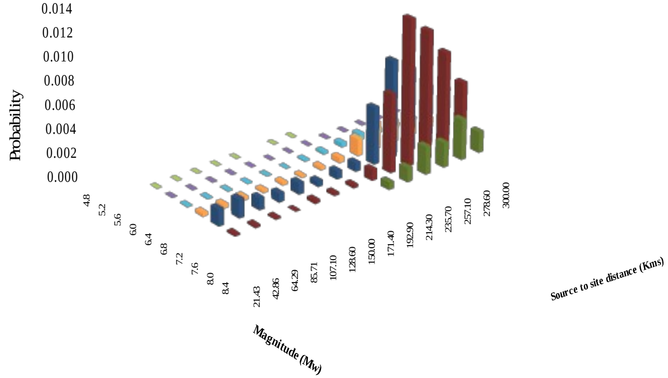

Grid 46

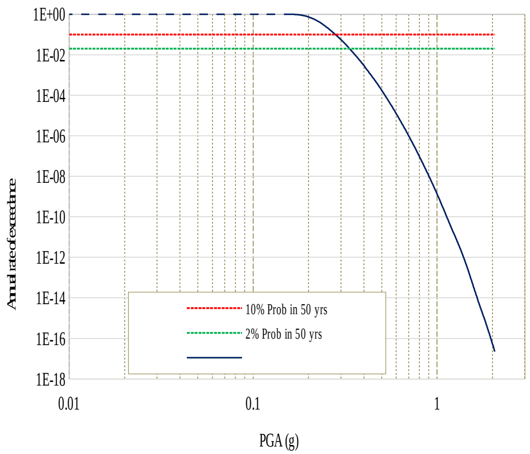

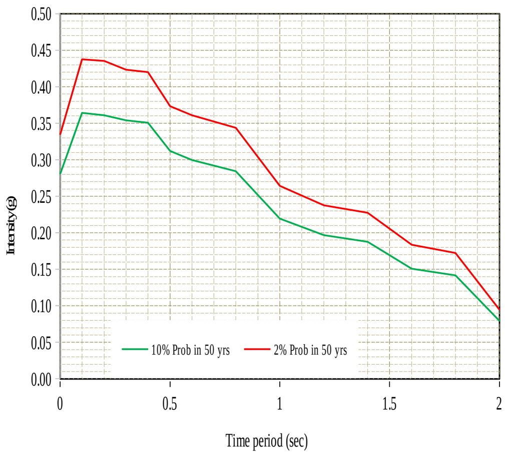

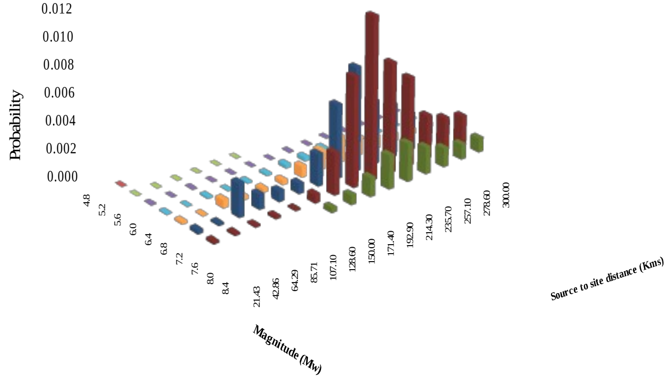

Grid 47

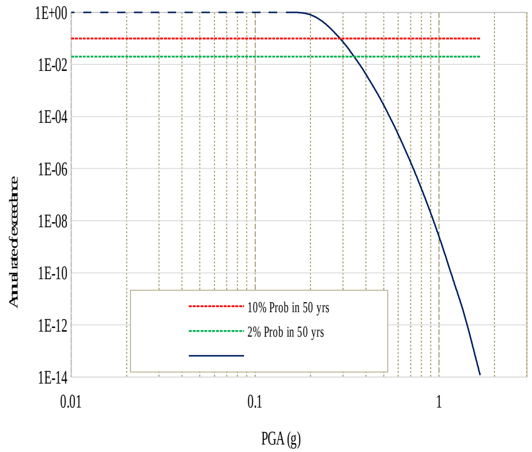

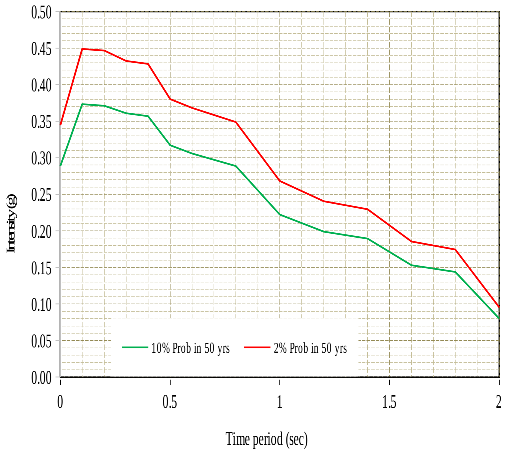

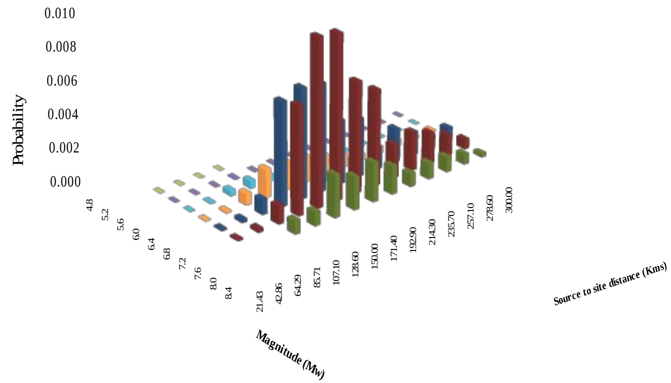

Grid 48

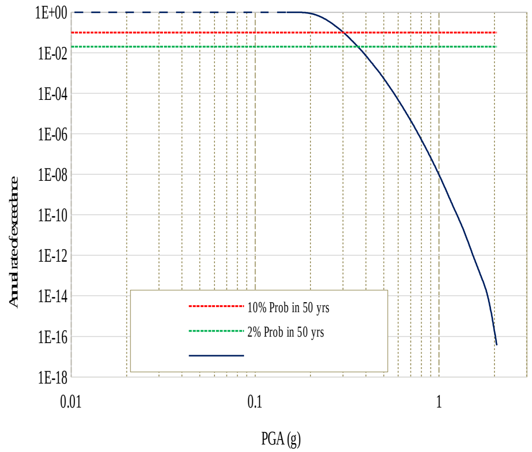

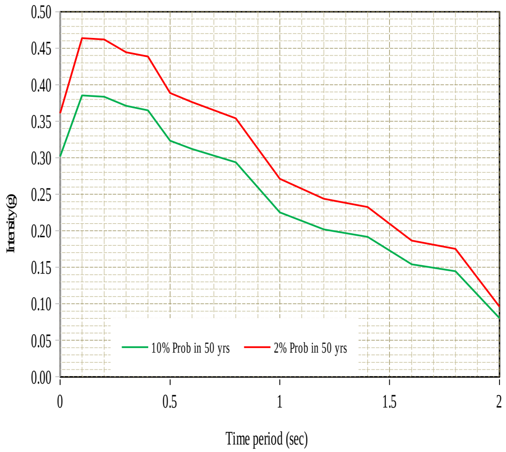

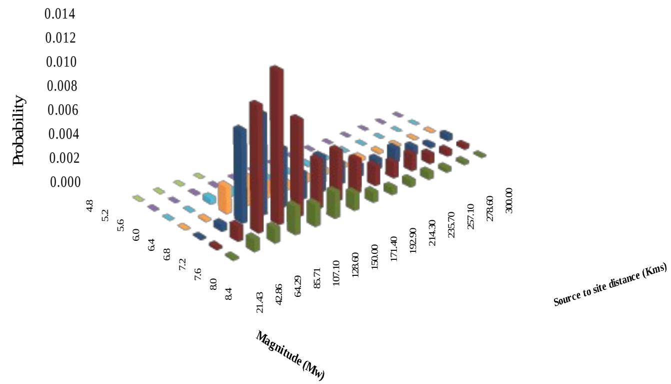

Grid 49

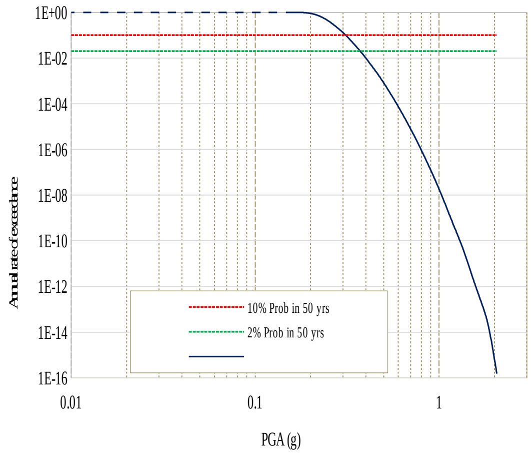

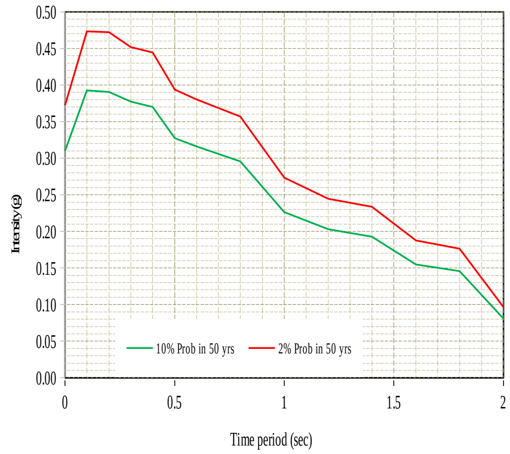

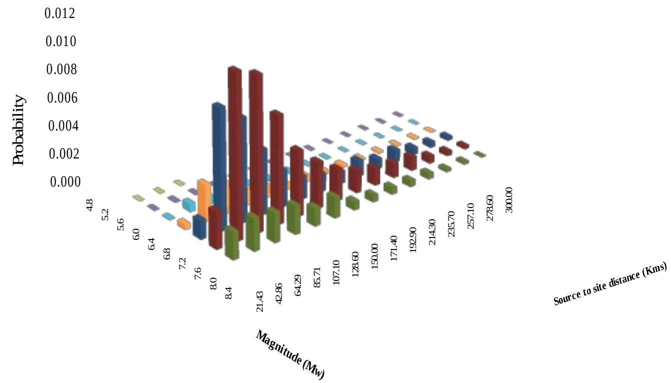

Grid 50

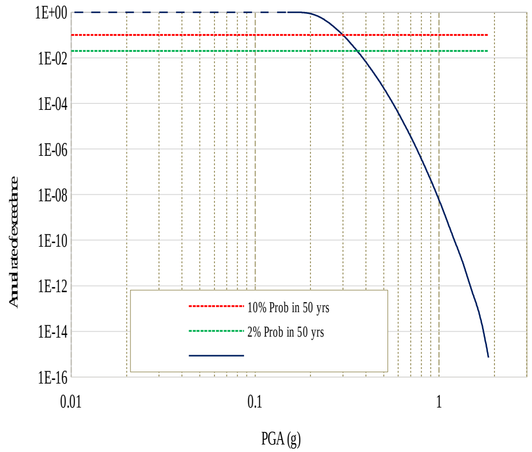

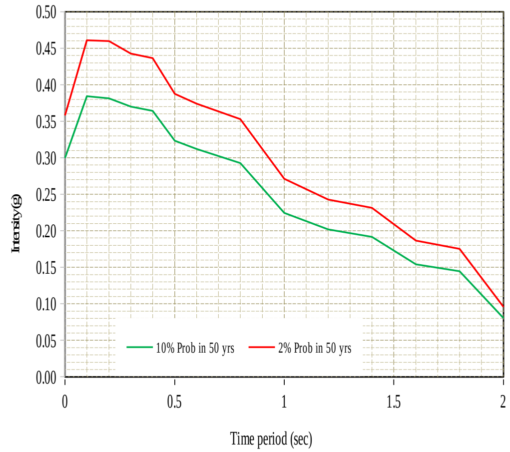

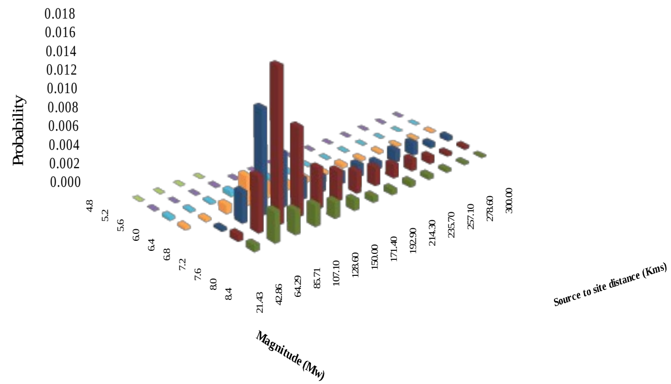

Grid 51

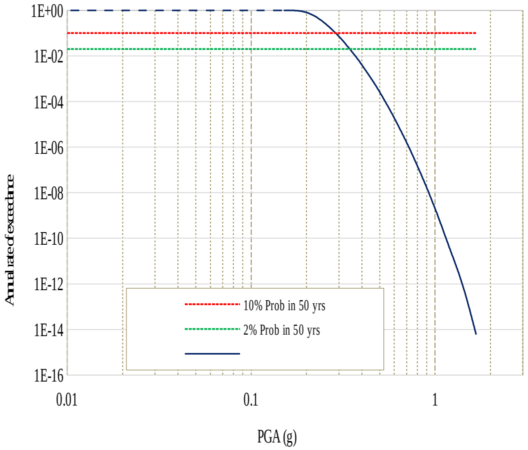

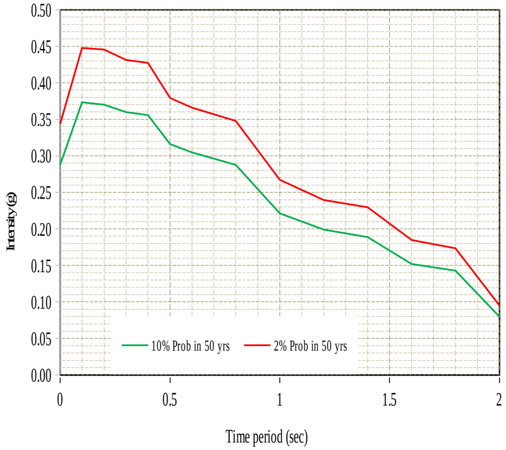

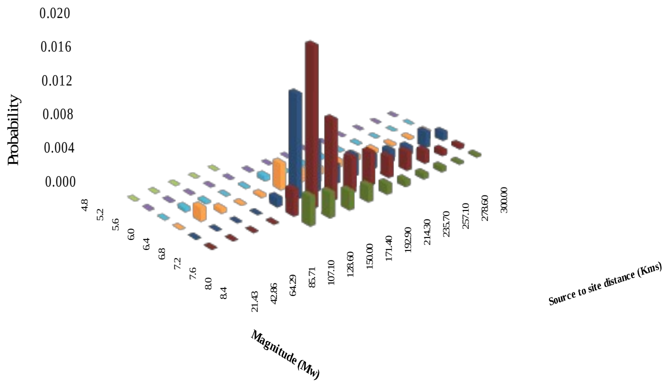

Grid 52

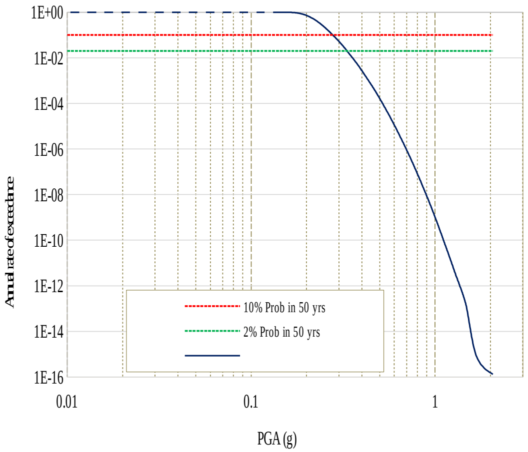

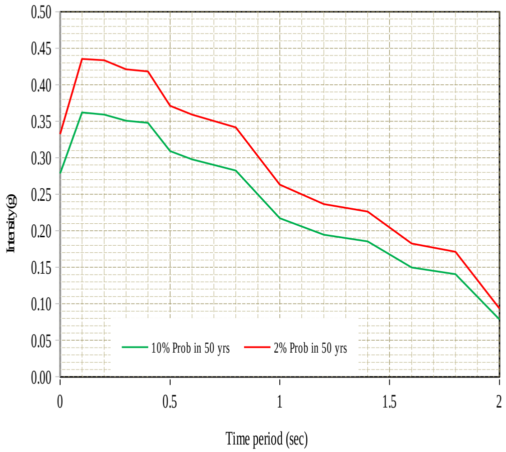

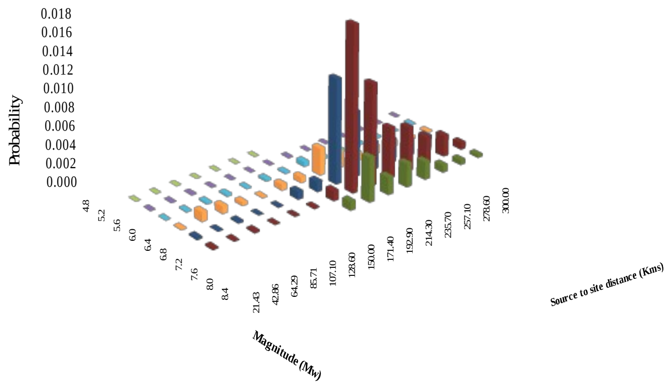

Grid 53

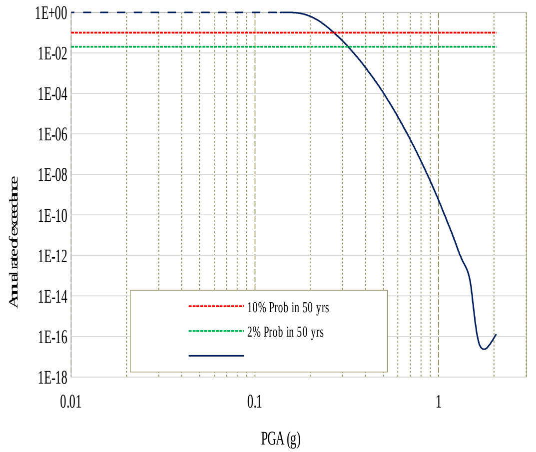

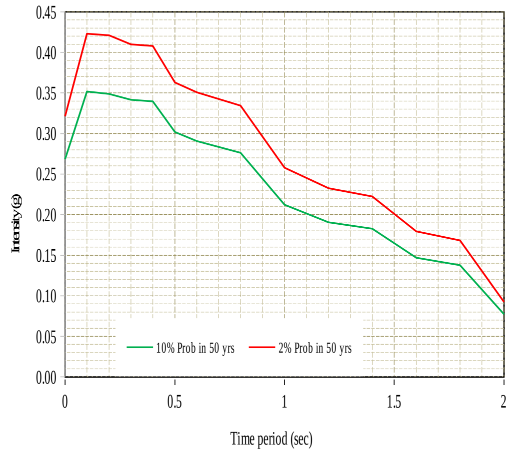

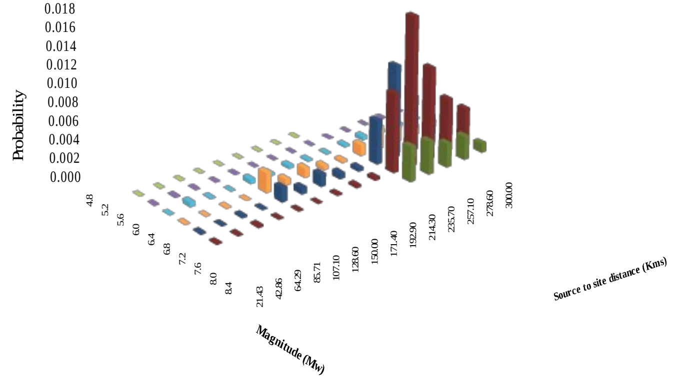

Grid 54

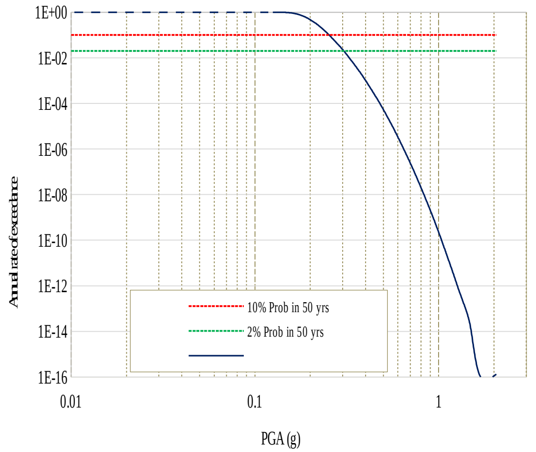

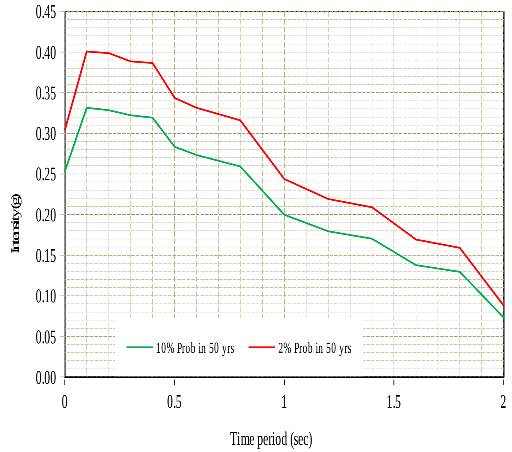

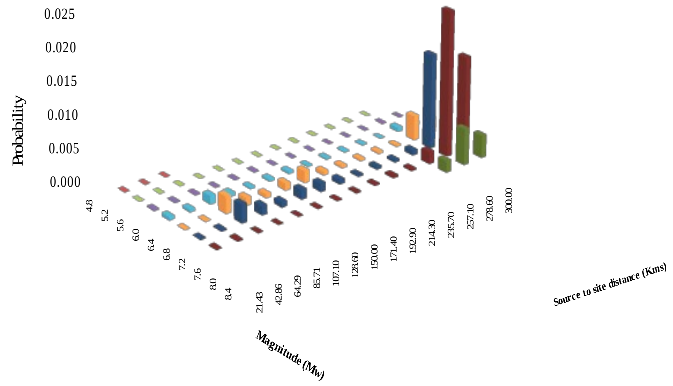

Grid 55

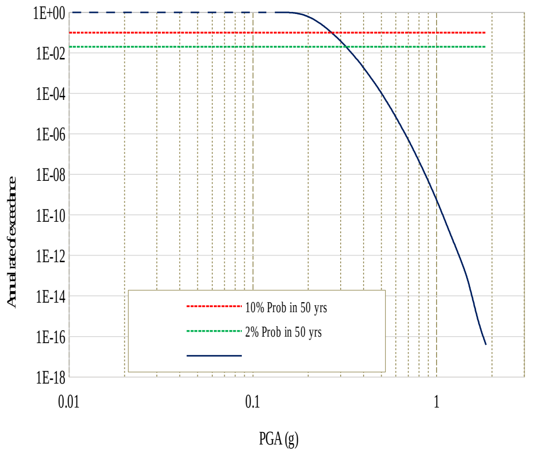

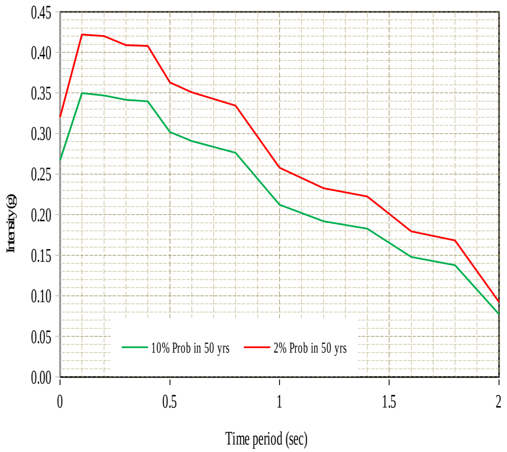

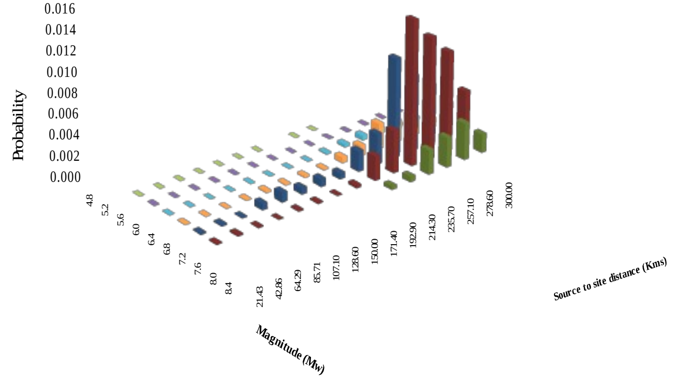

Grid 56

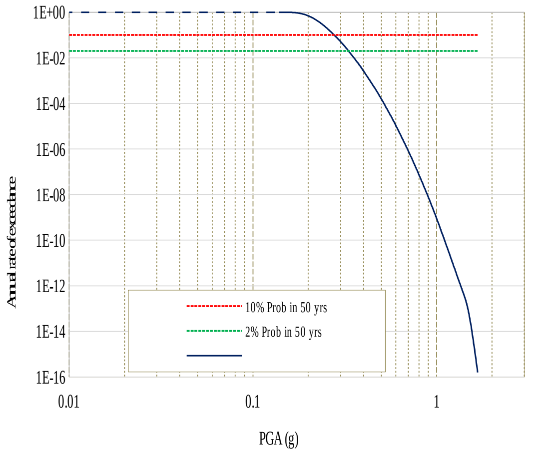

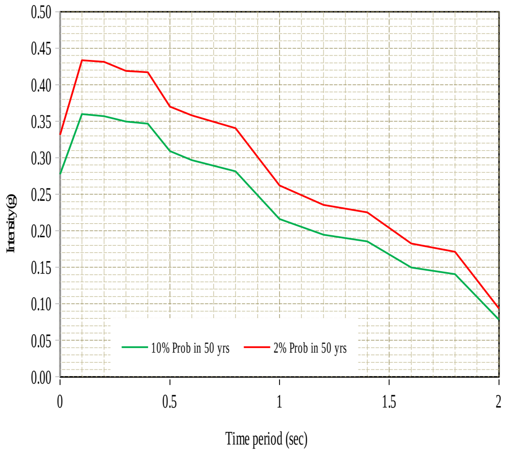

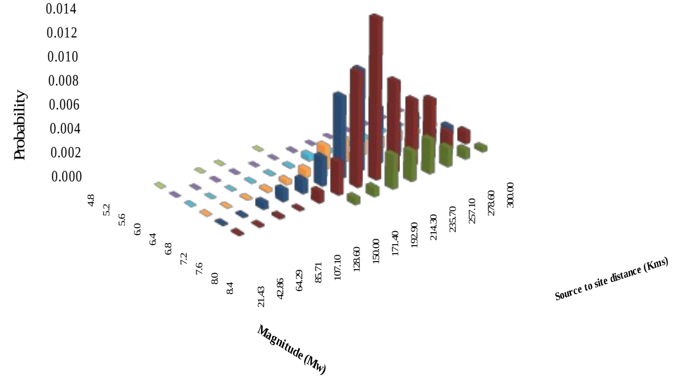

Grid 57

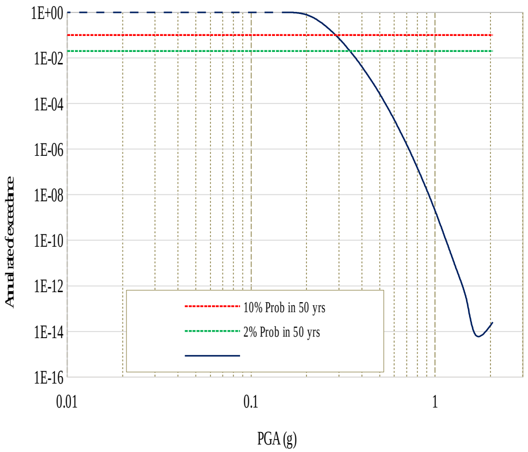

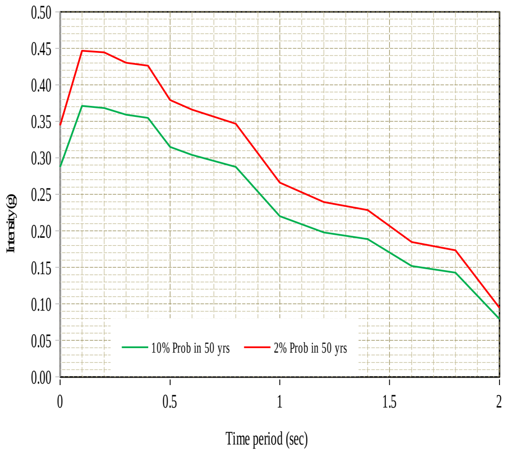

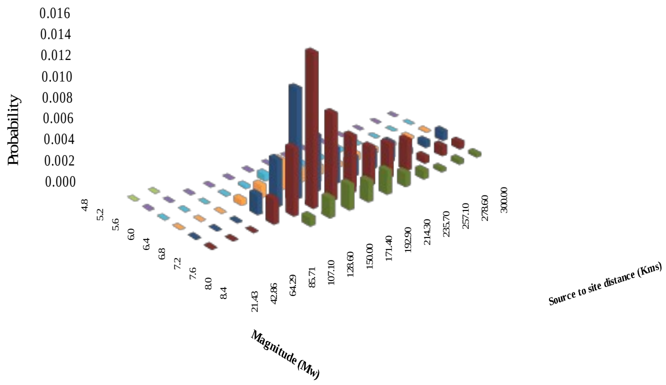

Grid 58

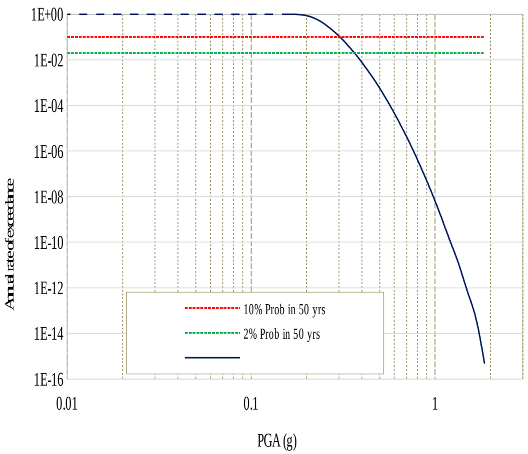

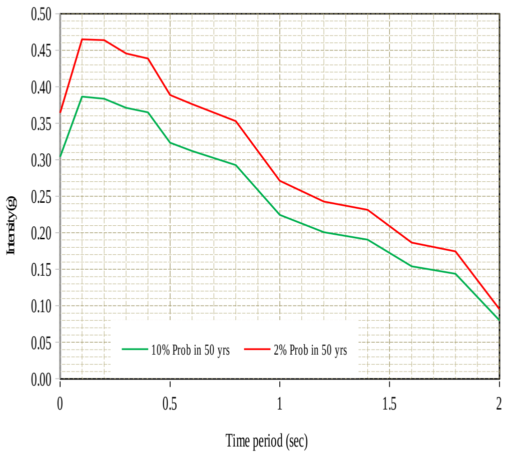

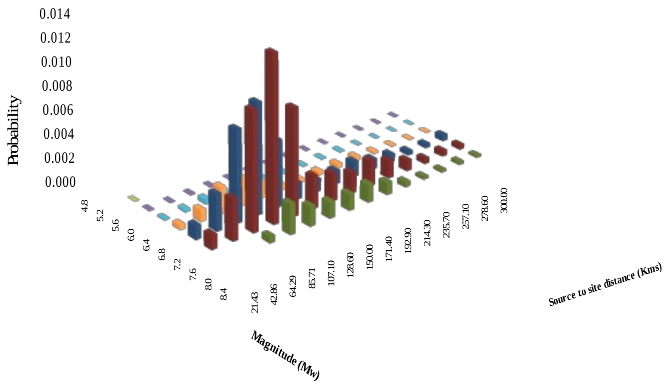

Grid 59

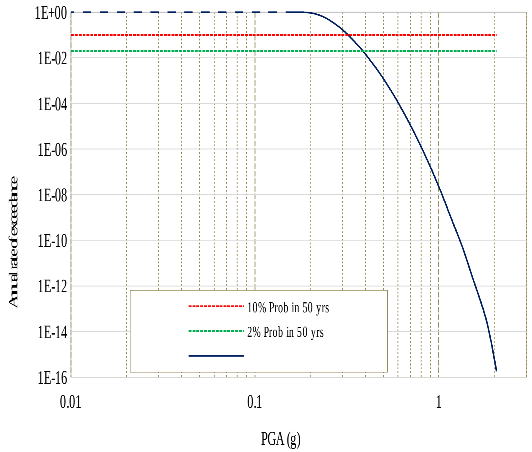

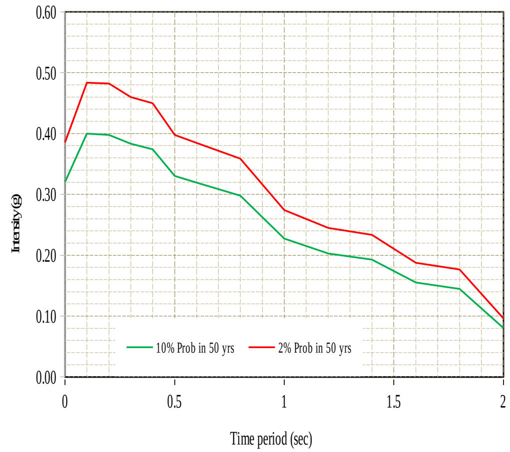

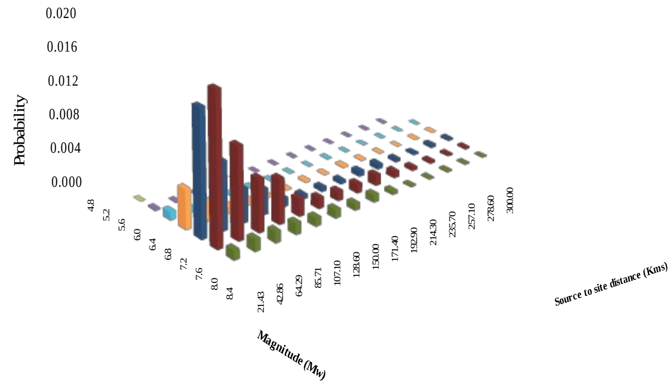

Grid 60

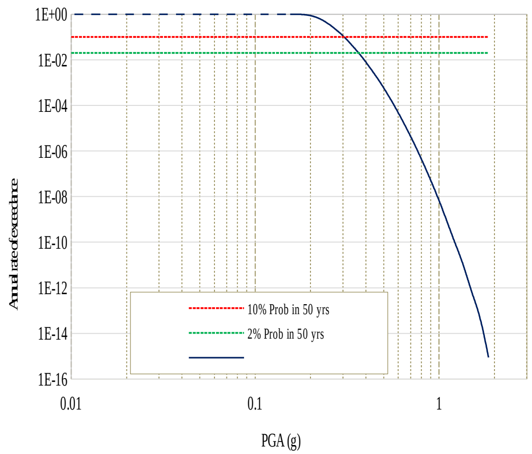

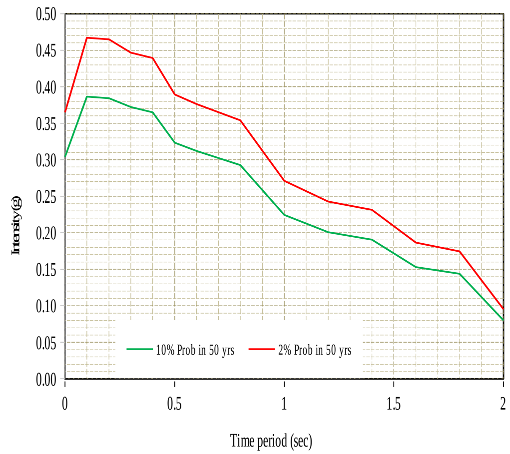

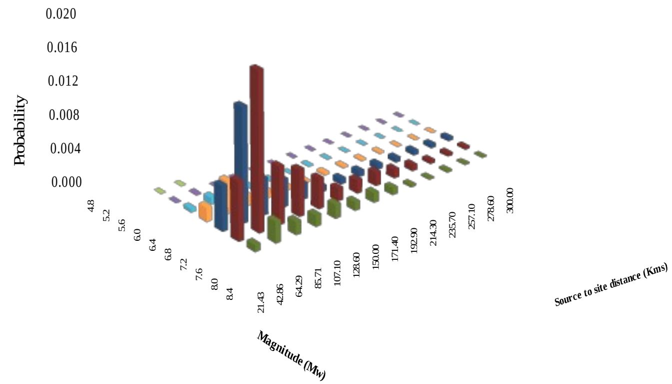

Grid 61

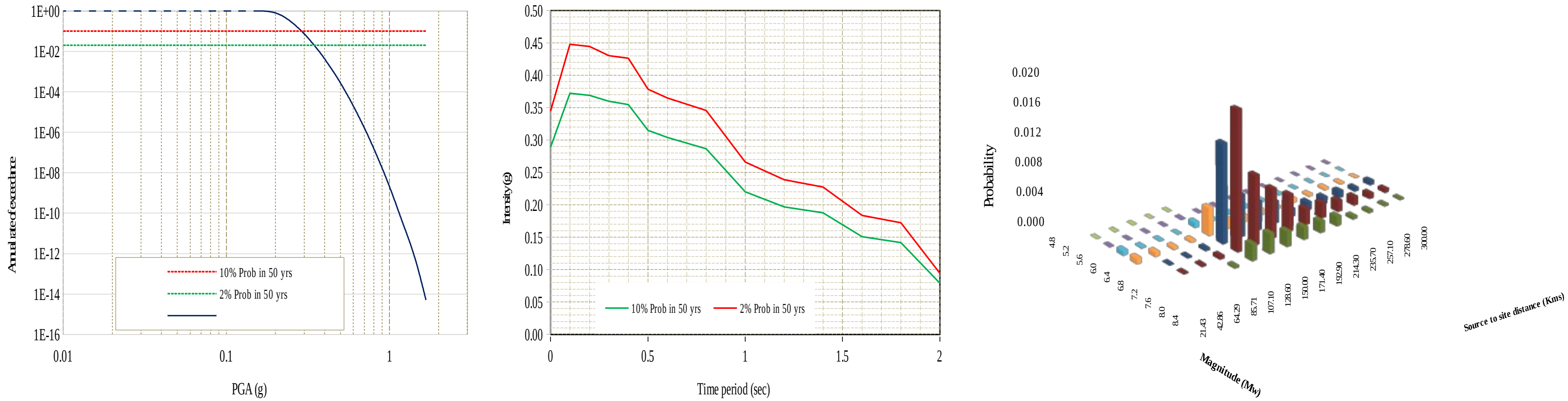

Grid 62

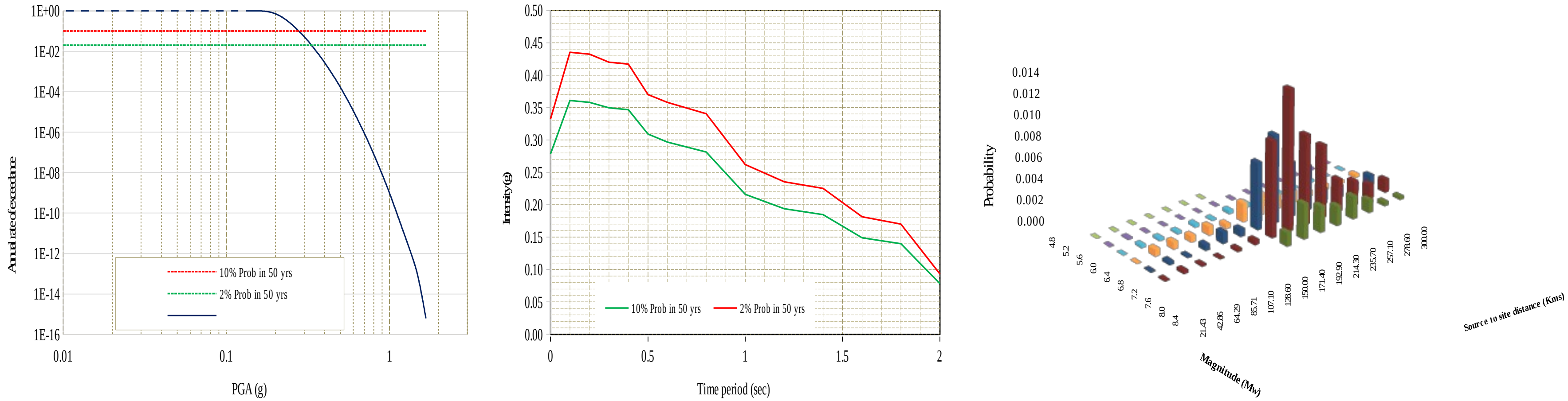

Grid 63

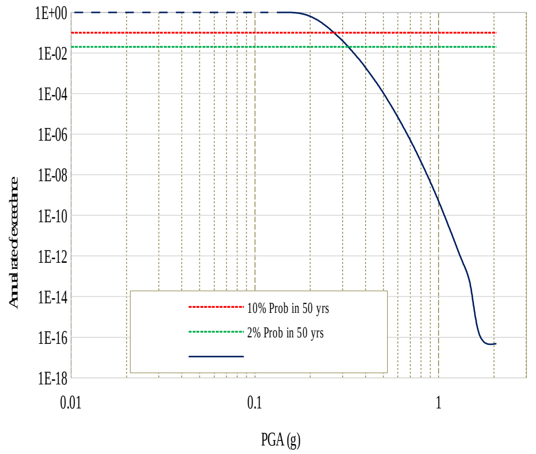

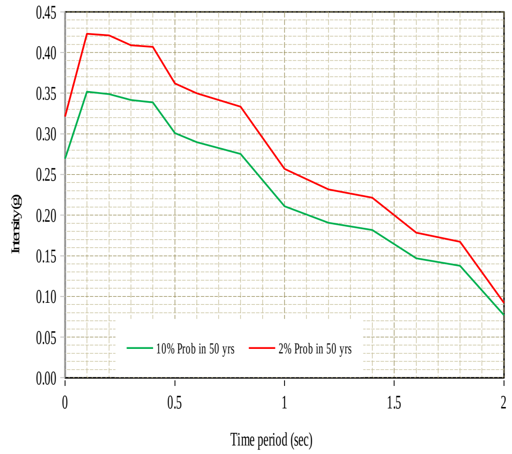

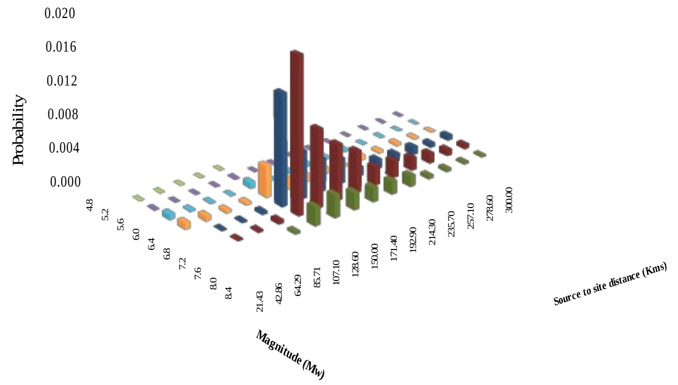

Grid 64

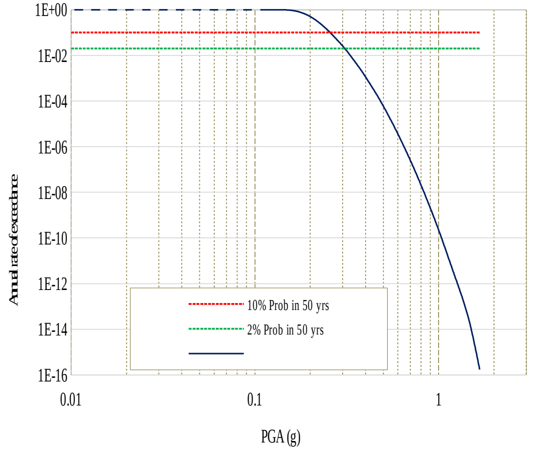

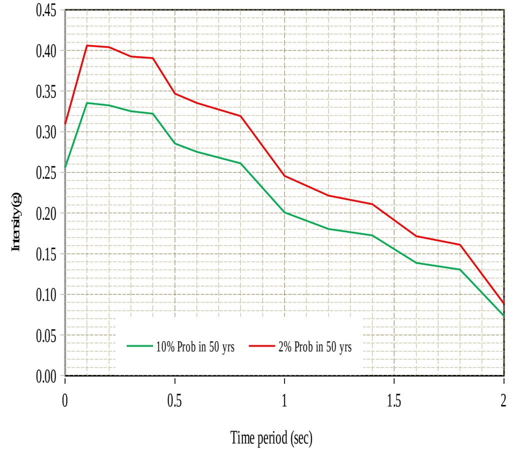

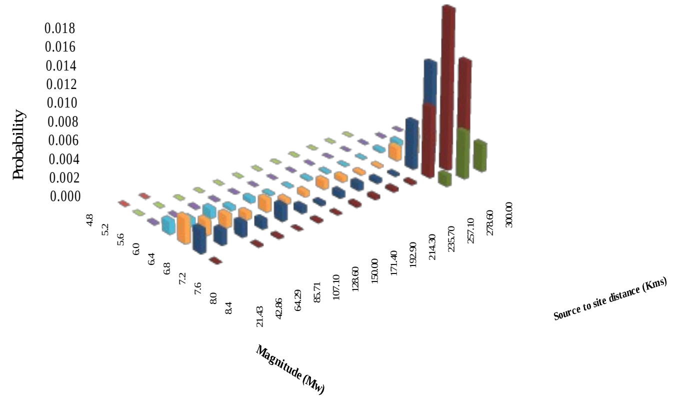

Grid 65

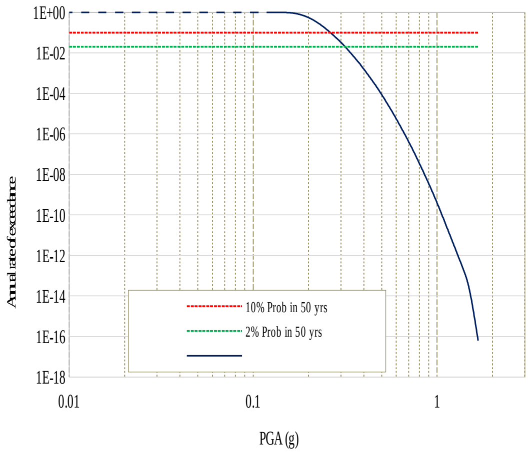

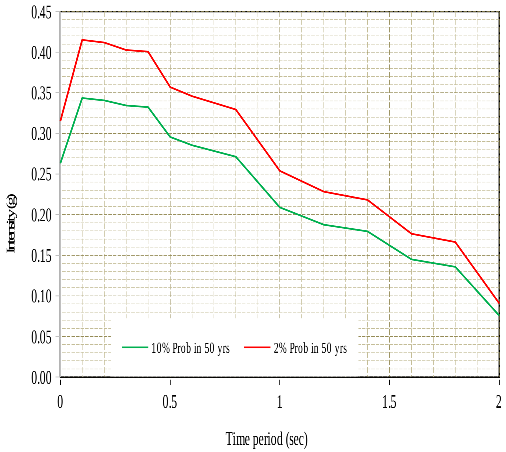

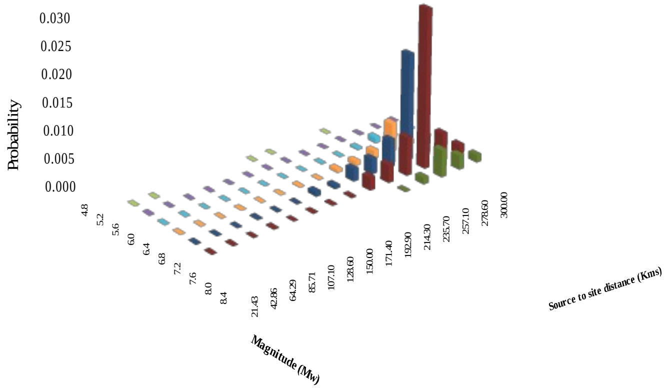

Grid 66

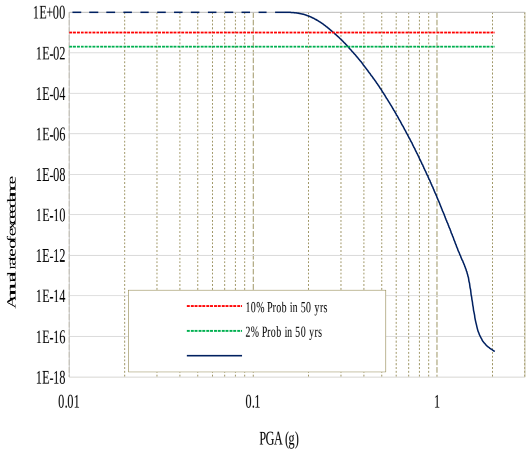

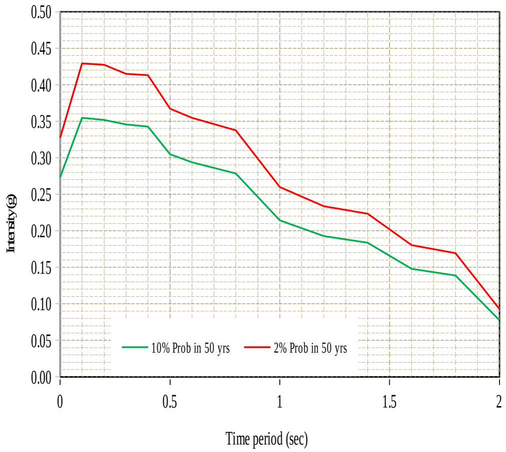

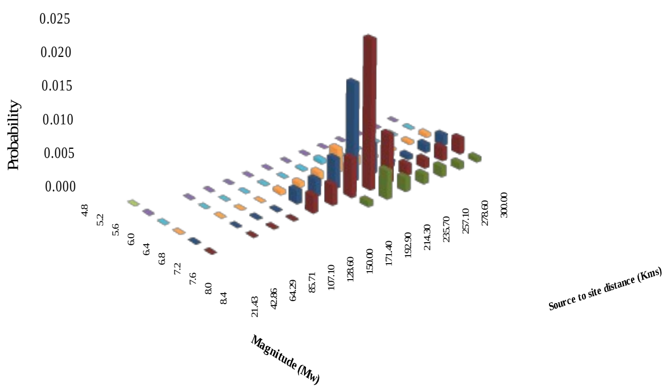

Grid 67

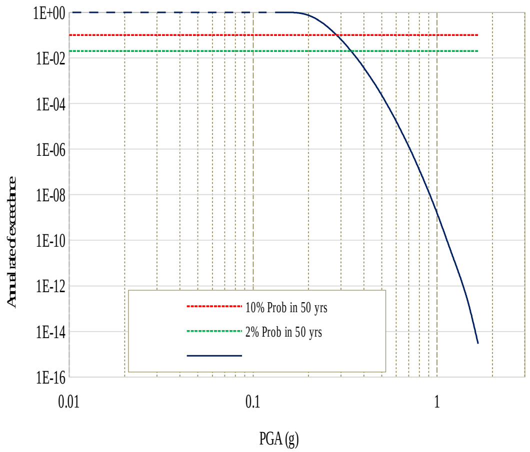

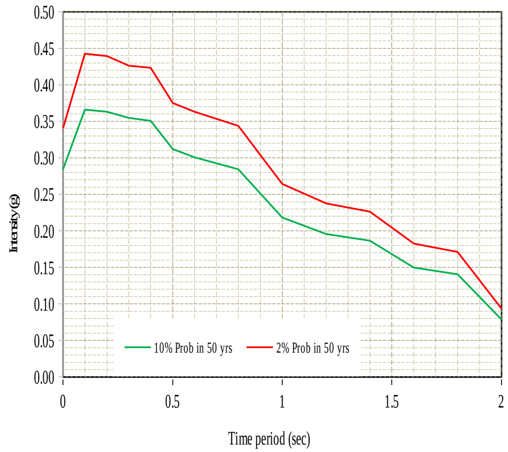

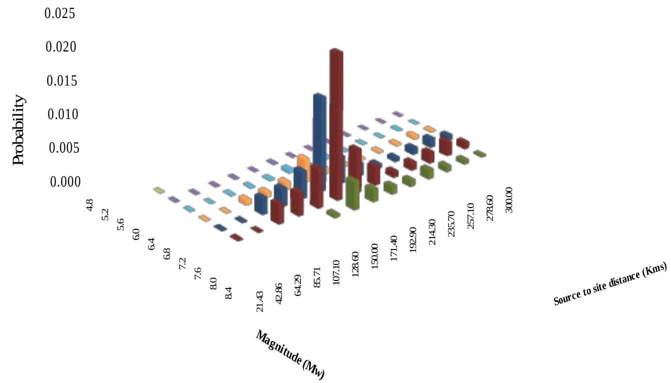

Grid 68

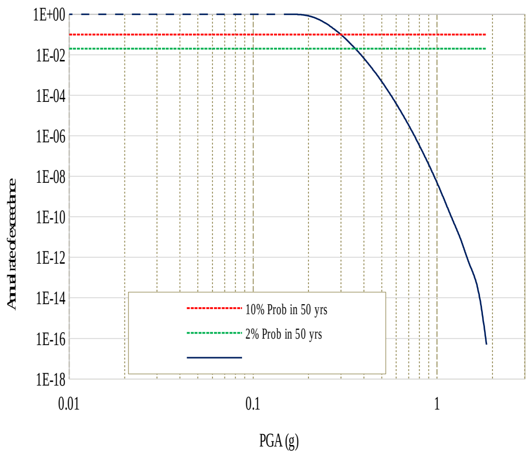

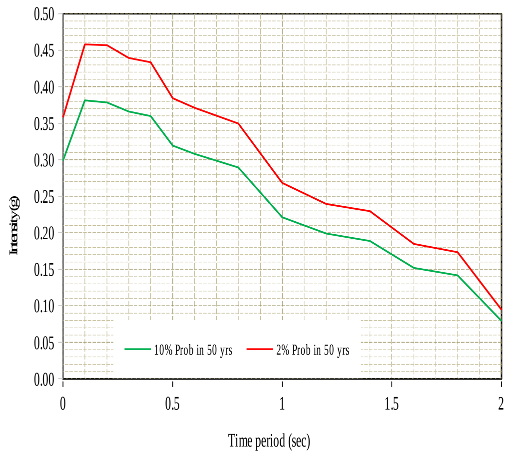

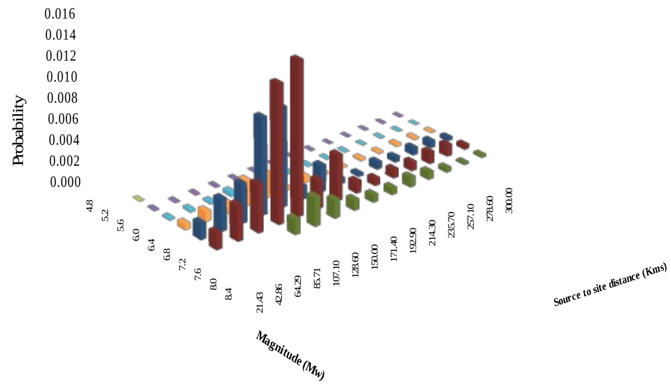

Grid 69

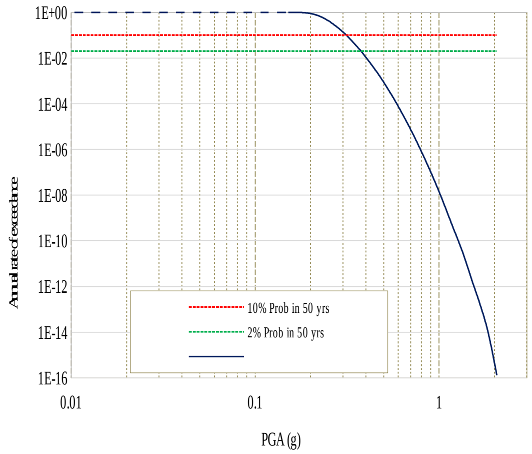

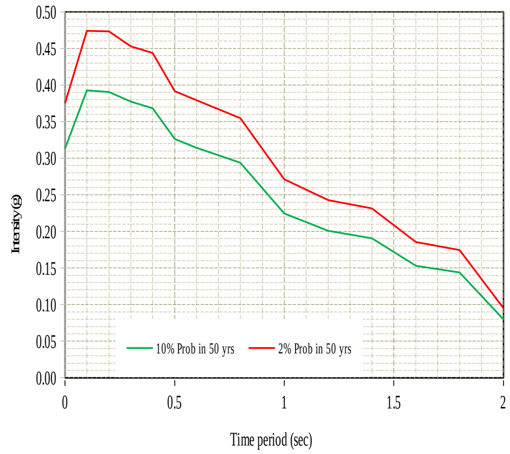

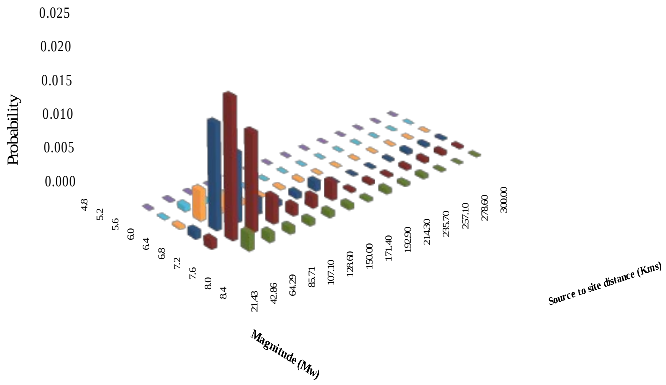

Grid 70

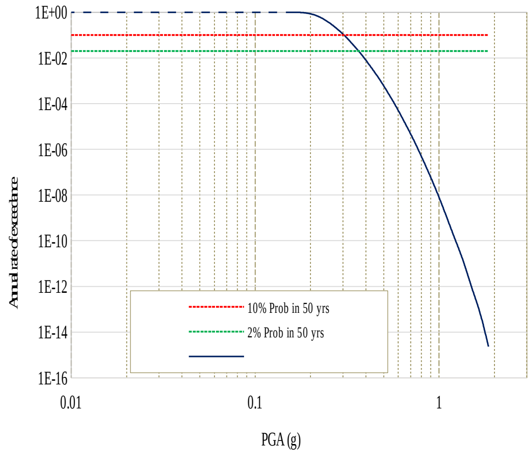

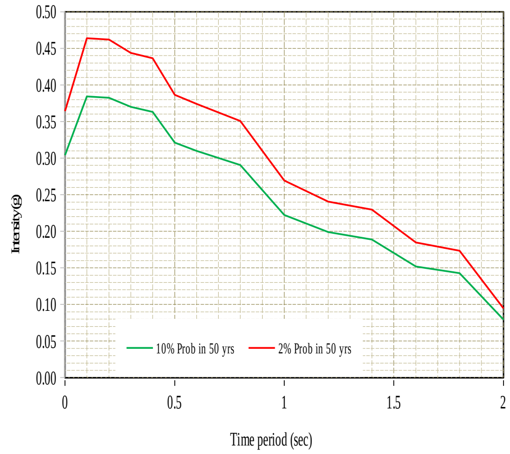

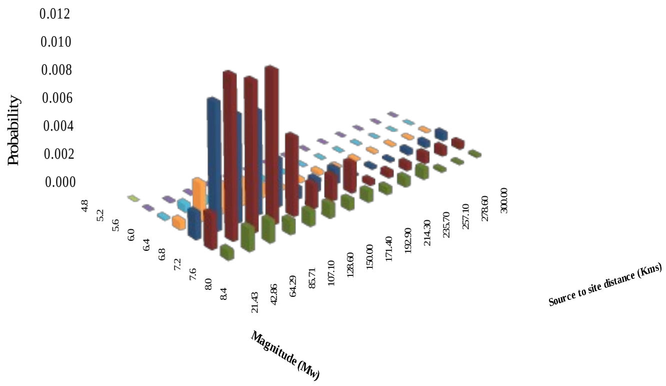

Grid 71

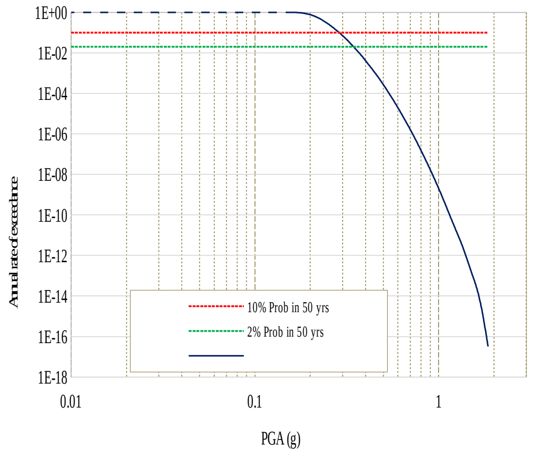

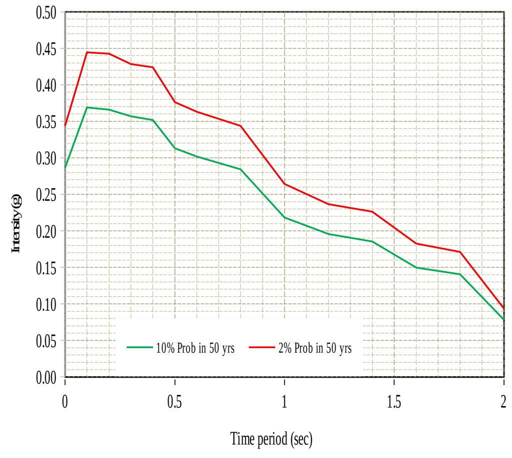

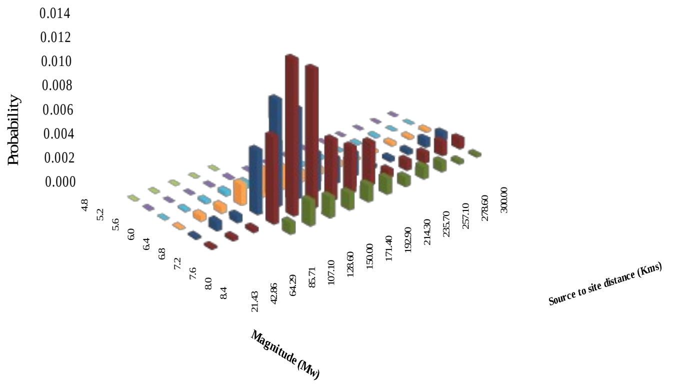

Grid 72

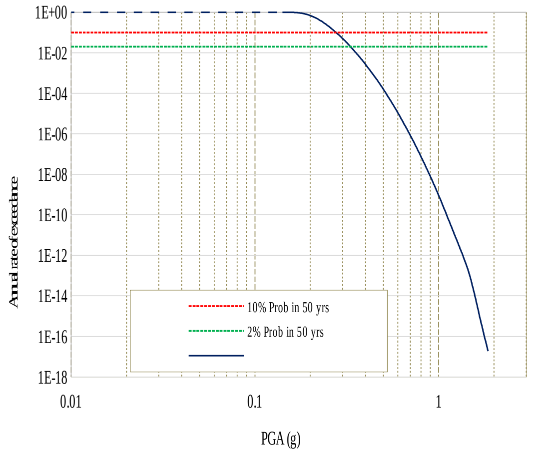

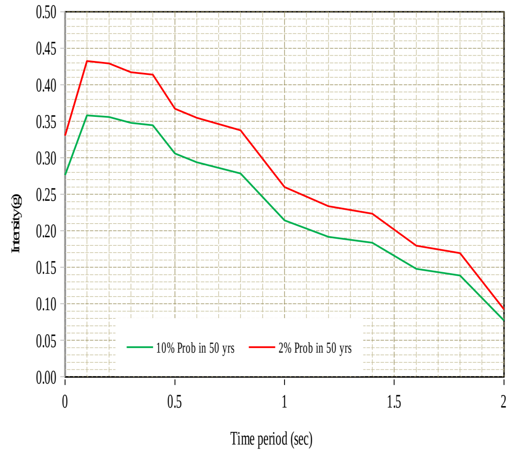

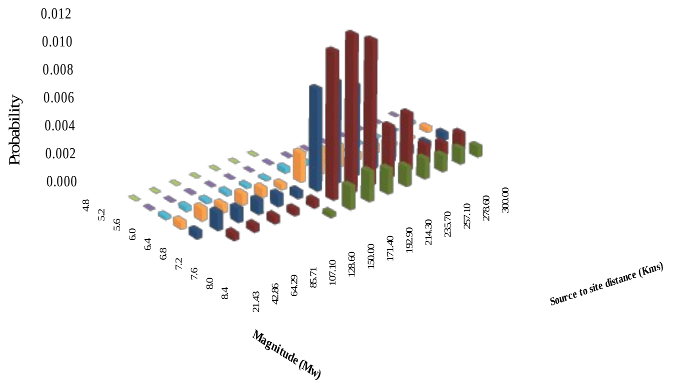

Grid 73

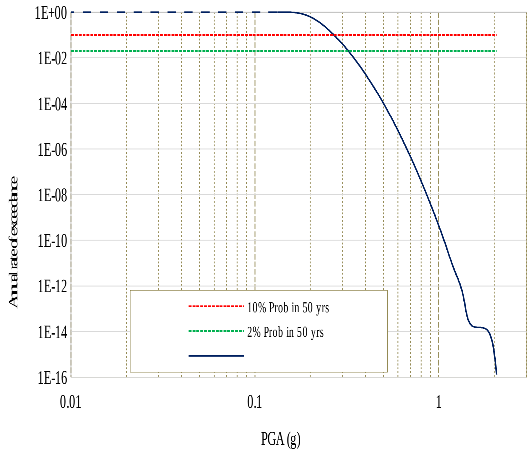

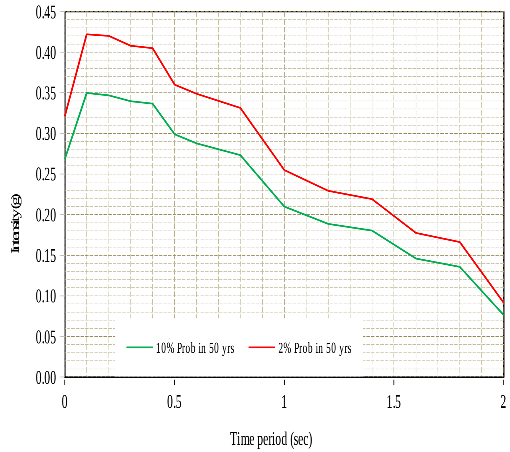

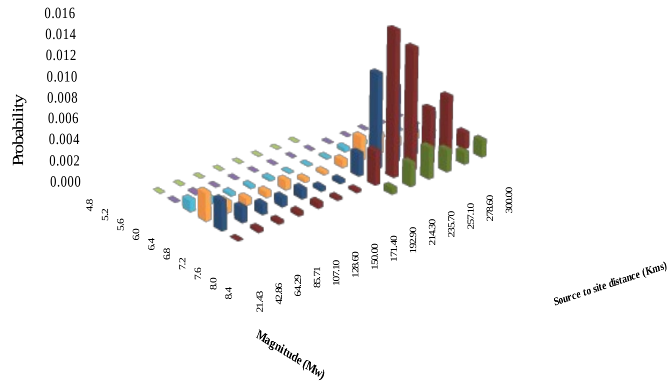

Grid 74

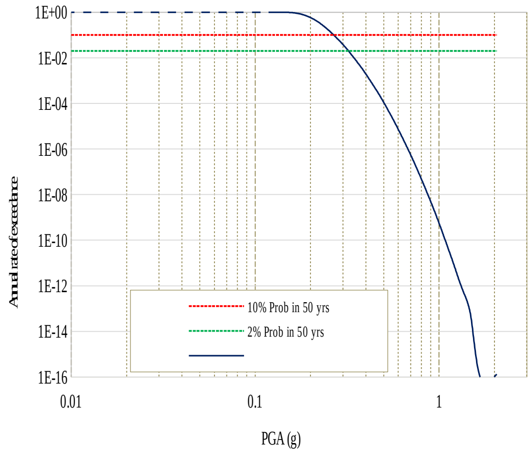

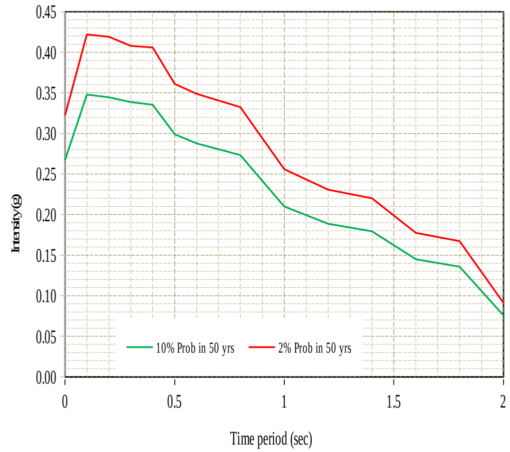

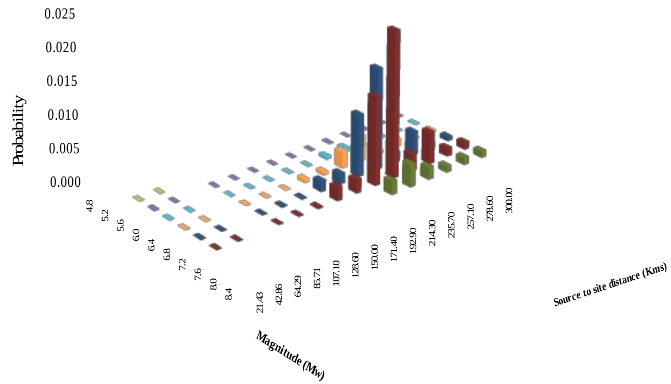

Grid 75

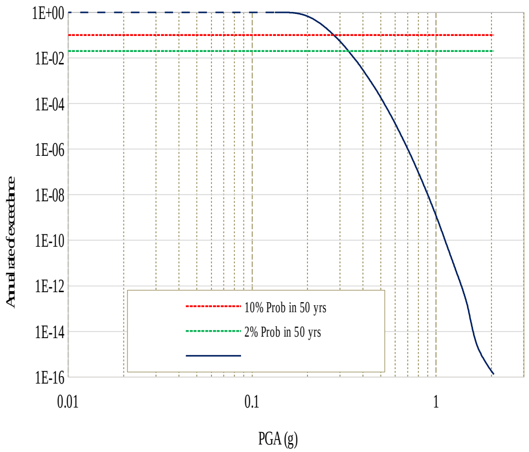

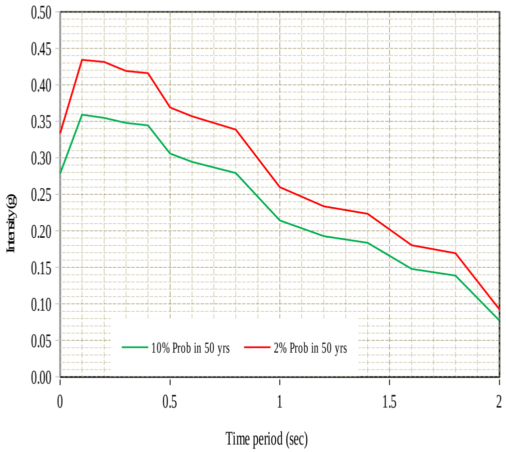

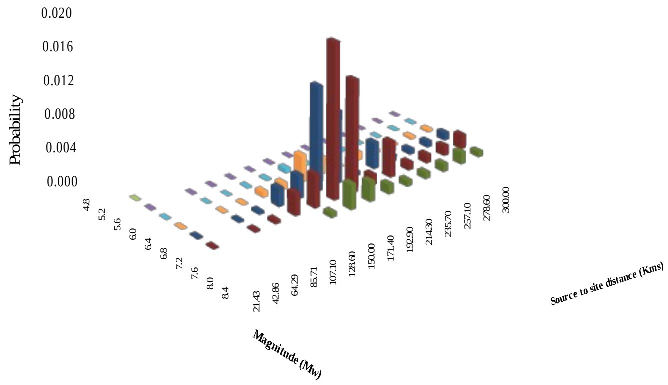

Grid 76

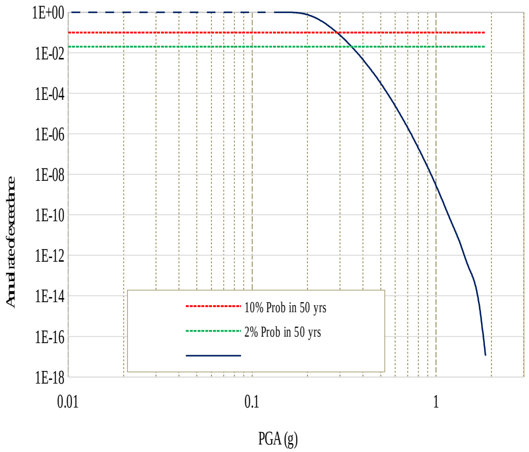

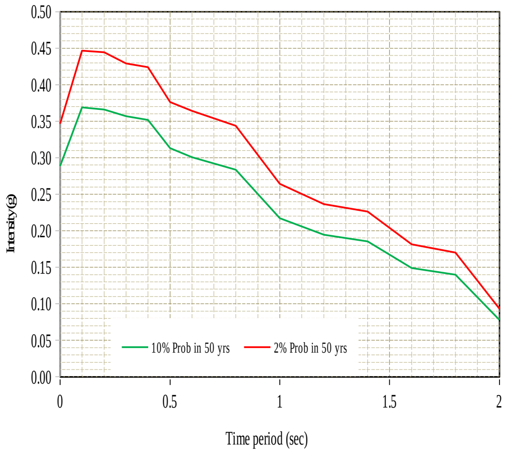

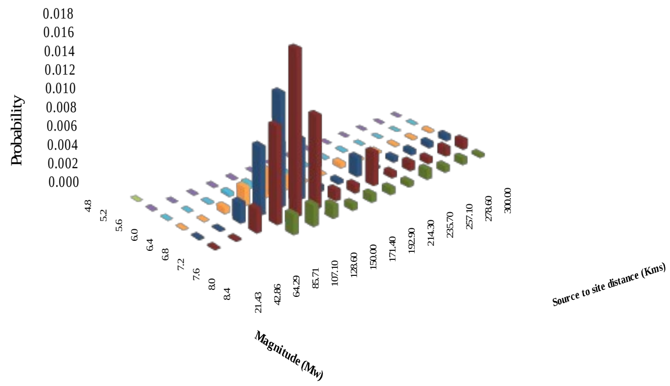

Grid 77

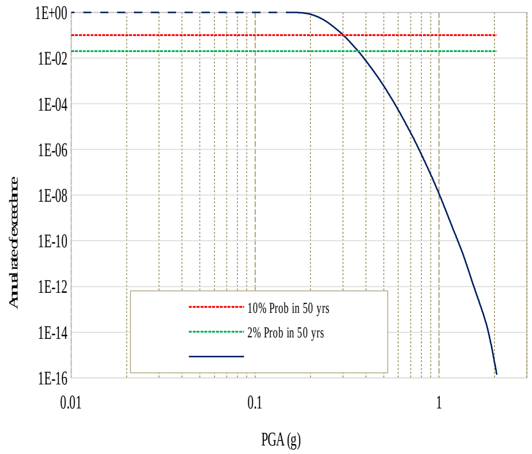

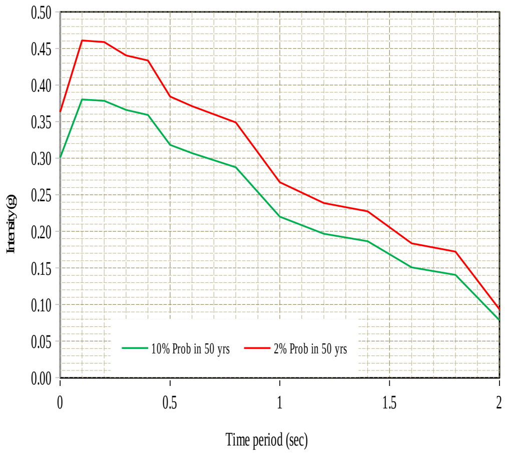

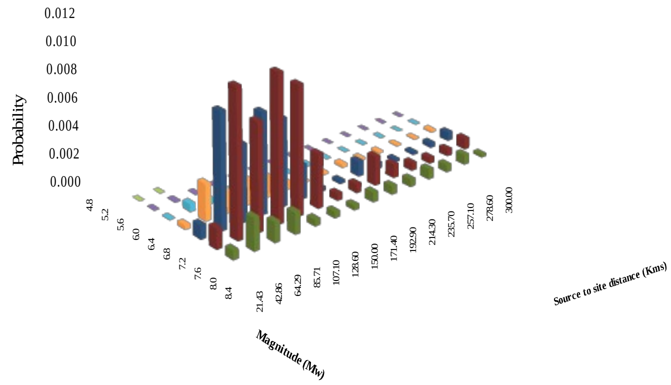

Grid 78

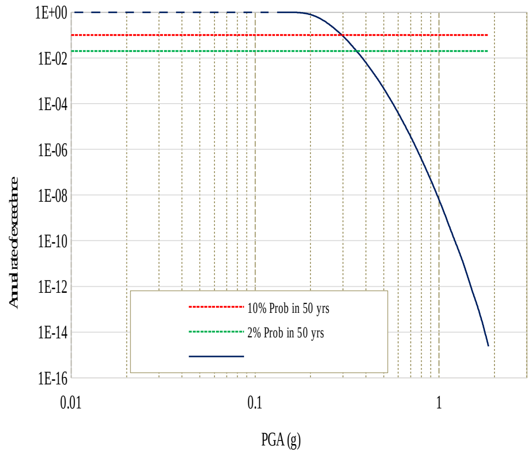

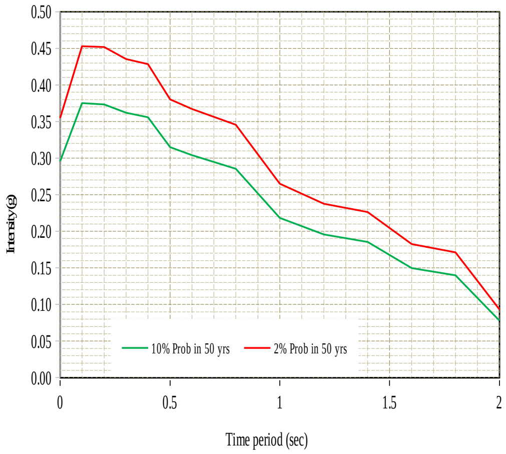

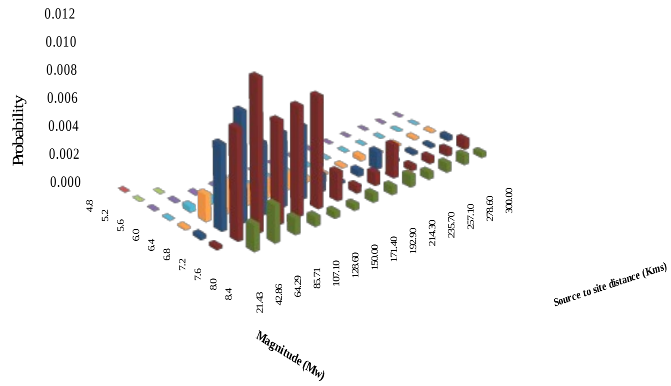

Grid 79

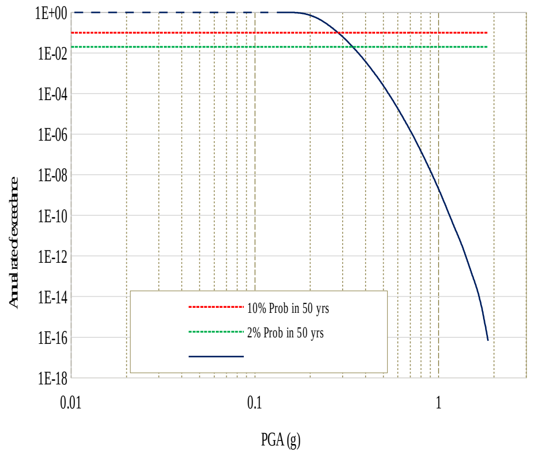

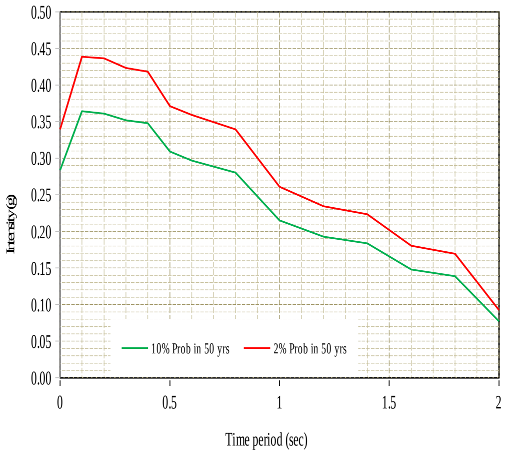

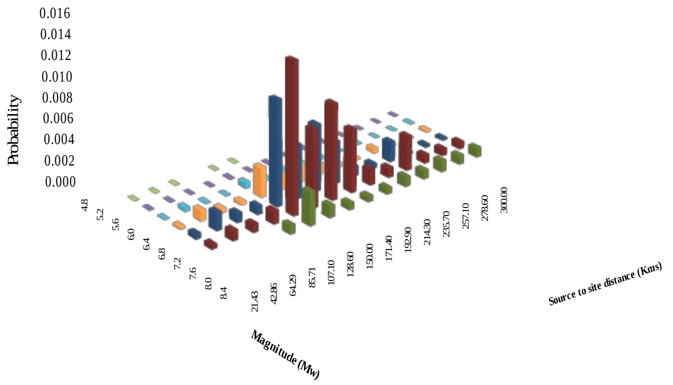

Grid 80

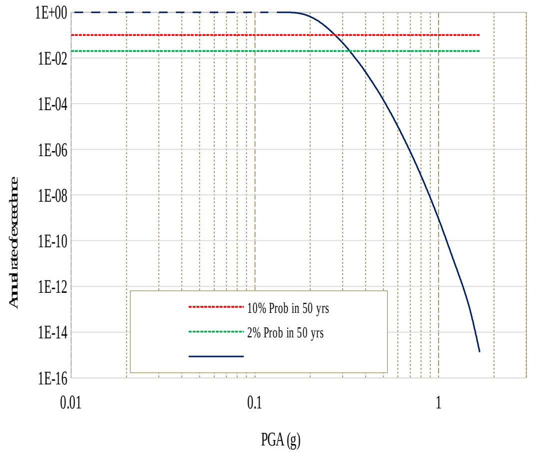

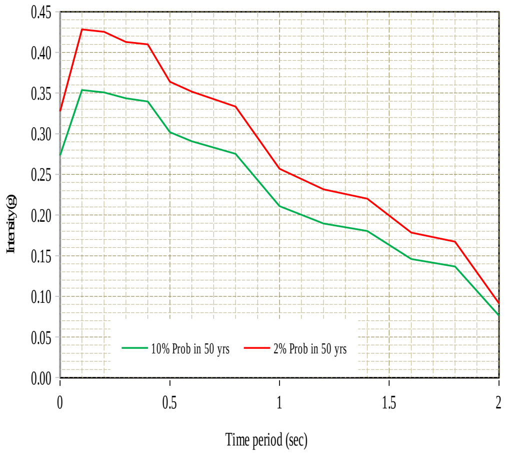

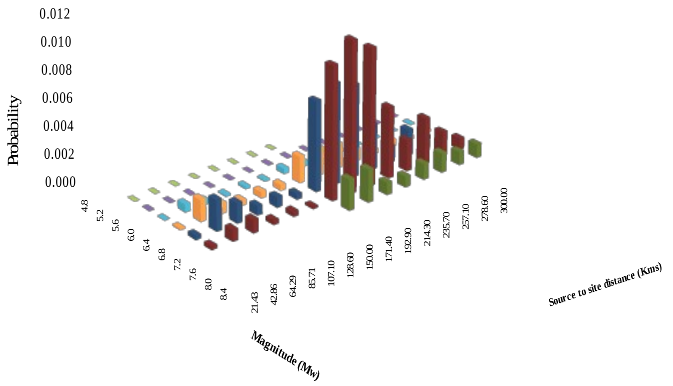

Grid 81

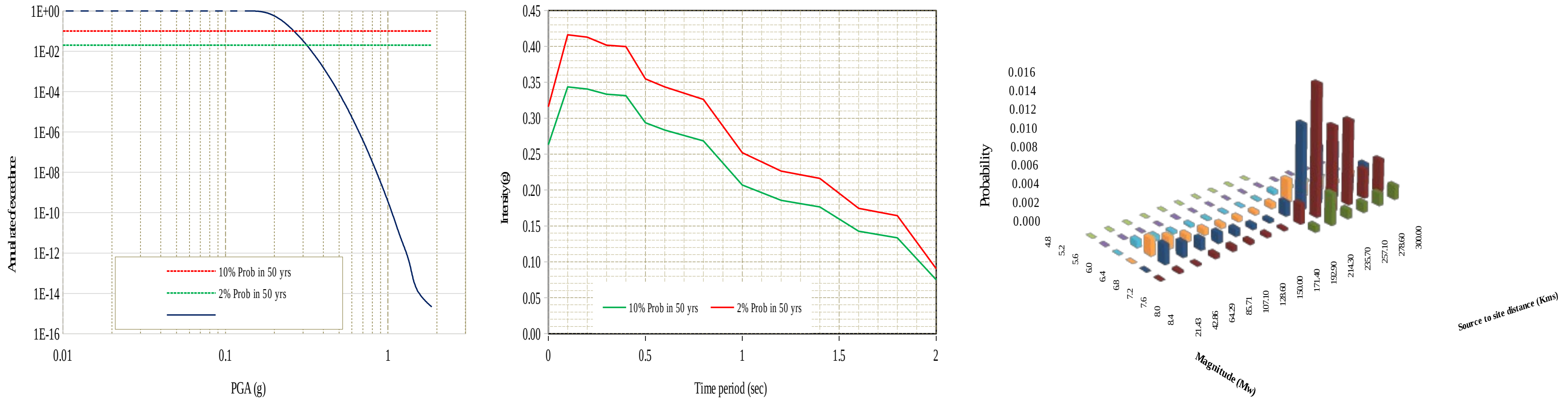

Grid 82

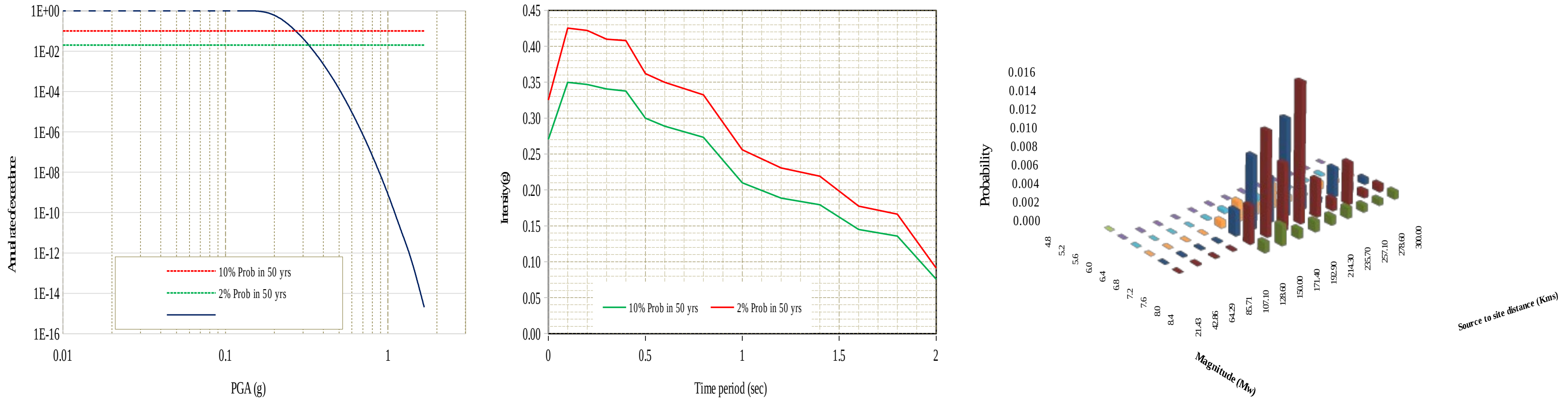

Grid 83

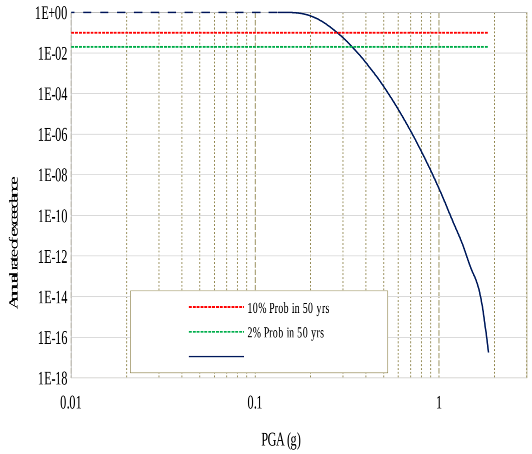

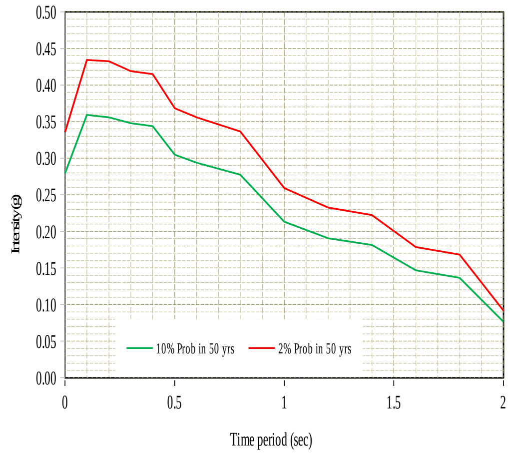

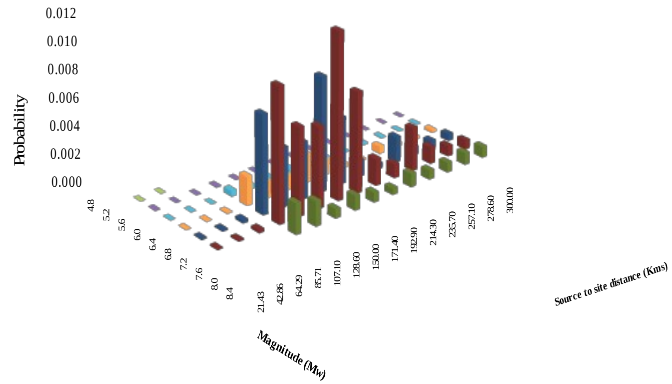

Grid 84

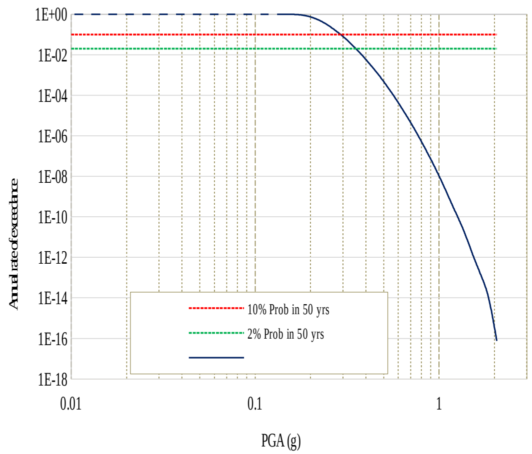

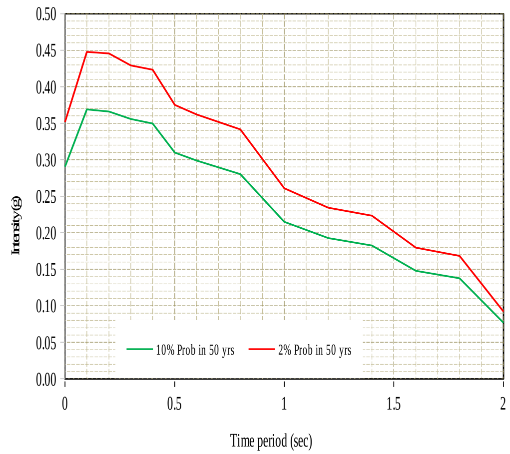

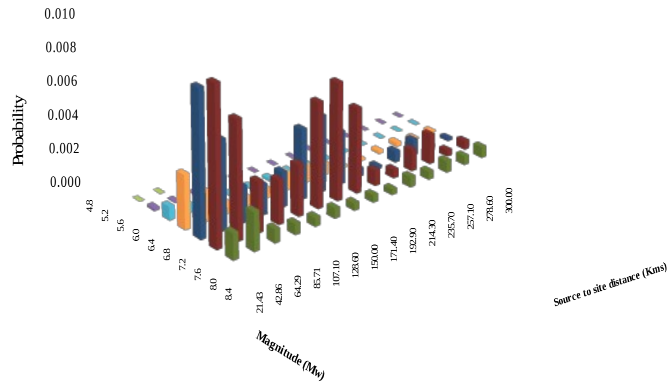

Grid 85

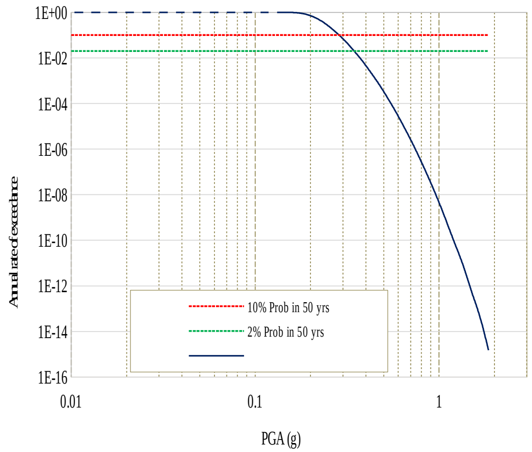

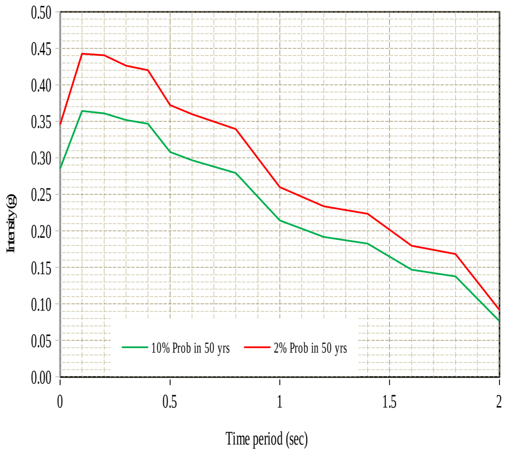

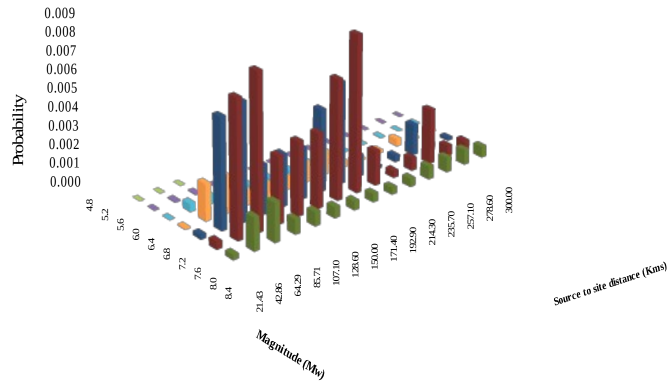

Grid 86